Combustion Characteristics of Lean Premixed Methane / Higher Hydrocarbon / Hydrogen Flames

Seif-Eddine Mehdi Zitouni

A thesis submitted in partial fulfilment of the requirements for the Degree of:

Doctor of Philosophy

Cardiff University,

School of Engineering,

Gas Turbine Research Centre

March 2020

Summary

Declining indigenous resources, increased dependence on imports and intermittent renewable energy, have resulted in an increasingly diverse energy-generation landscape. As a result, gas turbine operators face new challenges with respect to gas turbine flexibility in terms of combustion efficiency, safety and emission control. Increased reliance on liquefied natural gas, potentially containing high concentrations of heavier hydrocarbons, typically ethane and propane, coupled with the emerging prospect of hydrogen injection into national gas grids, presents associated combustion impacts not fully appreciated. This new reality underlines the necessity of developing understanding of fundamental combustion characteristics, ultimately guiding the design of future highly flexible gas turbines. This thesis aims to characterise fundamental combustion performance of methane/higher-hydrocarbon/hydrogen fuels, through a combination of experimental and numerical techniques, with a focus on natural gas blends representative of fuel variations and at air fuel ratios expected in premixed low-carbon power generation facilities.

The parameters identified to investigate fuel behaviour were the laminar burning velocity, Markstein Length and the Lewis Number, yielding essential physiochemical and thermo-diffusive flame information. These properties are of value when attempting to predict flame behaviour in turbulent environments, reflective of most practical gas turbine applications. The main components of natural gas, and relevant hydrogen enriched binary and tertiary mixtures were parametrically investigated, with respect to stretch-related and flame propagation behaviour at lean air fuel ratios, in addition to a comparison of numerically simulated results obtained from chemical kinetics. Effective Lewis Number models were appraised and compared to experimentally measured data, employing theoretical formulations relating Markstein Length to Lewis Number as proposed in literature. The influence of hydrogen and propane addition to the lean stability limits of premixed turbulent methane flames was examined, using a generic swirl burner, at various inlet temperature and thermal powers, with measured lean blow off limits in correlation with measured Markstein length behaviour.

Acknowledgements

For giving me the opportunity to do a PhD, I would like to thank Prof. Phil Bowen. For all the discussions, advice and time, I would like to thank Dr. Andrew Crayford. For the support, encouragement, and patience, many thanks are extended to Dr. Dan Pugh. Without these people I would not have been able to succeed.

For assisting during testing campaigns, a thank you to Mr. Steve Morris, Mr. Terry Treherne and Mr. Jack Thomas.

A thank you to all the people sharing my office. It has been four fun years.

Ultimately, I would like to express my deepest gratitude and recognition to all my family and friends, particularly to my mother, for being the wonderful person that she is, and my aunt for supporting me, as well as all my brothers, in all our educational endeavours.

Finally, a thought for my Grandfather, who I'm sure, would have been very proud.

To all the above, Thank You.

Published & Presented Work

Seif-Eddine Zitouni, Dan Pugh, Andrew Crayford, Phil Bowen: *Prediction of Impact of Natural Gas Composition and Hydrogen Addition on Fundamental Flame Characteristics.* Meeting on Current Research in Combustion, Institute of Physics Combustion Group, Sheffield University, United Kingdom, 19th Sept. 2019.

Seif-Eddine Zitouni, Dan Pugh, Andrew Crayford, Phil Bowen: *Influence of Natural Gas Composition and Hydrogen Addition on Fundamental Flame Characteristics.* 9th European Combustion Meeting, Lisbon, Portugal, 2019.

Seif-Eddine Zitouni, Dan Pugh, Andrew Crayford, Phil Bowen: *Influence of Natural Gas Composition and Hydrogen Addition on Premixed Flame Propagation.* 60th UKELG Discussion Meeting on ''Emerging Technology Explosion Hazards'', Sheffield University, United Kingdom, 11th Oct. 2018.

Seif-Eddine Zitouni, Dan Pugh, Andrew Crayford, Phil Bowen: *Influence of Natural Gas Composition and Hydrogen Addition on Fundamental Flame Characteristics.* 57th UKELG Discussion Meeting on ''Explosion Hazard of Power Generation'', Imperial College, London, United Kingdom, 30th Mar. 2017.

Contents

List of Figures

List of Tables

Nomenclature:

Burnt Density, ρ_b

Chemical Time Scale, T_C

Critical Pressure, P_c

Critical Temperature, T_c

Critical Velocity Gradient, g_f

Critical Volume, V_c

Damköhler number, **Da**

Density, ρ

Equivalence Ratio, Φ

Expansion Ratio, σ

Experimental Lewis Number based upon Bechtold & Matalon formulation, Le_{-BM}

Experimental Lewis Number based upon Chen formulation, Le_{-CHEN}

Experimental Lewis Number based upon Sung and Law formulation, Le_{-LAW}

Flame curvature, α_C

Flame radius, r_f

Flame Temperature adiabatic, T_{ad}

Flame Temperature, T_f

Flame Thickness Gradient Method, δ_G

Flame Thickness Kinetic (diffusion), δ_K

Flame Thickness, δ

Flow-field strain, α_S

Global Activation Energy, E_a

Horizontal Plane of Measurement, **H**

Karlovitz number, **Ka**

Laminar Burning Velocity, U_L

Lewis Number diffusion-based formulation, Le_D

Lewis Number effective, Le_{eff}

Lewis Number heat-release based formulation, Le_H

Lewis Number volume-based formulation, Le_V

Lewis Number, **Le**

Limiting reactant layer radius, $\mathbf{r_R}$

Markstein Length burnt, $\mathbf{L_b}$

Markstein Length unburnt, $\mathbf{L_u}$

Markstein Number, **Ma**

Mass Burning Flux, $\mathbf{m^0}$

Mass Diffusion Co-efficient of fuel into mixture, $D_{1\text{-}mix}$

Mass Diffusion Co-efficient, $\mathbf{D_{i,j}}$

Mass Fraction of Species i, $\mathbf{Y_i}$

Mole Fraction of component n, $\mathbf{X'_n}$

Mole Fraction of Species i, $\mathbf{X_i}$

Non-dimensional heat release, $\mathbf{q_i}$

Numerical Markstein length based upon Bechtold & Matalon formulation, $\mathbf{L_{b\text{-}BM}}$

Numerical Markstein length based upon Chen formulation, $\mathbf{L_{b\text{-}CHEN}}$

Overall Heat of Reaction, **Q**

Pressure, **P**

Quenching Distance, $\mathbf{d_q}$

Residence Time, $\mathbf{T_R}$

Specific Heat, $\mathbf{C_p}$

Stretch rate, $\boldsymbol{\alpha}$

Stretched Flame Speed, $\mathbf{S_n}$

Surface Area, $\boldsymbol{A}$

Thermal Conductivity, $\boldsymbol{\lambda}$

Thermal Diffusivity, $\mathbf{D_T}$

Thermal Layer radius, $\mathbf{r_T}$

Time, **t**

Unburnt Density, $\boldsymbol{\rho_U}$

Unburnt Temperature, $\mathbf{T_u}$

Universal Gas Constant, $\mathbf{R^0}$

Unstretched Flame Speed, $\mathbf{S_u}$

Vertical Plane of Measurement, **V**

Volumetric fraction of component 'i', $\mathbf{x_i}$

Zel'dovitch Number, **Ze**

Acronyms:

Constant Volume Combustion Bomb – (**CVCB**)

Dry Low Emission Combustors – (**DLE**)

Gas Turbine – (**GT**)

Green House Gases – (**GHG**)

Hydrocarbon – (**HC**)

Linear Model – (**LM**)

Linear Model based on Curvature – (**LM(C)**)

Linear Model based on Stretch – (**LM(S)**)

Liquified Natural Gas – (**LNG**)

Natural Gas – (**NG**)

Non-Linear Model based on Stretch – (**NM(S)**)

Non-Linear Model – (**NL**)

Power-to-gas – (**PtG**)

Spherically Expanding Flame – (**SEF**)

Wobbe Index – (**WI**)

Chemical Formulas:

Methane – **CH_4**

Ethane – **C_2H_6**

Propane – **C_3H_8**

n-Butane – **C_4H_{10}**

Hydrogen – **H_2**

Nitrogen – **N_2**

Oxygen – **O_2**

Carbon Monoxide – **CO**

Carbon Dioxide – **CO_2**

Nitrogen Oxides – **NO_X**

Water Vapour – **H_2O**

Chapter 1. Introduction

1.1 Thesis Context

Poverty alleviation, fair socio-economic cohesion and human well-being on a world-wide scale are crucial goals to strive towards in any advanced society. In order to succeed in this enduring and persistent challenge for global development, access to energy is key. Historically, burning of biomass and other organic matter, was the traditional energy source. At the end of the 19th century biomass accounted for nearly half of worldwide energy consumption [1]. Since, the energy needs of society have increasingly been supported by abundant and cheap hydrocarbon fossil fuels, firstly solid-based coal was utilised, then liquid-oil fuel during the 20th century, followed by natural gas (NG). Today's energy mix is heavily dominated by hydrocarbon fuels, with coal, crude oil and NG accounting for nearly three-quarters of our global primary energy consumption, see Figure 1.1 [1].

Fossil fuel combustion has important associated environmental impacts. Climate change can lead to ecological adversities; extreme weather events (heatwaves, droughts, floods, etc.), altered crop-growth, sea-level rise due to ice shrinkage around the poles, and disrupted water systems [2]. These environmental realities have obliged the world to shift towards more friendly and renewable energy sources namely: solar, wind, geothermal, hydro-electric and hydrogen, among others, to shape a more sustainable future. Thus, today more than ever before, the role of low carbon electrification technologies is required to generate a balanced trajectory between development, progress and cohesion with the environment. However, identifying and implementing such synergistic strategies within the energy sector, is particularly difficult [3].

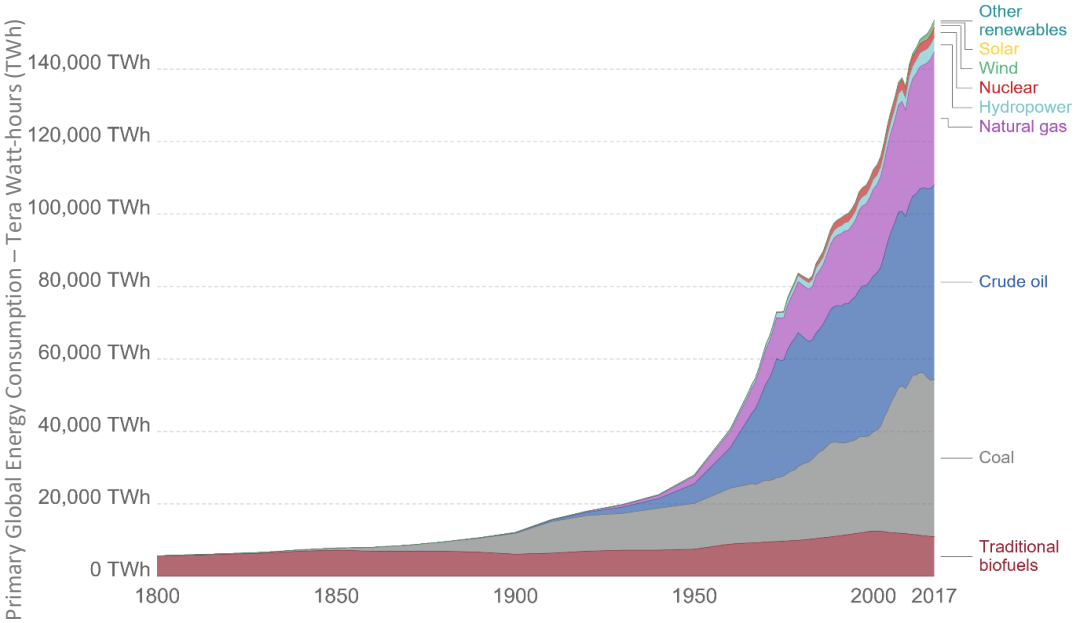

Figure 1.1 – Global Primary Energy Consumption – Historical Perspective – Graphic from [1] Data from [4], [5]

1.1.1 Green House Gas Emissions

Greenhouse gas (GHG) is a term to indicate gases which at elevated concentrations in the atmosphere contribute to global warming. Such gases include carbon dioxide (CO_2), methane (CH_4), water vapour (H_2O) and nitrous oxides (N_2O). Since the industrial revolution, GHG levels have increased in the environment due to the aforementioned use of hydrocarbon-based energy, altering the radiative balance of the atmosphere. Effectively, GHG absorb a portion of outgoing heat radiation and reradiate it back towards the earth's surface, resulting in a warming up of the lower atmosphere [6]. The concentrations of GHG (particularly CO_2 & CH_4) have increased significantly over the last 250 years and are still rising. Figure 1.2 illustrates the global average long-term atmospheric concentration of CO_2 & CH_4 [7]. The contribution of CO_2 emission from fossil fuel combustion and industrial processes on the total global GHG emission increase from 1970-2010 was around 78%; with similar percentage contribution for the period 2000-2010 [8]. CO_2 emissions registered its fastest growth for seven years in 2018, growing by 2%[4].

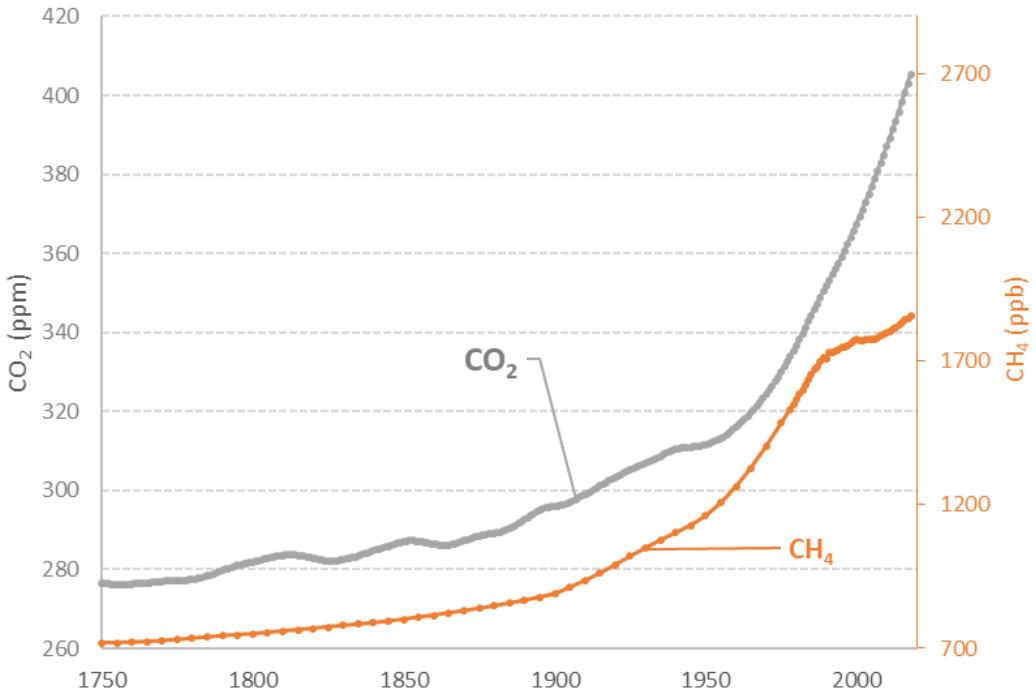

Figure 1.2 – Atmospheric CO_2 & CH_4 Concentration – Global Annual Averaged Long-Term Atmospheric Concentration of CO_2 and CH_4 measured in parts per million (ppm), and parts per billion (ppb), respectively – Data from [7]

1.1.2 Climate Agreements

In the past, commitments have been made by the international community to reduce GHG emissions. Progress nevertheless has been limited to-date. This is due in part to the fact that the United Nations Kyoto Protocol in 1997 was non-binding for emerging economies of the time and the non-ratification of the United States of America (US). However, global

pledges have been renewed with the United Nations Paris agreement in 2015. For such a broad and ambitious energy policy to be effective, in-depth local regulations are essential to frame the decarbonization of the electrical power generation sector. As of 2018, out of the 197 signatories, only 16 countries have actually defined national climate policies and plans ambitious enough to fulfil their pledge [8]. The recent withdrawal of the US from the agreement [9] is of concern, as the US produces nearly 15% of global CO_2 emissions but accounts for less than 5% of the world's population, placing the US in the top bracket of countries with highest emissions per capita (16.2 Tonnes of CO_2 per person per year, as of 2018) [10]. Comparatively, China the world's largest CO_2 emitter and second largest economy, generates roughly 28% of global CO_2 emissions, whilst accounting for nearly a fifth (18%) of the world's population, (7.1 Tonnes of CO_2 per person per year, as of 2018) [10].

The Intergovernmental Panel on Climate Change (IPCC), in their Fifth Assessment Report (AR5) [11], warned that society has till 2030 to fundamentally reshape current economies and energy systems. The AR5 predicted that failing to implement a change would result in the world suffering severe effects of climate change for generations to come, associated with a global average temperature rise of +2 (^{0}C) by 2060, with a continual rise of temperature afterwards. The global average land-sea temperature, relative to the 1961-1990 average temperatures, are presented in Figure 1.3. Since pre-industrial times (1850), the global average temperature has increased by 1.2 ^{0}C, bringing us ever closer to the 2 ^{0}C threshold.

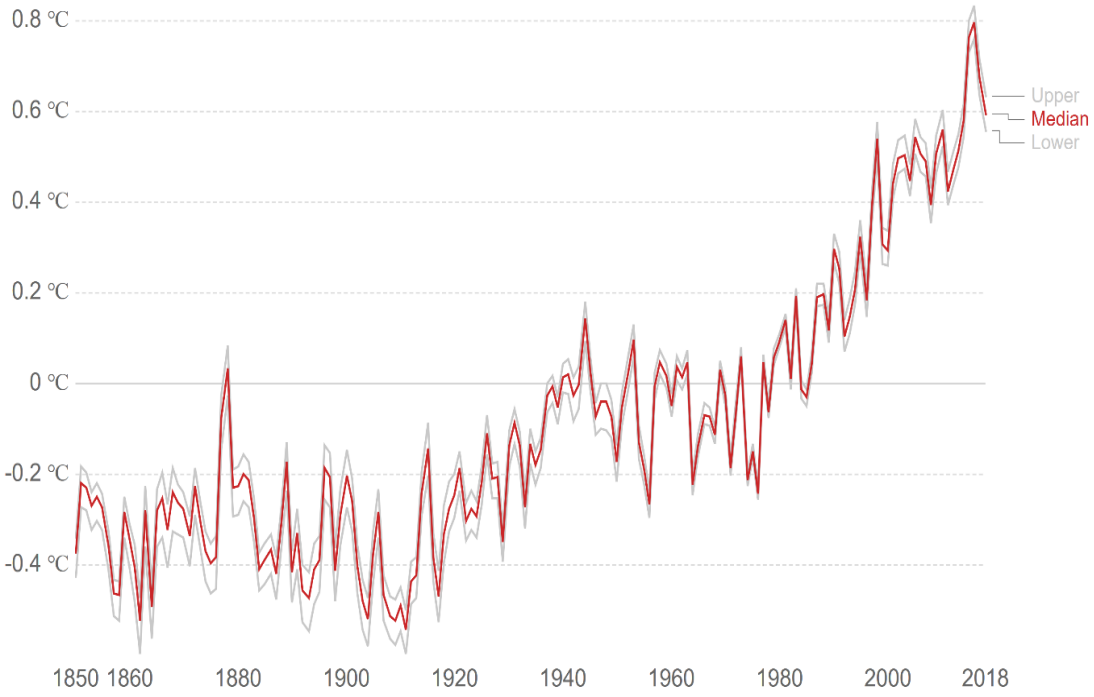

Figure 1.3 – Global Average Temperature Rise – Global average land-sea temperature relative to the 1961-1990 average temperature in degrees Celsius (^{0}C). The redline represents the median average temperature change, and grey lines represent the upper and lower 95% confidence intervals - [7].

1.2 The Importance of Natural Gas

In 2018, global primary energy consumption has grown at its fastest rate since 2010 (2.9%), equating to nearly double its previous 10-year average of 1.5% per annum. This growth is supported in large part by NG, which registered its largest levels of usage since 1984, accounting for more than 40% of the aforementioned global energy growth [4], [12]. Since the financial crisis of 2009, global production of NG has increased at an annual compounded growth rate of 2.8% [13]. The mounting importance of NG in our energy mix is not new, particularly with respect to electricity production. Since the 1970s, NG has increased its share in electricity production worldwide, with an increase from 12.33% in 1971, to 21.92% in 2014, mainly at the expense of oil, from 21.44% down to 3.6% over the same period [14]. This trend is expected to continue, due to the convenience of already existing infrastructure.

Gas-fired gas turbines provide flexibility in balancing energy requirements through coupling and support of intermittent renewable energy technologies. Furthermore, NG possesses the lowest carbon intensity compared to other fossil fuels, emitting less CO_2 per unit of energy due to its inherent molecular structure (approximately 50% less emissions when compared to a typical coal-powered plant [15]), a valuable quality in times of ever more stringent emission policies and environmental concern. It also has an important advantage over other fossil fuels such as oil, as only limited processing is required before it is suitable for end-use. Thus, optimised NG-fired contemporary systems have been able to penetrate many different markets including electrical power generation, commercial and domestic heating, and several industrial processes.

Consumption of NG is mainly driven by the US (78 billion cubic meters (bcm)), China (43 bcm) and Russia (23 bcm). In terms of NG production, the US (86 bcm) accounted for nearly half of the recorded annual growth, due to exploitation of unconventional gas resources, most notably low-cost shale gas and tight oil. Additionally, Russia (34 bcm), Iran (19 bcm) and Australia (17 bcm) made notable contributions [4]. Aside from historical producers, China's NG production has more than tripled between 2005 and 2017, with an additional 8.3% growth in 2018 [13]. Chinese government policies target 10% of gas share in their national energy mix by 2020, with a projection of 15% by 2030 [12].

1.2.1 Natural Gas Projections

Projections of various statistical and energy outlooks reviews [4], [13], [16]–[18], all point to the increasingly vital role NG will play in bridging our carbon intensive past and a carbon-free renewable future. On a global perspective, NG demands are expected to grow strongly, mainly due to support in broad-based demand, low-cost supplies, and the

increasing availability of Liquified Natural Gas (LNG). NG is the only source of energy, along with renewables, whose share in primary energy is currently increasing, with estimations of this growth ranging between 25% to 50% to 2035-40 [12], [16]. Most of this additional gas is absorbed by the growth in power and industry demand, with NG share in the global power sector staying relatively stable at around 20%. The coal-to-gas switching China is expected to undertake to improve air-quality also largely supports gas demand worldwide. Domestic consumption in the US is predicted to expand, supported and driven by economical shale gas and tight oil resources [17].

1.2.2 Liquified Natural Gas – The development of a Global Market

A major contributor to the sustained predicted growth of NG, is the availability and development of Liquified Natural Gas (LNG) trade. Historically, the NG market had not taken the same accelerated globalization highway compared with its crude oil counterpart, mainly due to its gaseous form, rendering it a high-volume low-energy commodity, and thus naturally disadvantaged in terms of transmission and storage. NG supplies are delivered through pipelines to the market, and the transportation costs reflect a much larger fraction of the overall costs compared to the crude oil market. Till recently, these characteristics have limited the evolution of a truly global gas market to a much more regional structure.

The evolution of the 'spot market' in LNG trade, to some degree, has laid foundations for a truly global market. The 'spot market' refers to a method of contract purchasing where buyer and seller are committed for a short period of time, typically less than a month and at a single volume price, which contrasts with the complexity of traditional long-term contracts [19]. In 2018, 32% of global LNG imported was on a 'spot' or short-term basis [20]. High sustained oil prices for much of the 21st century, and dwindling reserves in Europe and Asia have also helped development of LNG trade. The share of LNG in the global gas trade now represents 34.3%, with increases in LNG imports observed in all OECD (Organisation for Economic & Co-operation Development) regions in 2018. LNG volume growth is predicted to more than double, from 400 bcm in 2018, to 900 bcm by 2040 [16]. As of 2018, there are now 42 importing countries, up from 18 a decade ago.

The potential for a robust and integrated global and competitive gas market, depends in-part of the availability and timing of investment to finance this considerable expansion. It is likely that the development of the LNG market will continue to be associated with periods of volatility, due to the cyclical nature of LNG investments. Nevertheless, Asia will remain the dominant market of LNG trade, accounting for over three quarters of global demand (76%) [20]. Pattern shifts are to be expected, with transitioning of trade towards China and India, displacing more established Japanese and Korean markets [16]. China

became the world's largest gas importer, with LNG imports doubling over the last two years [12].

1.2.3 European Needs

From a European perspective, since the mid to late 1800s, town gas (or coal gas) has been used in both industrial and domestic appliances. The discovery of the giant Groningen (Netherlands) gas field in 1959, effectively launched the European NG industry. During 1960s and 70s NG emerged as major energy source, although it should be noted that only Norway, Britain, Holland, and Denmark had sufficient resources to satisfy domestic consumption.

Recently, due to gains in energy efficiency, an expected fossil fuel reduction in the primary energy mix over the upcoming decades is expected. However, dwindling and limited domestic hydrocarbon reserves result in projected increases in LNG import. By 2050, these imports could potentially reach 270 bcm net, mainly for Western European consumption in France, Germany, the Netherlands, and the United Kingdom [18]. Strong increase in gas-fired plants for low-carbon electricity, over the 2010-50 period, is expected to amount to 290 Giga Watt (GW), up 215 GW in 2010, with a focus in investment towards refurbishment and up-grading of already existing infrastructure, mostly Combined-Cycle Gas Turbine (CCGT) plants [18]. This capacity increase highlights the role that NG is expected to play as a fast response, flexible back-up technology complementing intermittent renewable energy sources.

1.2.4 American Renaissance

The story of the NG industry within the US is a perpetual cycle of feast and famine and genuinely testifies to the trouble of forecasting energy futures [21]. At the beginning of the century, confidence in gas was low and the adequacy of domestic gas supplies questioned, mainly due to declining conventional supplies and unconventional resources remaining economically unviable. The perception of shortage arose, coupled with the swift escalation of oil prices, created economically favourable conditions for large scale development of LNG import infrastructures, resulting in a record 47 terminals in permission phase [21]. The U.S import capacity rose from 0.056 bcm/day to over 0.756 bcm/day [19]. However, more recently the 'Shale Gas Revolution' resulted in the US again returning to a period of surplus, substantially altering the supply picture of the US and by ricochet altering global gas dynamics.

Based on the current positive economic environment around LNG, the US Energy Information Administration (E.I.A) in their Annual Energy Outlook (2019) [17], expects NG production to outpace consumption under all scenarios, resulting in higher levels of exports till 2030, before remaining steady during the later years of the projection period (2050) [17].

1.2.5 Change in Global Gas Dynamics

Taking into consideration the above information namely; (1) The US's predicted sustained NG production combined with the current 'climate-sceptic' American administration; (2) European dwindling fossil fuel reserves compounded with the difficulty it is encountering in developing its own shale gas resources and increasing dependence on foreign LNG; (3) the increase in world-wide demand driven largely by the Chinese coal-to-gas transition; global gas dynamics are set to become ever more flexible. At the same time, introduction of new producers and importers, the completion of liquefaction projects in the Americas and Australia, the embargo imposed on Iranian exports and the inherent flexibility of LNG contracts will enable important diversion of volumes of LNG around the globe within relatively short timeframes. The 'second gas revolution' projected by energy analysts could therefore result in the 'first LNG revolution'[20].

The above factors coupled with the increasing reliance on NG-fired gas turbine plants to fulfil low-carbon electricity generation, during both peak requirement and to support intermittent renewable generation during base-load, underpins the necessity of gas-fired power generators to operate more efficiently and flexibly.

1.2.6 Hydrogen Energy

The decarbonization of the electrical sector via the integration of renewable energies is a key issue faced by power system operators. This implementation generates higher risks of power system imbalances in real time, endangering grid stability. In the context of reducing carbon emissions whilst preserving security of supply, there may be a need to reconsider the management of energy systems. For example, coupling various energy sectors via power-to-heat and power-to-mobility, either with electricity directly or synthetic gas as an end fuel, could generate greater flexibility as well as allow the decarbonization of multi-sectorial power sectors simultaneously [22]. An emerging approach in this perspective is the use of hydrogen energy. This potential solution relies on the condition that hydrogen is produced through low-carbon technologies, such as renewable based electrolysis. However, today almost all hydrogen production (61 Mt per year in 2015) is supplied by fossil fuels, consuming 6% and 2% of global NG and coal, respectively [23].

Aside from the development of durable, low-cost and low-carbon hydrogen energy conversion systems, a major hurdle with respect to hydrogen deployment is the issue of reliable, economical and efficient storage and distribution infrastructure. Currently the development of novel compression/liquefaction technologies, materials and processes for chemical storage and safety issues relating to leak detection among others, are hurdles that are hindering the widespread usage of hydrogen to decarbonise energy systems [24].

Hydrogen use is expected to grow [23], [24] beyond current levels, whereby fertiliser production (via NH_3) accounts for > 80% of global hydrogen consumption [22].

1.2.7 The Power-to Gas Concept

The Power-to-Gas (PtG) concept consists of producing hydrogen utilising excess renewable electricity via water electrolysis. The resulting hydrogen can then either be used as a final energy carrier, or converted to synthetic gas, methane, chemicals or electricity [25]. Potentially, the PtG concept could facilitate hydrogen penetration into end-use sectors such as transport and residential heating or power appliances, or as chemical process agents in for example the steel-making industry. As of May 2018, over 128 PtG demonstration and research projects have been conducted/or are being realised across Europe, with Germany having the greatest share in realised demonstration projects. It should be noted that 32% of the aforementioned PtG projects relate to blending the produced hydrogen or converted methane into the NG grid [25].

Although there remain concerns with respect to material compatibility for pipelines and compressors, the integration of hydrogen into the NG infra-structure is being deployed in several countries across Europe. Trialled hydrogen levels range from 'minimal' concentrations, typically 0.1% to 0.5% on a volume basis (vol.%), which reflect typical background concentrations found in NG; to 'low', 'mid' and 'high' injection concentrations, 1-4%, 4-6% and 6-10% or higher, respectively (vol.%) [26]. Current permissible hydrogen addition levels of national gas grids across Western Europe are presented in Figure 1.4. There is no formal rules regarding the determination of allowable hydrogen concentrations, with restrictions generally based on safety limits referenced to NG operations, and local alignment with gas distribution and transmission system operators [26].

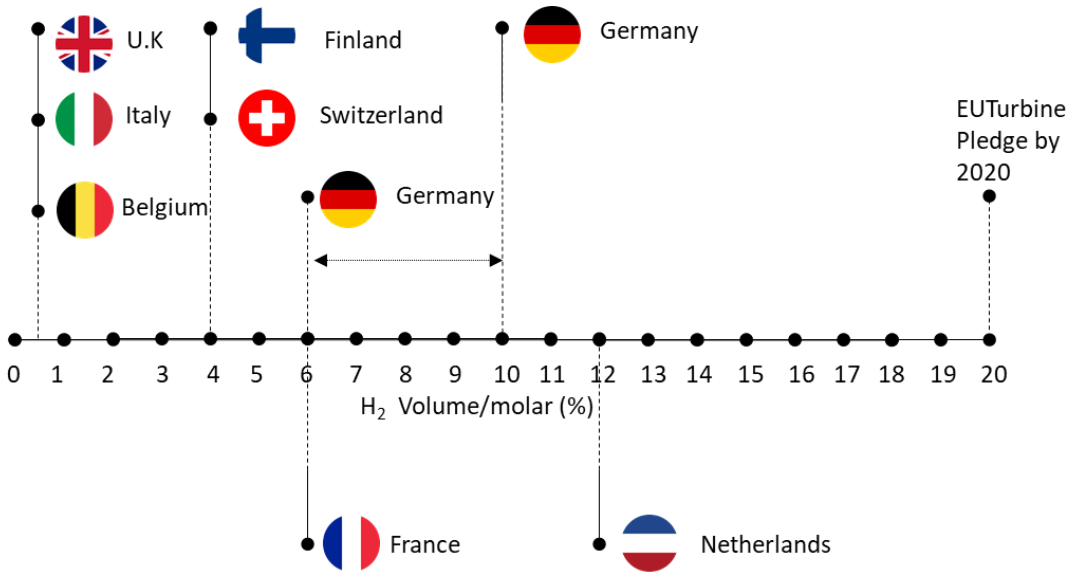

Figure 1.4 – Current Permissible Levels of H_2 Addition to National Grids for Different E.U Countries – Data: [26]

Several European countries are reviewing their gas regulations in relation to hydrogen injection, although there are currently no legal arrangements for revising permitted hydrogen thresholds to meet objectives related to the de-carbonisation of the energy sector. It is important that an EU regulatory framework encompassing hydrogen injection guidelines and PtG plant grid connections between hydrogen supplier and gas grid operators emerges. If not, structural and operational barriers will remain, in terms of divergent hydrogen levels both in transport and delivery. This will result in fragmentation of the gas market, severely constraining and preventing standardisation across the E.U [26].

1.3 The Issue of Interchangeability

Gas turbines (GT) have been specifically designed to operate on various types of gases, ranging from NG, high hydrogen content gases (refinery gases), syngas (biomass, coal, wastes gases) and steelwork gases (blast furnace and coke oven gas), all which have very different compositional make-up [27]. Following the introduction of emission regulations (i.e. NO_X) in the 90s, most modern power generation GTs switched to lean premixed combustion system, commonly referred to as Dry Low Emission (DLE). These new low emission combustors are significantly more sensitive to fuel variation, and are individually optimised, set-up and tuned to tolerate limited changes in fuel composition [28].

Local variations in fuel have typically been relatively slow and small, and thus have not been a major cause of concern. Thus, gas turbine manufactures have traditionally optimised their gas turbines to burn efficiently within a certain range, often reflecting the 'local' NG composition. However, the globalisation of LNG trade and imports, coupled with the potential of hydrogen injection, require a detailed understanding of the impact of fuel variability on combustion behaviour, to ensure high combustion efficiency and safe operation. Published and evaluated operating data by E.ON's UK gas turbine fleet [28], has shown that variations in fuel composition have impacted combustion dynamics, pollutant emissions and power output. Rapid changes in fuel composition have forced emergency shutdowns, impacting component life and revenue. An example of hardware damage (burner), and component failure due to excessive dynamics is shown in Figure 1.5 [28].

Figure 1.5 – New Burner (Left) Burner Damage (Right) Following Component Failure [28]

Original Equipment Manufacturers (OEMS), notably Siemens, SOLAR turbines and Mitsubishi-Hitachi Power Systems (MHPS), are developing and deploying fuel-flexible lean-premixed GTs, designed to operate on various blends of NG and hydrogen. Depending upon the combustion technology, the maximum allowable hydrogen content varies significantly for different OEMs. Currently, Siemen's more powerful GTs are marketed as suitable for up to 30% (vol.%) hydrogen [29]. MHPS have developed various combustors that can be used for co-firing of hydrogen, with combustion tests performed successfully with a 30% (vol.%) hydrogen mix in NG [29]. SOLAR turbines latest combustion system technology is promoted to run on mixtures of 5-25% hydrogen (vol.%) [29]. However, limited OEMs offer GTs designed to operate at hydrogen levels as high as 30-60% [29]. It should be noted that General Electrics (GE) market gas turbines that run on a 100% H_2 [29]. Siemens together with the industry body EUturbines, has committed to increase hydrogen capability in GTs, to 20% by 2020 with the aim to run on 100% hydrogen by 2030 [29]. As discussed, these are considerably higher levels than are currently permissible in E.U gas transmission networks, (Figure 1.4).

1.3.1 Natural Gas Composition

NG is comprised predominantly of methane (CH_4), commonly in the range of 55-98% of the total hydrocarbon content (vol.%). Other hydrocarbons (HC), namely ethane (C_2H_6) and propane (C_3H_8), also vary significantly, 0-15% and 0-25% (vol.%) respectively [30], [31]. Other heavier hydrocarbons and inert gases, notably CO_2 and Nitrogen (N_2), may be present in variable trace amounts, dependant on the source, extraction and refinement process. Compiled in Table 1.1, are compositions of NG extracted from various wells and geographic locations, highlighting expected variations [32], [33].

Table 1.1 – Composition of Different Natural Gases (vol.%) - from [32], [33]

	Frigg	Urengoi	Hassi R'Mel	Abu Dhabi		Matheson	Abu Madhi	Pittsburgh
	North Sea	**Russia**	**Algeria**	**UAE**	**Indonesia**	**Canada**	**Egypt**	**USA**
CH_4	95.7	98	83.5	82.07	89.91	96.62	92.8	85
C_2H_6	3.55		7.9	15.86	5.44	2.32	4.1	14
C_3H_8	0.04		2.1	1.89	3.16	0.54	1.2	
i-C_4H_{10}	0.01		1		1			
n-C_4H_{10}				0.06	0.75	0.12		
i-C_5H_{12}					0.03			
CO_2	0.3	0.8	0.2				0.7	
N_2	0.4	1.2	5.3	0.05	0.04	0.03	0.4	1

1.3.2 The Wobbe Index

The Wobbe Index (WI) is a common indicator used in the GT community to assess the incoming fuel's characteristics and interchangeability. Originally, the WI was developed to categorise different grades of NG. The WI is defined as the higher heating value of the fuel divided by the square root of the ratio of the fuel density to air density (ρ_{fuel}/ρ_{air}). This density ratio is defined as the specific gravity. The WI can be expressed as:

$$Wobbe\ Index\ (WI) = \frac{Higher\ Heating\ Value_{fuel,vol}}{\sqrt{\frac{\rho_{fuel}}{\rho_{air}}}} \qquad \text{Eqn. (1.1)}$$

The power input (P_{input}) into the burner, which is the product of the heating value (HV_{vol}) and the fuel volumetric flow rate ($\dot{Q}_f$), is often required to have limited fluctuations when operating a GT on a baseload basis [34]. The power input can be defined as the function of the pressure drop (Δp) at the burner, the density and the volumetric heating value, giving the following relationship:

$$P_{input} = Q_f \times (HV)_{vol} \propto \sqrt{\frac{\Delta p}{\rho_{fuel}}} \times HV_{vol} \propto \sqrt{\Delta p} \times WI \qquad \text{Eqn. (1.2)}$$

The rationale of the above relationship (Eqn. 1.2) is that for a given fuel supply and combustor conditions (temperature, pressure drop, burner geometry, control valve positions), two fuel mixtures of different compositions, but the same WI, will give the same power input into the system. It follows, that the greater the change in WI, the greater the flexibility demanded of the combustion and control systems to achieve the designed power output. Typically, GT manufactures specify in addition to the WI other limits, commonly heating value and other fuel bulk properties. For a GT installation, a range of ± 5% of the tuned WI is common. Ranges of ± 10% of the WI have been specified, although it is unlikely that the GT would not require some form of retuning or minor hardware changes [28]. Ranges as restrained as ± 2% have also been specified. Manufacture's requirements also account for compositional change by specifying the maximum levels of higher hydrocarbons, maximum amount of inert, and minimum methane amount. This is to ensure that the gas predominantly behaves as methane.

The WI range variation of different NGs transported/imported in the EU are plotted in Figure 1.6. The WI range of national indigenous gas production across the EU is wide, however, note that this does not necessarily mean that customers will experience such widespread ranges, since local gas composition may have little variation. Typically, LNG have a higher WI due to the presence of richer concentrations of higher hydrocarbons than usually consumed in the EU market. In 2017, over half of total NG consumption needs in the EU were provided by Russia (40%) and Algeria (11%) [35].

The EASEE-gas (European Association for the Streamlining of Energy Exchange) proposed WI range (Black lines; 46.46 – 54 MJ/m^3, Figure 1.6), is much broader than is customarily experienced in the EU. OEM's and operators have expressed worries concerning such wide WI ranges, with respect to efficiency, safety and emissions [36].

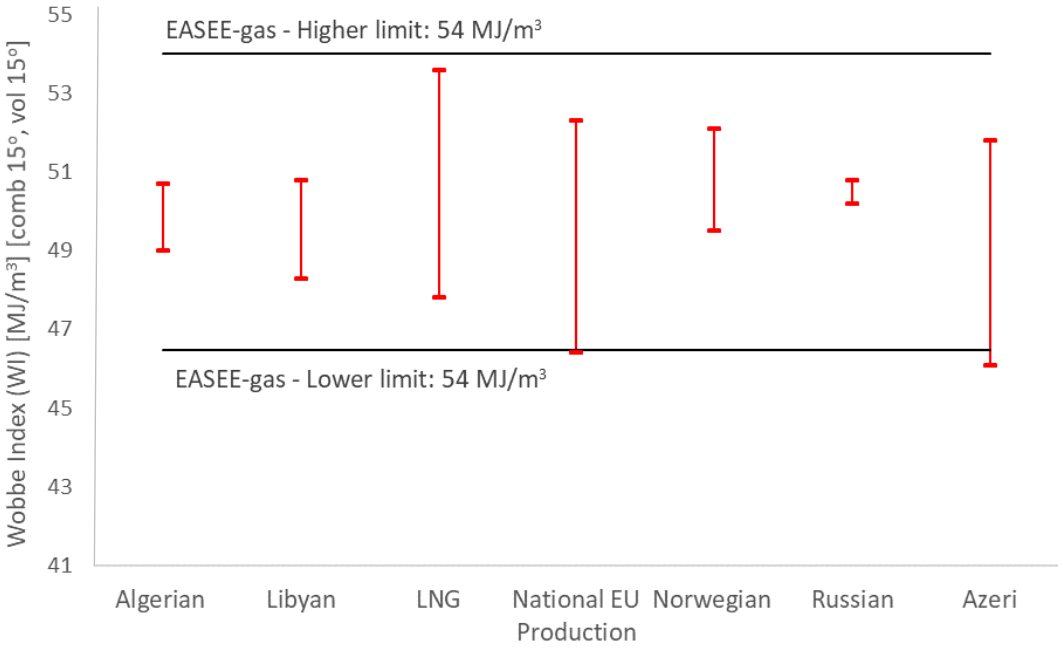

Figure 1.6 – Wobbe Index Range of Natural Gases Imported/Transported in E.U Countries – Solid Lines = Max and Min Limit Proposed by the EASEE-gas – Data from [37], [38]

1.3.3 Characteristics of Individual Fuel Components on Wobbe Index

As previously highlighted, hydrogen addition to NG has gained attention in recent years. It is indicated [29] that major re-configuration in GTs would not be necessary, if the NG/hydrogen mixtures fall within the 30-50 MJ/m^3 range. Hydrogen and methane possess very different fuel properties, as presented in Table 1.2, with hydrogen displaying a much lower heating value than methane. Nonetheless, both fuels have a very similar WI, in the range of 40-48 and 47-53 MJ/m^3, for hydrogen and methane, respectively. This is due to the low density of hydrogen which compensates its lower heating value. However, compared to hydrogen, hydrocarbons have a narrow flammability limit and relatively slower burning velocities, resulting in poor lean burn capabilities.

As illustrated by the similar WI's exhibited by hydrogen and methane, the WI may not capture fundamental changes in flame response brought about by fuel variation. This is due to the way the WI is calculated, using heating value and specific gravity, potentially masking the increased reactivity of alternative fuels. Hydrogen addition to a typical NG will result in the lowering of the heating value, whilst heavier hydrocarbons (ethane and particularly propane) will result in an increase in the heating value. The impact of varying concentrations of hydrogen and propane on the WI are graphically illustrated in Figure 1.7.

It is likely that different gas compositions with the same WI exhibit potentially very different combustion properties. Therefore, combustion of blends containing hydrogen or heavier hydrocarbons could result in unexpected variations in ignition delay times, flames speeds, flame temperature and flame chemistry. These variations may in-turn lead to detrimental phenomena in gas turbines such as flashback, auto-ignition or blow-off, as well as altered expected emissions.

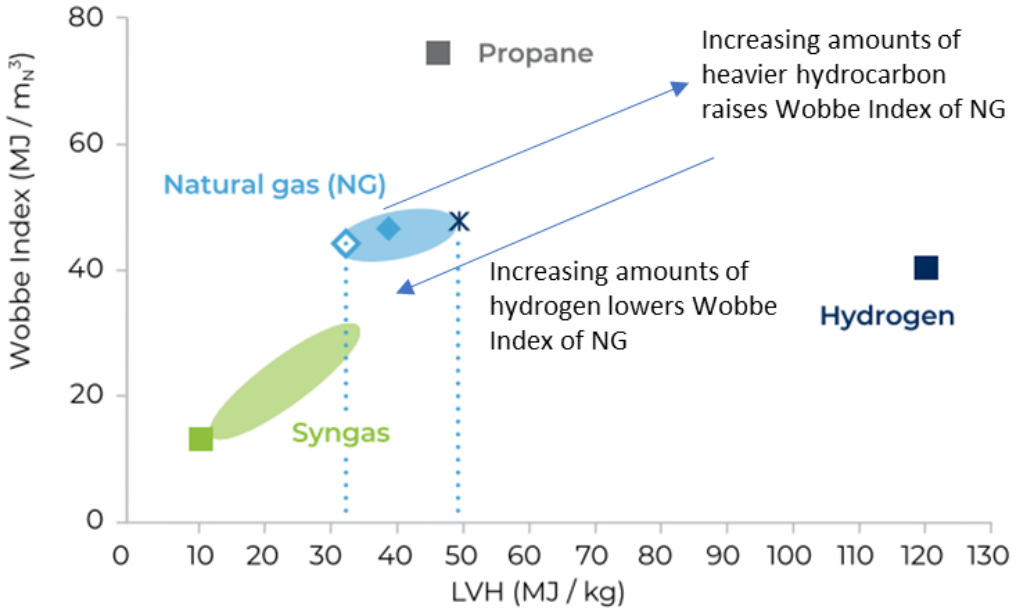

Figure 1.7 – Impact of Hydrogen and Propane Concentrations on Wobbe Index – Adapted from [29]

Table 1.2 – Fuel and Combustion Properties of Various Fuels – Source: For WI [34] Other from [39]

Properties	Natural Gas	Methane	Propane	Hydrogen
Density at 273 K, 1.1013 bar [kg/m^3]	0.7-0.9	0.72	2.01	0.09
Flammability limits [Vol% in air]	4.5-13.5	5-15	2.1-9.3	4-76
Lower Heating Value [MJ/ m$_N^3$]	31-41	35.9	93.1	10.8
Maximum laminar flame speed (in air, 1atm) [m/s]		0.40	0.45	2.85
Adiabatic Flame T [k]		2225	2280	2370
Wobbe Index [MJ/ m^3]	48-53	47-53	74.3	40-48

1.4 Research Aim

The role of low-carbon electrification technologies such as DLEs are required to fulfil the aim of balancing development, progress and cohesion with environmental impact. An emerging approach in this perspective is hydrogen injection into NG grids, with the aim of reducing the carbon intensity of power generation and domestic heating.

However, an increased facilitation of LNG trade coupled with the prospect of hydrogen injection in national gas grids generates new challenges, in terms of combustion efficiency, safety and emission control. Standardisation and regulatory alignment of distribution and system operators across inter-national pipeline distribution infrastructures will be required to avoid structural and operational barriers.

Furthermore, current parameters employed by the GT industry to characterise interchangeability, such as the Wobbe Index, may not be suitable for such a variable fuel supply. As a result, variations in ignition delay times, flames speeds, flame temperature and flame chemistry could potentially lead to detrimental phenomena in GTs, with associated emissions and safety issues. Thus, with ever-more fuel flexible, efficient, safe and clean combustors, fundamental research in fuel combustion properties is now required. This development of understanding will ultimately guide the design of future highly flexible GT's.

The general aim of this dissertation is thus to characterise fundamental combustion performance of blends of methane/higher-hydrocarbon/hydrogen fuels, representative of fuel variations expected in premixed low-carbon power generation facilities. Particular attention is directed towards the lean and ultra-lean spectrum, characteristic of low emission combustors.

In order to fulfil this aim, an extensive literature review is undertaken, identifying the knowledge gaps and fundamental flame parameters required to assess the impact of fuel variation.

Chapter 2. Literature Review

This chapter summarises published relevant research required to underpin the knowledge necessary to conduct the work presented in this thesis. Fundamental combustion properties are introduced, describing their relative importance in characterising operational fuel stability. A review of analogous fundamental alternative fuels combustion research is presented, necessary to both guide and 'benchmark' required experiments in this work.

As discussed in Chapter 1, today's energy mix is still dominated by the combustion of hydrocarbon fuels, with coal, crude oil and natural gas accounting for three-quarters of our global energy consumption [14]. Fossil fuel combustion has well publicised environmental impacts, due to pollutant emissions, such as Nitrogen Oxides (NO_x) and Carbon Monoxide (CO), leading to concern over environmental protection and global warming [7]. Furthermore, dwindling fossil fuel reserves coupled with an ever-increasing world-wide demand for energy have raised concerns over fuel security and supply. As such, this has driven development towards optimised fuel economy, minimised pollutants, and the potential adoption of alternative fuels and combustion techniques. Development of alternative and cleaner combustion systems has steered research towards lean premixed operating systems, air staging, exhaust gas recirculation, flame cooling and flameless combustion, among other techniques [40]. However, in order to implement these methods, detailed research must be conducted to gain insight and understanding of combustion behaviour, with measurement of physio-chemical properties a pre-requisite. Among quoted properties, the laminar burning velocity (U_L) may be regarded as an initial key step towards gaining this understanding of flame stability.

2.1 Laminar Burning Velocity

The laminar burning velocity is a fundamental physiochemical property of a premixed combustible mixture, resulting from the collective influence of thermal and mass diffusion of the reactants and mixture exothermicity [41]. The laminar burning velocity (sometimes termed as the laminar burning rate, or laminar flame speed, defined herein as U_L) reflects both the combustion process and the combustible mixtures reactivity, characterising a given fuels combustion behaviour. As such, the laminar burning velocity is a key parameter, helping describe premixed operational instabilities such as extinction, blow-off and flashback (detailed in Section 2.1.2), and a fundamental step towards characterisation of turbulent flame propagation [27], [42]. The laminar burning velocity is defined as the velocity at which a steady one-dimensional adiabatic flame front propagates normal to itself in the doubly-infinite domain [41]. This definition makes the laminar burning velocity particularly suitable

for calculations in one-dimensional computer codes which rely on thermodynamic and transport data, and by extension convenient in appraising and validating chemical kinetic mechanism and models. In practice, this definition renders the laminar burning velocity an idealistic parameter; since it is unfeasible to achieve quiescent unburned gas mixtures, with flame propagation affected by flame wall interactions, buoyancy effects and potential heat loss, when conducting experiments in a confined space [41]. As such, the laminar burning velocity is not a measurable quantity per se, it is derived from theoretical models based upon observables and assumptions.

2.1.1 Historical Empirical and Theoretical Combustion Developments

Initial research upon flame propagation began with work conducted by Bunsen and Roscoe [43], with measurements of hydrogen (H_2) and carbon monoxide (CO) mixtures using a cylindrical burner. Subsequently, Mallard and Le Chatelier [44] using horizontal tubes, discovered that for certain explosive mixtures, the flame propagated some distance at a ''*uniform*'' speed. Mason and Wheeler [45] demonstrated that this flame speed of ''*uniform movement*'' was related to tube diameter. Chapman and Wheeler [46] suggested a relationship between tube diameter and flame speed for methane air mixtures, with Coward and Hartwell [47] further investigating the proposed relationship using photographic analysis discovering that flames propagating in tubes are not flat and attempting to derive an average laminar burning velocity considering the conical surface of the flame front.

Further advancements were made in measurement techniques, including Hopkinson [48], who developed a confined chamber with central ignition using electric sparks to investigate flame propagation. Stevens [49] introduced the soap-bubble method based upon spherical flames. The combustible mixture would be ignited within a bubble film, subsequently freely expanding as combustion progressed, ensuring a constant pressure if the experiment is conducted in an open atmosphere [41]. Yet, much of the early work relied upon constant volume chambers, with rate of flame propagation evaluated using rise in internal pressure. Payman [50] endeavoured to correlate flame propagation of various fuel mixtures, and noted changes in attained flame speeds from different conditions. Continuing his work with Coward [51], Payman presented experimental influences upon flame propagation, including the motion of a combustible mixture and flame speed relative to it, and the impact of the configuring area upon flame size. Lewis and von Elbe [52], achieved noteworthy correlations between calculated flame speeds and experimental measurements using constant volume spherical flames, accounting for diffusion and heat flow. Lewis and von Elbe [53] subsequently introduced flame measurement techniques based upon particle imaging. Linnet [54] reviewed contemporary methods of measuring burning velocities and specific

associated definitions of burning velocity concluding that a precise definition equally applicable for both planar and spherically expanding flames seemed impossible. Powling [55] developed a burner to enable flame speed measurement using planar flame fronts allowing the quantification of quasi-laminar flat flames. Introduction of water cooling to this technique was developed by Botha and Spalding [56]. Subsequent advances produced by de Goey et al. [57] gave rise to the modern flat flame heat flux method.

Flame propagation is typically influenced by stretch, a term that incorporates the influence of aerodynamic strain, thermo-diffusive instabilities and surface curvature [41]. Karlovitz et al. [58] in their study of turbulent flames, presented the notion that variations in surface velocity gradients affect flame propagation, in view of the fact that local speed relates to the change of surface area (*A*) creation. This theory introduces a function known as the stretch rate (α), defined as the rate of change of flame area with time:

$$\alpha = \frac{1}{A} \times \frac{dA}{dt} \qquad \text{Eqn. (2.1)}$$

Markstein [59] linearly characterised the relationship between flame speed and the influence of curvature. Further work by Markstein [60], incorporated the influence of thermal and mass diffusion, through the dimensionless parameter known as the Lewis Number (Le), defined as the ratio of thermal to mass diffusivity. For single fuel/air mixtures, Le can be expressed as:

$$Le_i = \frac{\lambda}{C_p \rho_u D_{i,j}} = \frac{D_T}{D_{i,j}} \qquad \text{Eqn. (2.2)}$$

where (λ) represents thermal conductivity, (ρ_u) the unburnt density of the combustible mixture, (C_p) specific heat, which combine to give (D_T) the thermal diffusivity; and (D_{ij}) representing the binary mass diffusion co-efficient. Thermal diffusivity and mass diffusivity display similar temperature dependence, in the order of $D_T \sim T^a$ and $D_{i,j} \sim T^b$, with 'a' and 'b' lying in the range of 1.5-2.0, respectively [61]. Consequently, Le is only slightly dependent on temperature. Furthermore, Le is independent of pressure, since both mass and thermal diffusivity are inversely proportional to pressure (1/P) [61].

Non-equidiffusivity arises due to the imbalance of thermal to mass diffusivity, defined through Le. Non-equidiffusion, through preferential diffusion (also known as diffusional-thermal instability) impacts the combustion intensity of stretched flames, with respect to the flame propagation, stability and extinction characteristics [41]. From a phenomenological perspective, the flame releases energy to its surroundings whilst simultaneously gaining chemical energy from the surroundings due to an increase of the deficient reactant concentration. The heat and mass transport gradients are hence the driving forces behind flame propagation. Consequently, the diffusion of heat and mass govern the flame behaviour, and by extension the flame temperature. The flame is

unconditionally unstable when Le is below a critical value ($Le_{crit} \approx 1$), whereas it is stabilised through diffusion when Le > 1. When Le > 1, thermal diffusion is more dominant, and the flame loses heat in proportion to the surrounding reactant, and therefore accelerates as it expands. This is due to the impact of stretch effects, which are more pronounced when the flame is small, as the curvature is relatively larger [62]. As such, flames with Le > 1 become weakened and experience inhibition (burn slower) in turbulent (highly stretched) environments. Equally, the opposite holds true for fuel mixtures displaying an Le < 1. The effect of stretch on flame propagation was characterised by Markstein and is now known as the burned gas Markstein length (L_b). The effect of curvature on laminar burning velocity was later discussed by Sivashinsky and Frankel [63]. Wu and Law [64] proposed flame stretch corrections, suggesting that this was the reason behind the important scatter observed between experimental data. Similar suggestions were made by Tien and Matalon [65] whilst highlighting the importance of defining the reference position when measuring laminar burning velocities of stretched flames. Subsequently, non-linear stretch corrections have been proposed in an attempt to explain the effects of flame stretch on laminar burning velocity [66]–[68].

2.1.2 Operational Fuel Stability – The Importance of Laminar Burning Velocity

Flame positioning and constancy, coupled with instabilities generated from pressure oscillations, are key issues involved with premixed burner operability [34]. The laminar burning velocity directly characterises these parameters, and consequently is significant with respect to predicting flame behaviour [69]. The operational range of a premixed burner is determined by flame loss, either through blow-off (also termed blow-out, Lift-Off) on the low reactivity side, or flashback on the high reactivity side [70]. Simplistically, these phenomena result from an imbalance between the velocities of the reactant travelling from the burner and the speed of the flame towards the burner. Thus, if the incoming reactant flow is larger than the laminar burning velocity, the flame moves away from the burner and is blown off (blow-off/blow-out). Conversely, if the flame velocity is higher than the incoming fuel reactant velocity, the flame propagates upstream into the reactant flow towards the burner, with potential risk of flashback. A stabilised flame arises where the incoming reactant flow rate is balanced with the flame velocity [42].

Thus, flame propagation mechanisms effectively determine the fuels reactivity limits [70]. Naturally, these processes are dependent upon the fuel composition, which dictates chemical kinetics and the fuel flow rate into the fuel injection system, in order to achieve a target heat rate (thermal power). The laminar burning velocity of a specific fuel mixture can thus be utilised to predict/propose operating conditions for GTs [70], particularly with respect to the lower end of the reactivity scale (lean conditions). As the laminar burning

velocity decreases, a consequence of the fuel decreasing in reactivity, the blow-out phenomenon can destabilise the flame. Fuel reactivity is also controlled by the transport mechanism of various species across the flame front (thermo-diffusive effects), and the rate of kinetics [70]. Extensive studies have been conducted on blow-out, with physical or empirical correlations proposed to predict blow-off or flashback (i.e. turbulent flame speed approaches) [27]. In general, all agree upon the fact that blow-off occurs when the chemical time scale (T_C), which can be characterised as (D_T/U_L^2), known as the Damköhler number (Da), is larger than a characteristic residence time (T_R), $T_C > T_R$; meaning that the flame propagation takes more time than the residence time available for both mixing and reaction [27]. Likewise, the laminar burning velocity can be used to approximate a critical velocity gradient (g_f) resulting in boundary flashback through [42];

$$g_f = c \times \frac{U_L}{d_q} = c \times \frac{U_L^2}{D_T} \qquad \text{Eqn. (2.3)}$$

where (c) is a constant specific to the employed burner, (d_q) the quenching distance (which represents extinction of the flame due to heat loss at the burner wall) and (D_T) the thermal diffusivity of the flame. This association is simplified, with other parameters such as stretch and turbulent flow fundamental in describing changes in burner velocity gradients. Furthermore, in practice, there exists flame stabilisation mechanisms to reduce local flow velocity, for example the use of bluff bodies or by aerodynamically inducing recirculation zones by the use of swirl, which enables a region of stable flow between blow-off and flashback [42], [62]. Whilst changes in local fuel-air ratios and by extension laminar burning velocity will inevitably impact practical combustion systems, minimising their variation in order to enhance system stability is necessary.

2.2 Introduction to Measurement Techniques

Several experimental techniques have been developed to measure the laminar burning velocity of combustible mixtures. The most widely employed include the constant volume or pressure spherical flame method, the heat-flux method and the counter-flow (also known as stagnation) method, with the three methods schematically represented in Figure 2.1.

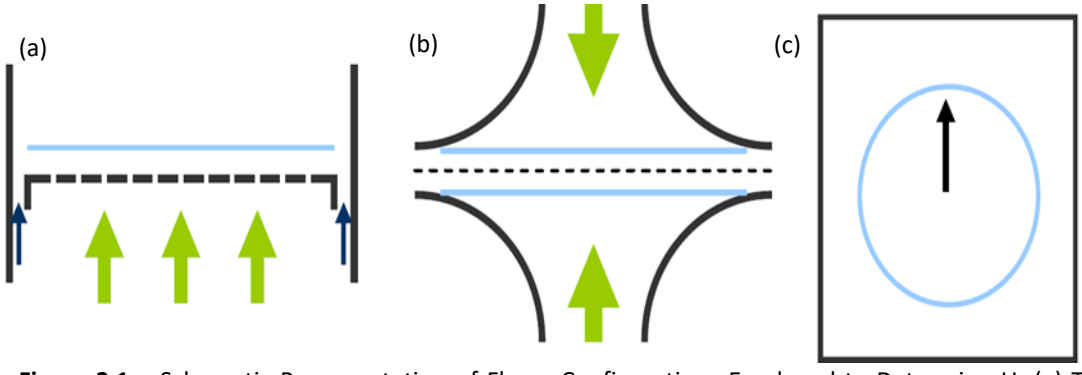

Figure 2.1 – Schematic Representation of Flame Configurations Employed to Determine U_L (a) The heat-flux (flat-flame) (b) Counter-flow (stagnation) flame (c) Outwardly propagating spherical flame, adapted from [62]. Note: Blue = flame outline

A recent critical review of the various combustion measurement techniques and associated stretch effects, including potential sources of uncertainties was presented by Egolfopoulos et al. [71]. Additionally, recent advances and updates have been reviewed by Konnov et al. [40]. As such, a brief review of the various experimental methods along with merits and limitations of each technique is presented herein.

2.2.1 The Heat Flux (flat-flame) Method (HFM) – This method is schematically depicted in Figure 2.1(a). In this configuration, the flame is planar and stationary, with the flame located normal to the burner exit. As such, due to the geometry, the laminar burning velocity equals the unburnt gas velocity flowing through the porous plug. An advantage of this technique is that the flame is subjected to practically no stretch (assuming the flame is perfectly flat). However, the measurement is inherently non-adiabatic due to heat loss to the porous plug. Adaptations have been proposed in order to quantify heat loss as suggested by Botha and Spalding [56]. By measuring different heat loss values to the plug by cooling to specific temperatures, the attained flow values can be extrapolated to adiabatic conditions. de Goey et al. [57] modified the burner set-up to compensate heat loss and stabilise adiabatic flat flames. This was achieved by heating the perforated burner externally with hot water, with the heat gained by the unburnt gases compensating the heat loss of the flame. There are however inherent limitations with this type of perforated burner. Combustible mixtures which display a laminar burning velocity > 80 cm/s cannot be experimented upon, as the hole sizes of the porous plug need to be reduced, rendering the burner fabrication difficult. Furthermore, measurements at higher mixture temperatures are difficult, as the distance between the flame and burner reduces, increasing quenching effects [40].

2.2.2 The Counter-Flow (Stagnation) Method (CF) – This method is schematically illustrated in Figure 2.1(b). Wu and Law [64] and Zhu et al. [72] first suggested this method for the determination of laminar burning velocity. This configuration requires the creation of a stagnation flow-field, achieved by directing two nozzle-generated combustible flows symmetrically, with twin flames formed (blue lines, Figure 2.1(b)). In this case, the stabilised flames do not experience any downstream heat losses (excluding negligible radiative heat loss) due to flame positioning and symmetry. As such only stretch generated due to non-uniform flows (hydrodynamic strain) influences the flame. For a well-characterised stagnation flow, stretch can be related to local velocity gradient and then related to the axial velocity gradient [40]. Extrapolation of velocities and stretch rate can then be used to quantify the laminar burning velocity. Uncertainties using this method relate to flow rate measurement and the requirement for perfectly matched flows makes this method comparatively more complex than other configurations.

2.2.3 Outwardly Propagating Spherically Expanding Flame Method (SEF) – This method is schematically illustrated in Figure 2.1 (c). In the spherically expanding flame configuration, a quiescent combustible mixture at a known fuel air ratio and initial temperature and pressure is filled inside a spherical/cylindrical chamber and centrally ignited. The rate of propagation of the outwardly, positively stretched spherical flame can then be measured. Several challenges are associated with this technique, namely, the impact of ignition energy and heat loss to the electrodes, confinement effects, buoyancy, and the expansion of the combusted gases must be considered [41]. The flame propagation is influenced by variations in flame curvature, diffusional instabilities and flow-field strain, summarised as stretch. The impact of stretch on the flame can be determined through the Markstein length, with extrapolation of measured stretched flame speeds to zero-stretch conditions required to evaluate the laminar burning velocity [41], [62].

This technique is particularly well suited for the investigation of multi-component fuels, such as NG, since all other methods necessitate a constant flow of unburnt gas. This renders precise determination of fuel blends more difficult and expensive, since several mass flow controllers would be required. Furthermore, this type of apparatus allows to precisely control the temperature and pressure of the unburnt combustible mixtures. Acknowledging that this experimental set-up will be extensively used to determine laminar burning velocities and stretch-related behaviour of various fuel mixtures, further detail related to the theory and flame configuration of this method are presented in Chapter 3.

2.3 Research Upon Alternative Fuels

Prior to overviewing contemporary literature, a fundamental parameter known as the equivalence ratio (Φ) needs to be defined. The combustion intensity of a fuel and an oxidizer mixture depends on the relative ratio of the reactants. Combustion intensity is highest when the ratio of reactants is balanced in such a way that all reactants are consumed [41], defined as stoichiometric combustion. The equivalence ratio indicates the mixture's concentration deviation from stoichiometry, and can be defined as [41]:

$$\Phi = \frac{(F/O)}{(F/O)_{stoic}} \qquad \text{Eqn. (2.4)}$$

where F/O is the ratio of the mass of the fuel to the mass of oxidizer in the mixture, and subscript 'stoic' indicates stoichiometric conditions. Consequently, fuel-lean (or lean), stoichiometric, and fuel-rich (or rich) conditions, imply an $\Phi < 1, = 1, > 1$, respectively.

2.3.1 Flame Speed and Markstein Length Research on Methane

Historically, early studies on flame speeds largely involved the combustion of methane (CH_4), (Section 2.1.1), partly because it is the main constituent of natural gas. The combustion characteristics of CH_4 have been widely reviewed, and as such this fuel is often used to benchmark methodologies and new experimental apparatus [40],[62],[71]. However, it should be noted that there remains relatively large scatter in attained laminar burning velocities. Peer-reviewed laminar burning velocities of CH_4 at standard conditions (T_u = ~298 K, P = 1 MPa), from lean to stoichiometric conditions ($\Phi \leq 1$) using various experimental configurations are plotted in Figure 2.2. The large discrepancies existing may be attributed to the employment of different flame configurations, and for similar experimental configuration the data extraction techniques relied upon [40], [71]. Furthermore, for the SEF apparatus, aside from the application of different techniques to correct for stretch (detailed in Section 3.1), discrepancies in U_L values are witnessed between the use of optical tracking techniques of flame front (i.e. Schlieren and shadowgraphy) and the use of pressure-time recordings to evaluate U_L [40].

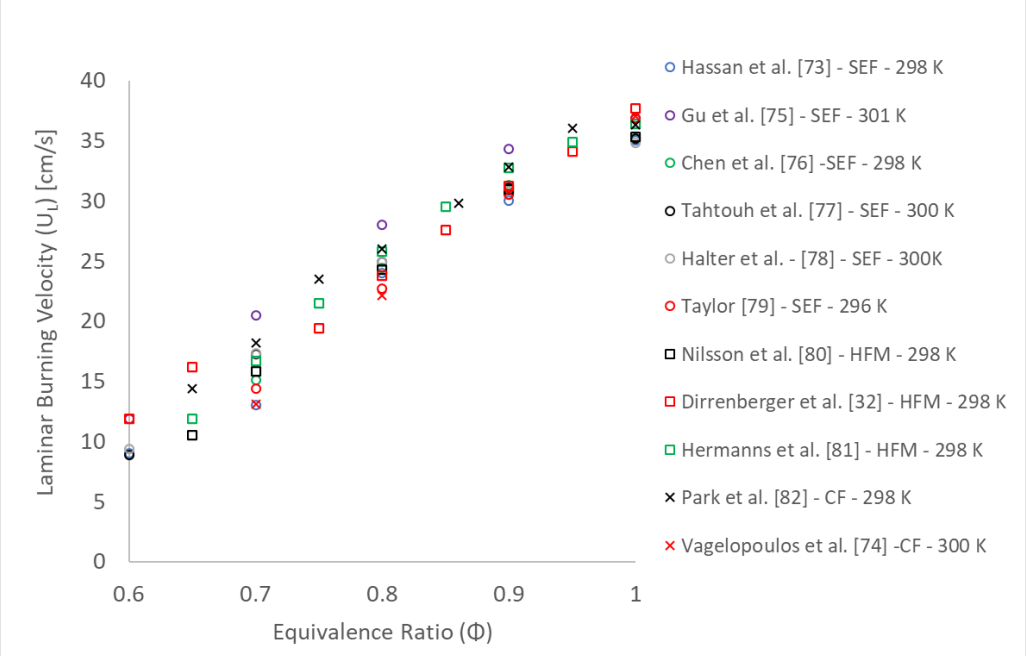

Figure 2.2 – Laminar Burning Velocity of CH_4/air at Standard Conditions (T_u≈298 K, P = 1 atm), Symbols: Circle (○) = Spherically Expanding Flame (SEF), Square (□) = Heat Flux Method (HFM), Cross (×) = Counterflow (CF)

Extensive work has been conducted with respect to sources of uncertainty/inaccuracy, notably by Chen [83], [84] on SEF as well as others [78], [85]–[87] covering the impact of mixture preparation (i.e. accuracy Φ, buoyancy, ignition, confinement, non-linearity and extrapolation technique utilised to extract U_L, detailed and quantified in Chapter 5). However, aside from a few exceptions [31], [88], [89], uncertainty analysis of attained experimental U_L values is often not presented, with uncertainty bars representing

minimum and maximum recorded values or two standard deviations, with little mention of the number of repeats conducted per experimental conditions (and when mentioned they are typically less than 3 repeats). With respect to the much more sensitive Markstein length (L_b), scatter in literature is even more important and can reach 100% or even larger, depending upon the extraction model employed to evaluate L_b [84] (further detailed in Chapter 3 and quantified in Chapters 6 & 7). Discrepancies in measured L_b using the SEF configuration are illustrated in Figure 2.3. Such large scatter is somewhat to be expected since one is effectively trying to derive a term at fractions of a millimetre from data representing flames travelling at tens of centimetres per second.

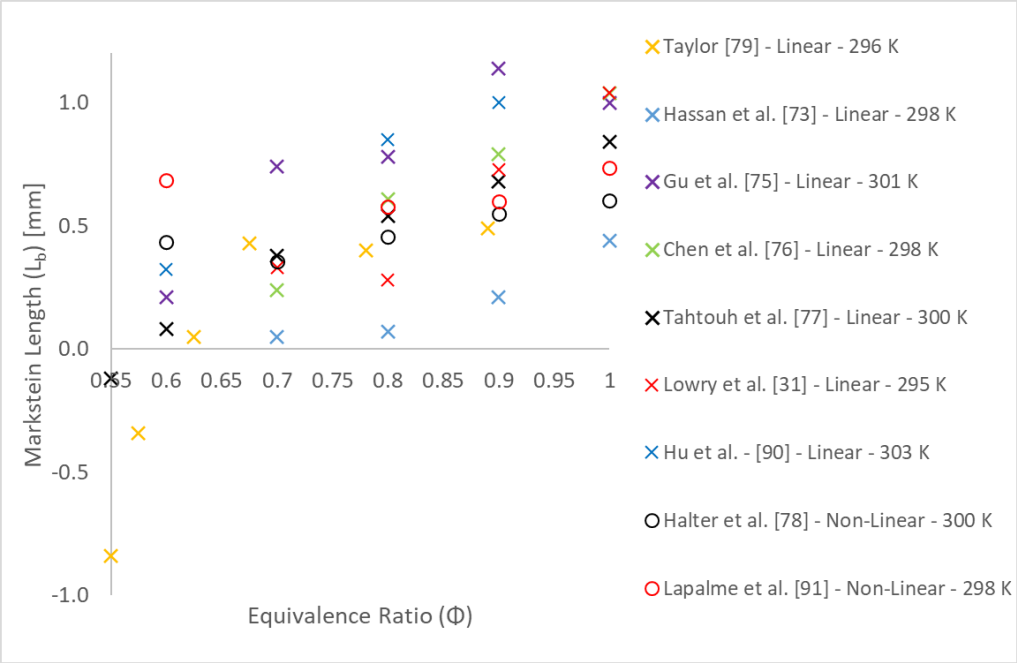

Figure 2.3 – Markstein Length of CH_4/air at Standard Conditions ($T_u \approx 298$ K, P = 0.1 MPa) measured using SEF, Symbols: Cross (×) = Linear Methodology, Circle (○) = Non-Linear Methodology

2.3.2 Higher Hydrocarbons

Flame characteristics of higher hydrocarbons (the term C_2+ will be used in this thesis when referring to ethane (C_2H_6), propane (C_3H_8) and n-butane (C_4H_{10}) as a whole), have been somewhat less studied than CH_4, although there exists substantial literature of flame speed measurements of ethane, for example [32], [79], [92]–[94], of propane [32], [79], [92], [95], [96], less so for measured L_b (particularly for ethane). Less research is published on n-butane, however limited examples can be found in [32], [68], [97]–[99]. A recent and exhaustive compilation of measured U_L for C_2+/air flames, using various experimental set-ups, is presented in [40]. Konnov et al. [40] highlight that ''*for propane-air mixtures no unstretched U_L data measured with the SEF configuration is available in literature and corrected for stretch using contemporary non-linear extrapolation schemes*''. To the author's best knowledge, this also applies to ethane-air mixtures. Moreover, Chen [84], in his investigation on the accuracy and performance of various stretch correction methodologies (linear and non-linear models,

detailed in Chapter 3) underlines that accuracy and performance of investigated stretch-models strongly depend on the Le of the mixture. Since, C_2+ fuels have known Le > 1 [41], and thus are strongly influenced by non-linear stretch effects, it would seem necessary to complement available data (for example n-butane/air U_L and L_b available in [68]) with measurements of U_L and L_b of C_2+ fuels employing appropriate extraction methodologies using the SEF apparatus.

When combusted in air, it is well established that methane has the lowest U_L of the fuels typically found in natural gas (C_2H_6 and C_3H_8), with ethane burning fastest at standard conditions. Propane has been shown to display a U_L closer to that of ethane at lean conditions, and methane in rich conditions [30], [32]. Furthermore, C_{1-4} (meaning CH_4, C_2H_6, C_3H_8 and n-C_4H_{10} in this thesis) alkanes all display a peak U_L at conditions slightly richer than stoichiometry ($\Phi \approx 1.05$-1.1), exhibiting relatively similar adiabatic flame temperatures and activation energies [98].

2.3.3 Methane – Higher Hydrocarbon Blends

Several studies have investigated the influence of higher hydrocarbons on methane combustion [31], [80], [88], [100]. It has been observed, using the heat flux method [32], [80] and SEF configuration [31], [88], that the addition of C_{2-3} compounds augment by a few cm/s the U_L of methane. Ravi et al. [88] analysed the reasons behind this measured increase, concluding that this was mainly a kinetic effect. Lowry et al. [31] witnessed that blending ethane and/or propane to methane made the CH_4/air flames less susceptible to flame instability. Aside from [31], research primarily attempts to elucidate the effect of blend composition on U_L with little focus on stretch-related behaviour. Furthermore, changes in fuel composition are often important (i.e. changes of 20%+ vol.%), with little research conducted on the impact of small additions of heavier hydrocarbons on CH_4 flame stability. It is thus unclear to what extent relatively small additions of C_2H_6 or C_3H_8 have on CH_4 based fuels, in terms of Markstein length behaviour in comparison to exhibited pure fuel characteristics.

2.3.4 Methane – Hydrogen Blends

A considerable amount of work relating to the impact of hydrogen enrichment on CH_4/air flames has been conducted. Flame speed measurements have been performed using the counterflow set-up [101], SEF configuration [90], [95], [102], [103] and heat-flux method [32], [80], [81]. Most experiments focus on H_2 additions of < 50% (vol%), with only Hu et al. [90], [104] employing the SEF configuration, generating data for U_L and L_b from lean to rich conditions and for hydrogen fractions of 0 to 100% (in 10% vol. increments). As such this dataset has been used by Ji et al. [105] to assess the performance of various reaction mechanisms, and by Bradley et al. [106] to validate empirical blending laws of CH_4/H_2

mixtures. It is worth highlighting, that Hu et al. [90], [104] employed a linear methodology to extract U_L and corresponding L_b. Under lean conditions ($\Phi < 1$), CH_4/H_2 mixtures exhibit Le close (or below) unity, with Le significantly decreasing the higher the concentration of H_2 and the leaner the conditions. According to Chen [84], for high hydrogen mixtures (Le << 1), a non-linear methodology should be applied in order to optimise accuracy, particularly with respect to the very-sensitive L_b parameter. A recent study by Liu et al. [107], evaluating U_L and L_b values upon application of a non-linear model for H_2/air SEF agrees with Chen's [84] conclusions. However, little to no data is found in literature which apply Chen's recommendations for CH_4/H_2 mixtures.

Although limited data is available for CH_4/H_2 mixtures containing > 60% H_2, Tang et al. [108] in their review on combustion of hydrogen enriched hydrocarbons highlight the existence of three distinct flame speed regimes for CH_4/H_2 blends, based upon Hu et al. [90] experimental data and Di Sarli et al. [109] numerical study of CH_4/H_2 blends. The first regime relates to H_2 additions of 0 - 50%, where small and gradual increases in U_L are exhibited with increasing H_2 fractions, indicating that combustion is dominated by CH_4. For H_2 fractions > than 80% (regime 3, ≈ 80 to 100% H_2), U_L decreases significantly with reduction in H_2 fraction, indicating that relatively small volumes of CH_4 drastically impact the combustion of H_2. For 60 to 80% H_2 (regime 2) the U_L increases respectively more and less significantly than regimes 1 and 3 [108]. These regimes are clearly visible when observing Hu et al.'s datasets [50], plotted in Figure 2.4, for various equivalence ratios (Φ). Augmentations in witnessed U_L of CH_4 flames upon H_2 enrichment are attributed to kinetic effects (enhanced oxidations chemistry), particularly an increase in production of radical (O, OH, H) in the flame reaction zone [90], [110].

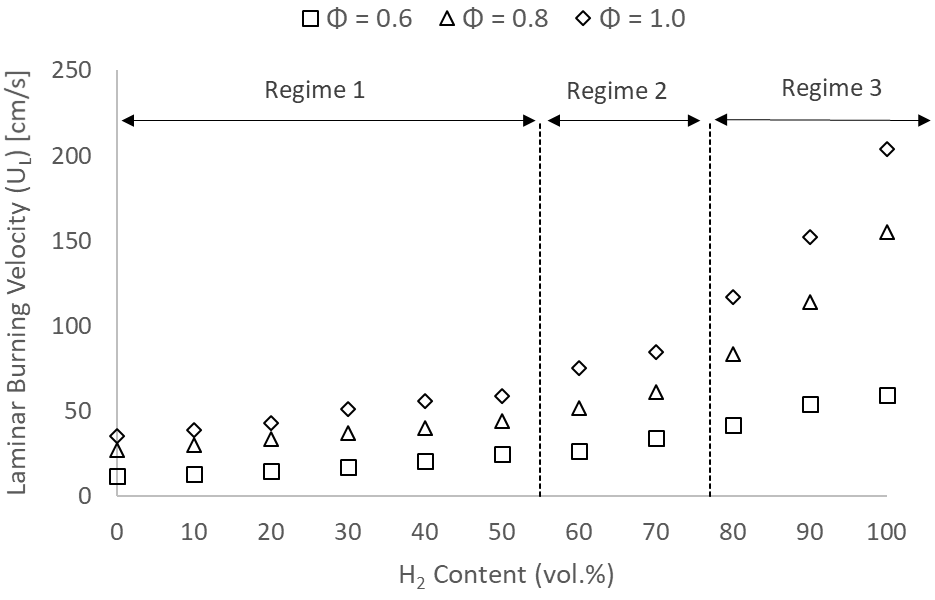

Figure 2.4 – Laminar Burning Velocity of H_2/CH_4/air Mixtures as a Function of H_2 Addition (vol.%) Φ = 0.6, 0.8, 1.0; Data Source: Hu et al. [90]

2.3.5 Higher Hydrocarbons – Hydrogen Blends

Numerical analysis on the impact of H_2 addition on laminar flame properties of C_{1-4} alkane/air mixtures has been conducted by Cheng et al. [111]. Results demonstrated that all flame parameters (i.e. Flame thickness, Activation Energy, defined in Chapter 3) including U_L and Le were significantly altered upon H_2 addition, with increasing dependence the more important the H_2 enrichment level. Detailed kinetic analysis revealed that U_L can be correlated to maximum molar concentrations of O and OH radicals. A few experimental investigations have been conducted to confirm those numerical findings. Wu et al. [112] used the SEF configuration to determine the impact of H_2 on C_2H_6, with tests conducted for a wide range of initial pressures (up to 20 atm). Conclusions agree with Cheng et al.'s [111] kinetic analysis, with results demonstrating a linear relationship between H_2 addition and U_L values, with those increases largely attributed to kinetic effects. Several experiments have been conducted on C_3H_8/H_2 blends, including Yu et al. [101] on the counterflow, and work by Tang et al. [113], [114] on the SEF configuration at atmospheric and elevated pressures (up to 7.5 bar). Tang and co-workers underline the impact of H_2 addition to C_3H_8 flame stability, attributed to a reduction in both the Le and flame thickness of the flame. Less work has been conducted on C_4H_{10}/H_2 mixtures, with first measurements recorded by Sher and Ozdor on a flat-flame burner, for additions of up to ~65% H_2 (vol.%). Tang et al. [115] further investigated the impact of H_2 on C_4H_{10} using the SEF set-up, from lean to rich conditions. A mechanistic investigation supplemented by a sensitivity analysis revealed that the augmentations witnessed in U_L were to be attributed to changes in global activation energy. Further calculations demonstrated similar behaviour for CH_4 and C_3H_8. Tang et al. [115] conclude that additional experimental investigation is warranted in order to generalise the correlations observed. Subsequently, as mentioned, Wu et al. [112] extended those findings to include C_2H_6/H_2 mixtures applying a similar sensitivity analysis, with such analysis yet to be conducted upon CH_4 or C_3H_8. It seems adequate to mention that most of the above investigations of C_{1-4}/H_2 generate valuable U_L measurements, however quantification of stretch-related behaviour through the Markstein length is not so readily available, with only Tang et al. [113] providing data. Furthermore, Tang et al. [113] apply a linear relationship, which is potentially not well suited for mixtures of propane containing low H_2 additions (<50% vol.) under lean conditions, since C_3H_8/H_2 mixtures at those conditions would exhibit Le >>1, as underlined by Chen [84].

2.3.6 Natural Gas – Hydrogen Blends

Some studies in literature investigate fixed compositions of NG or blends of CH_4 with higher hydrocarbons (generally C_2H_6 and/or C_3H_8) as surrogates of NG. Dagaut et al. [116] investigated the impact of H_2 enrichment upon the oxidation kinetics of CH_4/C_2H_6 (10:1) mixture in a jet-stirred reactor across lean to stoichiometric conditions. The study concluded that enhanced reactivity was due to the augmented production of OH radicals. Similarly, other studies [117], [118] using the SEF configuration investigated the impact of H_2 on NG, however those NG compositions were mainly composed of CH_4 (> 95% vol.), and as such outcomes are very similar to those related to CH_4/H_2 blends. Brower et al. [70] modelled the impact of H_2 addition to a fixed NG composition (containing ≈ 20% C_{2-4}) under practical engine-relevant conditions (T_u = 300 – 900 K, P = 1 – 30 atm). Results indicate that CH_4 is more prominently influenced by H_2 enrichment than the NG blend.

More recently, Nilsson et al. [80], using the HFM set-up, experimentally and numerically investigated the influence of H_2 (up to 50% addition) upon a NG blend composed of $CH_4/C_2H_6/C_3H_8$ (80/10/10 vol.%). The study likewise witnessed enhanced flame speed, attributed to increases in H and OH radicals. Very recently, Khan et al. [100] upon application of the SEF configuration examined the impact of H_2 addition (25%, 50%, 75% vol. enrichment levels) to different multi-component NG compositions ($CH_4/C_2H_6/C_3H_8$), evaluating the impact on both U_L and L_b. It was concluded that for lean mixtures, H_2 addition lowered Le and by extension L_b, with flames containing the highest concentrations of CH_4 most affected. Moreover, it was concluded that for additions of > 50%, H_2 dominates the overall oxidation of NG/H_2 blends.

Clearly, the experimental study on the addition of H_2 on NG blends containing varying quantities of higher hydrocarbons is scarce, and can to the author's best knowledge, be summarised to the recent studies of Nilsson et al.[80] using the HFM and Khan et al.[100] employing the SEF configuration. Whilst Khan et al.[100] experimented upon different composition of NG, thereby generating valuable data in terms of U_L and L_b (seemingly the only data set available in that respect), two of their three NG blends exhibit a Wobbe Index well above current regulations (and above proposed potential regulations, see Chapter 1). As such, it appears that to date, no experimental study in the literature that investigates practically relevant NG compositions respecting industrial Wobbe Index regulations.

2.4 Investigation Objectives

After undertaking the research presented in this chapter it was identified that the laminar burning velocity, the Markstein length and the Lewis number are essential physiochemical and thermo-diffusive flame properties. These parameters are of value when attempting to predict flame behaviour in turbulent environments, reflective of most practical gas turbine applications. As such, they have been chosen as the focus of this study. Several objectives were identified to fulfil the aim of this thesis, outlined in Chapter 1. These are listed below:

- First, to accurately measure flame propagation, the spherically expanding flame configuration will be employed. As such, appropriate extrapolation methods relating flame speed and stretch will need to be reviewed and evaluated, and appropriate analytical techniques developed.
- Work will be undertaken to better understand large scatter in published flame speed and Markstein length datasets observed for similar experimental conditions, ensuring accuracy of results presented.
- To correctly assess the thermo-diffusive behaviour of investigated fuels and the potential impact on exhibited stretch-related behaviour, theoretical relationships linking fundamental flame parameters and the Lewis number need to be explored. Moreover, computational methods enabling calculation of transport properties need to be developed and utilised to accurately evaluate the Lewis number of fuel mixtures.
- A range of representative fuel blends need to be selected for experimental examination, including investigation of the main components of natural gas, and NG/H_2 relevant binary and tertiary mixtures. Work will be undertaken to investigate the impact of varying content of hydrogen and higher hydrocarbons under lean conditions on combustion characteristics, flame front stability and propagation of methane-based fuels.
- To assess insights gained on the combustion behaviour of fuel mixtures tested, the behaviour of lean limit, turbulent flames, using a premixed generic swirl burner, more representative of GT configuration shall be investigated.
- Whilst gaining empirical trends for the combustion of selected fuels and blends, attention will also be directed towards computational chemical kinetic modelling. The performance of suitable reaction mechanisms will be appraised with respect to accuracy of modelling laminar burning velocities of gas mixtures.

Chapter 3. Flame Theory and Methodology of Numerical Calculations

This chapter outlines the theory and methods of calculations employed for this work. This includes a derivative analysis for measuring the laminar burning velocity (U_L) using the spherically expanding flame (SEF) configuration. Theoretical relationships linking Lewis number (Le) and Markstein length (L_b) are explored, as well as '*effective*' Lewis number formulations (Le_{eff}) proposed in literature to characterise multi-component fuel mixtures. Likewise, calculations employed to calculate various fundamental flame parameters necessary for the completion of the work undertaken are presented and assessed to ensure the correct application of methods and precision of attained values.

3.1 Flame Configuration and Analysis

The flame configuration and analysis described herein for an outwardly propagating spherical flame is an adaptation of the method initially developed by Dowdy et al. [119] and Taylor [79]. In this method, a quiescent combustible mixture at a known equivalence ratio (Φ, defined in Section 2.3, Eqn. 2.4) and initial temperature and pressure is introduced to a constant volume chamber and centrally ignited. The outward propagation rate of the positively stretched spherical flame can then be measured as it travels towards the chamber walls.

Several challenges are associated with this technique and potentially give rise to sources of uncertainty in attained measurement. Early flame propagation can be influenced by the ignition energy relied upon to initiate combustion [86] and potential heat loss to the electrodes, whilst slow-propagating flames are susceptible to buoyancy. Furthermore, the expansion of the combusted products leads to an augmentation of the flame speed, simultaneously increasing pressure within the vessel. This rise in pressure leads to a compression of the unburnt gas ahead of the flame, inhibiting flame propagation and simultaneously increasing the reactant's temperature [41]. As such, great care must be taken when selecting appropriate measured data ranges.

These factors are discussed and quantified in Chapter 5, which includes an uncertainty analysis related to the flame speed of lean and stoichiometric methane/air mixtures, at ambient conditions of temperature and pressure.

First, a derivative analysis for measuring the laminar burning velocity and Markstein length using the SEF configuration is presented. A schematic representation of the outwardly propagating spherical flame is depicted in Figure 3.1.

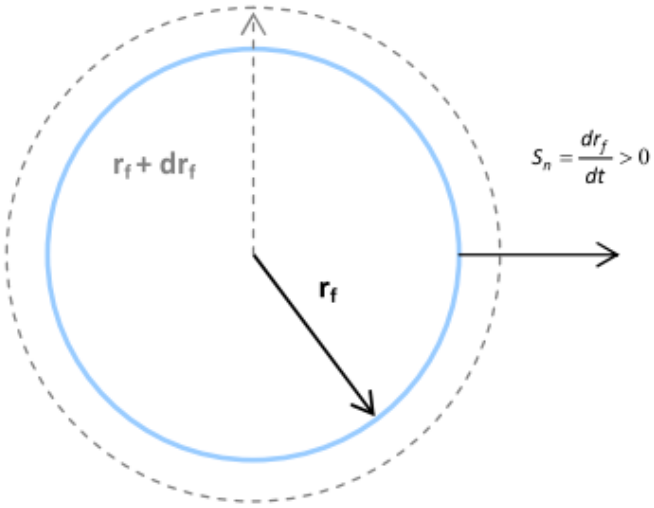

Figure 3.1 – Outwardly Propagating Spherical Flame Schematic [62]

The observed flame speed (S_n), is the measured rate of increase in the flame radius (r_f) with respect to time (t), giving:

$$S_n = \frac{dr_f}{dt} \qquad \text{Eqn. (3.1)}$$

This observed flame speed, being curved and non-stationary does not conform to the definition of the steadily freely propagating planar flame necessary to quantify laminar burning velocity. Furthermore, this observed flame speed has been accelerated by the expansion of the combusted products and is subjected to stretch effects. As such, this observed flame speed, shall be identified in text for the remainder of this thesis as the *stretched flame speed* (S_n). The effects of the expansion of combustion products and the influence of stretch must be removed in order to evaluate the experimental laminar burning velocity.

3.1.1 Stretch for Spherically Expanding Flames

The stretch rate (α), was previously defined as the rate of change of flame area with time (Section 2.1.1, Eqn. 2.1). For a SEF, stretch is defined in the ensuing manner [41], [62], [79], [119]. A spherical flame's surface area (A) can be defined as:

$$A = 4 \cdot \pi \cdot r_f^2 \qquad \text{Eqn. (3.2)}$$

Substituting Eqn. (3.2) into (2.1) for stretch rate, gives:

$$\alpha = \frac{1}{A} \cdot \frac{dA}{dt} = \frac{1}{4 \cdot \pi \cdot r_f^2} \cdot \frac{dA}{dt}$$

$$= \frac{1}{4 \cdot \pi \cdot r_f^2} \cdot \frac{dA}{dr_f} \cdot \frac{dr_f}{dt}$$

$$= \frac{1}{4 \cdot \pi \cdot r_f^2} \times (8 \cdot \pi \cdot r_f) \cdot \frac{dr_f}{dt}$$

$$= \frac{2}{r_f} \cdot \frac{dr_f}{dt} \qquad \text{Eqn. (3.3)}$$

Substituting Eqn. (3.1) into Eqn. (3.3) thus gives:

$$\alpha = \frac{2}{r_f} \cdot S_n \qquad \text{Eqn. (3.4)}$$

The stretch rate defined for this method of flame speed measurement encompasses both the influence of flame curvature (α_C) and flow-field strain (α_S), $\alpha = \alpha_C + \alpha_S$ as demonstrated by Bradley et al. [86]. Using this formulation, measured stretched flame speed can be corrected to attain the unstretched flame speed (S_u). In order to do so, several models relating S_u and L_b have been proposed over the last three decades and are discussed below.

3.1.2 Extrapolation Equations

In this thesis, three methods have been relied upon, to extract the unstretched flame speed.

3.1.2.1 Linear Extrapolation Techniques

The first methodology to extrapolate the measured flame speed to zero stretch and its associated relation was proposed by Wu and Law [64], and has since been the most commonly applied model. This linear relationship is based upon the assumption that mass and thermal diffusion are near equal (Le ≈ 1) and that the flame is weakly stretched [85]. Dowdy et al. [119] and Taylor [79], employed this reasoning, suggesting that α and flame speed are linearly related in the following manner:

$$S_u - S_n = L_b \cdot \alpha \qquad \text{Eqn. (3.5)}$$

with the burned Markstein length (L_b) being the parameter characterising the effect of stretch on flame propagation. Having measured S_n and calculated corresponding values of α, the two can be plotted, with the gradient representing L_b. Note that the sign and magnitude of L_b are directly related to Le. Extrapolation of the relationship can be undertaken to a corresponding intercept value (α = 0), equivalent to a flame speed influenced by zero stretch, thereby attaining the unstretched flame speed, for a theoretical spherical flame of infinite radius.

Fundamentally, the influence of stretch on flame speed originates from two sources [41], [85]. The first, as mentioned previously (Section 2.1, Eqn. 2.2), is the Lewis number and preferential diffusion, quantified through the Markstein number (Ma), $Ma = L_b/\delta_G$, where (δ_G) is known as the gradient flame thickness (defined later, Section 3.5). The second, through the Karlovitz number (Ka), identified as, $Ka = \alpha \times (\delta_G/S_n)$, which is measure of the flame time in

terms of the aerodynamic time (i.e. the normalised stretch rate) [41]. The combined effect is given as Ma × Ka.

Noting the above, Eqn. (3.5) can also be expressed as:

$$\frac{S_n}{S_u} = 1 - Ma \cdot Ka \qquad \text{Eqn. (3.6)}$$

The linear methodology has been extensively applied, for example in [73], [75]–[77], [79]. For fuel mixtures exhibiting Le deviating from unity, the application of the linear relationship has been demonstrated to over-predict both the laminar flame speed and the Markstein length [85], [120]. Consequently, the linear relationship is unable to account for observable non-linearity of S_n against α, when the flame is heavily influenced by stretch effects [68], [78]. This methodology will be referred to as LM(S) in text (i.e. Linear Model based on Stretch).

The second methodology is a model attributed to Frankel and Sivashinsky [121], which was originally proposed by Markstein [59], based upon the assumption of large flame radii. Frankel and Sivashinsky analysed a spherically expanding propane flame, considering the effects of thermal expansion and Lewis Number, and obtained the follow equation:

$$S_n = S_u - S_u L_b \cdot \frac{2}{r_f} \qquad \text{Eqn. (3.7)}$$

Eqn. 3.7 shows that the flame curvature (κ) = $(\frac{2}{r_f})$ and S_n vary linearly. As such, S_u and L_b can be obtained from linear extrapolation, based on the plot of S_u against $(2/r_f)$ [84], [85]. This methodology will be referenced in text as LM(C) (i.e. Linear Model based on Curvature).

3.1.2.2 Non-Linear Extrapolation Technique

The third methodology is a non-linear model proposed by Kelley and Law [68], based upon the theoretical work of Ronney and Sivashinsky [66]. This non-linear model allows for arbitrary Le and accounts for deviations in adiabatic and planar assumptions, which are more prominent for flames heavily influenced by stretch [62], [85]. This non-linear relationship can be expressed as:

$$\left(\frac{S_n}{S_u}\right)^2 \cdot In\left(\frac{S_n}{S_u}\right)^2 = -\frac{2 \cdot L_b \cdot \alpha}{S_u} \qquad \text{Eqn. (3.8)}$$

This methodology of extrapolation has been used frequently over the last decade, and has improved accuracy, as reported in [68], [78], [84]. This method will be referenced in text as NM(S) (i.e. Non-linear Model based on stretch).

Variations of this non-linear relationship has been proposed to improve accuracy [68], [78], [85], [122]. Work by Chen [84] demonstrated that extrapolation with LM(C) generated more accurate U_L for mixtures exhibiting Le > 1 (+ L_b) , whilst NM(S) should be

preferred for mixtures displaying Le < 1 (– L_b). Consequently, these recommendations have been adopted in this thesis.

3.1.3 Correcting Unstretched Flame Speed for Expansion of Combustion Products

Irrespective of the methodology employed, the influence of the expansion of the hot products on the unstretched flame speed must be considered to attain a representative laminar burning velocity. The adiabatic expansion, at constant pressure can be termed as the ratio of the burned (ρ_b) and unburned (ρ_u) gas densities, (ρ_b/ρ_u) [41], [62]. The laminar burning velocity can be thus evaluated through:

$$U_L = S_u \cdot \left(\frac{\rho_b}{\rho_u}\right) \qquad \text{Eqn. (3.09)}$$

Accounting for the influence of adiabatic expansion upon S_u to attain U_L in this manner is extensively applied, for example in [62], [73], [75]–[77], [79]. Evaluation of ρ_u is relatively straightforward, however this is not the case for ρ_b. For the purpose of this work, ρ_b was calculated using the CHEMKIN-PRO software. Detail of the chemical kinetic software and reaction mechanisms utilised are overviewed in Chapter 4, Section 4.3.

3.2 Lewis Number and Markstein Length

Markstein Lengths are indicative of the influence of stretch on flame speed. In premixed flames, instabilities result from hydrodynamic effects, known as Darrieus-Landeau (from the thermal expansion of gases) and preferential-diffusional (thermo-diffusive effects, i.e. Lewis Number) instabilities [41], [75]. As such, Markstein lengths represent a measure of a flame's susceptibility to instability, and should be viewed as indicator of the effect, not the cause. Several analytical formulations linking Le and L_b have been proposed in literature and will be explored. First, an explanation of the effects of stretch on a SEF in the presence of non-equidiffusion will be discussed.

3.2.1 Conceptual Explanation of Non-Equidiffusion on SEF

Considering a SEF, propagating outwards, which has flame radius (r_f) much larger than its thickness. This thickness is composed of a thermal and limiting reactant layer, denoted as (r_T) and (r_M), respectively [41]. For a time set interval, *d*t, the flame expands by *d*r_f, with this growth being much smaller than r_f, r_T, r_M, schematically depicted in Figure 3.2. As such, the volume of thermal energy will be augmented by approximately, $\frac{4}{3}\pi\ (r_T + dr_f)^3 - \frac{4}{3}\pi\ (r_T)^3$, i.e. (≈4 π r_T^2 *d*r_f). The same applies for reactant concentration, $\frac{4}{3}\pi\ (r_M + dr_f)^3 - \frac{4}{3}\pi\ (r_M)^3$, i.e. (≈4 π r_M^2 *d*r_f). Acknowledging that diffusive transport mechanisms travel

normal to the direction of the flame, thus for a non-unity Le interpretation, the increase in heat symbolizes an increase loss of heat transfer away from the flame to the surroundings. Conversely, an increase in the reactant concentration, signifies an increased amount of chemical supply from the surroundings to the flame. By extension, the flame temperature is impacted. Therefore, if $r_T > r_M$ (meaning Le > 1), then heat loss exceeds chemical energy gain, with the flame temperature (T_f) expected to be reduced from T_{ad}. Equally, the opposite holds true for $r_M > r_T$ (Le < 1).

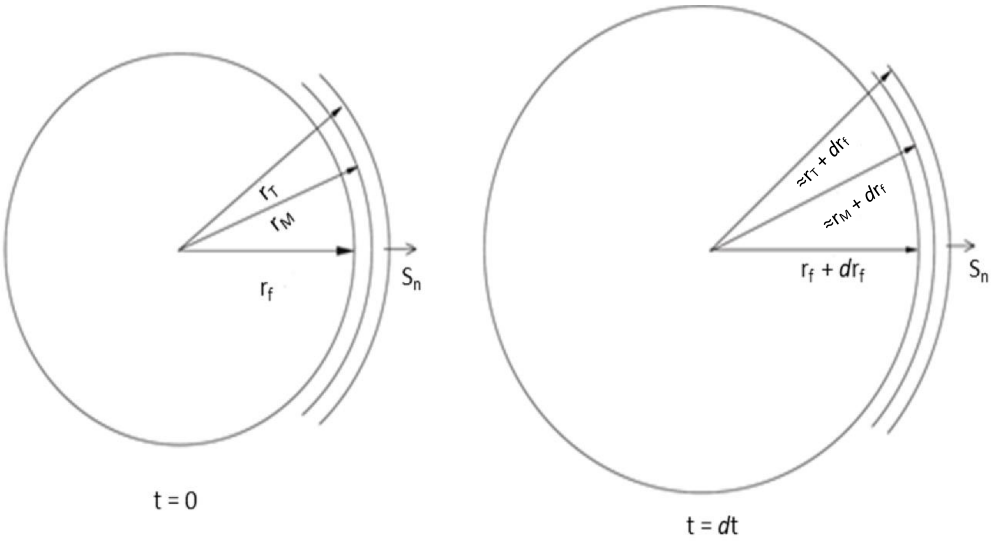

Figure 3.2 – Conceptual Schematic of Stretch Effects on Spherically Expanding Flames in the Presence of Non-Equidiffusion – Adapted from [41]

Counterintuitively, it could be thought that for a SEF exhibiting Le > 1, meaning $T_f < T_{ad}$, the flame would decelerate as it expands, whilst an expanding flame with Le < 1, meaning $T_f > T_{ad}$, the flame would accelerate, since flame speed is sensitive to temperature. However, stretch intensity is largest at small flame radii (early flame development), due to more important flame curvature. Consequently, as the flame expands, the stretch effects steadily decrease, with the flame temperature temporally varying with the stretch rate [41]. As such, for a SEF with an Le > 1, the flame would be accelerating, whilst the opposite holds for Le < 1. For this reason, flames displaying Le > 1 would be weakened in highly stretched (turbulent) environments, whilst flames exhibiting Le < 1 would accelerate. This thermo-diffusive flame response is fundamental and will inevitably impact the operation of practical combustion systems.

3.2.2 Lewis Number Calculation Methods

In order to evaluate the Lewis number, both the thermal diffusivity and mass diffusivity of the mixture must be determined (Section 2.1.1, Eqn. 2.2). The thermal diffusivity, $D_T = \lambda/(\rho_u/C_p)$, requires the calculation of the thermal conductivity (λ), the specific heat (c_p) and the unburnt mixture density (ρ_u). The calculation of the ρ_u and c_p were based on the ideal gas theory and are relatively straightforward. The evaluation of the λ_i and mass diffusion co-efficients (D_{ij}) are substantially more challenging and are detailed herein. Calculated values of D_T and D_{ij} are compared to the National Institute of Standards and Technology (NIST) chemistry web-book [123] and the STANJAN transport property calculator, available through the web-page of the Colorado State University [124], to ensure accuracy of determined values.

3.2.2.1 Specific Heat of Individual Species and Mixtures

The specific heat of each individual specie was evaluated using the Shomate equation as commonly recommended [41], [125]. The polynomial co-efficients for the various species are accessible in the NIST-JANAF Thermo-Chemical Tables [126] and the NIST chemistry web-book [123]. The Shomate equation takes the form of:

$$c_p = A_i + B_i T \ + C_i T^2 + \ D_i T^3 + \frac{E_i}{T^2} \qquad \text{Eqn. (3.10)}$$

The co-efficients, A_i, B_i, C_i, D_i and E_i for each individual specie can be found in Appendix – A.1. The specific heat of the mixture, ($c_{p,mix}$), was evaluated using the following mass-fraction weighted formulation:

$$c_{p,mix} = \sum_{i=1}^{N} Cp,_i \ x \ Y_i \qquad \text{Eqn. (3.11)}$$

where ($c_{p,i}$) and (Y_i) are the specific heat and mass fractions of the i^{th} species, respectively. For the purpose of this study, a 298 K temperature was used. The impact of selecting a higher isotherm (1000 K) for the calculation of Le is presented Chapter 6, Section 6.2.

3.2.2.2 Thermal Conductivity and Diffusivity of Individual Species and Mixtures

For the thermal conductivity of the combustible mixture to be calculated, the individual thermal conductivities of the gaseous components must be determined. The thermal conductivity of each individual species (λ_i) was calculated using the method employed by Clarke [127] and outlined by Poling et al. [125]. Using this method, λ_i is determined as a function of temperature only, by assuming a constant pressure of 1 bar. Between 1~10 bar the effects of pressure are relatively small, resulting in expected error of less than 5% [125], [127].

Two expressions were applied depending on which species was being assessed, expressed below:

$$\lambda_i = A + BT + CT^2 + DT^3 \quad \text{Eqn. (3.12a)}$$

$$\lambda_i = \frac{AT^B}{\left(1 + \frac{C}{T} + \frac{D}{T^2}\right)} \quad \text{Eqn. (3.12b)}$$

The co-efficients, A, B, C, and D for each individual species can be found in Appendix – A.1. Eqn. (3.12a) was utilised for the determination of λ_i for O_2, N_2, CH_4, C_2H_6 and C_3H_8, Eqn. (3.12b) was applied for C_4H_{10}.This method will be denoted in text as the Clarke method. A second method was evaluated, based upon the Chung et al.[128], [129] method, outlined by Poling et al. [125]. This calculation procedure uses a predictive method to estimate λ_i, and requires only the critical temperature (T_c), volume (V_c) and pressure (P_c) as inputs, available in [125], tabulated in Appendix – A.1. This correlation has been compared to extensive testing with experimental data and has demonstrated to be robust, with deviations of expected λ_i < 6% [129].

Differences between calculated λ_i for fuels investigated in this study using the Chung and Clarke methods with NIST values are presented in Table 3.1. Difference is evaluated on a percentage change basis, that is:

$$Percentage\ Change = \frac{(V_2 - V_1)}{|V_1|} \times 100 \quad \text{Eqn. (3.13)}$$

where (V_1) and (V_2) represent the original and new value. In this case, V_1 and V_2 correspond to λ_i from NIST and λ_i evaluated herein, respectively. As can be seen from Table 3.1, good agreement is seen with methods applied for this work and NIST values for all the major components of natural gas, with the evaluation of the λ_i for H_2 generating largest differences (≈7%). Note however, that NIST λ_i have a quoted uncertainty of ± 3% [123].

Table 3.1 – Differences in Thermal Conductivity Between Chung & Clarke Methods and NIST Values (at T_u=298 K, 1 atm)

Species	CHUNG [128], [129] (W/m.K) x10^{-3}	CLARKE [127] (W/m.K) x10^{-3}	NIST Values [123] (W/m.K) x10^{-3}	Difference With CHUNG (%)	Difference with CLARKE (%)
O_2	26.38	26.30	26.73	-1.31	-1.61
N_2	26.50	25.54	26.05	1.73	-1.96
CH_4	33.60	33.65	34.30	-2.04	-1.90
C_2H_6	21.10	21.18	21.96	-3.92	-3.55
C_3H_8	17.60	17.57	18.31	-3.88	-4.04
C_4H_{10}	16.31	16.18	16.56	-1.51	-2.29
H_2	172.39	/	185.63	-7.13	/

For multi-component fuels, the mixed average thermal conductivities (λ_{mix}) were calculated using Mathur et al.'s [130] suggestion:

$$\lambda_{mix} = \frac{1}{2}\left(\sum_{i=1}^{N} X_i\lambda_i + \frac{1}{\sum_{k=1}^{N}\frac{X_i}{\lambda_i}}\right) \quad \text{Eqn. (3.14)}$$

where (X_i) and (λ_i) are the mole fraction and thermal conductivity of the 'i^{th}' species, respectively. This method has been previously employed by Bouvet et al. [131]. To ensure the validity and correct application of the methodologies employed to calculate the thermal diffusivity, evaluated values are compared to values calculated using the STANJAN transport property calculator, for single, binary and tertiary multi-component mixtures, Table 3.2. Differences (calculated using Eqn. (3.13)) are generally less than ±3%, irrespective of the number of fuels composing the blend, thereby validating the robustness of the methodologies selected and their correct application.

Table 3.2 – Difference in Thermal Diffusivities between Methodology applied and STANJAN Transport Property calculator (T_u = 298 K, P = 1 atm, Φ = 1.0)

Fuel Designation (vol.%)	Thermal Diffusivity (D_T) (cm^2/s)	Thermal Diffusivity (D_T) (cm^2/s) STANJAN [124]	Difference (%)
CH_4 (100)	0.2193	0.2257	-2.84
C_2H_6 (100)	0.2065	0.2103	-1.79
C_3H_8 (100)	0.2024	0.2051	-1.30
C_4H_{10} (100)	0.2001	0.2030	-1.42
H_2 (100)	0.4570	0.4426	3.26
CH_4/C_3H_8 (50/50)	0.2073	0.2110	-1.75
CH_4/H_2 (50/50)	0.2745	0.2710	1.28
$CH_4/C_3H_8/H_2$ (68/17/15)	0.2225	0.2256	-1.34

3.2.2.3 Binary and Multi-fuel Mass Diffusion Co-efficients

Several methods have been proposed in literature to estimate binary mass diffusion co-efficients of low-pressure gases (< 10 bar), with empirical constants based upon experimental data [125]. Two methods have been employed in this work, the first based upon the propositions of Wilke and Lee [132], denoted in text as the *Wilke method*. The second, is based upon the proposals of Hirschfelder, Bird and Spot, detailed in [133], [134], and referenced in text as the *Hirschfelder method*. Values of binary mass co-efficients using both methods have been extensively tested against experimental data, with deviations in the order of 5-10% [125].

A detailed explanation of the assumptions behind both methods is beyond the scope of this thesis, with explanations and examples of application available in [125]. It is, however, necessary to validate the correct application of these methods. As such, selected binary mass diffusion co-efficients evaluated and relied upon for this work are compared to attained values calculated using the STANJAN transport property calculator [124]. Differences in attained values applying the Hirschfelder and Wilke methods (calculated using Eqn. 3.13) are presented in Table 3.3. The binary-mass diffusion co-efficients for all the binary compositions evaluated are listed in Appendix – A.1.

Table 3.3 – Differences in Binary Mass Diffusion co-efficients between Wilke & Hirschfelder Methods and STANJAN Transport Property Calculator (T_u = 298 K, P = 1 atm)

Selected Binary Combination	Wilke [132] (cm^2/s)	Hirschfelder [133], [134] (cm^2/s)	STANJAN [124] (cm^2/s)	Difference (%) with Wilke	Difference (%) with Hirschfelder
CH_4 -> N_2	0.234	0.219	0.223	4.92	-2.00
C_3H_8 -> N_2	0.123	0.113	0.113	8.99	0.04
H_2 -> N_2	0.710	0.739	0.788	-9.89	-6.21
CH_4 -> O_2	0.236	0.220	0.224	5.44	-1.68
C_3H_8 -> O_2	0.120	0.109	0.111	7.67	-1.39
H_2 -> O_2	0.749	0.779	0.817	-8.27	-4.61
CH_4 -> C_3H_8	0.130	0.121	0.123	5.63	-1.85
CH_4 -> H_2	0.672	0.703	0.748	-10.11	-5.98
N_2 -> O_2	0.221	0.204	0.207	6.90	-1.47

Differences between the binary mass diffusion co-efficients attained using the Hirschfelder method exhibit good agreement with values evaluated using the STANJAN transport calculator with differences no greater than ± 2% for the various binary combinations composed of hydrocarbons, O_2 and N_2. With the presence of H_2, the Hirschfelder method predicts smaller binary diffusion co-efficients in contrast to those evaluated using STANJAN, in the order of ≈ 5-6%. The Wilke method on the other hand generates larger differences, in the order of ± 5-10%, in line with expected deviation [125]. Overall, agreement is deemed suitable for the purpose of this work.

Once the binary co-efficients for the combinations of gases have been estimated, an effective formulation of the deficient species in to the mixture must be selected. Conventionally, it is assumed that for fuel-air mixtures the deficient reactant (fuel under lean conditions, Φ <1) is scare in proportion to the surrounding N_2 [41]. Consequently, the binary mass diffusion co-efficient ($D_{i,j}$) is taken as the fuel '*i* ' diffusing into N_2 (denoted with

subscript '*j* ') . Thus, the binary co-efficients are calculated upon the assumption that the fuel is diffusing into the N_2. As highlighted by Lapalme et al. [91], this may hold true for hydrocarbons, due to their high molar fuel-air ratio, but not for molecules that have low molar fuel-air ratio such as H_2. Thus, a mixed-average co-efficient of mass diffusion into the mixture was utilised as proposed by Fairbanks and Wilke [135]:

$$D_{1-mix} = \frac{1}{\frac{X'_2}{D_{1-2}} + \frac{X'_3}{D_{1-3}} + \cdots + \frac{X'_n}{D_{1-n}}} \qquad \text{Eqn. (3.15)}$$

where $D_{1\text{-}mix}$ is the diffusivity of compound 1 into the mixture, ($D_{1\text{-}n}$) the diffusivity of the binary pair, component 1 diffusing through component n, (X'_n) mole fraction of component *n* in the gas mixture evaluated on a component-1-free basis, that is:

$$X'_2 = \frac{X_2}{X_2 + X_3 + \cdots + X_N} \qquad \text{Eqn. (3.16)}$$

Having reviewed the methods utilised to precisely estimate the thermal diffusivity and mass diffusivity of single and multi-fuel fuel air mixtures, the formulations employed to characterise the Lewis number of multi-fuel blends is presented next.

3.3 Effective Lewis Number Formulations for Multi-Fuel Blends

Successful extractions of Lewis numbers for single-fuel mixtures have been previously performed in the framework of flame integral analysis by Sung and co-workers for C_3H_8 and H_2 air flames [136], [137]. Similarly, Jomaas et al. [138] upon application of asymptotic theory have determined Lewis numbers for C_2H_2/air flames at various conditions (pressures and O_2 concentration in air). Jomaas et al. [138] in their concluding remarks, underline that the Lewis number should be considered a global parameter of the flame and not of the free-stream mixtures, and consequently should be evaluated from properties affecting the flame, as for example would be the case when evaluating the global activation energy (E_a).

For multi-fuel blends, the calculations of the Lewis number can become challenging, since the diffusivity of each fuel must be considered. This is especially applicable to blends of H_2 and hydrocarbons, which exhibit different transport diffusion mechanisms and flame characteristics. The revival in interest of blending H_2 to natural gas in order to extend lean operational limits, and the inherent risks associated to the high reactivity of H_2, underline the importance of correctly assessing fundamental combustion properties. Whilst the calculation and definition of Le for single-fuel mixtures can be considered relatively straightforward, their still does not seem to exist a consensus on the correct formulation of Le to be employed for multi-fuel blends [131].

Bouvet et al. [131], identified three 'effective' Le formulations (Le_{eff}). The first, is derived from the asymptotic analysis of high pressure H_2/C_3H_8 laminar spherical flames conducted by Law et al. [139]. This formulation has been extensively applied to discuss the thermo-diffusive behaviour (i.e. stable, Le > 1 or unstable nature, Le < 1) of mostly binary and tertiary blends of hydrocarbons and hydrogen [90], [91], [113]–[115], [131], [140]. This formulation, is based upon the weighted average of the fuels non-dimensional heat release (q_i), and can be expressed as (Le_H):

$$Le_H = 1 + \frac{\sum_{i=1}^{f} q_i (Le_i - 1)}{\sum_{i=1}^{f} q_i} \qquad \text{Eqn. (3.17a)}$$

$$where\ q_i = \frac{Q\ Y_{i,unburnt}}{C_p T_u} \qquad \text{Eqn. (3.17b)}$$

where (Q) represents the overall heat of reaction. Eqn. 3.17(a) will be denoted in text as Le_H.

The second, is based upon a volumetric fraction weighted average formulation which stems from the computational study of Muppala et al. [141] on turbulent CH_4-H_2/C_3H_8 flames. This formulation lead to reasonable agreement with experimental burning velocities at low turbulence intensity. Differences between measured and modelled flame speeds increased at higher turbulent intensity, with modelled flame speeds significantly underpredicting burning velocities [141]. This formulation will be referenced in this work as (Le_V), and is expressed as:

$$Le_V = \sum_{i=1}^{f} x_i\ Le_i \qquad \text{Eqn. (3.18)}$$

where (x_i), is the fuel volumetric fraction of the component 'i'.

The third, is related to work by Dinkelacker et al. [140] on lean H_2/CH_4 flames. It is assumed that if flame curvature is dominant, then local enrichment of the most diffusive fuel at the flames leading edge can be expected. This overall reaction-rate enhancement is translated into a volumetric-weighted average of the fuel diffusivities. This formulation will be referenced in this work as (Le_D), and is expressed as:

$$Le_D = \frac{D_T}{\sum_{i=1}^{f} x_i D_{ij}} \qquad \text{Eqn. (3.19)}$$

Since the above formulations are based on the components of the mixture, when referring to Le_V, Le_D, and Le_H as a whole, these will be referenced as effective theoretical Lewis numbers, using the 'Le_{eff}' abbreviation.

Bouvet et al. [131] examined the validity of Le_V, Le_D, and Le_H, using the analytical developments of Chen [84], [120] (detailed in Section 3.4), linking the Markstein length to the Lewis number. Bouvet et al. [131] compared calculated numerical Markstein lengths derived using the different effective Lewis number formulations to experimentally measured Markstein lengths. Analysis was conducted for CH_4/H_2 (Φ = 0.80), C_3H_8/H_2 (Φ = 0.60), C_8H_{18}/H_2

(Φ = 0.80) and H_2/CO (Φ = 0.60). For H_2 and various alkane mixtures, Le_V exhibited best correlation with measured L_b, thereby validating the theoretical model proposed by Chen [84], [120] for these fuel mixtures. No Lewis number formulation adequately captured H_2/CO Markstein lengths (with Le_D generating closest agreement).

More recently, Lapalme et al. [91], applied a similar methodology to Bouvet et al. [131]. Instead of comparing numerical and measured Markstein lengths, as done by Bouvet et al. [131], effective Lewis number formulations were appraised through comparison with experimentally extracted Lewis numbers. These experimental Le were calculated through application of the theoretical relationships proposed by Chen [84], [120], Matalon and Bechtold [142], and Law and Sung [143] (detailed in Section 3.4), extending analysis to H_2/air, CH_4/air, H_2/CH_4 and H_2/CO mixtures, across a wide range of Φ. Lapalme et al. conclude that overall a Le_V formulation exhibited best agreement. They extend this conclusion to include syngas, disagreeing with results presented by Bouvet et al. [131] for that mixture.

3.4 Relationships linking Markstein Length to Lewis Number

Theoretical relationships linking the Markstein length and the Lewis number have been proposed in literature, by Chen [84], [120], Matalon and Bechtold [142], and Law and Sung [143], summarised in [91].

The first method is derived from the analytical developments conducted by Chen [84], [120] on spherically expanding flames, and has been employed by Lapalme et al. [91] and Bouvet et al. [131] in their research around the assessment of Lewis number formulations. This method is denoted herein as Le_{CHEN}, and can be expressed as:

$$Le_{-CHEN} = \left[\frac{L_b}{\sigma\,\delta} - \frac{Ze}{2}\right]^{-1}\left[1 - \frac{Ze}{2}\right] \qquad \text{Eqn. (3.20)}$$

where (Ze), is the Zel'dovitch number, (σ), the expansion ratio, and (δ), the flame thickness, with methods of calculations of fundamental flame parameters detailed in Section 3.5.

Eqn. (3.20) can be re-arranged to retrieve L_b, and will be defined as $L_{b\text{-}CHEN}$:

$$L_{b-CHEN} = \left[\frac{1}{Le} - \left(\frac{Ze}{2}\right)\left(\frac{1}{Le} - 1\right)\right]\sigma\,\delta \qquad \text{Eqn. (3.21)}$$

The second formulation was offered by Bechtold and Matalon [142], produced from their theoretical research on the dependence of the Markstein length on stoichiometry, and was demonstrated to be valid for off-stoichiometric condition. It was utilised by Jomaas et al. [138] for the determination of the Le of acetylene (C_2H_2) in air across a wide range of

conditions and employed by Lapalme et al. [91] for H_2/CO and H_2/CH_4 mixtures. This method is denoted herein as Le_{-BM}, and can be expressed as:

$$Le_{-BM} = 1 + \left[\frac{L_b}{\delta} - \frac{2}{\sqrt{\sigma}+1}\right]\left[\frac{2Ze}{\sigma - 1}\left\{\sqrt{\sigma} - 1 - \ln\left(\frac{1}{2}\left(\sqrt{\sigma}+1\right)\right)\right\}\right]^{-1} \quad \text{Eqn. (3.22)}$$

Eqn. (3.22) can be re-arranged to retrieve L_b, and will be defined as L_b BM:

$$L_{b-BM} = \delta\left[\frac{\gamma_1}{\sigma} + \left\{\frac{Ze}{2}(Le-1)\gamma_2\right\}\right] \quad \text{Eqn. (3.23)}$$

where γ_1 and γ_2 are functions of the expansion ratio:

$$\gamma_1 = \frac{2\sigma}{\left(\sqrt{\sigma}+1\right)} \quad \text{Eqn. (3.24)}$$

$$\gamma_2 = \left[\frac{4}{(\sigma-1)}\right]\left[\sqrt{\sigma} - 1 - In\left(\frac{\left(\sqrt{\sigma}+1\right)}{2}\right)\right] \quad \text{Eqn. (3.25)}$$

The third formulation results from the integral analysis of stretched H_2/air and C_3H_8/air flames conducted by Law and Sung [143]. The reference point of this formulation is based upon the unburnt Markstein length (L_u), evaluated from the burnt Markstein length (L_b), see Eqn. (3.28). This method is denoted herein as Le_{-LAW}, and takes the form of:

$$Le_{-LAW} = 1 + \frac{2\left(1-\frac{1}{\sigma}\right)}{\mathrm{Ze}\left(\frac{1}{\sigma}\right)(1-\bar{\alpha})}\left[\frac{L_u}{\delta} + \left(1-\frac{1}{\sigma}\right) - \left(\frac{1-\bar{\alpha}}{1-\frac{1}{\sigma}}\right)\right] \quad \text{Eqn. (3.26)}$$

where ($\bar{\alpha}$) and (L_u) are given by:

$$\bar{\alpha} = 1 + \ln\left[\frac{1}{\sigma} + \left(1 - \frac{1}{\sigma}\right)\exp(-1)\right] \quad \text{Eqn. (3.27)}$$

$$\mathrm{L_u} = \frac{L_b}{\sigma} + \left(\bar{\alpha} - \frac{1}{\sigma}\right)\delta \quad \text{Eqn. (3.28)}$$

Theoretical correlations of L_b and Le as proposed in literature require the calculation of various flame parameters. The methods employed in this thesis for their evaluation are presented next.

3.5 Evaluation of Fundamental Flame Parameters

The relationships between L_b and Le are explicitly related to fundamental flame parameters, with the Zel'dovitch Number (Ze), the flame expansion ratio (σ), and the flame thickness (δ). All flame parameters were numerically calculated using CHEMKIN-PRO software with the PREMIX code. Further detail of the chemical kinetic software and reaction mechanisms utilised are presented in Chapter 4, Section 4.3.

3.5.1 Activation Energy and Zel'dovitch Number

The Zel'dovitch number is defined as the non-dimensional form of the single-step activation energy (E_a) [41]. It can be calculated using the expression:

$$\mathrm{Ze} = \frac{E_a(T_{ad} - T_u)}{(R^0 T_{ad}^2)} \qquad \text{Eqn. (3.29)}$$

where, (R^0), the universal gas constant, (T_u), the temperature of the unburnt mixture and (T_{ad}), the adiabatic flame temperature. The activation energy, E_a, is defined as the slope of the mass burning flux and the inverse adiabatic flame temperature at constant equivalence ratio (Φ) and pressure (p), and can be empirically determined through:

$$E_a = -2\,R^0 \left[\frac{\partial ln\,(m^0)}{\partial\left(\frac{1}{T_{ad}}\right)}\right]_{\Phi,p} \qquad \text{Eqn. (3.30)}$$

in which the mass burning flux, (m^0) is the eigenvalue of laminar flame propagation, and can be replaced by $m^0 = \rho_u \times U_L$, as recommended by Egolfopoulos and Law [144].

Two common methods are applied to vary the mass burning flux in order to evaluate the differential. The first by slightly perturbing the diluent concentration as done by [91], [131], [137], [144]. Kumar and Sung [145] note that by varying m^0 and T_{ad} through different levels of nitrogen dilution, the reactant concentrations are also altered. As such, a second method based upon preheating the unburnt gas is advised. The preheat method was applied herein, which was achieved by varying the unburnt gas temperature in PREMIX, as done by [88], [145]. Depicted in Figure 3.3 (a), is the Arrhenius plot demonstrating the dependence of the mass burning flux on adiabatic temperature for CH_4/air mixtures across varying Φ (T_u = 298-450 K, P=0.1 MPa), with the slope of the linear regression proportional to the overall activation energy. The linear variation of (*In* m^0) with ($1/T_{ad}$) witnessed during this work validates this extraction method, with R-squared values (R^2) of at least 0.999. Note, however that Eqn. (3.30) is only valid for sufficiently off-stoichiometric conditions and E_a values for mixtures near stoichiometry have to be interpolated [138], as illustrated in Figure 3.3 (b).

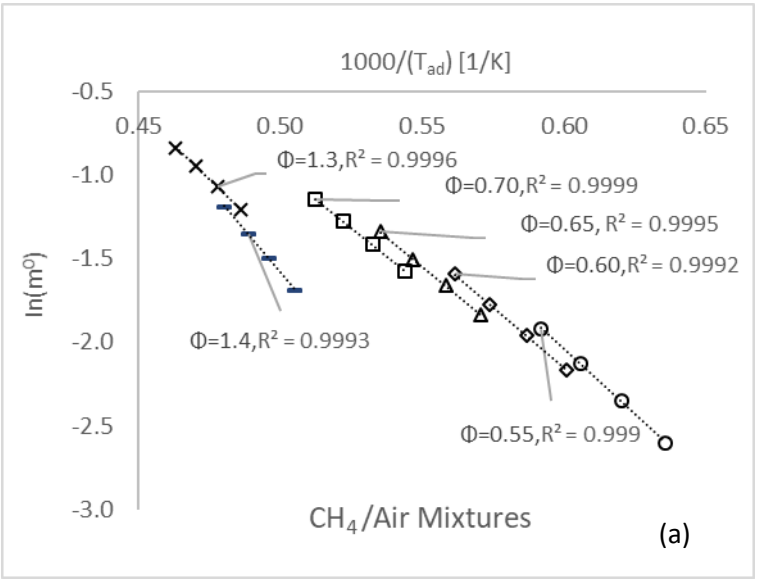

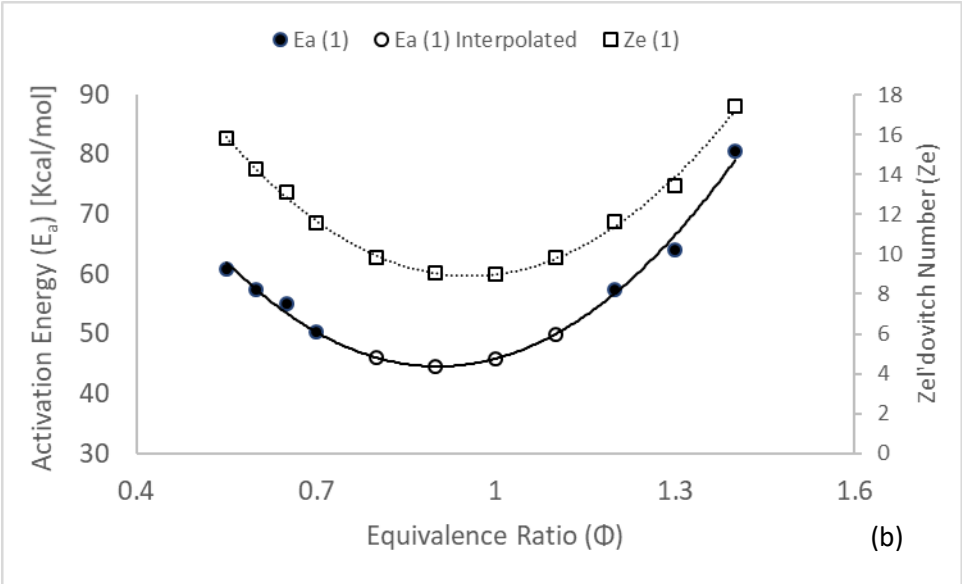

Figure 3.3 – (a) Arrhenius Plot Demonstrating the Dependence of the Mass Burning Flux on Adiabatic Temperature for CH_4/air Mixtures across Φ (b) Plot of E_a and Ze as a Function of Φ for CH_4/air

Müller et al. [146] propose an approximation to calculate Ze, based upon the inner layer temperature (T_0) as a supplementary variable, in the form of:

$$Ze = 4\,\frac{(T_{ad} - T_u)}{(T_{ad} - T_0)} \qquad \text{Eqn. (3.31)}$$

T_0, is the inner layer temperature demarking the start of the reaction zone. T_0 can be extracted as the maximum point of the slope of the temperature profile and the flame co-ordinate system, using CHEMKIN-PRO software, see Figure 3.4. As discussed in literature [41], [100], for Ze → ∞, Ze can be assessed through:

$$Ze = \frac{E_a}{R^0}\,\frac{(T_{ad} - T_u)}{T_{ad}^2} \qquad \text{Eqn. (3.32)}$$

As such after calculating Ze using Eqn. (3.31), the E_a can be evaluated using Eqn. (3.32), as done in [100]. For the purpose of this work, the E_a and Ze evaluated using both methods are compared and presented in Chapter 6. In order to distinguish between both methodologies,

E_a (1) and Ze (1) will refer to values attained using the pre-heat method [144], whilst E_a (2) and Ze (2) will refer to values attained using the approximation proposed by Müller et al. [146].

3.5.2 Flame Thickness

Two definitions of the laminar flame thickness have been proposed and employed in literature [41]. The first, commonly referred to as the kinetic (or diffusion) thickness, (δ_K), is given by:

$$\delta_k = \frac{\lambda}{\rho_u \, c_p \, U_L} \qquad \text{Eqn. (3.33)}$$

where (λ) represents thermal conductivity, (ρ_u) the unburnt density of the combustible mixture, and (c_p) the specific heat. Jomaas et al. [138], underline the ambiguity of this definition, most notably the temperature at which the (λ/c_p) ratio should be assessed (T_u = 298 K for this study) . As such an expression of the flame thickness relying upon the extraction of the gradient of the temperature profile with axial distance through the flame is proposed [41], [138]. This approximation relies upon the application of a linear gradient as the tangent of the inflection, which corresponds to $(dT/dx)_{max}$, from unburnt (T_u) to burnt conditions (T_{ad}), numerically modelled using the CHEMKIN-PRO software [41], [62]. This flame thickness, (δ_G), schematically depicted in Figure 3.4, can be expressed as:

$$\delta_G = \frac{T_{ad} - T_u}{\left(\frac{dT}{dx}\right)_{max}} \qquad \text{Eqn. (3.34)}$$

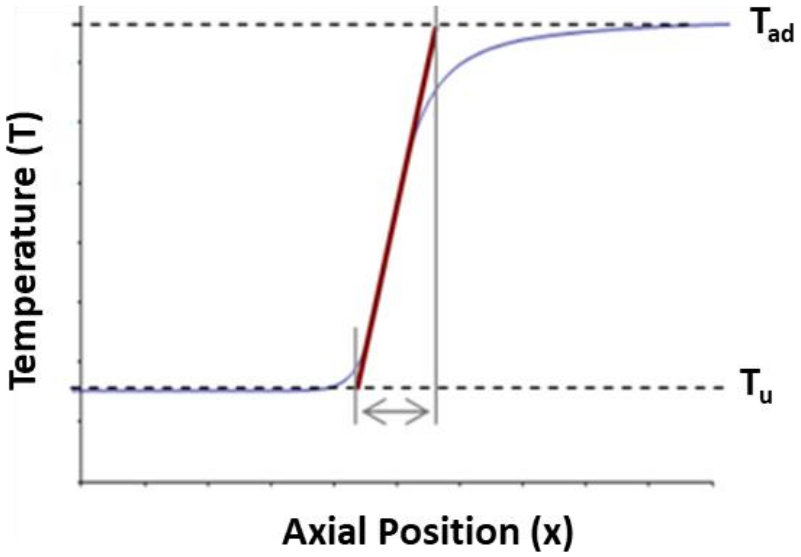

Figure 3.4 – Theoretical Use of Temperature Profile to Obtain Gradient Flame Thickness (δ_G) [41], [62]

The diffusion flame thickness (δ_K) definition is consistent with the approach detailed by Chen [84], [120], whilst the gradient flame thickness definition is consistent with approach detailed by Law [143] and Sung and Bechtold and Matalon [142], and thus will be utilised accordingly.

3.5.3 Thermal Expansion Ratio

The thermal expansion ratio (σ) applied herein is defined as $\sigma = \rho_u/\rho_b$, consistent with the approach described by Matalon [138], [142] , but the reciprocal of the one employed by Chen [84], [120].

3.6 Chapter Summary

Spherically expanding flame theory and various linear and non-linear models commonly employed to evaluate L_b and U_L were introduced. Relationships between L_b and Le were presented alongside methods utilized to evaluate fundamental flame parameters.

Effective Le formulations to characterise multi-component fuels were reviewed. Since there does not appear to exist a consensus on the correct formulation of Le to be employed for multi-component fuel blends, effective Le formulations will be appraised for the variety of fuel mixtures studied in this work.

Methods employed to calculate mass diffusion and thermal diffusivity for single and multi-fuel blends generated good agreement with the STANJAN property calculator (based on the CHEMKIN library), thereby validating correct application and ensuring accuracy of numerical Le values presented in this thesis

Reference properties, constants and co-efficients employed, including the evaluated thermal conductivities and binary mass diffusion co-efficients are provided in Appendix – A.1.

Chapter 4. Experimental Equipment, Data Processing & Benchmarking

Spherically expanding flames (SEF) experiments were conducted in a well characterised [62], [89], [147] cylindrical constant volume combustion bomb (CVCB), located at the Gas Turbine Research Centre (GTRC), affiliated to Cardiff University. This chapter overviews the specifications of the major system components, employed experimental procedure and data acquisition techniques. A benchmarking exercise was undertaken on lean methane/air flames, to ensure the correct utilization of apparatus and data-extraction methods employed.

4.1 Experimental Equipment - System Overview

A simplified schematic overview of the experimental set-up, with labelled ancillary components is presented in Figure 4.1. The CVCB is constructed using stainless steel (316 grade) and possesses an internal volume of 0.0349 m^3 (~35 Litres). Burke et al. [87] in their study on the effect of cylindrical confinement on outwardly propagating flames, advise a usable flame radius range of no more than 30% of overall chamber dimensions, in order for the flame speed to be relatively unaffected by confinement effects. The constant volume vessel employed has an internal diameter of 260 mm, thereby giving 39 mm of available flame radius data. These design parameters allow for a sufficiently long experimental time lapse to capture flame propagation within the constant pressure region [62]. Four diametrically opposed 100 mm in diameter quartz windows allow for optical access, permitting high-speed image capturing of the SEF inside the combustion chamber.

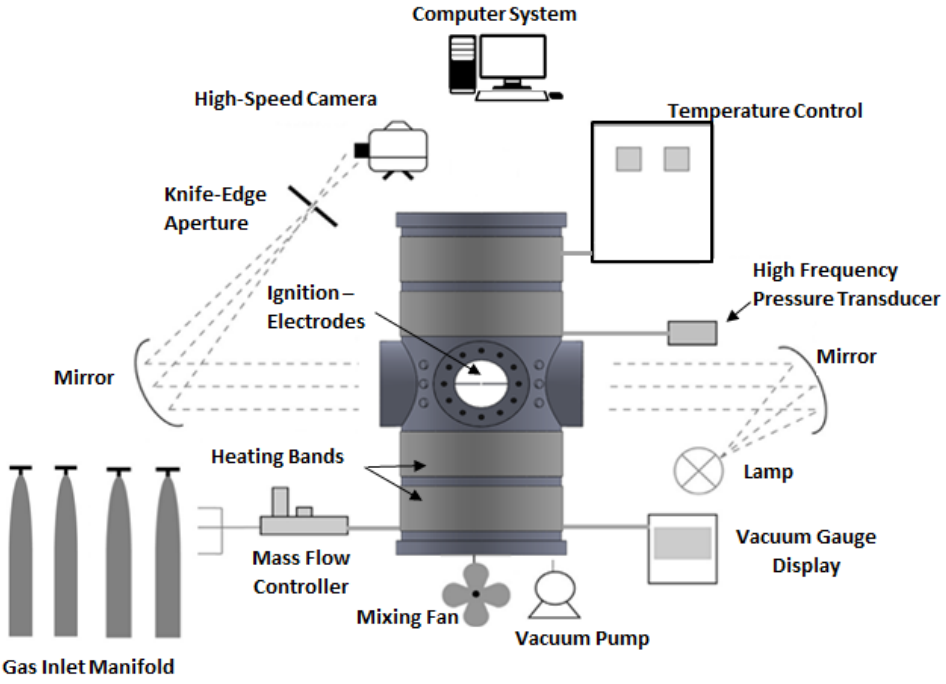

Figure 4.1 – Schematic Overview of Experimental Set-Up, adapted from [62]

4.1.1 Schlieren Optical Imaging Set-up

The flame front was tracked via a Z-type Schlieren cinematographic system, as suggested by Settles [148]. This technique is widely utilised in analogous research, examples of which can be found in [31], [89], [139]. The Schlieren system employed, which is schematically illustrated in Figure 4.2, consists of a light source, two mirrors, an aperture and a high-speed camera.

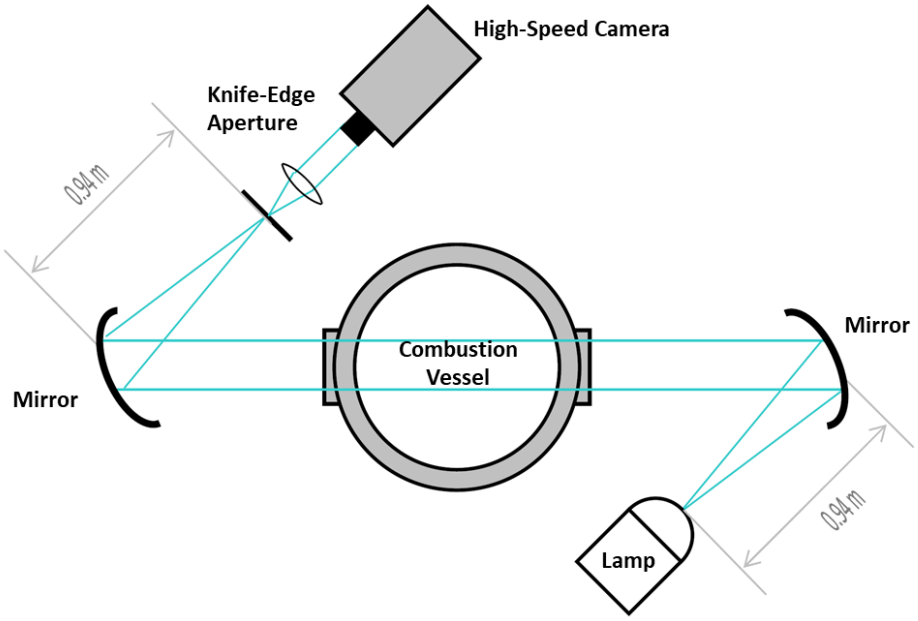

Figure 4.2 – Schematic Representation of Schlieren System Employed in this Work, adapted from [62]

Conceptually, light which is emitted from a filament lamp, is collimated using a converging mirror through two of the diametrically opposed quartz windows. This allows for the parallel light to pass through the centre of the combustion chamber. The light beam is then reflected a second time onto the aperture, with the high-speed camera capturing the refracted light beam not blocked by the knife-edge. This visualization technique exploits light intensity gradients due to the variation in refractive index generated from disparities in gas densities [148]. Consequently, the flame leading edge is represented by either brightened or shadowed fronts. Those captured edges are the result of combustion, representing isotherms were significant density changes are present. These density variations determine the delimitation between burnt and unburnt gases, enabling recording of the temporal evolution of the flame leading edge.

The portion of refracted beam light that passes through the aperture is imperfect and is focussed through a lens and captured by a high-speed motion camera (Photron FASTCAM APX-RS). A specified filming rate of 5000 frames per second was used for all experiments. This frame speed setting allows for the capture of as many usable frames as

possible. Practically, frame-rate is limited by the power and intensity of light in the system as well as shutter speed and image size [149]. The internal processor of the camera controls the timing of the frame capture rate, with a specified full-scale accuracy of 0.005% [149]. Example images from this study are provided in Figure 4.3, underlining the quality of images taken using the Schlieren optical set-up.

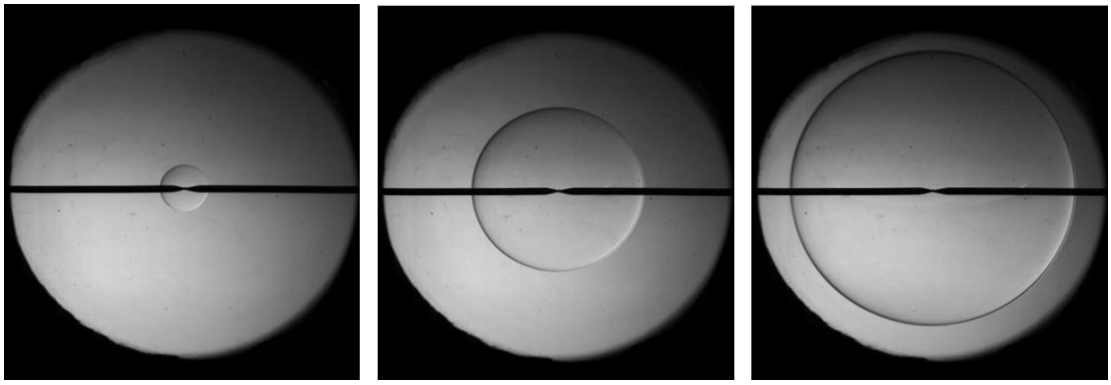

Figure 4.3 – Temporal Evolution of a Spherically Expanding Flame using Schlieren Cinematography

4.1.2 Experimental Equipment – Main Ancillary Components Overview

4.1.2.1 Gas Delivery and Mixing System

Fuel and oxidiser were independently introduced to the combustion chamber using a low flow Coriolis mass flow meter (Bronkhorst mini CORI-FLOW M13). This mass-flow controller uses the Coriolis principle of operation. The Coriolis effect describes the deflection of objects moving in a straight path, when viewed from a rotating frame of reference. The gas flows through a tube which is vibrating, generating changes in amplitude, frequency or phase shift, proportional to the mass flow through the tube. The fluid density is given as a secondary output, allowing to precisely measure the throughput of gas [150]. This contrasts with other flow meter principles which rely on the measurement of the volume, velocity or differential pressure, consequently requiring correction for density, temperature and pressure in order to determine the mass [150].

A dynamic data exchange client program (FlowDDE) was used to communicate between the mass-flow controller and a computer. This allowed for data to be exchanged to and from the mass-flow instrument. An application (FlowView) allowed direct entry of various parameters, including desired mass set-point and counter configuration. A set-point control mode permitted real-time visualization of mass flow output, enabling precise control of desired flow. The mass flow accuracy for a gas using this type of Coriolis flowmeter is ± 0.5% of flow rate [150].

Four fuel valves were connected into a manifold using ¼ inch stainless steel tubing. Those fuel valves were connected to their corresponding fuel lines, with cylinders placed in

a dedicated open-air delimitation zone. Multiple fuel feeds allowed for easy blending of multi-component fuels. An air valve connected to zero-grade cylinder air was also connected to the manifold, as well as an exhaust line. An isolation valve was placed between the manifold exit and the mass-flow controller entry point. This enabled purging of the fuel and air lines connected to the manifold, thereby ensuring the accuracy and control of fuel composition and air entering the combustion chamber, allowing precise determination of desired air fuel ratio. Fuel delivery from cylinders was set to 4 bar for all gases, however, this was revised for hydrogen. Due to the high diffusivity of hydrogen, the fraction of time necessary for the mass-flow controller to open and close its entry point was sufficient for hydrogen to overshoot the set-point. This was confirmed via the internal partial pressure of the combustion vessel, which was used as a verification method to assess correct mass flow input. By lowering the hydrogen fuel delivery line to 2 bar, sufficient time was allowed for the mass-flow controller to respond, ensuring accuracy of mixtures containing hydrogen.

Once the appropriate fresh fuel-air mixtures filled the combustion chamber, the fuel air blend was mixed prior ignition. An internal fan, placed at the bottom of the chamber, ensured adequate mixing. The fan was controlled by an external motor connected to a variable voltage supply. Integrity of vacuum was ensured around the motor shaft with the use of O-ring seals (Rotary Viton fluoroelastometer) which remain functional up to ~500K. The mixture in all experiments would be allowed to mix for an average of one minute, at the same rotational velocity. Once mixing was achieved, the fuel blend rested for 2 minutes. During this time, integrity of the combustion vessel was ensured by observing the internal pressure readout, with a rise indicating a leak. When necessary, appropriate maintenance was undertaken.

4.1.2.2 Vacuum System

A dry-scroll vacuum pump (SCROLLVAC SC15D) was used to remove the contents from inside the combustion chamber. The combustion chamber's internal pressure was available in real-time through the connection of a pressure sensor (Edwards D35727000 ASG 0-2000 mbar) to a real-time pressure instrument controller read-out (Edwards D39700000 TIC 3 head). The pressure sensor has a resolution of 0.1 mbar and a full-scale accuracy of ± 0.2%. Although fresh gases were filled with a mass-flow controller, this set-up allowed to double-check correct fuel composition and air/fuel ratio using internal partial pressure. Exposure to gaseous products was mitigated by placing the combustion vessel under a ventilation hood, with vacuum output and exhaust lines both connected to the extract ventilation system.

4.1.2.3 Temperature Control System

The temperature inside the combustion vessel was regulated using eight external heating bands. The bulk of the combustion vessel was heated using four large external bands, whilst other small localised heaters were employed to avoid cold-spot formation around the viewing windows. Two k-type thermocouples were located inside the combustion vessel, one pointing upwards the other downwards. Those thermocouples were connected to a temperature probe allowing to record temperature. The temperature control system was calibrated using a high precision thermocouple in combination with a dry-block calibrator (Hart Scientific 9100 HDRC). The temperature difference between both thermo-couples was no more than 0.5 ^{o}C. An average of both temperatures was logged as the final temperature.

4.1.2.4 Ignition System

The ignition of fuel mixture was achieved by using a variable voltage supply and auto-ignition coil generating a capacitor ignition system. The variable voltage supply had a range of up to 350 V, and seven capacitors arranged in parallel gave a theoretical summated capacitance of 2.79 µF. The use of a variable voltage supply allowed for the ignition energy to be regulated, giving a theoretical maximum ignition energy of approximately 170 mJ:

$$e = \frac{C \,.\, V^2}{2} \qquad \text{Eqn. (4.1)}$$

where, e= ignition energy (Joules, J), C= capacitance (Farad, F), and V = Voltage (Volts, V). Ignition was triggered using a pulse generator (Farnell PG102 TTL). The high-speed camera and the pulse generator were connected, allowing sequencing of video capture data at the point of ignition. Two stainless steel pointed tip electrodes were placed at a 45-degree angle to the Schlieren plane of measurement, with this set-up decreasing the display of disturbances due to the ignition in Schlieren video images [77].

The electrode gap was varied between 1mm – 3mm whilst a theoretical maximum ignition energy of 170 mJ was kept constant. It was found that a 2mm gap was able to ignite leaner mixtures more repeatably than a smaller 1mm spark gap. The 3mm spark gap was unable to create a repeatable electric arc, however it did allow to drive to leaner conditions when ignition did occur. Consequently, 2mm spark gap was employed for all experiments conducted in this work.

4.2 Experimental Procedure and Data Acquisition

This section describes the detailed step-by-step experimental procedure employed. Following on data acquisition and processing techniques will be discussed.

4.2.1 Test Procedure – Methodology

Each test was conducted in the manner listed below:

1) Before testing, it was ensured that the laboratory and rig environment were set-up according to specific risk assessments and health and safety requirements. Gas monitors (BW Honeywell Micro-clip) placed next to fuel delivery lines, working space and on-self ensured quick detection to possible gaseous product exposure. Personnel protective equipment was used when necessary.
2) The extraction ventilation hood above the combustion rig was switched on.
3) In order to attain the desired temperature inside the combustion vessel, the heating control system was switched on. The temperature probe attached to the two thermocouples inside the CVCB was then monitored until test temperature was achieved. Before the commencement of each new test campaign, the equipment was left on condition for 30 minutes to ensure uniform distribution of heat within the combustion rig. Minor adjustments of heat were sometimes necessary as the day progressed, particularly in colder months.
4) In the meantime, the fuel delivery system was pressure tested for any possible leaks to and from the rig, using nitrogen at 8 bar. If no drop of pressure was recorded during a 20-minute timespan, the fuel lines would then be purged three times. To ensure no left-over residue of nitrogen within the delivery system, the fuel lines would then be vacuumed through the rig using the vacuum pump, to an absolute pressure of 30mbar. Out of caution, the first test conducted each day was not recorded to avoid possible influence of nitrogen contamination. The required fuel cylinders were connected and set at the required pressure.
5) The imaging set-up of the Schlieren system was then conducted. The camera was set to the suitable specifications of frame capture rate, shutter speed, and image size. The effective image darkness would then be standardised against light supply. Image scaling of the camera was then performed using a set of Vernier callipers (detailed in Section 4.2.3). Communication between camera and ignitor was initialised with a chosen trigger mechanism.
6) Communication between the mass-flow controller and the computer was enabled.
7) Mixing and ignition were activated and verified.

8) The contents of the combustion chamber were removed by opening the isolation valve to the vacuum pump. Between each test, any moisture and combustion products would be evacuated, to an absolute pressure of 50mbar. The combustion vessel would then be filled to atmospheric pressure with zero-grade air and evacuated again to an absolute pressure of 50mbar, with this air-purge repeated twice. The choice of using a 50mbar threshold was imposed to some degree by the rate of evacuation of the vacuum pump. As chamber pressure decreased, it would take increasingly more time to reach lower values of pressure. As a comprise between accuracy and time-efficiency the two-purge solution was deemed adequate. Thus, after the second air-purge, it was assumed that the residual pressure contained within the combustion bomb could be added to the air fraction when calculating the air fuel ratio. A contamination level of < 0.1% is generate by using this procedure.
9) Once the starting partial pressure was attained, the system was ready for introduction of fuel and air. Each fuel line was delivered to a separate fuel valve all connected to a manifold. The manifold was also connected to the air supply and an exhaust line. An isolation valve was placed between the mass flow controller and the manifold. The fuel valve would be opened, and the fuel would flow into the manifold. The fuel valve would then be closed, and the pipe manifold purged. This process would be repeated 5 times. This was conducted to ensure that there was no other gas in the manifold, but the desired fuel. The isolation valve would then be opened, allowing the fuel to flow to the mass-flow entry point. The desired mass-set point of fuel was then inserted into the mass-flow application program and delivery of fuel into the combustion vessel commenced. Real-time visualization of mass flow output was available. A screen warning was triggered once desired fuel mass was achieved through the mass-flow controller. The isolation valve would then be closed. Internal pressure of vessel was then verified using the real-time pressure controller read-out and compared to calculated values. This allowed to double check that the correct output of mass had been inserted into the system. This process was repeated depending on the number of fuel component within the blend. Air was inserted into the rig following the same procedure.
10) Once the correct air/fuel mixture had filled the combustion chamber, mixing was enabled using a fan located at the bottom of the chamber. The mixture was then allowed to rest for 2 minutes to allow settlement of any turbulences. Simple analysis at the start of this work was undertaken to determine influence of mixing and settlement time. A methane/air blend at Φ = 0.70 and 1.0 Φ was mixed for 30, 60 and 90 seconds, and allowed to settle for 1, 2 and 5 minutes. No visual impact was

seen on flame sphericity, and corresponding laminar burning velocities fall within experimental uncertainties. It was assumed that a mixing and settlement time of 1 minute was enough.

11) The lamp used for the Schlieren system would be switched on. The camera would be set to record with the trigger mechanism set. The camera would continuously record in a loop of 1200 frames, with the centre frame designated by the eventual trigger point. This allowed for easy location of the first frame of the spherically expanding flame.
12) A final safety check was conducted. The pulse generator was triggered and the spherically expanding flame recorded.
13) After ensuring that combustion had occurred, either visually or from the live temperature read-out, the exhaust valve would be opened allowing for the evacuation of the hot products and residual pressure through the vacuum pump.
14) In the meantime, all relevant data was stored and copied to an external hard drive for post processing. The processing of data is covered in detail in the following section.

4.2.2 Video Processing

The temporal evolution of the spherically expanding flame was measured using the data files recorded by the high-speed camera. The video files were saved as a series of 8-byte grey-scale sequential frames in .tif format. These were then imported into the MATLAB software. A code was then used to facilitate the processing of the files. The following section covers how this script works, with the full code available in Appendix A – 3.

The MATLAB script follows the same algorithm as employed by [62], and is schematically represented in Figure 4.3.

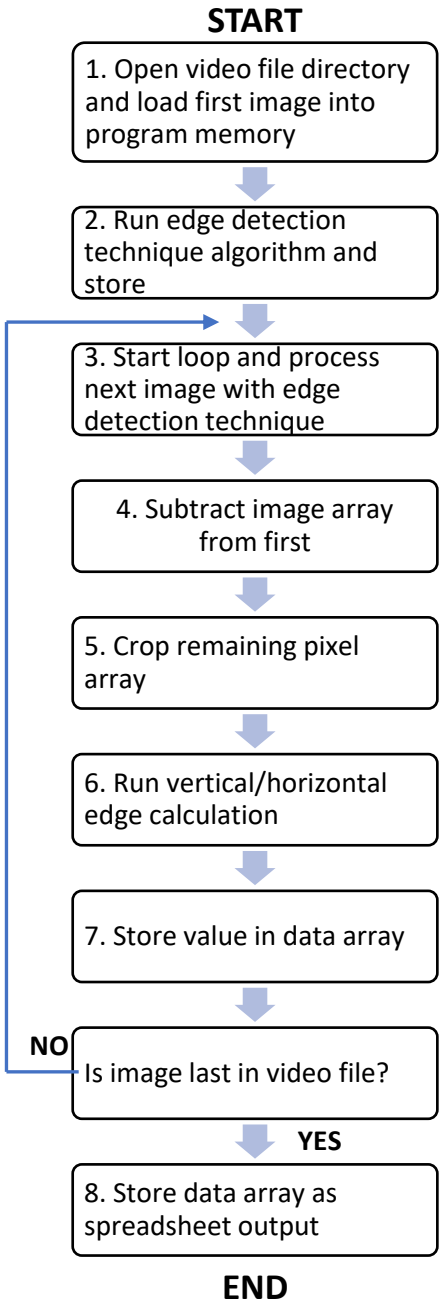

Figure 4.3 – Flow Chart of Employed MATLAB Algorithm, from [62]

The general algorithm operation remained the same for all experiments, with only minor adjustments necessary between tests. Modifications included adjustment in entering centre location of sphere, which was always set to the midpoint between the electrode spark gap. This would change slightly depending on initial positioning of camera. To ensure as little adjustment as possible, the position of all the components of the Schlieren optical system were marked, as to allow similar placing for all test campaigns. Other adjustments include cropping settings for the horizontal and vertical measurement planes, to ensure cropping at the centre of the flame as well as number of images being processed. The algorithm processed the images in the following way:

1. Prior to processing the program memory was cleared and with the image files placed into the image file directory. The camera saved each image in ascending numerical order, the first image representing a flameless image prior to ignition whilst the last image captured the fully developed spherical expanding flame. The program would access the first image which served as a background blank for the rest of the frames processed in the algorithm loop.
2. The program would convert the greyscale intensity value of each pixel in the first image into a numerical array. Each pixel would be attributed a value between zero and one, representing white and black. The *Canny* method was then employed to detect both weak and strong edges. The technique can be broken down into the following steps:

   (a) A Gaussian filter is applied to smoothen the image in order to reduce/remove noise (b) The derivative of the Gaussian filter is used to find the intensity gradients of the image (c) The *Sobe*l operator was used to determine potential edges at the points where the gradient of the image is maximum. This is done by comparing the vertical, horizontal and diagonal pixels around a single pixel. If the pixel intensity exceeded a specified threshold value, then an edge is assigned to that point. Depending on flame front strength and image brightness this threshold was kept between 0.060 to 0.090. All the edges are assigned a numerical value of one, with all other pixels assigned a zero value. This allows for the collection of pixels to be converted into a binary image.

   Practically, the Gaussian filter was only able to remove limited noise. Noise in this case would be generated by a combination of potential dust setting on the camera lens or mirrors and residue of combustion products on the windows of the combustion vessel. In order to alleviate this issue, noise was removed through an area opening operation on the binary image. This operation would remove all connected objects (edges) that had fewer than a specified

number of pixels. This threshold was kept between 0-30 depending on amount and size of noise. A second binary image was then produced with reduced noise. During early flame kernel formation and propagation (< 3mm radius) using an area opening operation would effectively remove segments of the growing flame. However, these initial data points are not used for the measurement process due to the influence of ignition energy (detailed in Chapter 5). This second binary image was then stored in the program memory in a separate array for further processing. Figure 4.4 gives an example of the effectiveness of the algorithm used for the edge detection technique, with (a) the actual Schlieren flame and (b) the binary flame image after using the edge detection technique and (c) the binary flame image after the open area operation. The remaining frames were now processed using a loop. The edge detection algorithm was thus applied to all the frames sequentially.

3. Effectively each binary image was numerically subtracted from the newly processed array and stored in the program memory. This would theoretically subtract any motionless pixels (edges) such as the electrodes or noise and leave only the outline of the spherically expanding flame. In practice this was not the case, most probably due to the intensity of light reflection varying with flame propagation. To remedy this an area opening operation was applied on the binary images after the edge detection technique, as explained in step 2.
4. In order to gain computing time, the binary images of the spherical flame were now cropped, horizontally and vertically. The cropped section would require the input of length and width parameters to generate the appropriate cropping section.
5. Measurement of the flame diameter was achieved using the *find* operator. The *find* operator searches for indices and values of nonzero elements within a specified array. The array is the cropped section of the binary image and nonzero elements are pixels identified as edges within that cropped array. The *find* operator would then locate the indices of the first and last pixel. This was done by counting sequentially downwards through each pixel column of the cropped array. For vertical analysis, this value would be subtracted by the total column length, thus giving the difference between the two. For horizontal analysis, the first and last indices were divided into the number of pixels in each column. That number would then be rounded up, giving integers corresponding to the column number in which they are located. The horizontal diameter was then calculated by subtracting these column numbers.

A similar process was used in order to calculate the left and right horizontal radius, with the rounded first and last column numbers subtracted from a specified centre point. This was also applied to vertical top and bottom hemispheres. However, due to the slow-moving nature of the flames at ultra-lean conditions ($\Phi < 0.65$), the flames would be subject to buoyancy. Practically, this meant that the flames would rise as the flame propagated. In these circumstances only the horizontal attained data was used.

6. The value attained for the diametric pixels both horizontal and vertical, as well as the upper/lower and right/left hemispheres were stored in a new dataset. This database would grow with every frame processed, giving increasing values of radius or diameter.
7. The radial and diametric dataset would cease growing once the final frame in the loop was processed. This dataset was then exported and saved into a spreadsheet.

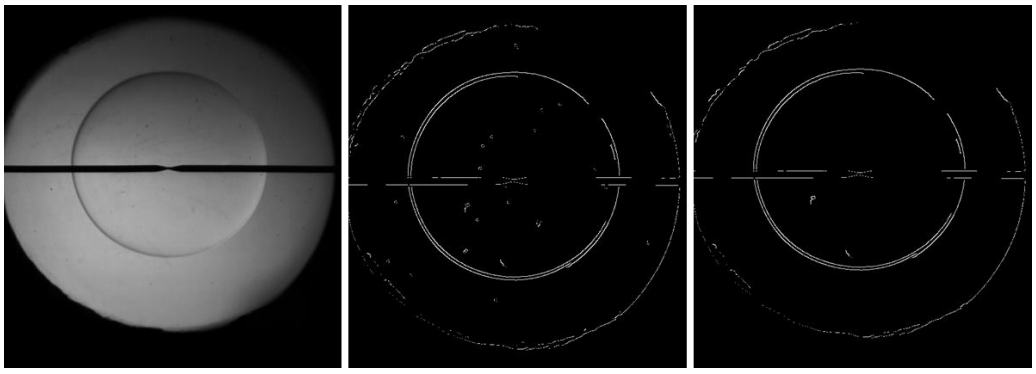

(a) (b) (c)

Figure 4.4 – (a) Schlieren Image (b) Binary Image of Schlieren (c) Binary image after Open Area Operation (noise removal)

4.2.3 Image Scaling

A scale for the binary images had to employed in order to accurately measure the distance travelled by the SEF using the diametric and radial pixel datasets. To do so, a digital set of Vernier callipers was used. Practically, the Vernier callipers were prepared at a set distance and placed in front of the collimated light beam between the first mirror and the optical window within the Schlieren set-up. The Vernier callipers would then be photographed in the centre, top, bottom, right and left positions. This process would be repeated for three distances, 5 mm, 10 mm, and 15 mm, for both horizontal and vertical scales.

These scaling images were then computationally processed individually using the MATLAB script described in Section 4.2.2. The photographs were transformed into binary images using the edge-detection technique, and the linear number of pixels, at five different

locations across the teeth of the Vernier calliper was evaluated. This process was repeated for all the Vernier scale positions (top, bottom, centre, left, right) and set distances (5, 10, 15 mm). An average of the linear pixel count was then used to determine the number of pixels per distance. An example of the Schlieren and binary scaling images are presented in Figure 4.5.

This calibration procedure was adhered to at the beginning of each day before the commencement of any testing. If at any point the mirrors or the camera had been inadvertently knocked, testing would be suspended in order to allow recalibration of scaling. The components of the Schlieren optical system (camera, light source, mirrors, aperture) were marked as to allow for them to be repositioned in similar locations every time. This proved to be very useful, as nominal differences in scale (<1%) were observed throughout the course of this work.

Finally, the Vernier callipers could be held at various distances between the window and the mirror with no impact on recorded scale distance. This gave a confident indication that the source of light was being collimated properly. The scaling process gave a spatial resolution of between 0.14 to 0.16 mm per pixel, depending on horizontal or vertical axis measurement (due to the pixels in the camera not being perfect squares). The calibrated Vernier scales afforded a degree of precision of 0.02 mm. This meant that the Vernier callipers were one order of magnitude more accurate than the pixel resolution of the camera. This was considered to give an acceptably accurate measure of scale.

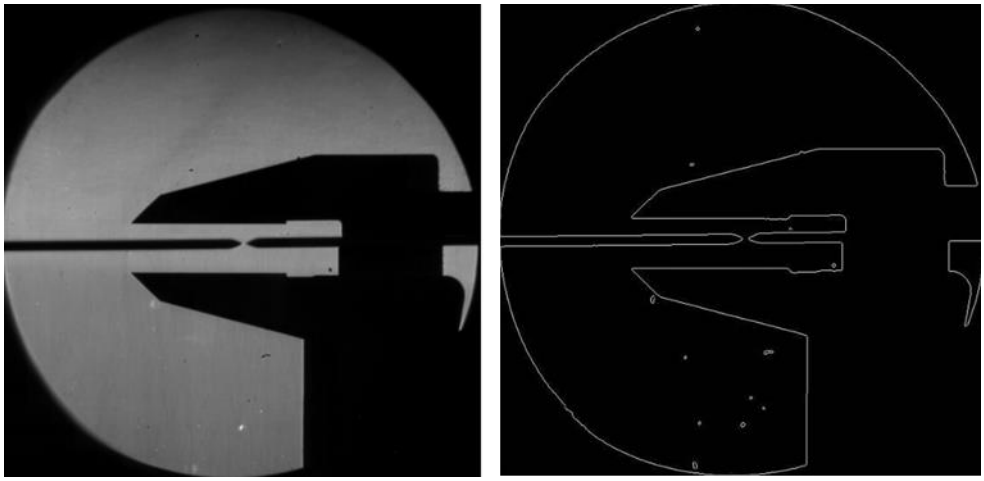

(a) (b)

Figure 4.5 – (a) Schlieren (b) Binary Image of Vernier Callipers for Scaling Calibration

An overview of the chemical kinetic program employed throughout the course of this thesis to evaluate numerical flame speeds and various other fundamental flame parameters is presented in the following section.

4.3 Chemical Kinetics Modelling

The various theoretical formulations described in Section 3.5, require the calculation of several flame parameters: the expansion ratio (σ), Zeldovitch Number (Ze), Activation energy (E_a) and flame thickness (δ). In order to so, a chemical kinetic modelling software was used. The CHEMKIN-PRO software package, developed by Sandia National laboratories, was chosen. This software facilitates the formulation, interpretation and solution of different problems involving elementary gas-phase chemical kinetics into simulations of fluid dynamics. The software offers modelling and simulation of freely propagating, adiabatic, one dimensional planar flame to obtain the laminar burning velocity. This permits comparison between experimental and computational simulation of flame speeds for the fuel and air blends investigated in this study. This software is heavily relied on in analogous fields of research, examples of which can be found in [62], [78], [151].The following section will be split into two parts, one describing the software package, with respect to the gas phase chemistry and transport properties for the premixed flame model, and the other overviewing the reaction mechanisms appraised.

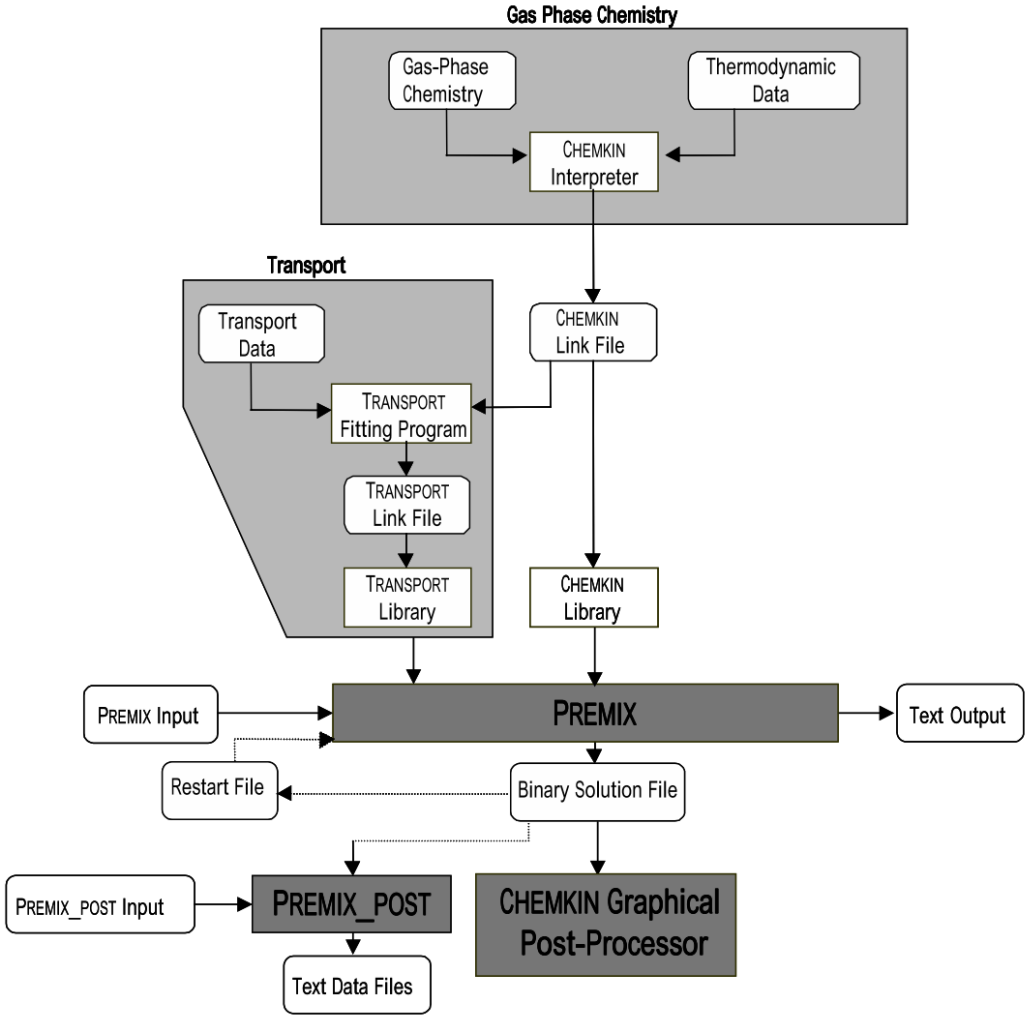

Figure 4.6 – Operational Algorithm of the CHEMKIN PREMIX Program [152]

4.3.1 Software Package Overview

To stimulate a premixed freely-propagating, adiabatic, one-dimensional planar flame the PREMIX program of the CHEMKIN-PRO software was used. The PREMIX program models spatial profiles of temperature and chemical species throughout a steady-state laminar flame front. For the purpose of this work a simulation domain of length 10cm was considered, with a total maximum number of a 1000 grid points allowed to resolve the computational domain.

The equations governing steady, isobaric, one-dimensional flame propagation modelling are summarised below [152]:

$Continuity$: Eqn. (4.2)

$$\dot{M} = \rho u A$$

$Energy$: Eqn. (4.3)

$$\dot{M}\frac{dT}{dx} - \frac{1}{C_p}\frac{d}{dx}\left(\lambda A\frac{dT}{dx}\right) + \frac{A}{C_p}\sum_{k=1}^{K}\rho Y_k V_k C_{pk}\frac{dT}{dx} + \frac{A}{C_p}\sum_{k=1}^{K}\dot{\omega}_k h_k W_k = 0$$

$Species$: Eqn. (4.4)

$$\dot{M}\frac{dY_k}{dx} + \frac{d}{dx}(\rho A Y_k V_k) - A\dot{\omega}_k W_k = 0 \ (k = 1, \dots, K)$$

$Equation\ of\ state:$ Eqn. (4.5)

$$\rho = \frac{p\overline{W}}{RT}$$

In the above equations, the mass flow rate ($\dot{M}$) is introduced in the continuity equation, with ρ and u, the density and velocity of the fluid mixture, respectively. The cross-sectional area of the stream encompassing the flame is represented by A, which by default is taken to equal unity and to be constant. The flame configuration is adiabatic, whereby definition there is no heat loss. In this case, temperatures are computed from the energy equation, which also introduces the spatial co-ordinate of the flame and thermodynamic properties including; the constant-pressure heat capacity (c_p), thermal conductivity (λ) and the specific enthalpy (h). Other properties including mass fraction (Y_k) and diffusion velocity (V_k) are defined in relation to specific chemical species (k=1,…,K). The molecular weight is defined for individual components and the mixture average ($\overline{W}$). The net chemical production rate of each species ($\dot{\omega}_k$), results from competition among all the chemical reaction involving that species.

Each reaction is assumed to follow the law of mass action and the forward rate co-efficients are obtained from the ensuing Arrhenius form [152]:

$$k_f = AT^{\beta} exp^{\left(\frac{-E_a}{R^0 T}\right)} \quad \text{Eqn. (4.6)}$$

where, (A) is the pre-exponential and β the temperature factors with respect to each chemical reaction, (R) the universal gas constant and (E_a) the global activation energy.

Other than the chemical reaction rates, the transport properties, for example diffusion co-efficients are also of concern. Two models are available when evaluating transport properties, one based on mixing-average formulas and the other using a multi-component diffusion model. The multi-component model was used to evaluate transport properties for the purpose of this work, as it is the most accurate approach but often more computationally intensive. A brief description is provided below, with full details available in the CHEMKIN transport manual [153].

A system of equations involving species mole fractions, binary diffusion co-efficients and molecular and thermodynamic properties of the species are computed to evaluate the multi-component diffusion coefficient, thermal conductivities and thermal diffusion co-efficients. The method by Dixon-Lewis [154] is followed by the program. The diffusion velocity (V_k), is assumed to be composed of two parts:

$$V_k = \mathcal{V}_k + \mathcal{W}_k \quad \text{Eqn. (4.7)}$$

where ($\mathcal{V}_k$) is the ordinary diffusion velocity and ($\mathcal{W}_k$) the thermal diffusion velocity. The ordinary velocity diffusion term is defined as:

$$\mathcal{V}_k = \frac{1}{X_k \overline{W}} \sum_{j \neq k}^{K} W_j D_{k,j} \boldsymbol{d_j} \quad \text{Eqn. (4.8)}$$

where (X_k), is the mole fraction, ($\overline{W}$), the mean molecular weight of the mixture, (W_j), is the molar mass of species *j*, and ($D_{k,j}$) is the binary diffusion co-efficient of species *k* into *j*. The term d_j is defined as:

$$\boldsymbol{d_j} = \nabla X_k + (X_k - Y_k) \frac{1}{p} \nabla p \quad \text{Eqn. (4.9)}$$

The thermal diffusion velocity ($\mathcal{W}_k$) is defined as:

$$\mathcal{W}_k = -\frac{{D_k}^T}{\rho Y_k} \frac{1}{T} \nabla T \quad \text{Eqn. (4.10)}$$

where (${D_k}^T$), is the thermal diffusion co-efficient for species *k*.

The operational algorithm of the CHEMKIN PREMIX code is represented in a flow-chart format in Figure 4.6 [152].

4.3.2 Reaction Mechanism Overview

The CHEMKIN PREMIX program is built up of two pre-processors that run-in conjunction, the CHEMKIN Gas-phase package and the Transport Property package (Figure 4.6). The Gas-phase deals with the chemical reaction mechanism, whilst the Transport package estimates polynomial fits for transport property calculations [152]. The PREMIX program depends upon user-supplied data as inputs to obtain a numerical solution. These reaction mechanism data files usually list most known species and chemical reactions for the complete combustion of a certain fuel. Reaction mechanisms can be split into three components. The first, is the CHEMKIN Interpreter that reads the user's description of the reaction mechanism, in which the activation energy and the pre-exponential factor and temperature exponent are specified (Eqn. 4.6). The CHEMKIN package then extracts the thermodynamic information of the relevant species from the second file. Essentially, this information is stored in the form of a table of polynomial co-efficients which are required to calculate most thermodynamic properties as a function of temperature. Data on chemical transport properties of each species make up the third file. This allows for the thermal and mass diffusion velocities to be evaluated (Eqn. 4.9 and Eqn. 4.10).

Typically, individual reaction mechanisms are optimised to model a certain fuel for specified temperature and pressure conditions. These mechanisms are often subjected to validation against reliable experimental combustion data of appropriate fuels, using various experimental set-ups. Four reaction mechanisms, namely: GRI-Mech 3.0 (1999 update) [155], USC-Mech II (2007 update) [156], Aramco-Mech 1.3 (2013 update) [157] and San Diego mechanism (2014 update) [158], were appraised, with numerical flame speeds compared to experimental results. Reaction mechanisms were also employed to evaluate various fundamental flame parameters (Chapter 3, Section 3.5).

The selected reaction mechanisms, all include H_2/CO chemistry, along with the oxidation of higher hydrocarbons at elevated temperatures, and thus should suitably represent the combustion of natural gas/hydrogen blends. GRI-Mech 3.0 was originally optimised for chemically modelling natural gas combustion, and consists of 325 reversible elementary reactions and 53 species, with oxidation up to C_1-C_3 hydrocarbons [155]. USC-Mech II was optimised for the high temperature oxidation of hydrogen, carbon monoxide and C_1-C_4 hydrocarbons. This mechanism is made up of 784 reactions and 111 species. Aramco-Mech 1.3 mechanism consists of 253 species and 1542 elementary reactions, with combustion up to C_1-C_3 hydrocarbons [157]. San Diego Mechanism is designed on a different approach to other mechanisms with number of species and elementary reactions kept to a

deliberate minimum, consisting of 50 species and 244 elementary reactions, up to C_4 hydrocarbon oxidation [158].

The summary of the reaction mechanisms employed in this study can be found in Table 4.1, with a comparison of the number of species and chemical reactions that the mechanisms have in common listed in Tables 4.2 & 4.3, respectively [151]. Full details and mechanism model specifications are included appropriately alongside presented results, as well as certain specific CHEMKIN calculation procedure details.

Table 4.1 – Main Details of Different Reaction Mechanisms

Mechanism Name	Author	Version	Number of reactions	Number of species
GRI 3.0	Smith et al.	1999	325	53
USC 2.0	Wang et al.	2007	784	111
Aramco 1.3	Curran et al.	2013	1542	253
San Diego	William et al.	2016	244	50

Table 4.2 – Reaction Mechanisms: Species in Common

	GRI 3.0 (53)	Aramco 1.3 (253)	USC 2.0 (111)
Aramco 1.3 (253)	35		
USC 2.0 (111)	34	66	
San Diego (50)	31	36	34

Note that the values in brackets are the number of species within each mechanism, whilst the number in the table is the number of identical species. Sourced from [151].

Table 4.3 – Reaction Mechanisms: Reactions in Common

	GRI 3.0 (325)	Aramco 1.3 (1542)	USC 2.0 (784)
Aramco 1.3 (1542)	49;88		
USC 2.0 (784)	93;72	120;124	
San Diego (247)	21;77	29;80	28;89

Note that the values in brackets are the number of reactions within the mechanism. The first value in the table is the number of reactions with identical Arrhenius constants, whilst the second number is the number of identical reactions but with different reaction rate constants. Sourced from [151].

4.4 Benchmarking of Experimental Apparatus

The numerical procedure undertaken to analyse experimental data is presented for stoichiometric CH_4/air, exemplifying application of linear and non-linear models employed to evaluate flame speed and Markstein length. Experimental and statistical uncertainties are explored in Chapter 5.

4.4.1 Experimental Data – Numerical Processing

Once the Schlieren SEF is recorded, the frames are computationally processed, outputting a growing pixel count (Section 4.2). This growing pixel count represents the development of the expanding Schlieren flame, with the pixel database scaled to give a propagating Schlieren flame radius (r_{sch}), as illustrated in Figure 4.7.

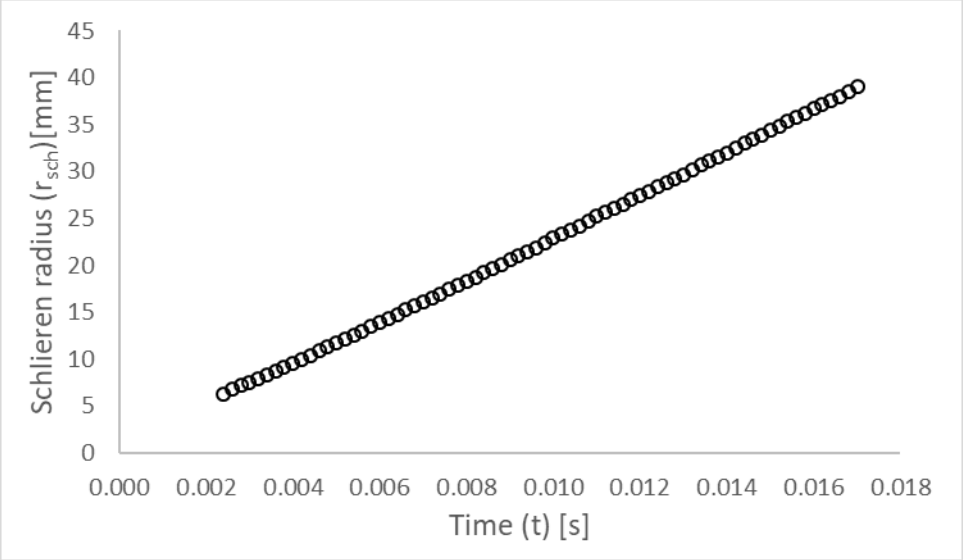

Figure 4.7 – Schlieren Radii of CH_4/air Spherical Flame Propagation (Φ = 1.0, T_u= 298 K, P = 0.1 MPa)

Influence of ignition phenomena on early flame radius propagation was studied by Bradley et al.[86], concluding that radial distances greater than 6mm are independent of ignition effects. Similarly, Burke *et al.* [87] in their study on the effect of cylindrical confinement on outwardly propagating flames, advise a usable flame radius range of no more than 30% of overall chamber dimensions, in order for the flame speed to be relatively unaffected by confinement effects. For the experimental rig used, this allows for processing of flame radii up to 39mm. This limit was respected for this exercise and explored in more detail in Chapter 5.

A third-order polynomial regression is fitted to the Schlieren flame front across the 6-39 mm flame radius range. Fitting a higher polynomial degree generates more noise in the velocity and stretch evolutions, as they tend to be less smooth (more 'lumpy') then lower order polynomials [77]. Moreover, fitting a higher degree polynomial than necessary is

undesirable as this can lead to cases where infinite number of solutions are possible. To quantify the error between the observed Schlieren radius and the fitted polynomial radius (r_{poly}) the root-square error for each data point is calculated using Eqn. 4.11.

$$r_{error} = \sqrt{\left(r_{sch} - r_{poly}\right)^2} \qquad \text{Eqn. (4.11)}$$

The error induced by the polynomial fit is plotted in Figure 4.8. The R-squared value (R^2), known as the coefficient of determination, is a statistical measure on how accurately the data is fitted to the regression line. For this work, R^2 is obtained up to 10 significant figures, with the example shown yielding R^2= 0.99998916, with this precision of fitting maintained for all tests. As can be seen, the errors in-between the polynomial fitting boundaries (r_{sch} = 6-39 mm, Figure 4.8) are smaller than the resolution of the optical system (0.14mm – dotted black line, Figure 4.8), with larger errors observable around the end points of the polynomial fitting.

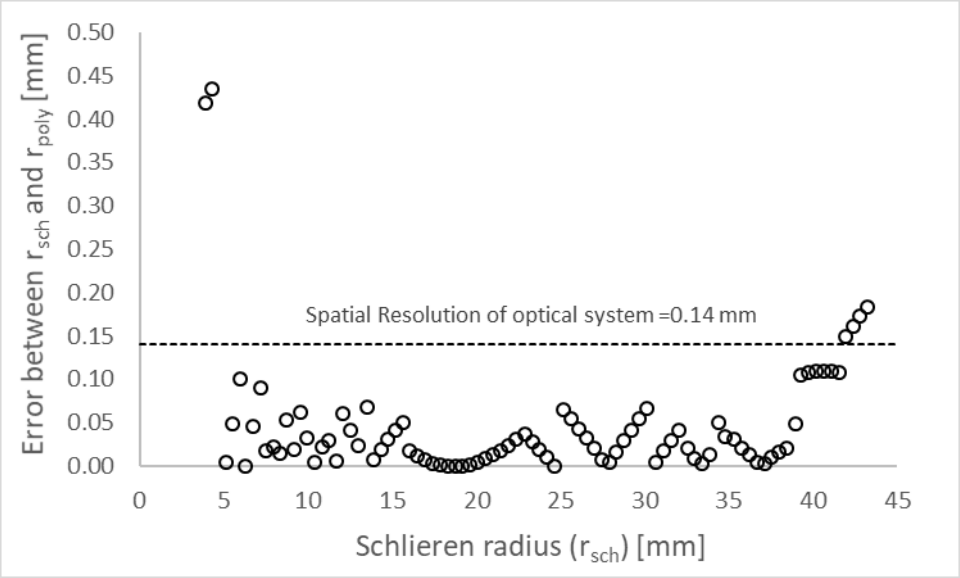

Figure 4.8 – Plotted Error between Observed and Predicted Polynomial Radius

Tahtouh et al. [77] in their study on the extraction of laminar flame properties from SEFs discuss the accuracy of such regressions, observing that such polynomial fittings generate distortions around the end points, consequently inducing largest errors at the polynomial extremities. When applying a differentiation process on the polynomial fit, to obtain the stretched flame speed (S_n) and corresponding stretch rate (α) noise generation is amplified. Consequently, to minimise these end-point distortions, usable data is further trimmed, with usable data range reduced from 6-39mm to 10-35 mm. The influence of flame radius selection on yielded flame speed and corresponding L_b values are explored and quantified in Chapter 5.

The temporal evolution of the stretched flame speed and corresponding stretch rate and curvature are depicted in Figure 4.9 and 4.10, respectively. Clearly, as can be seen from Figure 4.10, as the flame is expanding, flame curvature reduces and so does the influence of stretch (since stretch includes the effects of flame curvature, Eqn. 3.4), with Figure 4.11 illustrating the influence of both stretch and curvature on flame speed. To obtain a flame speed uninfluenced by stretch (S_u), linear and the non-linear theoretical relationships, LM(S), LM(C) and NM(S), correspondingly, must be applied.

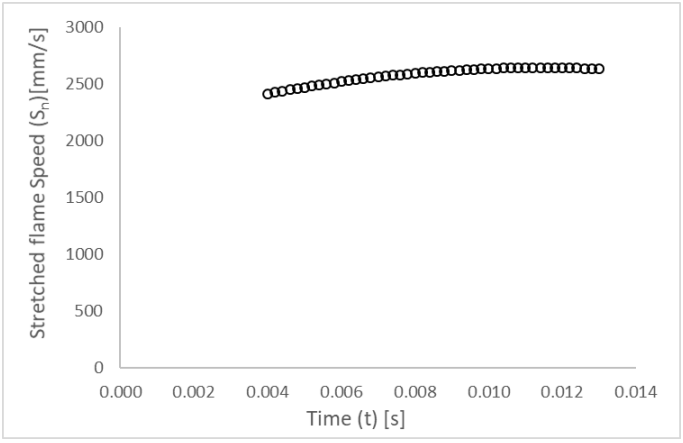

Figure 4.9 – Temporal Evolution of S_n for a CH_4/air Flame

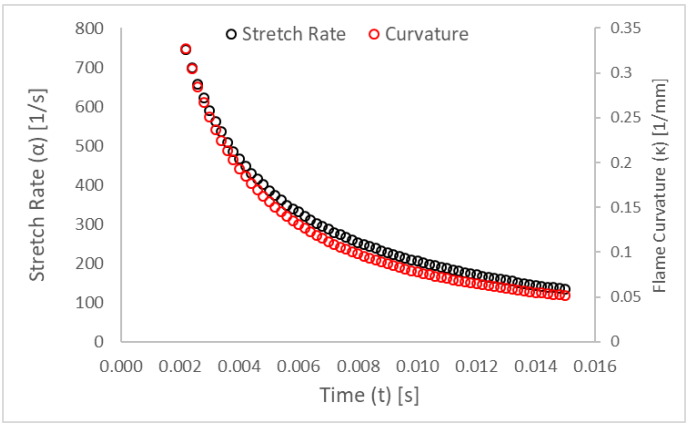

Figure 4.10 – Temporal Evolution of Stretch Rate and Flame Curvature for a CH_4/air Flame

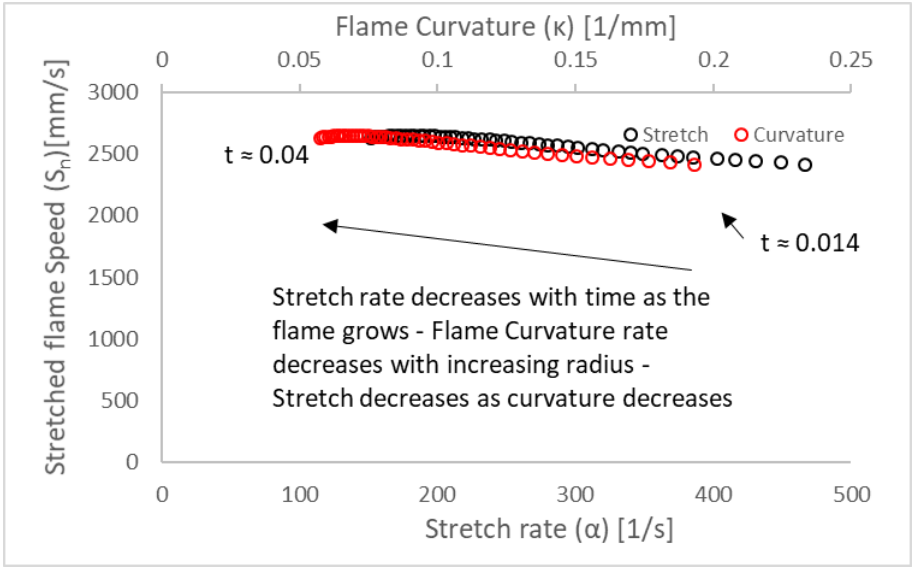

Figure 4.11 – Plotted CH_4/air Values of S_n vs α and κ

4.4.1 Linear Methodology

As previously detailed, (Section 3.1.2), LM(S) suggests a linear relationship between stretched flames speed (S_n) and α. By fitting a linear relationship to the data and extrapolating down to zero stretch conditions (α = 0), the y-intercept equates to S_u, with the gradient representing the flame response to stretch (L_b). Similarly, LM(C), implies a linear relationship between the S_n and flame curvature (κ). Thus, S_u and L_b can also be obtained by linear extrapolation based on the plot S_n versus κ. Figure 4.12 illustrates the appraised linear extrapolation methods, with the forecasted linear relationship to zero stretch or curvature superimposed.

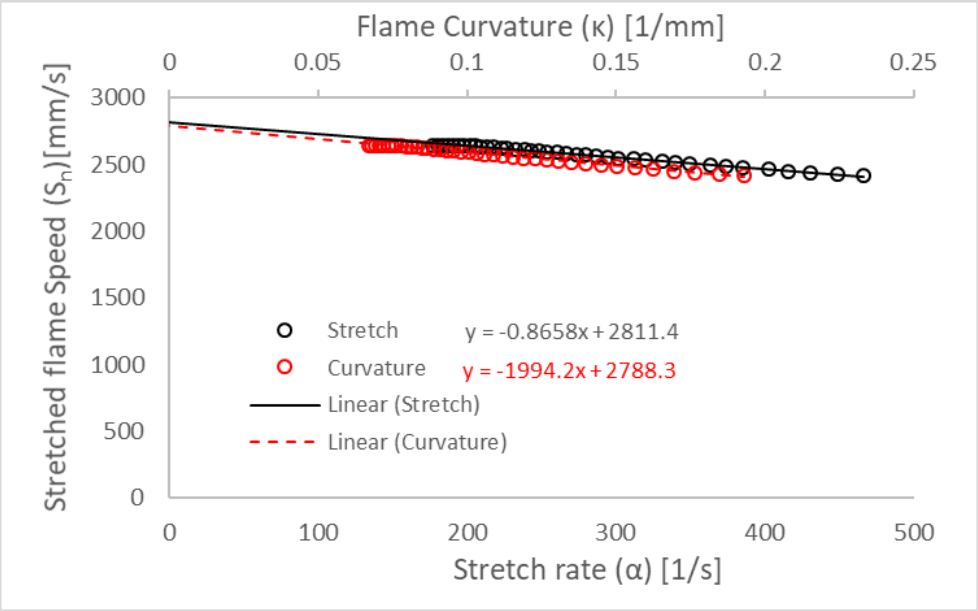

Figure 4.12 – Stoichiometric CH4/air of S_n versus α or κ with Linear Relationships Superimposed

With respect to LM(S), the sample test conducted for stoichiometric CH_4/air, yields an unstretched flame speed of **2811.4 mm/s** and a corresponding Markstein length of **0.87 mm,** (black line, Figure 4.12). In relation to LM(C), the unstretched flame speed is equal to **2788.3 mm/s** and a corresponding Markstein length of **0.70 mm**, (red line, Figure 4.12). Note that for LM(C), the gradient must be divided by S_u to evaluate L_b (i.e. 1994.2/2788.3 = 0.70 mm). To evaluate the laminar burning velocity (U_L), S_u must be corrected for the expansion of hot products, (Section 3.1.3, Eqn. 3.09). For the purpose of this example, the Aramco 1.3 reaction mechanism [157] was employed in combination with the CHEMKIN-PRO software.

The expansion ratio is equal to = **0.13275**

Thus, using S_u from LM(S), U_L = **37.32** cm/s

and using S_u from LM(C), U_L = **37.01** cm/s

4.4.2 Non-Linear Methodology

The non-linear methodology, NM(S), employs the relationship described in Section 3.1.2. Eqn. 3.08 must be solved for each value of S_n and corresponding α to evaluate S_u and L_b. Least square non-linear regression was used to fit the relationship to the plotted points. Thus, Eqn. 3.08, can be rearranged as:

$$\left(\frac{S_n}{S_u}\right)^2 . In\left(\frac{S_n}{S_u}\right)^2 + \frac{2 . L_b . \alpha}{S_u} = 0 \qquad \text{Eqn. (4.12)}$$

with any divergence from zero added as the dependent uncertainty used for the iteration process. Figure 4.13 illustrates the fitted non-linear relationship superimposed upon the fitted dataset.

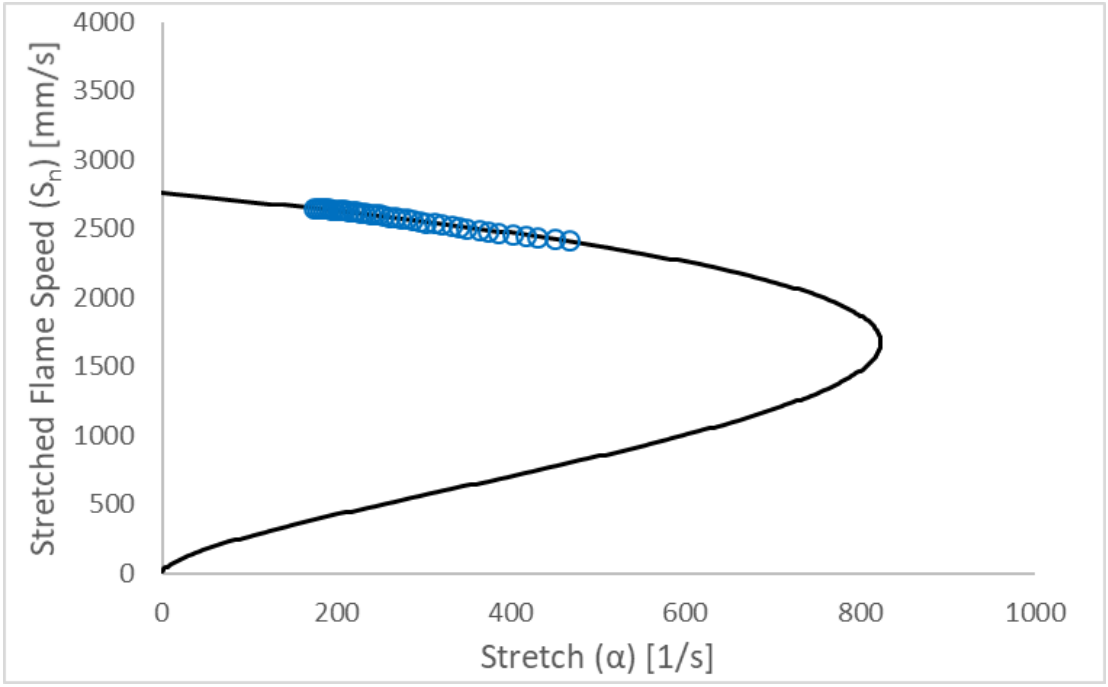

Figure 4.13 – Non-Linear Relationship with CH_4/air Values of S_n and α (Φ=1.0, T_u=298 K, P=0.1 MPa)

The non-linear methodology results in S_u = **2760 mm/s** and L_b equal to **0.62 mm**. Applying the same expansion ratio as for the linear methods yields U_L = **36.64** cm/s.

4.5 Benchmarking Methane/Air Combustion for lean conditions

A benchmarking exercise was undertaken for lean methane/air mixtures ($\Phi \leq 1$) at standard conditions (T_u=298 K, P = 0.1 MPa) for CH_4/air mixtures, with three nominally identical experiments conducted at each tested condition. Results are compared to peer-published datasets, to ensure correct application and utilisation of extrapolation methods and data-processing techniques.

The datasets of lean CH_4/air mixtures are presented in Figures 4.14, illustrating the relationships between the stretched flame speed (S_n) and stretch (α) using both linear and non-linear methodologies and that between S_n and curvature (κ). Clearly, with increasing Φ the influence of stretch becomes more significant, reflected by an increase in the steepness of the gradients (Figure 4.14). All appraised extrapolation methodologies result in similar S_u, irrespective of tested Φ, (see y-intercept, Figure 4.14). Differences in extrapolated values are presented in Table 4.4, evaluated with respect to LM(S) and NM(S), which generated highest and lowest values, respectively. Marginal differences (<1%) are observed for S_u, with differences in measured L_b significantly more important, increasing as conditions get richer.

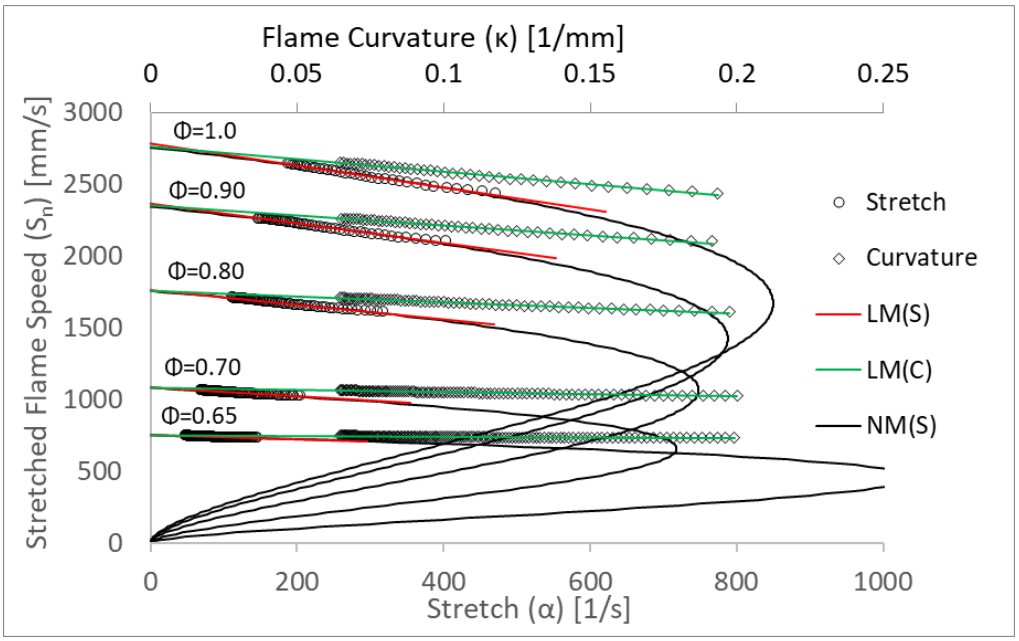

Figure 4.14 – Lean CH_4/air Mixtures Sn vs α and κ (T_u=298 K, P=0.1 MPa)

Table 4.4 – Difference in predicted S_n and L_b between Linear and Non-Linear Methodologies

Average Percentage difference between Linear and Non-linear Models		
Equivalence Ratio (Φ)	Unstretched Flame Speed (S_n) (%)	Markstein Length (L_b) (%)
0.65	0.02	7.37
0.70	0.16	11.02
0.80	0.44	18.72
0.90	0.72	24.32
1.00	0.88	27.23

Experimental scatter for S_u and L_b is graphically presented in Figure 4.15 and 4.16, respectively.

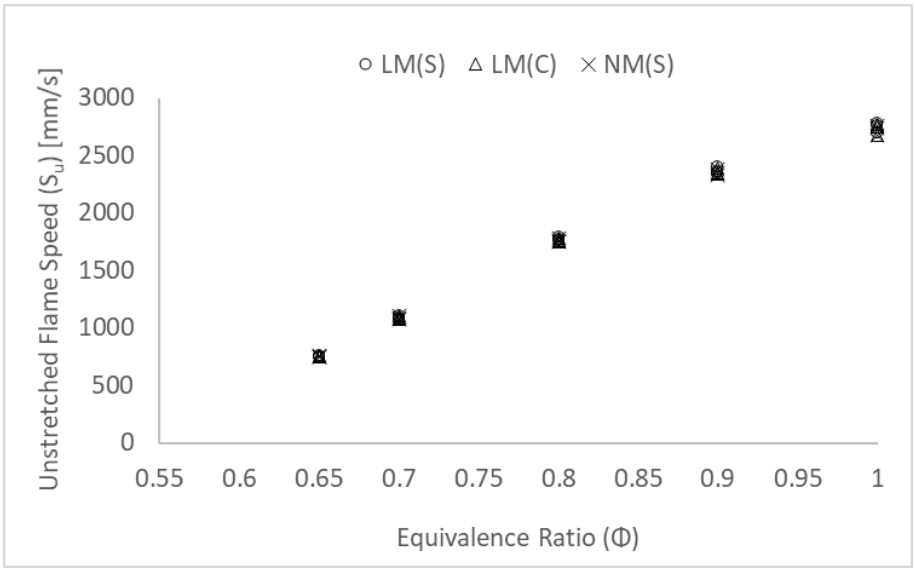

Figure 4.15 – Experimental Scatter in S_u for CH_4/air mixtures across lean Φ (T_u=298 K, P=0.1 MPa)

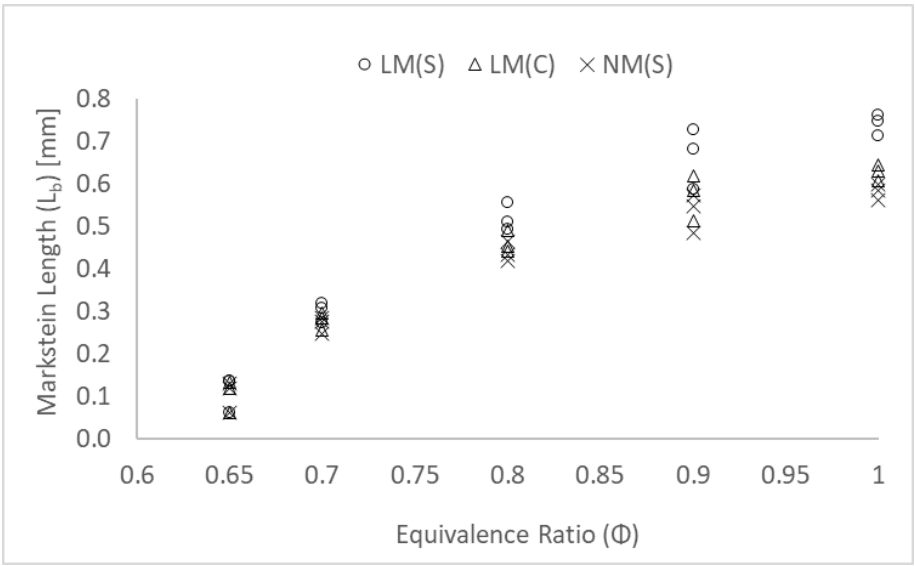

Figure 4.16 – Experimental Scatter L_b– CH4/air mixtures across lean Φ (T_u=298 K, P=0.1 MPa)

Scatter for S_u, appears to suggest good experimental repeatability, with average differences below <1%, (Figure 4.15). Scatter observed for measured L_b by employing different extraction models is much more significant, increasing with increasing Φ, (Figure 4.16). The observed level of scatter is in agreement with theoretical work conducted by Chen [84], underlining that the accuracy of different extrapolation methods is strongly related to the Lewis number (Le) of the fuel mixture. Thus, since CH_4/air mixtures exhibit Le ≈ 1, differences in attained values are small (at least for S_u, less so for the more sensitive L_b), irrespective of relationship employed.

4.5.1 Comparison with analogous datasets

4.5.1.1 Markstein Length

Comparison between average measured L_b of CH_4 and published research is presented in Figure 4.17. It is observed, that application of NM(S) (denoted by circles, Figure 4.17) results in narrower divergence than LM(S) (crosses, Figure 4.17), however this could be attributed to the limited number of datasets available for comparison. Historically, LM(S) has been extensively used, with L_b from this work situated comfortably between maximum and minimum reported L_b values.

All datasets exhibit the same trend, a rise of L_b with rising Φ, denoting an increasing Le, alluding to a thermally driven flame. L_b slope inversion (from positive to negative) has been reported at ultra-lean conditions (Φ< 0.60, Figure 4.17) [73],[77], indicative of a mass driven combustion process, with this reported change in CH_4 behaviour further investigated in Chapter 6.

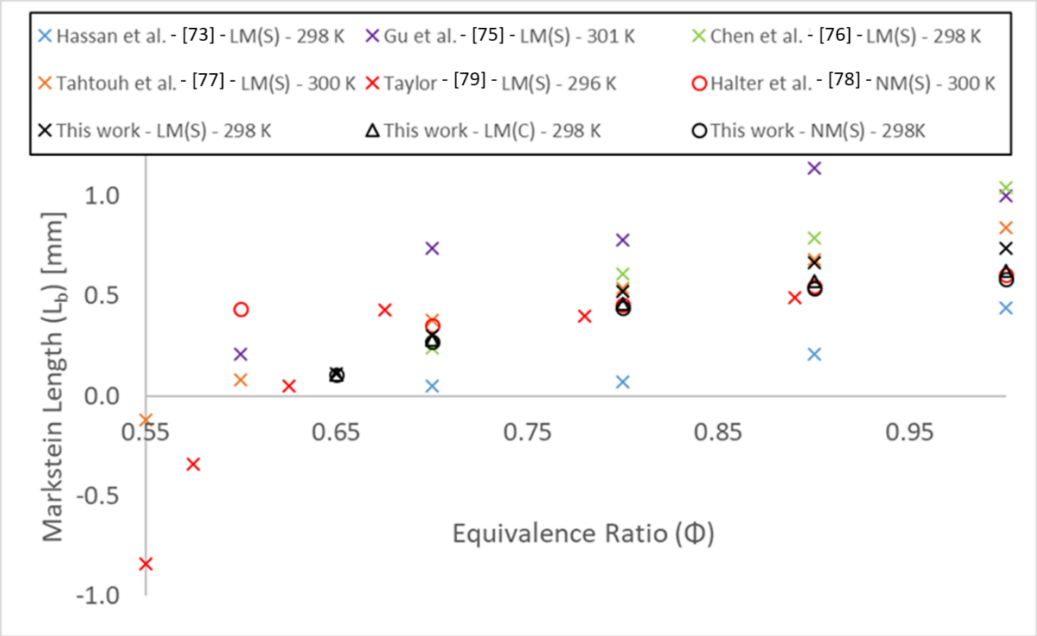

Figure 4.17 – Comparison of measured Average L_b with Published Data for Lean CH_4

4.5.1.2 Laminar Burning Velocity

The average experimental U_L of the tested CH_4 dataset are compared in Figure 4.18 to numerical U_L values generated using various reaction mechanisms [155]–[158], (Section 4.3.2). For the kinetic-modelling, the CHEMKIN PREMIX model was employed, assuming an air composition of 79% N_2 – 21% O_2, with multi-component diffusion included. All appraised reaction mechanisms yield similar numerical U_L values, with Aramco 1.3 [157] displaying best agreement with measured values (Figure 4.18).

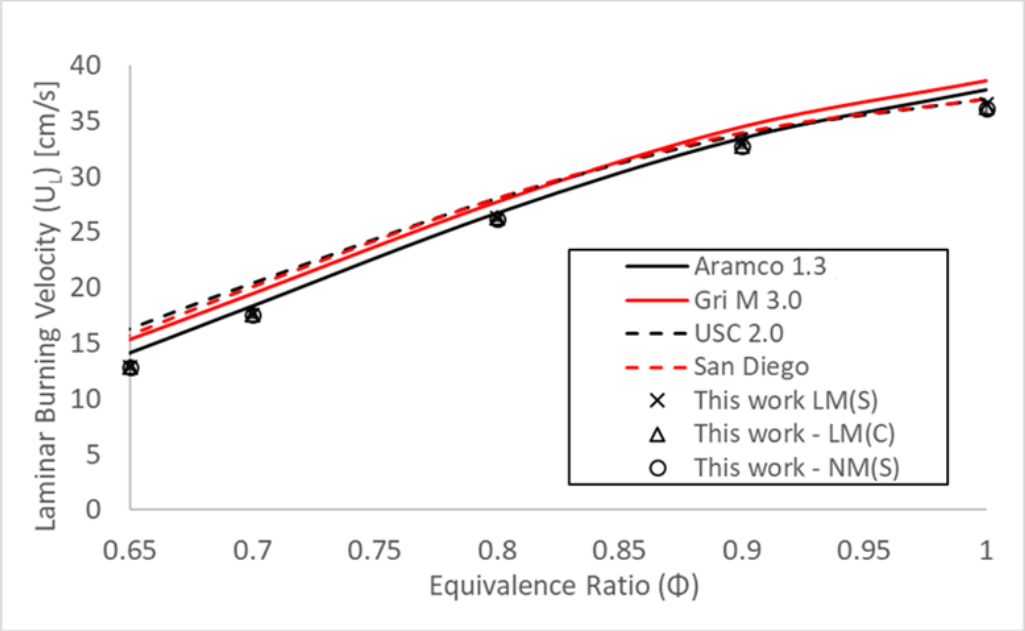

Figure 4.18 – Comparison of Average U_L for CH_4/air Flames with Numerical Predictions (T_u=298 K, P=0.1 MPa)

The average experimental U_L yielded from this benchmarking exercise are compared to published datasets in Figure 4.19, alongside numerical predictions using Aramco 1.3 [157].

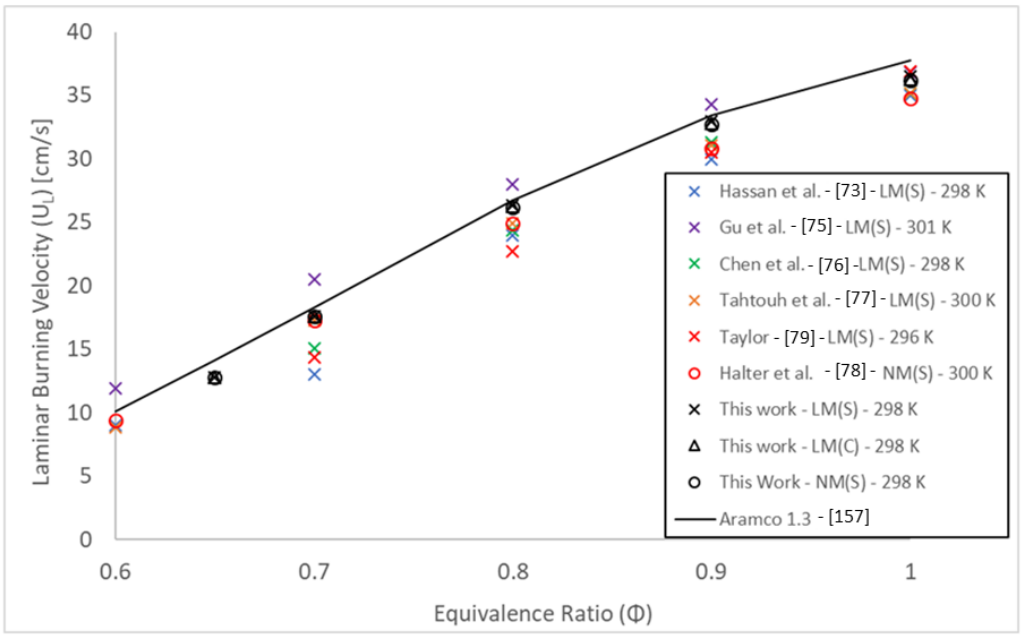

Figure 4.19 – Comparison of Average U_L Against Published Datasets

As previously highlighted in Chapter 2 (Section 2.3.1, Figure 2.2), important scatter in U_L is observable between peer-assessed datasets generated using the SEF configuration at nominally identical experimental conditions. Better agreement is witnessed at stoichiometric conditions (Φ = 1.0), with scatter increasing as conditions get leaner, particularly at Φ=0.70. As can be seen in Figure 4.19, limited research has been conducted for CH_4/air mixtures at ultra-lean conditions (Φ < 0.65). As such, the lack of observable scatter may potentially be

attributed to the fact that limited datasets are available for comparison, rather than a perceived enhanced accuracy at leanest conditions. It was demonstrated by Chen [83] that uncertainties related to the accuracy of Φ and unburnt temperature have greater influence on U_L at leanest conditions. As such, higher levels of scatter as conditions get leaner would be expected, in agreement with increasing levels of scatter displayed with decreasing Φ (0.70 – 1.0, Figure 4.19). Data measured using the Cardiff combustion chamber falls in-between reported published data, thereby validating both the correct application and utilisation of extrapolation methods and data-processing techniques employed.

4.6 Chapter Summary

The experimental equipment, data-processing methods and chemical kinetic software employed was overviewed. A benchmarking exercise was undertaken on the Cardiff CVCB, to gain familiarity with experimental procedure and assess correct application of extrapolation methodologies utilised to evaluate U_L and L_b.

The benchmarking work demonstrated good agreement with corresponding peer-assessed datasets, employing similar spherically expanding flame configurations and data-extraction methodologies. As such, the use of the combustion system and data processing methods is deemed by the author to be reliable, accurate and repeatable for the characterisation of fuel mixtures investigated in this thesis. Variations in evaluated U_L and L_b values employing different extraction models agree with theoretical published work. Therefore, to avoid confusion and enhance accuracy, plotted results will follow those recommendations, with the use of LM(C) for mixtures displaying Le > 1 and NM(S) for mixtures exhibiting Le < 1, with appropriate comparison undertaken when deemed necessary.

The important amount of observable scatter for both L_b and U_L across well referenced works, using similar SEF configurations at nominally equivalent testing conditions is evident. To better understand these divergences and ensure the accuracy of datasets presented in this thesis, sources of uncertainty and errors, are explored and quantified in the following chapter.

Chapter 5. Uncertainty Analysis of Measurements

It is apparent that large scatter exists in published attained laminar burning velocities (U_L) and Markstein lengths (L_b), for comparable testing conditions using spherically expanding flames (Section 4.5.1, Figure 4.17 and 4.19). In general, due to time and economic constraints, published U_L or L_b are presented as an average generated from 1-5 repeats (usually ≤ 3), with error bars representing either 1 or 2 standard deviations or maximum and minimum measured values. To better understand levels of expected uncertainty, a series of experiments at nominally identical conditions were conducted over a one-year period, following procedures outlined in Section 4.2. In total, 20 test results were generated for CH_4/air mixtures at both stoichiometric (Φ = 1.0) and lean (Φ = 0.70) conditions, at ambient temperature and pressure (defined herein as T_u = 298 K, P = 0.1 MPa). All experimental conditions were kept as constant as possible, including use of same high-purity methane fuel (99.9%). The only change that was necessary was with respect to the utilised zero-grade air cylinder, which required replacement due to the volumes required.

There are several factors known to impact the repeatability of combustion testing [83], for example the precision of experimental instrumentation utilised to control and measure pressure, mass and temperature, impact both the ambient conditions and air fuel ratio (AFR). Similarly, fuel and combustion air purity impact AFR and witnessed flame properties. Hence differences in published U_L and L_b datasets from various research institutions are to be expected. Coupled with experimental error, data analysis techniques employed to calculate S_u and L_b, for example, the use of linear or non-linear regression models (see Section 4.4.1), introduce further uncertainty, particularly for fuels that exhibit strong stretch-related behaviour (Le deviating significantly from unity). The above factors, among others, have been thoroughly evaluated by Chen [83], [84] and Wu et al.[85].

5.1 Uncertainty Criteria

Prior to quantifying sources of uncertainty for this work, the influence of data-selection range was explored. Since an important portion of presented datasets in subsequent chapters includes lean fuel mixtures containing various hydrogen contents, it is anticipated that these mixtures will be diffusionally unstable due to their low Lewis number (Le << 1). Under such conditions, as the stretch rate decreases the flame will self-accelerate, with potential cellularity (further detailed in Section 6.1.3 & 8.2) arising at early stages of flame propagation. Consequently, the usable pressure unaffected radius range may potentially be diminished. As such, to maintain accurate and consistent comparison between

datasets generated for different fuel mixtures, determination of the impact of radius selection on attained flame speed and L_b is deemed necessary.

Note the influence of data-processing range was examined with respect to the measured unstretched flame speed (S_u), rather than the laminar burning velocity (U_L) which requires the use of modelled expansion ratios for its determination, which introduces further uncertainty into the analysis. Furthermore, the non-linear method proposed by Kelley and Law [68] (detailed as NM(S) in section 3.1.2.2) was employed to yield S_u and L_b values. As previously discussed, NM(S) has been demonstrated to be more consistent and less sensitive to flame radius range selection [83]. Additionally, several studies [84], [85] highlight introduced uncertainties generated using the linear model based on stretch (LM(S),detailed in section 3.1.2.1) for fuel blends exhibiting Le deviating from unity. Similarly, the linear model based on curvature LM(C), has been demonstrated to be less accurate for fuels displaying Le below unity compared to NM(S) [84]. For near stoichiometric CH_4/air mixtures (Le ≈ 1) differences in attained values of S_u and L_b using the different models was found to be relatively small (Section 4.5, Table 4.4). However, to maintain clarity, and since much of the work presented in this thesis deals with fuel blends which exhibit Le varying across a wide range, it was decided to employ NM(S) for data-range selection analysis. The recorded spherically expanding flames were analysed as follows:

(1) With respect to axis plane of measurement – Two growing radial datasets are generated in both the horizontal and vertical axis (Section 4.2.2). For the rest of this section, note that when referencing to the measurement plane, ‘V’ and ‘H’ will be used to denote the vertical and horizontal axis, respectively.

(2) Initial data range – The data ranges upon which a polynomial is fitted was set to 8-39 mm (Section 4.4.1). Bradley et al. [86], demonstrated that the impact of ignition energy on flame growth dissipates by the time the flame radius has grown to 6 mm. In the case of this study 8 mm was utilised to ensure spark impact was limited. Burke et al. [87] in their study on the effect of cylindrical confinement on outwardly propagating flames, advised a usable flame radius range of < 30% of overall chamber dimensions, was required to ensure flame speed unaffected by confinement effects. The experimental rig used for this work afforded a flame radius ≤ 39mm.

(3) The extrapolation differential range – The flame radius extrapolation range upon which the polynomial fitting is differentiated (Section 4.4.1) was assessed at 10-25mm, 10-30mm and 10-35mm respectively.

The above limits are graphically illustrated in Figure 5.1, as a radial propagation chart (Schlieren radius versus time).

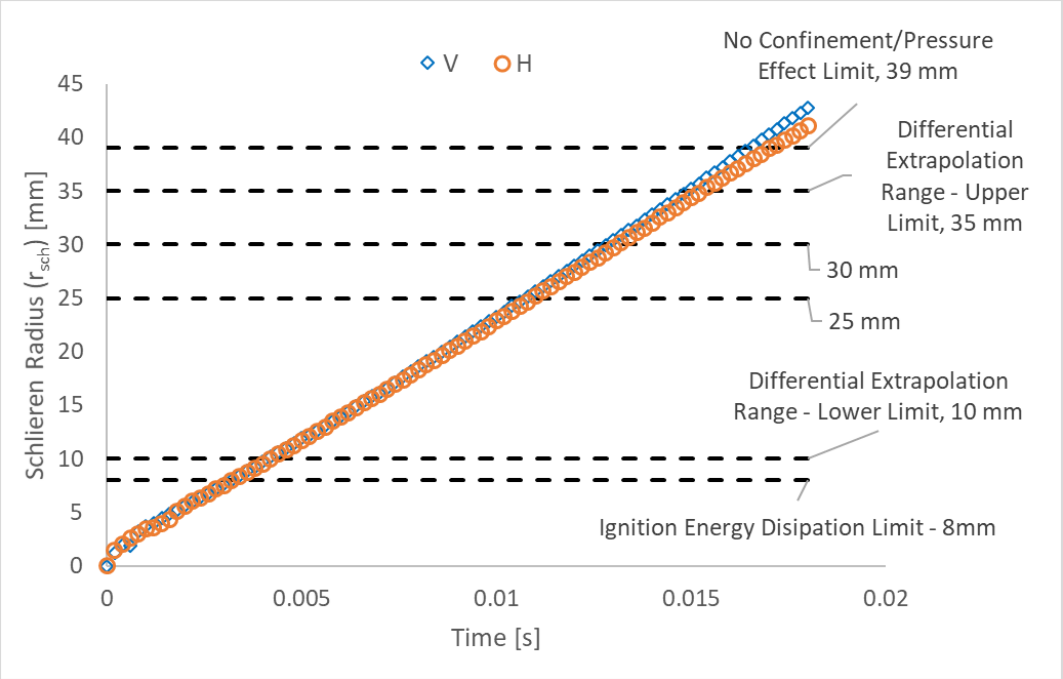

Figure 5.1 – Schlieren Radius vs Time Graph Highlighting Criterions and Limits used for Uncertainty Analysis of Data-Range Selection (CH_4/air mixture (Φ = 1.0)

Theoretically, assuming perfect spherical growth and the impact of buoyancy to be negligible, little variation in S_u and L_b should be present when analysing either plane of measurement, if confinement is not impacting flame growth. Nevertheless, several assumptions are made when processing the data that may result in differences. First with respect to the ignition energy. It is assumed that the flame ignition point occurs at the centre point between the electrodes, required when fixing V and H centre locations (Section 4.2.2). This may not always be the case, as spark-ignition is not a point source, thus could arise at any location within the 2mm spark gap. However, this should not impact measurements in either plane, as the numerical procedure employed calculates the flame diameter with respect to the largest point of circumference. Secondly, it is assumed that the spark-ignition constantly produces the same amount of energy, for a set voltage and capacitor ignition system. However, the ignition event is a random process, thus small variations are unavoidable and will impact early flame propagation. This impact is assumed to dissipate by the time the flame radius has grown to 6mm, as suggested by Bradley et al. [86]. Third, with respect to the H axis of measurement. Due to the presence of the electrodes, measurement is not taken precisely at the leading edge of the flame but slightly above, resulting in analysis which may not truly represent the largest point of circumference (in the order of 5-8 pixels ≈ < 1mm). Finally, heat loss of the flame to the electrodes in the H plane possibly impacts flame propagation. By placing the electrodes at a 45^0 angle to the measurement plane, this was effectively reduced particularly as the flame becomes larger. Nevertheless, early flame propagation will still be influenced by heat loss to the electrodes. All the above are assumed to be negligible but are mentioned for the sake of completeness.

5.2 Stoichiometric Methane Analysis

The variation in measured S_u for the 20 stoichiometric CH_4/air (Φ = 1.0) repeats are plotted in Figure 5.2, for both the H and V planes of measurements. Superimposed black lines represent tests conducted on the same day, whilst the red line denotes a change in the zero-air grade bottle used for the experiments. Results were generated upon application of an initial radius range of 8-39 mm and a differential extrapolation range of 10-30 mm.

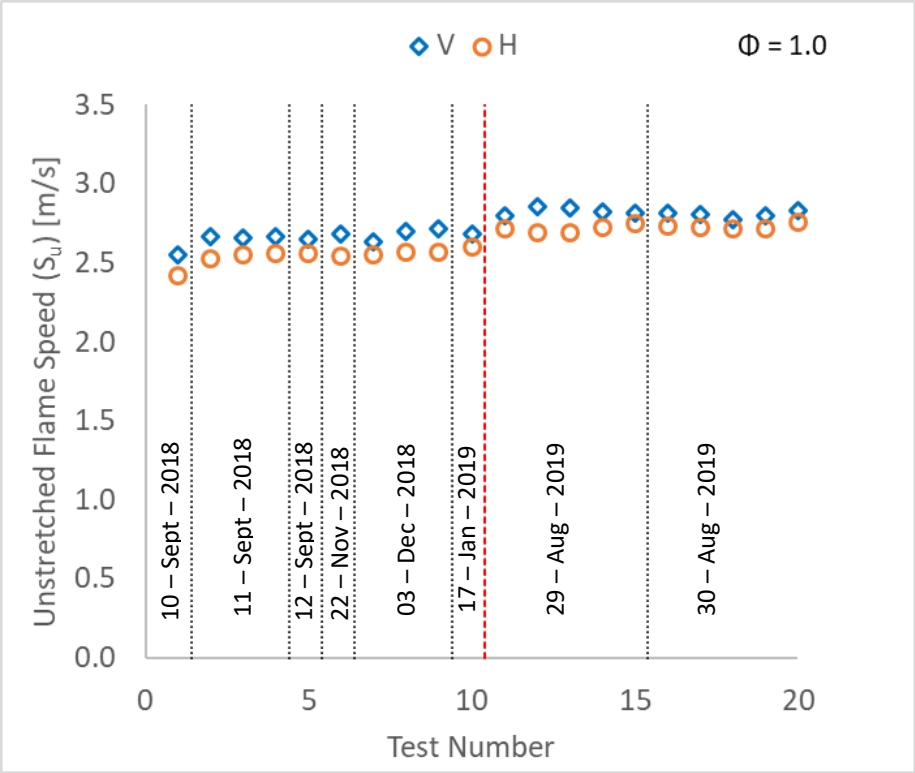

Figure 5.2 – Variations in S_u for CH_4/air Repeats (Φ = 1, T_u = 298 K, P = 0.1 MPa) – Black lines denote tests conducted on the same day, red line denotes change in zero-air grade bottle used for experiments - Radius range = 8 - 39 mm, Differential extrapolation range = 10-30 mm

With respect to S_u, two noticeable trends are apparent in Figure 5.2. The first is that measured V-S_u (vertical-unstretched flame speed) is consistently faster than H-S_u (horizontal unstretched flame speed). The relative variations between both planes of measurements (calculated with respect to the H-plane) are on average < 4%, with a maximum relative difference of ~6%, with differences discussed further later. Another observation is a perceptible increase in S_u, from test 11 onwards, denoted by a red line in Figure 5.2. Retrospective consultation of noted experimental details, suggest this bias in S_u is a consequence of a change in the zero-air grade bottle, which occurred between the 17th of January and 29th August 2019 (tests 10 and 11). The zero-grade air bottles manufactured by BOC [159] have quoted impurity values of; total hydrocarbons < 5 parts per million (ppm), moisture <5 ppm, CO_2 < 3 ppm, and thus their impact on flame propagation is deemed insignificant. However, it has been subsequently determined that the synthesized air bottles,

manufactured for low impurity contamination, have a relatively large quoted range of 19.9% - 21.9% O_2 in N_2 balance [160]. To understand the potential impact of the O_2 concentration, this range was modelled in CHEMKIN-PRO, for Φ =1.0 and 0.70 at 298 K and 0.1 MPa, using the GRI-M 3.0 reaction mechanism [155]. The relative difference in S_u modelled using a ratio of 21/79 (O_2/N_2) as a reference, against the quoted range (19.9% - 21.9% O_2) is depicted in Figure 5.3.

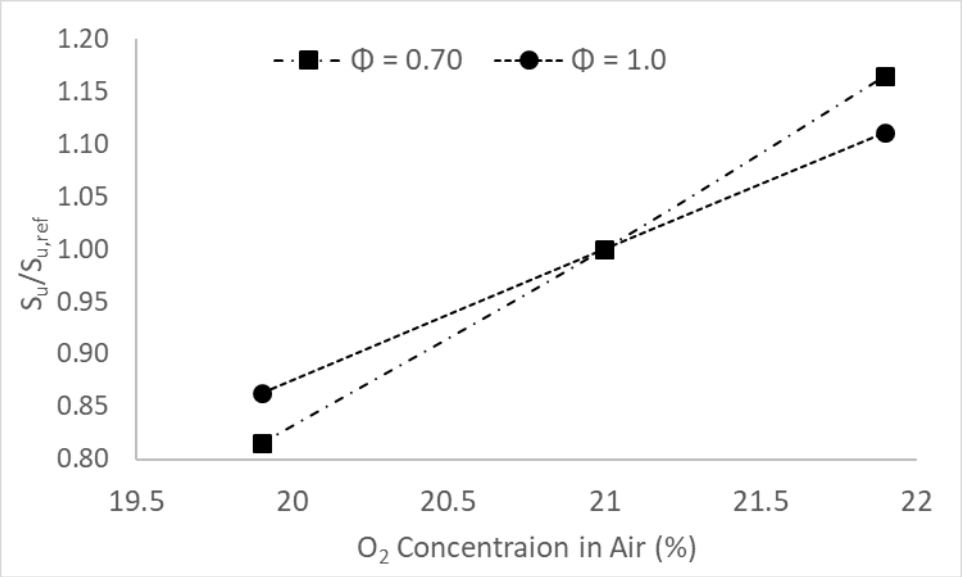

Figure 5.3 – Influence of Modelled Variations in O_2/N_2 Ratio on S_u - $S_{u,ref}$ is S_u at reference temperature Tu=298K, and P = 0.1 Mpa and O2/N2 ratio (21/79) modelled using the CHEMKIN-PREMIX code with GRI - M 3.0 [155]

It is observed that small variations in O_2/N_2 ratio have a significant impact on S_u, with a potential variation of up to ±10% for stoichiometric CH_4/air flames (with the impact of O_2/N_2 increasing at leaner conditions). Acknowledging the unlikelihood that both zero-grade air bottles employed correspond to the higher and lower quoted N_2/O_2 range, average relative differences between tests 1-10 and 11-20 are < 4% (for either plane of measurement) falling well within modelled differences. To be confident that this observed bias in S_u was due to a change in O_2/N_2 ratio within the two air cylinders, a gas analyses of the bottles would have been required. However, unfortunately this was not possible as the initial air cylinder was sent back to the manufacturer before potential issues in permissible oxygen concentrations were highlighted.

Aside from the noticeable step-change in S_u between test 10 and 11 (and test 1 with a S_u noticeably slower than tests 2-10 conducted using the same zero-air grade bottle) there seems to be little variation and good repeatability. This is expected due to the closed nature of the combustion system employed, with variations in laboratory conditions, for example temperature or humidity, having no obvious impact on results. The temperature within the combustion chamber is controlled via a closed loop PID system, with sufficient time during

fuel and oxidiser mixing (approximately 15 minutes including fan-mixing for 2 minutes) ensuring that the fuel and air reach temperature equilibrium within the chamber. The contamination level due to imperfect vacuum was calculated as < 0.1% (see Section 4.1) and would be a constant over the test duration and thus not have a noticeable impact on results. The only perceived variability therefore relates to the set-up of the optical Schlieren system. However, to limit this impact the system components were marked permitting accurate repositioning, with scaling factors in both the H and V plane noted as < 1% across the duration months of testing.

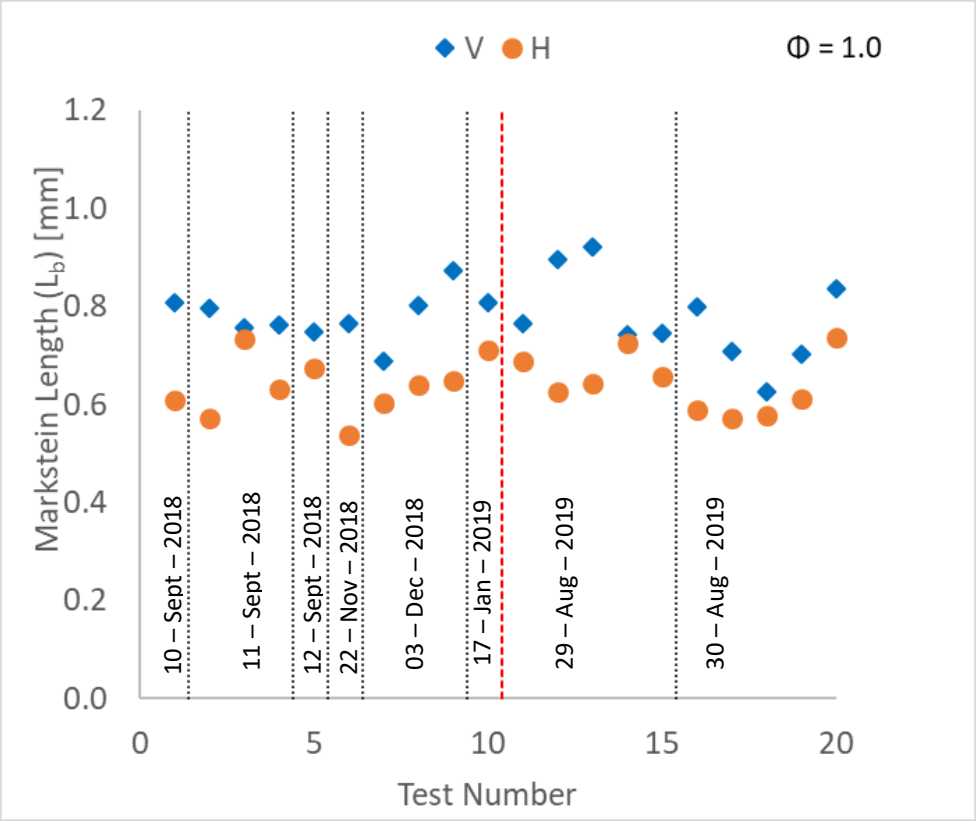

Figure 5.4 – Variations in L_b for CH_4/air Repeats (Φ = 1, Tu = 298 K, P = 0.1 MPa) – Black lines denote tests conducted on the same day, red line denotes change in zero-air grade bottle used for experiments - Data range = 8 - 39 mm, Differential extrapolation range = 10-30 mm

The L_b of the corresponding S_u stoichiometric CH_4/air tests (Figure 5.2), are plotted in Figure 5.4. As witnessed for the measured S_u again for the case of L_b, the vertical (V-L_b) measurement is systematically larger than the horizontal (H-L_b) counterpart. The difference in L_b between both measurement planes is not constant, with relative differences ranging from a minimum of ~2% to a maximum of ~30%, with an average ~17% difference. With such important differences generated using the same experimental apparatus and data-extraction methodology, the high level of scatter witnessed in literature (see Figure 4.17) becomes comprehensible.

The precise control of the choice of isotherm using the Schlieren optical system is difficult, possibly explaining the observed differences. Although care is applied to ensure that measurements are taken relative to the unburnt side, potential changes in measured isotherm have an important associated impact on measured L_b, whilst having very little influence on measured S_u [161]. Furthermore, when measuring L_b using a Schlieren set-up, one is effectively attempting to measure changes in the order of <0.1mm per time step of 0.0002 seconds (5000 frames per second) on a flame propagating at > 30cm/s. Additionally, it should be noted that the spatial resolution of the optical system employed was 0.14 mm, which is of the same order of magnitude as the flames thickness, rendering precise control of isotherm selection difficult.

The scatter in measured L_b (irrespective of measurement plane) are as important (and on some repeat points even larger) than variations that would be expected to be generated between the use of the linear and non-linear models (Section 4.5, Table 4.4). As expected, there seems to be no correlation between date of experiment and measured L_b, with variation seemingly random. The change in oxygen concentration due to the zero-air grade being replaced (red line Figure 5.4), does not notably impact L_b.

Considering that the repeated tests were conducted at stoichiometric conditions, factors that could possibly generate differences in the flame propagation in the H or V plane, namely the impact of buoyancy or loss of sphericity should not be present and were not witnessed during the post-processing of photographic-images. Additionally, the impact of changes in ambient pressure, temperature or Φ would generate sources of uncertainties when comparing different tests. However, for one test, those differences should affect the flame propagation in the same manner, irrespective of measurement plane (V or H). Consequently, this would not explain the differences measured between both planes. Thus, an attempt to better understand the observed differences, analyses was undertaken by processing the flame speeds using different radius ranges to investigate if pressure effects were impacting flame growth in the H plane.

As discussed, the usable data range of flame propagation was fixed at 8-39 mm (upon which the initial polynomial is fitted, Section 4.4.1) and the differential of the flame radius polynomial range altered between 10-25 mm, 10-30 mm and 10-35mm. It was assumed that by fixing the initial data range to 8-39mm and varying the differential polynomial range, measured S_u should stay relatively constant if uninfluenced by pressure/confinement effects.

The relative differences in V-S_u, normalised to a radius range of 10-25 mm, are illustrated in Figure 5.5. The corresponding L_b, employing the same relative difference approach, are depicted in Figure 5.6.

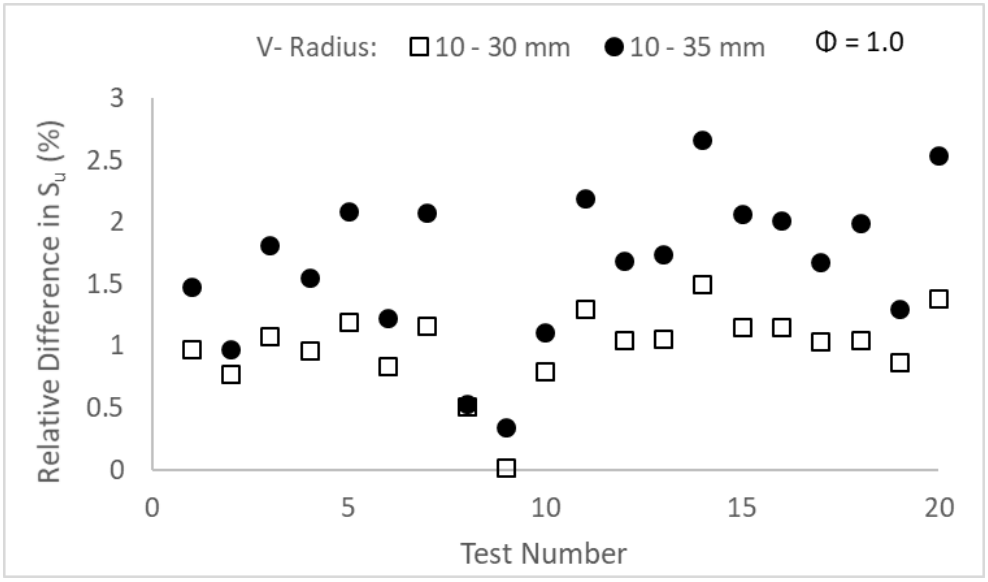

Figure 5.5 – Impact of Radius Range on S_u – Vertical Plane (Φ = 1, T_u=298 K, P = 0.1 Mpa) Relative Difference Normalised to 10-25mm Radius Range

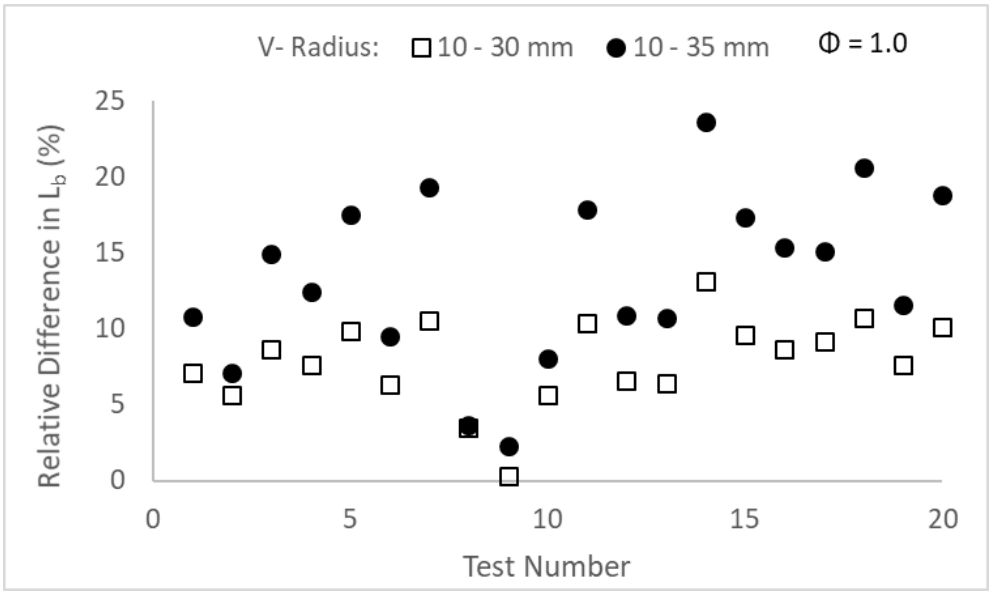

Figure 5.6 – Impact of Radius Range on L_b – Vertical Plane (Φ = 1, T_u=298 K, P = 0.1 MPa) Relative Difference Normalised to 10-25mm Radius Range

As can be seen from Figure 5.5, small increases in V-S_u are exhibited when the 10-35 mm flame radius range was employed. This confirms that in the V-plane of measurement, the spherically expanding flame is not inhibited by confinement (at least till 39mm), rather a subtle acceleration is witnessed. Nevertheless, average differences are < 1% and < 2% for a 5mm and 10mm flame radius increase. This is in agreement with similar analysis conducted by Chen [83] around the accuracy of extracted flame parameters using spherically expanding flames. Chen notes that uncertainty related to the flame radius range varies between 3-5% for methane/air mixtures with Φ ≤ 1.0 (at standard temperature and pressure). Following work and recommendations by Jayachandran et al. [162] and Varea et al. [163], Chen suggests that instead of using the extracted S_u (or U_L), the stretched flame speed (S_n) versus stretch or flame radius should be employed when validating chemical kinetic models. In doing

so, associated uncertainties related to extrapolation and choice of flame radius would be removed. With respect to the V-L_b, differences are considerable, as illustrated in Figure 5.6. Clearly, L_b is significantly more sensitive to radius range than S_u, with average relative differences of 8% and 13% for a modest increase in interrogated flame radius, respectively.

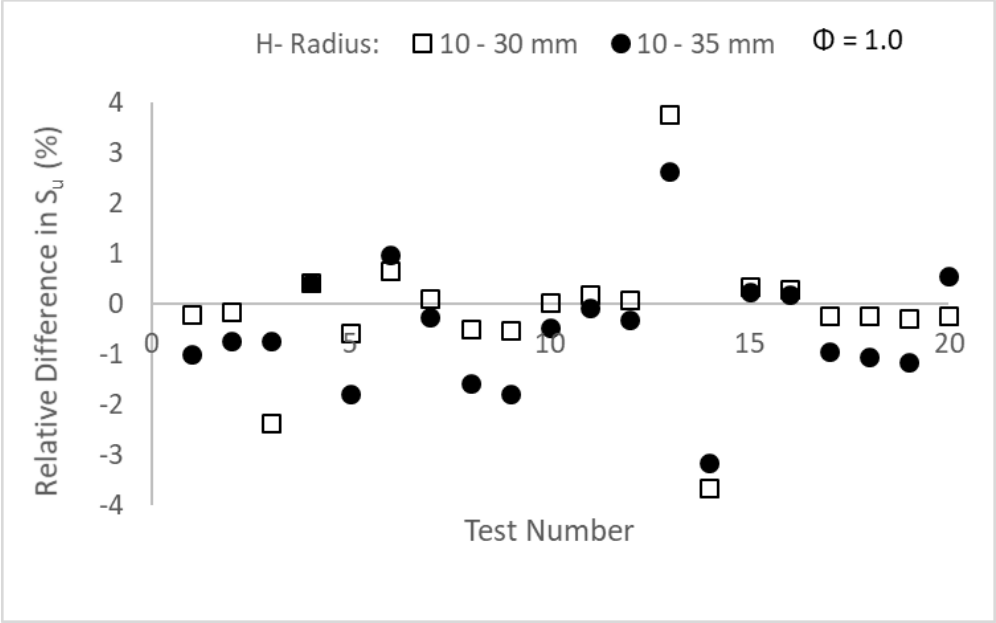

Figure 5.7 – Impact of Radius Range on S_u – Horizontal Plane (Φ = 1, T_u = 298 K, P= 0.1 MPa) Relative Difference Normalised to 10-25mm Radius Range

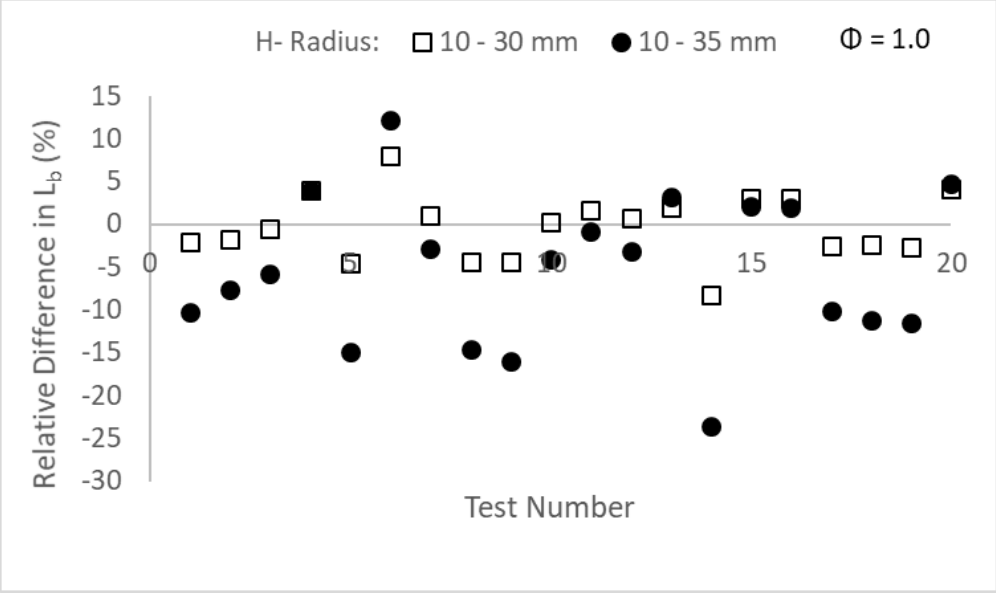

Figure 5.8 – Impact of Radius Range on L_b – Horizontal Plane (Φ =1, T_u = 298 K, P = 0.1 MPa) Relative Difference Normalised to 10-25 mm Range Radius

The impact of flame radius selection upon H-S_u and H-L_b is illustrated in Figure 5.7 and Figure 5.8, respectively. A deceleration of the flame is observable for most of the repeats, with an average deceleration of < 0.5% and 1%, for a 5mm and 10mm increase. Although subtle, this should not be the case, as all tests have positive L_b, representative of an acceleration with reducing stretch effects (flame growth). This observable flame inhibition on the H-plane may possibly be attributed to confinement effects and/or the inability to

measure precisely the leading flame edge on the horizontal plane due to location of electrodes. Nevertheless, these differences fall well within the uncertainty range proposed by Chen [83] of 3-5% for CH_4/air mixtures with $\Phi \leq 1.0$. The impact of flame radius selection on H-L_b is plotted in Figure 5.8. For the tests exhibiting a flame deceleration, L_b reduces on average by 4% and 10% for a 5mm and 10mm flame radius increase.

For the stoichiometric CH_4 repeats, differences in attained S_u between the H and V planes, for different radius ranges are illustrated in Figure 5.9. Note that differences are calculated relative to the H-plane. Clearly, differences between attained V-S_u and H-S_u augment with growth in flame radius, with average differences of ≈ 3%, 4% and 5%, for 10-25, 10-30, and 10-35 radius selection, respectively.

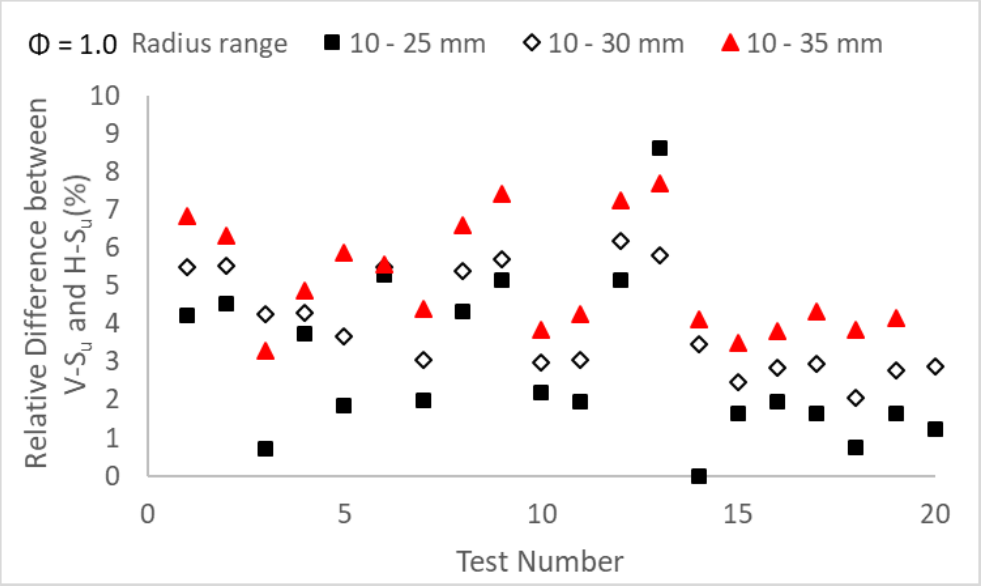

Figure 5.9 – Difference in S_u Between H and V Planes for 10-25, 10-30, and 10-35 mm Flame Radius Ranges – Differences are Calculated with Respect to the H Plane (Φ = 1, T_u = 298 K, P = 0.1 MPa)

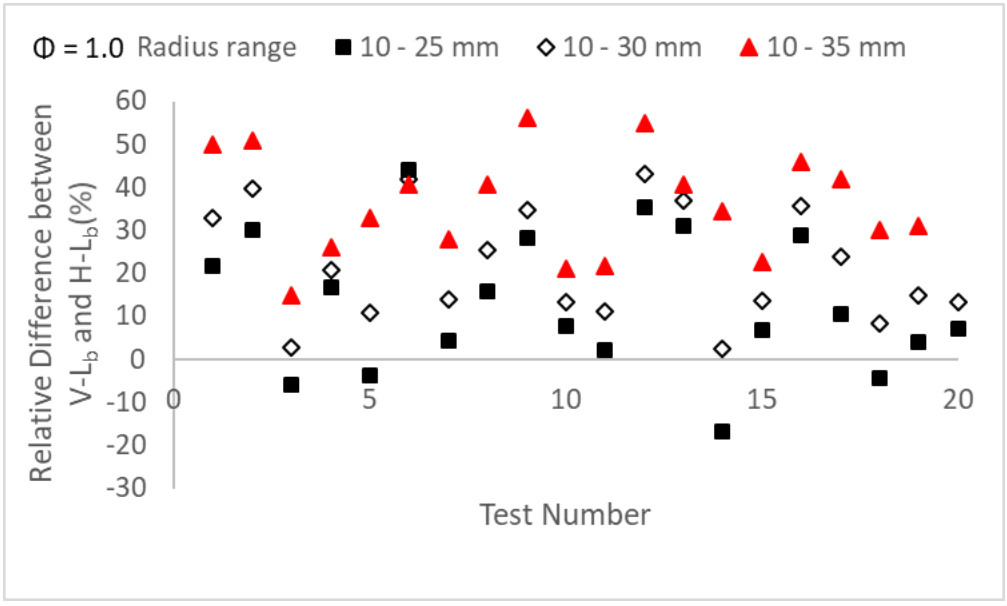

Figure 5.10 – Difference in L_b Between H and V planes for 10-25, 10-30 and 10-35 Flame Radius Ranges – Differences are Calculated with Respect to the H Plane – (Φ = 1, T_u = 298 K, P = 0.1 MPa)

In terms of L_b, differences are significant, with the same trend present; an increasing difference between measured H and V values as flame radius grows, illustrated in Figure 5.10. Average differences amount to 13%, 22% and 35%, for 10-25, 10-30, and 10-35 radius selection, respectively, with maximum differences considerably higher than the average (up to 50%).

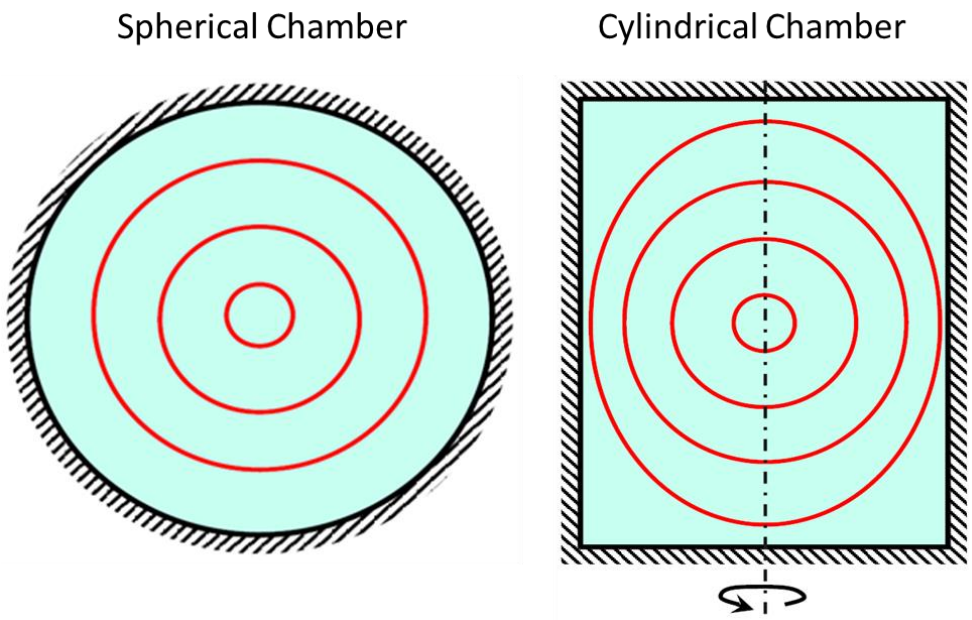

Figure 5.11 – Schematic Representation of the Effect of Chamber Geometry on Sphericity of Expanding Flame – From [164]

The subtle flame deceleration (< 1%) witnessed on the horizontal plane with growing flame radius, (Figure 5.7), coupled with the small acceleration (< 3%) witnessed on the vertical plane, (Figure 5.5), potentially indicates that flame propagation is being influenced by chamber geometry. The impact of a cylindrical or spherical chamber on the sphericity of the expanding flame is schematically represented in Figure 5.11. For cylindrical chambers, after a certain flame radius, flame propagation is constrained on the horizontal axis due to confinement, with those effects arising earlier than on the vertical plane due to the proximity of the chamber walls. Consequently, as the flame grows, the spherical flame becomes elliptical. Although the recommendation on confinement effects of Burke et al. [87], (confinement effects are negligible when using a flame radius < 30% of total combustion volume, 39 mm for employed rig) and that of Chen [83] (R_f/R_w < 25%, where R_f is the flame radius, and $R_w=(3V/4\pi)^{1/3}$ for non-spherical chambers of volume V, $R_f/R_w \approx 20\%$ for a 39 mm radius for the rig employed) were respected, possible influence of confinement on the spherically expanding flame may have still been present.

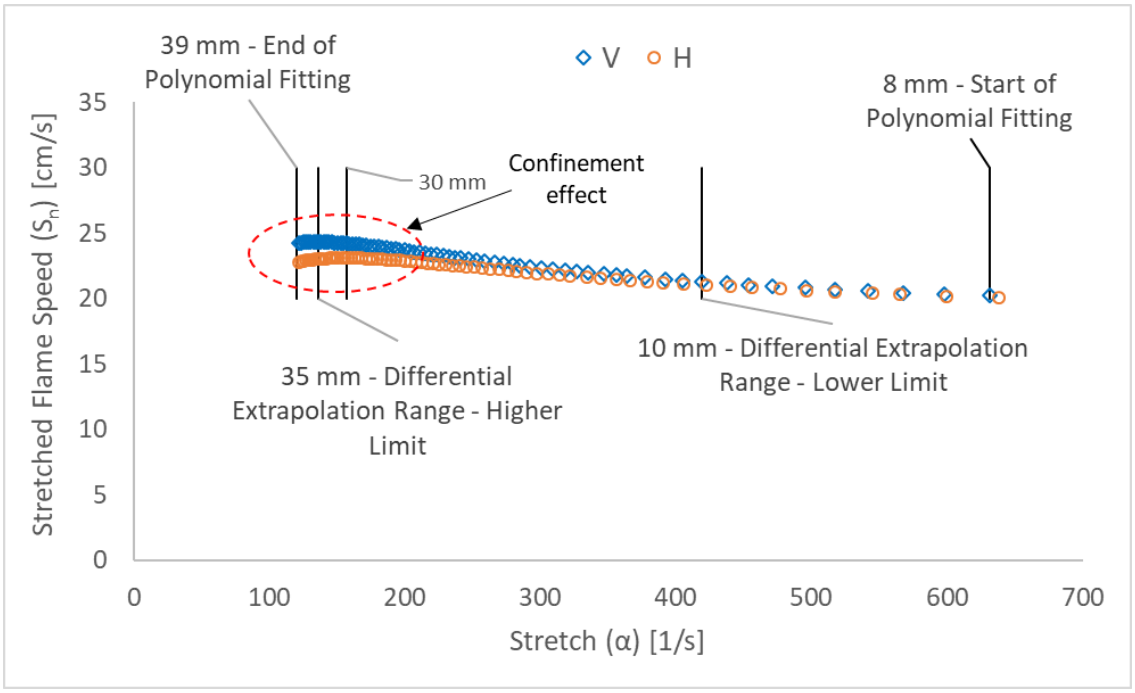

Figure 5.12 – Stretched Flame Speed vs Stretch – Radius range 8 mm – 39 mm, Differential Range 10-35 mm (Φ = 1, T_u = 298 K, P = 0.1 MPa)

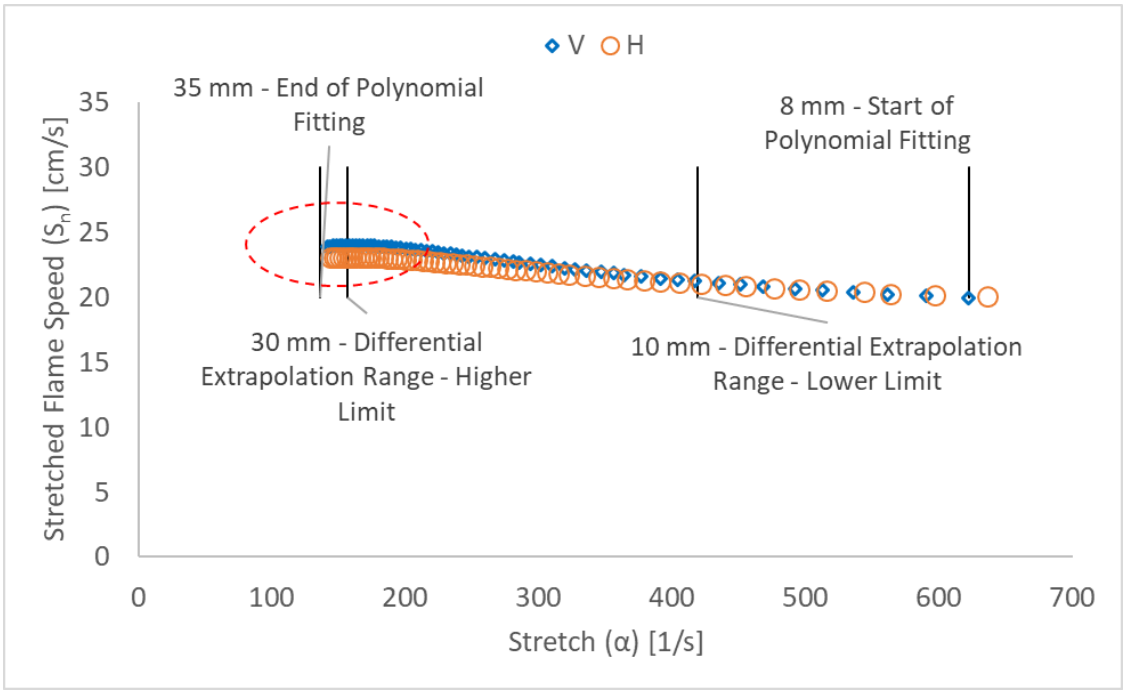

Figure 5.13 – Stretched Flame Speed vs Stretch – Radius Range 8 mm – 39 mm, Differential Range 10-30 mm (Φ = 1, T_u = 298 K, P = 0.1 MPa)

In order to minimise differences in attained S_u in the vertical and horizontal plane, the flame radius range was reduced from 39 mm to 35 mm (i.e. 8 – 35mm), with a differential polynomial fitting of 8 – 30mm. Figure 5.12 and Figure 5.13, illustrate the flame propagation versus stretch using the initial radius range (8 – 39mm) and the reduced range (8 – 35mm), respectively. Note that the both Figure 5.12 and 5.13 exemplify the stoichiometric repeat which yielded the largest difference in attained S_u and L_b between both planes of measurement. It is evident from Figure 5.12, that once the H flame had grown to a radius greater than 35mm, deceleration occurred (see superimposed circle). Upon application of the reduced radius range, Figure 5.13, the H flame exhibits less deceleration, with differences between V-S_u and H-S_u minimised (see superimposed circle). Average differences in S_u between both planes of measurement upon application of the reduced radius range amount to < 3%, in good agreement with quoted values of 2-3% by Chen [83]. With respect to L_b, average differences between both measurement planes, drop from ~36% to ~20% with the use of the restrained flame radius range, a significant difference. Consequently, it was decided to apply a usable radius range of 8 – 35 mm with a differential polynomial range of 10-30 mm for the lean (Φ = 0.70) CH_4/air repeats.

5.3 Lean Methane Analysis

A series of 20 test results were generated for lean (Φ = 0.70) CH_4/air mixtures, at ambient temperature and pressure (defined herein as T_u = 298 K, P = 0.1 MPa). As with the stoichiometric CH_4/air repeats, all experimental conditions were kept as constant as possible. The only change that was necessary was with respect to the utilised zero-grade air source as discussed previously.

5.3.1 Critical Radius Evaluation

As highlighted in literature [78], [83], [86], early flame growth (small radii) is affected by ignition energy. It is thus important to quantify till which radius the flame is influenced by initial energy deposit. To do so, the flame propagation speed against stretch for the lean CH_4/air mixtures were analysed. Very lean CH_4/air mixtures (Φ = 0.60-0.70) exhibit a L_b close to 0, propagating almost linearly, independently of stretch influence. The evolution of the flame propagation (for this example the temporal evolution of the Schlieren flame radius), against stretch rate is illustrated in Figure 5.14, for both H and V planes of measurement.

As can be seen from Figure 5.14, there are two distinct propagation evolution regimes. The first exhibits very high stretch rates, due to the high associated curvature at small flame radii. The flame propagation speed for these small flame radii is strongly influenced by the initial ignition energy, which overdrives flame propagation. As the initial ignition energy dissipates, the flame propagation starts to act linearly. This transition denotes

the change of regime of the flame, delimitated by a critical radius, moving from an ignition affected region to a non-affected region [78] .

For the example used in Figure 5.14, this critical radius was determined to be ≈ 5.4 mm, for both H and V measurement planes. It can be assumed that beyond this critical radius the initial ignition energy has negligible impact on the proceeding flame propagation. This critical radius of 5.4 mm is similar to the 6mm recommendation of Bradley et al. [86] and that reported by Halter et al. 6.5 mm [78], consequently re-validating the use of an 8 mm radius, which was subsequently maintained for the remainder of the study. It should be noted that this unaffected flame radius will vary depending on fuel and Φ but should retain the same order of magnitude.

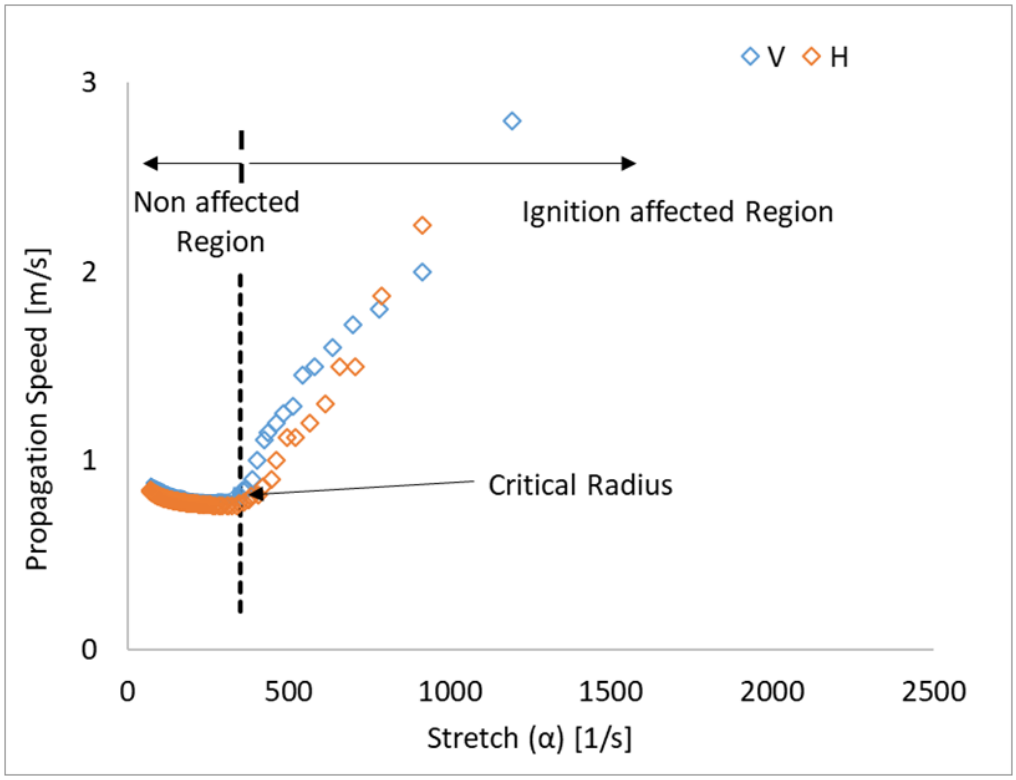

Figure 5.14 – Influence of Initial Ignition Energy on Horizontal and Vertical Flame Front Propagation (CH_4/air, T_u = 298 K, P = 0.1 MPa, Φ=0.70)

The variation in measured S_u and L_b for the lean CH_4/air (Φ = 0.70) repeats are plotted in Figure 5.15 and 5.16, respectively, for both the H and V planes of measurements. Again, the superimposed black lines highlight tests conducted on the same day, with the red line again denoting a change in the zero-air grade bottle. As per the recommendations of the previous section, results were generated upon application of an initial data range of 8-35 mm and a differential extrapolation range of 10-30 mm.

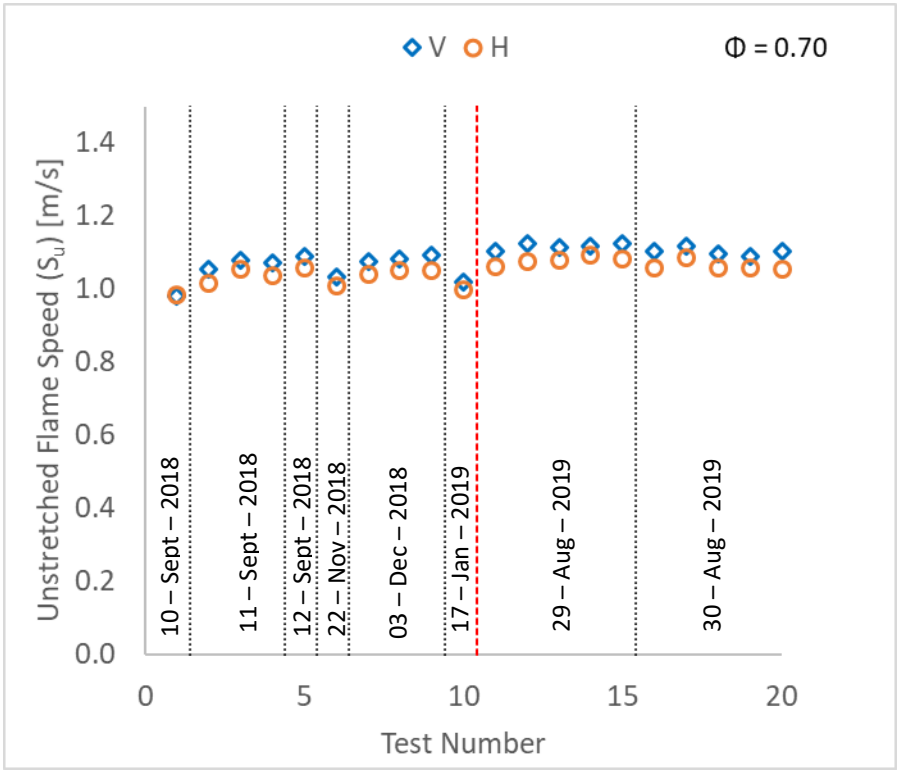

Figure 5.15 – Variations in S_u for Lean CH_4/air Repeats (Φ = 0.70, T_u = 298 K, P = 0.1 MPa) – Black lines denote tests conducted on the same day, red line denotes change in zero-air grade bottle used for experiments - Data range = 8 - 35 mm, Differential extrapolation range = 10-30 mm

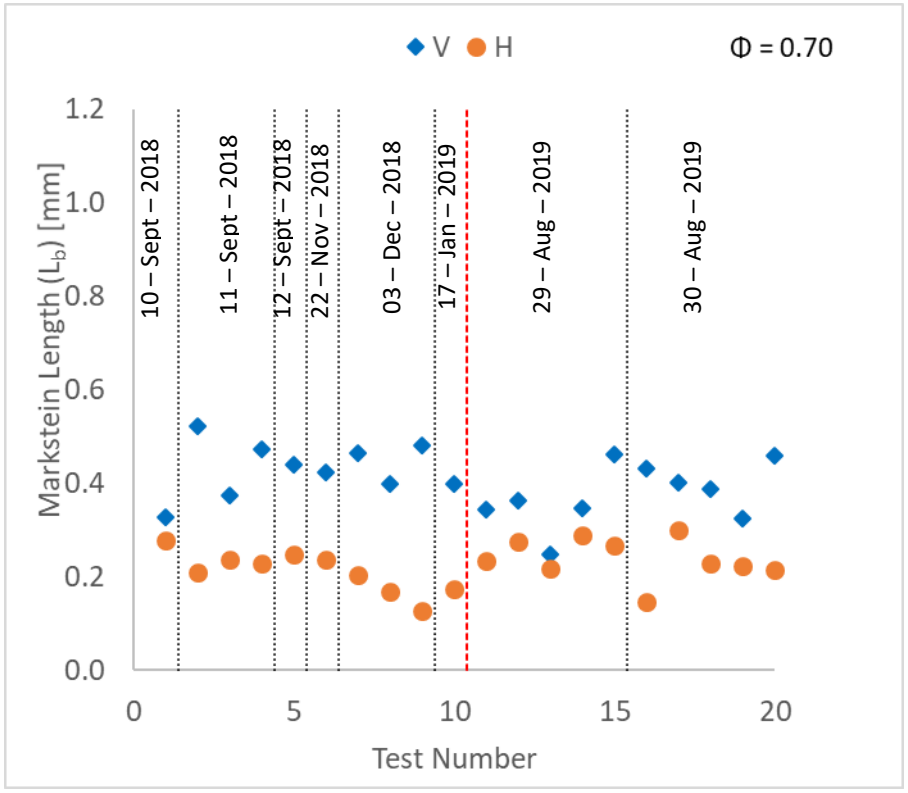

Figure 5.16 – Variations in L_b for Lean CH_4/air Repeats (Φ = 0.70, T_u = 298 K, P = 0.1 MPa) – Black lines denote tests conducted on the same day, red line denotes change in zero-air grade bottle used for experiments - Data range = 8 - 35 mm, Differential extrapolation range = 10-30 mm

From Figure 5.15, measured V-S_u remains marginally faster than corresponding H-S_u, as was witnessed with the stoichiometric CH_4 repeats, with an average relative difference < 3%. The maximum difference in measured S_u across the 20 repeats is ≈ 10%, irrespective of measurement plane. This difference can in part be attributed to the change in zero-air grade bottle, with a noticeable bias in S_u again witnessed between tests 10-11. For lean mixtures, the impact of O_2 concentration upon S_u is considerable, as illustrated in Figure 5.3. Modelled changes across the range of O_2 specified by the zero-air grade manufacturer (19.9% - 21.9% O_2) in CHEMKIN-PRO can lead to differences as large as ± 18%. However, other possible sources of uncertainty (temperature, ambient pressure, Φ) explored and quantified in the next section also contribute to the observed differences.

Variations in L_b across the 20 lean CH_4/air repeats are illustrated in Figure 5.16. Important differences are evident between the V and H measured L_b, with differences seemingly inconsistent. The H-L_b is consistently lower than the V-L_b, replicating the trend observed in S_u. Although differences in L_b across the 20 tests is significant, ≈ 50%, the observed scatter falls within literature reported values (Section 4.5, Figure 4.17).

From the stoichiometric and lean CH_4/air analysis it was decided that an 8 – 35 flame radius range would be applied for data-processing of subsequent result chapters. This range is deemed to be most appropriate, allowing sufficient data points whilst simultaneously minimising any potential confinement effect. Differences in attained S_u between both measurements plane is small < 3 % (for both Φ = 0.70 and 1.0), and thus should not impact reported results. Due to the lean nature of the tests conducted for this thesis, flames may potentially be impacted by buoyancy effects. Should this occur (at Φ<0.70), the flame vertical radius would rise outside of the camera focus, and consequently only the H-axis of measurement would be available for post-processing. Thus, in order to maintain consistency across the results generated, the horizontal plane of measurement was used for post-processing for all experiments in subsequent chapters. With respect to L_b, differences are significant, however measures of L_b will identify trends, with reported values thought to be smaller than those which would have been witnessed if the vertical plane was used.

Having determined the flame radius ranges to be used for post-processing whilst investigating the influence of flame radius range, confinement and ignition energy, quantification of other possible sources of uncertainty was undertaken next, with experimental uncertainty quantified in relation to S_u.

5.4 Quantifying Experimental Uncertainty

This section presents an overview of the uncertainty analysis conducted. The analysis herein is based upon the methods outlined by Moffat [165], in which total uncertainty estimate is given by Eqn. 5.1, where (B_{Su}) represents the total bias uncertainty, ($t_{M-1,95}$) is Student's *t* value at a 95% confidence interval and M-1 degrees of freedom, (σ_{Su}) is the standard deviation of the repeated experiments, and (M) the number of experimental repeats at each condition,

$$U_{Su} = \sqrt{B_{Su}^2 + \left(\frac{t_{M-1,95}\sigma_{Su}}{\sqrt{M}}\right)^2} \quad \text{Eqn. (5.1)}$$

The total bias uncertainty, given by Eqn. 5.2, relating changes in S_u with respect to an independent variable, (v_i, i.e. temperature, ambient pressure, Φ, etc.) and the fixed error linked to that variable (y_i),

$$B_{Su} = \sqrt{\sum_{i=1}^{n} \left(\frac{\partial S_u(v_i)}{\partial v_i} y_i\right)^2} \quad \text{Eqn. (5.2)}$$

In order to utilise Eqn. 5.2, the relationship between S_u and each independent variable must be established. These relationships were generated using estimations from appropriate chemical models, with GRI – M 3.0 reaction mechanism [155]. For each independent variable an example calculation will be shown for lean (Φ = 0.70) and stoichiometric (Φ = 1.0) CH_4/air mixture. Example of quantification of uncertainty for SEF experiments following this method can be found in [31], [62].

5.4.1 Influence of Ambient Temperature:

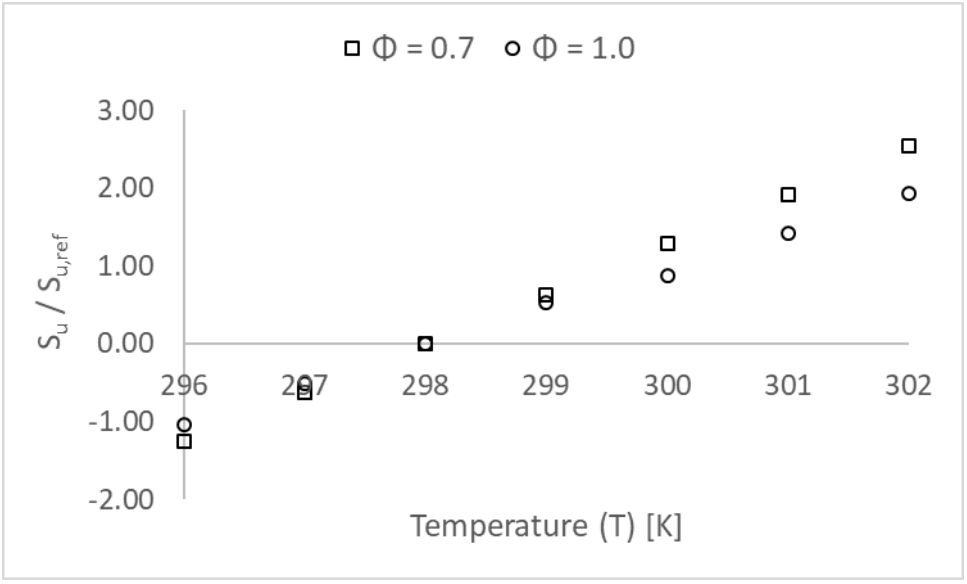

Figure 5.17 – Modelled Impact of Variations in Unburnt Reactant Temperature on S_u – CH_4/air (P = 0.1 MPa)

Using a reference temperature of 298 K, Figure 5.17 illustrates the impact of small differences in unburnt reactant temperature on S_u. With a change in 1 K in unburnt temperature, modelled results suggest a relative difference in S_u of ~0.70% and ~0.50% for an Φ = 0.70 and 1.0, respectively. This level of uncertainty is in good agreement with values found in literature, with a relative change of S_u of ±2% for a ± 3K variation quoted [83]. For the combustion system employed, the accuracy of the temperature control system (outlined in section 4.1.2.3) is ± 2 K. The average S_u recorded for 20 repeats was ~1050 mm/s (Φ = 0.70) and ~2633 mm/s (Φ = 1.0). This leads to an example uncertainty of approximately **~± 14.7 mm/s** (Φ = 0.70) and **~±26.4 mm/s** (Φ = 1.0).

5.4.2 Influence of Ambient Pressure:

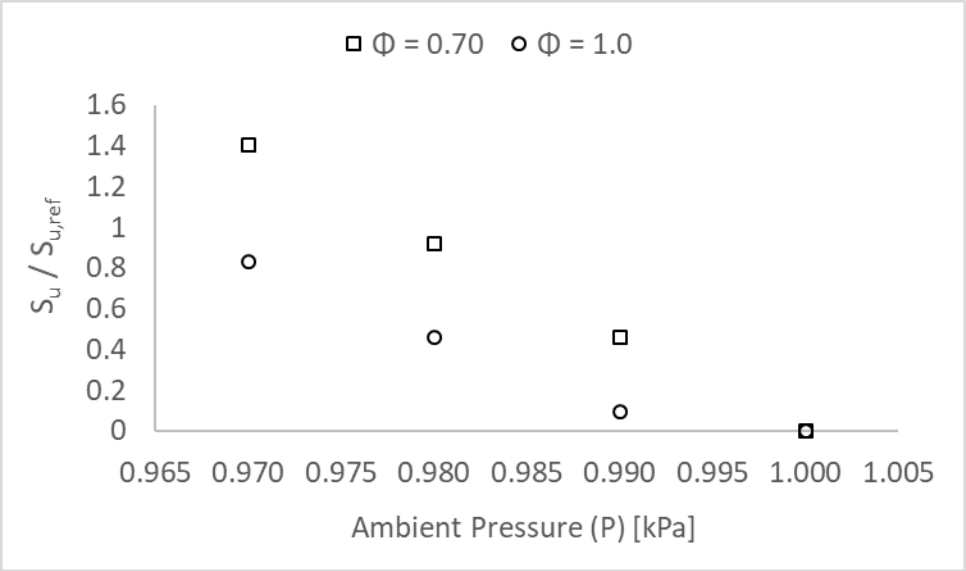

Figure 5.18 – Modelled Impact of Variations in Ambient Pressure on S_u – CH_4/air (T_u=298 K)

The ambient pressure was recorded before ignition of each test point. The targeted ambient pressure was of 0.1 MPa (100 kPa), with the pressure system measurement accuracy of ± 0.01kPa (1%). The maximum difference recorded between the targeted pressure and the actual recorded ambient pressure was ~975 kPa. Figure 5.18 illustrates the impact of small differences in ambient pressure on S_u. With a change of 0.01 KPa, modelled results suggest a relative difference in S_u of ~0.5% (Φ = 0.70) and ~0.3% (Φ = 1.0). This leads to an example uncertainty of approximately **~± 5.3 mm/s** (Φ = 0.70) and ~**±7.9 mm/s** (Φ = 1.0).

5.4.3 Influence of Equivalence Ratio:

For most of the testing, reactants were introduced using a high accuracy Coriolis mass flow controller (Section 4.1.2.1), however, on some occasions when the mass flow controller was unavailable, the mixing system utilised partial pressure to confirm blends. Unfortunately, when logging data, mention of type of delivery fuel system employed was

overlooked. Consequently, from a conservative perspective, uncertainty in Φ will be assessed with respect to the pressure gauge (± 0.01kPa – 1%) and not the more precise mass flow controller (± 0.5%).

The relationship proposed by Chen [83] was employed to evaluate the real Φ of the mixture. For the case of stoichiometric (Φ = 1.0) and lean (Φ = 0.70) CH_4, applying an error factor of ±0.01 KPa, yields a resultant range in specified Φ of **~0.994 – ~1.006** and **~0.693 – ~0.707**, respectively. Egolfopoulos et al. [71] discuss an uncertainty of circa 0.005 for CH_4/air mixtures of Φ =0.70, in good agreement with values evaluated using the relationship proposed by Chen [83]. Modelled results (Figure 5.19), suggest a difference of 4.20% (Φ = 0.70) and 0.70% (Φ = 1.0) for a change in Φ of **~± 0.006**. This leads to an example uncertainty of approximately **± 44.1 mm/s** (Φ = 0.70) and **± 18.5 mm/s** (Φ = 1.0).

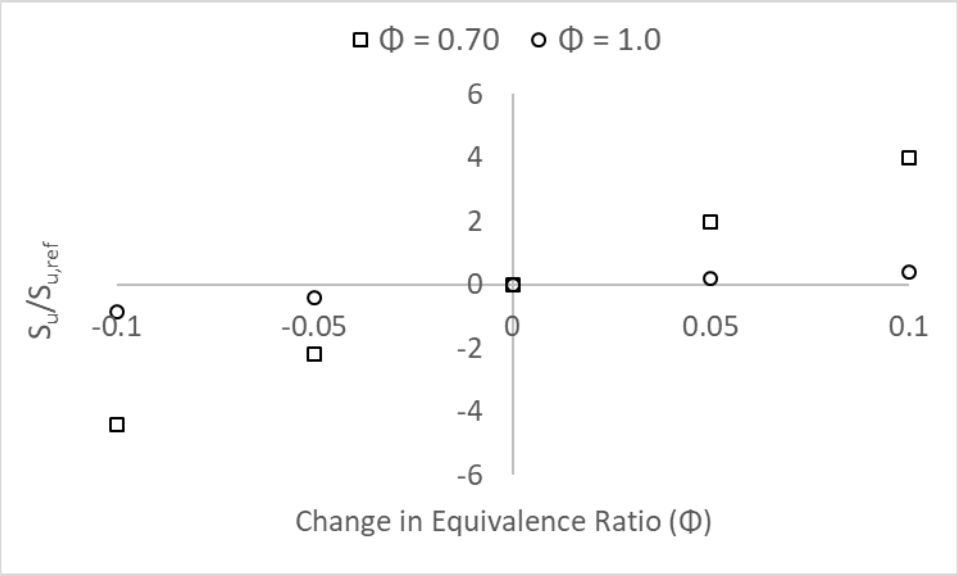

Figure 5.19 – Modelled Impact of Variations in Φ on S_u – CH_4/air (T_u=298 K, P = 0.1 MPa)

5.4.4 System Optics:

The spatial resolution of the digital image produced is ~0.14mm per pixel, yielding a potential oscillation around ±0.07 mm per time step. Since the error induced by the polynomial fitting is approximately of the same size, to maintain a conservative approach, the fluctuation was doubled back to 0.14mm. A filming rate of 5000 frames per second was employed for all tests conducted, yielding an initial uncertainty of 700mm/s (0.14/0.0002). This uncertainty is averaged across the number of frames used per experiment as it represents the uncertainty across the whole dataset. On average, the lean CH_4/air tests had 160 usable frames, and the stoichiometric tests 60 frames. This generates an uncertainty of **±4.5 mm/s** and **±12 mm/s** for 0.70 and 1.0 Φ, respectively. The inaccuracy in filming rate which was specified to 5000 f.p.s +/- 0.25 frames, was deemed negligible, with a resultant error in the order of 0.01%.

5.4.5 Gas Mixture Quality:

The gas mixture quality of the methane fuel used was of 99.9% purity [159], with a contamination percentage, due to imperfect vacuum calculated to be ~0.1%, (Section 4.2.1). Summing these two uncertainties gives a total maximum contamination of ~0.20%. The resultant uncertainty would therefore be **±2.1 mm/s** and **±5.34 mm/s** for the lean and stoichiometric methane mixtures, respectively. Note that application of error calculation in this way assumes an impurity will not accelerate S_u by a greater amount than the opposing zero assumption.

5.4.6 Influence of N_2/O_2 concentration:

The flame speed also depends on the O_2/N_2 ratio of air utilised. The impact of the oxygen concentration is analysed due to the use of two different zero-air grade bottles during testing. Although, no gas analysis was performed on the employed synthesised air bottles to precisely quantify the difference in O_2 concentration, computational modelling was performed with respect to the manufacturer's quoted O_2/N_2 balance (19.9 – 21.9 % O_2 in N_2). The impact of small changes in O_2 concentration upon S_u are illustrated in Figure 5.3. Modelled results indicate a significant impact on S_u, approximately ~± 15% (Φ = 0.70) and ~±10% (Φ = 1.0), relative to a 21/79 (O_2/N_2) ratio, in good agreement with values found in literature (6 – 11% for a O_2 volumetric change from 21% to 20.5% [83]). This leads to an uncertainty in S_u of ~± ~±157.5mm/s and ~±263.3 mm/s, for lean and stoichiometric conditions, respectively. Considering the unlikelihood of employed zero-grade air bottles spanning the entirety of the manufacture's specifications, a change in ±0.5% in O_2 composition (relative to a 21% O_2 concentration) was assumed. This leads to an example uncertainty of **~±94.5 mm/s** and **~±184.3 mm/s** for the 0.70 and 1.0 Φ CH_4 mixture, respectively.

5.4.7 Others Possible Source of Uncertainty:

Other possible sources of uncertainty have been deemed negligible. The impact of ignition energy on flame propagation has been demonstrated to dissipate when flame radius > 6mm [86]. As a precaution, an 8 mm flame radius was utilised for the processing of datasets. According to Ronney and Wachman [166], for flames that exhibit U_L > 15 cm/s, as is the case for CH_4/air flames at Φ = 0.70 and 1.00, influence of buoyancy can be deemed negligible. Other possible sources of uncertainty related to flame radius range and confinement have been analysed in section 5.5.1.

5.4.8 Uncertainty Calculation for lean and stoichiometric CH_4

Having established the relationship between S_u and each independent variable, Eqn. 5.2 is employed to evaluate the total bias uncertainty:

$$B_{Su,(\emptyset=0.70)} = \sqrt{14.70^2 + 5.25^2 + 44.11^2 + 4.50^2 + 2.10^2 + 94.51^2} = \pm \mathbf{105.58\ mm/s}$$

$$B_{Su(,\emptyset=1.0)} = \sqrt{26.32^2 + 7.90^2 + 18.43^2 + 12^2 + 5.26^2 + 184.28^2} = \pm \mathbf{187.68\ mm/s}$$

The standard deviation of the lean and stoichiometric CH_4 data (M=20) was 28.47 mm/s and 96.35 mm/s, respectively. Using a t-value at a 95% confidence level for M-1 (19) repeats is 2.093 [167], giving U_{Su} (Eqn. 5.1) values of:

$$U_{Su,\Phi=0.70} = \sqrt{105.58^2 + \left(\frac{2.093\ x\ 28.47}{\sqrt{20}}\right)^2} = \mathbf{\pm\ 105.74\ mm/s}$$

$$U_{Su,\Phi=1.0} = \sqrt{187.68^2 + \left(\frac{2.093\ x\ 96.35}{\sqrt{20}}\right)^2} = \mathbf{\pm\ 188.92\ mm/s}$$

The total bias uncertainty for the lean and stoichiometric CH_4 dataset is illustrated in Figure 5.20 and 5.21 respectively, with one standard deviation superimposed as red lines. The total uncertainty is large, respectively ~± 10% and ~± 7% for the lean and stoichiometric CH_4 datasets. Unsurprisingly for Φ = 0.70, all S_u repeats fall within the total uncertainty range, see Figure 5.20. For Φ = 1.0, 19 of the 20 repeats fall within calculated total uncertainty, see Figure 5.21, with test 1 exhibiting a comparatively spurious S_u.

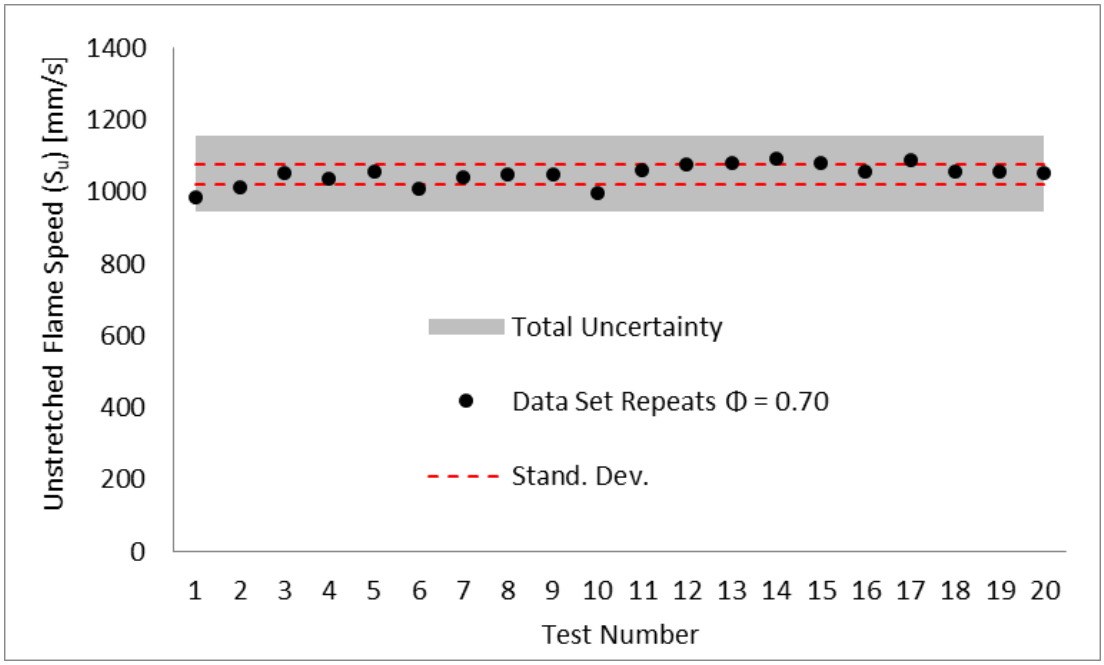

Figure 5.20 – S_u of Lean CH_4 Repeat Dataset with Superimposed Uncertainty

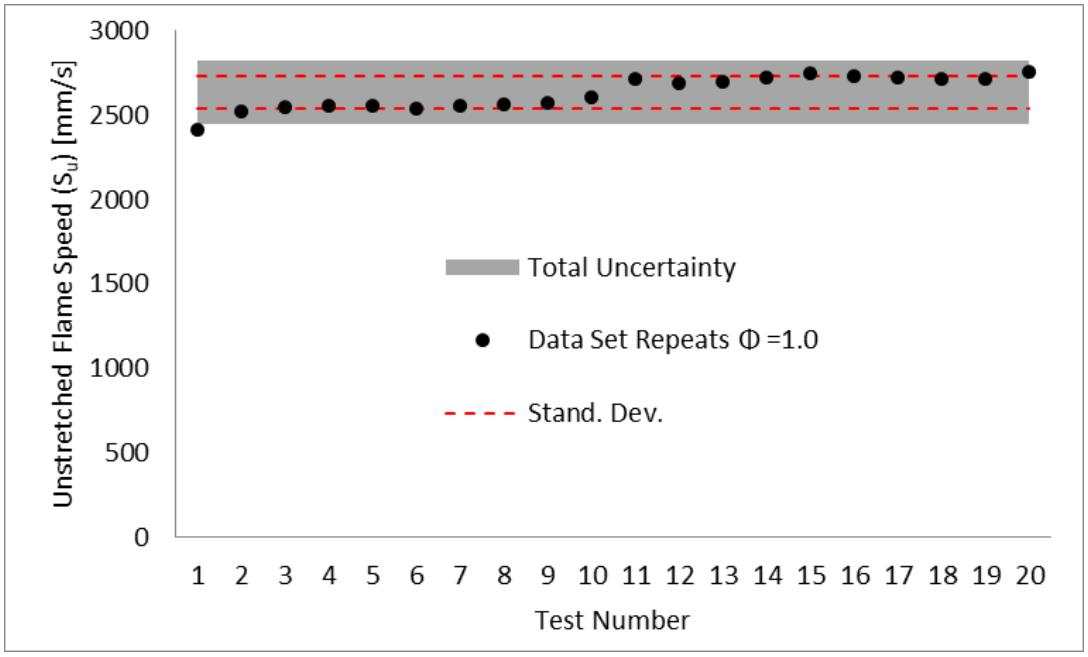

Figure 5.21 – S_u of Stoichiometric CH_4 Repeat Dataset with Superimposed Uncertainty

A significant fraction of the total uncertainty can be attributed to the impact of changes in O_2/N_2 ratio on S_u (~55% for Φ = 0.70 and ~75% for Φ = 1.00 of total uncertainty). In order to confirm that the visible step-change in S_u between tests 10 and 11 was due to a change in zero-grade air supply, total uncertainty was calculated with respect to the average of tests 1-10 and 11-20. By doing so, the uncertainty related to a change in O_2/N_2 is removed since each dataset (i.e. 1-10 and 10-20) was generated on a different zero-grade air bottle, and as such on the same O_2/N_2 ratio. Figure 5.22 illustrates the total uncertainty calculated with respect to tests 1-10 and 11-20 for the lean and stoichiometric CH_4 repeats.

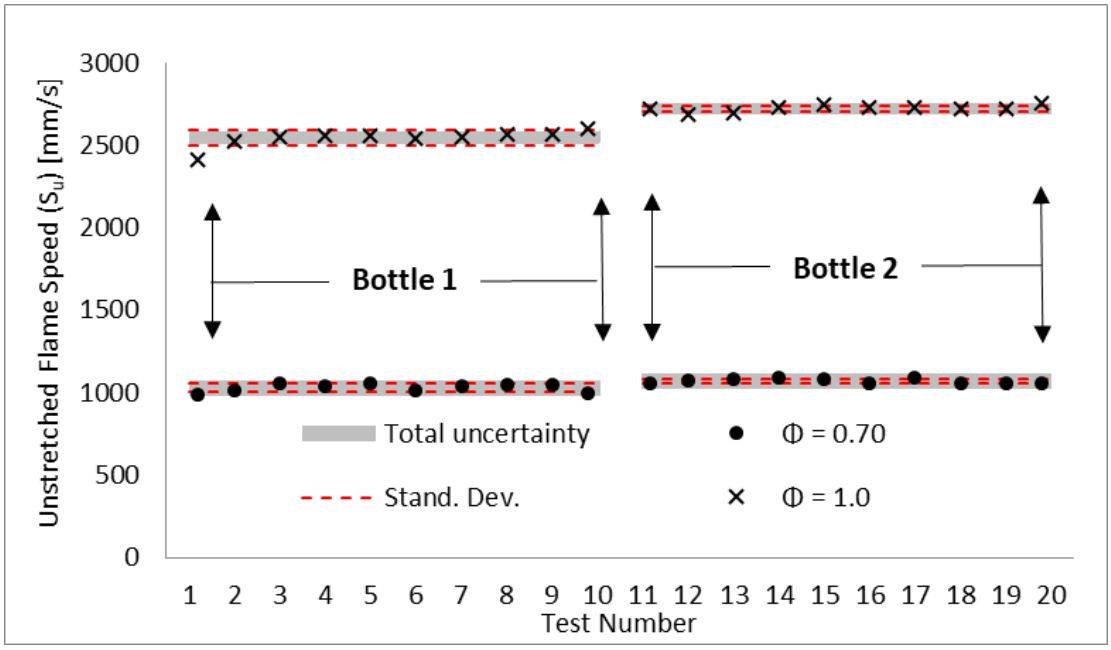

Figure 5.22 – S_u of Lean and Stoichiometric CH_4 Repeat Dataset with Superimposed Uncertainty – Excluding N_2/O_2 Uncertainty

It is evident from Figure 5.22, that very good repeatability is witnessed, with co-efficients of variation (relative standard deviations) of ~2% (for tests 1-10 and 11-20) and ~1% (11-20), for the lean and stoichiometric methane repeats, respectively. The only exception to this overall trend is the standard deviation associated to tests 1-10 for the stoichiometric methane dataset (bottle 1, see Figure 5.22), with a comparatively spurious test point (N.1) increasing the standard deviation of the dataset, and consequently the total uncertainty. It should be noted that the total uncertainty increases from 1-2% for the stoichiometric datasets to ~4.5-5% for the lean datasets, of the corresponding average S_u values. This increase in uncertainty is to be expected since changes in the independent variables appraised (particularly Φ) influence lean flames more than stoichiometric flames. Considering the good repeatability witnessed for the lean and stoichiometric methane repeats, for the remainder of this research thesis, error bars superimposed for S_u and U_L datasets reflect measured maximum and minimum values, with the average value of all the repeats plotted.

It should be noted that whilst the influence of systematic uncertainties was appraised for S_u, a corresponding analysis for L_b was not undertaken. It was deemed that the calculations required to determinate B_{Su} for L_b would be potentially too inaccurate to give worthwhile values. Thus, L_b data presented in subsequent result chapters have superimposed error bars to represent again only maximum and minimum measured values.

5.5 Chapter Summary

A series of 20 experiments on lean and stoichiometric CH_4/air mixtures at nominally identical conditions was conducted in order to better understand the nature of the important levels of S_u and L_b scatter exhibited in literature. The influence of flame radius range on S_u and L_b values was analysed, in both the horizontal and vertical planes. Impact of flame radius selection on S_u is < 3-4% for a 10 mm radius increase, with significant differences in L_b values. For the combustion vessel employed, analysis demonstrated that flame radius range of 8-35 mm, with an extrapolation range of 10-30 mm yielded results devoid of ignition or confinement influences in both planes of measurement, and as such will be employed for the remainder of this study.

Experimental uncertainties related to the apparatus utilised were quantified for the lean and stoichiometric CH_4 mixtures using modelled results. Excellent repeatability was exhibited for S_u, less so for L_b. Due to the important spread in L_b, results will primarily be analysed for overall stretch influence, opposed to exact quantification of precise values.

Variations in the S_u values obtained was shown to be of the same order as quantified systematic and statistical uncertainties. The influence of small variations in the O_2/N_2 ratio of air utilised was determined to generate substantial discrepancy in S_u measurement. As such, it is proposed that the precise ratio of employed O_2/N_2 ratio should be included alongside published S_u datasets, in order to allow for fair comparison and re-scaling.

Appendix – B.1 provides details of the experimental results obtained and described in this chapter. Full test specifications are provided, together with the returned individual and averaged values, alongside co-efficients obtained for quantifying the apt levels of uncertainty (total bias and standard deviation).

Chapter 6. Combustion Properties &Characteristics of Pure Fuels

Building on the results of Chapters 4 (Section 4.5) and 5, which demonstrated both the representativeness of the experimental apparatus employed and levels of uncertainty witnessed in the experimental set-up and data-analysis utilised, it was deemed necessary to quantify the combustion properties of the main individual components of Natural Gas (NG). Spherical expanding flame (SEF) experiments were conducted under lean fuel/air conditions for C_1-C_4 alkanes. The measured flame propagation and Markstein length (L_b) behaviour were analysed and compared to published datasets, with preferential diffusion of the individual fuels analysed in terms of measured stretch behaviour and Lewis Number (Le). Relationships proposed in the literature linking Le to L_b were explored and analysis of fundamental flame properties undertaken. The aim of this chapter is to gain insight of individual fuel combustion behaviour to inform thermo-diffusive behaviour of binary and tertiary mixtures, which are more representative of typical NG compositions.

6.1 Flame Propagation of Pure Fuel Components of Natural Gas

As discussed in Chapter 2, the combustion characteristics of methane (CH_4) have been extensively examined (Section 2.3.1). However, as highlighted, the flame attributes of ethane (C_2H_6) and propane (C_3H_8) have been somewhat less studied, with no unstretched flame speed (S_u) and L_b data measured using the SEF configuration currently found in literature which is corrected for stretch using contemporary non-linear extrapolation methods [40]. Similarly, limited published research has been conducted on n-butane (C_4H_{10}), with Kelley and Law [68] providing the only S_u and L_b using the relevant non-linear methodologies. To the author's best knowledge, little work using a contemporary linear model based on curvature is available in published research for any of the fuels investigated in this chapter, which given this is argued as the most accurate method [84] for such fuels (Le >1) was a knowledge gap this work aimed to fill.

All flame measurements of outwardly propagating flames were measured at atmospheric pressure and temperature (0.1 MPa, 298K). Repeatability was ensured by conducting a minimum of three nominally identical experiments at each data point. The filming rate of the Schlieren flame images was kept constant at 5,000 fps for all tests. Four reaction mechanisms which include H_2/CO chemistry [155]–[158], were deemed suitable for hydrocarbon (HC) combustion hence these are appraised in conjunction with experimentally measured flame speeds. For pure hydrogen (H_2) combustion, two mechanism namely; the

O'Conaire [168] and San Diego [158] were employed, with full reaction mechanism presented in Section 4.3.2.

6.1.1 Radial Propagation of Pure Fuels

The temporal propagation of radial hydrocarbon/air mixture flames are plotted in Figure 6.1 (a-d), with gradients representing stretched flame speed. With respect to CH_4, (Figure 6.1 (a)), the propagation speed is constant across all the tested Φ (0.60-1.0). For the heavier HCs (C_2H_6, C_3H_8, C_4H_{10}), it is witnessed in Figure 6.1 (b-d), that at small flame radii (< 15mm) stretched flame propagation is influenced by stretch, highlighted by initially shallow gradients which are particularly noticeable in the leanest flames (Φ < 0.70). It is observed that as the flame grows, stretch effects gradually weaken, with stretched flame speeds tending to an asymptotic value. To underline this behaviour, Figure 6.2 (a-b) groups the radial propagation of the tested HC/air mixtures by Φ, at 0.65 and 0.90, respectively. At near stoichiometric conditions (Φ = 0.9) the radial propagation of all alkanes is constant, whilst at leaner conditions (Φ = 0.65), initial more pronounced stretch influences are displayed at small flame radii particularly in the case of C_3H_8. This increasing and strong stretch response (for C_2-C_4 HCs) is an indication that as the reactive mixture is deviating from stoichiometric conditions, the concentration of heat and mass diffusion are unequal, alluding to a Le deviating from unity. The destabilising hydrodynamic instabilities linked to the small flame radii, are counterbalanced by the thermo-diffusive instabilities exhibited by the mixture [77], enabling combustion to proceed.

Analysis of ignition behaviour of fuel mixtures reinforces non-unity Le interpretation. Heavier hydrocarbons (C_4H_{10}) could not be ignited reliably at the leanest conditions (Φ <0.70), using the ignition energies tested, whereas CH_4 and C_2H_6 reliably ignited at Φ=0.60, and C_3H_8 at Φ=0.65. With respect to tested C_3+ HCs, upon ignition at the leaner conditions (Φ < 0.65), rising flame kernels were witnessed as combustion progressed, with flames extinguishing prior the establishment of full flame propagation, presumably due to the associated stretch effects at small flame radii. From a phenomenological perspective, the flame releases energy to its surroundings whilst simultaneously gaining chemical energy from its surroundings due to an increase of the deficient reactant concentration, with changes in heat and mass transport gradients driving flame propagation. Consequently, diffusion of heat and mass dictate flame behaviour and by extension flame temperature. As such, upon the ignition of C_3+ fuels, initially, heat loss largely exceeds chemical mass gain, reducing flame temperature to a point whereby flame propagation cannot be sustained resulting in extinction [143]. As such, for fuel mixtures that exhibit Le>1, there seems to exist a maximum/critical stretch limit above which flame propagation is unsustainable.

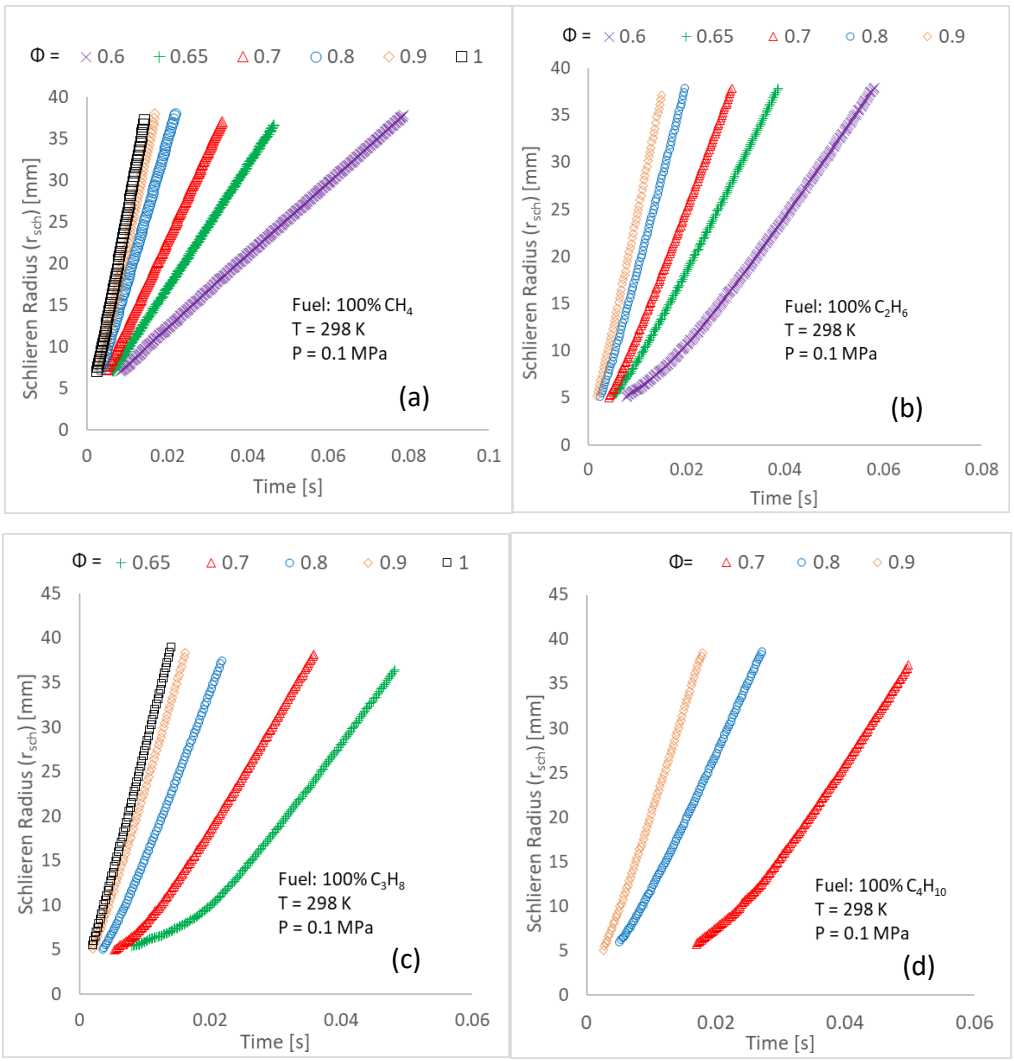

Figure 6.1 – Radial Propagation Rates for (a) CH_4 (b) C_2H_6 (c) C_3H_8 (d) C_4H_{10}

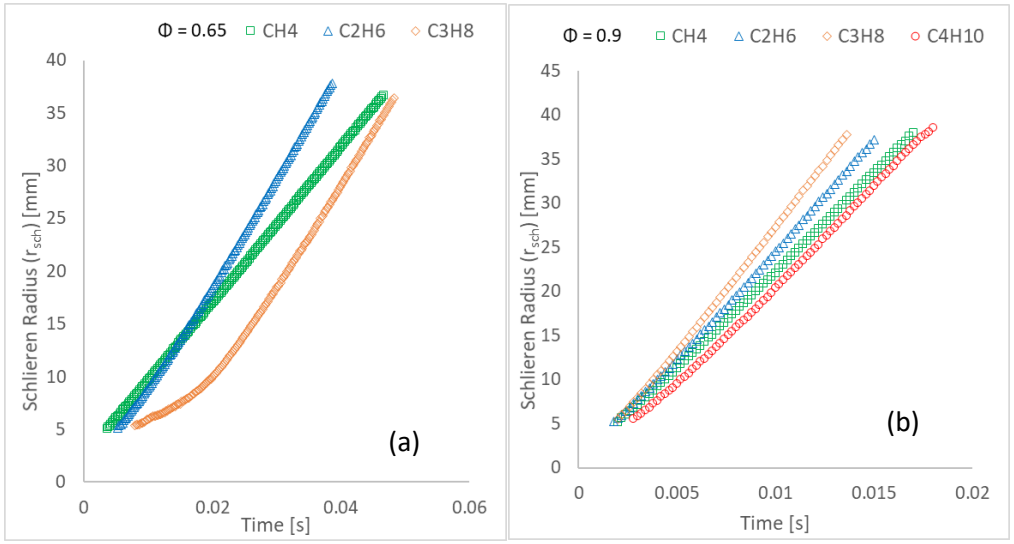

Figure 6.2 – Radial Propagation Rates for (a) C_{1-3} at Φ = 0.65 (b) C_{1-4} at Φ = 0.90

6.1.2 Stretched Flame Propagation of Pure Fuels

Further processing the datasets presented in Section 6.1.1 affords flame stretch to be plotted against stretched flame speed (S_n) for CH_4, C_2H_6, C_3H_8 and C_4H_{10} as given in Figures 6.3-6.6. As can be seen, plotted relationships between S_n and stretch (α) can be derived using numerous linear and non-linear methodologies namely, LM(S) and NM(S), and that between S_n and curvature (κ), using LM(C) as described previously (Section 3.1.2).

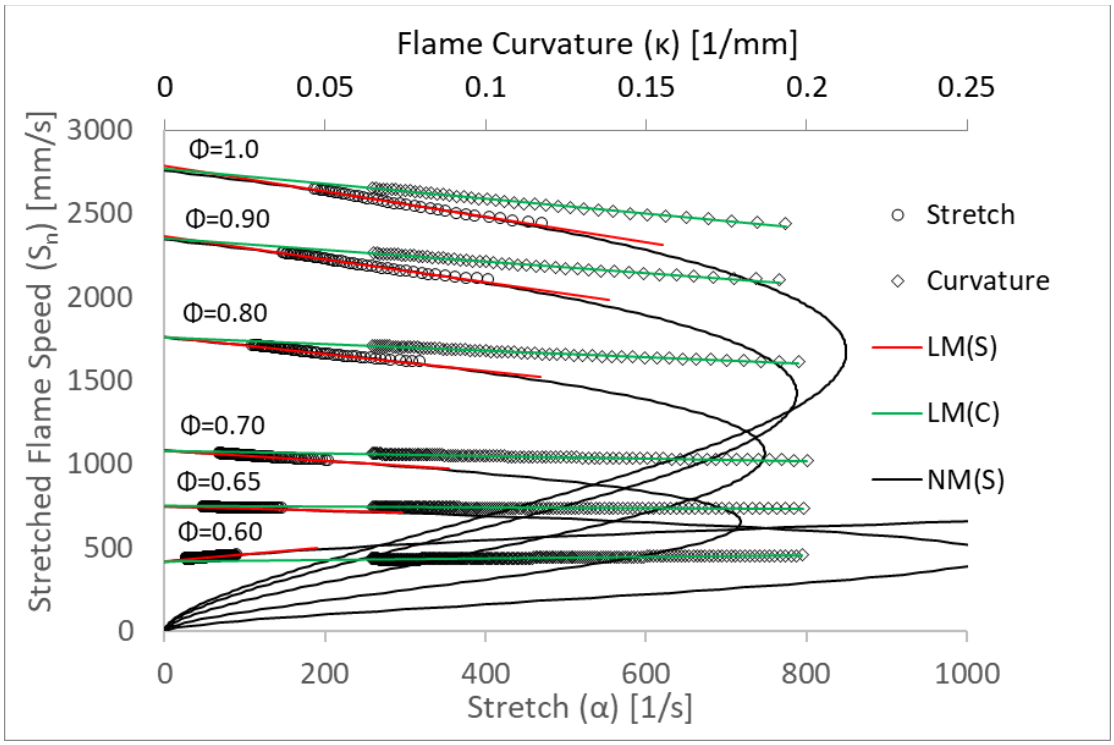

Figure 6.3 – S_n vs α and κ of Lean CH_4/air Mixtures (T_u=298 K, P=0.1MPa)

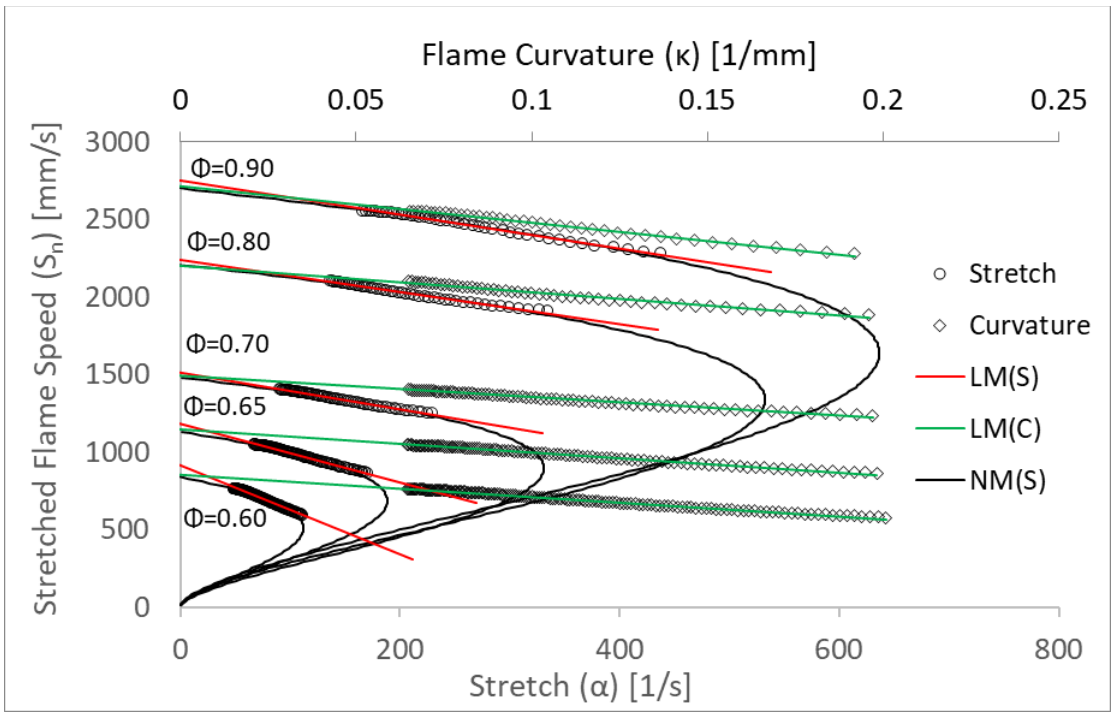

Figure 6.4 – S_n vs α and κ for Lean C_2H_6/air Mixtures (Tu=298 K, P=0.1MPa)

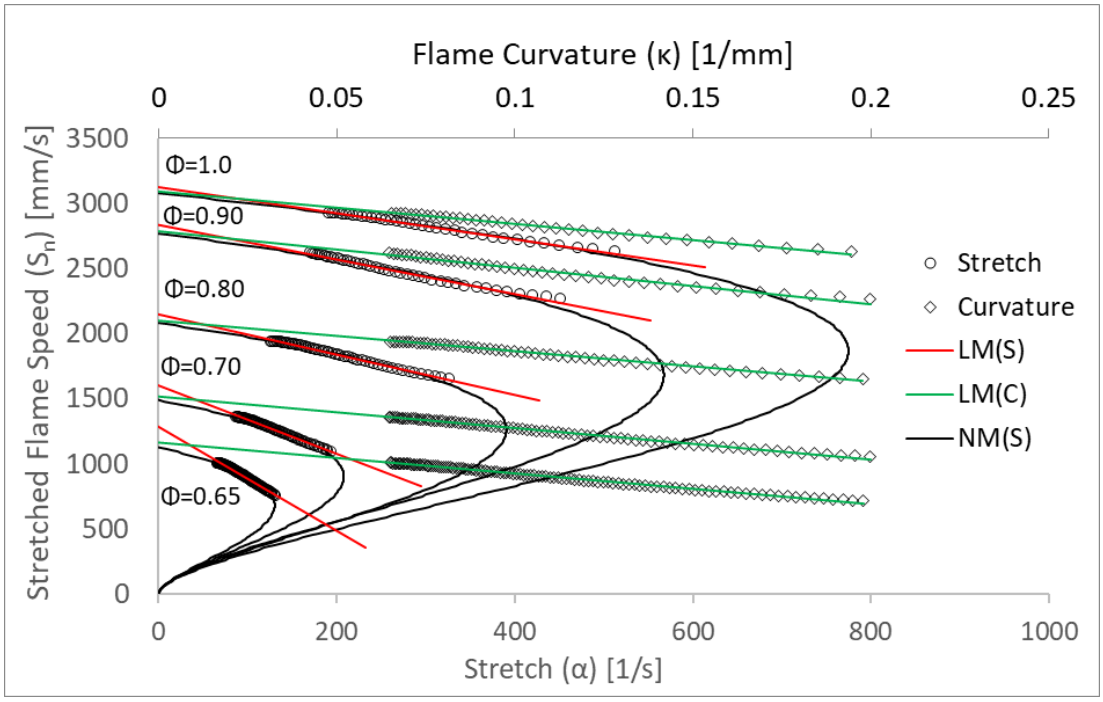

Figure 6.5 – S_n vs α and κ for Lean C_3H_8/air Mixtures (T_u=298 K, P=0.1MPa)

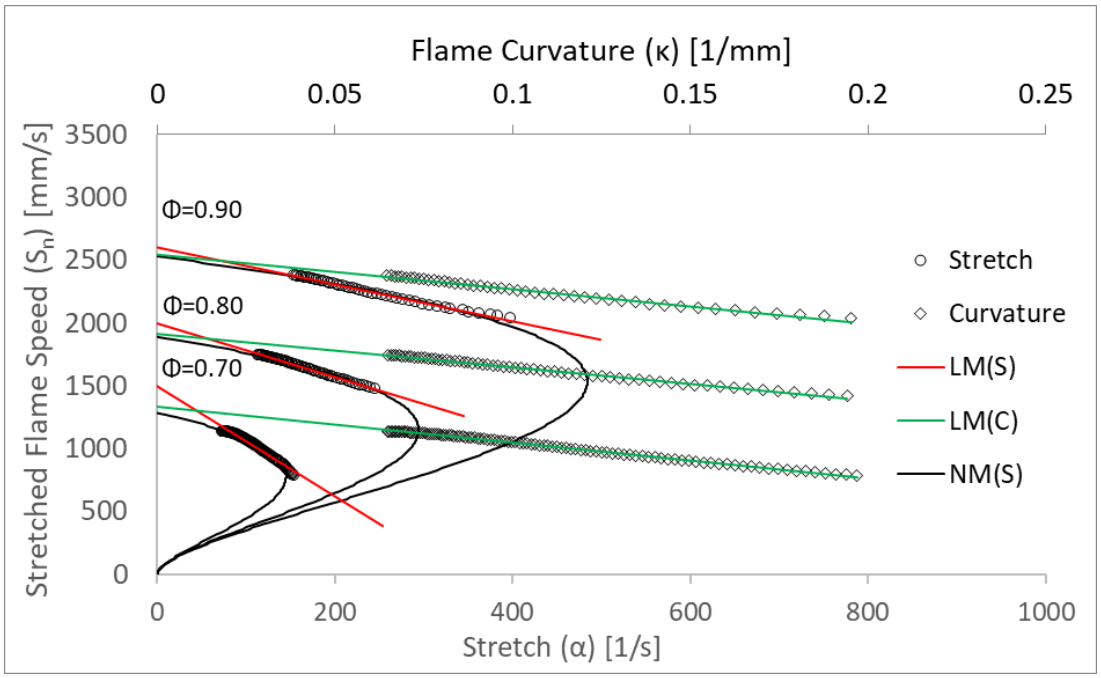

Figure 6.6 – Sn vs α and κ for Lean C_4H_{10}/air Mixtures (T_u=298 K, P=0.1MPa)

With respect to Figures 6.3-6.6, a negative gradient represents a deceleration in flame speed with increasing stretch/curvature, corresponding to positive values of L_b, exhibited by all the alkane air blends (except CH_4/air mixture Φ=0.60, discussed subsequently). Two opposite trends in stretch to Φ relationship are observable for CH_4 and C_2-C_4 HCs, respectively. For C_2+/air flames, as conditions get leaner, gradients increase, a consequence of unequal heat and mass diffusivities, with non-equidiffusion accentuated the heavier the HC. As a result, important differences in S_u are attained upon application of

different extrapolation methods, with differences between attained S_u values using LM(S) and NM(S) visible for C_2H_6 at Φ = 0.60, C_3H_8 at Φ = 0.65 and C_4H_{10} at Φ = 0.80-0.70, Figure 6.4,6.5 and 6.6, respectively, with application of LM(C) yielding S_u values closer to those attained using NM(S) than LM(S). Note that differences are explored and quantified subsequently (Figures 6.13 & 6.15).

At near stoichiometric conditions, CH_4 flames behave similarly to heavier HCs, albeit displaying weaker stretch related behaviour. With decreasing Φ, the stretched flame speed gradient increases, with gradients close to 0 registered at Φ 0.65-0.70. At these relatively lean conditions, propagation speed of CH_4/air flames is quasi-linear and independent of stretch rate, suggesting near equidiffusion of heat and mass transport mechanisms, exemplified with NM(S) (black lines, Figure 6.3), tending towards linearity (Φ=0.65, Figure 6.3), and thus reducing differences in linear and non-linear extrapolated values (i.e. S_u and L_b).

For CH_4/air flames slope inversion occurs at Φ=0.60, and a positive gradient is recorded, equating to a negative L_b, with the flame now accelerating with increasing stretch. Phenomenologically, stretch is now increasing concentrations of CH_4 within the flame front, rendering the ultra-lean CH_4/air mixture locally richer, leading to enhanced burning intensity, with domination of mass over heat diffusion typical of fuels displaying Le < 1. The flame front, which is subjected to hydrodynamic instabilities, tends to start developing cellularity under such conditions (Le < 1), however, no signs of cellular instability were witnessed upon visual inspection of recorded Schlieren images in the cases discussed. Tahtouh et al. [77], employing LM(S), similarly report slope inversion ($-L_b$) of CH_4 flames at very lean conditions (Φ = 0.55), attributed to error induced by polynomial fitting. To counteract this perceived issue a new methodology is proposed, based on fitting a flame radius polynomial using the exact solution of the differential equation, thereby removing errors linked to radius determination, and consequently registering a positive L_b, albeit very close to unity (0.01 mm). To address similar concerns, Chen [84] remarks that it is preferable for flames exhibiting acceleration with increasing stretch ($-L_b$), to apply a NM(S) fitting, which is adopted for this study. Note however that all models employed yielded a negative L_b for CH_4/air mixtures at ultra-lean conditions (Φ ≤ 0.60).

Overall, published research of CH_4 at ultra-lean conditions using SEF is limited, in part due to the difficulty in repeatedly igniting such mixtures. However, slope inversion of L_b for CH_4 at Φ<0.60 has been reported numerous times [73], [79], with opposed ($+L_b$) Markstein lengths consistently reported [75], [78]. A quantitative explanation behind the reported divergences has yet to be proposed, with behaviour either attributable to a physical-chemical

phenomenon or uncertainty generated when extrapolating data. Published evaluations of the lean Le limit for CH_4 flames (Section 6.3), range between 0.955 [140] and 1.01 [91], marginally above and below the critical value (Le ≈ 1). Consequently, two opposite flame behaviour are predicted for the same limit (1 < Le > 1), with both measured experimentally (negative and positive L_b). From a simple mass diffusion of species perspective (N_2, O_2, CH_4 in this case) the relative diffusivities of the reactants relative to N_2 gives $CH_4 > O_2$. For ultra-lean CH_4/air mixtures stretch would increase local CH_4 concentration within the flame front, thereby increasing burning intensity (through augmented flame temperature), impacting flame behaviour. As a result, self-acceleration of flame could occur, potentially yielding $-L_b$ measurements.

6.1.3 Markstein Length of Pure Fuels

Prior to presenting Markstein length results, it is important to underline that Markstein Lengths are indicative of the influence of stretch on flame speed. In premixed flames, instabilities result from hydrodynamic effects, known as Darrieus-Landeau (from the thermal expansion of gases) and preferential-diffusional (thermo-diffusive effects) instabilities [41], [75]. In this thesis, experimental Markstein lengths are utilised as a measure of a flame's susceptibility to instability, and should be viewed as indicator of the effect, not the cause.

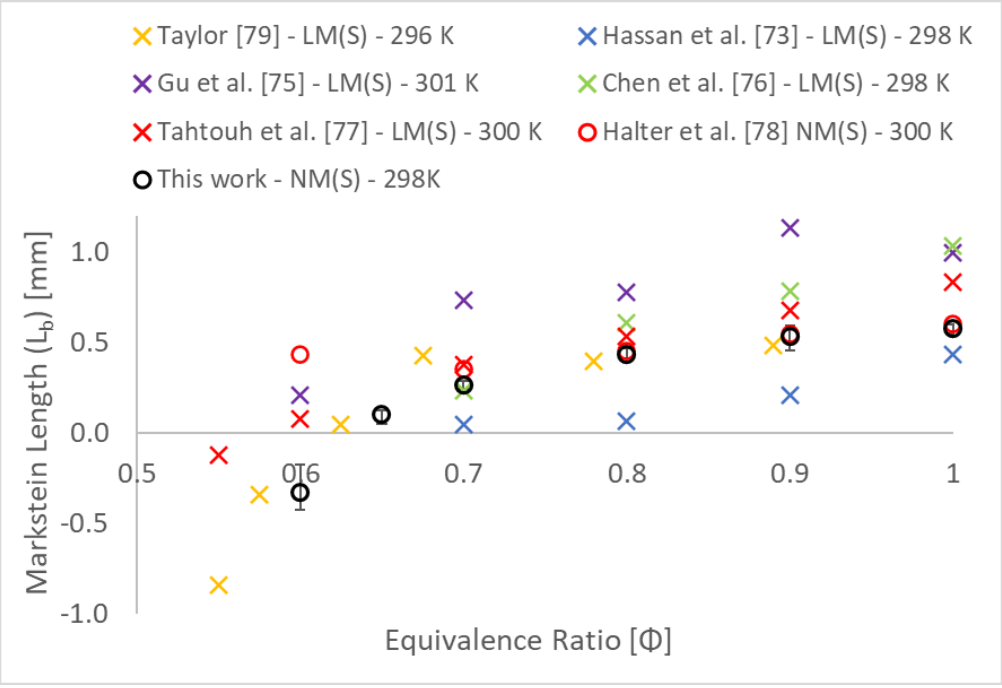

Figure 6.7 – Comparison of Measured and Published L_b Datasets for CH_4/air Mixtures

Measured L_b of CH_4, C_2H_6, C_3H_8 and C_4H_{10} are illustrated in Figures 6.7 – 6.10, respectively, alongside previously published values, with errors bars on this works data representing maximum and minimum measured values, around the average of repeated tests. It should be noted that all datasets presented in Figures 6.7 – 6.10 were conducted at similar initial

temperature and pressure conditions, to those employed for this work. Standard temperature has various definitions depending on geographical location (ranging between ≈ 293-298 K), and thus temperature quoted within each study is listed alongside the reference within the legend of the plots. Note that if standard temperature was specified without further precision, a temperature of 298 K was assumed. Furthermore, in order to facilitate fair comparison, the relationship relating flame speed to stretch utilised to extrapolate L_b is also referenced. Since limited recent research has been conducted on the subject, most the published data presented employ a historical linear relationship between S_u and L_b (i.e. LM(S)), as they were analysed prior to Kelley and Law's [68] non-linear model developments (i.e. NM(S)), with no relevant data applying LM(C) found in published literature.

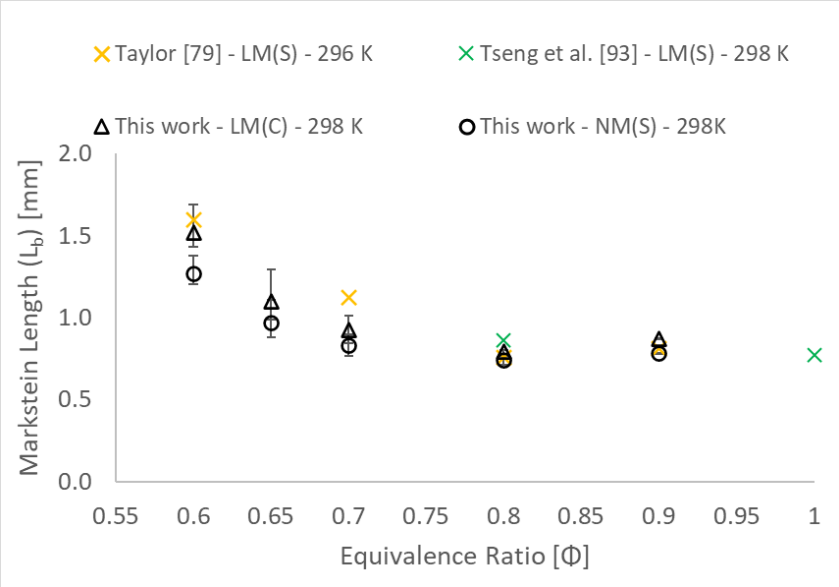

Figure 6.8 – Comparison of Measured and Published L_b Datasets for C_2H_6/air Mixtures

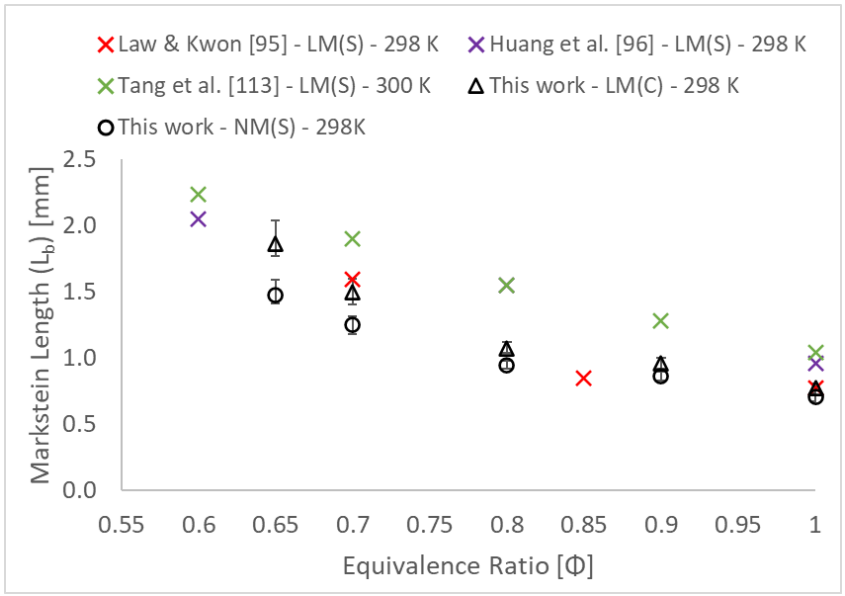

Figure 6.9 – Comparison of Measured and Published L_b Datasets for C_3H_8/air Mixtures

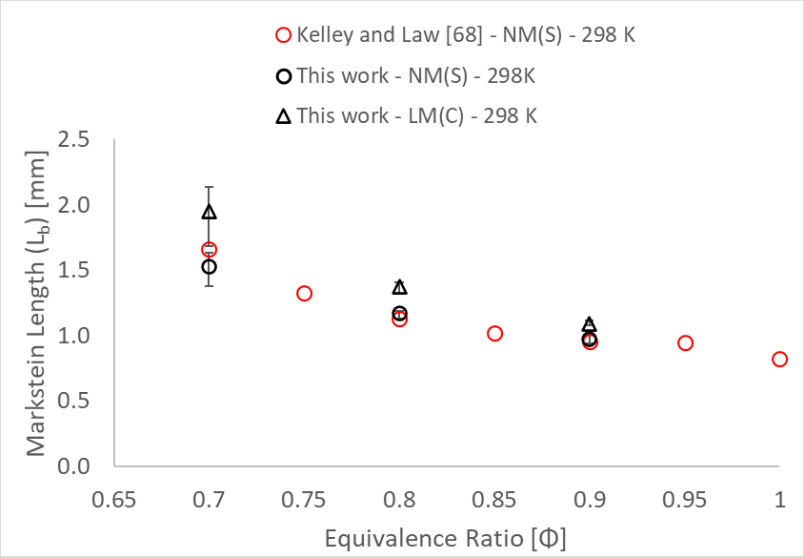

Figure 6.10 – Comparison of Measured and published L_b Datasets for C_4H_{10}/air Mixtures

As underlined in Section 2.3.1 and discussed in Section 4.5.1.1 important differences are noticeable in published CH_4 L_b datasets. In Figure 6.7, only L_b extrapolated using NM(S) from this work is illustrated, since differences in measured L_b using different extrapolation methodologies yield relatively small differences for CH_4 flames (Section 4.5, Table 4.4). Presented data agrees best with Halter et al. [78], who also applied a NM(S) methodology. At leaner conditions (Φ=0.60), negative L_b is measured, in agreement with Taylor [79] and Tahtouh et al. [77] (upon application of the LM(S)). In general, irrespective of methodology employed for evaluation of L_b, the same trend is displayed by all datasets, highlighting a decreasing L_b with decreasing Φ. This trend is opposite to the C_{2+} alkanes and analogous to that displayed by H_2/air mixtures (discussed next, Figure 6.11).

Nominal differences in unburnt temperature have limited effect on measured L_b, however, the relationship employed to yield L_b from S_u will have a significant impact, particularly for flames subjected to important stretch influence. Chen [84], underlines the enhanced accuracy of LM(C) and NM(S) for fuels exhibiting Le > 1 and Le < 1, respectively. Although C_2+ HCs exhibit Le > 1, both LM(C) and NM(S) are depicted in Figures 6.8-6.10, since little to no L_b published data is available using those extrapolation models.

As can be seen in Figure 6.8 and 6.9, published L_b datasets of C_2H_6 and C_3H_8 using LM(S) demonstrate good agreement with L_b measured in this study (for both LM(C) and NM(S)) with the same general trend exhibited, increasing L_b with decreasing Φ. For C_3H_8, Figure 6.9, best agreement is seen at stoichiometric conditions, before differences gradually increase with decreasing Φ. Note that minimal changes in L_b are measured between Φ = 0.80 – 1.0, before important incremental changes in L_b occur as conditions get leaner, in agreement with work from Law and Kwon [95], with this behaviour recorded in the case of the three different extrapolation models used to evaluate L_b (NM(S) and LM(C) in this study,

LM(S) in Law and Kwon [95]). Other work conducted by Tang et al. [96] (Figure 6.9), displays a much more linear relationship, with changes in L_b constant between Φ = 0.6 – 1.0.

In the case of C_4H_{10} (Figure 6.10) available L_b data is limited. Upon application of NM(S) excellent agreement is displayed between this work and that of Kelley and Law [68], with all corresponding datapoints falling within maximum and minimum recorded measurements. As expected, L_b values using LM(C) exhibit higher values, with those differences considerable at Φ=0.70. Once more, little change in L_b behaviour is exhibited at near stoichiometric conditions, with incremental changes in L_b the leaner the condition becomes.

Two distinct L_b behaviour are displayed by the tested C_2-C_4/air mixtures. First, small changes in L_b are registered near stoichiometric conditions ($\Phi\approx$ 0.80 – 1.0), with similar stretch related behaviour recorded for all HCs (including CH_4). However, at leaner conditions, important variations in measured L_b occur rapidly, for all alkanes, with CH_4 and C_2+ HCs exhibiting opposite L_b behaviour.

Due to safety issues and problems associated with flame cellularity, pure H_2/air mixtures at lean Φ were not been experimentally investigated during this study. However, H_2 is a fuel that has been extensively studied, with abundant published datasets [79], [113], [169], [170], hence this data is presented in Figure 6.11. Extrapolation methods utilised to yield L_b rely on there being a sufficiently large stable non-cellular flame regime. However, H_2 flames are particularly diffusionally-unstable due to their low Le (Le<<1), with cellularity arising at early stages of flame propagation (at very small radii), with flame acceleration witnessed at decreasing stretch [170]. It was demonstrated by Gu et al. [75] that flame acceleration related to cellular instabilities occur at a certain critical Peclet number (where the critical Peclet number = critical radius at which the flame accelerates due to cellularity / the laminar flame thickness).

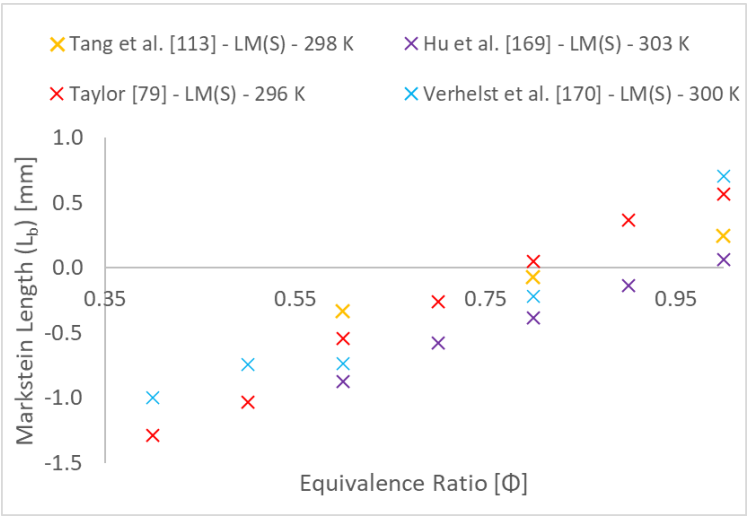

Figure 6.11 – Comparison of Published L_b Datasets for H_2/air Mixtures

As can be seen in Figure 6.11, in the case of H_2/air flames L_b increases as conditions get richer, with relatively good agreement displayed in published datasets, with L_b sign inversion from negative to positive captured by all groups at Φ 0.75-0.85. At Φ < 0.70 L_b behaviour indicates that H_2 is losing more mass than heat to the surroundings, a direct consequence of the much higher mass diffusivity of H_2 compared to the O_2 molecule. As a result, H_2/air blends exhibit an acceleration with increasing stretch ($-L_b$), with stretch augmenting concentration of H_2 in the flame front, thus increasing flame burning intensity and consequently increasing flame temperature, generating a 'self-accelerating' flame. This phenomena is physically observable when viewing Schlieren hydrogen flame images, with an obvious transitioning from stable to cellular combustion [170]. A change in combustion dynamics occurs at Φ ≈ 0.80-0.85, at which point the flame loses more heat with respect to mass diffusion, implying a Le>1, and a much more diffusionally stable flame, similar to behaviour exhibited by the tested C_{1-4} HC flames (Φ>1).

The L_b measurements extrapolated using LM(C) for the C_{1-4} HCs, are presented in Figure 6.12. Clearly, all tested alkane/air blends exhibit similar stretch related behaviour at conditions near stoichiometry. Opposite trends are displayed by CH_4 and C_{2+} hydrocarbons as conditions get leaner, with decreasing and increasing stretch-related behaviour respectively. Note that most significant variations occur at leanest conditions, representative of modern low emission combustion systems, with those differences expected to increase at ultra-lean conditions (Φ < 0.60), typically employed in DLE GT systems.

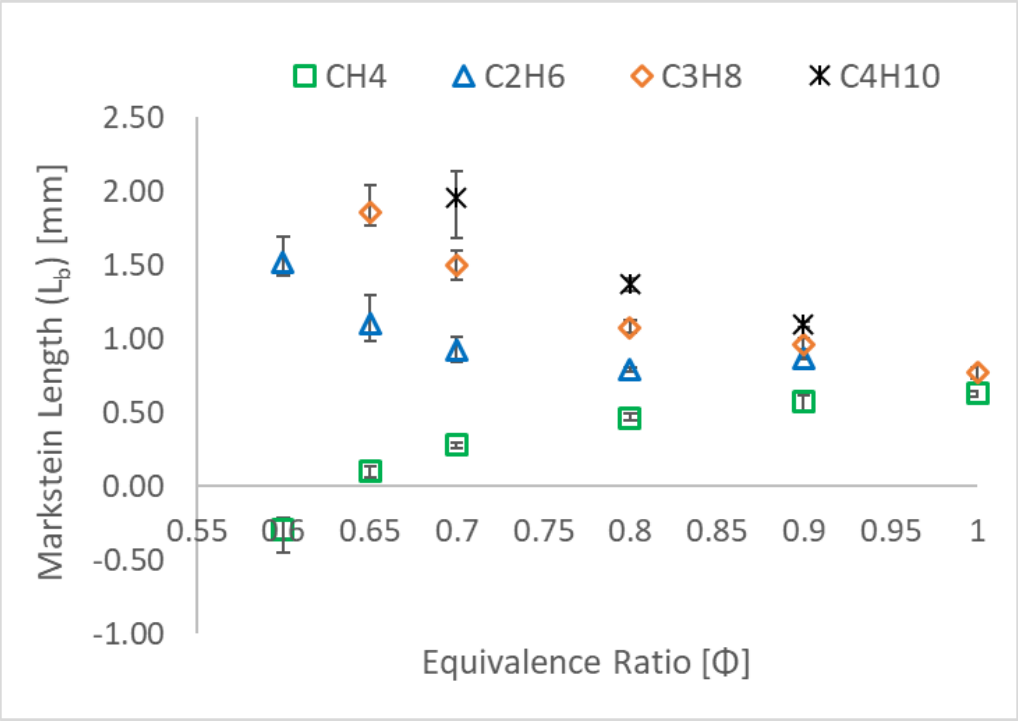

Figure 6.12 – Measured L_b for Tested C_{1-4}/air Mixtures (T_u =298 K, P =0.1MPa)

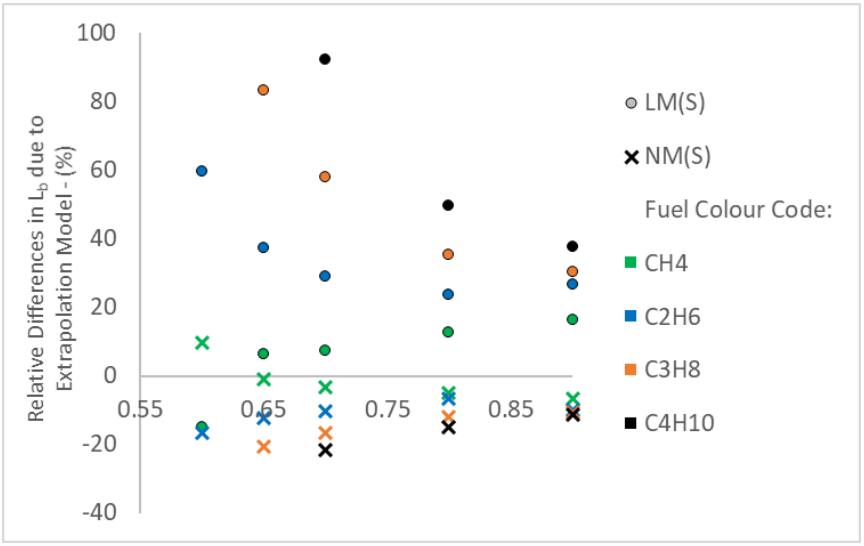

Figure 6.13 – Relative Differences in L_b Values Employing LM(S) and NM(S) Normalised to LM(C) for Lean C_{1-4}/air Mixtures (T_u =298 K, P =0.1MPa)

To exemplify the impact of the extrapolation model employed on attained L_b values, Figure 6.13 depicts average relative differences in L_b values of lean C_{1-4}/air mixtures yielded using LM(S) and NM(S) normalised to LM(C). Clearly, the influence of employed extrapolation method yields significant differences in evaluated L_b values, noticeably LM(S) which substantially overpredicts L_b values of fuels exhibiting Le>>1 (i.e. C_2+ HCs), with differences augmenting with increasing alkane number and decreasing Φ (reflecting an increasing Le). Smaller differences are recorded in relation to NM(S), in good agreement with Chen [84]. Note that attained L_b (and corresponding S_u) values employing all appraised extrapolation methods for C_{1-4}/air mixtures are available in Appendix – C.1

6.1.4 Unstretched Flame Propagation of Pure Fuels

The S_u measurements yielded via LM(C), for the fuel/air mixtures tested are presented in Figure 6.14.

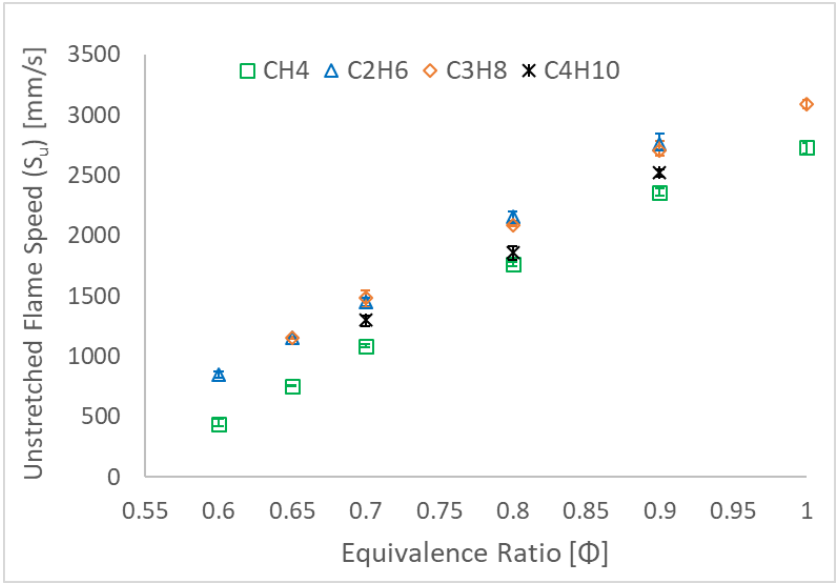

Figure 6.14 – S_u versus Φ for CH_4, C_2H_6, C_3H_8, and C_4H_{10} air Mixtures (T_u =298 K, P = 0.1 MPa)

It is observed that at lean conditions, CH_4 and C_2H_6 exhibit the slowest and fastest S_u, respectively, with C_3H_8 displaying S_u values very similar to that of C_2H_6, albeit minimally slower. Measured S_u for C_4H_{10} sit in-between those of C_3H_8 and CH_4, albeit closer to the latter. S_u of the tested C_{2-4} HCs under lean conditions are a priori related to their hydrogen/carbon ratio (H:C), with S_u decreasing with declining hydrogen to carbon ratio (H:C). However, this explanation does not consider the much slower S_u recorded for CH_4 which has a higher H:C ratio. The flame propagation behaviour of the individual alkane fuels is intricately linked to flame temperature and the thermal diffusivities of the fuels, discussed in the following section.

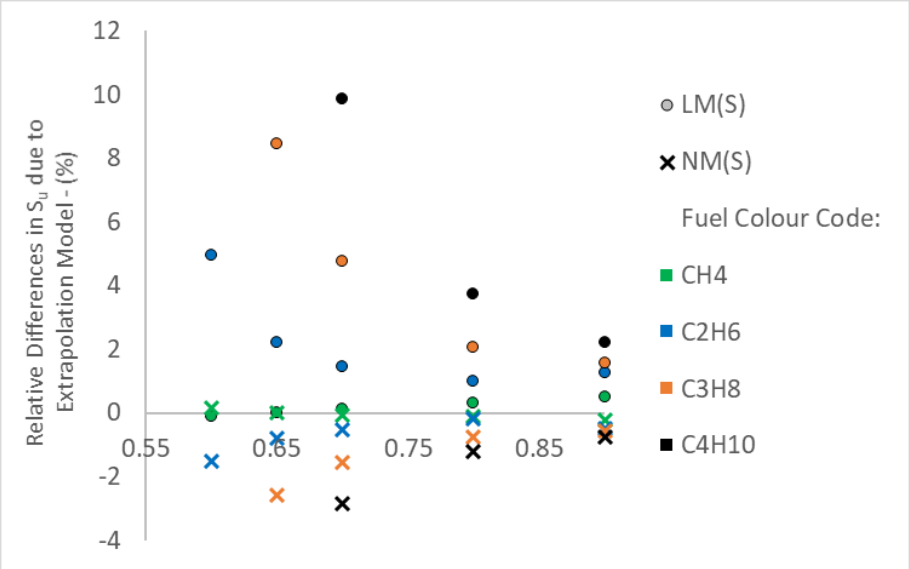

Figure 6.15 – Relative Differences in S_u Values Employing LM(S) and NM(S) Normalised to LM(C) for Lean C_{1-4}/air Mixtures (T_u = 298 K, P = 0.1MPa)

Average relative differences in S_u values of lean C_{1-4}/air mixtures yielded using LM(S) and NM(S) normalised to LM(C), are illustrated in Figure 6.15. For CH_4/air mixtures (Le ≈ 1), all extrapolation methods yield negligible differences in attained S_u (< 1%), however, application of LM(S) for fuels displaying Le>>1 (C_2+ HCs) generates considerable differences at leanest conditions, with differences augmenting with alkane number (↑ Le). NM(S) yields significantly smaller differences in S_u values for fuels displaying Le>>1, with differences < 3%, in agreement with analysis conducted by Chen [84].

6.1.5 Laminar Burning Velocities of Pure Fuels

As previously underlined, in order to determine the laminar burning velocity (U_L) value from S_u, calculation of the adiabatic density ratio of the burned and unburnt gases is required. In order to do so a chemical kinetic simulation using a suitable reaction mechanism must be utilised. Four different reaction mechanisms were investigated namely; Aramco 1.3[157] as was previously employed for the benchmarking exercise (Section 4.5.1.2), GRI-M 3.0 [155], USC II [156], and San Diego [158]. All are suited for hydrocarbon oxidation; however

it should be noted that Aramco 1.3 & GRI M 3.0 only include up to C_3 chemistry, and all include H_2/CO chemistry which was deemed necessary in the later cases when analysing H_2 addition blends. Full details of reaction mechanisms are provided in Section 4.3.2. The resultant density ratios of all appraised mechanisms are available in Appendix – A.4.

Differences in attained burned to unburned density ratios are typically < 0.05%. Thus, the uncertainty associated to the selection of a single mechanism for the calculation of density ratios was deemed insignificant with respect to possible influences of other experimental uncertainty (Chapter 5). The density ratios generated using the USC II mechanism [156] were chosen for the determination of U_L, since it includes chemistry up to C_4. Data is presented in Figures 6.16 – 6.19, with comparison to both relevant published literature and numerical modelled U_L for different reaction mechanisms appraised (presented as lines). Due to the various experimental methodologies available (Section 2.2.1 – 2.2.3), there is abundant resource available for U_L comparison. With respect to CH_4, Figure 6.16, data was again sourced from [73], [75]–[78] as employed previously for L_b comparison. For C_2H_6, due to the limited availability of datasets using SEF, U_L measured using different experimental equipment are presented and compared to present data, sourced from [32], [92], [94], as illustrated in Figure 6.17. For the case of C_3H_8 U_L, Figure 6.18, depicts datasets from numerous authors [32], [92], [95], [96], including data from Dirrenberger et al. [32] whom used the heat-flux method. Finally, C_4H_{10} data were sourced from both SEF [68], [97], and counterflow flames [98], [99] as presented in Figure 6.19.

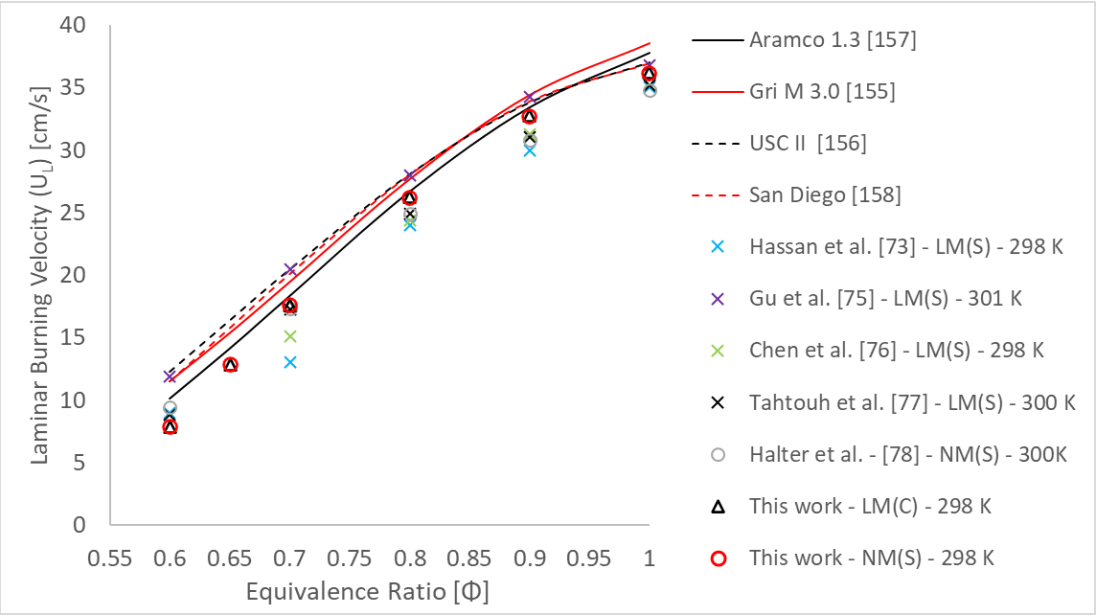

Figure 6.16 – Comparison of Measured and Modelled U_L for CH_4/air Mixtures (T_u =298 K, P =0.1MPa)

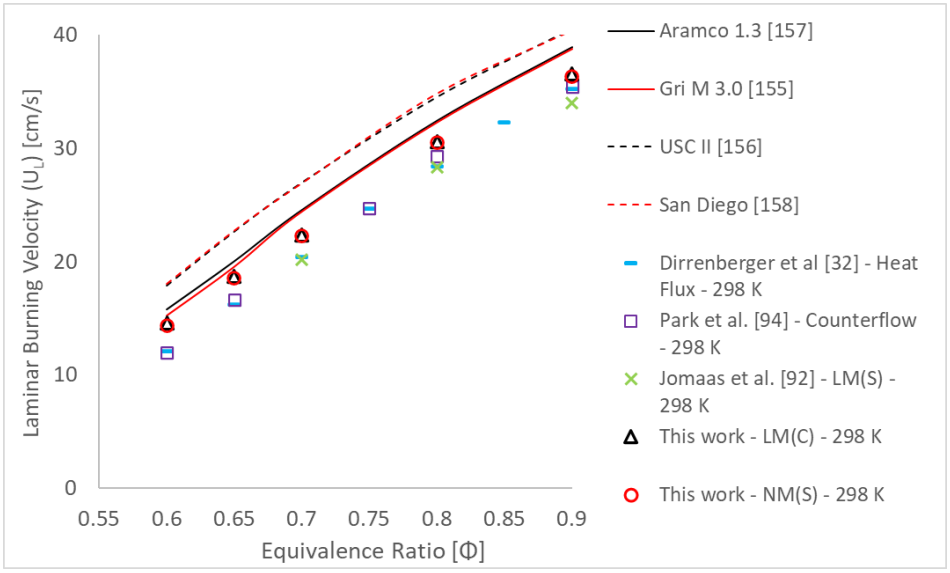

Figure 6.17 – Comparison of Measured and Modelled U_L for C_2H_6/air Mixtures (T_u =298 K, P =0.1MPa)

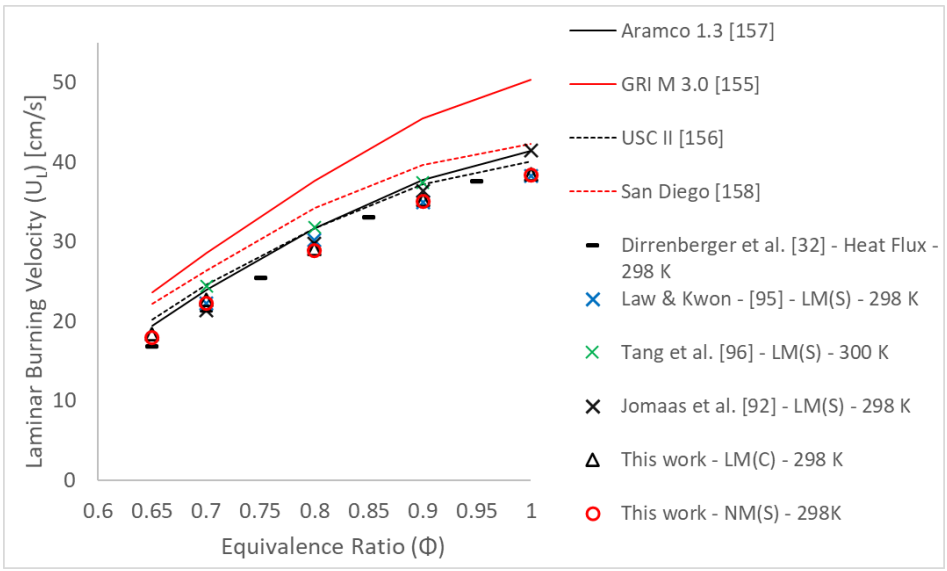

Figure 6.18 – Comparison of Measured and Modelled U_L for C_3H_8/air Mixtures (T_u =298 K, P =0.1MPa)

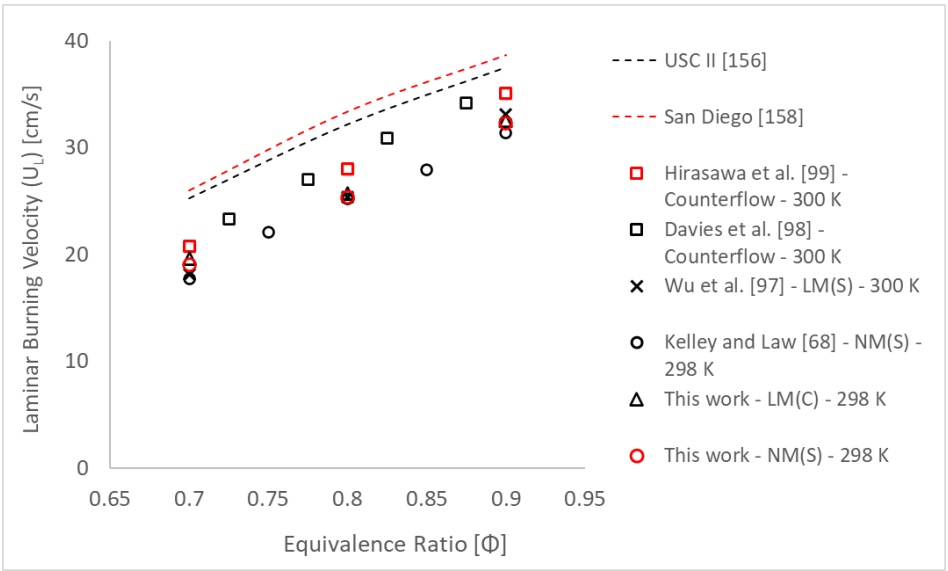

Figure 6.19 – Comparison of Measured and Modelled U_L for C_4H_{10}/air Mixtures (T_u=298 K,P =0.1MPa)

As previously discussed relatively important differences are witnessed when comparing peer-assessed datasets of U_L for CH_4 combustion, Figure 6.16, with differences increasing at leanest conditions. The dataset generated from this study falls in-between published values, with good agreement observed across the tested Φ. With respect to appraised chemical reaction mechanisms, all predict similar U_L, with best agreement witnessed with the chemical kinetic modelling utilising Aramco 1.3 [157].

With respect to C_2H_6, (Figure 6.17), good agreement is seen between all compared datasets, irrespective of experimental apparatus employed. It is observed that all reaction mechanisms over predict U_L values across the lean Φ spectrum as compared to experimental values, with again best agreement displayed by Aramco 1.3 [157] and GRI-M 3.0 [155]. Little scatter is observed for measured C_3H_8 U_L in comparison to other tested HCs, with agreement between all datasets, including heat-flux measurements, illustrated in Figure 6.18. Again, best correlation is observed with Aramco 1.3 [157], and USC II [156] also performing well in this case. GRI-M 3.0 [155] largely overpredicts C_3H_8/air U_L values, with significant differences registered as conditions get richer. With respect to C_4H_{10}, Figure 6.19, good agreement is present with U_L extracted from SEF, whether linear or non-linear methodology is applied, whilst important differences are witnessed with numerically attained U_L values. Flame speeds measured using the counter-flow setup are faster than those measured using SEF whilst remaining slower than numerical values. Overall, good agreement is seen between reaction mechanisms (particularly Aramco 1.3), experimental data from this study, and published work for C_1-C_3 U_L. For the lesser studied C_4H_{10} alkane, differences are witnessed, between reaction modelling and measured data.

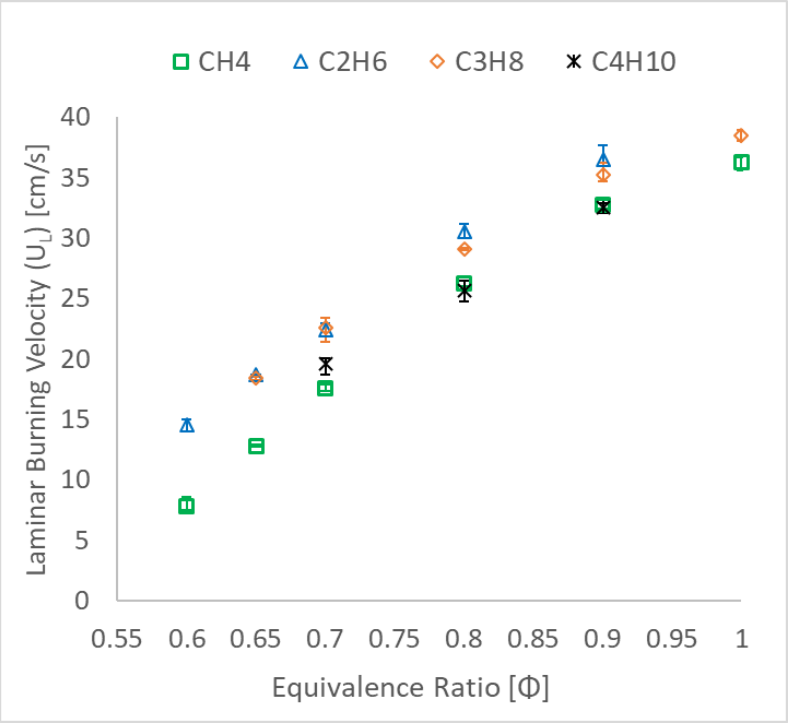

Figure 6.20 – Experimental U_L for Lean C_{1-C4}/air Mixtures (T_u=298 K, P =0.1MPa)

It is well established [41], [98] that U_L is heavily influenced by flame temperature. The adiabatic flame temperature for the tested C_{1-4}/air mixtures was calculated using CHEMKIN-PRO, using the four appraised reaction mechanisms, and are presented in Appendix – A.4. As with the density ratios, differences in attained adiabatic flame temperatures are minimal, with maximum relative differences of < 1% observed. All HCs have inherently similar molecular structures (with CH_4 an exception due its single carbon atom and thus no C-C bond) whilst all exhibiting similar adiabatic flame temperatures and flame speeds.

In order to remove the reliance of the burning intensity on the mixture density (and by extension the molecular weight of the fuel), U_L may be multiplied by the unburnt density (ρ_u) of the fuel/air mixture ($m = \rho_u \times U_L$), resulting in the laminar burning rate per unit area (the burning flux) [98]. The burning flux for the four fuels tested is presented in Figure 6.21. When comparing Figures 6.20 (U_L vs Φ) and 6.21 (burning flux vs Φ), as expected the same trend is witnessed (albeit a greater difference is observable between CH_4 and C_4H_{10}). This implies that the global reaction rate '*w*', and the density compensated diffusivity of the mixture (λ/C_p), via $m \sim (\lambda/C_p\ w)^{1/2}$, is behind the variations witnessed in flame speed, as demonstrated by Davis and Law in there study of HC fuel structure effects on U_L [98]. The thermal conductivity (and diffusivity) of the C_2+ mixtures decreases with increasing carbon number, analogous to the decreasing U_L values.

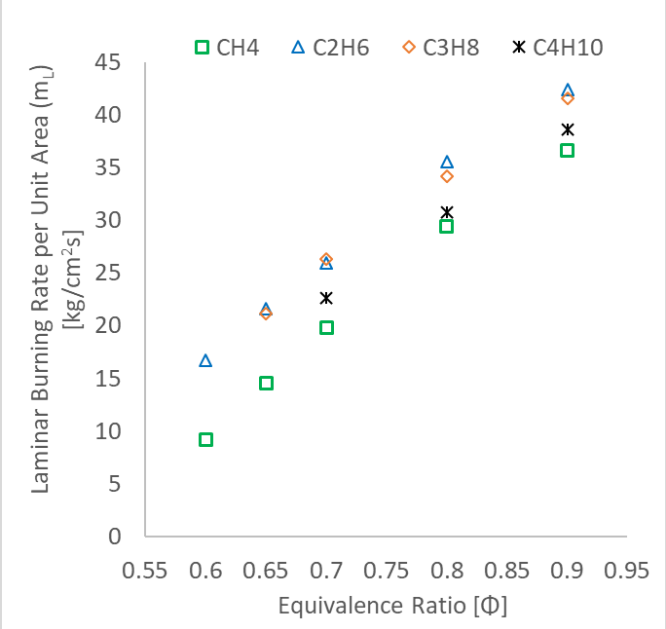

Figure 6.21 – Laminar Burning Rate per unit Area of Tested Alkanes against Φ

For purpose of comparison, U_L values of H_2/air mixtures are illustrated in Figure 6.22 and were compiled using the same sources as used for comparison of L_b (Figure 6.11) [79], [113], [169], [170]. Superimposed on Figure 6.22, are modelled U_L values from the O'Conaire mechanism [168] modelled for H_2 oxidation and San Diego mechanism [158]. The O'Conaire mechanism was employed as it was specifically optimised for H_2 combustion. Scatter across

measured values is relatively small, with experimental data in good agreement with computationally modelled values. Evidently, H_2 burns faster than the tested C_1-C_4 HCs (practically an order of magnitude), with measured values at Φ=0.50 exhibiting faster flame propagation than maximum hydrocarbon U_L registered at Φ=1.0. Note that peak flame speeds for C_1-C_4 alkanes is Φ≈ 1.05 U_L≈0.35-0.45 m/s, compared to H_2 Φ≈1.6-1.85 U_L ≈ 2.6-2.9 m/s, at 298K and 0.1 MPa [168].

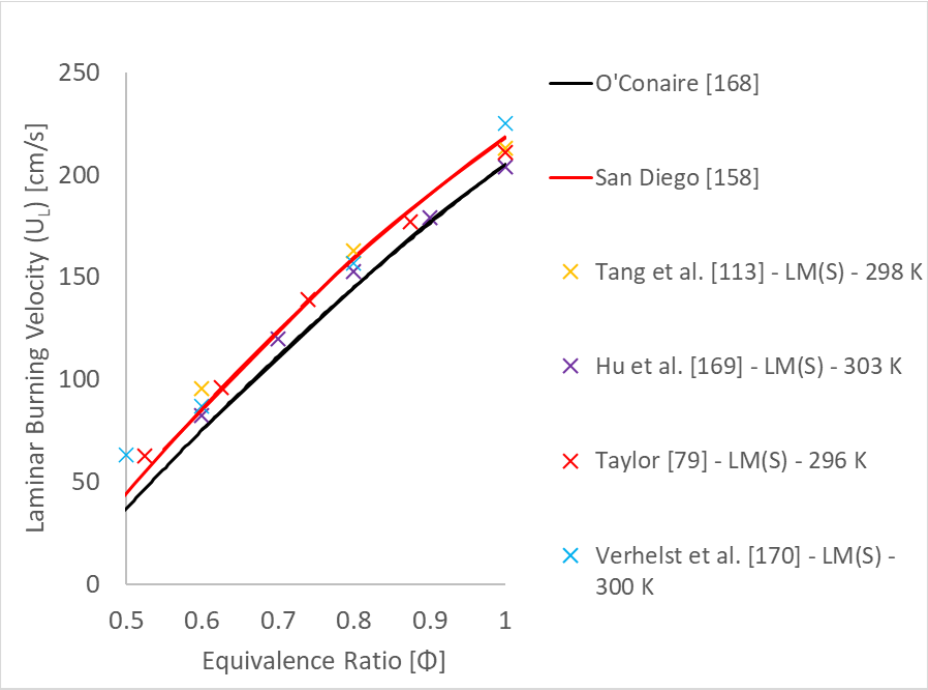

Figure 6.22 – Comparison of Published and Modelled U_L for H_2/air Mixtures (P =0.1MPa)

6.2 Fundamental Flame Characteristics of Individual Fuels

In order to better understand stretch behaviour of C_1-C_4 HCs and H_2 flames, detailed research characterising exhibited thermo-diffusive properties was undertaken. Fuel transport properties are determinant in characterising combustion phenomena, with fluctuations in mass and heat transport mechanisms critical in assessment of flame behaviour. The Lewis number (Le), discussed in Section 3.2.1 and defined in Eqn. 2.2, quantifies non-equidiffusion through preferential diffusion. The diffusional-thermal instability impacts the combustion intensity of stretched flames, characteristic of most practical combustion systems, with respect to propagation, stability and extinction [41]. This holds true for both laminar and turbulent flames, underlying the importance of correctly estimating changes in Le. The flame is unconditionally unstable when Le is below the critical threshold (Le_{crit} ≈ 1), whereas it is stabilised through diffusion when Le > 1 [139]. This transition, from 1 < Le > 1 (i.e. – to + L_b) was demonstrated for H_2 flames across varying Φs in Figure 6.11, highlighting that this not only a function of the fuel but also the local concentrations of that fuel.

6.2.1 Lewis Number of Alkanes and Hydrogen

The method of calculating Le for single fuels was fully reviewed in Section 3.2.2. As discussed, various parameters are needed for its calculation including, thermal conductivity (λ), specific heat capacity (c_p), and binary mass diffusion co-efficients (D_{ij}), both for single species and mixtures. Since determining precise binary mass diffusion co-efficients for fuel mixtures is experimentally challenging, methodologies and recommendations of both Hirschfelder [133], [134] and Wilke and Lee [132] reviewed by Pooling et al. [125] were employed in this work. Note that in the following subsection, D_{ij} – Wilke and D_{ij} – Hirsch refer to Le calculated using the Wilke and Hirschfelder mass diffusion coefficient methods, respectively.

Dunn-Rankin and Weinberg [171] investigated the location of the measured isotherm temperature of Schlieren images (equivalent to the stretch-rate isotherm) using premixed SEF, highlighting that the Schlieren isotherm of measurement is likely closer to that of the luminous zone (i.e. reaction zone), than the unburnt temperature, with the separation between the two of equal magnitude to the flame thickness. Consequently, Dunn-Rankin and Weinberg conclude that the flame area based on Schlieren images may be smaller than the actual value, and thus potentially underestimates values of measured L_b. For stoichiometric methane combustion, Dunn-Rankin and Weinberg reference an 856 K Schlieren temperature of measurement. Bradley et al. [172], used particle image velocimetry to measure SEF laminar burning velocities, exploiting droplets with an associated evaporation temperature of 570 K. The study concluded that depending on the stretch-rate isotherm selected (defined by the droplet evaporation at 570 K), an associated degree of underestimation of L_b values, of 4-12%, could be present.

A main difficultly in assessing Le is concerned with the ambiguous definition of the properties used for its calculation, for example, the temperature at which the (λ/c_P) ratio should be assessed. In order to determine the potential impact on calculated results, two temperatures were evaluated, firstly at 298 K reflecting unburnt temperature second, and secondly at 1000 K, more representative of the flame temperature, and potentially the Schlieren temperature of measurement.

The author notes that the aim of this study is not to generate precise quantitative calculations of Le, but rather to highlight rigorous qualitative trends. The Le numbers for the pure fuels across the tested Φ are presented in Figures 6.23 (a-e). Two different Le are illustrated (varying due to application of either D_{ij} – Wilke and D_{ij} – Hirsch) for the same Φ and (λ/C_p) ratio. The difference between them is coloured to give a perception of the possible Le range.

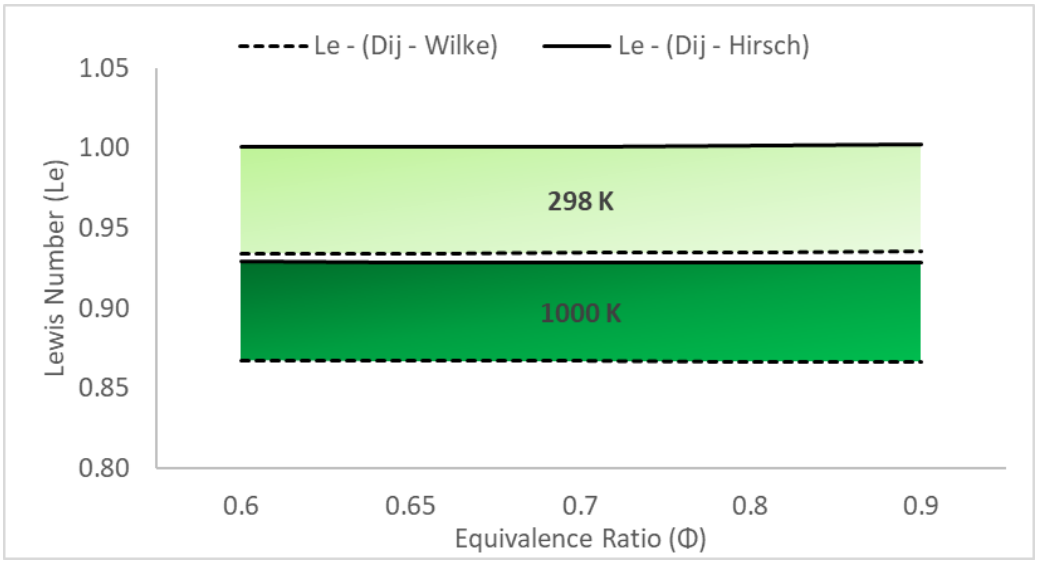

Figure 6.23 (a) – Theoretical Le for CH_4 at different (λ/C_P) ratio (298 & 1000 K) across lean Φ

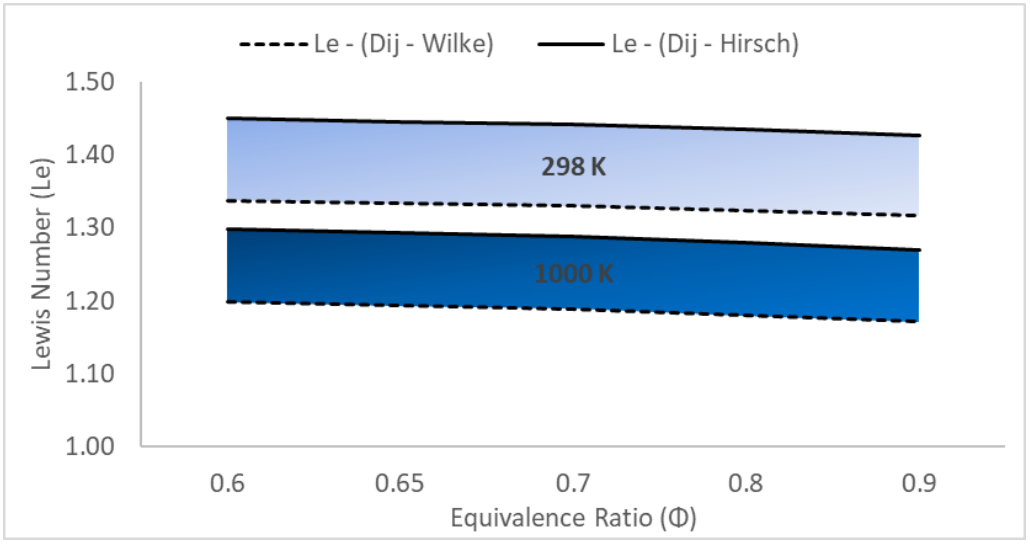

Figure 6.23 (b) – Theoretical Le for C_2H_6 at different (λ/C_P) ratio (298 & 1000 K) across lean Φ

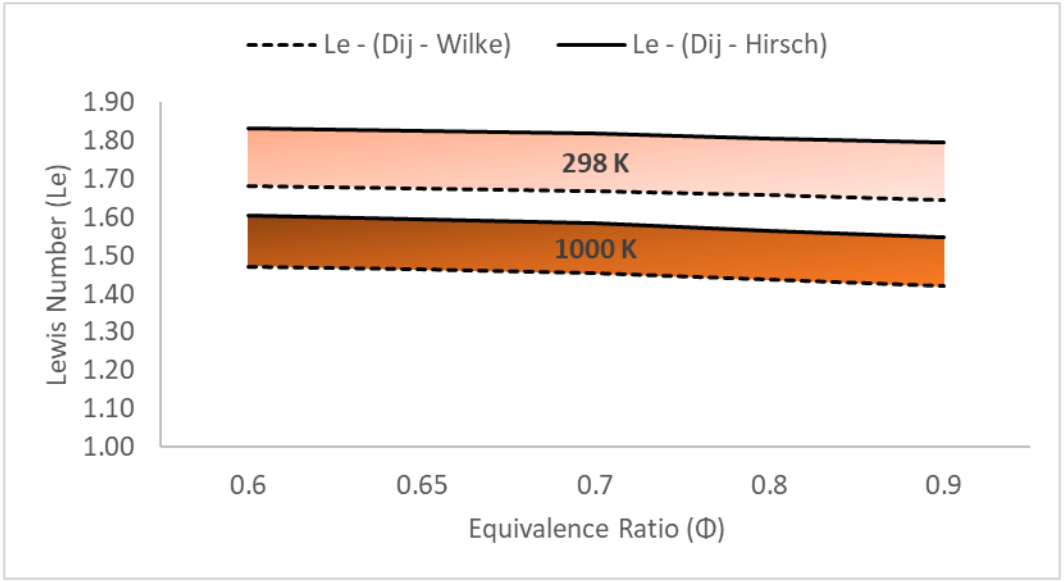

Figure 6.23 (c) – Theoretical Le for C_3H_8 at different (λ/C_P) ratio (298 & 1000 K) across lean Φ

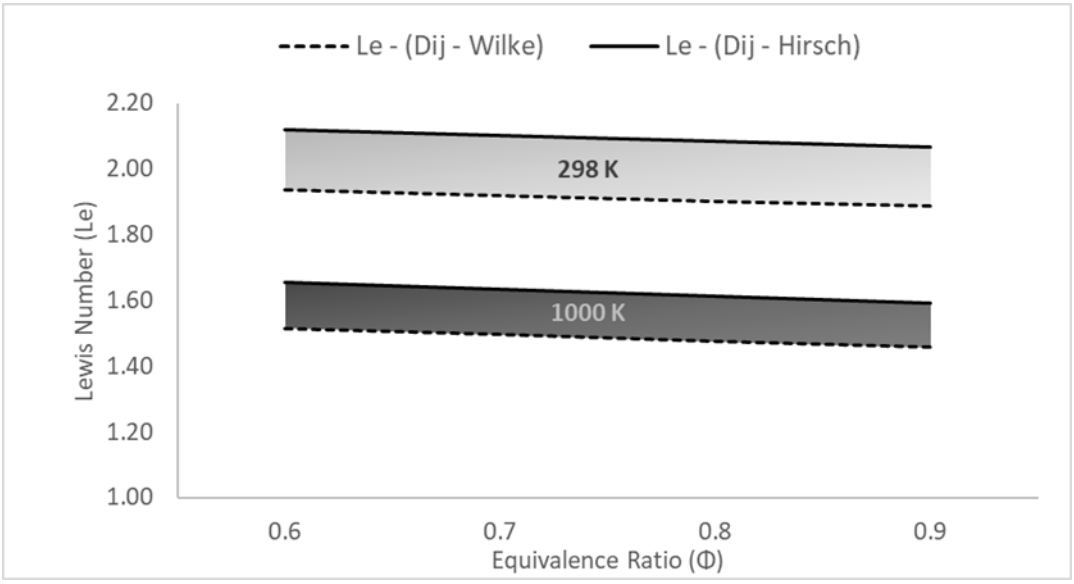

Figure 6.23 (d) –Theoretical Le for C_4H_{10} at different (λ/C_P) ratio (298 & 1000 K) across lean Φ

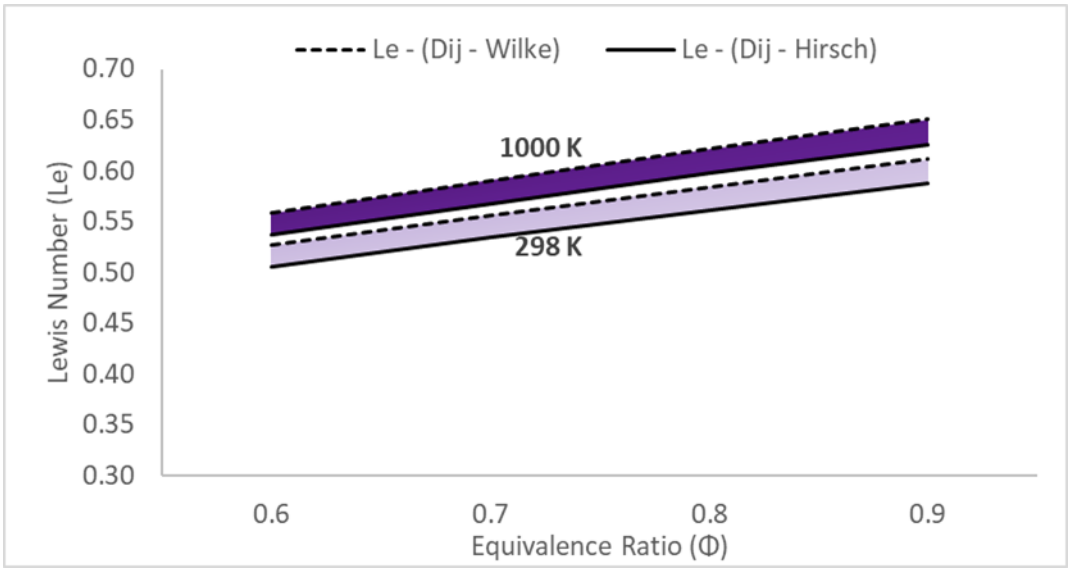

Figure 6.23 (e) – Theoretical Le for H_2 at different (λ/C_P) ratio (298 & 1000 K) across lean Φ

With respect to CH_4, Figure 6.23 (a), calculated the Le appears to be insensitive to Φ. Applying the Hirschfelder method for mass diffusion co-efficients predicts Le ≈ 1, whilst application of the Wilke method yields Le values slightly below 1 across the tested Φ. Both methodologies predict Le numbers representing near-equidiffusion, aligned with values found in literature [41]. However, the C_2-C_4 alkanes (Figures 6.23 (b-d)) display more sensitivity to Le across the lean spectrum, with decreasing Le as Φ increases, analogous to their respective experimentally measured stretch behaviour (L_b). Again, the Hirschfelder method predicts higher Le for all C_2-C_4 compounds than the Wilke method. With respect to H_2, (Figure 6.23 (e)), a comparable assessment can be made, with Le increasing with rising Φ, again aligned with the measured stretch behaviour. However, at reported L_b slope inversion Φ≈0.80 (Figure 6.11), calculated Le remains far from unity, irrespective of mass diffusion methodology employed.

A downwards shift in Le for CH_4 is displayed upon employment of a higher λ/c_P ratio (1000K), with calculated values below unity, predicting a change in thermo-diffusive behaviour aligned with that associated with H_2. However, this shift is small and constant, thus may not be fully representative of the measured stretch behaviour. With respect to the C_2-C_4 alkanes, Le calculated at a higher isotherm yields a decrease in Le of ≈ 11%, 14% and 25%, respectively, thus not significantly altering expected thermo-diffusive behaviour, with flame behaviour largely dominated by heat transport mechanisms. It is observed that an increase in reference temperature shifts Le numbers for H_2 mixtures by ≈ 6% towards unity, the smallest difference witnessed for any of the evaluated fuels.

Upon reflection, relatively small shifts in Le at a higher isotherm are anticipated, since thermal diffusivity (D_T) and mass diffusivity (D_{ij}) display a similar temperature dependence, in the order of $D_T \sim T^a$ and $D_{ij} \sim T^b$, with 'a' and 'b' varying from 1.5-2.0, respectively [61], demonstrating that Le is only slightly sensitive to temperature. With respect to the mass diffusion coefficient formulations proposed by Wilke and Hirschfelder, both methods give approximately similar Le values irrespective of fuel appraised.

Although Le characterises the sensitivity of flame to stretch, rigid analogous correlations are not to be expected with the method of calculation preformed above. Fundamental flame parameters; for example global activation energy, thermal expansion, flame thickness, all vary significantly for non-stoichiometric mixtures and impact the stretched flame sensitivity (L_b) [142]. Variations in those fundamental flame parameters are not considered within the above methodology, since Le is calculated from properties related to the free-stream mixture. As such, Le was also evaluated from properties affecting the flame, as recommended by Jomaas et al. [138], as detailed in Section 3.4.

6.2.2 Relationships between Markstein Length and Lewis Number

As discussed previously (Section 3.4), three theoretical relationships linking L_b to Le have been proposed in literature, by Chen [84], [120], Matalon and Bechtold [142] and Law and Sung [143], referenced in text as Le_{-CHEN}, Le_{-BM}, and Le_{-LAW}, respectively. These analytical theoretical formulations require the calculation of several flame parameters namely, the Zeldovitch number (Ze), flame thickness (δ), and expansion ratio (σ), with the methods employed to evaluate these fundamental flame properties described earlier in Section 3.5.

For C_1-C_4 HCs and H_2, average experimentally measured L_b values (extrapolated using LM(C)) and L_b values sourced from Hu et al. [169], respectively, were utilised when appraising Le_{-CHEN}, Le_{-BM} and Le_{-LAW}. With respect to the reaction mechanisms employed to evaluate fundamental flame parameters note that Aramco 1.3[157], GRI-M 3.0[155], USM II[156], and San Diego[158], were all appraised for C_{1-3} HCs. For C_4H_{10} and H_2, the USM II [158] and

O'Conaire [168] mechanisms, respectively, were relied upon. Finally, if fundamental flame parameters varied significantly using one reaction mechanism or another, comparisons when appropriate are made.

6.2.3 Activation Energy of Pure Fuels

In order to assess predictions of Le_{-CHEN}, Le_{-BM}, and Le_{-LAW}, the global activation energy (E_a) (and by extension the Zeldovitch number (Ze), the dimensionless number of E_a) had to be calculated. As discussed previously, two methods were assessed, the first recommended by Egolfopoulos and Law [144] and the second recommended by Müller et al. [146], (Section 3.5). Each method will be denoted respectively as E_a (1) and E_a (2).

Variations in attained values of E_a (1) are to be anticipated when employing different reaction mechanisms, simply due to the number of identical reactions within each mechanism with variable associated Arrhenius co-efficients (tabulated in Section 4.3.2.). Likewise, less differences in yielded values utilising E_a (2) are expected since good agreement was witnessed between the spatial temperature profiles generated by the different reaction mechanisms. However, it is of interest to evaluate differences generated between both methods.

To give an example of differences observed, Figures 6.24 (a-b) plots the activation energy for CH_4 calculated using both methods (i.e. E_a (1) and E_a (2)) employing different reaction mechanisms, with Figure 6.25 (a-b) applying the same principle for C_3H_8. The differences in Ze (same as the E_a) between both methods are tabulated in Table 6.1, for each fuel and reaction mechanism investigated.

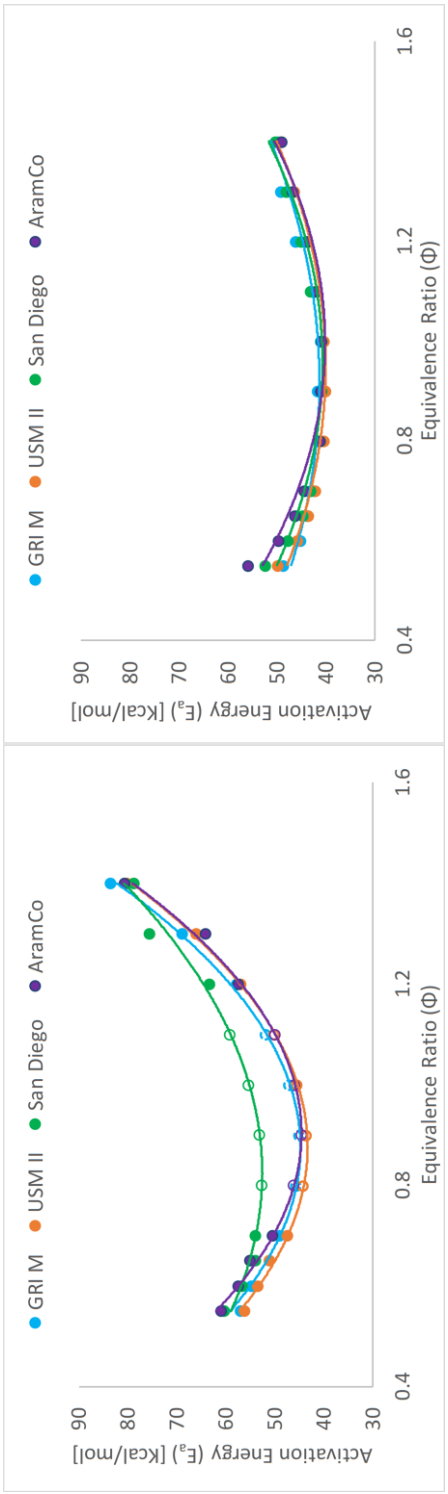

Figure 6.24 (a-b) – Activation Energy (E_a) against Φ for CH_4 – For Different Reaction Mechanisms (a) E_a (1) (b) E_a (2) Methods

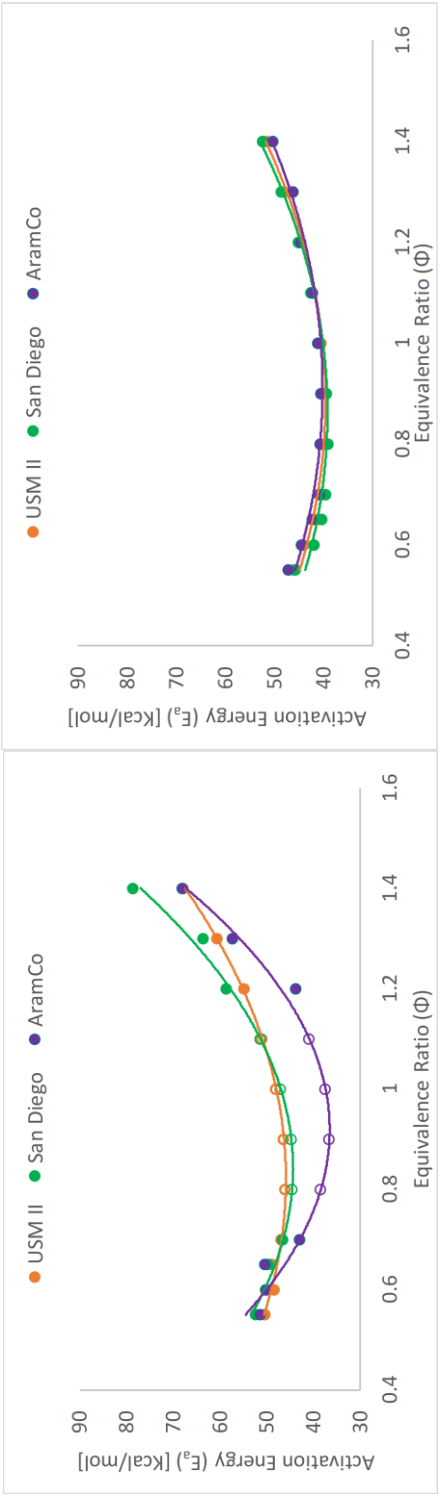

Figure 6.25 (a-b) – Activation Energy (E_a) against Φ for C_3H_8 – For Different Reaction Mechanisms (a) E_a (1) (b) E_a (2) Methods

Table 6.1 – Differences (in %) in Predicted Ze between E_a (1) and E_a (2) using Different Reaction Mechanisms for C_{1-4} Hydrocarbons and H_2

Φ	Aramco 1.3	GRI-M 3.0	USM II	San Diego	Aramco 1.3	GRI-M 3.0	USM II	San Diego	Aramco 1.3	USM II	San Diego	USM II	San Diego	O'Conaire	San Diego
	CH_4				**C_2H_6**				**C_3H_8**			**C_4H_{10}**		**H_2**	
0.6	14.38	18.92	15.35	16.9	14.89	15.42	17.63	17.48	11.95	9.85	18.19	11	11.88	-71.66	-70.13
0.65	16.96	22.46	15.69	18.56	17.64	18.02	22.21	21.78	17.96	17.36	20.83	16.42	16.74	/	/
0.7	12.64	14.42	11.55	22.3	17.4	13.94	20.61	17.85	5.01	15.52	16.38	15.02	12.63	-72.5	-69.49
0.8	11.15	8.77	8.67	24.46	19.87	12.28	23.69	18.16	-5.48	14.91	13.38	14.47	8.48	-69.91	-67.46
0.9	8.08	7.38	7.77	25.96	19.05	9.82	24.04	17.84	-9.9	14.35	12.85	15.54	7.29	-67.67	-64.96
1	11.34	13.34	11.44	29.77	21.11	10.25	23.98	20.1	-9.11	16.99	14.46	17.96	8.83	-71.66	-70.13

Calculated E_a (1) and E_a (2) values for CH_4 using various reaction mechanisms are presented in Figures 6.24 (a-b), respectively. In relation to E_a (1), all appraised reaction mechanisms yield similar E_a values, with only San Diego mechanism displaying higher values near stoichiometric conditions. Nevertheless, all follow a similar parabolic curve, with a minimum E_a registered at conditions slightly leaner than stoichiometry ($E_{a,min}$ $\Phi \approx 0.9$). With respect to differences witnessed for CH_4 upon application of E_a (2) (Figure 6.24 (b)), variations between yielded E_a values are smaller in comparison to results attained using E_a (1), however the same parabolic relationship is maintained. When comparing attained E_a values between both methods, important differences are noticed for non-stoichiometric conditions, particularly on the rich side, with values generated through E_a (1) 20-30 kcal/mol larger than with E_a (2). On the lean spectrum (0.6-0.7), relative differences vary between 10-20% depending on fuel and reaction mechanism employed, with relative differences summarised in Table 6.1.

Similar statements can be made when analysing C_3H_8, Figure 6.25 (a-b). Both E_a methods follow a similar parabolic curve, with differences between both methodologies again resulting in larger observed differences on the rich side. Excluding C_3H_8 (at Φ = 0.8-1.0, using Aramco 1.3), predicted values using the Ea (1) methodology are consistently larger for all the C_1-C_4 alkanes (Table 6.1).

The experimental evaluation of the overall activation energy of fuel-air mixtures is not straightforward, with two methods largely employed, namely; the preheating method and the dilution method. Both methods utilise the laminar burning velocity, and its associated relationship with either the initial temperature of the unburnt mixture or dilution of fuel-air mixtures with inert components (generally N_2 or CO_2). A review of literature reveals that both experimental techniques estimate widely varying activation energies, underlining the difficulty in precisely assessing this parameter. For example, the reported minimum E_a values for C_3H_8/air flames range between 40-87 kcal/mol depending on experimental set-up [173]. To assess E_a in this study, the initial unburnt temperature was varied (in relation to the E_a (1) methodology, Section 3.5) using chemical kinetic programs, analogous to the experimental preheat method described in literature. Calculated values of C_3H_8/air at Φ=1.0 produced E_a values of ≈ 37-47 kcal/mol (depending on mechanism employed). These are closer to those experimentally registered when applying the dilution method (≈40 kcal/mol) than the preheat method (87 kcal/mol).

Although relatively important differences are seen upon application of E_a (1) and E_a (2) (particularly for rich-off stoichiometric conditions), both E_a methodologies predict a similar parabolic curve (for all tested C_1-C_4 fuels); with minimum E_a located at slightly leaner than stoichiometric conditions ($E_{a,min}$ Φ ≈ 0.9). For the C_1-C_4 alkanes, the laminar flame speed and the flame temperature peak at conditions slightly richer than stoichiometric conditions (Φ ≈ 1.05-1.10), underlining the sensitivity of flame propagation to flame temperature. The fact that the minimum activation energy is located at similar conditions, underlines the dictating influence of flame temperature on the global activation energy. Due to flame temperatures peaking at around stoichiometric conditions, temperature-sensitive branching reactions are facilitated, thereby leading to overall faster reactions, as highlighted by Jomaas et al. [138]. The influence of flame temperature on both U_L and E_a (represented by Ze) with respect to Φ, are depicted in Figure 6.26 for the case of CH_4. Although the heavier C_{2-4} alkanes were not specifically examined it is anticipated that similar trends would be exhibited.

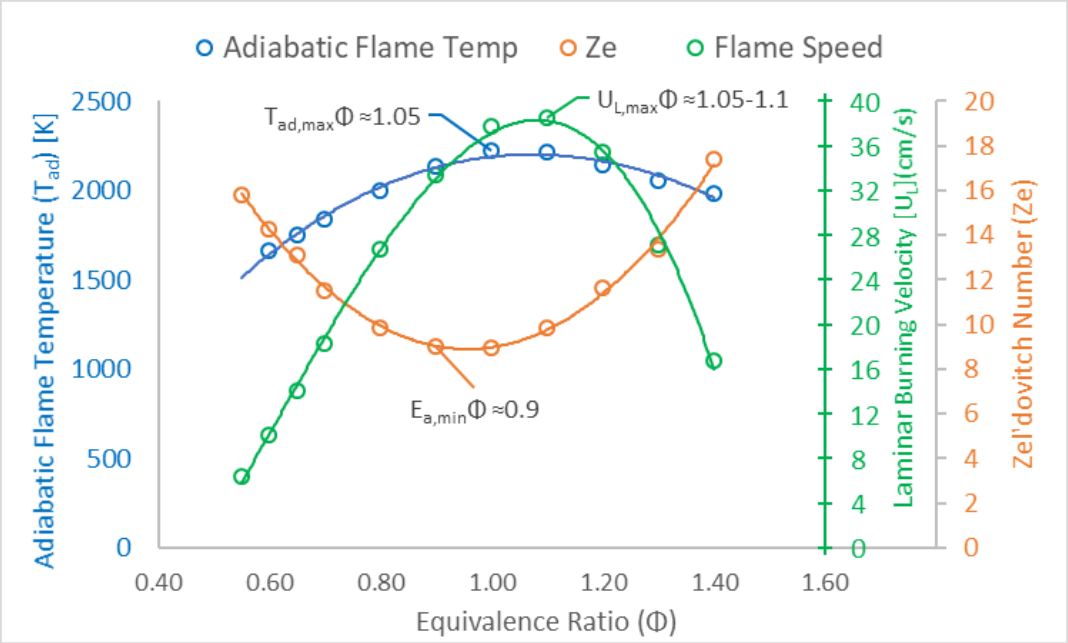

Figure 6.26 – Adiabatic Flame Temperature, Laminar Burning Velocity and Zel'dovitch Number against Φ for CH_4/air Mixtures (T_u = 298 K and P = 0.1 MPa)

In relation to H_2, both methods predict quasi-linear relationship between E_a and Φ, illustrated in Figure 6.27 (a-b). Clearly, differences are substantial between both methodologies. E_a (1) predicts H_2 values alike those witnessed for alkanes, whilst E_a (2) generated values that are considerably smaller, 50-55 kcal/mol and 25-26 kcal/mol, respectively. Upon review of available literature, reported E_a values for H_2 vary considerably, from 20 kcal/mol to 40 kcal/mol [142]. It was thus decided that E_a (1) would be used for alkanes and E_a (2) for H_2, which overall best reflect expected behaviour of global activation energies for those fuels as reported in literature.

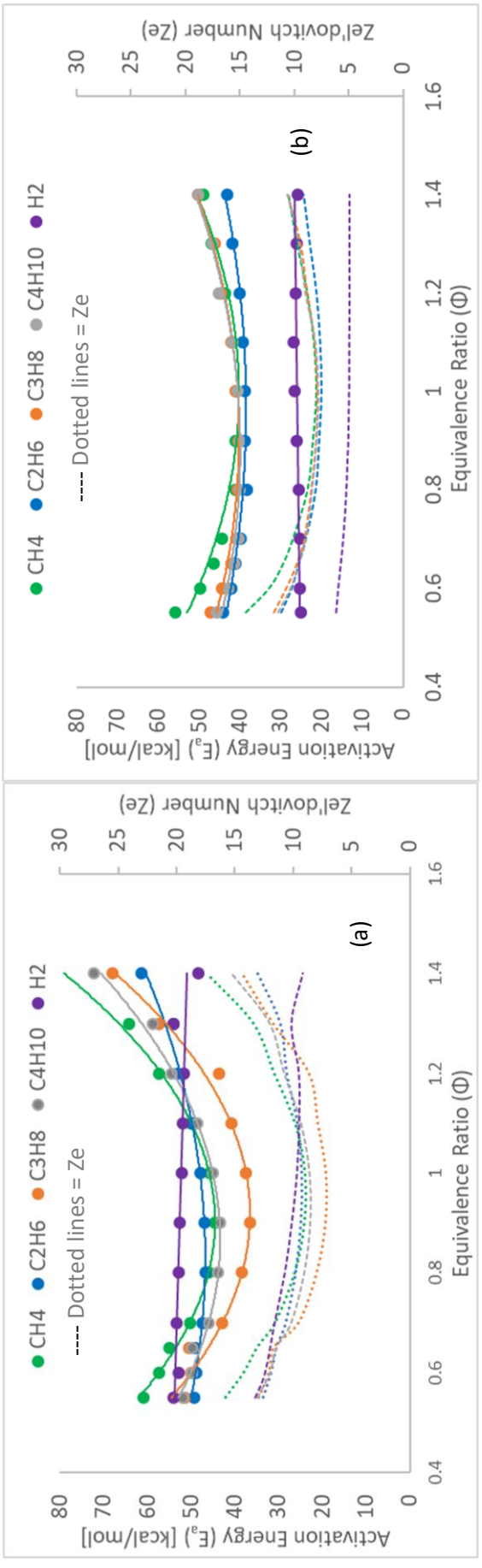

Figure 6.27 (a-b) – Activation Energy and Ze against Φ for $C_{1\text{-}4}$ Alkanes and H_2 – (a) E_a (1) (b) E_a (2) Methods

(T_u = 298 K and P = 0.1 MPa)

Note that the linear trend witnessed for the E_a of H_2 is a small segment of a similar parabolic relationship analogous to that exhibited by C_{1-4} alkanes, with Figure 6.28 illustrating the relationship between flame temperature, the laminar flame speed and E_a (represented by Ze) of H_2 across a much wider range of Φ (up to Φ = 4.20). Evidently, although H_2 flame temperature peaks at similar conditions to that of alkanes (Φ≈1.1), both the flame speed and minimum values of E_a are located at much richer conditions (U_L Φ≈1.6-1.8, $E_{a,min}$ Φ≈1.4-1.6). This shift in flame speed to richer conditions (and by extension the reduced influence of flame temperature on U_L) has been attributed to the much larger values of Le (Le>>1 at Φ>1.6 for H_2), with flame acceleration a consequence of preferential diffusion [138]. As a result, the minimum E_a witnesses a corresponding shift to richer conditions, since E_a is directly extracted from the flame speed. Thus, a transport mechanism (i.e. the thermo-diffusive response of the fuel – Le >> 1) generates a change of response in the flame speed, which subsequently impacts a chemical property (the E_a), highlighting the interrelation of transport and chemical properties. Simply put, E_a aims to provide a global response to detailed reaction chemistry, with the progress of reactions determined by the availability and concentrations of intermediates, which are reliant on transport mechanisms (and thus Le). This is of importance when attempting to understand behaviour of fuel blends which possess dissimilar transport properties (as is the case with H_2 and HCs) and the subsequent consequence this has on flame behaviour.

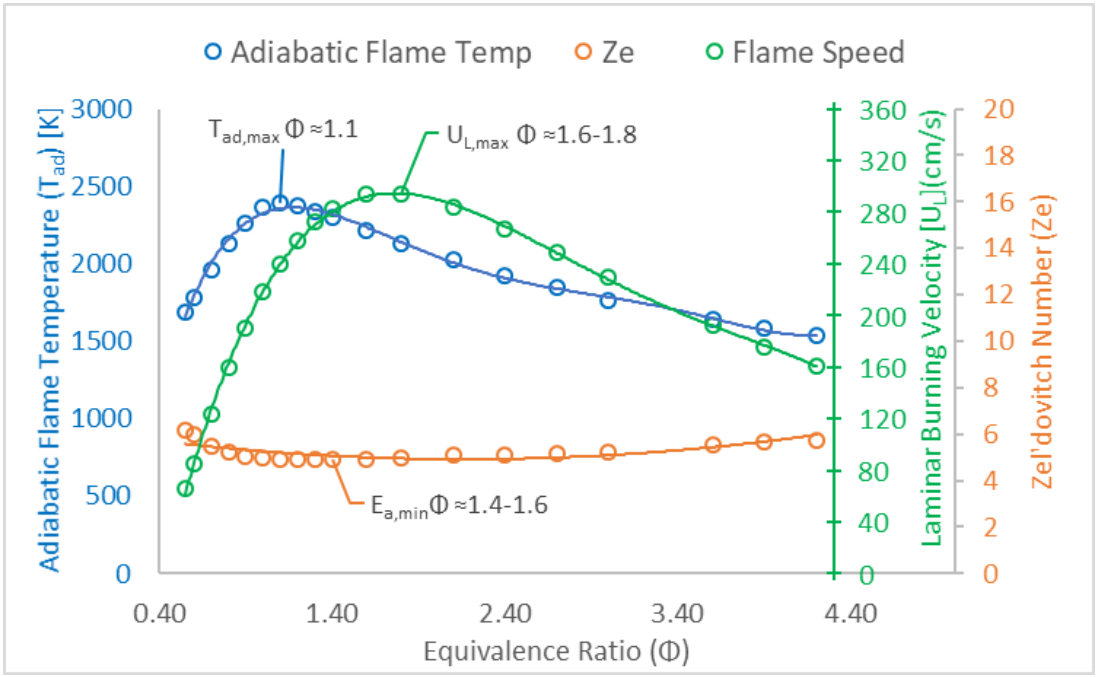

Figure 6.28 – Adiabatic Flame Temperature, Laminar burning Velocity and Zel'dovitch Number against Φ for H_2/air Mixtures (T_U = 298 K and P = 0.1 MPa)

6.2.4 Flame Thickness of Pure Fuels

Once the global activation energy has been calculated, the flame thickness of the flame must be theoretically determined. As detailed in Section 3.5, several algebraic formulations for flame thickness can be found in literature [41], [138], two of which have been investigated in this study; the kinetic/diffusion and gradient flame thickness defined by Eqn. 3.33 and 3.34, referred to as δ_G and δ_K in text, respectively.

Calculated flame thickness of CH_4/air mixtures are presented in Figure 6.29, providing an indication of variations in attained flame thickness generated from the use of different reaction mechanisms. Greatest variations are witnessed at leanest conditions, with differences of up to 13% (for both δ_G and δ_K), with disparities decreasing as conditions get richer. Although both definitions predict a thicker flame as conditions get leaner, differences between both definitions amount to an order of magnitude, in agreement with the literature [41]. From a phenomenological perspective, δ_K would be representative of the very thin reaction zone in which the kinetic chemical reactions occur, whilst δ_G can be viewed as encompassing both the pre-heat zone and the reaction zone of the flame.

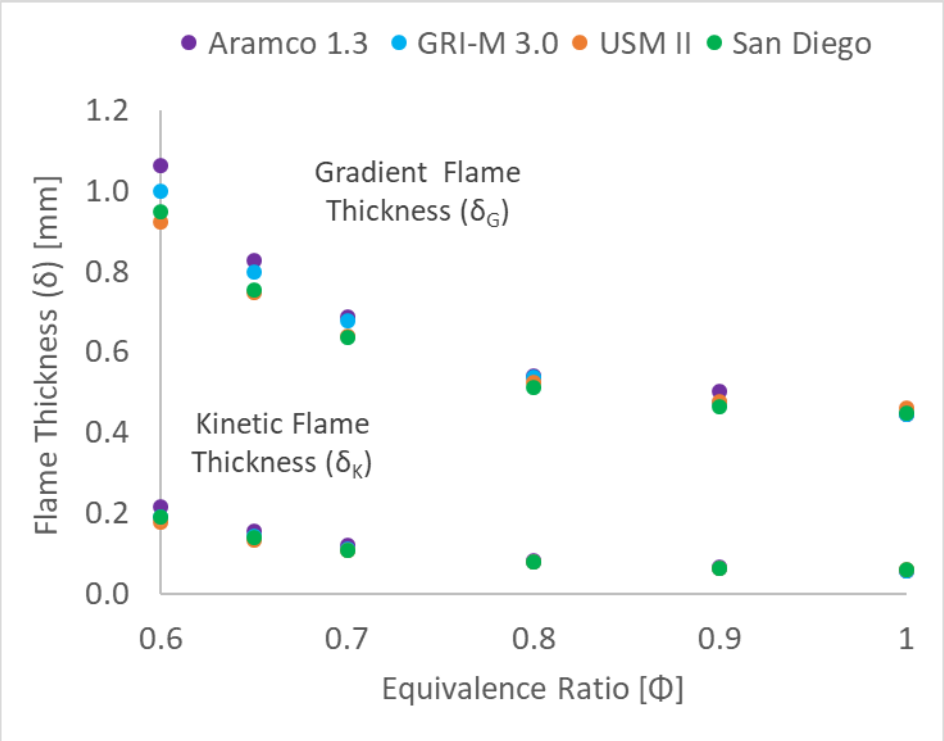

Figure 6.29 – Variation in Flame Thickness vs Φ Evaluated using Various Reaction Mechanisms for CH_4/air mixtures (T_u = 298 K & P = 0.1 MPa)

As evident from Figure 6.30, δ_G exhibited by C_{1-4} HCs and H_2 at Φ = 1 are similar. As conditions get leaner, for C_1-C_4 HCs δ_G increases gradually, with CH_4 displaying a much thicker flame thickness than the C_2-C_4 HCs that display very similar δ_G. Differences augment from ≈15% at Φ = 1, to ≈40% at Φ = 0.60. H_2 displays a constant δ_G, close to those of C_{1-4} HCs at Φ

= 1, whilst significantly thinner at leaner conditions. The same general trend of increasing flame thickness with decreasing Φ for C_{1-4} HCs is followed in Figure 6.31, which depicts δ_K. However, all the tested C_1-C_4 HCs display very similar δ_K (a direct consequence of their similar thermal and mass diffusion properties), unlike differences witnessed when applying δ_G. Note that C_4H_{10} exhibits a somewhat thicker flames, a consequence of its slower U_L. With respect to H_2, the same constant δ_K trend across Φ is predicted, an order of magnitude smaller than δ_G. However, near stoichiometric conditions, differences between δ_K of H_2 and C_1-C_4 are important, contrasting with the similarity witnessed at the same conditions with δ_G.

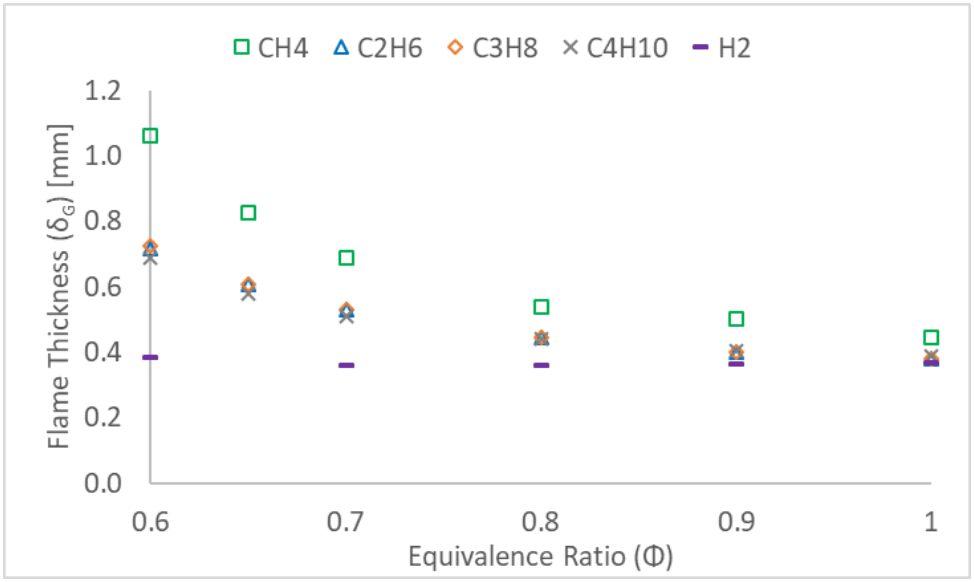

Figure 6.30 – Variation in Gradient Flame Thickness vs Φ for C_{1-4}/air and H_2/air Mixtures (T_u = 298 K and P = 0.1 MPa)

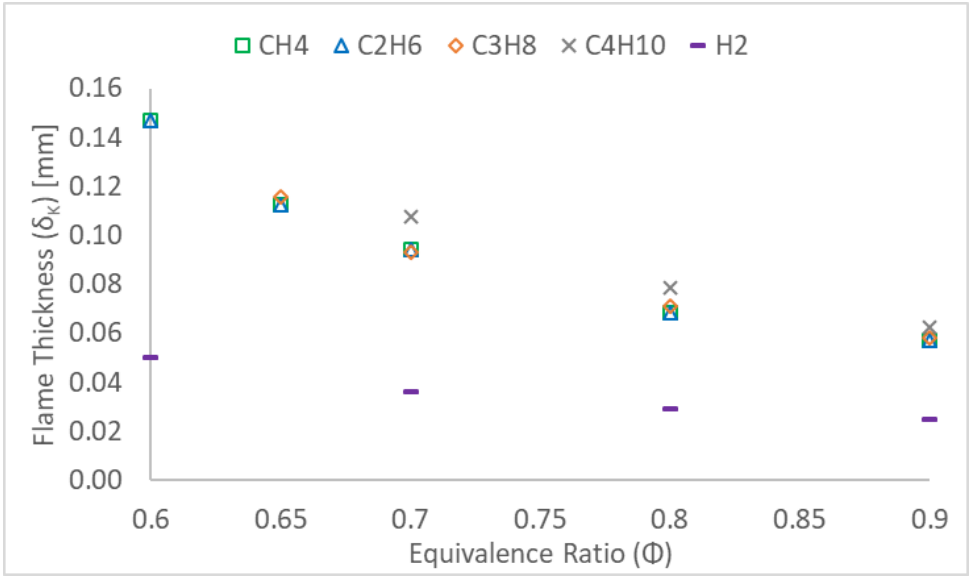

Figure 6.31 – Variation in Kinetic Flame Thickness vs Φ for C_{1-4}/air and H_2/air Mixtures (T_u = 298 K and P = 0.1 MPa)

6.3 Evaluation of Proposed Relationships for Pure fuels

Having evaluated the necessary fundamental flame parameters, relationships linking L_b and Le proposed by Chen [84], [120], Matalon and Bechtold [142] and Law and Sung [143] (Section 3.4), can now be appraised. Since experimentally measured L_b is employed for evaluation of the formulations, generated Le will be referenced as '*experimental*' Le in text (in the format Le_{-CHEN}, Le_{-BM}, and Le_{-LAW}), with Le calculated using the free-stream properties of the mixture referred as '*theoretical*' Le numbers (Section 6.2.1).

In order to assess Le_{-CHEN}, Le_{-BM} and Le_{-LAW}, the lean and rich Le limits of the fuel/air mixtures tested must be evaluated. These limits effectively delimitate minimum (lean) and maximum (rich) plausible Le values for ultra-lean or rich mixtures, respectively, with evaluated Le limits summarised in Table 6.2 (a-b). Lean limits are largely dictated by mass-diffusion of fuel into N_2 (for $\Phi<1$), with rich limits dictated by mass diffusion of O_2 into fuel (for $\Phi>1$). Le Limits were assessed using the mixture averaged diffusion co-efficient of the fuel or O_2 into the mixture. Although no experiments under rich conditions were conducted in this study, illustrating these rich limits allows understanding of plausible variations of Le with changing Φ, with Le limits denoted as Le_{fuel} and Le_{O2}, for lean and rich limits, respectively, on Figures 6.32 – 6.36. In order to evaluate those limits, the upper and lower flammability limits of the fuels were utilised, sourced from [174].

Table 6.2 (a) – Lean and Rich Limits of Le for C_1-C_4/air and H_2/air mixtures (λ/C_p ratio = 298 K)

Fuel	Lean Limits (Le_{Fuel})		Rich Limits (Le_{O2})		Air Fuel Conditions	
	Mass Diffusion Methodology Employed					
	Wilke	Hirschfelder	Wilke	Hirschfelder	UFL-LFL (conc.% in air)	Φ_{min}-Φ_{max}
CH_4	0.93	1.00	0.98	1.06	5-15	0.5-1.7
C_2H_6	1.34	1.46	0.94	1.01	3-12	0.5-2.2
C_3H_8	1.72	1.87	0.92	0.99	2.1-9.5	0.5-2.4
C_4H_{10}	1.86	2.04	0.88	0.96	1.8-8.4	0.6-2.8
H_2	0.35	0.33	1.86	1.90	4-75	0.1-7.1

Table 6.2 (b) – Lean and Rich limits of Le for C_1-C_4/air and H_2/air mixtures (λ/C_p ratio = 1000 K)

Fuel	Lean Limits (Le_{Fuel})		Rich Limits (Le_{O2})		Air Fuel Conditions	
	Mass Diffusion Methodology Employed					
	Wilke	Hirschfelder	Wilke	Hirschfelder	UFL-LFL (conc.% in air)	Φ_{min}-Φ_{max}
CH_4	0.87	0.93	0.92	1.00	5-15	0.5-1.7
C_2H_6	1.21	1.31	0.84	0.92	3-12	0.5-2.2
C_3H_8	1.51	1.65	0.78	0.85	2.1-9.5	0.5-2.4
C_4H_{10}	1.52	1.66	0.73	0.79	1.8-8.4	0.6-2.8
H_2	0.34	0.33	1.98	2.02	4-75	0.1-7.1

A challenging aspect of this work is the suitable selection of a methodology to calculate fundamental flame parameters (E_a, Ze, δ). Note that for the tested C_1-C_4 fuels Ze was calculated using E_a (1) method and applying the USM II reaction mechanism (since it includes up to C_4 chemistry). The method named E_a (2) was relied upon to calculate Ze for H_2 with the use of the O'Conaire mechanism [168]. With respect to flame thickness definition, δ_G was used in association with Le_{-LAW} and Le_{-BM}, whilst δ_K was utilised with Le_{-CHEN}, consistent with each respective approach, denoted as $Le_{-CHEN\ (K)}$, $Le_{-LAW\ (G)}$ and $Le_{-BM\ (G)}$ on Figures 6.32 – 6.36. Since $Le_{-CHEN\ (K)}$ relies upon the δ_K definition, the laminar burning velocity must be employed (Section 3.5). If otherwise not stated, the experimentally measured U_L was used. Finally, L_b employed in the above formulations to generate Figures 6.32 – 6.36 were derived experimentally from this study (upon application of LM(C)), except for H_2 which were extracted from Hu et al. [169]. If other L_b were relied upon for comparison purposes, the dataset source is referenced within the legend of the corresponding graph.

Prior to discussing the results, note that extraction of Le for single fuel mixtures using asymptotic theory and integral analysis has already been achieved, resulting in the formulations detailed in Section 3.4. The aim herein, is therefore to firstly compare those formulations for different single fuel mixtures, and secondly to analyse whether the Le trends are analogous to experimentally measured L_b trends.

Figures 6.32 – 6.36 all follow the same illustration guidelines. Two lean and rich Le limits are denoted, reflecting a 298 K and 1000 K (λ/c_p) ratio selection (straight and dotted lines, respectively). The widest possible limits are depicted, irrespective of mass-diffusion co-efficient methodology employed.

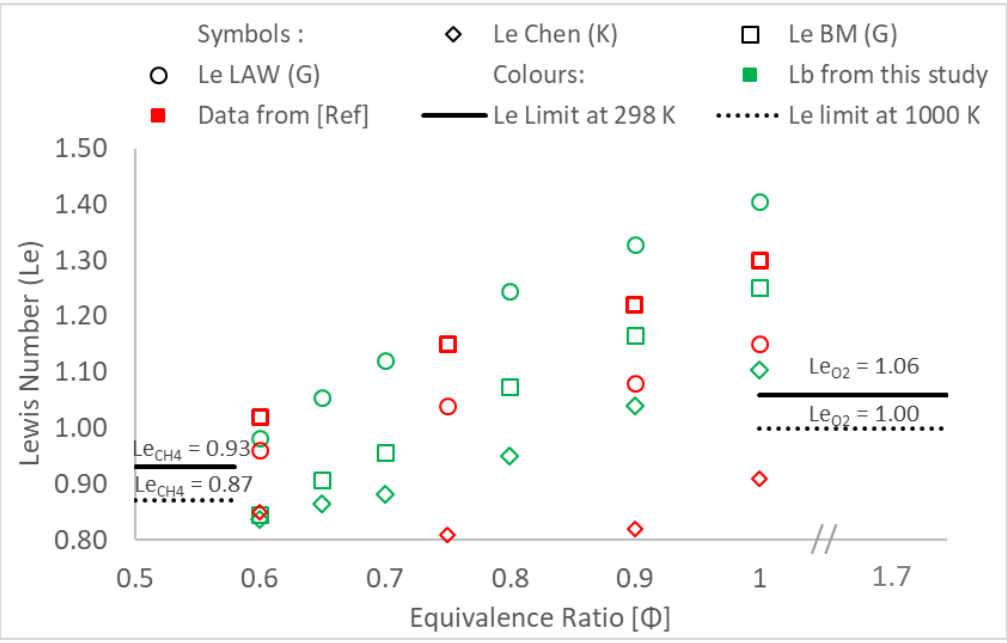

Figure 6.32 – CH_4/air Mixtures Experimental Le Comparison

The experimental Le of CH_4/air mixtures, alongside the evaluated lean and rich limits are presented in Figure 6.32. The lean Le limit is given as 0.93, minimally smaller than those reported in literature, with Dinkelacker et al., [140] referencing 0.955, Hawkes and Chen [175] 0.98 and Lapalme et al. [91] a 1.01 Le limit. These differences are essentially due to the methodology and reference conditions employed to calculate Le. For example, applying the Wilke or Hirschfelder mass-diffusion methodology generates Le of 0.93 and 1.00, respectively, essentially covering the quoted range of published lean Le limits. On the rich side, an Le of 1.06 is denoted, marginally lower than other published rich limits with 1.10 cited in Lapalme et al. [91]. Nevertheless, these very small Le limits for CH_4 with Le very close to unity on either side of stoichiometric conditions, highlight the equi-diffusive nature of CH_4. Le limits calculated at a 1000 K (λ/c_p) ratio decrease only marginally, underlining that Le is minimally sensitivity to temperature.

Clearly, all formulations predict a rising trend in Le, analogous to measured stretch behaviour of CH_4 with increasing Φ. $Le_{-BM\ (G)}$ and $Le_{-LAW\ (G)}$ yield Le values at lean conditions (Φ≈0.8-0.9) which are larger than the rich limits, with this trend expected to increase towards stoichiometric conditions (since at rich conditions L_b increases for CH_4). $Le_{-CHEN\ (K)}$ also yields the same rising trend, however it is less pronounced with values at Φ = 1 still relatively close to calculated rich limits. Work from Lapalme et al. [91] on precise assessment of Lewis number, employed a similar methodology to the one utilised herein for CH_4/air mixtures, plotted in red in Figure 6.32. Lapalme and co-works also witness similar rising trends, confirming the above observations. Note that due to the associated uncertainty linked to calculation of fundamental flame parameters (method employed, reaction mechanism utilised) coupled with experimental uncertainty related to L_b measurement, it is unsurprising that differences in calculated values are present. Overall, $Le_{-CHEN\ (K)}$ presents best agreement with both expected trend and Le limits, with $Le_{-LAW\ (G)}$ and $Le_{-BM\ (G)}$ yielding values considerably higher than the theoretical Le rich limits.

The experimentally derived Le of C_2H_6/air mixtures and associated Le limits are illustrated in Figure 6.33. The lean limit (1.46) agrees well with Hawkes and Chen [175] value of 1.47, whilst no comparatives were found for rich limit. The expected Le trend would be a gradual decrease as conditions get richer, analogous to that displayed by C_2H_6 L_b. Clearly, no formulation captures this behaviour, with all formulations yielding an initial decreasing Le across Φ 0.6-0.70, before experimental Le numbers increase at Φ = 0.70-0.80. Note that employing L_b extrapolated using LM(S) and NM(S) (not shown in Figure 6.33) shift experimental Le upwards and downwards, respectively, irrespective of Le – L_b appraised relationship. Overall, all three formulations generate similar results, however $Le_{-CHEN\ (K)}$ generates experimental Le values that better respect the lean limits.

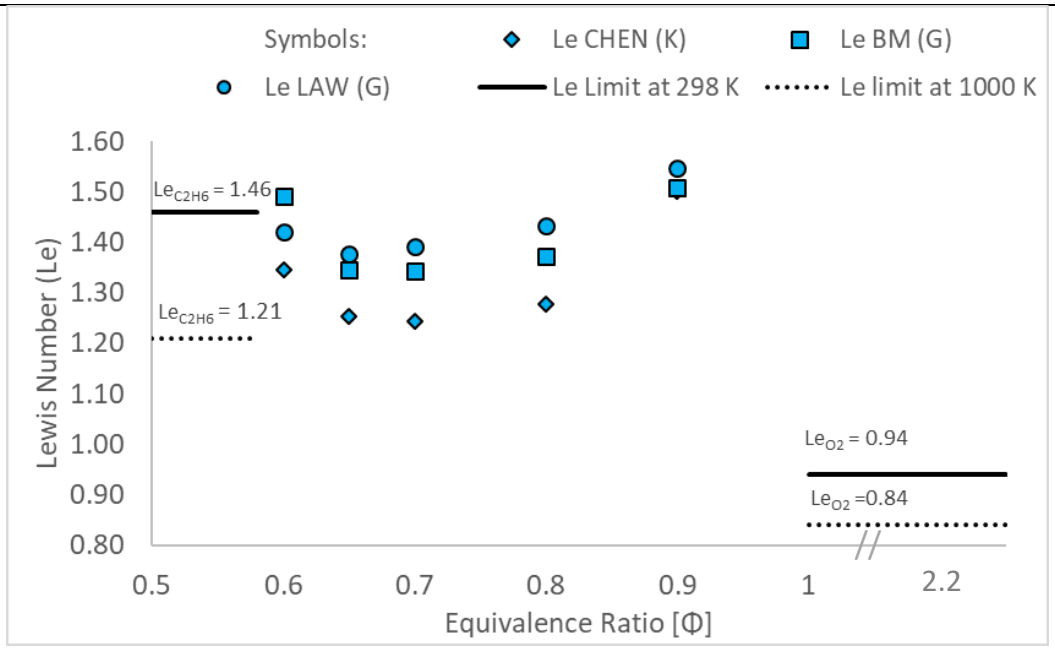

Figure 6.33 – C_2H_6/air Mixtures Experimental Le Comparison

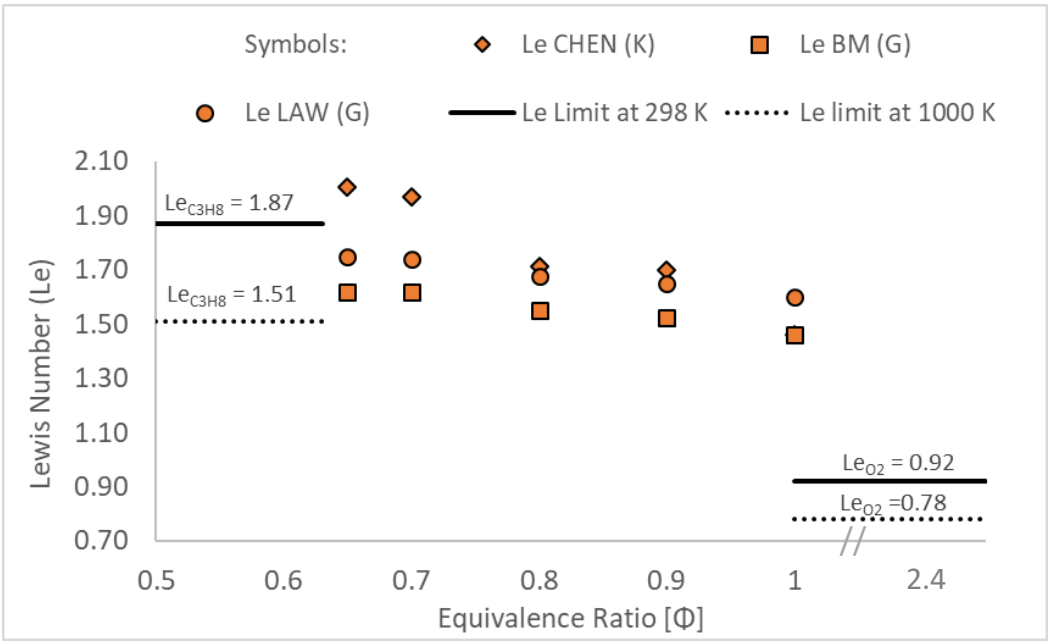

Figure 6.34 – C_3H_8/air Mixtures Experimental Le Comparison

The experimentally derived Le for C_3H_8/air mixtures are plotted along lean and rich Le limits in Figure 6.34. Evaluated lean limits (1.87) are marginally higher than cited by Law and Sung (1.83) [143] whilst good agreement is seen for rich limits (0.92 and 0.93, respectively). All formulations predict very similar experimental Le, with a decreasing Le with rising Φ, analogous to witnessed stretch related behaviour. $Le_{-CHEN\ (K)}$ yields highest Le values, marginally higher than lean limits (Φ = 0.65-0.70) before exhibiting Le values alike $Le_{-LAW\ (G)}$ and $Le_{-BM\ (G)}$.

The experimentally derived Le values alongside lean and rich limits of C_4H_{10} are presented in Figure 6.35. No sources were found in order to compare the Le limits for this

fuel, with lean and rich limits slightly higher and lower, respectively, than those of C_3H_8. Since limited experiments were conducted, insight of experimental Le is thus restricted. However, the expected trend of decreasing Le with increasing Φ is exhibited by all formulations, most pronounced upon application of $Le_{-CHEN\ (K)}$. $Le_{-BM\ (G)}$ and $Le_{-LAW\ (G)}$ both demonstrate very good agreement.

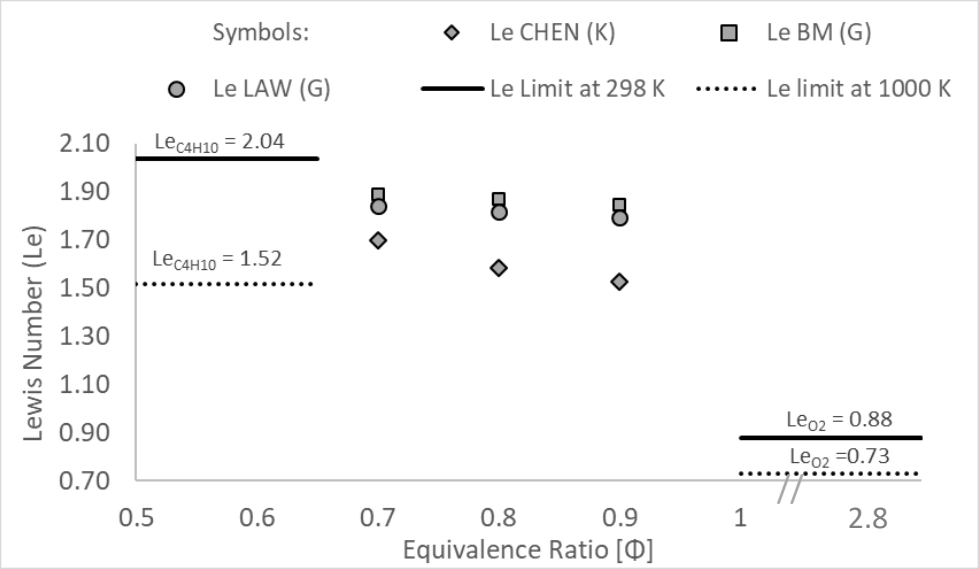

Figure 6.35 – C_4H_{10}/air Mixtures Experimental Le Comparison

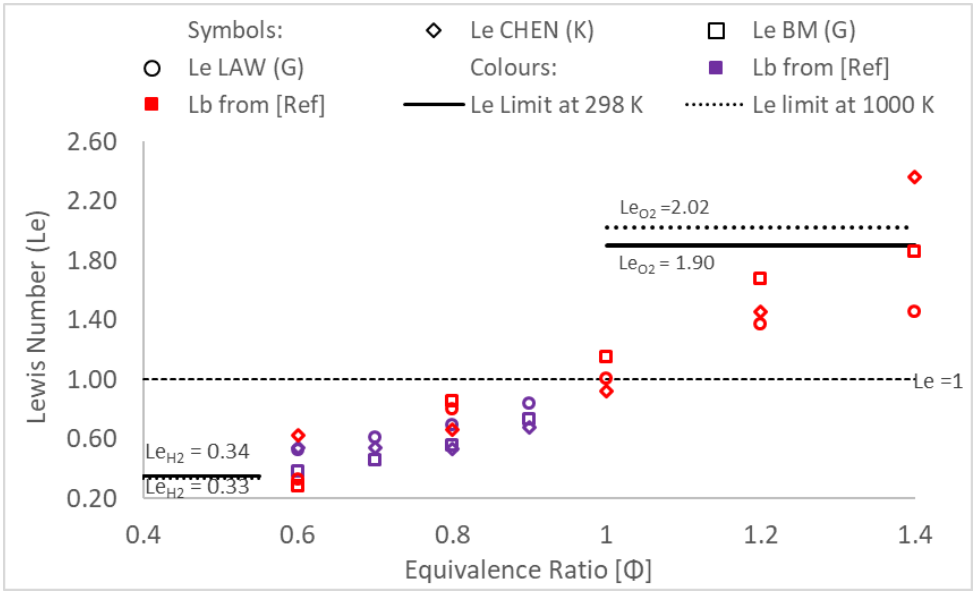

Figure 6.36 – H_2/air Mixtures Experimental Le Comparison

The experimentally derived Le values of H_2/air mixtures are shown in Figure 6.36, alongside the Le limits. The Le lean limit of 0.34 is minimally higher than the 0.29 quoted in [91], [175] and 0.33 in [143]. Important differences with respect to the rich limit are noted, with a calculated value of 2.02 in this work, significantly smaller than other cited rich limits, 2.32 in [143] and 2.58 in [91], potentially due to the observed underestimation of H_2 mass-diffusion co-efficients upon application of Wilke and Hirsch methods (Section 3.3, Table 3.2).

The L_b dataset from Hu et al. [169] was employed to evaluate experimental Le, plotted in purple in Figure 6.36. Since the flammability limits of H_2 are much wider than for alkanes, work from Lapalme et al. [91] related to assessment of Le methodology for H_2 across both lean and rich conditions is plotted, denoted by red symbols. Clearly all formulations predict experimental Le that is rising with Φ, in agreement with experimentally measured stretch behaviour (rising L_b). This increasing trend is analogous to experimental Le generated for CH_4; albeit less significant. At lean conditions, $Le_{-CHEN\ (K)}$ stays relatively insensitive to Φ (0.60-0.80, also captured by [91]), before increasing, unlike $Le_{-BM\ (G)}$ and $Le_{-LAW\ (G)}$ that continually increase, which better portrays expected H_2 behaviour. Slope inversion of L_b at Φ≈0.80 (Figure 6.11) signifying a change in thermo-diffusive response (Le > 1) is not well captured irrespective of formulation, with all predicting this change at stoichiometric conditions (Φ≈1). Finally, as underlined by Lapalme et al. [91], $Le_{-CHEN\ (K)}$ rises exponentially with increasing Φ foretelling higher than the limit Le with increasing Φ. From the plotted Lapalme dataset, $Le_{LAW\ (G)}$ and $Le_{-BM\ (G)}$ both seem to start plateauing at around Φ = 1.3-1.4, much earlier than at Φ = 3.0 evaluated by Law and Sung [143]. For lean conditions all Le formulations display similar values, with $Le_{-LAW\ (G)}$ and $Le_{-BM\ (G)}$ better capturing H_2 thermo-diffusive behaviour.

Generally, Le limits of the individual fuels give a good indication of how sensitive a fuel is to stretch. Important variations in L_b across lean Φ was experimentally measured for C_2-C_4 alkanes, with increasing stretch behaviour exhibited as conditions got leaner. This increasing stretch behaviour is analogous to the increasing lean Le limits of those hydrocarbons (1.46, 1.87 and 2.04 for C_2-C_4, respectively). A similar assessment can be made for H_2, which displays the largest Le limits coupled with the most sensitivity to stretch. For CH_4, significant variations in L_b with Φ were experimentally measured. This is not reflected in associated Le limits which are much smaller than the other alkanes and predict near equidiffusion. At leanest conditions -L_b were measured in agreement with lean limits of Le<1.

With respect to the appraised formulations, no formulation satisfactorily captured Le behaviour for CH_4, with $Le_{-CHEN\ (K)}$ best respecting Le limits, as was the case for C_2H_6. Variations in Le for the heavier $C_{2\text{-}4}$ HCs was better captured by the relationships, with Le_{-CHEN}, Le_{-LAW} and Le_{-BM} predicting a decreasing Le trend with increasing Φ for C_3H_8 whilst respecting evaluated Le limits. The application of linearly derived L_b shifted experimental Le numbers outside the limits, underlining the validity of applying non-linear models or linear models-based on curvature for highly stretched flames. Finally, for H_2 all formulations displayed the correct trend with relatively good agreement between experimental Le. Unfortunately, none of the formulations precisely captured expected change in thermo-diffusive behaviour at Φ≈0.80, predicting this change at slightly richer conditions (Φ≈1) than reported in published experimental datasets, with $Le_{-BM(G)}$ and $Le_{-LAW(G)}$ best reflecting expected H_2 Le variation.

6.4 Chapter Summary

The combustion behaviour of C_1-C_4 hydrocarbons and H_2 across lean equivalence ratios was investigated. Experimentally extrapolated flame parameters were analysed and compared to peer-published datasets and computational models. Theoretical relationships proposed in literature characterising the thermo-diffusive response of flames were explored as well as various methodologies and definitions to calculate fundamental flame parameters. From this work the following can be concluded:

- Unstretched flame speeds (S_u) and Markstein lengths (L_b) were evaluated using three different extrapolation techniques (i.e. LM(S), LM(C), NM(S)), complementing published datasets, with all presented measurements tabulated in Appendix – C.1. Application of LM(S) for fuels exhibiting Le>>1 (C_2+ HCs) results in significant overprediction of L_b and S_u values yielded (L_b up to 80%, S_u < 10%, for lean $C_{2\text{-}4}$/air mixtures), with NM(S) marginally underpredicting L_b and S_u values (L_b < 20%, S_u < 3%).
- Results were obtained for unstretched flame speeds and corresponding laminar burning velocities of C_1-C_4 fuels. In agreement with the literature CH_4 exhibited the slowest flame propagation, with C_2H_6 exhibiting marginally faster flame speeds than C_3H_8. The C_2+ hydrocarbons displayed a reduction in speed with increasing alkane number, analogous to their decreasing thermal diffusivity. Overall, relatively good agreement is observed between experimental and numerical data (particularly with Aramco 1.3) for C_1-C_3 laminar flame speeds. For the lesser studied C_4H_{10}, differences are more pronounced, between reaction modelling and data measured using different experimental apparatus.
- The influence of stretch was quantified using measured values of L_b. All hydrocarbons tested displayed similar stretch behaviour near stoichiometric conditions. Important variations in measured L_b occur rapidly as conditions get leaner, for all tested alkanes. A transition point at Φ = ~0.80 is observed at which significant changes in stretch behaviour occur, with CH_4 and C_2-C_4 exhibiting opposite trends with decreasing Φ.
- Analysis of thermo-diffusive response of the fuels was assessed using the free-stream properties of the mixture, with evaluated Le values displaying little variation across tested Φ for CH_4, with correct decreasing and increasing Le trends displayed by C_{2+} and H_2, respectively, analogous to measured stretch behaviour (for C_2+ fuels).
- Le limits of fuels evaluated provide an indication of how sensitive a fuel is to stretch, except for CH_4 which displays narrow Le limits, whilst important variations in L_b were measured. With respect to appraised formulations, $Le_{\text{-CHEN (K)}}$ best captured expected CH_4 Le behaviour. Correlation was displayed for C_3H_8 & C_4H_{10} for all formulations, with trends in Le analogous to measured L_b. $Le_{\text{-BM(G)}}$ and $Le_{\text{-Law(G)}}$ yielded best agreement with H_2.

Chapter 7. Combustion Properties &Characteristics of Fuel Blends

Having gained insight regarding the combustion characteristics of the primary components of natural gas (NG) and Hydrogen (H_2), work was undertaken to analyse the behaviour of binary mixtures. Spherical expanding flame (SEF) experiments were conducted at lean conditions ($\Phi<1$) for CH_4, C_2H_6, C_3H_8 and C_4H_{10} fuels blended with 15% volumetric additions of H_2; an enrichment level representative of contemporary industrial standards [23]. Firstly, the impact of H_2 on the investigated fuels was quantified in relation to flame propagation, stretch-related effects and thermo-diffusive stability. Secondly, a parametric study was performed investigating the impact of C_3H_8 addition on CH_4, with focus on volumes typically found in NG, with specific attention towards experimentally measured changes in Markstein length (L_b) behaviour and flame speed.

The aim of this section was therefore to quantify both the impact of H_2 addition on NG relevant HCs and to gain insight of the impact of C_3H_8 on CH_4 flames, thus enabling better understanding of the surrogate NG/H_2 mixtures subsequently examined.

7.1 Hydrogen Addition to Hydrocarbons

As reviewed in Chapter 2, extensive research (Section 2.3.4) has been conducted in relation to the impact of H_2 addition upon combustion characteristics of lean CH_4/air flames. Flame characteristics of H_2 addition to heavier HCs have been somewhat less explored (Section 2.3.5), with the general knowledge tending towards smaller combustion enhancements, as highlighted by Tang et al. [115].

All flame measurements of outwardly propagating flames were conducted at atmospheric pressure and temperature (0.1 MPa, 298K), with three nominally identical experiments for each data point used to determined repeatability. H_2 (15% by vol.) was blended to the tested C_1-C_4 fuels, with this level of H_2 enrichment corresponding to the 'higher' range of H_2 injection currently permissible in European NG infrastructure (Figure 1.4, Section 1.2.7), and comparable in volume to commitments made by the GT industry, targeting 20% H_2 capability by 2020.

Again, the four reaction mechanisms [155]–[158] suitable for hydrocarbon fuel combustion, all including the H_2/CO chemistry were appraised with appropriate numerical details provided within the relevant sub-sections. Note that unless otherwise stated, error

bars represent maximum and minimum recorded values, around an average plotted value for graphical illustrations depicting experimental L_b, S_u and U_L values.

7.1.1 Radial Propagation of Hydrocarbon/H_2 Flames

The temporal evolutions of the radial flame propagation, for the HC/H_2 mixtures are illustrated in Figure 7.1 (a-d), with the gradients representing the stretched flame speed. With respect to CH_4, (Figure 7.1 (a)), there are contrasting inflection points near the base of the curve, with stretched flame speeds curving outwards, for Φ 0.55-0.70, and opposite curvature exhibited for Φ ≥ 0.80. This behaviour suggests L_b of opposing signs, witnessed at Φ = 0.60 for CH_4 combustion (Figure 6.1(a), Section 6.1.1). Clearly, relatively small additions of H_2 alter stretch behaviour of CH_4 flames, particularly at lean conditions.

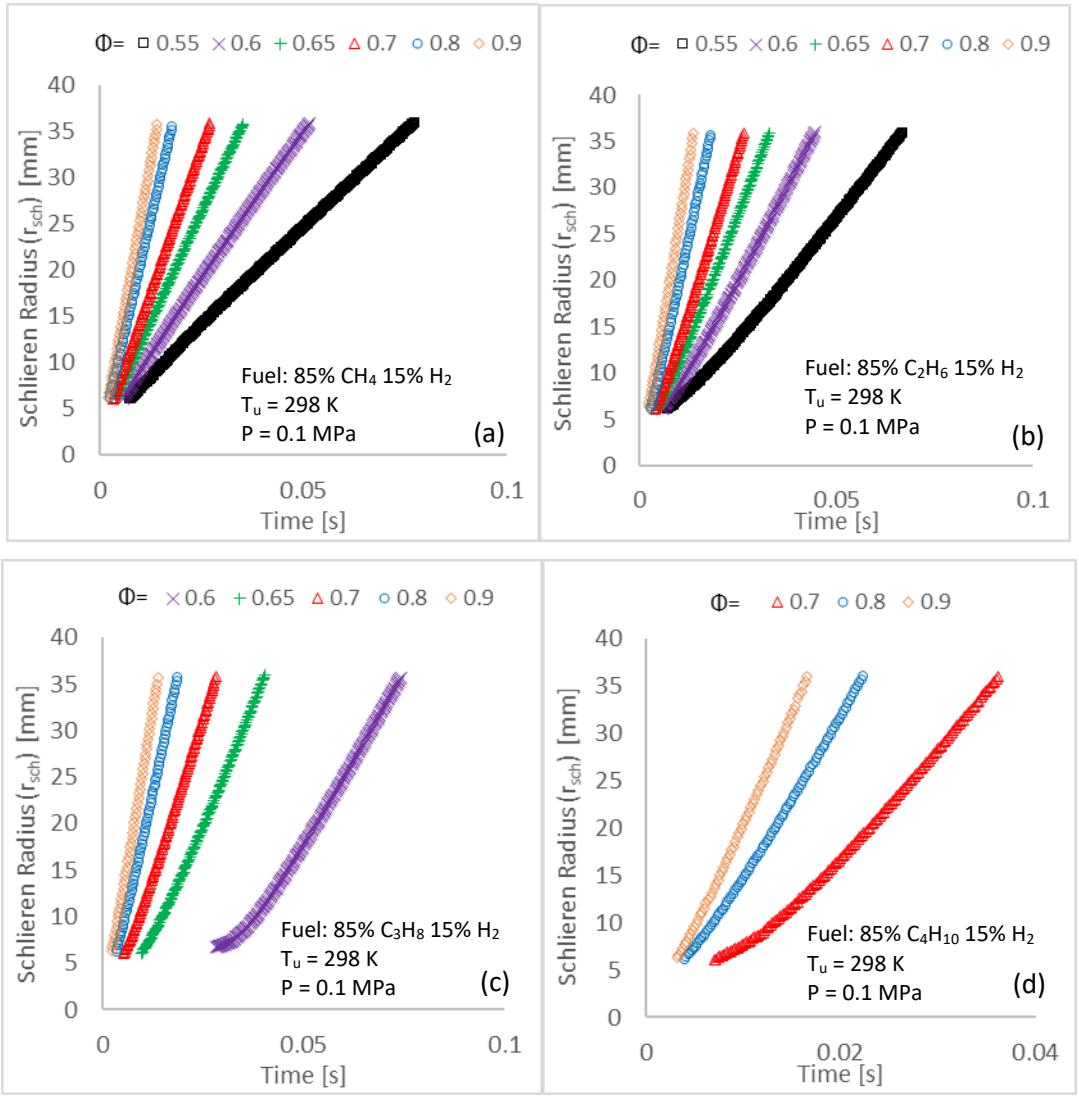

Figure 7.1 – Radial Propagation Rates for Lean H_2 enriched (15% vol.) - (a) CH_4 (b) C_2H_6 (c) C_3H_8 (d) C_4H_{10}/air mixtures

In relation to the heavier fuels tested, (Figure 7.1 (b-d)), H_2 addition seems to have limited impact, with strong stretch-behaviour again observable at small flame radii,

discernible at the leanest conditions, prior to establishment of full flame propagation, in agreement with earlier observations of the C_2-C_4/air flames (Figure 6.1 (b-d), Section 6.1.1).

For the tests conducted throughout this thesis, ignition energy was kept as constant as possible to limit the influence of initial energy deposit on early flame propagation, however, it was noticed that small volumetric additions of H_2 (15%) extended lean limits of HCs investigated. Reliable ignition was observed for H_2 enriched CH_4 and C_2H_6 at Φ= 0.55 (from Φ=0.60), C_3H_8 at Φ= 0.60 (from Φ= 0.65), with lean limits of C_4H_{10} unaffected (Φ=0.70). Recognising the above, relatively small additions of H_2 are seen to augment the burning intensity, the result of facilitated diffusion. Thus the enhanced reactivity of the mixture due to the presence of H_2, potentially alters the critical stretch limit of the HC fuels tested, consequently extending the lean limits of the mixtures.

7.1.2 Stretched Flame Propagation of Hydrocarbon/H_2 Flames

The datasets of the HC/H_2 mixtures are presented in Figures 7.2-7.5, illustrating the relationships between the stretched flame speed (S_n) and stretch (α) using both linear and non-linear methodologies and that between S_n and curvature (κ).

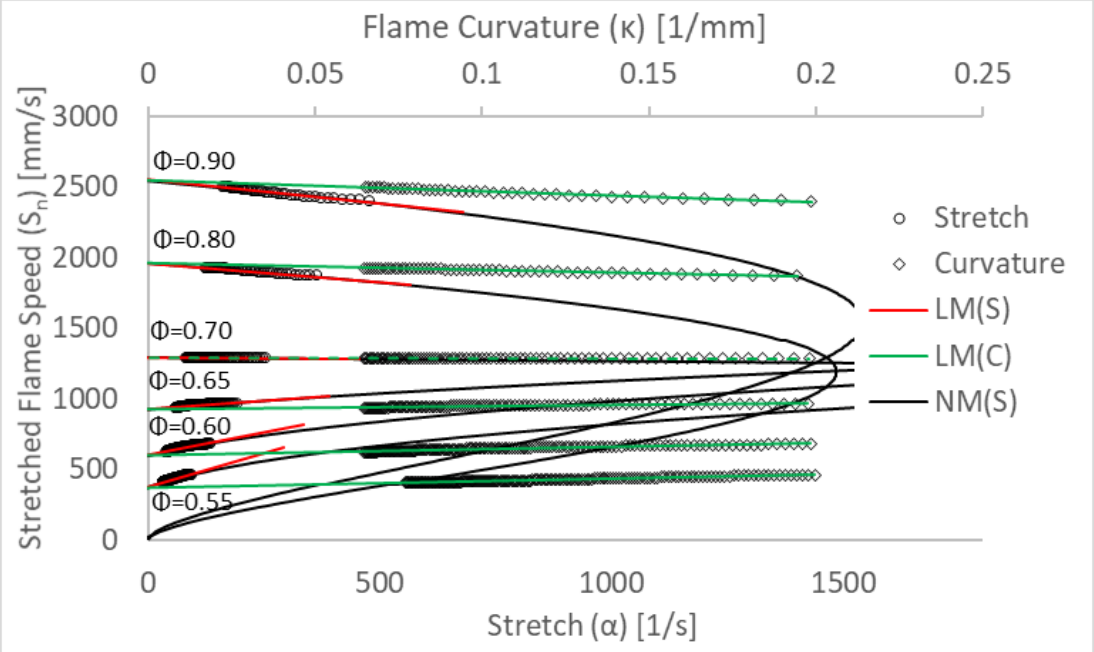

Figure 7.2 – S_n vs α and κ for Lean CH_4/H_2 air Blends (85/15 vol.%) – (T_u=298 K, P=0.1MPa)

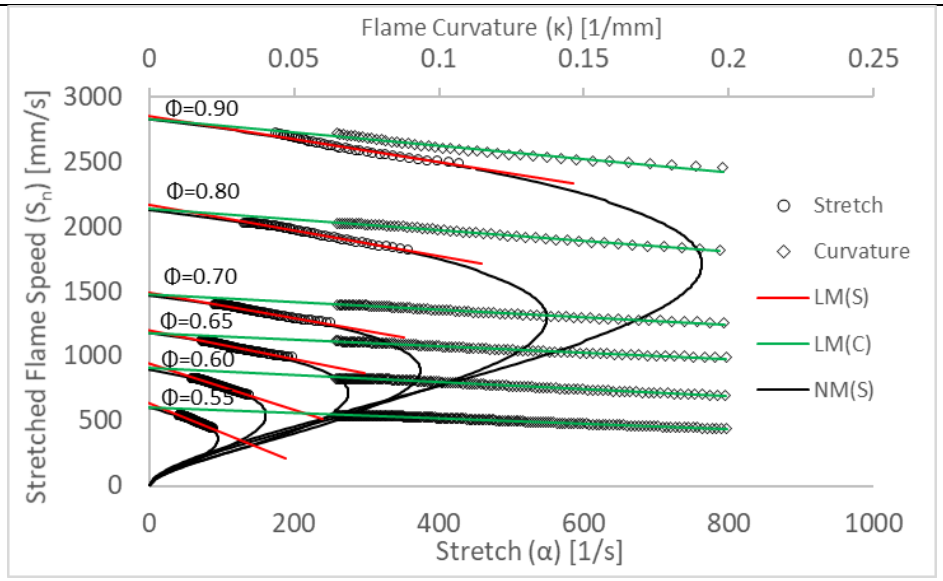

Figure 7.3 – S_n vs α and κ for Lean C_2H_6/H_2 air Blends (85/15 vol.%) – (T_u=298 K, P=0.1MPa)

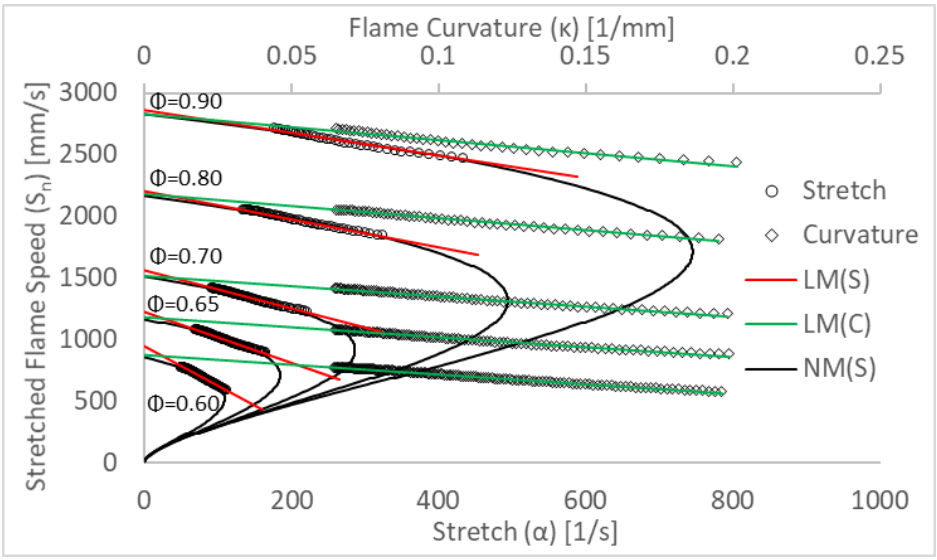

Figure 7.4 – S_n vs α and κ for Lean C_3H_8/H_2 air Blends (85/15 vol.%) – (T_u=298 K, P=0.1MPa)

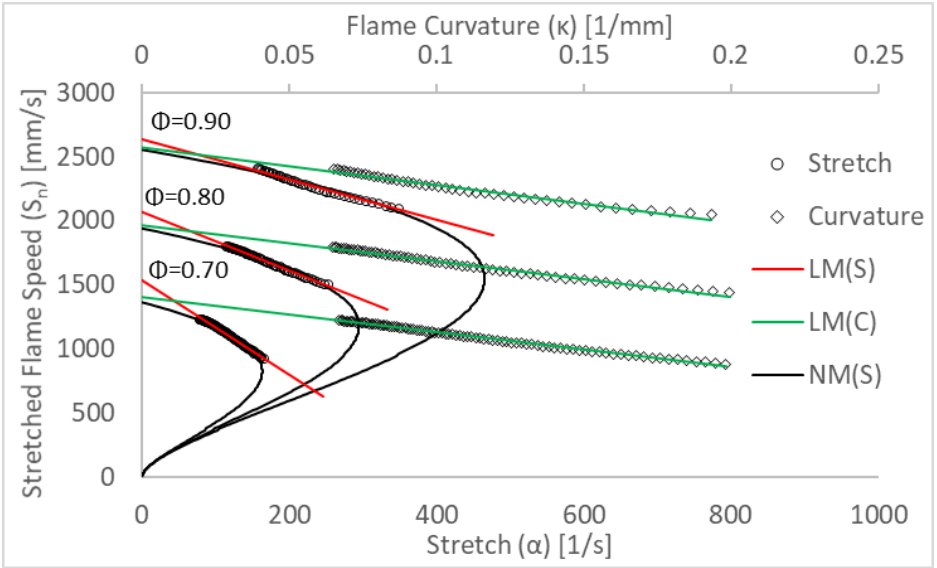

Figure 7.5 – S_n vs α and κ for Lean C_4H_{10}/H_2 air Blends (85/15 vol.%) – (T_u=298 K, P=0.1MPa)

With respect to Figures 7.2-7.5, again a negative gradient represents a deceleration in flame speed with increasing stretch/curvature rates, equating to + L_b values. As seen from Figure 7.2, nominal change in CH_4 stretch behaviour is witnessed at near stoichiometric conditions (Φ = 0.90) upon H_2 addition. Quasi-equidiffusion of heat and mass transport mechanisms (L_b≈0, Le≈1) is observable at Φ=0.70, with flame propagation practically independent of stretch and curvature effects, exemplified with gradients close to zero evaluated by all extrapolation methodologies employed. Significant changes are seen at leaner conditions (Φ= 0.55-0.65), with slope inversion shifting to richer conditions, and positive gradients measured at Φ=0.65, indicating a negative L_b and flame acceleration with increasing stretch rates, driven by facilitated mass diffusivity due to the presence of H_2. As such, small fractions of H_2 have the propensity of diffusionally destabilising ultra-lean CH_4 flames, promoting preferential diffusion instabilities, somewhat unsurprisingly since CH_4 L_b behaviour (↑L_b with ↑Φ) is more similar to that exhibited by H_2 (↑L_b with ↑Φ) than HC flames (↓L_b with ↑Φ).

Figures 7.3-7.5 illustrate the relationship between flame stretch/curvature and flame propagation of lean C_{2+}/H_2 (85/15, vol.%) flames, with H_2 addition seemingly having little impact on C_{2-4} flame behaviour, albeit minimally less step gradients are observed. To some extent, minimal changes are to be expected since H_2 and C_{2-4} HCs display opposite L_b and Le behaviour at lean conditions. Furthermore, significant differences in molecular mass between H_2 and C_2+ fuels tested diminish the influence of small volumetric additions of H_2 (15% vol.). Tang et al. [113] highlight that for lean C_{2+} mixtures, enrichments levels > 50% (vol.%) are required to enable H_2 to dominate the combustion process, dictating flame stability and behaviour.

Note that important differences in extrapolated S_u (and L_b) values are visible upon application of different extrapolation methodologies, with differences in yielded S_u exacerbated with decreasing and increasing Φ and molecular weight, respectively, particularly visible for C_4H_{10} (Φ=0.70, Figure 7.5), with differences quantified subsequently (Figure 7.7).

7.1.3 Markstein Lengths of Hydrocarbon/H_2 Flames

Measured L_b of H_2/HC mixtures are illustrated in Figure 7.6, alongside previously presented C_{1-4} L_b (plotted as lines) and H_2 L_b as measured by Hu et al. [90], to facilitate comparison and discussion. Due to the perceived greater accuracy for fuel displaying Le >> 1, L_b values yielded using LM(C) are plotted in Figure 7.6, with individual test results generated using all employed extrapolation methodologies available in tabulated format in

Appendix – C.1. Finally, for the sake of completeness, note that for CH_4/H_2 Φ=0.55, results reflect two nominally identical experiments, with all other conditions repeated at least three times.

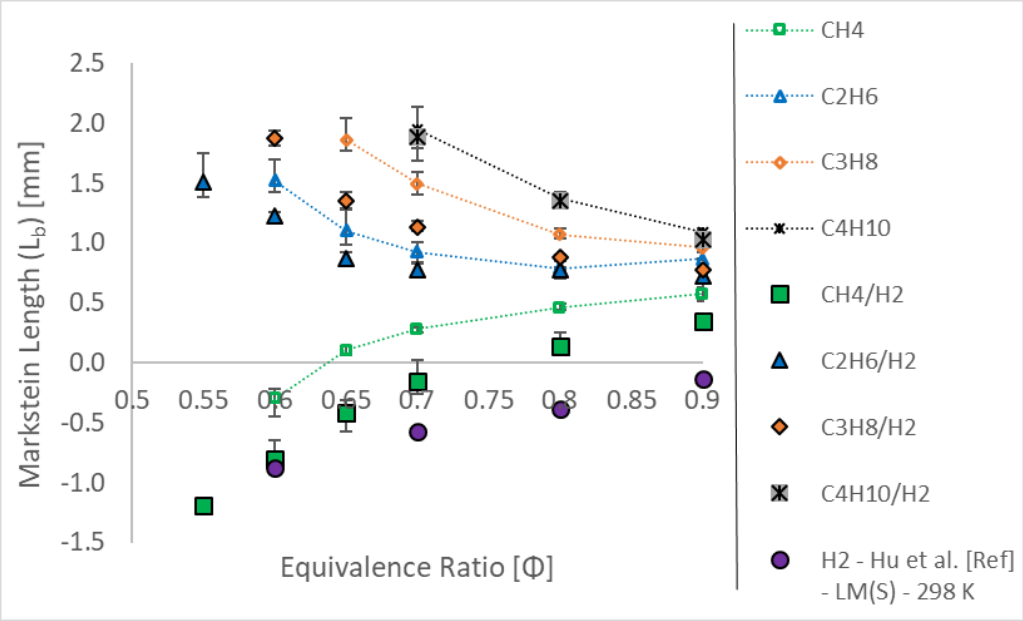

Figure 7.6 – Measured L_b of Lean C_{1-4}/air and C_{1-4}/H_2/air Mixtures (H_2 = 15% vol.)

As indicated by the S_n vs α plots (Figures 7.3-7.5), small H_2 additions to C_{2-4} fuels has limited impact on L_b, due to H_2 and C_{2-4} fuels displaying similar stretch behaviour at near stoichiometric conditions (Φ =0.8-0.9). However, it is noticeable that the influence of H_2 on C_{2-3} flames augments as conditions get leaner, a consequence of the individual fuels increasingly opposite response to stretch and Le behaviour. Nominal differences in measured L_b are registered for C_4H_{10} upon H_2 addition.

H_2 addition (15% vol.) generates fundamental changes in lean (Φ<0.70) CH_4/flames, with L_b sign inversion (from + to –) observed at Φ=0.70-0.8 (Figure 7.6). Note that L_b published dataset comparison for H_2/air flames (Figure 6.11), L_b slope inversion was measured at Φ=0.75-0.85 (for Hu et al., [90] plotted in Figure 7.6, L_b slope inversion was measured at Φ ≈ 1). As such, it may appear that only small volumes of H_2 are required to significantly influence CH_4 flame stability. Recognising that lean CH_4 flames exhibit quasi-equidiffusion of heat and mass, with lean H_2 flames driven by mass diffusion (Le<<1), small additions of H_2 at ultra-lean conditions (Φ<0.65) would lower the effective Le of CH_4 (on a diffusional, volumetric and heat-release base, discussed subsequently in Section 7.1.6). However, although the above holds true, near equivalent stretch behaviour were exhibited by H_2 and CH_4/H_2 (85/15% vol.) mixtures as measured by Hu et al. [90] and during this work, respectively, using SEFs at nominally identical experimental conditions. Note that the only perceived difference is related to the methodology employed to yield L_b values, LM(S) and LM(C), applied by Hu et

al. [90] and in this study, respectively. As previously underlined, most published research using SEFs employ the historical linear relationship between flame speed and stretch, (Section 3.1.2.2). Chen [84] assessed the accuracy of L_b values yielded using LM(S), concluding that significant underprediction of L_b is observed, with differences as high as 100% for fuels that exhibit Le < 0.65, as is the case for lean H_2 flames (with calculated 'theoretical' and 'experimental' Le < 0.60, see Figures 6.23(e) and 6.36) recommending the use of NM(S) for fuels exhibiting Le <<1. It thus seems likely that L_b measurements of H_2/air flames published using LM(S), greatly underpredict L_b values, with H_2 possibly displaying much lower (more negative) L_b than reported, in part explaining the similarity witnessed between H_2/air and CH_4/H_2 flames at Φ=0.60 in Figure 7.6.

For fuels exhibiting Le >> 1, such as C_{2-4}/H_2 blends (85/15% vol.), Chen recommends [84] employing LM(C). Thus, to exemplify the impact of extrapolation model employed on attained L_b values, Figure 7.6 depicts average relative differences in L_b values of lean C_{1-4}/H_2 blends yielded using LM(S) and NM(S) normalised to LM(C). Two distinct observations can be made from Figure 7.7, firstly that LM(S) and NM(S) overpredict and underpredict L_b values, respectively for fuels displaying Le>>1, secondly, that those differences augment with increasing Le. As expected, differences in attained L_b values for the CH_4/H_2 mixture are significantly smaller than those exhibited by the C_{2+}/H_2 mixtures, a consequence of CH_4's quasi-equidiffusivity of mass and heat (Le =1), with differences in yielded L_b values increasing with decreasing Φ, indicating deviation from Le = 1 for ultra-lean CH_4/H_2 mixtures.

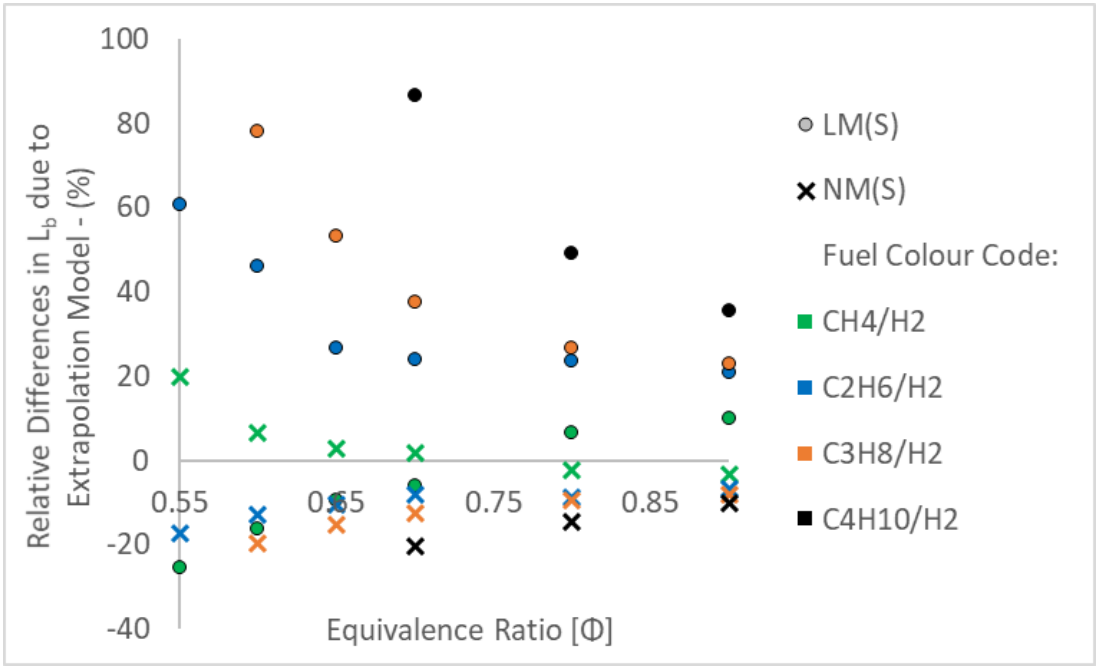

Figure 7.7 – Relative Differences in L_b Values Employing LM(S) and NM(S) Normalised to LM(C) for Lean C_{1-4}/H_2 Blends (85/15% vol.)

7.1.4 Unstretched Flame Propagation of Hydrocarbon/H_2 Flames

The S_u measurements attained via application of LM(C), for the HC/H_2/air (85/15% vol.) mixtures tested are presented in Figure 7.8. The relative increase in S_u of the C_{1-4} flames due to H_2 enrichment is illustrated in Figure 7.9, with Figure 7.10 depicting relative differences in yielded S_u utilising LM(S) and NM(S) normalised to that of LM(C). With respect to Figure 7.8, whilst the CH_4/H_2 blend maintains the slowest S_u in comparison to the tested C_{2-4}/H_2 mixtures, differences have considerably reduced, with measured CH_4/H_2 S_u comparable to those displayed by C_4H_{10}/H_2 flames, whilst C_2H_6/H_2 and C_3H_8/H_2 mixtures exhibit quasi-identical S_u.

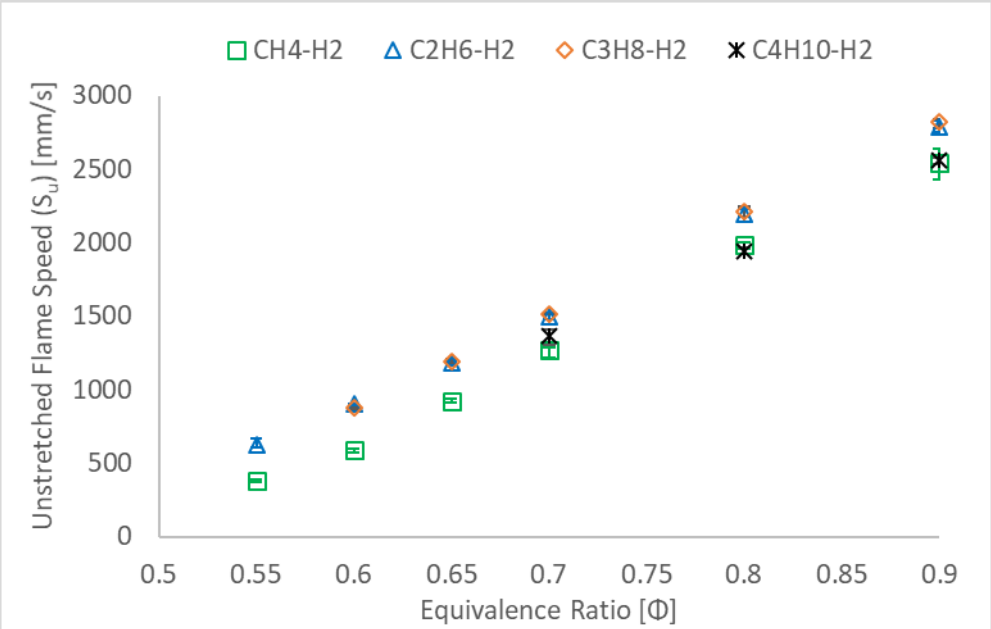

Figure 7.8 – S_u of C_1-C_4/H_2/air Mixtures across Lean Φ (T_u=298K, P = 0.1MPa)

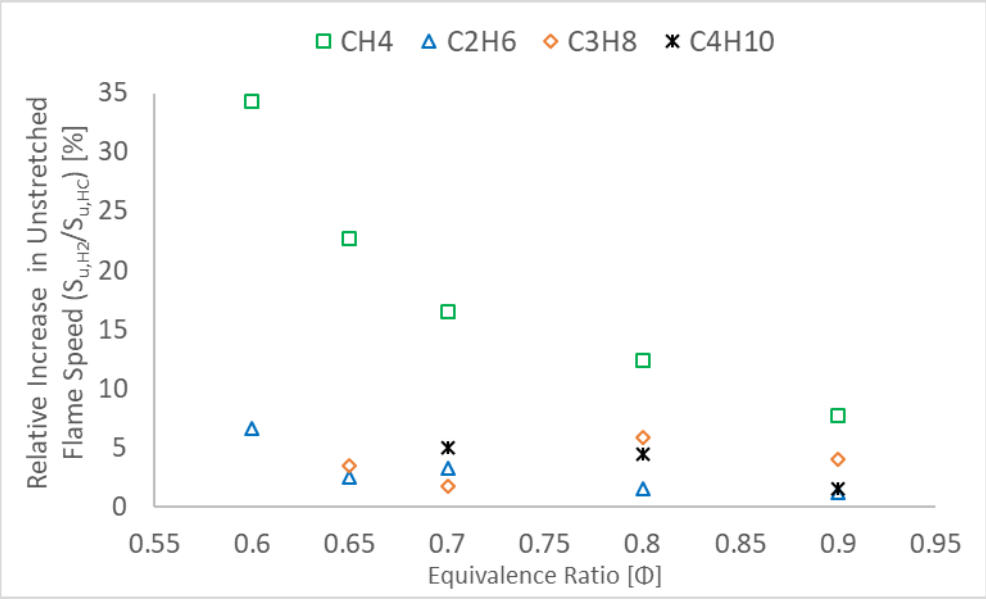

Figure 7.9 – Relative Increase in S_u of C_1-C_4 Fuels upon H_2 Addition (15% vol.) across Lean Φ (T_u=298K, P = 0.1MPa)

Evidently, H_2 addition to lean CH_4 flames generates significant impact in attained S_u, as illustrated in Figure 7.9, with enhancement of S_u augmenting with decreasing Φ, analogous to measured changes in L_b (Figure 7.6). H_2 enrichment generates relatively small augmentations in measured S_u (<10%) for C_{2-4} HCs, in comparison to CH_4, with recorded relative increases > 30% at Φ = 0.60. As expected, H_2 addition alters the thermo-kinetic and transport properties of lean HC/air mixtures, with CH_4 most prominently affected; possible reasons behind this enhancement in burning intensity are explored in more detail in Section 7.1.5.

Relative differences in average yielded S_u employing LM(S) and NM(S) normalised to LM(C) for the tested lean C_{1-4}/H_2 blends are plotted in Figure 7.10, as previously performed for the tested mixtures respective L_b values (Figure 7.7). Again, two observations can be made from Figure 7.10, first, for CH_4/H_2 mixtures minimal differences in attained S_u values (<2%) are witnessed upon application of LM(S) or NM(S), second, differences are considerably more significant for the C_{2-4}/H_2/air mixtures (Le >>1), with LM(S) overpredicting S_u, (i.e. ≈10% for C_4H_{10}/H_2 Φ=0.70), whilst NM(S) underpredicts S_u ≈ 1-4% depending on HC compound, with the observed differences increasing with increasing Le, particularly at leanest conditions.

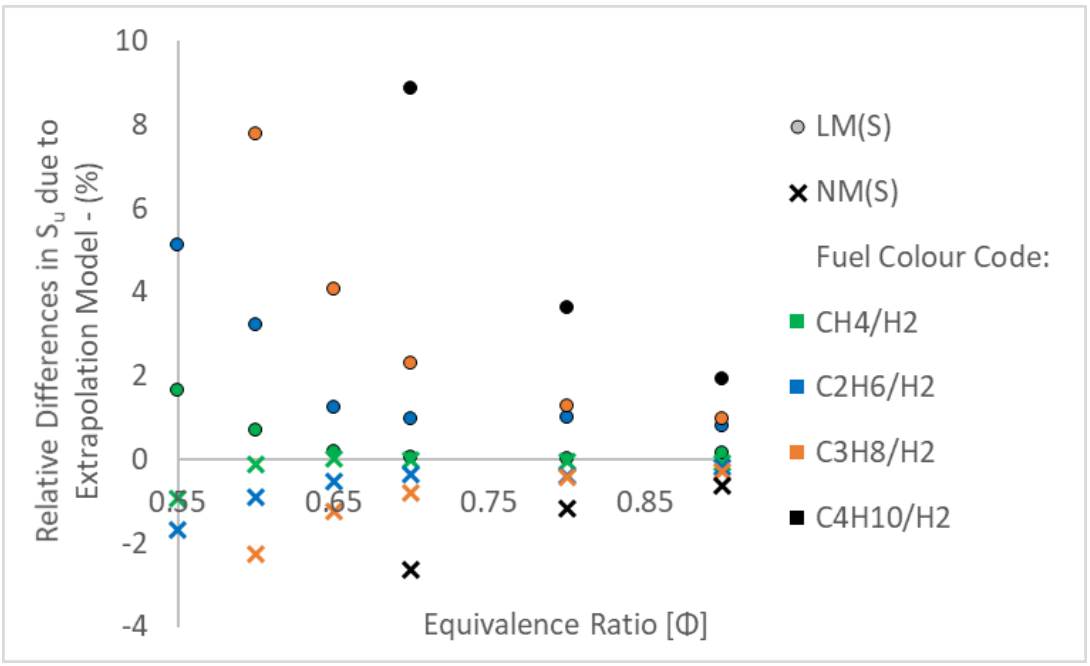

Figure 7.10 – Relative Differences in S_u values employing LM(S) and NM(S) Normalised to LM(C) for Lean C_{1-4}/H_2 blends (85/15% vol.)

7.1.5 Laminar Burning Velocity of Hydrocarbon/H_2 Flames

The laminar burning velocities (U_L) of the C_{1-4}/H_2 blends are presented in Figure 7.11. Clearly, the CH_4/H_2 mixture exhibits higher U_L values than those attained by the C_4H_{10}/H_2 flame, a significant change in comparison to U_L values displayed by pure CH_4 and C_4H_{10} flames

(Figure 6.20). C_2H_6/H_2 and C_3H_8/H_2 flames exhibit comparable U_L, marginally higher than U_L attained by CH_4/H_2 flames, with differences decreasing with increasing Φ, with comparable U_L values attained at near stoichiometric conditions (Φ=0.9) by the C_{1-3}/H_2 blends.

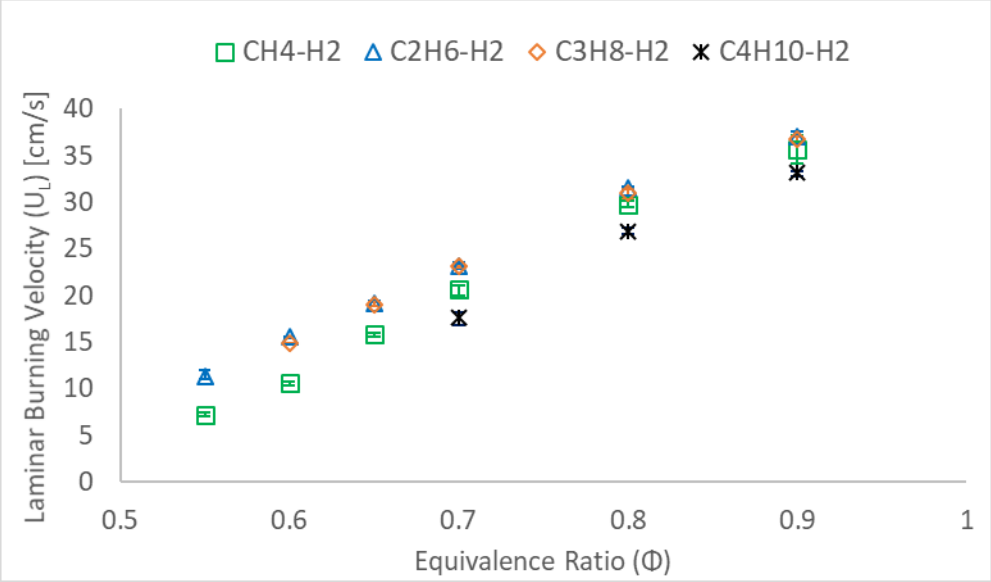

Figure 7.11 – U_L of C_1-C_4/H_2/air Mixtures (85/15% vol.) across Lean Φ (T_u =298 K, P =0.1 MPa)

Numerical simulations of U_L values for the C_1-C_4/H_2 mixtures was conducted using CHEMKIN-PRO and associated PREMIX code. Again, four reaction mechanisms were appraised [155]–[158], all suitable for HC/H_2 combustion, with numerical solutions plotted in Figures 7.12 – 7.15, for CH_4/H_2, C_2H_6/H_2, C_3H_8/H_2 and C_4H_{10}/H_2, respectively, alongside experimental data.

It is seen that there is excellent agreement between measured and numerically attained U_L values using the Aramco 1.3 mechanism (Figure 7.12), with all appraised mechanisms predicting very similar values. With respect to C_2H_6/H_2 blends (Figure 7.13), there is again correlation between experimental and predicted U_L values from GRI-M 3.0 and Aramco 1.3 for Φ < 0.7, however differences augment with increasing Φ, with measured U_L marginally slower than predicted numerical solutions. Larger discrepancies are displayed in the case of C_3H_8/H_2 flames (Figure 7.14), with GRI-M 3.0 significantly over-predicting U_L values at near stoichiometric conditions (Φ=0.8-0.9). Best agreement is observed again with Aramco 1.3, with measured values minimally slower than numerical solutions across the tested Φ. Finally, with respect to C_4H_{10}/H_2 (Figure 7.15), all assessed reaction mechanisms significantly over-predict U_L, as previously witnessed for C_4H_{10}/air flames (Figure 6.19). Overall, measured U_L values of C_1-C_3/H_2 mixtures display best agreement with Aramco 1.3, as previously witnessed for the pure C_1-C_3 fuel/air mixtures. For the lesser studied C_4H_{10}, differences are apparent between measured U_L values and numerical predictions.

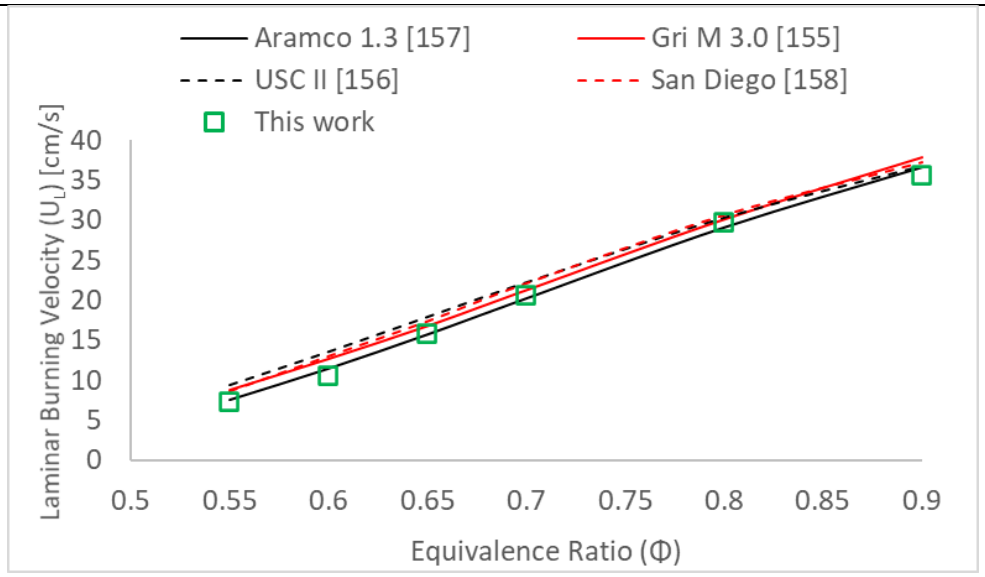

Figure 7.12 – Numerical and Measured U_L values for CH_4/H_2 Mixtures (T_u=298K, P =0.1MPa)

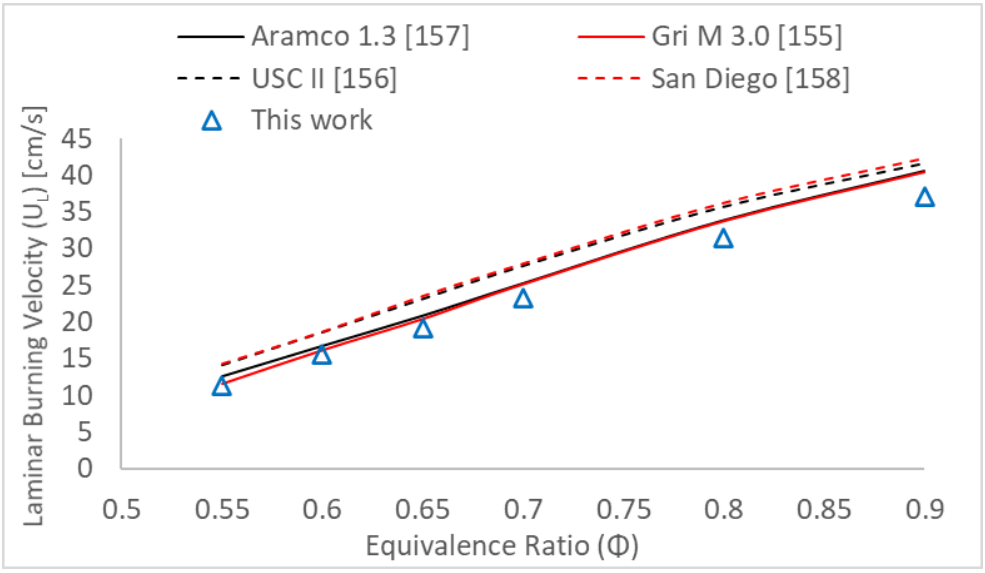

Figure 7.13 – Numerical and Measured U_L values for C_2H_6/H_2 Mixtures (T_u =298K, P = 0.1MPa)

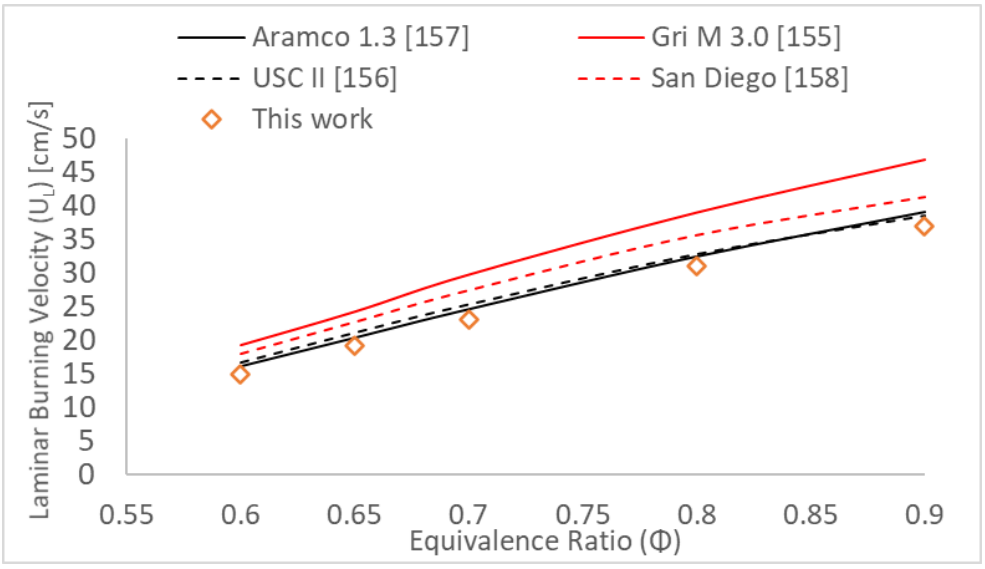

Figure 7.14 – Numerical and Measured U_L values for C_3H_8/H_2 Mixtures (T_u =298K, P = 0.1MPa)

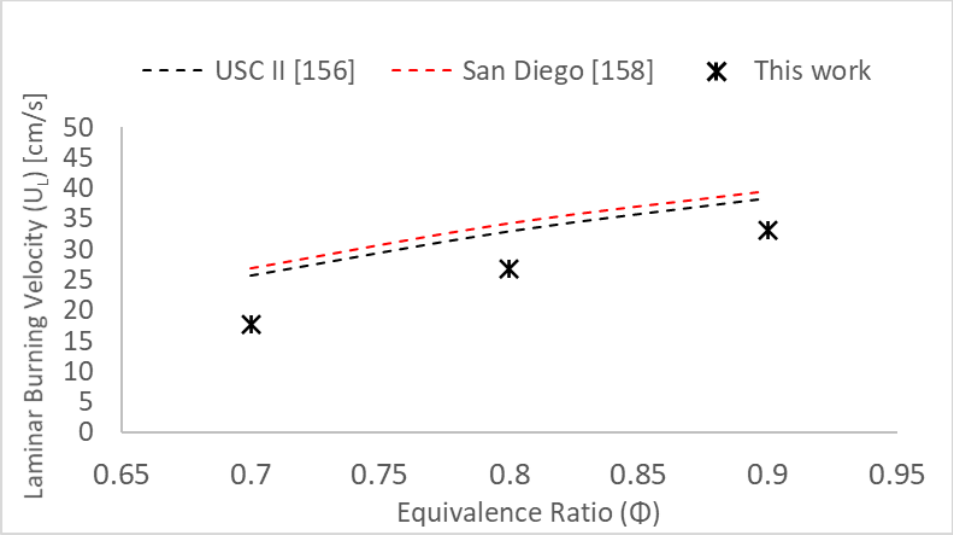

Figure 7.15 – Numerical and Measured U_L values for C_4H_{10}/H_2 Mixtures (T=298K, 0.1MPa)

It is evident from the measured changes in S_u (Figure 7.8-7.9), relatively small amounts of H_2 (15% vol.) are seen to augment the burning intensity of C_{1-4} HCs, with CH_4 most prominently affected. Modelling work (applying the same conditions as those employed to predict U_L values plotted in Figures 7.12-7.15) was undertaken to evaluate the relative increase in volumetric heat release rate (Q') of the HC flames upon H_2 enrichment, presented in Figure 7.16. The Aramco 1.3 and USC II reaction mechanisms were employed for evaluating increases in Q' for C_1-C_3/H_2 and C_4H_{10}/H_2, respectively, since those reaction mechanisms displayed best agreement with experimental U_L values. Clearly, as can be seen from Figure 7.16, small H_2 additions significantly augment the burning intensity of lean CH_4 flames, with relative differences in volumetric heat release rates intensifying with decreasing Φ, analogous to average relative increases in S_u (Figure 7.9). With respect to the tested C_{2-4} fuels, H_2 enrichment results in modest increases in modelled heat release rate, in agreement with the limited measured changes in S_u exhibited by the tested C_{2-4}/H_2 mixtures.

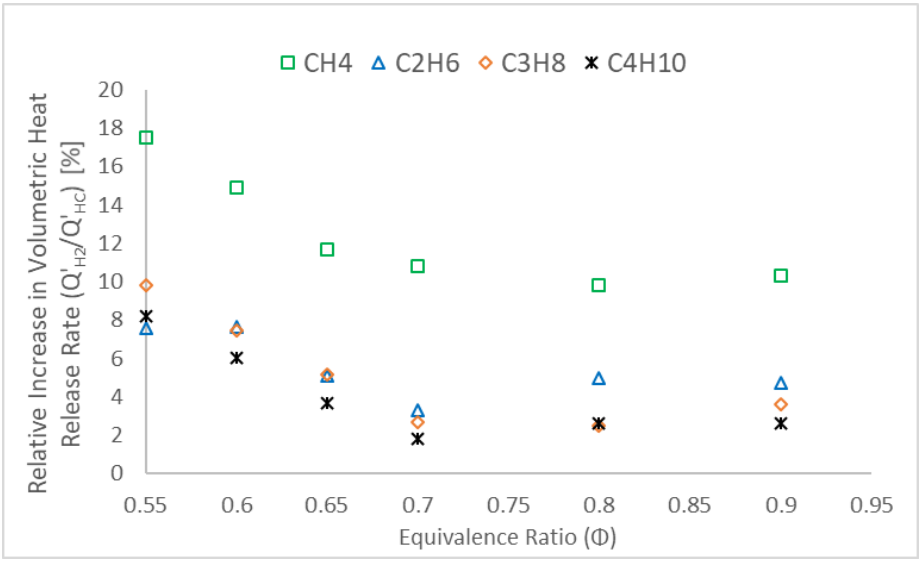

Figure 7.16 – Relative Increase in Q' of C_1-C_4 Flames upon H_2 Addition (15% vol.) across Lean Φ

Recently, Nilsson et al. [80] experimentally and numerically studied the chemical kinetic effects of H_2 enrichment (up to 50% vol.) on U_L of NG blends containing higher HCs (C_2-C_3, 20% vol.), concluding that H_2 addition affected the overall oxidation mechanism of CH_4 more significantly than C_{2-3} HCs, attributing the enhanced reactivity of CH_4 to significant increases in concentration of active radicals (H, O, OH) at leanest conditions. Modelled average relative increases in H radical concentrations for the C_1-C_4/H_2/air experiments conducted are illustrated in Figure 7.17, and are in good agreement with trends published by Nilsson et al. [80].

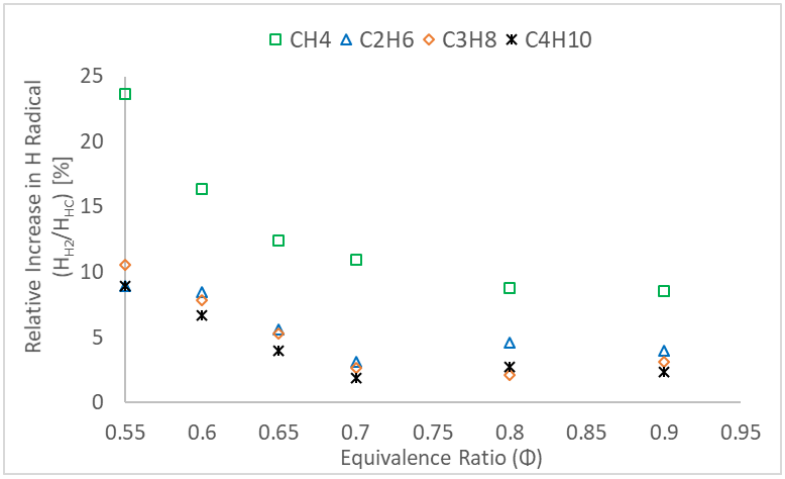

Figure 7.17 – Relative Increase in H radical of C_{1-4} Flames upon H_2 Addition (15% vol.) across Lean Φ

7.1.6 Lewis Number of Bi-Component Fuels

As evident from measured changes in L_b and S_u, lean CH_4/air flames are particularly susceptible to H_2 enrichment, with limited impact displayed by the C_{2-4} fuels. To better understand these thermo-diffusive changes, analysis of Lewis number (Le) behaviour of HC/H_2 flames is undertaken. For multi-fuel blends, evaluation of Le can become challenging, since the diffusivity of each component fuel must be considered. As discussed previously, Bouvet et al. [131] identified three 'effective' Le formulations, namely: volume based Le (Le_V), diffusion based Le (Le_D) and heat-released based Le (Le_H) (Section 3.3). Since the above formulations were based on the free-stream properties of the mixture, when referring to Le_V, Le_D, and Le_H as a whole, these are henceforth referenced as 'effective theoretical' Le, using the 'Le_{eff}' abbreviation.

Figures 7.18 (a-d) illustrates Le_{eff} for the H_2 enriched CH_4, C_2H_6, C_3H_8, and C_4H_{10} mixtures, respectively, with Le_D, Le_V and Le_H following the colour-code blue, red, green, correspondingly, maintained throughout this work. As previously, for evaluation of single fuel Le (Section 6.2.1), the binary-mass diffusion co-efficients of the HC/H_2 blends are calculated employing the Hirschfelder and Wilke methodologies, as detailed in [125], and described in Section 3.2.1.3, denoted by full and broken lines, respectively, with the difference coloured to give a perception of possible Le range, evaluated at a (λ/c_p) ratio of T = 298 K.

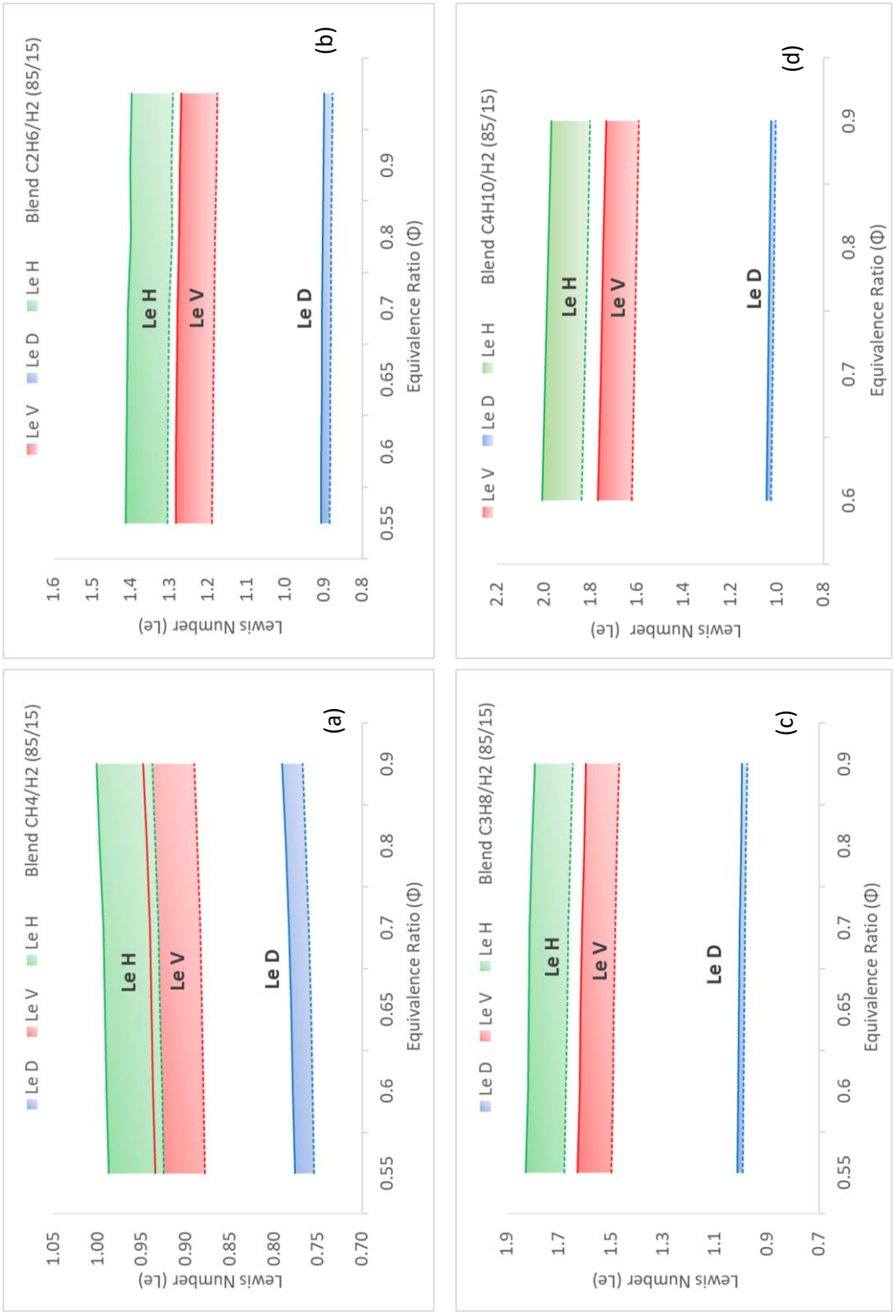

Figure 7.18 – Theoretical Le_{eff} Formulations for (a) CH_4/H_2 (b) C_2H_6/H_2 (c) C_3H_8/H_2 (d) C_4H_{10}/H_2 flames (85/15% vol.) across lean Φ

With respect to the CH_4/H_2 mixture (Figure 7.18 (a)), all Le_{eff} formulations predict Le close to or below unity, with rising Le with increasing Φ, reminiscent of the mixture's experimentally measured L_b. For the C_2-C_4 HCs (and in general for all heavier HCs), Le_{eff} models predict an important Le range, above and below unity (1< Le <1, Figure 7.18 (b-d)), implying opposite thermo-diffusive properties and stretch-related behaviour for the same condition. Recognizing this apparent incompatibility, Le_{eff} formulations are investigated using relationships proposed by Chen [84], [120] and Matalon and Bechtold [142] (referred to CHEN and BM in text, Section 3.4), and thus requiring assessment of fundamental flame parameters, evaluated following methods described in Section 3.5.

7.1.7 Fundamental Flame Parameters for Hydrocarbon/H_2 Flames

Fundamental flame parameters namely Zel'dovitch number (Ze) and flame thickness (δ) of the tested C_1-C_4/H_2 flames are evaluated (methods employed are detailed in Section 3.5), with impact of 15% H_2 (vol.%) enrichment analysed. Note that the Aramco 1.3 [157] and USC II [156] reaction mechanisms were utilised to yield Ze and δ results, for C_{1-3}/H_2 and C_4/H_2 mixtures, respectively, since best agreement was observed between measured and numerically attained U_L values for the respective blends and reaction mechanisms. As discussed in Chapter 6 (Section 6.2.3) E_a (2) yields values that better represents expected E_a (and thus Ze) of H_2 whilst simultaneously respecting the parabolic E_a behaviour of HCs (Figure 6.27 (a-b)), and thus was employed for the H_2/HC blends presented in this section. Relative differences in Ze and δ (δ_G & δ_K) between the tested C_{1-4}/air and C_{1-4}/H_2/air mixtures are presented in Table 7.1 and 7.2, respectively.

Table 7.1 – Relative Differences (%) in Ze between C_1-C_4/air and C_1-C_4/H_2/air blends (85/15% vol.)

Φ	CH_4	C_2H_6	C_3H_8	C_4H_{10}
0.55	-7.38	-1.30	/	/
0.60	-4.58	-1.30	-0.61	/
0.65	-2.94	-1.02	-1.61	/
0.70	-2.75	-1.71	-1.19	-0.25
0.80	-1.33	0.06	-0.84	-1.21
0.90	-2.50	-1.41	-0.58	0.01

Table 7.2 – Differences (%) in δG & δK between C_1-C_4/air and C_1-C_4/H_2/air blends (85/15% vol.)

Φ	CH_4		C_2H_6		C_3H_8		C_4H_{10}	
	δ_G	δ_K	δ_G	δ_K	δ_G	δ_K	δ_G	δ_K
0.60	-8.80	-24.44	-3.27	-6.38	/	/	/	/
0.65	-6.82	-19.10	-2.45	-1.37	-2.63	-3.16	/	/
0.70	-6.18	-12.20	-1.87	-3.14	-1.71	-1.04	-1.07	-2.95
0.80	-5.27	-7.52	-2.29	-2.52	-1.52	-3.98	-1.21	-1.48
0.90	-10.63	-5.12	-2.08	-1.51	-1.80	-2.01	-1.20	-0.37

Since E_a of H_2 is approximately half that of the tested C_1-C_4 fuels at ultra-lean conditions (at Φ= 0.60, E_a H_2 ≈ 25 kcal/mol, E_a C_1-C_4 ≈45-55 kcal/mol, Figure 6.33), H_2 addition is expected to lower E_a of the tested HC/H_2 blends, with calculated relative decreases in Ze illustrated in Table 7.1. Two observations can be made from Table 7.1, first, that small H_2 additions have greater impact on E_a of HC fuels at leanest conditions, with differences diminishing with increasing Φ, this is expected considering the parabolic relationship of C_{1-4} E_a (with minimum E_a registered at Φ≈0.90-1.0, Figure 6.26) coupled with the 'flat' parabolic E_a of H_2 (with minimal changes in E_a across Φ=0.40-4.40, Figure 6.28). Second, the impact of H_2 enrichment is most pronounced for CH_4 than the tested C_{2-4} HCs, which is reasonable since E_a is seen to decrease with increasing alkane number, with relative differences decreasing with increasing carbon number, Table 7.1.

The impact of H_2 on flame thickness is presented in Table 7.2, with results showing a reduction of the flame thickness (both δ_G & δ_K) for all HCs across the tested Φ, with CH_4 most prominently affected. Note that the thinning effect of H_2 on δ decreases with increasing alkane number. Intriguingly, the thermal expansion ratio ($\sigma = \rho_u/\rho_b$) remains almost constant (<1.2% variation across tested Φ) for all the HC/H_2 mixtures. Consequently, a reduction in flame thickness and constant σ would have the combined effect of promoting hydrodynamic instabilities, with CH_4 most affected due to greatest reduction in flame thickness. Furthermore, H_2 enrichment decreases Le exhibited by CH_4 to values below/or close to unity, thus promoting diffusional-thermal instabilities, which is not the case for the C_{2-4} HCs which exhibit Le>>1. Consequently, it is be expected that lean CH_4 flames will display greater sensitivity to small additions of H_2 than C_{2-4} flames, as confirmed by experimental values of L_b, which represents the flame's sensitivity to both hydrodynamic and thermal-diffusional instabilities, with H_2 addition yielding greatest measured changes in CH_4 flames (Figure 7.6).

7.1.8 Evaluation of Le_{eff} for Hydrocarbon/H_2 flames

In order to assess Le_{eff} models, the experimentally measured L_b are compared to theoretical L_b yielded using the analytical relationships between L_b and Le as proposed by Chen [84], [120] and Matalon and Bechtold [142] (denoted in text as L_b-CHEN and L_b-BM) . By re-arranging the CHEN and BM formulations (Section 3.4) in the form of Eqn. 3.21 and 3.23, respectively, and substituting the various Le_{eff} models (i.e. $Le_{V,}$ Le_D and Le_H) a 'theoretical' L_b (i.e. $L_{b\text{-}CHEN}$ and $L_{b\text{-}BM}$) for each Le_{eff} is calculated; enabling comparison to experimental L_b measurements. Since this approach differs from the one employed in Chapter 6 for single fuel mixtures (Section 6.3), results are first presented for CH_4, C_3H_8 and H_2/air flames, with Figure 7.19 illustrating $L_{b\text{-}CHEN}$ and $L_{b\text{-}BM}$, alongside selected peer-published L_b datasets and measurements from this work.

As depicted in Figure 7.19, BM and CHEN formulations correctly predict a rising and decreasing trend in L_b with increasing Φ for H_2 and C_3H_8, respectively, yielding excellent agreement with measured L_b values from this study and peer-published datasets. For CH_4 there is disagreement, between theoretical and experimental L_b values, with minimal changes in L_b predicted by both formulations, whilst a rising L_b with increasing Φ was experimentally captured. Overall, the appraised theoretical formulations yield good agreement with measured changes in H_2 and C_{2+} stretch related behaviour, qualitatively and quantitatively, whilst less correlation is observed for CH_4, as previously witnessed when evaluating Le (Section 6.3).

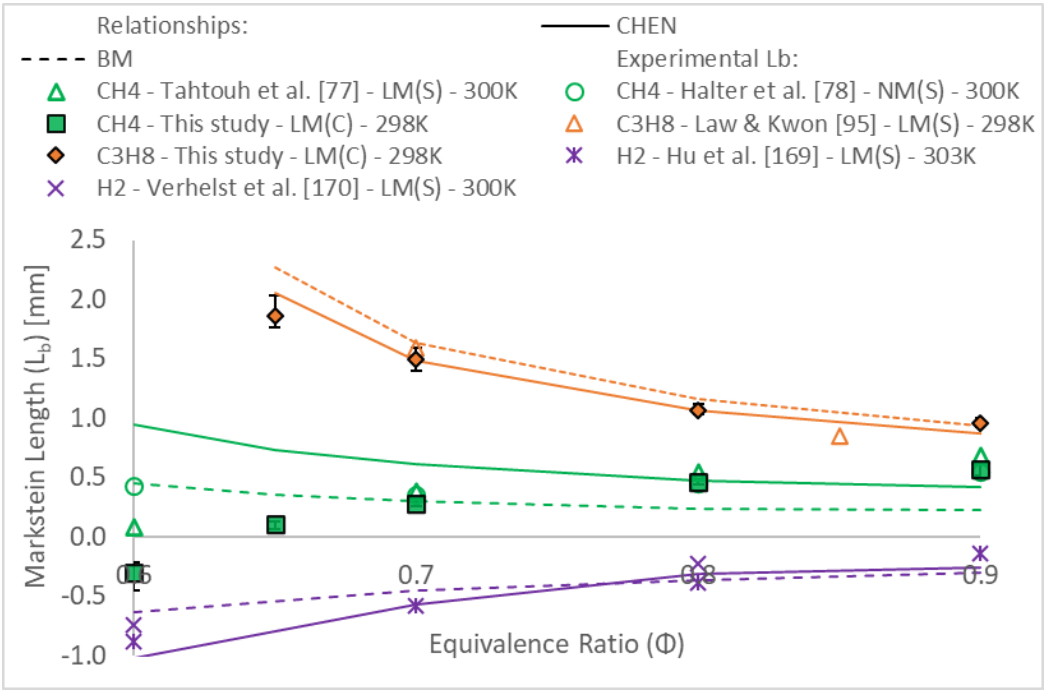

Figure 7.19 – Comparison of $L_{b\text{-}CHEN}$ & $L_{b\text{-}BM}$ with Measured L_b for CH_4/air, C_3H_8/air and H_2/air
Colour Code: Green – CH_4, Orange – C_3H_8, Purple – H_2

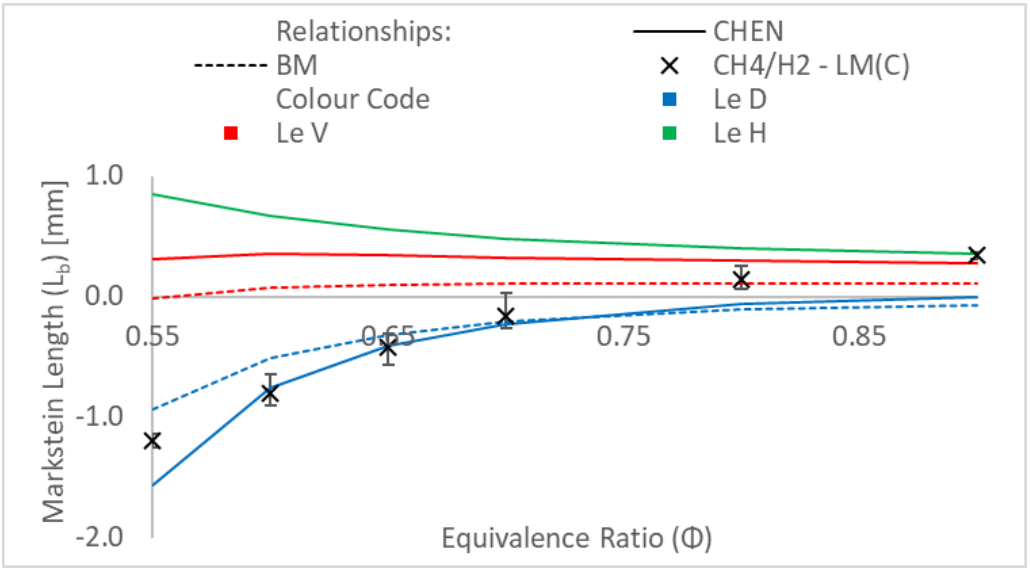

Figure 7.20 – Comparison of $L_{b\text{-}CHEN}$ & $L_{b\text{-}BM}$ using Le_{eff} for CH_4/H_2 vs Measured L_b – (85/15% vol.)

$L_{b\text{-}CHEN}$ and $L_{b\text{-}BM}$ for CH_4/H_2 and C_3H_8/H_2 mixtures (85/15% vol.) are illustrated in Figure 7.20-7.21, respectively, alongside experimentally measured L_b values from this study. With respect to Figure 7.20, correlation is witnessed at lean conditions (Φ<0.75) between measured L_b and the use of Le_D, with better agreement displayed with Le_V at richer condition (Φ = 0.80-0.90). Notice that Le_D and Le_V predict the correct trend of rising L_b with increasing Φ; albeit distinctly more pronounced for Le_D. The use of Le_H, irrespective of appraised theoretical formulation, yields an incorrect trend of decreasing L_b with increasing Φ. For the C_3H_8/H_2 blend (Figure 7.21), all Le_{eff} formulations witness the correct trend (decreasing L_b with increasing Φ), with remarkable qualitative agreement exhibited with Le_V definition. The use of Le_D and Le_H, significantly underpredicts or marginally overpredicts, respectively, the influence of flame stretch.

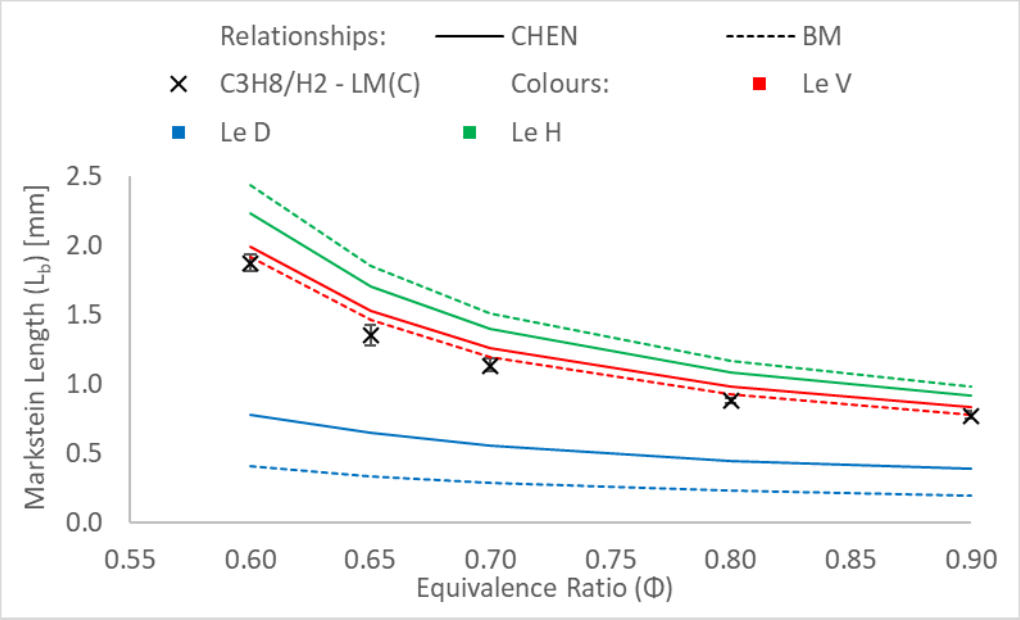

Figure 7.21 – Comparison of $L_{b\text{-}CHEN}$ & $L_{b\text{-}BM}$ using Le_{eff} for C_3H_8/H_2 vs Measured L_b – (85/15% vol.)

For small volumetric additions of H_2 to CH_4 (and to a certain extent C_3H_8) flames, Le_H is seen to systematically overestimate the influence of the HC on flame stability characteristics. Since the Le_H model is based upon heat of combustion per mass (Section 3.3), the significant differences in molecular mass between H_2 and HCs reduces the influence of small additions of H_2 even though the heat of combustion per mass of H_2 is higher than that of HCs.

Although Le_D yielded best agreement with CH_4/H_2 blends, for the C_3H_8/H_2 blend, the diffusion-based model considerably over estimated the influence of H_2. Le_D is based upon the assumption that if flame curvature is dominant, then local enrichment of the most diffusive fuel at the flames leading edge can be expected [140]. This concept may be applicable to certain fuel mixtures (as demonstrated with lean CH_4/H_2 flames) but does not seem to be suitable for blends containing significant amounts of heavier C_2+ fuels (as demonstrated with

the lean C_3H_8/H_2 flames). Finally, Le_V yielded best agreement for C_3H_8/H_2 mixtures, but significantly overpredicted L_b for CH_4/H_2 mixtures at leanest conditions (albeit correctly assessing L_b trend). As highlighted by Bouvet et al. [131], the use of individual Le numbers to form any of the Le_{eff} formulations presupposes that each fuel reacts independently. Consequently, an effective Le formulation based on a volumetric weighted average of each individual fuel would seem most logical and appropriate, however, significant changes in CH_4/H_2 flame behaviour are observable at leanest conditions, which are better captured by the Le_D model.

7.2 Parametric Study of the Influence of C_3H_8 on CH_4

Having gained insight on the influence of H_2 enrichment on the tested C_1-C_4/air flames, a parametric study related to the influence of C_3H_8 on CH_4 flame characteristics was undertaken. Results presented in Chapter 6 demonstrated that CH_4 and the tested C_2+ HC flames exhibited opposed stretch and thermo-diffusive behaviour at lean conditions ($\Phi \leq 0.70$), AFR's representative of modern premixed dry-low NO_x GT operating ranges ($\Phi \approx 0.45$-0.60 [176]). Consequently, it is was deemed of interest to measure the influence of small additions of C_3H_8 on stability of CH_4 based flames. To do so, a series of SEF experiments were conducted at atmospheric temperature and pressure across a range of lean CH_4/C_3H_8 blends (2%,4%,6%,8%,10% and 15%, C_3H_8 by vol.) representative of typical ranges found within NG [30]-[31].

7.2.1 Markstein Length and Le of CH_4/C_3H_8 mixtures

Processed datasets of the CH_4/C_3H_8 blends highlighting the measured L_b are plotted in Figure 7.22. Owing to tightly clustered data (particularly at Φ 0.8-1.0), a line of best fit was superimposed, to assist with the visualisation of trends, with the line of best fit for 100% C_3H_8/air blend extrapolated to $\Phi = 0.60$ to aid discussion. Stretch effects dominate early flame propagation at conditions below $\Phi = 0.65$ for C_3H_8/air mixtures (L_b>1.5 mm; Le >>1), it was observed that developing flame kernels would extinguish before self-propagation was achieved (Section 6.1.1), consequently, no data could be obtained for pure C_3H_8 at $\Phi < 0.65$ using the ignition system employed in this study.

As identified earlier, CH_4 and C_3H_8 display similar stretch-related behaviour at near stoichiometric conditions (Φ = 0.8-1.0), with decreasing Φ exposing increasingly divergent L_b behaviour, a consequence of the respective fuels opposite Le (at $\Phi \leq 0.60$, CH_4 Le ≤ 1, C_3H_8 Le >>1). As discussed in Chapter 6, evaluated experimental Le for CH_4 increases with rising Φ (Figure 6.32), with the calculated Le switching from below to above unity. This switch denotes

a change in flame dynamics from a mass to a heat-driven combustion process, converse to pure C_3H_8 flames which are driven by thermal diffusion at lean conditions.

Recognising the above, at stoichiometric conditions, all blends display very similar stretch behaviour, as expected, with important differences exhibited with decreasing Φ. As can be seen from Figure 7.22, for Φ = 0.8-1.0, all CH_4/C_3H_8 blends exhibit L_b behaviour analogous to that of CH_4 (↓L_b with ↓Φ), indicating that mass diffusion is becoming more prevalent (since L_b is decreasing), though still not the dominant transport mechanism. Below Φ = 0.80, mixtures containing ≤ 4% C_3H_8, exhibit similar behaviour to that of CH_4 (↓L_b with ↓Φ), however, no L_b slope inversion is observed, with a 2% C_3H_8 enrichment sufficient to maintain +L_b behaviour at Φ =0.60 (with -L_b measured for CH_4 at Φ=0.6). It is noted that using extrapolation of best line fits, to conditions leaner than those tested, predict L_b slope inversion (+ to –) for blends containing 2% and 4% C_3H_8 (vol.%) at Φ ≈ 0.55 and Φ ≈ 0.45, respectively. These AFR's fall within GT operation, hence in practical systems there may be observed an acceleration in flame propagation due to the highly stretched turbulent environment.

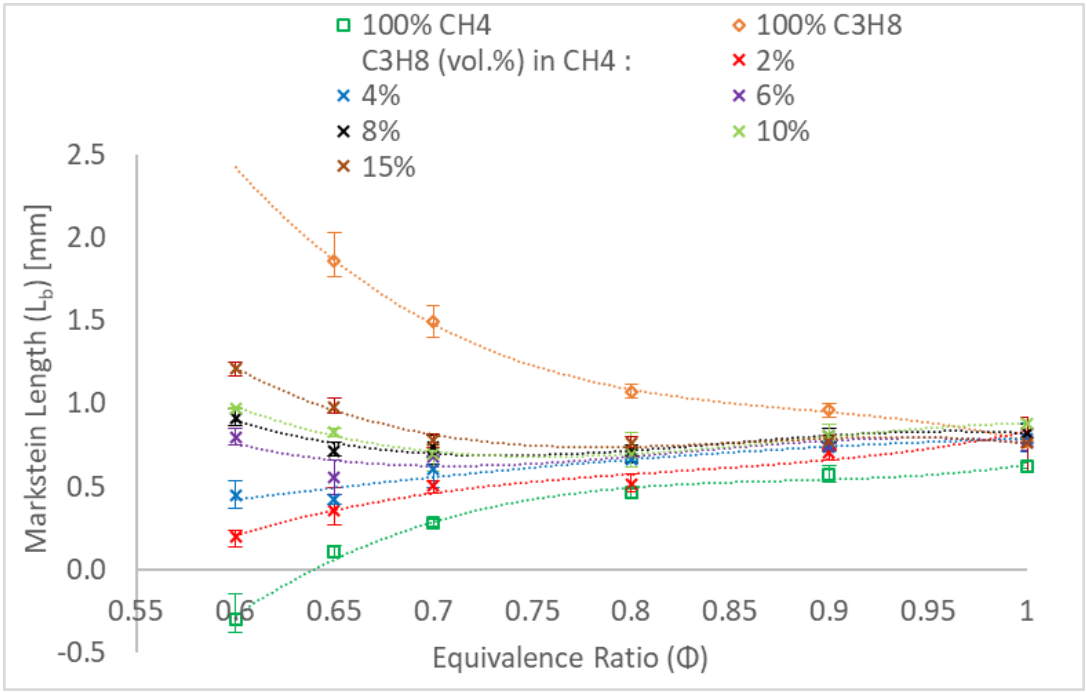

Figure 7.22 – L_b Measurements of Lean CH_4/C_3H_8 air Flames – (T_u =298K, P =0.1MPa)

At the leanest conditions (Φ ≤ 0.70) blends containing ≥ 6% of C_3H_8 (vol.%) displayed behaviour akin to C_3H_8/air flames (↑L_b with ↑Φ), although the mixture is predominantly CH_4 (molecular weight ratio ≈ 5.5:1 for a 94/6 CH_4/C_3H_8 (vol.%) blend), with small concentrations of C_3H_8 dictating stretch related behaviour, with a transition point observable at Φ = 0.70-0.8. Differences between the measured L_b for these blends is therefore most important at leanest conditions, a response comparable to that of the pure individual fuels, at which point Le behaviour is most divergent.

As witnessed, at leanest conditions, C_3H_8 addition to CH_4 has the propensity to stabilise CH_4 flames from a thermo-diffusive perspective, a direct consequence of the blends increased Le_{eff}. Changes in Le_{eff} are plotted in Figure 7.23 for an $\Phi = 0.60$ (mass-diffusion co-efficients evaluated using Hirschfelder method [133], [134], Section 3.2.1.3). All Le_{eff} models predict an increase in Le with increasing C_3H_8 concentrations, in agreement with measured stretch behaviour; with Le_H best capturing this change, Le_D seemingly underpredicting Le whilst Le_V yields values between those of Le_D and Le_H.

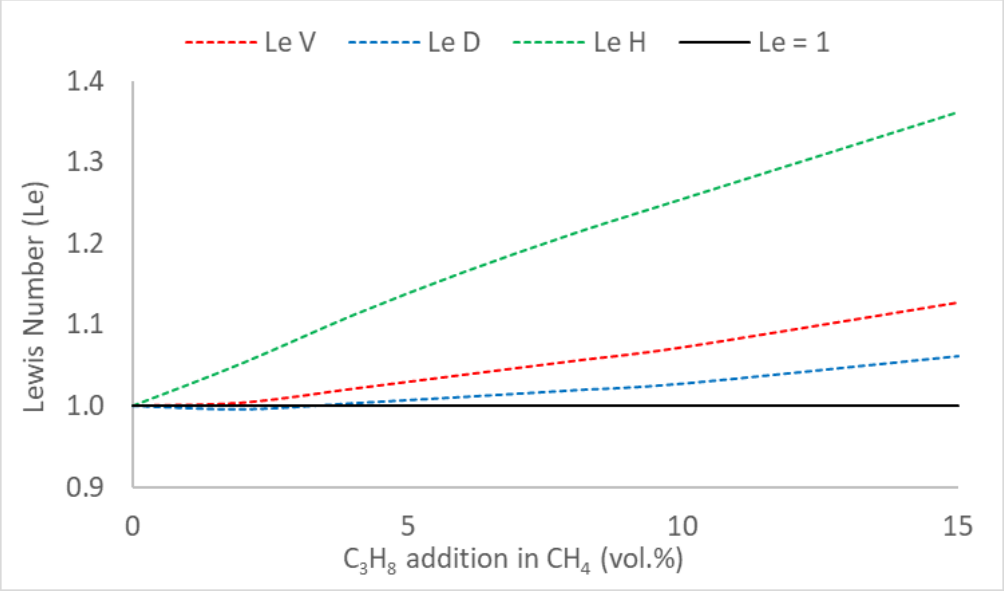

Figure 7.23 – Effective Lewis Number Formulations for CH_4/C_3H_8 ($\Phi = 0.60$)

The impact of C_3H_8 addition to CH_4-based mixtures was quantified in relation to changes in E_a, with differences presented in Table 7.3, with E_a represented by Ze, and evaluated utilising the $E_a(2)$ method employing Aramco 1.3 [157], facilitating comparison to earlier results (Section 7.1.7). Variations in flame thickness are presented in Table 7.4.

Two observations are noted from Table 7.3, first, C_3H_8 addition lowers E_a of CH_4-based fuels, somewhat unsurprisingly since C_3H_8 exhibits a lower E_a than that of CH_4, with differences decreasing with increasing Φ. Secondly, for equal volumetric additions (15%) C_3H_8 enrichment yields a greater influence on E_a of lean CH_4 flames than H_2 enrichment (see Φ= 0.60, Table 7.1 and Table 7.3), although H_2 displays E_a values significantly lower than those of C_3H_8, likely the result of the significant differences in molecular weight between H_2 and C_3H_8. Regarding the impact on flame thickness (Table 7.4), C_3H_8 addition to CH_4 flames results in a considerable reduction in flame thickness (both δ_K and δ_G), comparable in magnitude to reductions calculated for lean CH_4/H_2 (85/15 vol.%, Table 7.2).

Table 7.3 – Relative Differences (%) in CH_4 Ze due to C_3H_8 enrichment – (T = 298K, P = 0.1 MPa)

Φ	Vol. % of C_3H_8 in CH_4			
	4	6%	8	15
0.6	-2.58	-2.63	-4.01	-6.14
0.65	-1.37	-2.61	-2.13	-4.41
0.7	-1.29	-2.00	-2.73	-5.00
0.8	-0.49	-0.95	-0.94	-1.43

Table 7.4 – Differences (%) in CH_4 δ_G & δ_K due to C_3H_8 Enrichment – (T = 298K, P = 0.1 MPa)

Φ	Vol. % of C_3H_8 in CH_4							
	4%		6%		8%		15%	
	δ_K	δ_G	δ_K	δ_G	δ_K	δ_G	δ_K	δ_G
0.6	-13.08	-4.92	-23.10	-6.52	-30.41	-8.31	-32.54	-13.37
0.65	-13.66	-3.62	-16.09	-3.62	-17.96	-6.68	-21.25	-10.69
0.7	-6.86	-3.03	-11.11	-3.03	-13.33	-5.48	-14.36	-8.95
0.8	-1.33	-2.12	-3.87	-2.12	-4.48	-4.00	-9.50	-6.52

7.2.2 Flame propagation of CH_4/C_3H_8 mixtures

S_u measurements attained via application of the most applicable linear methodology LM(C), for the CH_4/C_3H_8 mixtures tested are presented in Figure 7.24. The average relative increase in S_u of CH_4 flames due to C_3H_8 enrichment is illustrated in Figure 7.25.

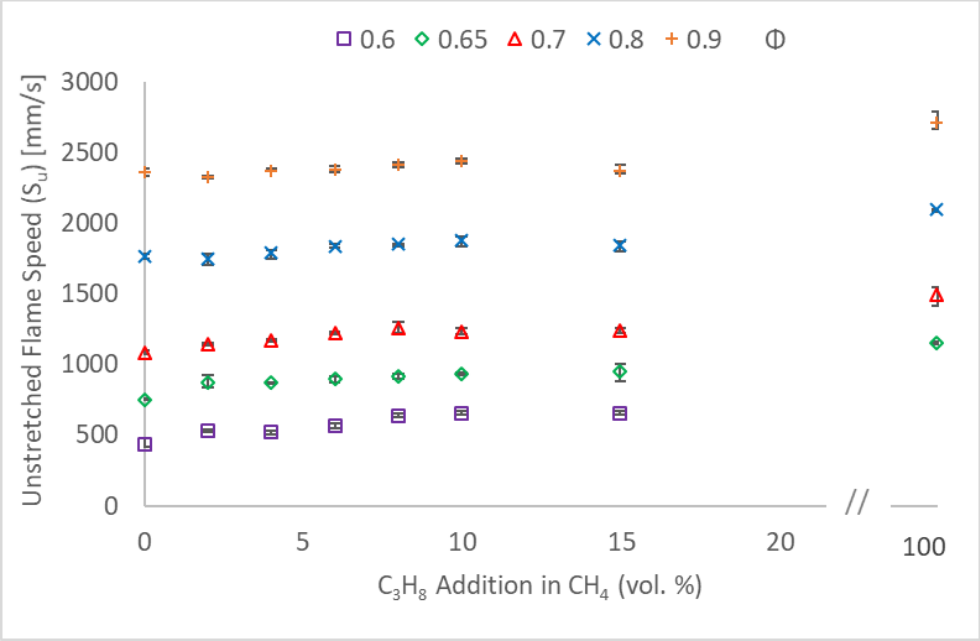

Figure 7.24 – Unstretched Flame Speed of Lean CH_4/C_3H_8 Blends – (T=298K, P=0.1MPa)

As can be seen from Figure 7.25, at near stoichiometric conditions (Φ=0.8-0.9), C_3H_8 enrichment (up to 15% vol.) of CH_4 based flames generates relatively small enhancements in measured S_u (<10%), with augmentation in S_u substantially increasing with decreasing Φ, with recorded average relative increases of > 50% for 15% C_3H_8 addition at Φ=0.60.

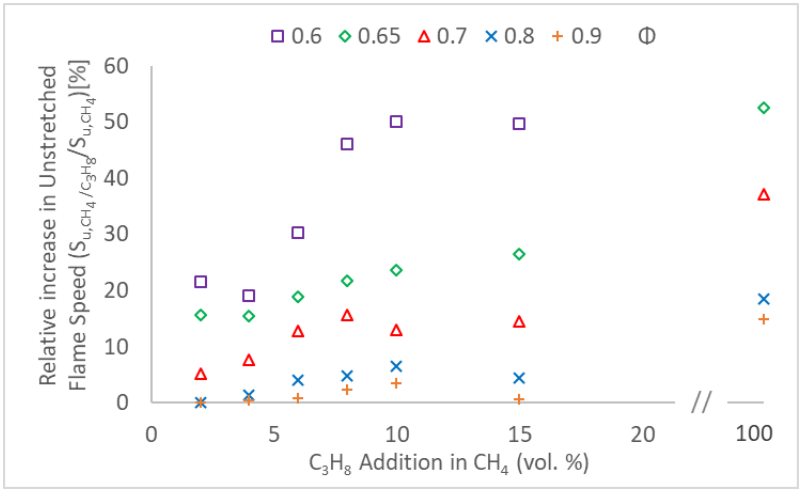

Figure 7.25 – Relative Increase in S_u of CH_4 Flames from C_3H_8 Addition

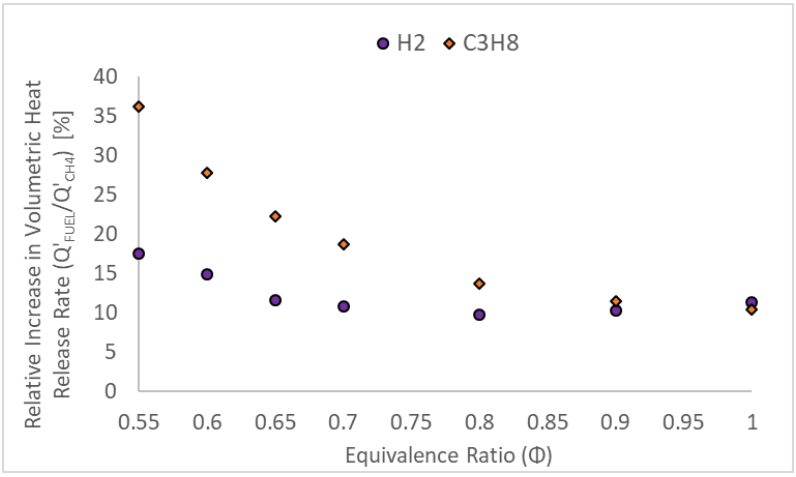

Figure 7.26 – Relative Increase in Q' of CH_4 Flames with H_2 or C_3H_8 Addition (15% vol.) across Lean Φ

Interestingly, volumetric additions of 15% C_3H_8 or H_2 to ultra-lean CH_4 flames produce comparable flame propagation enhancements effects. With respect to H_2 enrichment, the increased reactivity of lean CH_4/H_2 mixture was attributed to an augmentation in burning intensity, with oxidation of CH_4 intensified due to significant increases in radical production (notably H), resulting in enhanced reactivity and consequently flame propagation (Figure 7.16-7.17). Comparison of modelled increases in volumetric heat release rate (Q') of CH_4 flames due to C_3H_8 and H_2 addition (15% vol.) are depicted in Figure 7.26. Evidently, C_3H_8 or H_2 addition to CH_4 flames yield practically similar relative increases in Q' at near stoichiometric conditions (Φ=0.80=0.90), however, as conditions get leaner, C_3H_8 additions yield higher relative increases in Q' than H_2 addition, practically double at leanest conditions, in agreement with witnessed S_u augmentations. Note however, that the heat of combustion per mass (KJ/mol) of H_2 is two to three times greater than that of C_3H_8 ($H_2 \approx 286$; $C_3H_8 = 105$ [KJ/mol]), however it is noted that there are significant differences in terms of molecular mass between both fuels ($H_2 = 2.0159$; $C_3H_8 = 44.0956$ [g/mol]) which suppresses the higher heat of combustion exhibited by H_2.

Comparison of relative increases in production of radical fractions in CH_4 flames due to the addition of H_2 or C_3H_8 (15% vol.) are plotted in Figure 7.27. Modelled values predict an enhanced production of radicals related to the presence of C_3H_8 than H_2 (for equal volumetric additions), underlining the importance of small amounts of HCs on the oxidation mechanics of CH_4. When no other fuel is present, CH_4 oxidation is initiated by its reaction with O_2 and by thermal dissociation [41] [177]. In the CH_4/C_3H_8 blends, C_3H_8 reacts first, leading to the formation of radicals (O, H, OH) which enhances the oxidation mechanics of CH_4, leading to increased burning intensity and reactivity, reflected in augmented flame speeds. Thus, both H_2 and C_3H_8 promote flame propagation of lean methane-based fuels, to a similar extent for 15% volumetric enrichment levels, however, yield opposite stretch-related and Le behaviour.

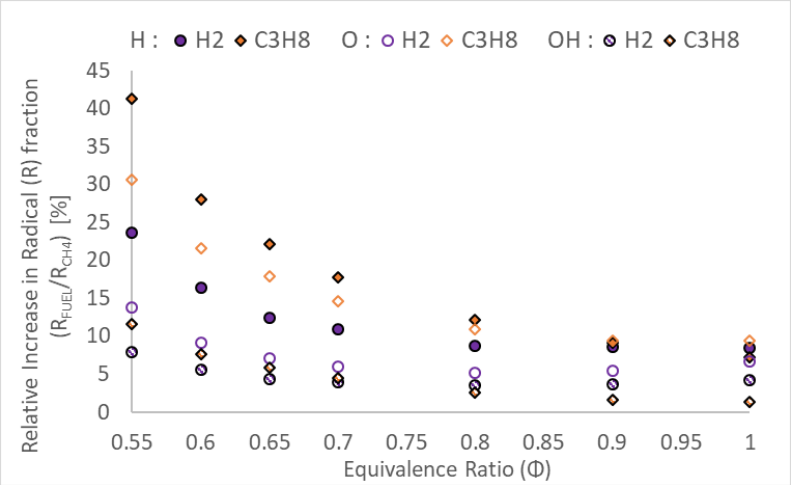

Figure 7.27 – Relative Increase in Modelled Radical (H, O, OH) Concentrations in CH_4 Flames upon H_2 or C_3H_8 Addition (15% vol.) across Lean Φ

The attained U_L values of CH_4/C_3H_8 blends are depicted in Figure 7.28, with numerical simulations using the Aramco 1.3 mechanism [157] superimposed as lines. In general, there is good correlation between the numerical and experimental measured U_L values at Φ= 0.60-0.80 and 2-10% C_3H_8 volumetric additions. It is observed that for the CH_4 blends containing 15% C_3H_8 (at Φ = 0.8-0.9) experimental U_L are discernibly slower than numerical simulations.

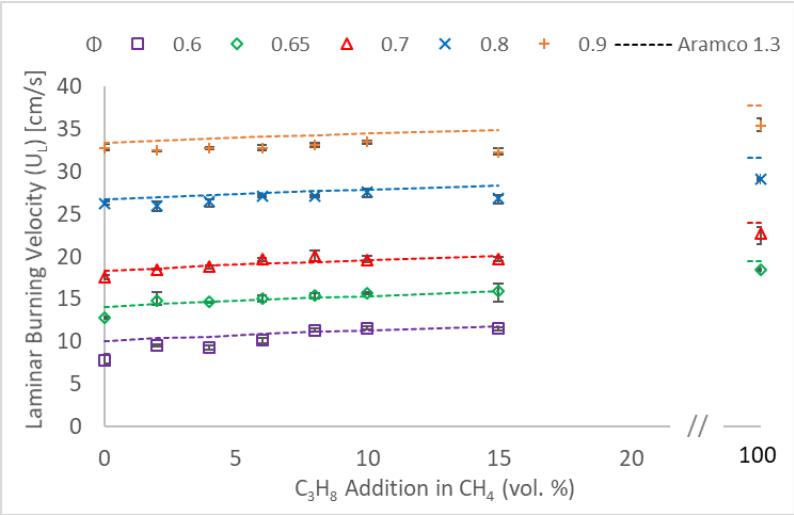

Figure 7.28 – Laminar Burning Velocity of CH_4/C_3H_8 Blends – (T_u =298K, P =0.1MPa)

7.3 Chapter Summary

The combustion behaviour of lean C_{1-4}/H_2 (85/15 vol.%) and CH_4/C_3H_8 (up to 15% C_3H_8 vol.%) blends was experimentally investigated including analysis of measured stretch-related behaviour and flame speed propagation. Effective Lewis number formulations were appraised for the mixtures tested using theoretical relationships proposed in literature relating L_b to Le. The impact of H_2 enrichment on C_{1-4} fundamental flame parameters was examined. Modelling work was presented analysing the influence of H_2 and C_3H_8 addition on volumetric heat release rate and production of key radicals (O, H, OH) within lean CH_4-based flames. From this work, the following conclusions can be taken:

- H_2 addition (15% vol.) has the propensity of diffusionally destabilising ultra-lean ($\Phi \leq 0.65$) CH_4 flames, promoting preferential diffusional instabilities, reflected by negative measured L_b values. For the tested C_{2-4} fuels, limited impact on measured L_b was observed, with influence of H_2 augmenting with decreasing Φ. C_3H_8 addition (up to 15% vol.) yielded a diffusionally stabilising effect on ultra-lean CH_4 flames, with blends containing ≥ 6% C_3H_8 displaying L_b behaviour akin to C_3H_8/air flames (↑ +L_b with ↑Φ).
- Both H_2 and C_3H_8 addition to ultra-lean CH_4-based flames result in comparably significant relative increases in S_u, with augmentation in S_u substantially decreasing at near stoichiometric conditions. Overall, correlation is displayed by numerically attained U_L and experimental U_L values for all blends tested, with the Aramco 1.3 mechanism exhibiting best agreement of all appraised reaction mechanisms.
- Modelling work suggests that measured augmentations in flame propagation of ultra-lean CH_4-based fuels upon H_2 or C_3H_8 addition is predominantly a consequence of enhanced production of key radicals, notably H, facilitating CH_4 oxidation mechanisms, with C_3H_8 yielding a greater influence than H_2 for equal volumetric enrichment fractions.
- H_2 addition (15% vol.) to the tested C_{1-4} fuels resulted in a reduction in overall activation energy and flame thickness, with the influence of H_2 decreasing with increasing alkane number and Φ, with CH_4 most significantly affected. C_3H_8 (15% vol.) enrichment to CH_4 yielded a similar reduction in overall activation energy and flame thickness, comparable in magnitude to the influence of H_2 addition on CH_4/H_2 (for equal volumetric additions).
- For the evaluated effective Le formulations, a diffusional and volume-based model (Le_D and Le_V) yielded best agreement with measured L_b of lean CH_4/H_2 and C_3H_8/H_2 mixtures, respectively, with Le_H (heat-release based model) best representing L_b behaviour of ultra-lean (Φ= 0.60) CH_4/C_3H_8 blends.

Chapter 8. Binary Blends at Ultra-Lean Conditions

As discussed in Chapter 7 the influence of H_2 and C_3H_8 additions (15% vol.) on CH_4/air flames resulted in diverging stretched related behaviour at increasingly leaner conditions. This phenomenon is attributed to the opposite thermo-diffusive characteristics displayed by H_2 and C_3H_8. Consequently, in this chapter experimentation is undertaken at ultra-lean conditions (Φ = 0.65) to examine the impact of these opposite trends on the stability and propagation of spherically expanding flames (SEF) for several binary blends.

The influence of C_2H_6 and C_3H_8, the two main heavier hydrocarbons (HC) commonly found in natural gas (NG), on CH_4 flames is studied, complementing the parametric study conducted in Chapter 7. The impact of H_2 on the tested $C_{1\text{-}3}$ fuels is extended from 15% to 50% volumetric additions, focused upon measured changes in flame propagation speed, stretch-related behaviour and thermo-diffusive stability. To better understand the nature of measured augmented burning intensity of $C_{1\text{-}3}/H_2$ flames, a sensitivity analysis related to the contribution of major flame enhancing pathways (thermal, diffusive, kinetic) is conducted. In-line with methods discussed previously, four reaction mechanisms [155]–[158], which include H_2/CO chemistry, are analysed and compared with experimentally measured data. Finally, theoretical relationships linking Markstein length (L_b) and Lewis number (Le) are evaluated and appraised for the binary mixtures tested.

The aim of this chapter is to first gain insight of the combustion characteristics NG/H_2 relevant binary fuel mixtures, at lean conditions representative of dry low emission (DLE) gas-turbine operating windows (Φ = 0.45 – 0.60 [176]). Secondly, to further examine and quantify the impact of H_2 on NG combustion at lean conditions (Φ <0.70) and interrogate stretch related behaviour at ultra-lean conditions.

8.1 Binary $C_{1\text{-}3}$ Blends

As discussed in Chapter 2, CH_4/HC blends have been considerably studied using SEFs and heat flux method [32], both at atmospheric [88] and high pressure [31]. However, research primarily attempts to elucidate the effect of blend composition on U_L with little focus on stretch-related behaviour, with the majority of data at relatively richer air fuel ratios ($0.70 \leq \Phi \leq 1.4$). Furthermore, the impact of subtle changes in fuel composition (i.e. changes of ≤ 10% vol.% in C_2+ HC content) appear to be missing from the published literature.

In this section, the parametric study related to CH_4/C_3H_8 mixtures, presented in Chapter 7, is broadened to include the influence of C_2H_6, with volumetric additions of HCs extended from 15% to 85%, focussing on ultra-lean conditions (Φ =0.65). All SEF experiments

were conducted at atmospheric pressure and temperature (T_u = 298 K and P = 0.1 MPa), with repeatability ensured by conducting a minimum of three nominally identical experiments for each data point. Note that unless otherwise stated, error bars represent maximum and minimum recorded values, around an average measured plotted value.

8.1.1 Markstein Length of Binary C_{1-3} Blends

The datasets of the experimentally measured L_b (employing LM(C)) for CH_4/C_2H_6 and CH_4/C_3H_8 blends are depicted in Figure 8.1, with similar data in the case of C_2H_6/C_3H_8 mixtures presented in Figure 8.2. The full datasets of L_b values measured in this chapter are available in Appendix – C.1.

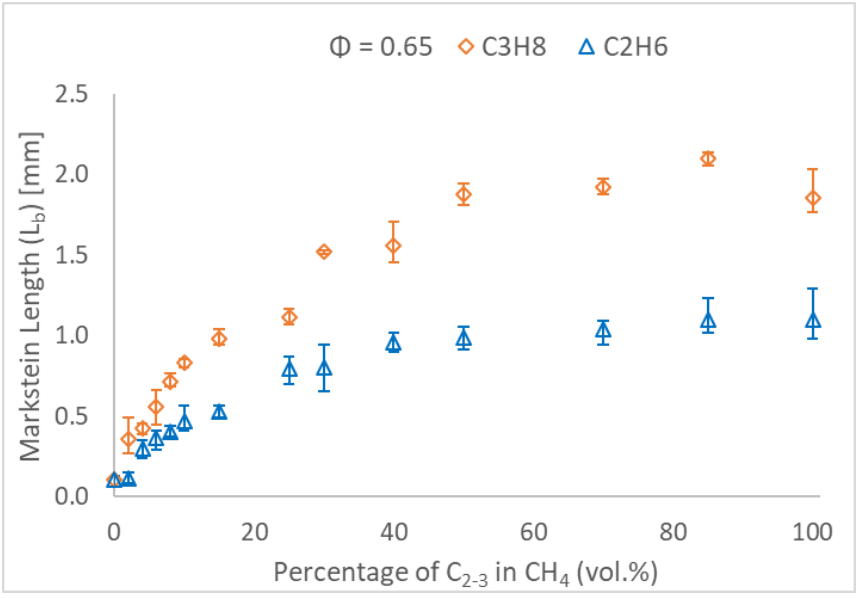

Figure 8.1 – Measured change in L_b for CH_4/C_2H_6 and CH_4/C_3H_8 Blends (T_u=298K, P=0.1MPa)

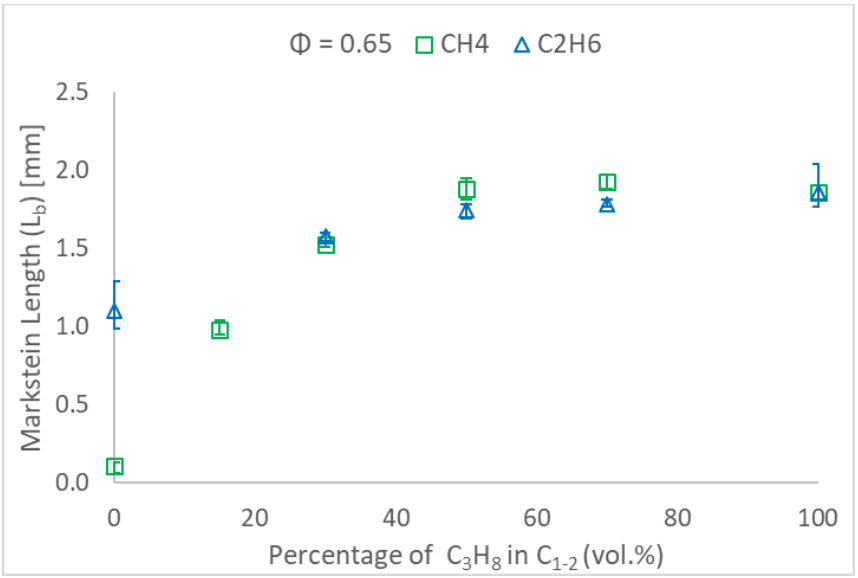

Figure 8.2 – Measured Change in L_b for CH_4/C_3H_8 and C_2H_6/C_3H_8 Blends (T_u=298K, P=0.1MPa)

As identified in Chapter 6, lean C_2H_6 and C_3H_8/air flames exhibit very similar stretch-related behaviour (+L_b, Le>>1), and thus unsurprisingly the tested C_{2-3} fuel blends with CH_4 display comparable trends, as shown in Figure 8.1. As discussed in Chapter 7 (Figure 7.22) small volumetric additions of C_3H_8 (2-15%) resulted in significant incremental changes in ultra-lean CH_4 L_b behaviour (Φ=0.60-0.65), with C_2H_8 enrichment (for equal vol. additions, 2-15%) yielding a similar influence, in agreement with Figure 8.1. Note that for 15% (vol.) additions of tested C_{2-3} fuels, the ratio of molecular weight of CH_4/C_{2-3} is ~3:1 and ~2:1, respectively, thus although the blends are composed predominantly of CH_4, relatively small additions of the higher HCs yielded a considerable impact on the stretch-sensitivity. As can be seen from Figure 8.1, small variations in measured L_b for C_2H_6 addition ≥ 30% (vol.) are observed, with CH_4/C_2H_6 mixtures exhibiting L_b akin to that of C_2H_6/air flames. It is also noted that L_b plateauing is observed when the molecular weight ratio of the CH_4/C_2H_6 blend ~1:1.

As seen in Figure 8.2, changes in L_b are more subtle since the tested C_{2-3} fuels display similar stretch-sensitivity in comparison to CH_4. From Figure 8.2 it can be observed that, C_2H_6/C_3H_8 blends containing > 30% C_3H_8 (vol.) exhibit L_b behaviour akin to that of C_3H_8, with marginal changes in measured L_b upon further C_3H_8 addition. These changes in stretch sensitivity are a direct consequence of the blends increasing Le as discussed in Section 8.1.2.

8.1.2 Effective Lewis Number Formulations for Binary C_{1-3} Blends

The Le_{eff} of CH_4/C_2H_6 and CH_4/C_3H_8 mixtures are illustrated in Figure 8.3, evaluated using the mixtures free-stream properties assessed at (λ/c_p) ratio of T=298 K, with mass-diffusion co-efficients evaluated using the Hirschfelder method [133], [134], discussed earlier (Section 3.2.1.3). It is noted, that unless otherwise stated, all Le_{eff} values presented in this chapter, were evaluated in a similar manner.

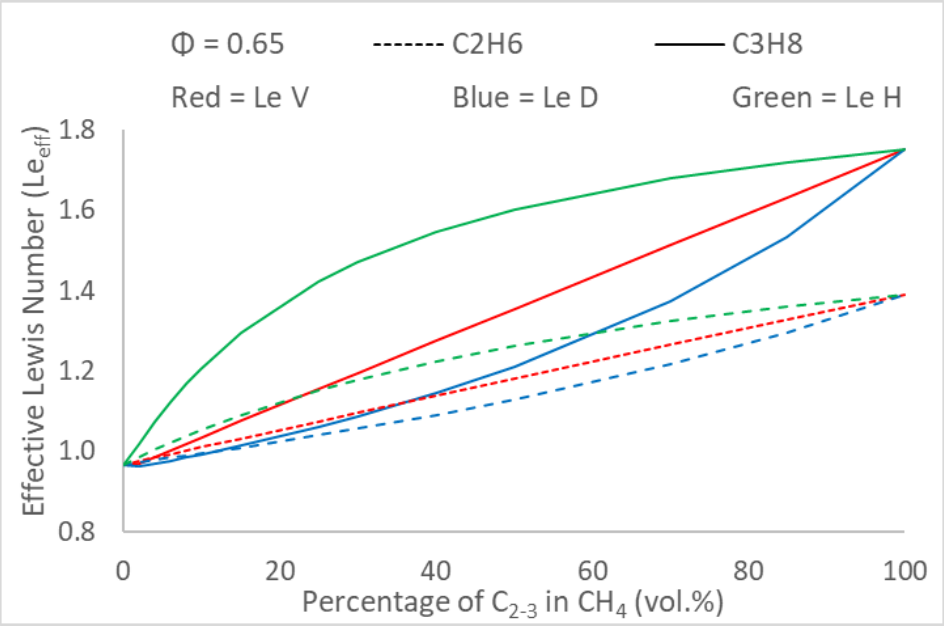

Figure 8.3 – Effective Lewis Number for C_{2-3}/CH_4 Binary Mixtures (T_u = 298 K, P = 0.1 MPa)

In order to assess the validity of Le_{eff} plotted in Figure 8.3, relationships linking L_b to Le as proposed by Chen [84], [120] and Bechtold and Matalon [142] (Section 3.4) are appraised, requiring the evaluation of various fundamental flame parameters (i.e. Zel'dovitch Number (Ze), flame thickness (δ) and expansion ratio (σ)), as discussed in Section 3.5. In agreement with methods presented earlier (Section 7.1.8), the L_{eff} models for volume, mass-diffusion and heat-release (i.e. Le_V, Le_D and Le_H) are employed to yield a numerical L_b, using the CHEN and BM relationships (Section 3.3 & 3.4), referred to in text as $L_{b\text{-}CHEN}$ and $L_{b\text{-}BM}$, respectively. Numerically derived L_b are then compared to experimentally measured L_b, allowing assessment of Le_{eff} models.

Similar work has been conducted by Bouvet et al. [131] and Lapalme et al. [91]. Bouvet employed the CHEN formulation to evaluate Le_{eff} models for CH_4/H_2 (Φ = 0.80) and C_3H_8/H_2 (Φ = 0.60) blends, and Lapalme utilised both CHEN and BM relationships for H_2/CO and H_2/CH_4 mixtures (lean and rich Φ). This work aims to extend analysis and insight to ultra-lean CH_4/C_2H_6, CH_4/C_3H_8 and C_2H_6/C_3H_8 mixtures, as well as to binary blends of $C_{1\text{-}3}/H_2$ presented in Section 8.2.

Note that resemblance between Le_{eff} trends (Figure 8.3) and numerical L_b trends (i.e. $L_{b\text{-}CHEN}$, $L_{b\text{-}BM}$) is to be expected, since only the Le_{eff} value changes when substituted in the CHEN and BM formulations whilst other evaluated fundamental flame parameters stay constant for a fixed fuel blend composition and Φ. Furthermore, it is noted that the aim of such analysis is not quantitative in nature, rather qualitative trends are sought, to validate which Le_{eff} models best represent the exhibited stretch-related behaviour of the evaluated blends.

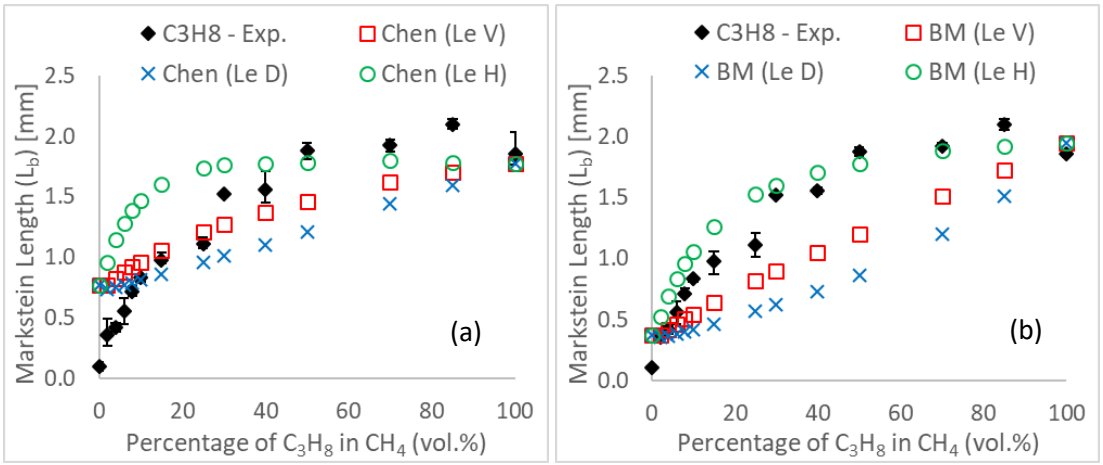

Figure 8.4 – (a) $L_{b\text{-}CHEN}$ and (b) $L_{b\text{-}BM}$ for CH_4/C_3H_8 Mixtures using Le_{eff} (Φ = 0.65, T_u= 298 K, P= 0.1 MPa)

Assessed $L_{b\text{-}CHEN}$ and $L_{b\text{-}BM}$ values for the CH_4/C_3H_8 blends are presented in Figures 8.4 (a & b), respectively, alongside experimentally measured L_b values. For the CH_4/C_3H_8 blend (Φ= 0.65) illustrated in Figure 8.4(a), $L_{b\text{-}CHEN}$ with Le_H captures quasi-linear incremental increases in L_b resulting from small additions of C_3H_8 up to 15% vol., albeit yielding

significantly underestimated L_b values. For volumetric C_3H_8 additions >25%, a plateauing in $L_{b\text{-}CHEN}$ with Le_H is observed, in disagreement with measured L_b trend, which displays incremental changes in L_b. As seen in Figure 8.4 (b), in the case of the BM formulation, both qualitative and quantitative agreement is observed with Le_H, with minimal differences witnessed between measured L_b and numerical $L_{b\text{-}BM}$ across the mixture concentration. Clearly, Le_D significantly underpredicts L_b values, with Le_V yielding a linear L_b transition from pure CH_4 to C_3H_8, unlike the measured L_b trend observed, which displays significant incremental changes in L_b measured for small C_3H_8 enrichment fractions (2-15% vol.). Furthermore, it is also noticeable that $L_{b\text{-}BM}$ better captures the measured L_b of pure CH_4 compared to $L_{b\text{-}CHEN}$ (Figures 8.4 (a)).

Numerically derived L_b using CHEN and BM for the CH_4/C_2H_6 blend is illustrated in Figures 8.5 (a & b) respectively, and again compared with measured L_b values. As witnessed in Figure 8.5(a), CHEN overpredicts L_b, irrespective of the Le_{eff} model employed, with best qualitative agreement yielded applying Le_H, particularly for C_2H_6 additions < 15% (vol.). Similarly, as observed in Figure 8.5 (b), BM again yields quantitative and qualitative agreement for Le_H and measured L_b values, particularly at C_2H_6 additions > 25% (vol.).

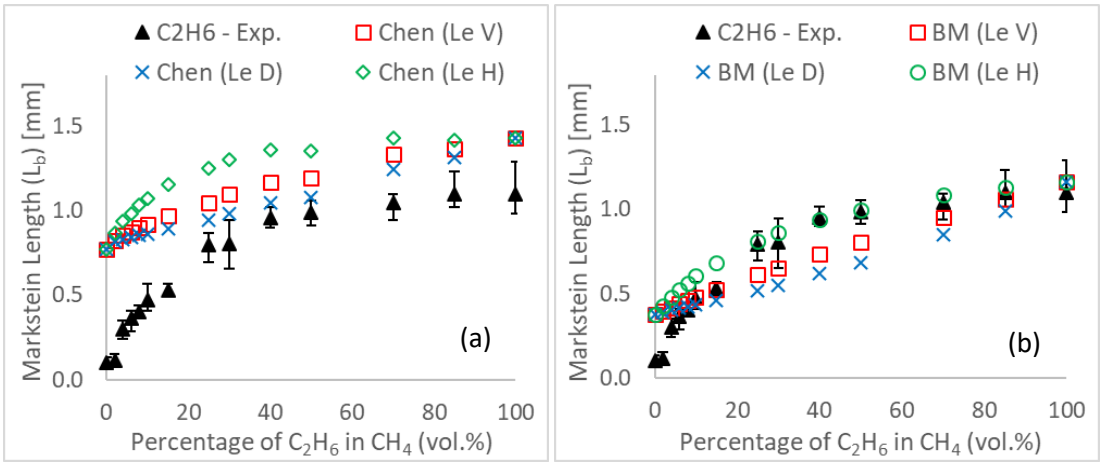

Figure 8.5 – (a) $L_{b\text{-}CHEN}$ and (b) $L_{b\text{-}BM}$ for CH_4/C_2H_6 Mixtures using Le_{eff} (Φ =0.65, T_u = 298 K, P= 0.1 MPa)

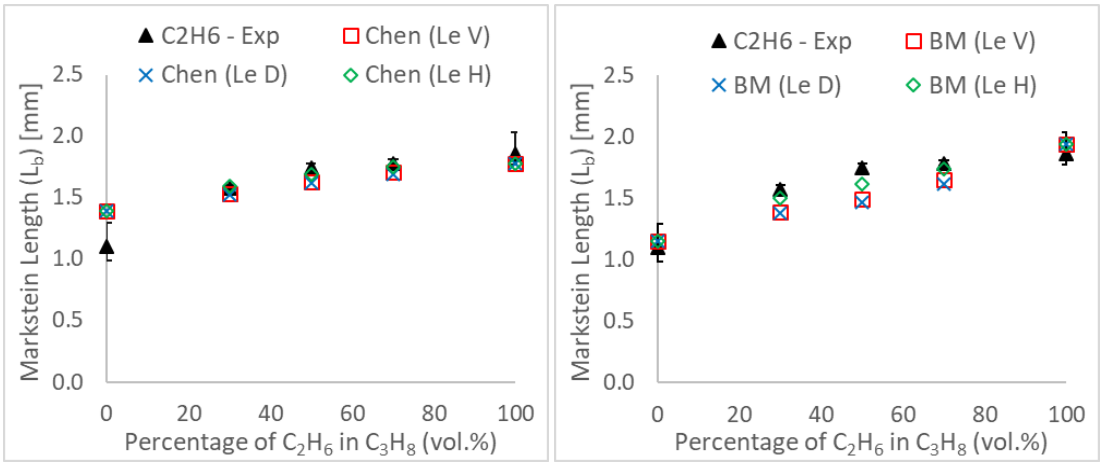

Figure 8.6 – (a) $L_{b\text{-}CHEN}$ and (b) $L_{b\text{-}BM}$ for C_2H_6/C_3H_8 Mixtures using Le_{eff} (Φ=0.65, T_u = 298 K, P= 0.1 MPa)

With respect to C_2H_6/C_3H_8 blends, $L_{b\text{-}CHEN}$ and $L_{b\text{-}BM}$ values are compared to experimental L_b data in Figure 8.6 (a & b). Note that all Le_{eff} models result in similar Le values, a consequence of the similar mass and thermal diffusion properties of C_2H_6 and C_3H_8. Both the CHEN and BM formulations exhibit good agreement with measured L_b values, irrespective of L_{eff} model employed.

Overall, it is seen that best agreement is exhibited using Le_H in association with the BM relationship for the tested lean $CH_4/C_{2\text{-}3}$ mixtures, with qualitative and quantitative numerical agreement observed between measured and theoretical L_b values for $C_{2\text{-}3}$ additions >30% (vol.). In general, irrespective of the formulation appraised (CHEN or BM) applying Le_D results in an underpredicted L_b value when compared to the measured value. Le_V yielded a linear L_b relationship, hence did not correctly capture the qualitative trend of measured L_b for the tested $CH_4/C_{2\text{-}3}$ blends. With respect to C_2H_6/C_3H_8 mixtures, CHEN and BM formulations display agreement with measured L_b irrespective of Le_{eff} model utilised. It is however noted that the BM formulation is significantly more complex and intricate than the CHEN relationship (Section 3.4), consequently the fact that the BM model better captures stretch-sensitivity of the evaluated blends is to be expected. From the above analysis, it is therefore concluded that for lean $CH_4/C_{2\text{-}3}$ air mixtures, changes in L_b behaviour are best captured by the Le_H model, based upon a heat-release formulation.

8.1.3 Flame Propagation of Binary $C_{1\text{-}3}$ Blends

Measured unstretched flame speeds (S_u) for CH_4/C_2H_6 and CH_4/C_3H_8 air mixtures are presented in Figure 8.7, with values evaluated using LM(C) (S_u datasets using other extrapolation methods are presented in Appendix–C.1), with relative increases of S_u brought about by $C_{2\text{-}3}$ HC enrichment as compared to the pure CH_4 flame illustrated in Figure 8.8.

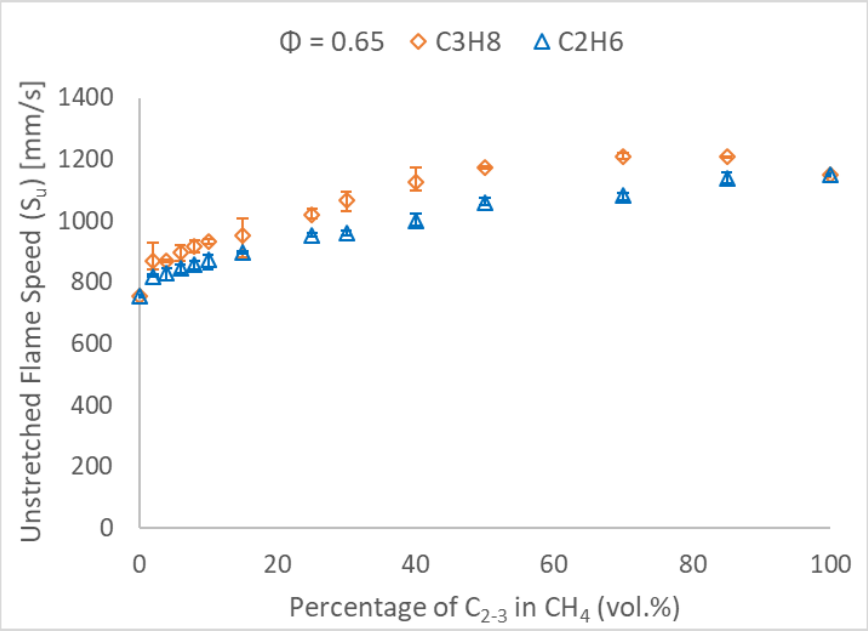

Figure 8.7 – Unstretched Flame Speed for CH_4/C_2H_6 and CH_4/C_3H_8 Blends (T_u =298 K, P= 0.1 MPa)

As expected, it can be seen from Figure 8.7, that C_2H_6 or C_3H_8 additions to CH_4 flames result in similar measured S_u, a direct consequence of the similar flame temperatures and thermal diffusivity, with C_3H_8 enrichment yielding marginally faster S_u. Relative increases in S_u due to the tested $C_{2\text{-}3}$ fuel enrichment are illustrated in Figure 8.8, with a linear relative increase in S_u observed for C_2H_6 addition and minimal relative changes exhibited for C_3H_8 additions > 60% (vol.) As discussed in Section 7.2, increased flames speeds of lean $CH_4/C_{2\text{-}3}$ blends potentially result from the higher reactivity of the $C_{2\text{-}3}$ HCs, due to their relative lower E_a, promoting the formation of key radicals (Figure 7.27), which subsequently enhances the oxidation of CH_4 [177], ultimately augmenting flame speed.

The laminar burning velocities (U_L) of the CH_4/C_2H_6 and CH_4/C_3H_8 mixtures are presented in Figure 8.9, with attained U_L values of the C_2H_6/C_3H_8 blend illustrated in Figure 8.10, with superimposed lines representing numerically derived U_L values, attained employing both the Aramco 1.3 and USC II reaction mechanisms [156], [157]. It is noted that the GRI-M 3.0 [155] mechanism is not at this time presented as it was previously shown to significantly overpredict blends containing C_3H_8 (Figures 6.17 and 7.14).

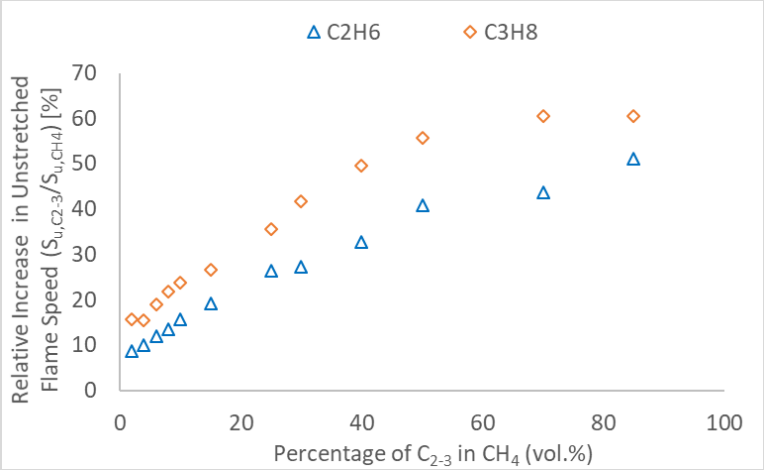

Figure 8.8 – Relative increase in S_u for CH_4 Flames upon Addition of C_2H_6 or C_3H_8

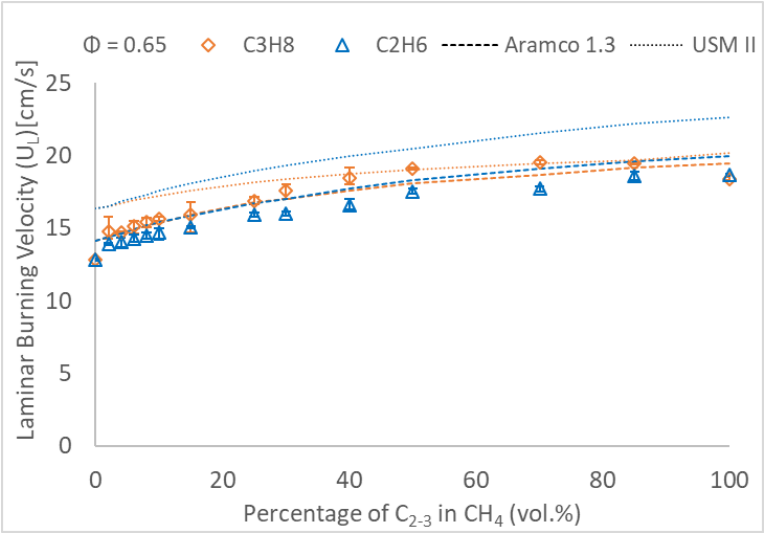

Figure 8.9 – Measured and Modelled U_L of CH_4/C_2H_6 and CH_4/C_3H_8 Blends (T_u=298 K, P=0.1MPa)

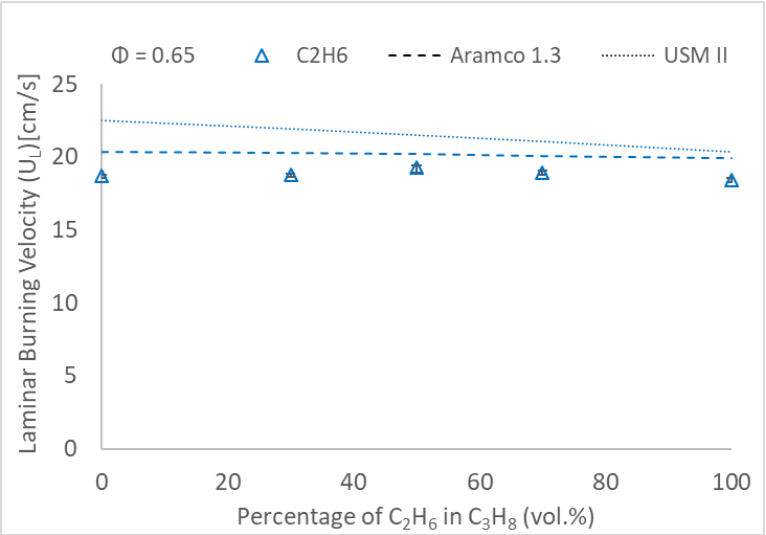

Figure 8.10 – Measured and Modelled U_L of C_2H_6/C_3H_8 Mixtures (T_u=298 K, P=0.1MPa)

As can be seen in Figure 8.9, the Aramco 1.3 mechanism more accurately predicts U_L values for CH_4/C_2H_6 and CH_4/C_3H_8 blends, with marginal differences in numerical U_L witnessed for C_{2-3} HC additions > 50% (vol.). It is observed that compared to numerical predictions, the opposite enhancement effect was measured, with C_3H_8 addition yielding faster U_L values than C_2H_6 enrichment. Again, it is witnessed in Figure 8.10, for C_2H_6/C_3H_8 flames, better agreement is exhibited with Aramco 1.3 when compared to USC II which constantly predicted higher U_L values than those experimentally measured.

8.2 Binary H_2/C_{1-3} HC Blends at ultra-lean conditions

As discussed in Chapter 2, a considerable amount of work relating to the impact of H_2 enrichment on CH_4/air has been conducted using SEFs [90], [95], [102], [103]. Research related to flame characteristics of H_2 addition on heavier HCs fuels has been somewhat less studied, with the general knowledge tending towards smaller combustion enhancements than exhibited by CH_4 based fuels, as highlighted by Tang et al. [115]. For the following work, CH_4 was enriched with H_2 at volumetric additions of 10%, 15%, 25%, 30%, 40% and 50%, respectively. Similarly, C_2H_6 and C_3H_8 were blended with 15%, 30% and 50% H_2 (vol.%). Again, all SEF tests were conducted at atmospheric pressure and temperature (T_u = 298 K and P = 0.1 MPa), at an Φ = 0.65, with three nominally identical experiments attained for each data point.

8.2.1 Markstein Length of H_2/C_1-C_3 binary blends

Due to known instability issues associated with H_2 combustion, minor modifications in usable flame radius selection were required to accurately measure L_b and S_u of ultra-lean CH_4/H_2 blends containing ≥ 30% H_2 (vol.). As discussed previously (Section 6.1.2), lean fuel mixtures which exhibit Le <<1, are thermo-diffusionally unstable (displaying –ve L_b values). During data-processing, it was observed that the stretched flame speeds (S_n) of CH_4/H_2 mixtures (H_2 ≥ 30% vol.) would decelerate with increasing flame radius as expected, however, at a flame radius > 30 mm, an acceleration of the flame was observed. The stretched flame speed versus Schlieren radius of the tested CH_4/H_2 is illustrated in Figure 8.11, with flame acceleration clearly visible for blends containing H_2 ≥ 30% (vol.) (red circle). Upon inspection of the Schlieren images, flame surface cracking was discernible for flames containing ≥ 30% H_2, with flames containing H_2 < 25% showing no discernible signs of cellularity within the data range employed to yield S_u and L_b values. Examples of Schlieren images depicting both stable and cracking of the flame surface area, are illustrated in Figure 8.12 (a-d).

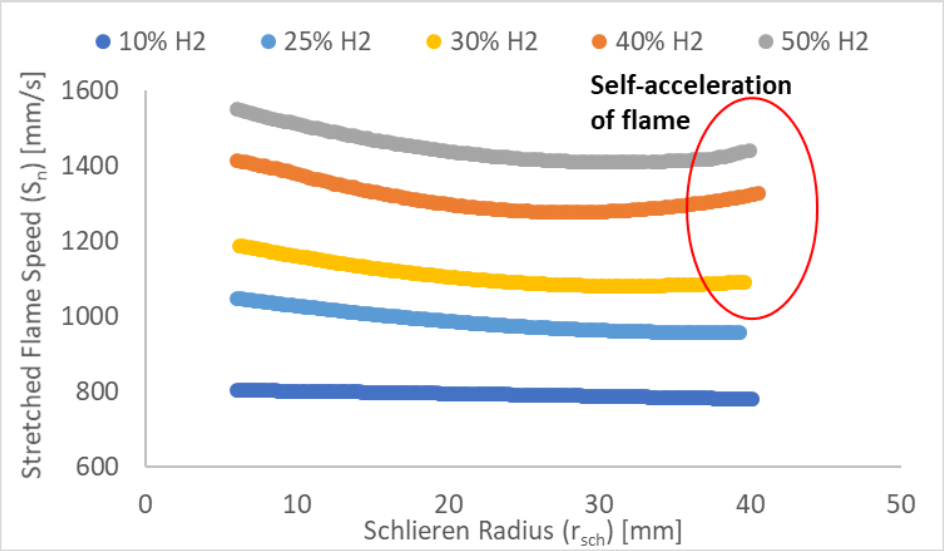

Figure 8.11 – Stretched Flame Speed vs Flame Radius for CH_4/H_2 Flames (T_u=298K,0.1 MPa, Φ=0.65)

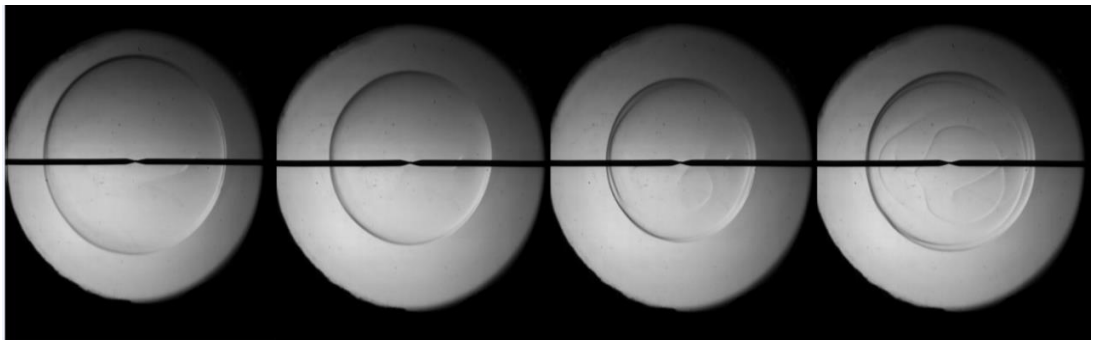

(a) H_2 = 10% (b) H_2 = 25% (c) H_2 = 40% (d) H_2 = 50%

Figure 8.12 – Schlieren Images Illustrating Development of Cracking of Flame Surface Area for Different CH_4/H_2 Flames (T_u=298K, P = 0.1 MPa, Φ=0.65)

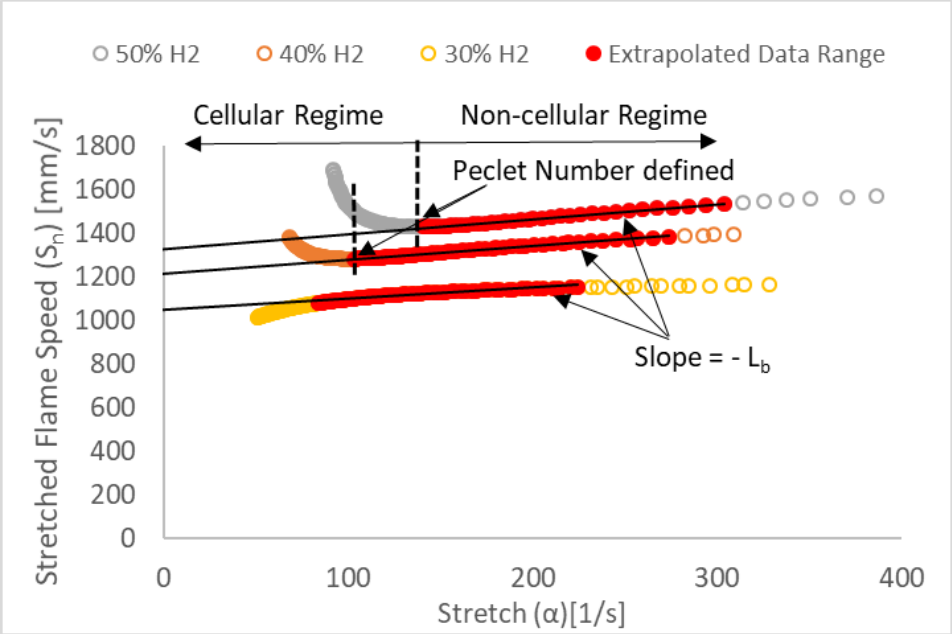

Figure 8.13 – Measured Flame Speed at Different Stretch Rates for CH_4/H_2 Flames (T_u=298K, P = 0.1 MPa, Φ=0.65)

The reduction and then acceleration of the flame with increasing flame radius due to cellularity must be accurately considered in order to provide meaningful S_u and corresponding L_b values. Consequently, a critical radius, which denotes the flame radius beyond which as stretch decreases the flame self-accelerates was determined. This transition point is defined as the critical Peclet number (defined as the critical flame radius / the laminar flame thickness [75], [170]), illustrated in Figure 8.13. The critical radius was determined to be approximately 25 mm for CH_4/H_2 mixture (50% H_2 vol.), with this critical radius increasing with reduction in H_2 concentration (i.e. ≈ 30 mm for the 30-40% H_2 blend).

From the uncertainty analysis conducted in Chapter 5, it was concluded that an initial flame polynomial range of 8-35 mm and a differential range of 10-30mm allowed for measurements, devoid of confinement or ignition influence. Since it was determined that self-acceleration of CH_4/H_2 flames was observable at a critical radius of ≈ 25 mm (for the 50/50 CH_4/H_2 blend) it was necessary to reduce the initial polynomial range to 8-22 mm (inclusive of a further 3 mm uncertainty factor), consequently reducing the differential range to 10-20 mm. Although the critical radius increased with decreasing H_2 fraction, to ensure comparability it was decided to apply the same flame radius range for all the CH_4/H_2 blends tested. It is noted that for the CH_4/H_2 blends containing ≤ 30% H_2, average relative differences between the initial and reduced flame data range (i.e. 10-30 and 10-22) were < 3% and < 25%, for yielded S_u and L_b values respectively, in agreement with conclusions from Chapter 5.

Datasets of the experimental L_b values for the CH_4/H_2, C_2H_6/H_2, and C_3H_8/H_2 blends are plotted in Figure 8.14. Following Chen's recommendations [84], LM(C) was employed for C_2H_6/H_2 and C_3H_8/H_2 mixtures (Le >1), whilst NM(S) was utilised for CH_4/H_2 blends (Le <1), with full L_b data-sets employing all appraised extrapolation methods available in Appendix – C.1.

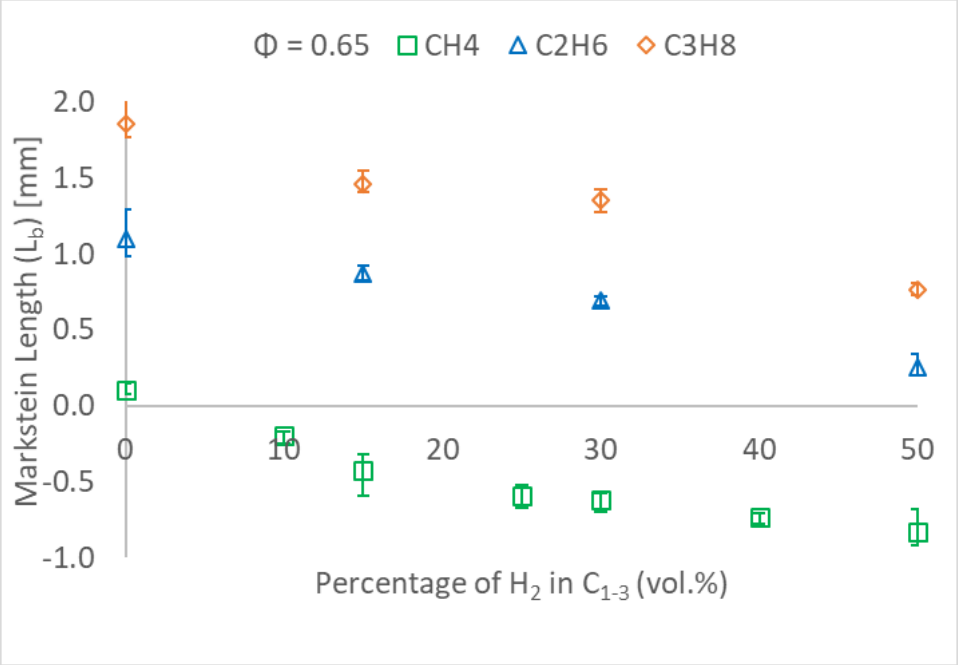

Figure 8.14 – Measured L_b of CH_4/H_2, C_2H_6/H_2, and C_3H_8/H_2 Blends (T_u=298K, P = 0.1 MPa)

As can be seen from Figure 8.14, CH_4/H_2 flames exhibit measured L_b changing from positive (100% CH_4) to increasingly negative values with increasing H_2 fractions, consequently fundamentally changing the flames response to stretch. Clearly, for ultra-lean CH_4/H_2 mixtures, increasing volumetric enrichments of H_2 have a destabilising effect, with the flame fronts becoming diffusionally unstable and cellular (Figure 8.12 (c) – (d)). This change in flame stability are a consequence of hydrodynamic instabilities (known as the Landau-Darrieus instability) and thermo-diffusive effects (diffusional-thermal instabilities) [41]. Hydrodynamic instabilities, in freely propagating flames, originate from the thermal expansion of gases. In the case of the CH_4/H_2 flames, the thermal expansion ($\sigma = \rho_u/\rho_b$), remains almost constant (relative differences < 2%), with increasing H_2 fractions (up to 50% vol.), whilst the kinetic flame thickness (δ_k) decreases with H_2 addition as seen in Figure 8.15; in effect promoting hydrodynamic instabilities. On the other hand, the effects of preferential diffusion, are a consequence of the higher mass diffusivity of H_2 and CH_4 compared to the O_2 molecule. Since, Le of the CH_4/H_2 decreases with increasing H_2 concentration, diffusional-thermal instabilities are promoted. For lean CH_4/H_2 flames, changes in measured L_b are thus potentially the result of the competing hydrodynamic and thermo-diffusive instabilities.

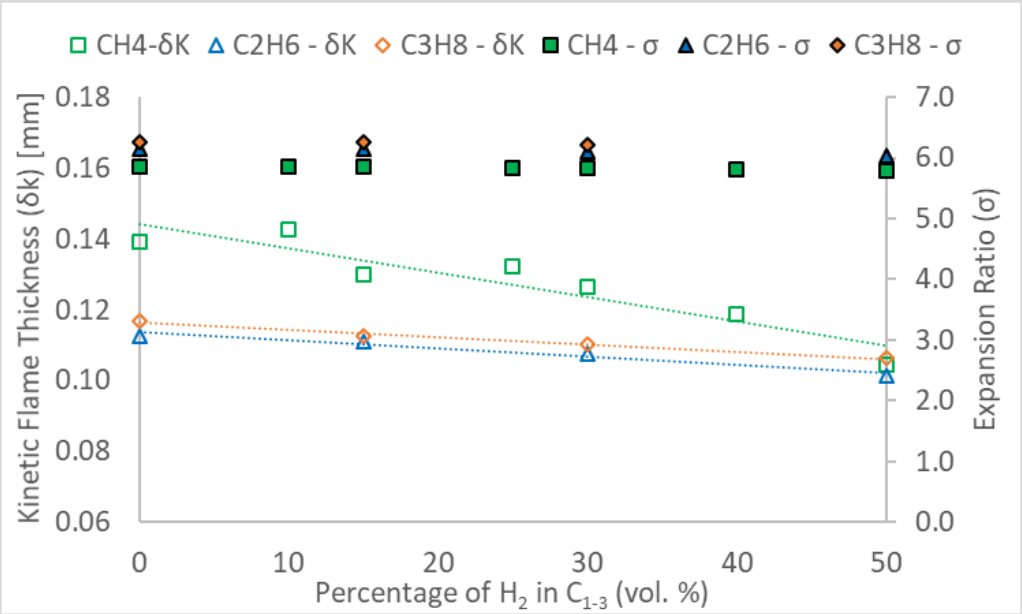

Figure 8.15 – Variations in Kinetic Flame Thickness (δ_K) and Expansion Ratio (σ) of $C_{1\text{-}3}/H_2$ Mixtures (T_u=298K,0.1MPa, Φ=0.65)

With respect to the C_2H_6/H_2 and the C_3H_8/H_2 mixtures, the same trend of decreasing L_b with increasing H_2 fraction as that of the CH_4/H_2 blend is displayed. However, all recorded L_b exhibit positive values, underlining the stabilising influence of the heavier HCs on flame stretch behaviour, with no signs of flame surface cracking on Schlieren images observable for H_2 additions of up to 50% (vol.%). The thermal expansion remained relatively constant for both the H_2 enriched C_2H_6 and the C_3H_8 mixtures (differences < 2% at 50% H_2 addition). The decreasing kinetic flame thickness with increasing H_2 enrichment as seen in Figure 8.15 effectively meant that hydrodynamic instabilities were promoted. However, since the mass diffusivity of C_3H_8 (and to a lesser extent C_2H_6) is lower than that of air, diffusional-thermal effects (Le>1) seem to have the propensity of moderating hydrodynamic instabilities, yielding a stabilising influence on the flame.

From the experimental values of L_b, which represents the flame's sensitivity to stretch (including both hydrodynamic and thermal-diffusional instabilities), it was observed that changes in L_b for ultra-lean C_2+/H_2 flames are potentially a consequence of hydrodynamic and thermo-diffusive effects, with the latter having a stabilizing influence on the flame (+L_b, Le >1). With respect to the CH_4/H_2 flames, measured changes in L_b result from the competing hydrodynamic and thermo-diffusional instabilities, with the latter promoting flame instability (–ve L_b, Le <1).

8.2.2 Effective Lewis Number formulations for H_2/C_1-C_3 binary blends

The impact of thermo-diffusional instabilities on measured L_b for the tested C_{1-3}/H_2 blends are characterised by changes in the mass to thermal ratio. Le_{eff} models, for CH_4/H_2, C_2H_6/H_2 and C_3H_8/H_2 mixtures are plotted in Figure 8.16.

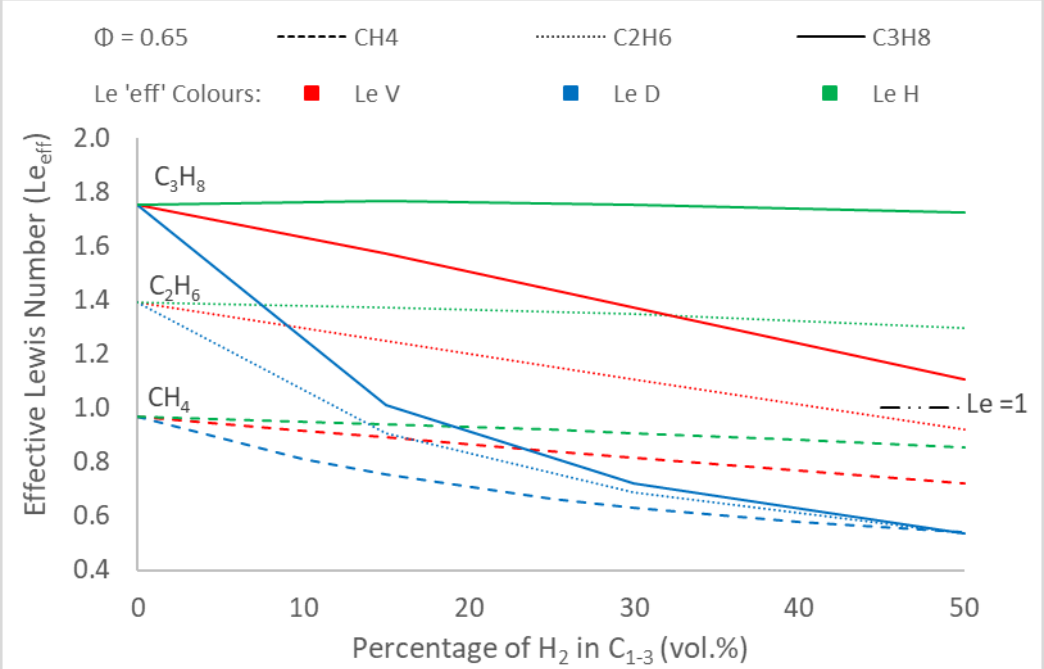

Figure 8.16 – Effective Lewis Number for C_{1-3}/H_2 Binary Mixtures (Φ = 0.65, T_u = 298 K, P = 0.1 MPa)

As seen in Figure 8.16, for the tested C_{2-3}/H_2 mixtures, different Le_{eff} models (i.e. Le_V, Le_D, Le_H) predict opposite thermo-diffusive behaviour, for identical blend composition and Φ, with this apparent incompatibility exacerbated with increasing carbon number (i.e. $Le_D << 1$, with $Le_H >> 1$ for a C_3H_8/H_2 mixture containing 50% H_2 vol.). It is observed that the Le_D formulation is clearly unsuited for C_2+/H_2 mixtures, predicting Le << 1 for H_2 volumetric enrichments of 20%, whilst $+L_b$ values were measured at 50% H_2 additions, with Schlieren images depicting smooth flame surfaces, in contradiction to flame fronts that exhibit Le <<1.

However, it is noted that Le_V and Le_H formulations predict behaviour (Le>1) in better agreement with measured L_b of C_{2-3}/H_2 mixtures. With respect to the CH_4/H_2 blends, illustrated in Figure 8.16, all Le_{eff} models predict plausible thermo-diffusive behaviour, with $Le_{eff} < 1$, in accordance with measured –ve L_b. In order to assess the validity Le_{eff}, relationships linking L_b to Le proposed by Chen [84], [120] and Bechtold and Matalon [142] are appraised (denoted in text as $L_{b\text{-}CHEN}$ and $L_{b\text{-}BM}$) and compared to measured L_b datasets, following the same procedure employed for the earlier presented CH_4/C_{2-3} binary blends (Section 8.1.2).

Experimentally measured and predicted (CHEN and BM) L_b for the CH_4/H_2 blends are presented in Figures 8.17 (a & b), respectively. With respect to $L_{b\text{-}CHEN}$, Figure 8.17 (a), best qualitative agreement is displayed employing Le_D, with slope inversion (i.e. + to – L_b) predicted for 10% H_2 enrichment, in agreement with measured L_b values. For volumetric H_2 additions > 25%, differences become incrementally more important, with measured L_b considerably smaller than numerically calculated Le_D, with the influence of H_2 over-estimated. $L_{b\text{-}CHEN}$ employing Le_V predicts L_b slope inversion (+ to – L_b) at ~30% H_2 addition. Whilst –ve L_b was measured for 10% H_2 fractions, it is noted that cracking of flame surface was only observable for blends containing H_2 additions ≥ 30%. Le_H under-estimates the influence of H_2, with +L_b values for 50% H_2 enrichment levels, in contradiction to measured +ve L_b values and observed flame cracking (Figure 8.12).

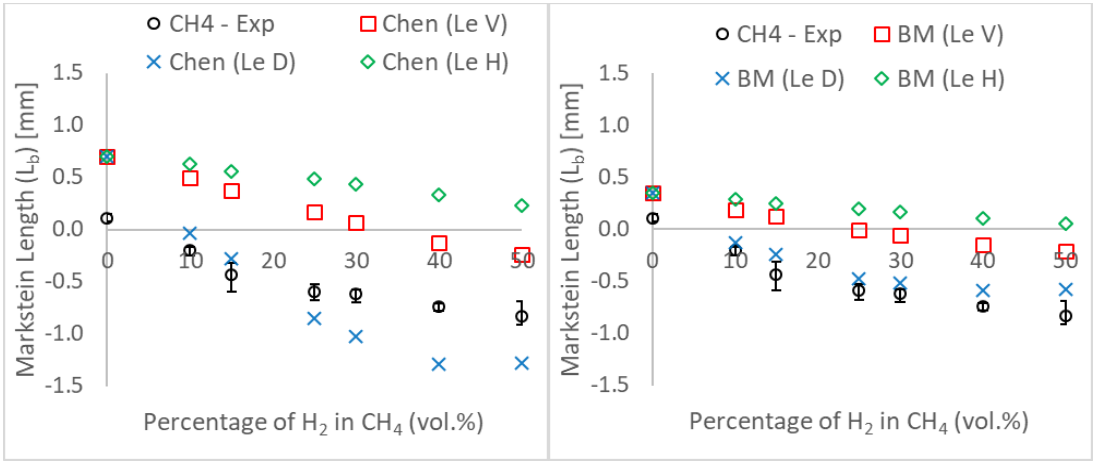

Figure 8.17 – (a) $L_{b\text{-}CHEN}$ and (b) $L_{b\text{-}BM}$ for CH_4/H_2 Mixtures using Le_{eff} (Φ =0.65, T_u = 298 K, P = 0.1 MPa)

In relation to $L_{b\text{-}BM}$, Figure 8.17 (b), both quantitative and qualitative agreement is witnessed with Le_D and experimental L_b values. It is observed that a smaller range in L_b values is predicted using the BM formulation in comparison to the wider L_b range yielded employing CHEN relationship. In general, the Le_D formulation, irrespective of the proposed relationship between L_b and Le (CHEN and BM), displays the best agreement with experimentally extracted L_b data. This agreement is expected given the Le_D formulation was derived from modelling of lean turbulent premixed CH_4/H_2 air flames [140], using the assumption that flame curvature is dominant, hence local enrichment of the most diffusive fuel at the flames leading edge is predicted. Since for ultra-lean conditions H_2 and CH_4 have higher mass diffusivities than O_2, the above flame concept demonstrates best agreement with measured CH_4/H_2 L_b datasets.

Bouvet et al. [131] conducted similar research, concluding that the Le_V model employing the CHEN relationship better captured changes in thermo-diffusive response of CH_4/H_2 flames. However, Bouvet and co-workers evaluated CH_4/H_2 flame behaviour at richer conditions then presented herein, (Φ = 0.80). Referring to results presented in Section 7.1.8

(Figure 7.20), application of $L_{b\text{-}CHEN}$ in combination with Le_V demonstrated better agreement with measured L_b of CH_4/H_2 (15% H_2 vol.) mixtures at Φ = 0.80-0.90, in agreement with Bouvet et al. [131]. Consequently, it appears that for ultra-lean CH_4/H_2 blends (Φ < 0.70), Le_D best depicts expected thermo-diffusive behaviour, whilst at near stoichiometric conditions, Le_V model appears more suitable.

Again, measured and numerical L_b for C_2H_6/H_2 mixtures are presented in Figures 8.18 (a & b), respectively. With respect to $L_{b\text{-}CHEN}$, Figure 8.18 (a), Le_V displays the best agreement with measured L_b, exhibiting progressively better quantitative agreement with increasing H_2 fractions. As previously underlined, Le_D considerably over-estimates the influence of H_2 upon C_2+ HC stretch-behaviour, whilst little variation is observed employing Le_H. With respect to $L_{b\text{-}BM}$, Figure 8.18 (b), quantitative agreement is displayed between experimental L_b values and Le_V. Again, the BM formulation tends to result in a tighter L_b range in combination with Le_{eff} in comparison to results using the CHEN formulation.

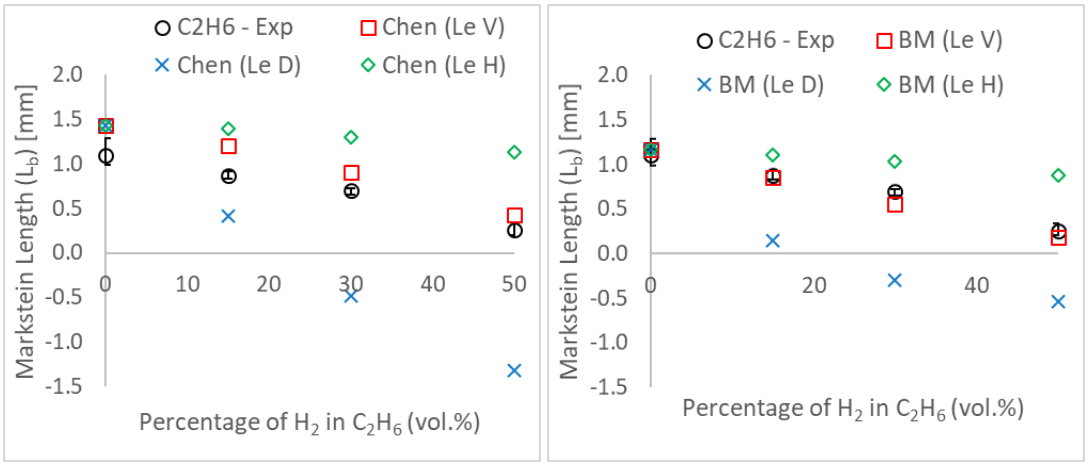

Figure 8.18 – (a) $L_{b\text{-}CHEN}$ and (b) $L_{b\text{-}BM}$ for C_2H_6/H_2 Mixtures using Le_{eff} (Φ = 0.65, T_u= 298 K, P= 0.1 MPa)

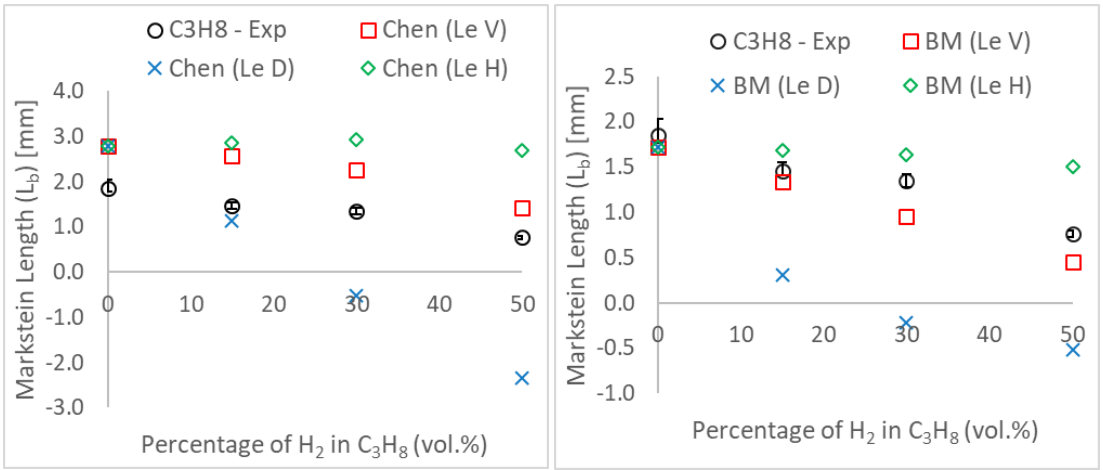

Figure 8.19 – (a) $L_{b\text{-}CHEN}$ and (b) $L_{b\text{-}BM}$ for C_3H_8/H_2 Mixtures using Le_{eff} (Φ = 0.65, T_u= 298 K, P= 0.1 MPa)

Experimental and modelled L_b values for C_3H_8/H_2 mixtures are plotted in Figures 8.19 (a & b), respectively. Generally, the same discussion expressed for the C_2H_6/H_2 mixtures can be extended to the C_3H_8/H_2 blends. Overall, $L_{b\text{-}CHEN}$ and $L_{b\text{-}BM}$ with Le_V exhibit best qualitative

agreement with experimental L_b data, in agreement with conclusions made by Bouvet et al. [131] (with respect to $L_{b\text{-}CHEN}$ for C_3H_8/H_2, $\Phi = 0.60$). $L_{b\text{-}BM}$ again demonstrates best agreement from a quantitative perspective. Once again, Le_H tends to overpredict the influence of heavier HCs on flame stability characteristics, with the Le_H model based upon the heat of combustion per mass formulation. Consequently, the significant differences in molecular mass between H_2 and C_2+ reduces the influence of H_2, even though the heat of combustion per mass of H_2 is significantly greater than that of HCs, with this effect exacerbated the heavier the HC (the impact of increased molecular weight).

Overall, for the ultra-lean CH_4/H_2 mixtures, $L_{b\text{-}CHEN}$ and $L_{b\text{-}BM}$ yield best qualitative agreement when combined with Le_D model. For the tested $C_{2\text{-}3}/H_2$ blends, the Le_V definition results in greatest qualitative agreement, irrespective of evaluated theoretical formulation (CHEN and BM). Finally, for all fuel blends tested, again the much more intricate BM formulation linking L_b and Le through various fundamental combustion properties generates better quantitative agreement with experimental values compared to that of CHEN, particularly for CH_4/H_2 fuel mixtures.

8.2.3 Unstretched Flame Propagation of H_2 C_1-C_3 binary blends

The unstretched flame speeds (S_u) attained for the CH_4/H_2, C_2H_6/H_2 and C_3H_8/H_2 mixtures are presented in Figure 8.20. NM(S) was employed to extrapolate S_u for CH_4/H_2 blends, with LM(C) utilised for $C_{2\text{-}3}/H_2$ mixtures, as per Chen's recommendations [84], with full S_u data-sets employing all evaluated extrapolation methods, located in Appendix – C.1.

Evidently, as can be seen from Figure 8.20, H_2 additions to CH_4 based fuels results in significantly increased S_u, in comparison to more modest S_u gains measured for the tested $C_{2\text{-}3}/H_2$ mixtures, in good agreement with relevant literature [105], [115]. With respect to the CH_4/H_2 mixture, measured S_u for 50% volumetric H_2 additions are closer to those displayed by pure CH_4 than pure H_2 (from this study, S_u ~1.4 m/s for CH_4/H_2 (50% H_2) and S_u ~ 0.8 m/s for 100% CH_4 at Φ =0.65, T_u = 298 K, P=0.1MPa; with S_u ~4.5 m/s for 100% H_2/air flames at Φ = 0.60, T_u = 303 K, P = 0.1MPa, obtained from [90]). For equal 50% volumetric additions of H_2, CH_4 flames exhibit equivalent S_u to that of C_2H_6, and marginally faster than those of C_3H_8, a significant change when compared to exhibited measured S_u of the pure $C_{1\text{-}3}$ alkane compounds.

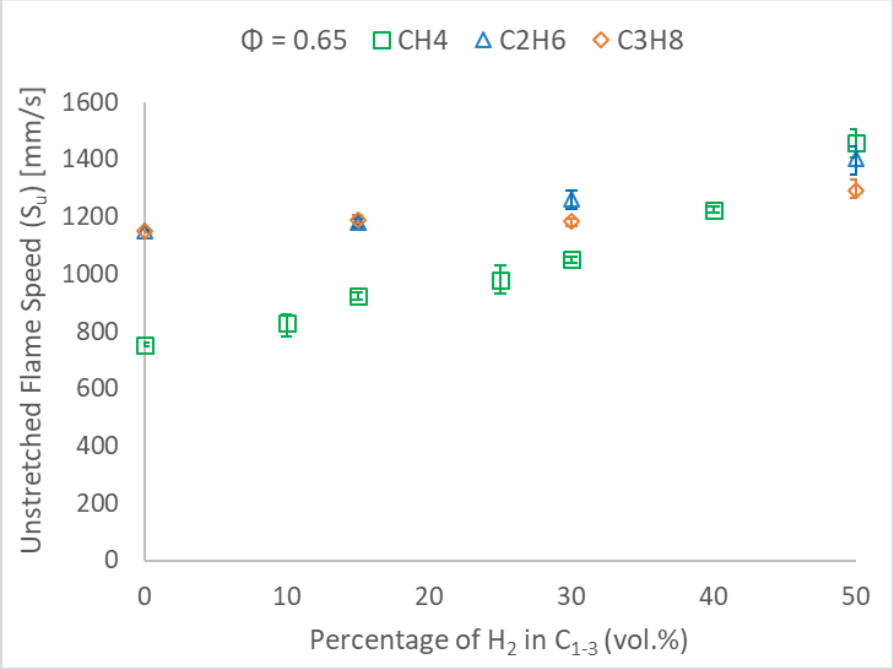

Figure 8.20 – Unstretched Flame Speed for CH_4/H_2, C_2H_6/H_2 and C_3H_8/H_2 Blends (T_u=298 K, 0.1 MPa)

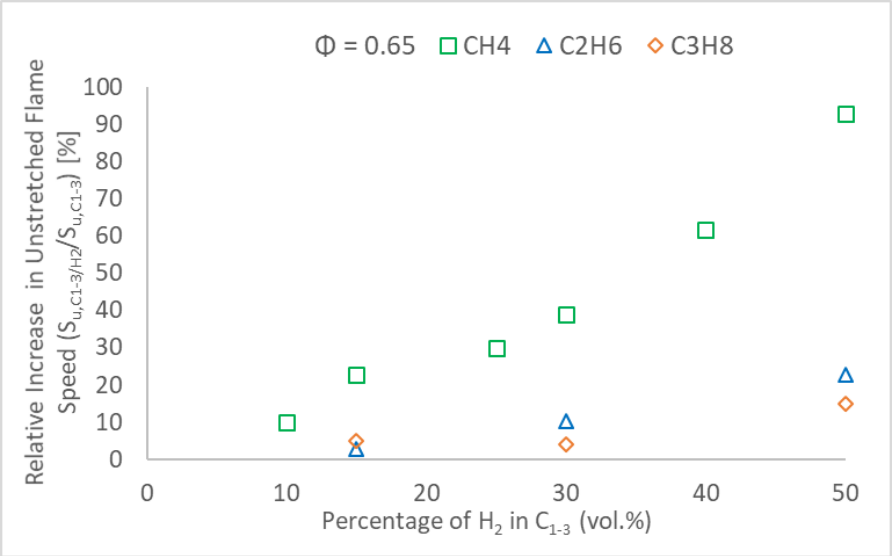

Figure 8.21 – Relative Increase in S_u for C_{1-3} Flames upon Addition of H_2 (T_u=298 K, P = 0.1 MPa)

To better capture the impact of H_2 on flame propagation, the relative increases in S_u of the tested C_{1-3}/H_2 blends, normalised to that of the pure HC (i.e. CH_4 for the CH_4/H_2 mixture), are illustrated in Figure 8.21. It can be observed that enhancements of CH_4 flame speeds upon H_2 additions (up to 50% vol.) appear to be quasi-linear, with average relative increases in S_u ~70% for CH_4 (50% H_2 vol.), with more modest average relative increases ~20% and ~15% for C_2H_6 and C_3H_8, respectively (for 50% H_2 fractions). For an Φ = 0.65, enhancement of S_u due to the presence of H_2 follows the order of $CH_4 > C_2H_6 > C_3H_8$, reflective of the decreasing H:C ratio, and increasing molecular weight of the fuels.

Modelling of freely propagating flames was undertaken, using the CHEMKIN-PRO software package with the PREMIX code employed [153]. The computational solutions were based on an adaptive grid of 1000 points, including multi-component diffusion and an assumed air composition of 79% N_2 – 21% O_2. The Aramco 1.3 [157] reaction mechanism was utilised to generate numerical adiabatic flame temperatures (T_{ad}), volumetric heat release rates (Q') and concentration of mole fractions of active radicals (O, OH and H). Modelled increases in T_{ad} upon H_2 addition on C_{1-3} alkane flames were observed to be modest (< 25 K), however, modelling work predicts a significant augmentation of burning intensity (through the volumetric heat release rate Q'), due to the presence of H_2, with relative increases in Q', normalised to that of 100% of the pure HC, presented in Figure 8.22.

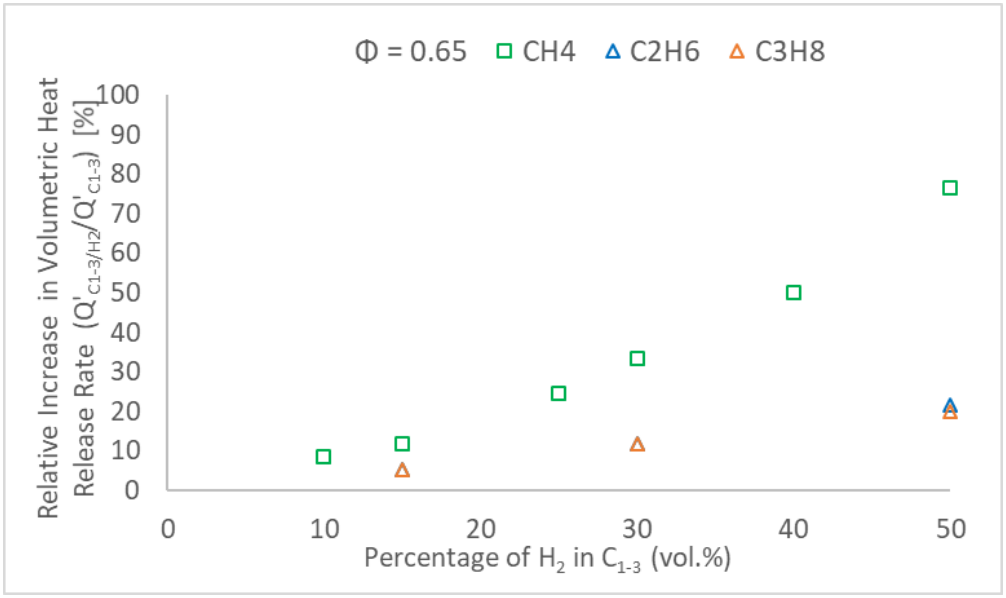

Figure 8.22 – Relative Increase in Q' for C_{1-3} Flames upon Addition of H_2 (T_u=298 K, P = 0.1 MPa)

Relative increases in modelled Q' for the C_{1-3}/H_2 blends are depicted in Figure 8.22, with the same linear trend exhibited in relative increases in Q' than those previously observed for S_u (Figure 8.21). As previously discussed, (Section 7.1 & 7.2), augmented volumetric heat release rates result in enhanced production of key radicals, notably H, with modelled values of relative increases in H radical production depicted in Figure 8.23.

Again, the relative increases in the production of H radical, Figure 8.23, exhibit a similar linear trend to that displayed by changes in measured S_u and modelled Q'. The flame speed, burning intensity (Q'), and production of H radical, appear to be highly correlated, in agreement with experimental work and sensitivity analysis conducted by Hu et al. [169]. Results from this work extend these conclusions to lean C_2H_6/H_2 and C_3H_8/H_2 mixtures for volumetric H_2 addition up to 50%. This linearity and correlation between flame propagation, volumetric heat release and production of H radical is graphically illustrated in Figure 8.24.

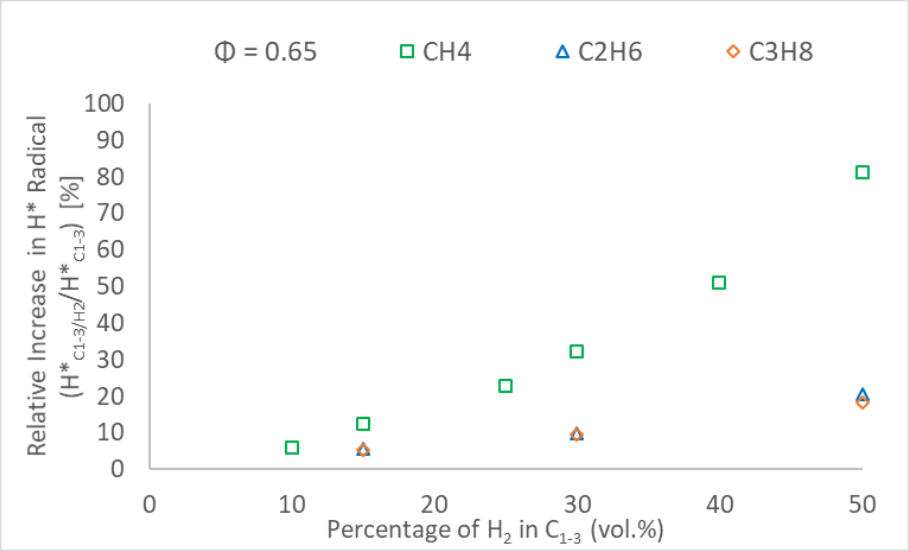

Figure 8.23 – Relative Increase in H Radical for C_{1-3} Flames upon H_2 Addition (T_u=298 K, P = 0.1 MPa)

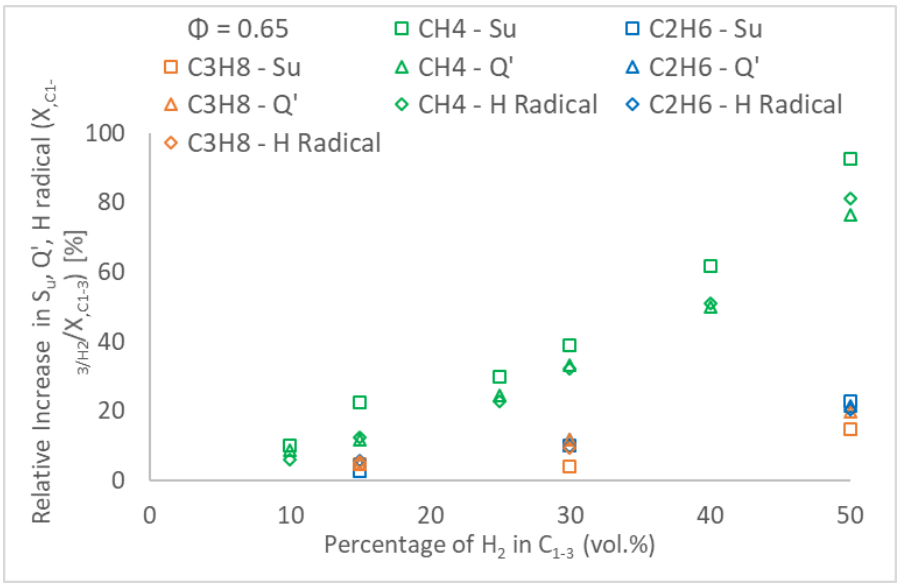

Figure 8.24 – Linear Correlation between Relative Increases in Measured S_u, Modelled Q' and H Radical Production for C_{1-3}/H_2 Mixtures (T_u=298 K, P = 0.1 MPa)

H_2 addition through facilitated diffusion, substantially alters thermo-diffusive behaviour (decreases Le), reduces global activation energy (E_a, discussed in Section 7.1.7), and generates small increases in flame temperature (quantified through changes in adiabatic flame temperature) of lean C_{1-3} alkane compounds, substantially altering their burning intensity; with CH_4 most prominently affected (Figure 8.22). Consequently, it seems that the measured enhancement of C_{1-3}/H_2 flame propagation may not primarily be a thermal effect (since modelled changes in T_{ad} are modest) but potentially a diffusional or kinetic effect. As such, further study was undertaken to investigate the main causes (thermal, diffusional, kinetic) behind the witnessed augmented burning.

8.2.4 Laminar Burning Velocity of H_2/C_1-C_3 Binary Blends

Experimental U_L values for CH_4/H_2, C_2H_6/H_2 and C_3H_8/H_2 mixtures are presented in Figure 8.25, alongside numerical U_L generated using the Aramco 1.3, USC II, and San Diego reaction mechanisms [156]–[158].

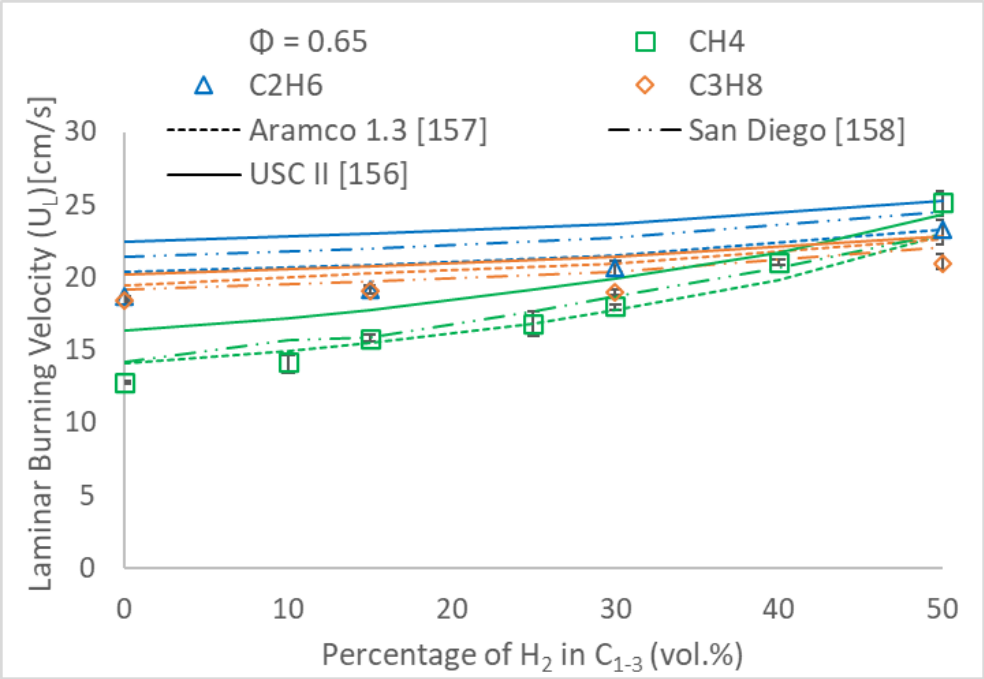

Figure 8.25 – Measured and Modelled U_L of C_{1-3}/H_2 mixtures (T_u=298 K, P=0.1MPa)

For volumetric H_2 additions of 50%, all appraised reaction mechanisms predict marginally faster numerical U_L values for CH_4 than C_3H_8 based mixtures, in agreement with experimental U_L values. In this study, CH_4/H_2 displayed marginally faster flame speeds than those witnessed by C_2H_6/H_2 flames (for 50% H_2), in contradiction to reaction modelling. However, it is noted that the observed differences are marginal, < 1 cm/s. Quantitively, again measured CH_4/H_2 blends exhibit best agreement with Aramco 1.3 for H_2 fraction up to 30%. With respect to C_2H_6/H_2 and C_3H_8/H_2 mixtures, experimental U_L values are observed to be marginally slower than numerically attained U_L, with best agreement again displayed with Aramco 1.3 and San Diego, for C_2H_6/H_2 and C_3H_8/H_2, respectively.

8.2.5 Sensitivity Analysis of H_2/C_1-C_3 binary blends

The enhancing effects of H_2 addition upon C_{1-3} fuels in terms of flame propagation, can be categorised as a combination of thermal, kinetic and diffusive effects [41], [88], [115]. The individual impact of each effect upon U_L can be modelled as [115]:

$$U_L \sim (D_T \cdot \mathrm{Le})^{1/2} \exp\left(\frac{-T_a}{2T_{ad}}\right) \quad \text{Eqn. (8.1)}$$

Where

$$T_a = \left(\frac{E_a}{R_u}\right) \quad \text{Eqn. (8.2)}$$

where T_a is the activation energy, and R_u the universal gas constant, with all other terms remaining as previously defined. For methods and example calculations of parameters (i.e. E_a, D_T, Le) refer to Sections 3.3 – 3.5.

With respect to Eqn. 8.1, the right-hand term [$(D_T \cdot \mathrm{Le})^{1/2}$ – the product of the thermal diffusivity and Lewis number of the mixture] reflects the diffusive influence. The left-hand term [$\exp(-T_a/2T_{ad})$] represents the Arrhenius factor, which encompasses the role of the global activation energy through the activation temperature [$T_a = (E_a/R_u)$] and the adiabatic flame temperature (T_{ad}). These individually represent the kinetic (T_a) and thermal (T_{ad}) influences on flame speed. With respect to Le definition, it was determined that Le_D and Le_V formulation, best captured changes in thermo-diffusive behaviour, for CH_4/H_2 and tested C_{2-3}/H_2, respectively, at ultra-lean conditions (Φ = 0.65), (Section 8.2.2). This conclusion is maintained irrespective of the employed theoretical relationship linking the Le to L_b (appraised for Chen [84], [120] and Matalon [142]), and consequently applied for the following analysis.

Similar research has been conducted by Ravi et al. [88], Tang et al. [115] and Wu et al. [112]. Ravi et al. [88], studied the enhancement effects of C_2H_6 and C_2H_4 (ethylene) addition to CH_4, performing a sensitivity analysis which revealed that flame speed enhancements were predominantly an Arrhenius effect (primarily kinetic), whilst thermal and diffusive pathways contributed equally to measured enhanced flame speeds for CH_4/C_2H_6. Tang et al. [115] investigated the augmentation effect of H_2 enrichment on C_4H_{10} flames, with sensitivity analysis identifying that kinetic effects had greatest influence. Tang et al. [115], suggest that if the same behaviour is maintained for methane and propane, potential generalisation of the phenomena could be concluded. Following this recommendation, work is undertaken to extend analysis to lean CH_4/H_2, C_2H_6/H_2 and C_3H_8/H_2 blends, up to 50% H_2 fractions (vol.%).

The following results are presented at an Φ = 0.65, all normalised to that of the pure fuel case. Thus, for example, in relation to the Arrhenius factor; $\exp(-T_a/2T_{ad})/ \exp(-T_a^*/2T_{ad}^*)$ and the diffusive factor; $(\alpha Le)^{1/2}/(\alpha^* Le^*)^{1/2}$, where the asterisk (*) denotes the normalisation of the parameter by the exhibited value of the pure (i.e. by CH_4 for a CH_4/H_2 blend). The variation in Arrhenius and diffusion factors (from Eqn. 8.1) upon several H_2 fraction additions to CH_4 are presented in Figure 8.26.

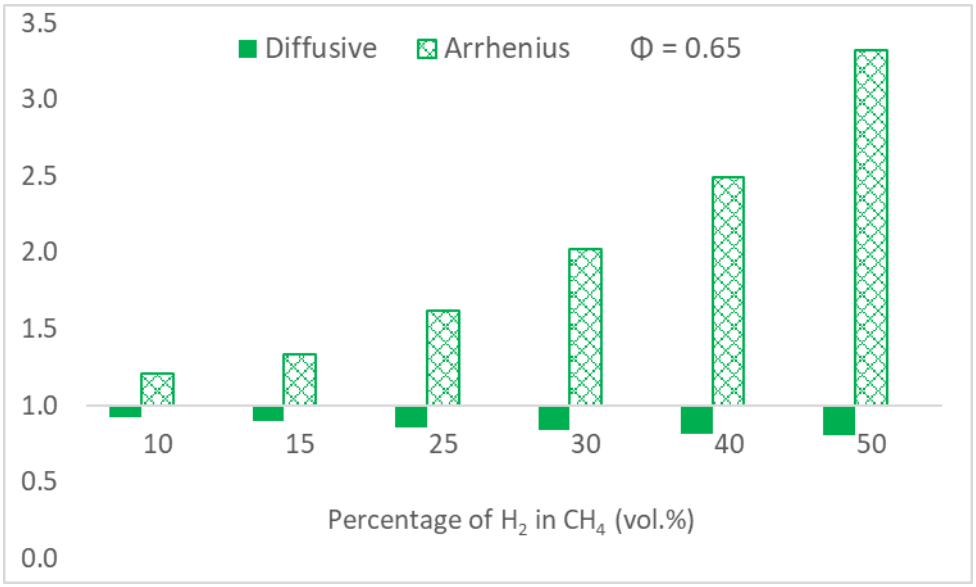

Figure 8.26 – Relative Arrhenius and Diffusive Effects of H_2 Addition to CH_4 – All Factors Normalised by those of Pure CH_4

As can be seen in Figure 8.26, for CH_4/H_2 blends, the Arrhenius factor plays the dominant role by comparison to that of the diffusive factor, whereby a positive or negative sensitivity equates to flame speed enhancement or inhibition. For CH_4/H_2 flames, under fuel-lean conditions, the Arrhenius factor and the diffusive factor impact flame propagation in opposite manners, with a displayed positive and negative sensitivity, respectively. This behaviour is consistent with trends in the global activation energy (and by extension T_a) and adiabatic flame temperature, which decrease (T_a) or increase (T_{ad}), respectively, upon the addition of H_2; consequently, combining into a positive enhancement of flame speed. Conversely, the negative sensitivity displayed by the diffusive factor, correlates with decreases in Le of the CH_4/H_2 mixture with increasing H_2 fractions. Note that this diminution of Le is maintained irrespective of Le_{eff} model employed (i.e. Le_V, Le_D, Le_H). Only the magnitude of decrease of Le will change upon application of different definitions, thus maintaining the same general trend.

The variations in Arrhenius and diffusive factors for the C_2H_6/H_2 and C_3H_8/H_2 blends are illustrated in Figure 8.27, alongside CH_4/H_2 blends for comparison (for equal volumetric H_2 additions). Evidently, with respect to the diffusive factor, the same trend is maintained for all tested $C_{1\text{-}3}/H_2$ blends, displaying negative sensitivities (consistent with the decreasing

trend of Le of the tested C_{1-3} fuels upon H_2 addition). The Arrhenius factor maintains a positive sensitivity for all blends, its impact however, is drastically reduced for C_2H_6 and C_3H_8 in comparison to CH_4. This is consistent with the measured flame speeds, with H_2 addition significantly impacting CH_4 flames, whilst smaller gains in flame speed were exhibited by the C_2H_6/H_2 and C_3H_8/H_2 blends. Note that in terms of magnitude, the opposite effects of the Arrhenius and diffusive factors upon flame speed of the C_{2-3}/H_2 blends maintains an overall positive sensitivity (in adequation with the measured subtle increases in flame speed).

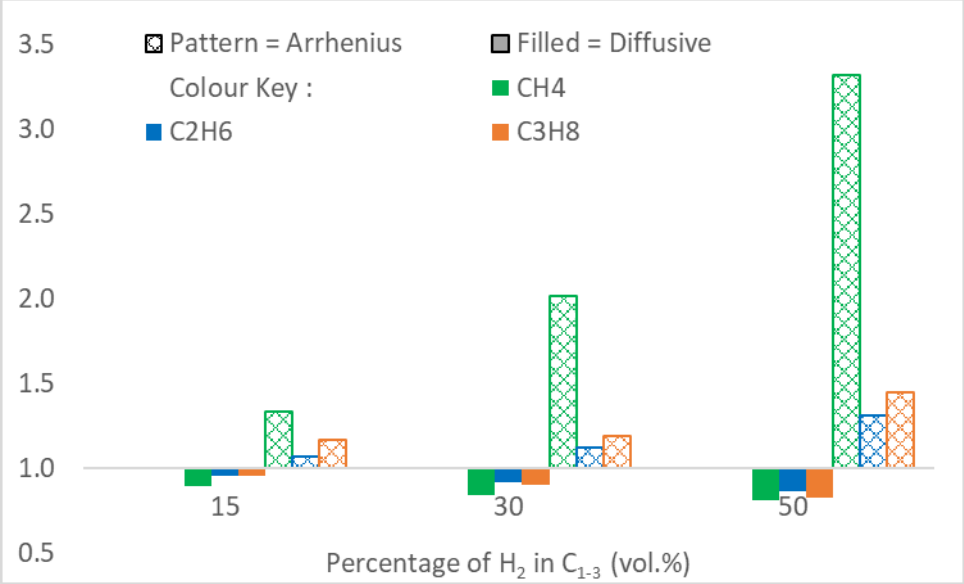

Figure 8.27 – Arrhenius and Diffusive Effects of H_2 Addition on CH_4, C_2H_6 and C_3H_8 – All factors Normalised by those of Pure Hydrocarbon (i.e. CH_4 for a CH_4/H_2 blend)

As demonstrated, the Arrhenius factor is the major contributor to flame speed enhancement displayed by CH_4 flames upon H_2 addition. For tested C_{2-3}/H_2 blends, the diffusive and Arrhenius factors are comparable in strength, with the latter being marginally more dominant. Their opposite sensitives explain the witnessed smaller flame speed enhancements. The vastly different enhancement rates between CH_4 and the heavier HCs in H_2 blends, and the contribution of each pathway (thermal, diffusive, kinetic) on the overall enhancement or inhibition of flame speeds deserves further investigation. Thus, using Eqn. 8.3, the overall sensitivity co-efficient may be expressed by [115]:

$$\frac{1}{U_L}\frac{dU_L}{dx} = \frac{1}{2D_T \cdot Le}\frac{d(D_T.Le)}{dx} - \frac{1}{2T_{ad}}\frac{dT_a}{dx} + \frac{T_a}{2T_{ad}^2}\frac{dT_{ad}}{dx} \qquad \text{Eqn. 8.3}$$

where *x* is the volume fraction of H_2 in the individual fuel blend. Note that the three terms on the right-hand side denote the influence, respectively, of the diffusive, kinetic, and thermal effects.

Sensitivity analysis for the CH_4/H_2 blend is presented in Figure 8.28, where the diffusion effect, is quantified for both the Le_D and Le_V definition. This comparison underlines the importance of employing an appropriate Le model. Clearly, as depicted in Figure 8.28,

either definition maintains the same qualitative sensitivity trend (negative sensitivity increasing with higher H_2 fractions, consistent with Le trend), however the magnitude of inhibition upon flame speed enhancement is significantly different, with application of a Le_D formulation predicting greater inhibition than Le_V. This is of importance since two different conclusions could be drawn from Figure 8.28. The first, employing Le_D, that the diffusive factor has a greater influence than the thermal factor. The second, utilising Le_V, that both the diffusive and thermal effects are of comparable influence. Nevertheless, the enhancement rate is primarily a kinetic effect, with the dominant mechanism of flame speed enhancement occurring through the reduction of the activation energy (and by extension the activation temperature).

With respect to the thermal effect, its impact is marginal in comparison to that of the kinetic factor. The influence of the thermal effect correlates with modelled changes in adiabatic flame temperatures, with increases < 25 K upon 50% H_2 addition (vol.) on CH_4 flames. This confirms the earlier hypothesis that changes in flame enhancement for CH_4/H_2 may not primarily be thermal in nature, but rather kinetic. As previously discussed, variations in adiabatic flame temperatures between reaction mechanisms are negligible (<0.63%), with Aramco 1.3 [157] values employed for this sensitivity analysis.

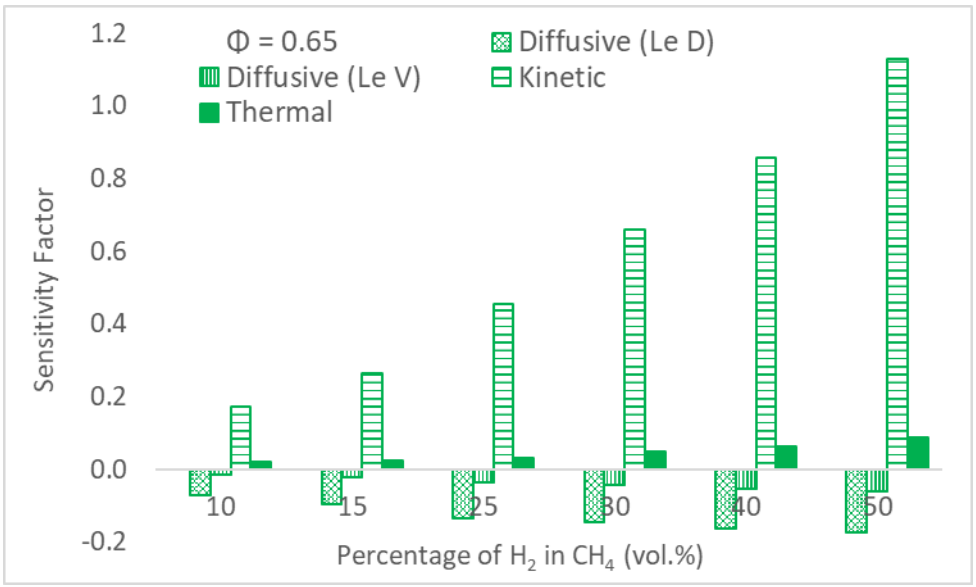

Figure 8.28 – Sensitivity of CH_4/H_2 Flame Speeds to Diffusive, Thermal, and Kinetic Effects

Analysis of the CH_4/H_2, C_2H_6/H_2 and C_3H_8/H_2 blends are presented in Figure 8.29, highlighting the thermal, kinetic and diffusive sensitivities. In terms of the influence of diffusion, all blends display a negative sensitivity, of comparable magnitude for the C_2H_6 and C_3H_8 mixtures. The kinetic effect displays positive sensitivity for all the tested $C_{1\text{-}3}/H_2$ blends and is the dominant mechanism behind measured enhancements of flame speed, with its impact most heavily pronounced on CH_4/H_2 flames, in agreement with experimental measurements of flame speeds. Finally, the thermal effect, shows a positive sensitivity for all

tested hydrocarbon hydrogen blends, respecting subtle increases in adiabatic flame temperatures resulting from H_2 addition at ultra–lean conditions. The fact that the thermal effect is less pronounced with increasing alkane number mirrors the adiabatic flame temperatures of the pure fuels, in the order C_3H_8 > C_2H_6 > CH_4, with that of H_2 marginally higher than those of the HC's at the tested fuel/air ratio.

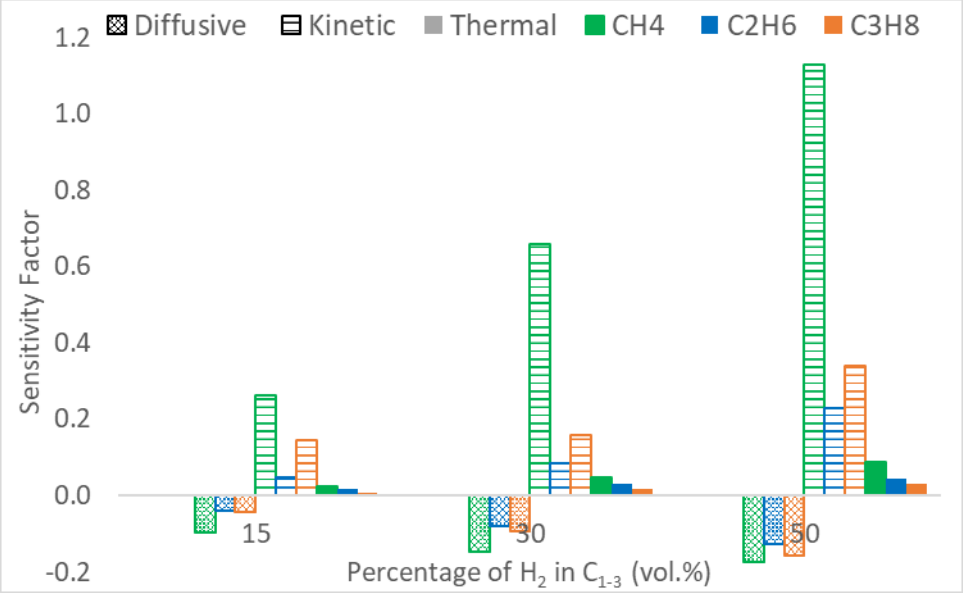

Figure 8.29 – Sensitivity of C_{1-3}/H_2 Flame Speeds to Diffusive, Thermal, and Kinetic Effects (Φ = 0.65)

Upon analysis conducted from first principles, it has been demonstrated that the measured augmentation of the flame speeds for CH_4 with H_2 addition is principally an Arrhenius effect rather than a diffusive one. Sensitivity analysis reveals that the dominant mechanism of flame speed enhancement is kinetic in nature, through the reduction of the global activation energy. The diffusive effect had an inhibiting effect (negative sensitivity), comparable to that of the thermal effect (which displayed positive sensitivity) upon application of a Le_V formulation, whilst it was stronger using Le_D model. These conclusions agree with earlier observations, particularly with the apparent linear correlation (noteworthy from a qualitative and quantitative perspective) displayed between measured relative increases in S_u and modelled heat releases (Q') and concentration of H radicals. With respect to the measured enhancement of the flame speeds for C_2H_6 and C_3H_8 with H_2 addition, sensitivity analysis reveals that the dominant mechanism is also kinetic. However, its effect is substantially weaker than for CH_4/H_2 flames. The diffusion pathway (negative sensitivity) is stronger than the thermal effect (positive sensitivity), reflecting the more prominent changes in Le in comparison to the minimal changes in adiabatic flame temperatures. These conclusions agree with the marginal exhibited gains in flame speeds witnessed upon H_2 addition to the heavier hydrocarbons, as well as the modelled modest relative increases in heat release (Q') and H radical concentration.

Overall, conclusions herein agree with the study conducted by Tang et al. [115] on C_4H_{10}/H_2 with respect to the fact that the kinetic effect is the most important factor behind enhancement of C_{1-4} hydrocarbon flame speeds upon H_2 enrichment. Note that the subsequent discussion only applies for the conditions tested herein (lean spectrum – 50% H_2 additions), since Tang et al., [115], extended their sensitivity analysis to include stoichiometric and rich conditions (Φ = 1.4) at volumetric H_2 additions of up to 70-90%. As demonstrated herein, the kinetic mechanism is significantly stronger upon CH_4 flames than heavier alkanes (including C_4H_{10}). Disagreement arises between conclusions from this study and those formed by Tang et al. [115] in terms of the strength of the diffusion factor. Agreement is maintained in terms of the general impact of the diffusion factor, with negative sensitivity displayed in both studies for all alkane fuels tested (C_{1-4}) under fuel-lean conditions, leading to inhibition of flame propagation. The strength of the diffusion factor was concluded herein to be stronger than the thermal effect, whilst the inverse was concluded by Tang et al., [115]. As demonstrated earlier, the Le model utilised impacts significantly the magnitude of the diffusion pathway and could possibly explain sources of disagreement. Furthermore, it was observed that differences are subtle, with both studies agreeing that the thermal and diffusive pathways have opposite effects, and that changes in flame speed are mainly to be attributed to the impact of H_2 on activation energy (kinetic effect).

Finally, it is noted that conclusions should be taken from a qualitative point of view rather than a quantitative perspective, given there exists several different theoretical formulations to evaluate the same fundamental flame property. For example, the global activation energy (E_a) can be assessed using two different methods [144], [146], (Section 3.5). Differences in attained values in the lean spectrum (Φ = 0.60 – 0.70) between both methods fluctuates between 10-20% depending on the investigated fuel, with differences significantly exacerbated on the rich side (Table 6.1). Furthermore, differences are to be expected by applying different reaction mechanisms, due to the number of identical reactions within each mechanism that have different associated Arrhenius co-efficients (Section 4.3.2, Tables 4.2 & 4.3). As exemplified by changing Le_{eff} model (Le_D and Le_V) in the CH_4/H_2 sensitivity analysis, Figure 8.28, different quantitative conclusions can be drawn. Note however, that qualitative trends should remain valid, and thus performing such sensitivity analysis from first principles remains relevant with potentially useful insight gained.

8.3 Chapter Summary

The combustion behaviour of ultra-lean (Φ = 0.65) CH_4/C_{2-3} (up to 85% C_{2-3} vol.), C_2H_6/C_3H_8 and C_{1-3}/H_2 (up to 50% H_2 vol.) mixtures was experimentally investigated including analysis of measured Markstein length (L_b) and flame speed propagation. Effective Lewis number formulations were appraised for the tested mixtures using theoretical relationships proposed in literature associating L_b to Le. A sensitivity analysis related to the contribution of major flame enhancing pathways (thermal, diffusive, kinetic) was conducted from first principles to clarify the nature of measured augmented burning intensity of C_{1-3}/H_2 flames. From this work, the following conclusions can be taken:

- Changes in measured L_b of ultra-lean CH_4/H_2 and C_{2-3}/H_2 (50% H_2 vol.) result from competing hydrodynamic and thermo-diffusional instabilities, with the latter promoting flame instability in CH_4/H_2 blends (-L_b, Le <1) whilst having a stabilising influence on C_2+/H_2 flames (+L_b, Le >1). For blends composed predominantly of CH_4, small additions of C_{2-3} alkanes yield considerable impact on measured stretch-related behaviour.
- For equal volumetric H_2 additions (50%), CH_4 flames exhibit equivalent S_u to that of C_2H_6 and marginally faster than C_3H_8 flames, with enhancement of S_u due to H_2 enrichment following the order CH_4>C_2H_6 > C_3H_8. For CH_4-based fuels, C_2H_6 and C_3H_8 enrichment have quasi-identical impact on measured augmented flame propagation. In general, experimental U_L values for all tested blends display best correlation with the Aramco 1.3 mechanism.
- Modelling and experimental work suggests that ultra-lean CH_4/H_2 flame speed, burning intensity (Q') and H radical concentrations are highly correlated, in agreement with literature, with the above correlation extendable to C_2H_6/H_2 and C_3H_8/H_2 mixtures (volumetric H_2 addition up to 50%).
- Measured augmentations in flame speed of ultra-lean CH_4/H_2 blends was demonstrated to be principally an Arrhenius effect (kinetic), through the reduction of E_a (and thus T_a), with diffusive and thermal pathways comparable in strength (with opposite sensitivities). For the tested C_{2-3}/H_2 blends, enhanced flame speed was kinetic in nature, however, substantially weaker than for CH_4/H_2 flames, in good agreement with marginal exhibited gains in measured flame speed and modest modelled increases in Q' and H radical production.
- For the evaluated effective Le formulations, a heat release based model (Le_H) yielded best agreement with measured L_b of ultra-lean CH_4/C_{2-3} HC blends, with diffusional and volume-based models (Le_D and Le_V) best representing measured L_b behaviour of ultra-lean CH_4/H_2 and C_{2-3}/H_2, respectively.

Chapter 9. Natural Gas mixtures, with Practical Implications to Premixed Swirling, Lean Limit Flames

Having examined and quantified the lean combustion characteristics of CH_4, C_2H_6, C_3H_8 and C_4H_{10} and their blends with H_2 (15% vol.) (Chapters 6 and 7), as well as the influence of H_2, C_2H_6 and C_3H_8 additions on ultra-lean CH_4 based flames (Chapter 8), an understanding of the impacts of tertiary blends was sought. Consequently, a series of spherically expanding flame (SEF) experiments was conducted at atmospheric pressure and temperature (T_u= 298 K, P= 0.1 MPa), at fuel lean conditions Φ =0.6, 0.7 and 0.8, for $CH_4/C_3H_8/H_2$ mixtures, representative of five hydrogen-enriched Natural Gas (NG) blends, with compositions detailed in Table 9.1.

Table 9.1 – Composition of Selected Natural Gas Blends

Fuel Designation	Fuel Composition (Volume %)			CH_4:C_3H_8 mol. fraction Ratio	CH_4:C_3H_8 Mass fraction Ratio
	CH_4	C_3H_8	H_2		
NG 1	68	17	15	4:1	1.45:1
NG 2	73.1	11.9	15	6.14:1	2.23:1
NG 3	76.5	8.5	15	9:1	3.27:1
NG 4	78.2	6.8	15	11.5:1	4.18:1
NG 5	79.9	5.1	15	15.6:1	5.70:1

As discussed previously (Section 1.3.1) depending on the source, extraction and refinement process, NG is comprised predominantly of CH_4, with other heavier hydrocarbons (HCs), namely C_2H_6 and C_3H_8, varying significantly, 0-15 vol.% and 0-25 vol.%, respectively [30]-[31]. It was previously demonstrated that, (Section 6.1, 7.1, 8.1), C_2H_6 and C_3H_8 exhibit comparable combustion properties, as both pure fuels and when enriched with 15% volumetric H_2, in addition to displaying similar effects in terms of stretch-related behaviour and flame propagation when blended with CH_4. As such, it was considered sufficient for the purpose of this work to represent the potential influence of concentrations of C_2+ HCs in NG combustion using only C_3H_8.

With respect to the NG compositions (Table 9.1), CH_4:C_3H_8 mol fractions were constituted to allow comparison with the previously investigated CH_4/C_3H_8 blends (Section 7.2), with NG 5 – 94/6% (CH_4/C_3H_8) blend, NG 4 – 92/8% blend and NG 3 – 90/10% blend, presenting identical CH_4:C_3H_8 mol fraction ratios, facilitating analysis related to the influence of H_2 enrichment. All NG blends contain a 15% volumetric addition of H_2, an enrichment level corresponding to present 'higher' permissible range within European NG infrastructure [26]

(Figure 1.4), representative of contemporary industrial targets (20% H_2 vol.). Furthermore, NG 2 – 5 have associated Wobbe Index (WI) values falling within the proposed European EASEE gas regulations (46.46 – 54 MJ/m^3 [36], Section 1.3.1, Figure 1.6).

As discussed in Chapter 2, some studies [117], [118] employing the SEF configuration have investigated the impact of H_2 on NG, however, the NG compositions employed were mainly composed of CH_4 (> 95% vol.), and as expected such results are hence very similar to those related to CH_4/H_2 blends. Limited experimental data concerned with the addition of H_2 on NG mixtures containing differing quantities of higher HCs (C_2H_6 and C_3H_8) is available in literature, including recent work by Nilsson et al.[80] using the heat flux method and Khan et al.[100] employing the SEF configuration. However, it appears to date, that no experimental study in the literature investigates practically relevant NG compositions respecting industrial Wobbe Index regulations.

With respect to chemical kinetic modelling, the Aramco 1.3 [157] and USC II [156] reaction mechanisms have consistently displayed best correlation with all tested fuel mixtures in this work, and thus again appraised in this chapter. Again, as with previous results, unless otherwise stated, the error bars represent maximum and minimum recorded values, around an average plotted value for graphical illustrations depicting experimental Markstein Length (L_b), unstretched flame speeds (S_u) and laminar burning velocities (U_L) values.

9.1 Stretch Behaviour of Natural Gas/H_2 Mixtures

Datasets of the NG/H_2 mixtures are presented in Figures 9.1 and 9.2, for Φ = 0.80 and 0.60, respectively, illustrating the relationships between the stretched flame speed (S_n) and stretch (α) using both linear and non-linear methodologies and that between S_n and curvature (κ).

It can be observed from Figure 9.1, that all tested NG blends irrespective of their compositional make-up, displayed a deceleration in flame speed with increasing stretch effects (represented by a negative gradient). At around those AFRs (Φ = 0.80 – 1.0), this behaviour is consistent with that previously measured for pure CH_4, C_3H_8 and CH_4/C_3H_8 binary mixtures (Section 6.1.2 – 7.2.1), with H_2 (15% vol.) as expected yielding nominal influence on flame stability characteristics (+L_b, Le >1). However, significant changes in flame behaviour are observable at leaner conditions (Φ =0.60, Figure 9.2), with variations in NG composition discernibly influencing flame stretch-propagation characteristics. NG 1 – 3 flames continue to decelerate with increasing stretch, however, a subtle increase in gradient (smoothening) is observed, with flames displaying a reduced sensitivity to stretch, a consequence of both the increasing CH_4:C_3H_8 ratio (decreasing C_3H_8 fraction), and greater influence of H_2 on flame stability at leanest conditions. NG 4 exhibits a gradient close to 0, with flame propagation

speed quasi-linear and thus practically independent of stretch rate, suggesting near equi-diffusion of heat and mass transport mechanisms (Le ≈ 1), behaviour analogous to that measured for pure CH_4 at minimally richer conditions (Φ = 0.65, Figure 6.3). NG 5, the blend containing the highest CH_4 fraction is observed to accelerate with stretch, in agreement with earlier results of CH_4 and H_2 (Φ = 0.60), alluding to a diffusionally mass-driven combustion process (Le < 1 and $-L_b$).

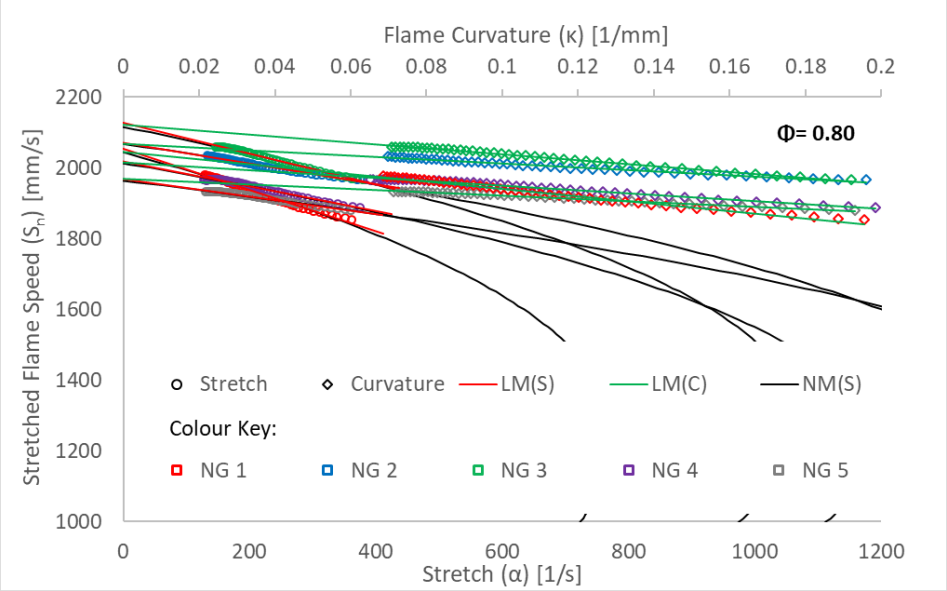

Figure 9.1 – S_n vs α and κ of NG/H_2 Blends (T_u = 298 K, P= 0.1 MPa)

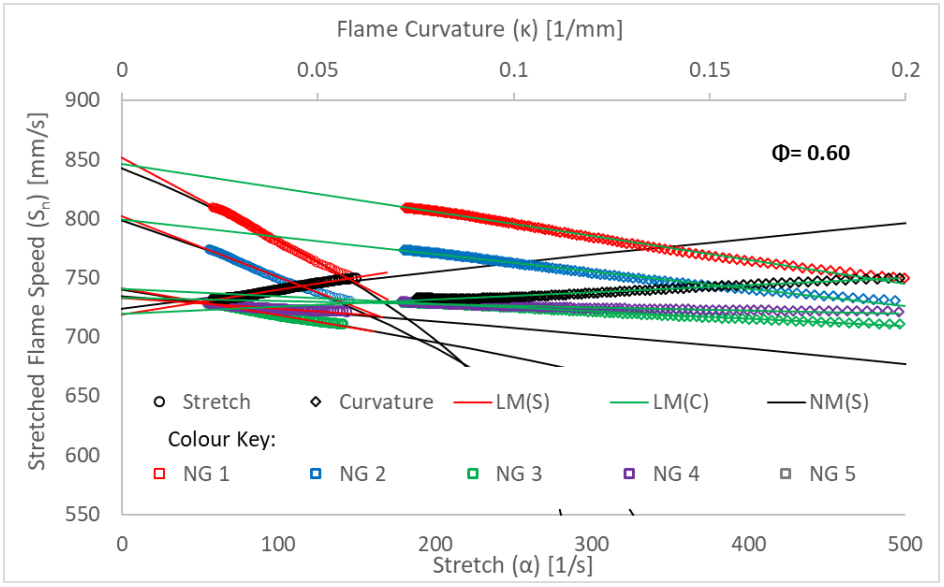

Figure 9.2 – S_n vs α and κ of NG/H_2 Blends (T_u = 298 K, P= 0.1 MPa)

9.1.1 Markstein Length of Natural Gas/Hydrogen Mixtures

Measured L_b of the NG/H_2 blends are illustrated in Figure 9.3, derived using LM(C), with individual test results generated using all employed extrapolation methodologies available in tabulated format in Appendix – C.1. The effective Lewis number (Le_{eff}, i.e. Le_V, Le_D, Le_H) of the NG blends are depicted in Figure 9.4, evaluated using the mixtures free-stream properties assessed at a (λ/C_p) ratio of T=298 K, with mass-diffusion co-efficients evaluated using the Hirschfelder method [133], [134] (Section 3.2.1.3).

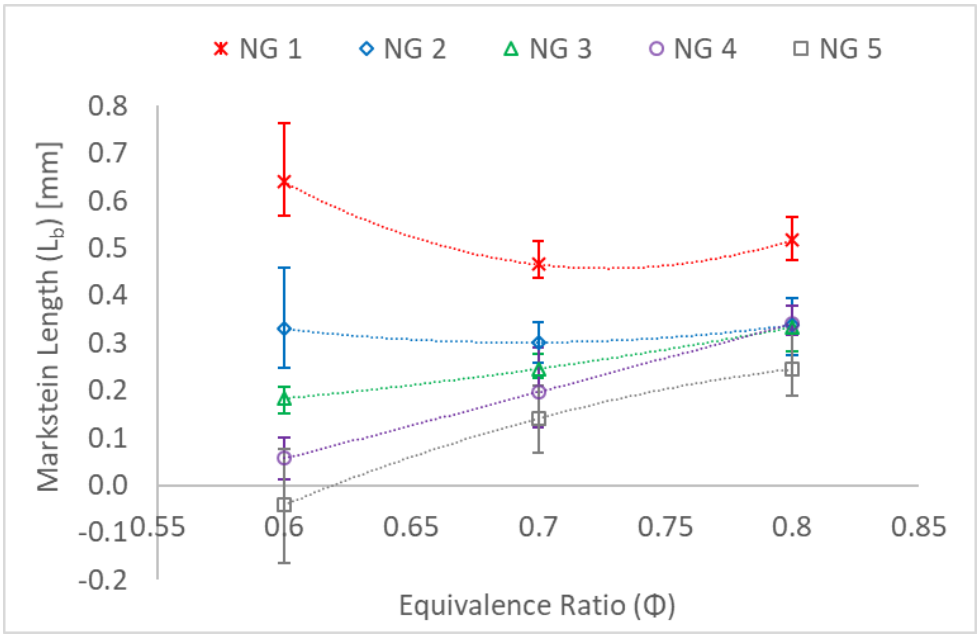

Figure 9.3 – Measured L_b vs Φ for the NG/H_2 Blends – (T_u= 298 K, P= 0.1 MPa)

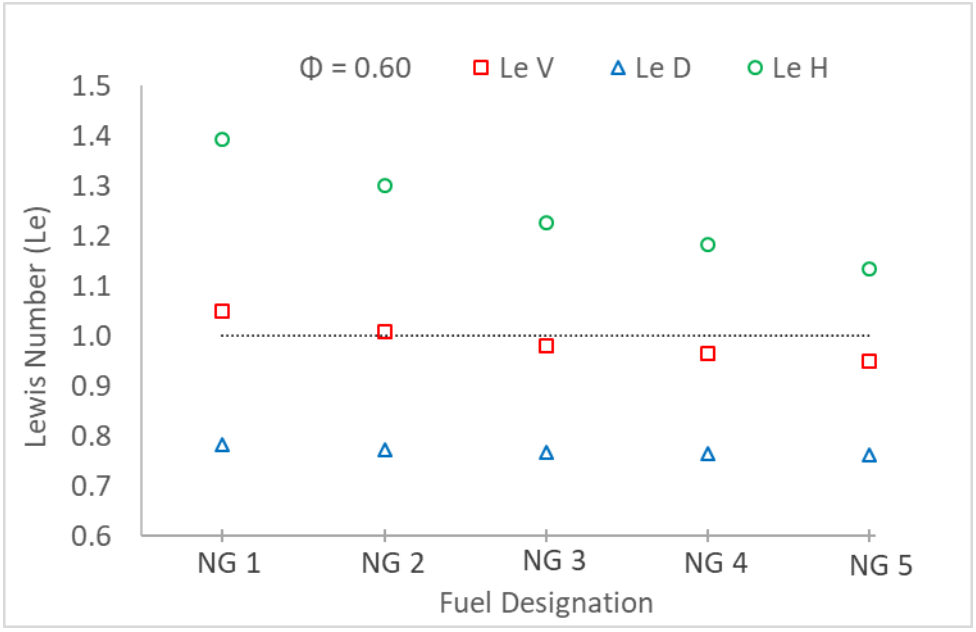

Figure 9.4 – Effective Lewis Number Formulation of NG/H_2 Blends – (Tu= 298 K, P= 0.1 MPa)

As expected, at near-stoichiometric conditions, all NG blends display comparable measured L_b values (Figure 9.3), a consequence of the similar stretch-related and thermo-

diffusive behaviour of CH_4 and C_3H_8 at those AFRs ($\Phi = 0.80$). At leaner conditions ($\Phi \leq 0.7$), NG 1 and NG 3 – 5 exhibit opposite $L_b - \Phi$ trends, increasing and decreasing, respectively, with NG 2 displaying little sensitivity to Φ, with minimal changes in average measured L_b. Variations in the NG's CH_4:C_3H_8 mol fraction ratios are behind the measured changes in L_b behaviour, with NG 1 and NG 5 containing the largest fractions of C_3H_8 and CH_4, respectively, behaving in equivalent manner to that of pure C_3H_8 (Le > 1, + L_b) and CH_4 flames (Le < 1, - L_b) at $\Phi = 0.60$. From a thermo-diffusive perspective (Le), H_2 and C_3H_8 promote opposite lean CH_4 based flame stability behaviour, with the influence of H_2 prominent for NG 3 – 5 ($\downarrow L_b$ with $\downarrow\Phi$), counter-acted by increasing fraction of C_3H_8 in NG 1 ($\uparrow L_b$ with $\downarrow\Phi$) and balanced for NG 2 (little change in L_b with $\downarrow\Phi$). Ravi et al. [100], measured L_b for different H_2 enriched NG ($CH_4/C_2H_6/C_3H_8$) compositions, remarking that L_b dropped with decreasing heavier HC fraction for a fixed volumetric H_2 addition, in good agreement with observed trends in this study.

The Le_{eff} formulations evaluated at $\Phi = 0.60$ for the NG mixtures are presented in Figure 9.4. Both a Le_H and Le_V model yield a reducing Le trend with increasing CH_4 fractions (i.e. decreasing C_3H_8, fixed H_2 fraction), correctly capturing the influence of changes in CH_4:C_3H_8 mol fraction ratios, and in agreement with measured changes in L_b. It should be noted that Le_H returns Le > 1 for all NG blends, with Le_V yielding Le > 1 (NG 1, highest C_3H_8 content), Le = 1 (NG 2) and Le < 1 (NG 5, highest CH_4 content). Again, the Le_D formulation overpredicts the influence of H_2 with Le << 1 for all NG blends, and thus unable to capture the thermo-diffusive influence of changes in NG compositions.

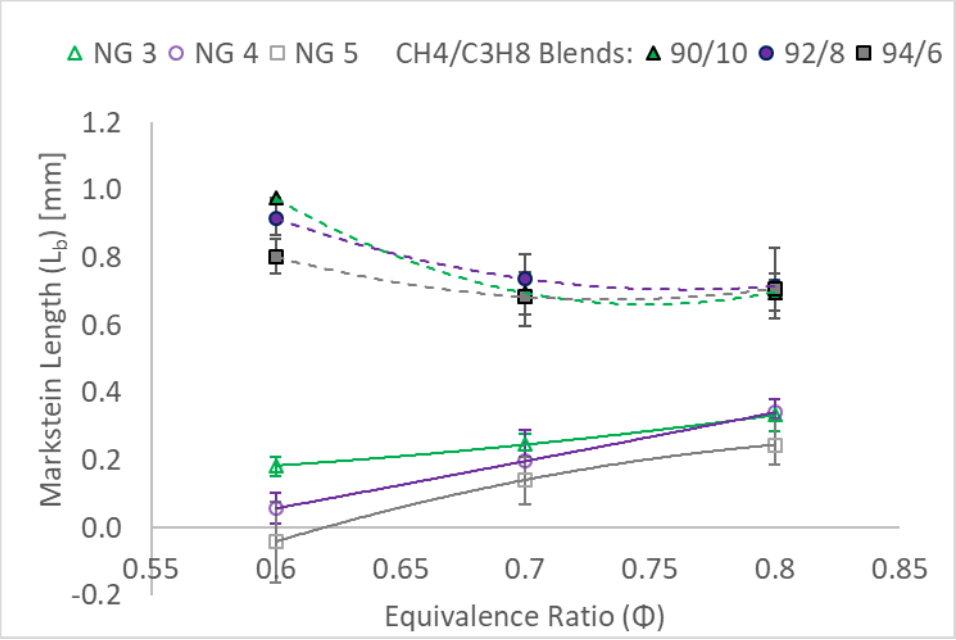

Figure 9.5 – Measured L_b vs Φ for NG/H_2 and CH_4/C_3H_8 Blends – (T_u= 298 K, P= 0.1 MPa)

Since NG 3, 4 and 5 display identical CH_4/C_3H_8 mol fraction ratios to previously investigated CH_4/C_3H_8 binary blends (i.e. NG 3 – 90/10, NG 4 – 92/8, NG 5 – 94/6 vol.%, Table 9.1), the impact of 15% H_2 volumetric enrichment can thus be evaluated. Measured L_b of NG blends 3 – 5 and the corresponding CH_4/C_3H_8 binary blends are depicted in Figure 9.5. As concluded from the CH_4/C_3H_8 parametric study (Section 7.2), at lean conditions ($\Phi \leq 0.70$), blends with a ~16:1 CH_4/C_3H_8 mol. fraction ratio resulted in flames exhibiting stretch related behaviour analogous to pure C_3H_8 ($\uparrow L_b$ with $\downarrow \Phi$, Figure 7.22). The influence of H_2 is clearly observable in Figure 9.5, with the $CH_4/C_3H_8/H_2$ blend (i.e. NG 3) containing a CH_4/C_3H_8 mol. fraction ratio of ~9:1 now exhibiting decreasing L_b as conditions get leaner (from $\uparrow L_b$ with $\downarrow \Phi$), indicating that mass diffusion is becoming more prevalent (since L_b is decreasing), though still not the dominant transport mechanism. Slope inversion (+ to – L_b) is registered for NG 5 (CH_4/C_3H_8 mol. fraction ratio (16:1)), a significant change in flame stability characteristics, with respect to the tested CH_4/C_3H_8 blend containing equal CH_4/C_3H_8 mol. fraction ratio, which exhibited behaviour analogous to C_3H_8 ($\uparrow L_b$ with $\downarrow \Phi$). Extrapolation of best line fits, to conditions leaner than those tested, predict L_b slope inversion (+ to –) for NG 4 at $\Phi \approx 0.55$, with this Φ falling within GT operation, hence in practical systems there may be observed an acceleration in flame propagation due to the highly stretched turbulent environment.

The influence of H_2 addition (15% vol.), on Le_{eff} values of the CH_4/C_3H_8 blends is illustrated in Figure 9.6. Both Le_V and Le_H correctly predict a decrease in Le_{eff} with H_2 addition (represented by NG 3 – 5, Figure 9.6), however Le_V yields better correlation with measured L_b values, with Le < 1 for NG 5.

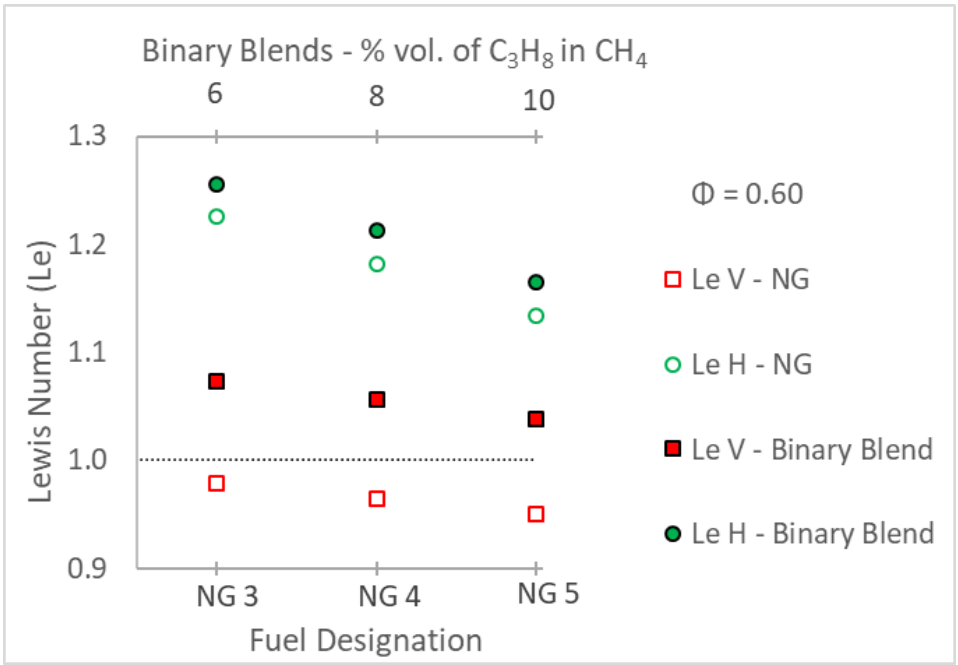

Figure 9.6 – Le_{eff} Comparison for NG and CH_4/C_3H_8 Blends – $\Phi = 0.60$ – (T_u= 298 K, P= 0.1 MPa)

9.1.2 Flame Propagation of Natural Gas/Hydrogen Mixtures

The unstretched flame speeds (S_u) attained for the NG mixtures are presented in Figure 9.7, with linear relationships superimposed to facilitate trend analysis and discussion. Note that S_u values were extrapolated utilising LM(C), with full S_u datasets employing all evaluated extrapolation methods located in Appendix – C.1

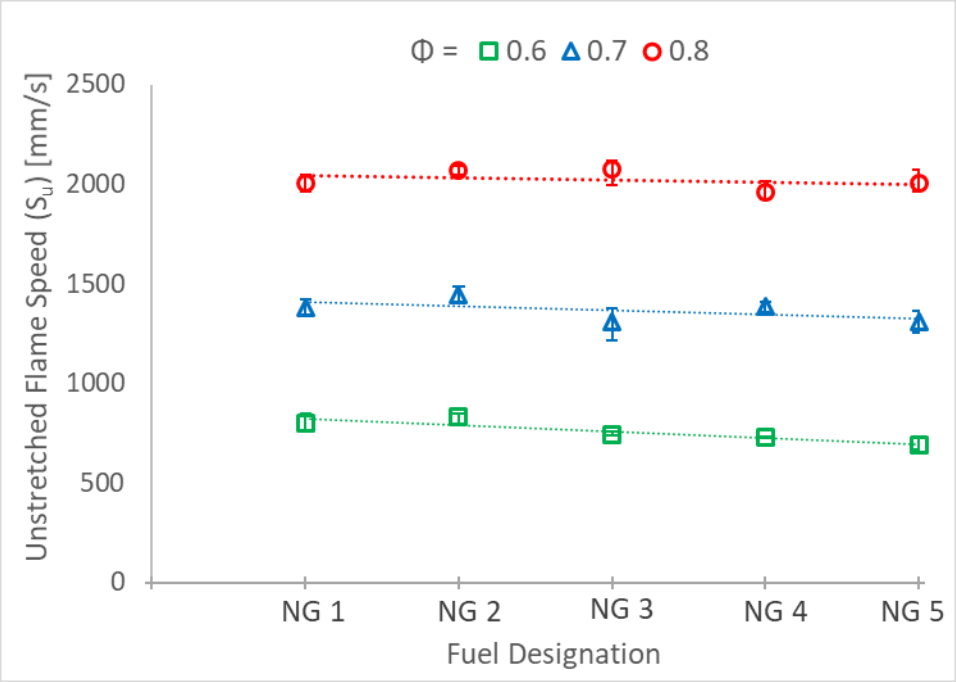

Figure 9.7 – Unstretched Flame Speed of Lean NG/H_2 Mixtures (T_u = 298 K, P = 0.1 MPa)

At near stoichiometric conditions (Φ = 0.8), all NG mixtures exhibit near identical S_u, with the linear fitted relationship displaying a gradient close to 0, consequently indicating that changes in CH_4:C_3H_8 fractions yield minimal impact on attained flame propagation. At equivalent Φ, the previously tested binary blends (CH_4/H_2, C_3H_8/H_2, CH_4/C_3H_8 (85/15%) vol.), CH_4 based fuels exhibited similar marginal gains in S_u upon H_2 or C_3H_8 addition, in good agreement with minimal variations in S_u observed for the tested NG blends. At leaner conditions, H_2 or C_3H_8 enrichment resulted in important relative increases in attained S_u for CH_4 based mixtures. This flame enhancement is also exhibited by the NG mixtures, with variations in CH_4/C_3H_8 fractions impacting attained S_u values, represented by the negative gradient displayed by the fitted linear relationship (i.e. green dotted line, Φ = 0.60, Figure 9.7). In terms of average relative difference, NG 1 (highest C_3H_8 fraction) with respect to NG 5 (lowest fraction of C_3H_8), displays an average augmentation in S_u of ~17%.

The sensitivity analysis performed in Section 8.2.5, concluded that observed augmentations in flame propagation of ultra-lean (Φ = 0.65) CH_4/H_2 flames (up to 50% H_2 vol.) was principally an Arrhenius effect (kinetic), through the reduction of the global activation energy (E_a), with this effect substantially weaker for C_2H_6/H_2 and C_3H_8/H_2 flames,

whilst still remaining the dominant factor. Modelled changes in adiabatic flame temperature (T_{ad}) and E_a (evaluated using the E_a (2) method utilising the Aramco 1.3 reaction mechanism [157], Section 3.5) for the NG blends are presented in Figure 9.8, normalised to that of NG 5 (highest amount of CH_4, highest E_a). Evidently, at Φ = 0.8, marginal reductions in E_a are exhibited by the NG blends, in agreement with minimal measured changes in S_u exhibited by the tested NG blends (red dotted line, Figure 9.7). However, at the leanest conditions, blends with the highest C_3H_8 content (decreasing in the order of NG1 → NG5) display greatest reduction in E_a, in correlation with enhanced augmentation in measured S_u (green dotted line, Figure 9.7). It is noted that relative changes in the adiabatic flame temperature exhibited by the NG blends are negligible (< 1%), (Figure 9.8), irrespective of tested Φ, re-affirming that changes in attained S_u are principally kinetic in nature, not thermal (Section 8.2.5).

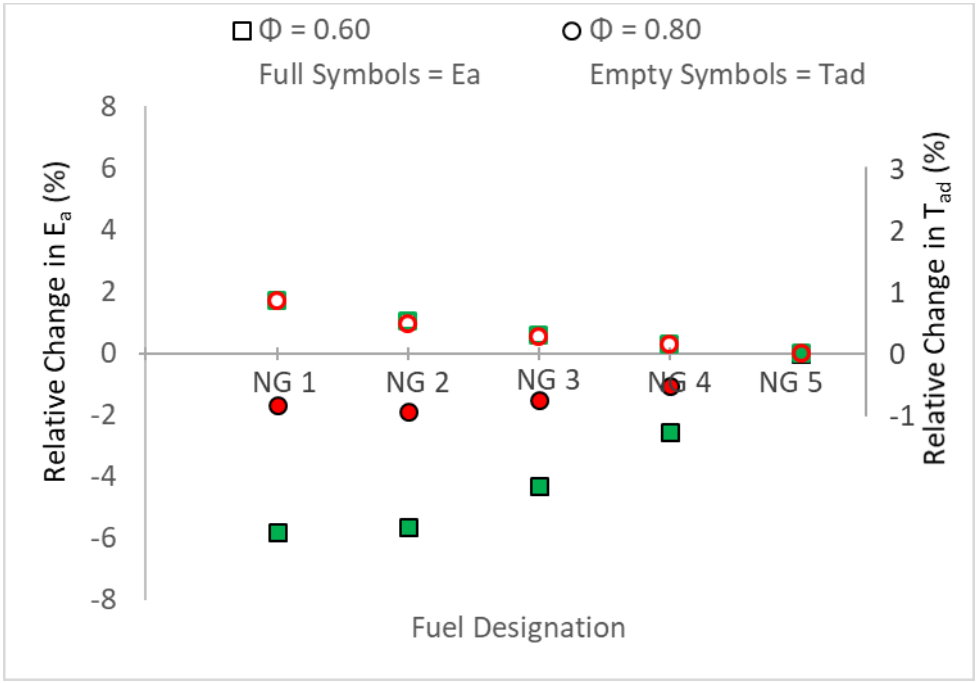

Figure 9.8 – Modelled Relative Change in E_a and T_{ad} for NG 1 – 5 – Normalized to that of NG 1

Since all tested NG compositions contain equal volumetric H_2 fractions (Table 9.1), changes in E_a are principally related to variations in CH_4:C_3H_8 content. The influence of small 15% volumetric additions of C_3H_8 and H_2 on E_a displayed by CH_4-based blends was previously quantified and discussed (Sections 7.1.7 – 7.2, Tables 7.1 – 7.3), with C_3H_8 addition yielding a greater reduction than H_2 on CH_4 flames (for equal volumetric fractions up to 15%). Since H_2 and C_3H_8 fuels display higher heat of combustion per mass than CH_4, as previously discussed, measured changes in S_u are directly correlated to changes in volumetric heat release rates (Q'), with production of key radicals, notably H, influencing CH_4 oxidation mechanisms. Relative changes in modelled Q' and concentrations of H radicals, for the NG 1 – 3 – 5, normalised to that of pure CH_4 are presented in Figure 9.9 and 9.10, respectively.

As expected, NG blends containing the highest volumetric concentrations of C_3H_8 and a fixed H_2 content (15% vol.) yield greatest augmentation in modelled Q', with enhancement promoted with decreasing Φ, as illustrated in Figure 9.9. The same trend is sustained with respect to modelled H radical production concentrations, depicted in Figure 9.10, further validating the trends in measured S_u of the NG blends (Figure 9.7).

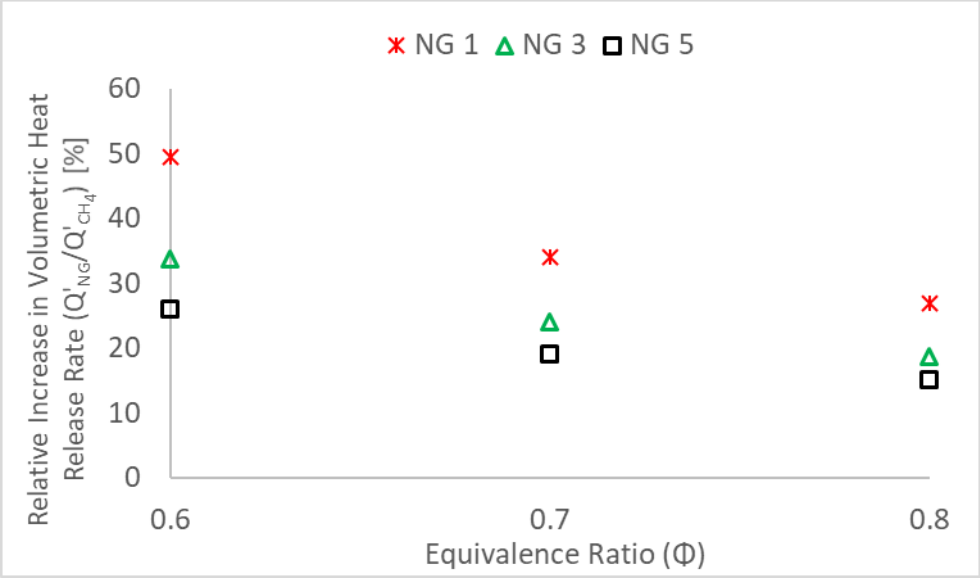

Figure 9.9 – Relative Increase in Modelled Q' for NG 1, 3, 5 Flames – Normalised to that of CH4

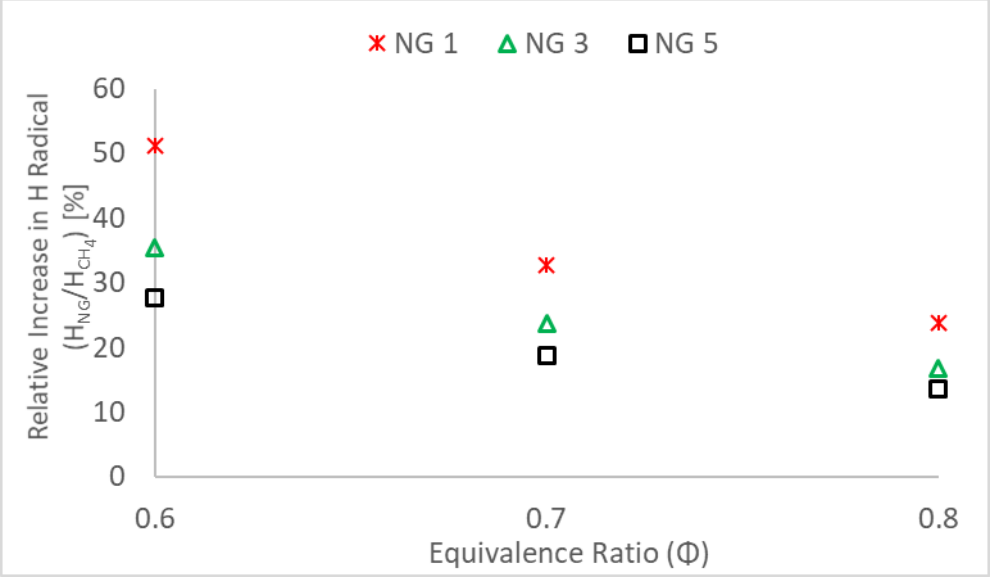

Figure 9.10 – Relative Increase in Modelled H Radical for NG 1, 3, 5 Flames – Normalised to that of CH_4

Experimental and numerical U_L values generated utilising the Aramco 1.3 [157] and USC II [156] reaction mechanisms for the tested NG mixtures are presented in Figure 9.11. The evaluated reaction mechanisms predict a marginal decrease in U_L with decreasing C_3H_8 concentration (NG 1→ NG 5), in agreement with measured U_L values, particularly at leanest conditions. In general, best agreement is again observed with Aramco 1.3, with most measured data points exhibiting correlation with numerical predictions.

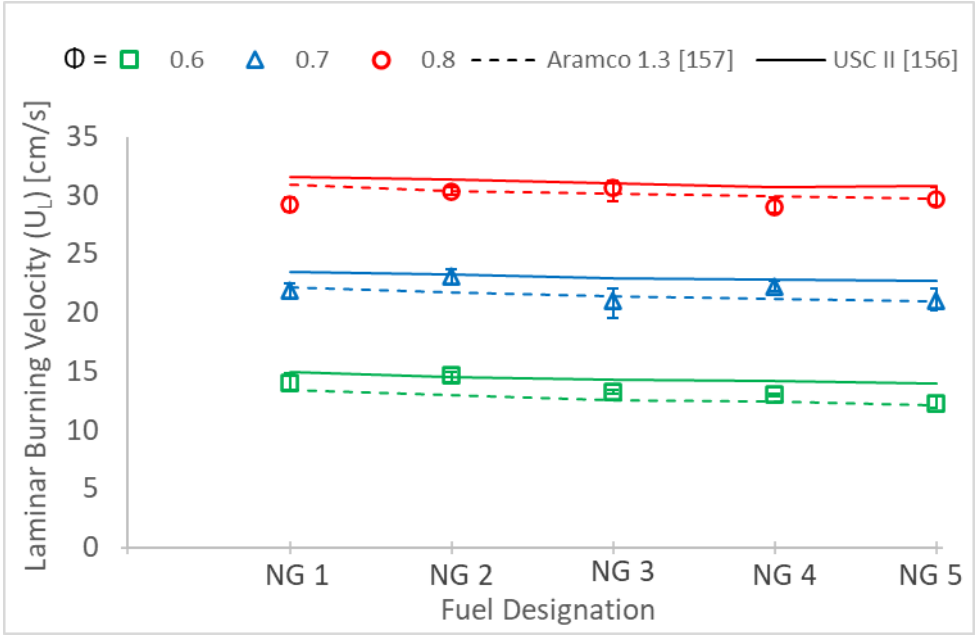

Figure 9.11 –Measured and Modelled U_L of NG Blends

Evidently, the presence of H_2 and C_3H_8 (~15% vol.) augments the burning intensity of ultra-lean CH_4-based fuels, potentially affording leaner blow-off limits, with associated decreased adiabatic flame temperatures, resulting in reductions in harmful emissions [105]. However, H_2 and C_3H_8 flames exhibit fundamentally different thermo-diffusive combustion mechanisms (Le << 1, - L_b, Le >>1, + L_b) yielding opposite susceptibility to preferential-diffusional instability on lean CH_4 flames, with divergences exacerbated at the leanest conditions. Since, dry low emission gas turbines (DLE-GT) operate at ultra-lean and highly turbulent (highly stretched) environments (Φ = 0.45 – 0.60), differences in stretch-related behaviour may possibly be intensified, altering expected flame behaviour, with potential for detrimental phenomena such as flashback. Likewise, DLE-GT are highly sensitive to fuel variation, and often individually optimised, set-up and tuned to tolerate limited changes in fuel composition [28]. With the increased facilitation of LNG trade coupled with the prospect of hydrogen injection in national gas grids (Section 1.2.2), the issue of interchangeability of NG is of importance and discussed in the subsequent section.

9.2 Practical Implications – Interchangeability of Natural Gas

As discussed in Chapter 1, the Wobbe Index (WI) (Eqn. 1.1, Section 1.3.2), is a common indicator employed in the GT industry to evaluate the incoming fuel's energy density and interchangeability, directly related to the power input into the burner (Eqn. 1.2), for a given fuel supply and combustor conditions. Thus, two fuel mixtures of different compositions, but exhibiting the same WI, will yield identical power input into the system. It follows, the greater the changes in WI, the greater flexibility is demanded from the combustion and control systems, to achieve the designed power output. Commonly, GT manufactures specify a range of ± 5% of the tuned WI (with ranges of ±2% and ±10% specified [28]), and maximum levels of heavier hydrocarbons (C_2+) and inert gases (i.e. N_2, CO_2), to ensure that the gas predominantly behaves as CH_4.

The EASEE-gas (European Association for the Streamlining of Energy Exchange), have proposed a WI range (46.46 – 54 MJ/m^3), much broader than customarily experienced in the E.U (Figure 1.6), with OEM's and operators having expressed concerns over such wide WI, with respect to efficiency, safety and emissions [36]. Several binary blends and NG mixtures investigated in this thesis display associated WI values falling within the proposed EASEE-gas regulations, with experimental work conducted at AFRs (Φ = 0.60) relevant to low emission power generation GT operating windows (Φ = 0.45 – 0.60). The influence of fuel composition variation on fundamental flame parameters has been numerically and experimentally quantified, allowing discussion of interchangeability of NG and analysis of proposed WI range.

Common gas quality indicators used in the GT industry namely; the WI, Higher and Lower Heating Value (HHV – LHV) and specific gravity are presented for tested NG and binary mixtures, in Tables 9.2 & 9.3 (a), with selected experimentally and numerically attained fundamental flame parameters given in Table 9.2 & 9.3 (b), respectively. Note that, fuel quality indicators were evaluated following ISO 6979 [178], at a reference temperature and pressure of 288.15 K and P = 0.11 MPa, for an N_2/O_2 air ratio of 79.05 – 20.95 (vol.%), utilising the application provided in [179]. Numerically attained fundamental flame parameters (T_{ad}, U_L) were calculated employing the Aramco 1.3 reaction mechanism [157] applying the same conditions as previously detailed. Extrapolation methods employed for experimentally derived values (L_b, U_L), follow Chen's recommendations [84], LM(C) and NM(S), for fuel mixtures exhibiting Le > 1 and Le < 1, respectively. Finally, building from conclusions drawn from this work, tabulated Le_{eff} values (i.e. Le_V, Le_D, Le_H) for presented blends represent models which yielded best correlation with measured L_b behaviour of the respective fuel mixtures.

Table 9.2 (a) – Fuel Quality Indicators of Natural Gas Mixtures

Fuel Designation ($CH_4/C_3H_8/H_2$) vol.%	Molar mass (Kg/Kmol)	Molar H:C Ratio	Mass H:C Ratio	Density (Kg/m^3)	Specific gravity	LHV (MJ/m^3)	HHV (MJ/m^3)	WI (MJ/m^3)
NG 1 – (68/17/15)	18.708	3.681	0.309	0.793	0.647	39.418	43.545	54.117
NG 2 – (73.1/11.9/15)	17.277	3.838	0.322	0.732	0.598	36.718	40.650	52.582
NG 3 – (76.5/8.5/15)	16.323	3.961	0.332	0.692	0.565	34.920	38.723	51.539
NG 4 – (78.2/6.8/15)	15.846	4.028	0.338	0.671	0.548	34.021	37.760	51.012
NG 5 – (79.9/5.1/15)	15.369	4.101	0.344	0.651	0.531	33.123	36.798	50.480

Table 9.2 (b) – Experimental and Numerical Fundamental Flame Properties of Natural Gas mixtures – $\Phi = 0.60$ ($T_u = 298$ K, P = 0.1 MPa)

Fuel Designation ($CH_4/C_3H_8/H_2$) vol.%	Flame Temp T_{ad} (K)	Laminar Burning Velocity U_L (cm/s) Experimental	Laminar Burning Velocity U_L (cm/s) Aramco 1.3 [157]	Markstein Length L_b (mm)	Effective Lewis Number (Le_{eff})
NG 1 – (68/17/15)	1688	14.06	13.36	0.639	$Le_V = 1.05$
NG 2 – (73.1/11.9/15)	1683	14.63	12.92	0.330	$Le_V = 1.01$
NG 3 – (76.5/8.5/15)	1679	13.19	12.57	0.183	$Le_V = 0.98$
NG 4 – (78.2/6.8/15)	1677	12.97	12.38	0.057	$Le_V = 0.96$
NG 5 – (79.9/5.1/15)	1674	12.31	12.13	-0.041	$Le_V = 0.95$

Table 9.3 (a) – Fuel Quality Indicators of Selected Blends

Fuel Composition (vol.%)	Molar mass (Kg/Kmol)	Molar H:C Ratio	Mass H:C Ratio	Density (Kg/m^3)	Specific gravity	LHV (MJ/m^3)	HHV (MJ/m^3)	WI (MJ/m^3)
CH_4 – (100)	16.042	4.000	0.336	0.680	0.555	34.016	37.781	50.724
CH_4/H_2 – (85/15)	13.938	4.353	0.356	0.590	0.482	30.432	33.913	48.860
CH_4/C_3H_8 – (85/15)	20.250	3.538	0.297	0.859	0.701	41.960	46.297	55.285
CH_4/C_3H_8 – (98/2)	16.604	3.923	0.329	0.704	0.574	35.073	38.915	51.351
CH_4/C_3H_8 – (96/4)	17.165	3.852	0.323	0.728	0.594	36.131	40.049	51.972
CH_4/C_3H_8 – (94/6)	17.726	3.786	0.318	0.752	0.613	37.189	41.183	52.587
CH_4/C_3H_8 – (92/8)	18.287	3.724	0.313	0.775	0.633	38.249	42.318	53.196
CH_4/C_3H_8 – (90/10)	18.848	3.667	0.308	0.799	0.652	39.308	43.454	53.800

Table 9.3 (b) – Experimental and Numerical Fundamental Flame Properties of Selected Blends – Φ = 0.60 (T_u = 298 K, P = 0.1 MPa)

Fuel Designation (vol.%)	Flame Temp. T_{ad} (K)	Laminar Burning Velocity U_L (cm/s) Experimental	Laminar Burning Velocity U_L (cm/s) Aramco 1.3 [157]	Markstein Length L_b (mm)	Effective Lewis Number (Le_{eff})
CH_4 – (100)	1664	7.85	10.12	-0.327	Le ≈ 1.00
CH_4/H_2 – (85/15)	1667	10.59	11.43	-0.855	Le_D = 0.78
CH_4/C_3H_8 – (85/15)	1681	11.54	11.83	1.215	Le_H = 1.36
CH_4/C_3H_8 – (98/2)	1666	9.51	10.41	0.197	Le_H = 1.05
CH_4/C_3H_8 – (96/4)	1669	9.30	10.55	0.452	Le_H = 1.11
CH_4/C_3H_8 – (94/6)	1672	10.14	10.93	0.801	Le_H = 1.17
CH_4/C_3H_8 – (92/8)	1674	11.35	11.15	0.916	Le_H = 1.21
CH_4/C_3H_8 – (90/10)	1676	11.62	11.38	0.975	Le_H = 1.26

The relationship between the WI and heavier HC content (C_2+) is illustrated in Figure 9.12, for tested NG and binary fuel blends and LNG mixtures from different locations (LNG compositions in Table 1.1)[32][33], with the proposed EASEE-gas WI guidelines superimposed.

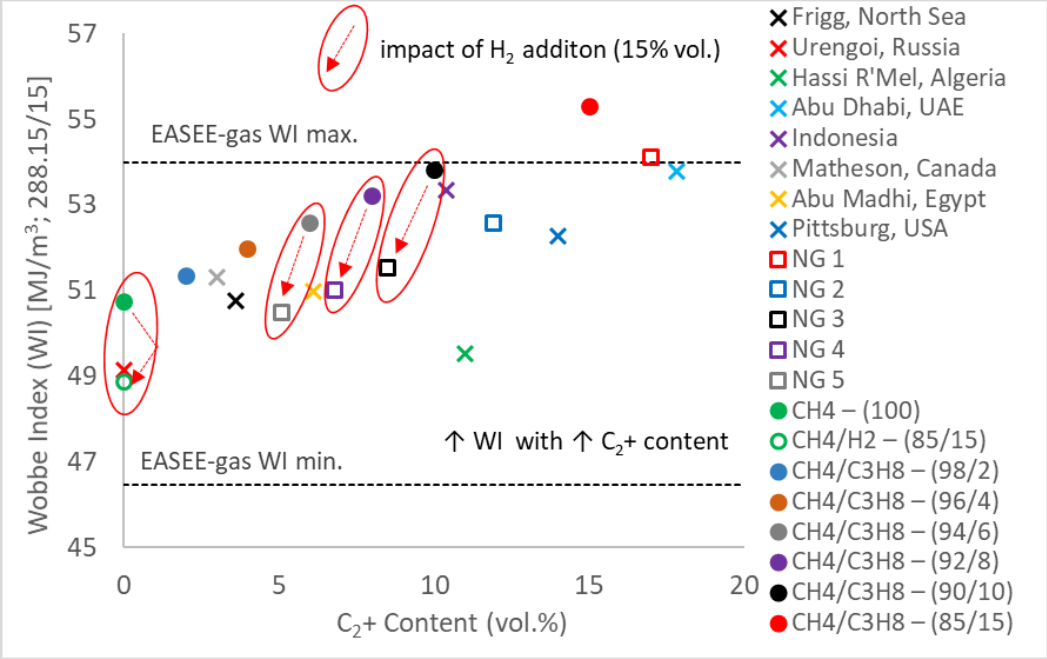

Figure 9.12 – Wobbe Index of Selected Fuel Mixtures vs Heavier Hydrocarbon Content

As expected, WI augments with increasing heavier hydrocarbon content, with a linear increase observable in WI of the CH_4/C_3H_8 blends with increasing C_3H_8 fraction (coloured circles, Figure 9.12). H_2 addition to NG yields a reduction in WI, exemplified by the downwards shift displayed by CH_4 and CH_4/C_3H_8 blends upon 15% volumetric additions of H_2 (superimposed red ellipses, Figure 9.12). This is a consequence of the method by which WI is evaluated, employing the specific gravity and heating values of the fuels (Eqn. 1.1). Although the heating values of H_2 are significantly lower than CH_4 (i.e. LHV/HHV: 10.22/12.10 and 34.78/37.78 (MJ/m^3) for H_2 and CH_4), they are compensated by H_2's low-density (specific gravity ~ 0.07 and 0.56 for H_2 and CH_4), resulting in similar WI values, 40-48 and 47-53 MJ/m^3 for H_2 and CH_4, respectively. Consequently, the wide EASEE proposed WI range would allow entry of most LNG sources into European pipeline distribution infrastructure, including Emirati LNG (Abu Dhabi, UAE) containing ~18% (vol.) C_2+ and CH_4/H_2 blends enriched up to ~34% H_2 (vol., WI = 46.47 (MJ/m^3)).

The WI of tested NG and binary blends are illustrated against measured L_b in Figure 9.13, for an Φ = 0.60, with depicted fuel mixtures possessing comparable adiabatic flame temperatures and numerical U_L values, with differences < 25 K and 3 cm/s (Tables 9.2 – 9.3 (a)), respectively, and differences in experimental U_L < 7 cm/s. However, illustrated fuel

mixtures in Figure 9.13, exhibit fundamentally different thermo-diffusive properties and measured stretch-related behaviour, with additions of H_2 and C_2+ fuels yielding opposite susceptibility to preferential-diffusional flame instability (Le << 1, - L_b, Le >>1, + L_b) of ultra-lean CH_4 based fuels (Figure 9.13). Clearly, the WI parameter, by its method of calculation masks potential changes in reactivity of alternative fuels (NG with high contents of C_2+ and H_2), with the WI unable to capture changes in thermo-diffusive response of the flame due to variations in compositional make-up of the fuel.

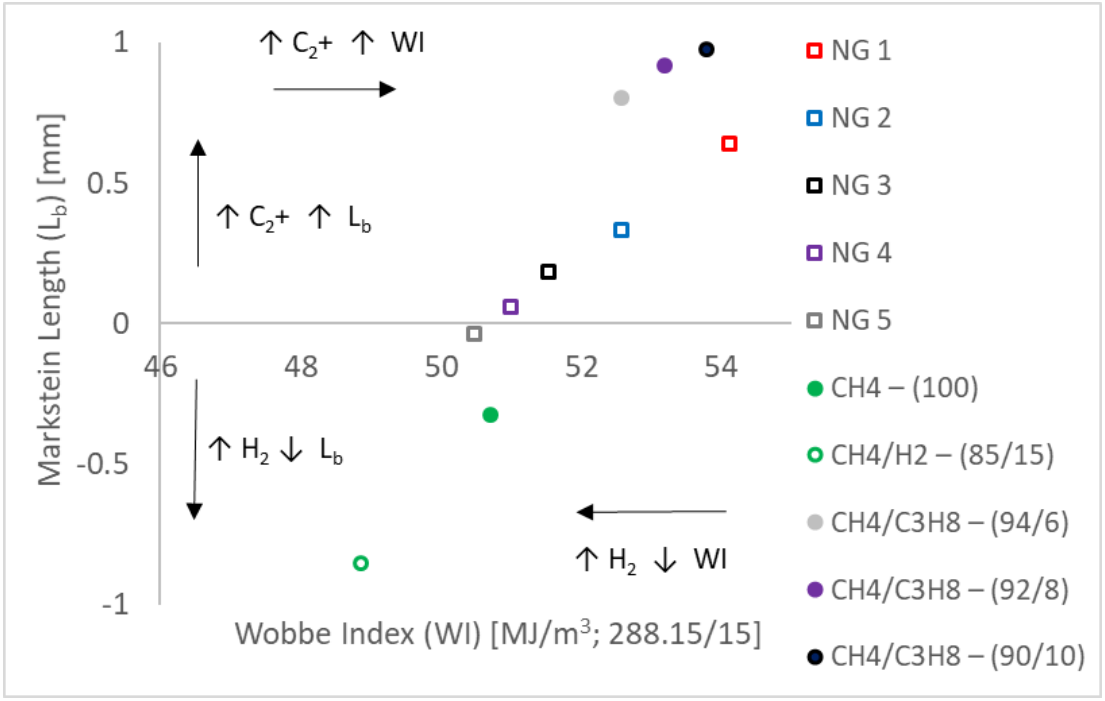

Figure 9.13 – Wobbe Index of Selected Fuel Mixtures vs L_b (Φ = 0.60, T_u = 298 K, P = 0.1 MPa)

Recognising the above, modern DLE-GT systems have feedback control systems that allow for smooth operation when the incoming NG WI deviates from the manufacture's requirements (typically ± 5% [28]). Since WI is unable to capture changes related to increased or decreased thermo-diffusivity, reactivity and physical flame response, contemporary control systems may not be adequate if relatively important variations in volumes of H_2/C_2+ HCs are present. Furthermore, control feedback systems only act retrospectively, meaning that sudden large variations in NG compositions or H_2 enrichment, may not be compensated quickly enough to avoid for example: flame blow-off (extinguishment), flashback, or the output of undesirable and excessive polluting emissions.

Acknowledging, that all presented experimental work is based on spherically expanding laminar flames, tested at atmospheric temperature and pressure, work was undertaken to practically assess gained insight to a premixed, lean limit, turbulent flame, using a premixed generic swirl burner.

9.3 Application to a Premixed, Swirling, Lean Limit, Turbulent Flame

A series of experiments were conducted using a premixed generic swirl burner, housed within a high-pressure optical chamber (HPOC), at Cardiff University's Gas Turbine Research Centre (GTRC). Combustion mechanisms in a GT combustor are far more complex and involved, due to turbulent chemistry interactions, aerodynamics of flow-fields and stretch and curvature effects, in comparison to freely propagating SEF presented in this thesis. Consequently, the following results do not intend to satisfactorily describe turbulent swirling flames, predict or attempt to match real engine behaviour which would require a detailed parametric study. The approach discussed here should be viewed as a first step towards an improved evaluation of the impact of thermo-diffusive instabilities due to changes in fuel composition on flame reactivity, with attention focused on the lean blow off (LBO) limit of alternative NG fuel mixtures. Potentially, a modified method based upon a Lewis number (Le) scaling could hypothetically be developed to improve the evaluation procedure of defining operational conditions potentially affording higher flexibility of GTs and thus extended acceptable fuel ranges. In order to so, comparison with full scale GT combustion tests would be required and measurement and quantification of certain turbulent combustion parameters necessary.

9.3.1 Lean Blow-off Limit

As discussed in Chapter 2, flame positioning and consistency, coupled with instabilities that are caused from oscillations in pressure, are important issues involved with premixed burner operability [34]. These parameters are directly related to U_L, with a stabilised flame occurring when the reactant flow is balanced with the flame velocity [42] (Section 2.1.2). As such, flame propagation mechanisms determine the operational range of a premixed burner, both with respect to the lower and upper reactivity scale (LBO and flashback, Eqn. 2.3). Fuel composition naturally controls these processes, dictating chemical kinetics and fuel flow rate into the system, in order to achieve a target thermal power. Combustion theory [27], [41] underlines that blow-off occurs when the flame propagation takes more time than the residence time available for both mixing and reaction (i.e. when the chemical time scale (T_C) is larger than a characteristic residence time (T_R), $T_C > T_R$).

Lipatnikov and Chomiak [69], in their extensive review upon the effects of molecular transport effects on turbulent flame propagation and structure, underline that weak and strong turbulent premixed combustion is affected by preferential diffusional instabilities (Le effects). The influence of thermo-diffusive instability was physically observed in Schlieren

images capturing the transition from smooth to cracked flame fronts of lean CH_4/H_2 flames (Φ = 0.65, 50% H_2 vol., Figure 8.12), a precursor to cellularity. Once the cellular structure has been established, the increased flame surface area results in flame acceleration, with instabilities leading to an autonomous regime [75], by which the cells continue to grow and divide, with evidence implying that, this phenomenon potentially results in '*self-turbulization*' of the flame [180], [181].

For a premixed turbulent flame, a dominant factor to assess the burning rate is the degree to which the flame front is wrinkled. Higher turbulences, generate enhanced wrinkling of the flame front, which consequently increase the turbulent burning rate [182]. Local variations in propagation speed are characterised by the Markstein number (Markstein Number = L_b/δ), with L_b as discussed throughout this thesis, representing a measure of the flame's response to curvature and strain, flame's sensitivity to stretch, and thus susceptibility to hydrodynamic instabilities.

9.3.2 Blend Selection and Rig description

Three fuel blends used in the SEF experiments were selected in relation to their exhibited fundamental flame parameters and opposite thermo-diffusive behaviour (Table 9.3(b)), namely 100% CH_4, CH_4/H_2 (85/15%) and CH_4/C_3H_8 (85/15%) (vol.%). As discussed earlier, at ultra-lean conditions (Φ = 0.65), CH_4 (100%) displays Le ≈ 1, suggesting near equidiffusion of heat and mass transport mechanisms, with measured slope inversion of L_b at ~0.6 – 0.65 ($L_b \approx 0$), thus exhibiting flame propagation practically independent of stretch rate. Upon H_2 addition, ultra-lean CH_4/H_2 based fuels exhibit negative L_b, implying a mass-driven combustion process (Le < 1), with flame propagation accelerating with increasing stretch. Upon C_3H_8 enrichment, the opposite behaviour was observed, with flames exhibiting + L_b, indicating a thermally driven combustion process (Le >1), with flame propagation decelerating with increasing stretch effects. Since, swirl burners can generate highly turbulent (i.e. stretched) environments, opposite behaviour in flame propagation are expected to be amplified, reflected in differences in attained LBO limits, despite similar U_L and adiabatic flame temperature (T_{ad}) values exhibited by all three fuel mixtures.

Experiments were conducted using an established, well-characterised [183]–[186] premixed generic swirl burner, with a multi-component schematic of the main elements of the burner and casing assembly illustrated in Figure 9.14. The fuel and oxidiser enter the burner inlet plenum (Fig. 9.14 (a)), through fixed piping or metallic flexible hose, with Coriolis meters (±0.35%) quantifying their respective mass flows. The burner resides within a pressure casing (Fig. 9.14 (b)) rated at 1.6Mpa at 900 K. Once the reactants enter the burner plenum, they move through the premix chamber (Fig. 9.14 (c)), to a single radial tangential

swirler (Fig. 9.14 (d)) and exit the burner nozzle (0.04 m diameter) ((Fig. 9.14 (e)). Optical access was available through diametrically opposed quartz windows (Fig. 9.14 (f)). A cylindrical quartz exhaust confinement tube with an expansion ratio of 3.5 from the burner exit nozzle was utilised during the tests. Thermocouples (k and n-type, ± 2.2 K) were mounted to measure key rig temperatures, recording the temperature of reactants entering the burner inlet plenum ((Fig. 9.14 (T1)), the recirculated and radiated heat from combustion ((Fig. 9.14 (T2)) and exhaust temperature at burner exist ((Fig. 9.14 (T3)).

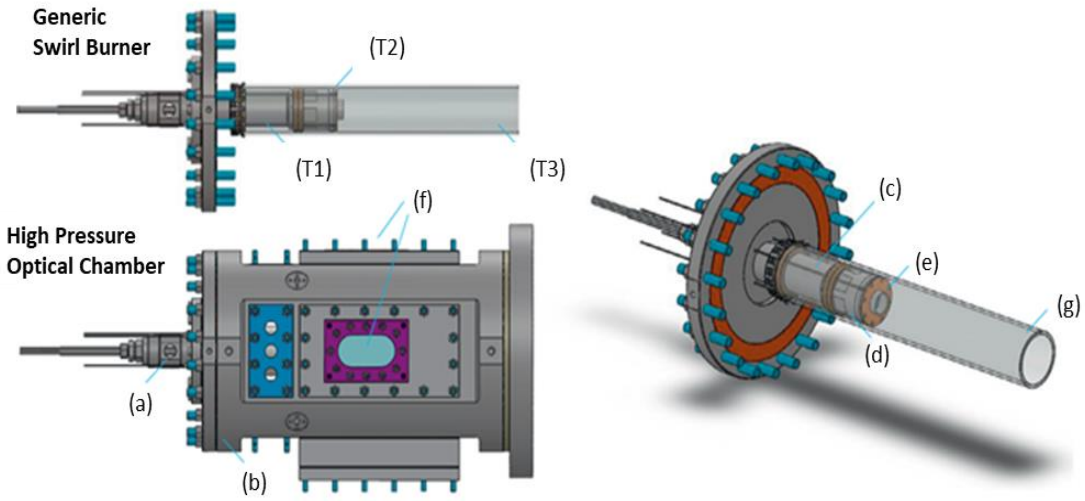

Figure 9.14 – Multi-component Schematic of Burner Assembly and Optical Casing (with Components as described in text) Adapted from [183]

9.3.4 Testing Procedure and Conditions

A series of experiments using the generic swirl burner were conducted at inlet temperature of 289 K (± 2K) and 579 (± 5K) (T1, Figure 9.14) at atmospheric conditions (0.11 MPa (± 0.005 MPa)), at three different thermal powers, namely: 25, 42, and 55 kW. For each experimental condition the lean stability limit was evaluated. To do so, the fuel mass flow was fixed, and the flame was stabilised at an Φ = 0.65. The Φ was driven towards leaner conditions by gradually increasing air mass flow rate using a digitally controlled needle valve at steps of ~0.2 g/s. Lean blow-off was defined as the Φ that generated a detachment from the outlet nozzle, resulting in a lifted flame, stabilising downstream in the quartz confinement tube, which was visually monitored. Figure 9.15 illustrates an example of a lean, swirling premixed stable CH_4/H_2 flame ahead of the burner edge. Prior research conducted at Cardiff University, using a similar experimental rig and methodology to evaluate lean blow-off limits of heavily carbonaceous syngas can be found in [183].

All experiments were conducted using a radial-tangential swirler, with a geometric swirl number of 0.8, with further information concerning the swirler geometry available in [184]. In order to minimise the impact of local heat loss for experiments conducted at elevated temperatures, the entire rig was pre-heated for ~60 mins prior to combustion trials, with temperature evaluated through monitoring at the quartz outlet (T3, Figure 9.14). The compressed air employed was dried in a chiller, prior to entering the distribution pipe network, with monitoring of a hygrometer measuring humidity at the plenum inlet effectively ensuring that the incoming combustion air could be assumed dry, with fuel delivered from cylinder packs with a 1% associated full-scale uncertainty for each mixture component.

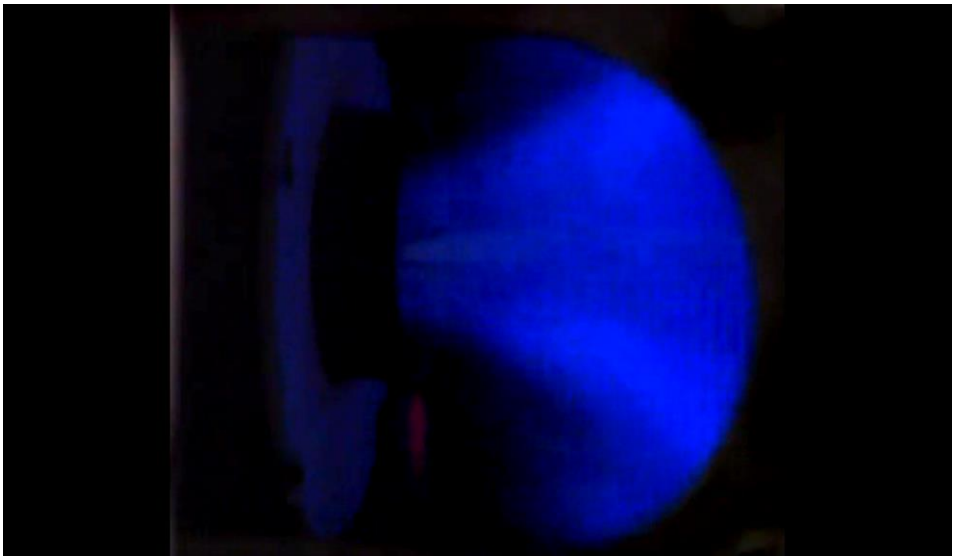

Figure 9.15 – Camera Still of a Lean Premixed Turbulent Swirling CH_4/H_2 Flame

9.4 Lean Stability Limit Results and Discussion

Rig data was acquired on a 1 second interval basis (i.e. temperature, pressure, mass flow rates of reactants, etc.) with all presented results representing an average of the relevant parameter over the course of 60 seconds prior to the recorded LBO limit. Three nominally identical experiments were conducted at each condition. The measured LBO limit of the tested fuels against thermal power and bulk exit velocity are illustrated in Figures 9.16 & 9.17, respectively, with empty and coloured symbols representing measurements at 289 K and 579 K, correspondingly. To assist discussion and analysis, Figures 9.18 and 9.19, illustrate modelled U_L and T_{ad} of the tested blends, respectively, evaluated at the measured LBO limit (Φ), employing the Aramco 1.3 reaction mechanism [157], with measured L_b behaviour of all three fuel mixtures depicted in Figure 9.20.

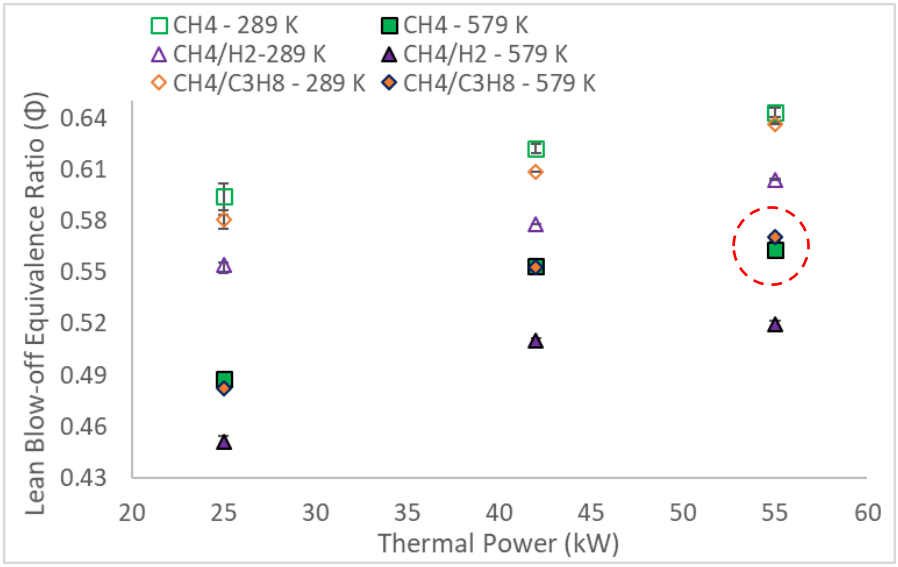

Figure 9.16 – Lean Blow-off limit of Selected Mixtures against Thermal Power

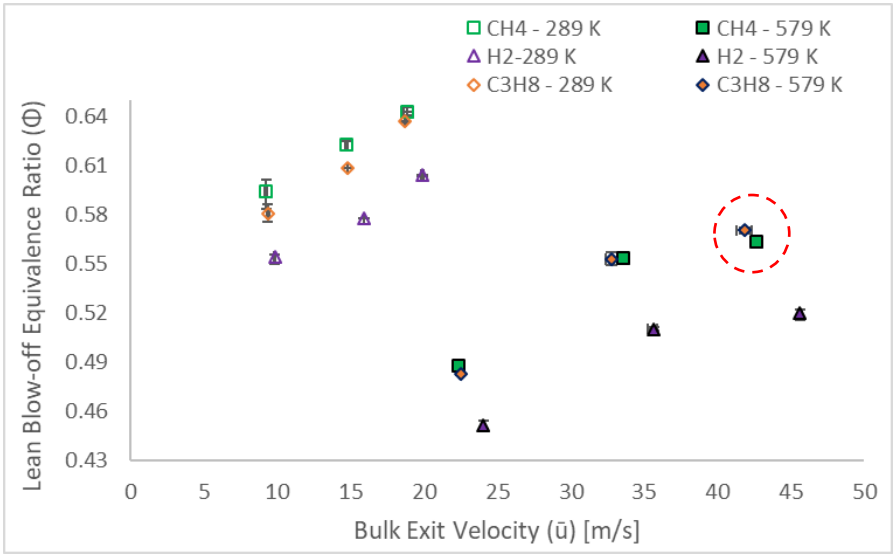

Figure 9.17 – Lean Blow-off limit of Selected Mixtures against Bulk Exit Velocity

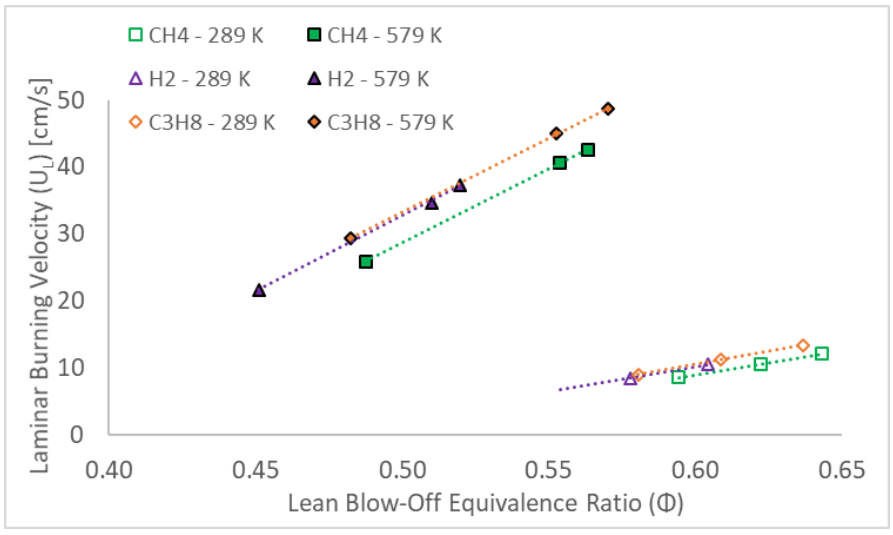

Figure 9.18 – Lean Blow off against modelled Laminar Burning Velocity

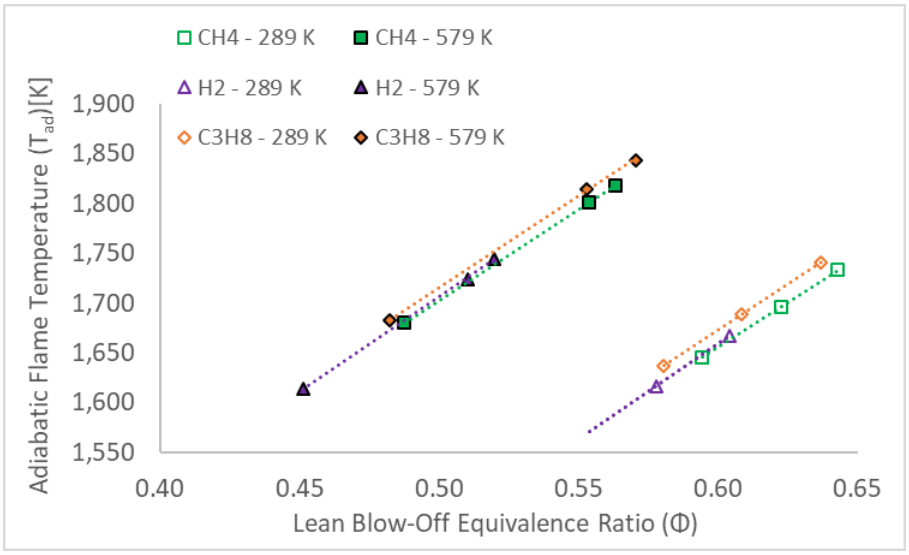

Figure 9.19 – Lean Blow Off against Modelled Adiabatic Flame Temperature

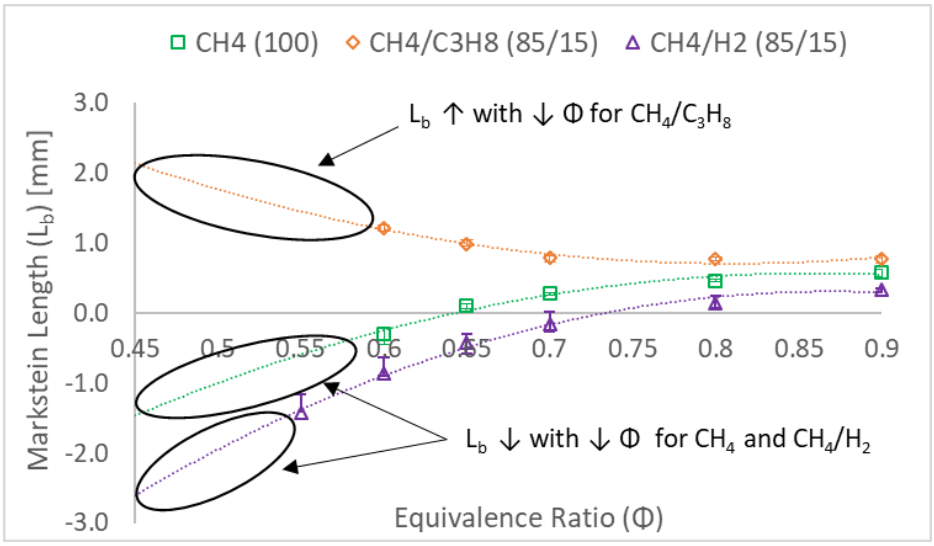

Figure 9.20 – Markstein Length of Blends – Experimental and Extrapolation

Prior to presenting results, note that analysis of measured of LBO limits is structured in two parts, with results at T = 289 K and 579 K discussed separately. At T = 289 K, CH_4/H_2 and CH_4/C_3H_8 flames attained significantly different LBO limits, with CH_4/H_2 stabilising at leaner conditions than CH_4/C_3H_8 (Figure 9.16), although the CH_4/C_3H_8 mixture exhibits marginally higher modelled U_L and T_{ad} values (Figures 9.18 – 9.19). These differences in LBO stability are believed to be a consequence of the H_2 and C_3H_8 opposite thermo-diffusive characteristics (Le < 1, – L_b; Le > 1, + L_b, respectively). As a result, CH_4/H_2 flames, exhibit a propensity of acceleration in turbulent environments, inherent to mass-driven combustion. As discussed in previous result chapters, equal 15% volumetric additions of H_2 and C_3H_8 have a similar impact on global activation energy, burning rate and production of key radicals of CH_4 based fuels. As such, differences in attained LBO limits are thought to be a consequence of preferential diffusion, influencing the relationship between flame stretch and propagation,

allowing the CH_4/H_2 mixture to achieve leaner flame stability. Furthermore, it is deemed important to underline that CH_4/H_2 (WI = 48.86) and CH_4/C_3H_8 (WI = 55.29) display a WI that fall within or marginally higher (for CH_4/C_3H_8, WI = 55.29) to the proposed EASEE-gas WI regulations (46.46 – 54 MJ/m^3), but exhibit substantially different LBO stability limits.

With respect to CH_4 and CH_4/C_3H_8 flames, at Φs reflective of attained LBO limits (Φ = 0.58 – 0.65) measured L_b (Figure 9.20), suggests that flame stretch has little influence on CH_4 flame speed ($L_b \approx 0$, Le ≈ 1), with inhibition of CH_4/C_3H_8 flame propagation expected (+ L_b). It is observed that CH_4/C_3H_8 maintains marginally leaner stability limits than those measured for CH_4, potentially a result of CH_4/C_3H_8 flames exhibiting marginally higher U_L and T_{ad} (Figure 9.18 – 9.19). However, it is observed that differences in measured LBO limits between CH_4 and CH_4/C_3H_8 is greatest at lowest thermal power tested (lower bulk exit velocity) with differences reducing with increasing thermal power, at conditions where flame stretch is perceived to be the greatest (higher bulk exit velocity, Figure 9.17), at which condition both fuels under scrutiny display near identical measured LBO limits.

Focusing on results achieved at a reactant temperature of 579 K, it is recognised that increasing the reactant temperature (289 K -> 579 K), naturally increases both U_L and T_{ad} attained by the fuel mixtures, however, the same general trend in U_L and T_{ad} is maintained, with $CH_4/C_3H_8 > CH_4/H_2 > CH_4$ (Figures 9.18 – 9.19). Furthermore, measured L_b retain their relevance (Figure 9.20), since L_b has been demonstrated to be insensitive to the initial unburnt temperature, as discussed by Giannakopoulos et al. [161]. Likewise, thermal diffusivity (D_T) and mass diffusivity (D_{ij}) display a similar temperature dependence, in the order of $\alpha \sim T^a$ and $D \sim T^b$, with the 'a' and 'b' lying in the range of 1.5-2.0, respectively [61]. Consequently, Le is only slightly dependent on temperature, as discussed in Section 6.2.1, with changes in Le minimal when assessed at a reference temperature of 1000 K, for pure CH_4, C_3H_8 and H_2 fuels (Figure 6.23 (a),(c),(e)). Additionally, an increase in reactant temperature allows for the blends to be driven leaner, consequently increasing volumetric flowrates and thus bulk exit velocity.

As expected, at T = 579 K, the CH_4/H_2 blend continues to maintain leaner flame stability with respect to CH_4 and CH_4/C_3H_8 mixtures (Figure 9.16). In comparison to attained LBO limits at 289 K, differences in LBO limits between CH_4 and CH_4/C_3H_8 are observed to reduce at 579 K, with CH_4 exhibiting leaner flame stability with increasing thermal power (higher bulk exit velocity), than CH_4/C_3H_8 flames as highlighted in Figure 9.16 & 9.17 (red circle). Thus, although the CH_4/C_3H_8 still displays higher modelled U_L and T_{ad} values then CH_4 at LBO Φ (Figures 9.18 – 9.19), CH_4 attained marginally leaner LBO limits likely linked to the stretch effects exhibited by the flame at the highest temperature and power tested, brought

about by increased volumetric flowrates, potentially resulting in an augmentation of CH_4 turbulent flame speed.

Unfortunately, SEF experiments could not be conducted at Φ equal to the measured lean stability limit attained for the 579 K tests, in part due to insufficient ignition energy, limits of rig heating system (max. temp. achievable ≈ 450 K), as well as important buoyancy effects associated with SEF at ultra-lean conditions. Thus, to aid discussion, a line of best fit was superimposed on Figure 9.20, extrapolated to reflect expected L_b behaviour at the observed LBO limits. Testing at elevated temperatures (579 K) allows the flames to be driven leaner (reflected in a shift in LBO limits, Figure 9.16), towards Φs where L_b is exacerbated in opposite directions for the CH_4 and CH_4/C_3H_8 blends (Figure 9.20). The opposite influence of stretch on flame propagation, a consequence of preferential diffusion, is thought to be impacting the ability of the CH_4/C_3H_8 flame to stabilise at leanest conditions, allowing CH_4 to achieve marginally leaner stability limits.

Acknowledging that a detailed parametric study would be required to satisfactorily describe turbulent flame speed, presented results in LBO behaviour tend to underline the importance of accurately considering thermo-diffusive interactions. Often the ratio of turbulent to laminar flame speeds (S_T/U_L) are directly related to the Damköhler number (Da) and Reynolds number (Re), with Da and Re being respectively, inversely or directly proportional to u'/U_L [187] (u' = root mean square of the turbulent intensity). Thus, as $u' \rightarrow 0$, implies that $Da \rightarrow \infty$, $Re \rightarrow 0$, and the ratio of S_T/U_L tends towards 1 (i.e. turbulent and laminar flame speed are equal). However, from the experiments conducted above, the turbulent flame speed is affected by preferential diffusion, influencing stretch behaviour of laminar premixed flames, as witnessed through changes in lean blow-off stability limits, and thus should also be considered.

Non-unity Lewis number effects have been examined for lean turbulent premixed combustion mainly through simulations [70], [182], [188] using either H_2, CH_4 and C_3H_8 or a combination of those fuels in mixtures (due to their different respective Le properties). All studies agree that local burning rate is related to thermo-diffusive behaviour, with CH_4 relatively insensitive to flame curvature, whilst H_2 and C_3H_8 flames, show strong sensitivities to curvature, with burning enhanced for negative (positive) curvature indicating a thermo-diffusively stable (unstable) flame for C_3H_8 (H_2), analogous to L_b behaviour. Furthermore, Chakraborty and Cant [188] demonstrated using Direct Numerical Simulation (DNS), that for identical values of turbulence intensity (u'/U_L) and length scale ratio (integral length scale/ laminar flame thickness), flames exhibiting Le = 0.34 and 0.60 show counter-gradient transport whilst flames with Le = 1.0 and 1.2 display gradient transport, with the extent of counter-gradient transport increasing with decreasing Le. Brower et al. [70] underline that

the use of planar laminar burning velocities in estimating turbulent flame speeds for mixtures exhibiting Le > 1 tend to be over-predicted, with underprediction of turbulent flame speeds in the case of mixtures displaying Le < 1. All the above tend to agree and explain variations in lean stability witnessed for the CH_4, CH_4/H_2 and CH_4/C_3H_8 mixtures.

It thus seems that estimating turbulent flame speeds employing Le scaling merits further exploration. Potentially, a scaling approach similar to that employed by Brower et al. [70] for H_2/CH_4 mixtures (applying Le_D model) could be extended to CH_4/heavier hydrocarbons/H_2 mixtures, applying corresponding Le_{eff} models. Work would have to be extended to include full scale GT combustion tests with measurement and quantification of turbulent combustion parameters necessary. As a result, a simplified method based upon Le scaling could hypothetically lead to an improved evaluation procedure to find operational conditions that allow higher flexibility of GTs and thus extend acceptable alternative fuel range.

9.5 Chapter Summary

The combustion behaviour of lean (Φ = 0.60 – 0.80) Natural Gas (NG) mixtures, containing differing heavier hydrocarbon (HC) content and 15% H_2 enrichment (vol. %), was experimentally investigated, including analysis of measured Markstein Length (L_b), flame speed propagation, and effective Lewis number (Le_{eff}) models. The issue of interchangeability of NG was investigated, with fuel quality indicators such as the Wobbe Index (WI) examined with respect to ability in capturing changes in thermo-diffusive, reactivity and flame response behaviour of alternative fuels. Finally, the lean blow-off (LBO) stability limits of premixed turbulent CH_4, CH_4/H_2 and CH_4/C_3H_8 flames were examined using a generic swirl burner at two different unburnt reactant temperature (T_u = 289 and 579 K) and three thermal powers (25, 42 and 55 kW). From this work, the following conclusions can be taken:

- Changes in measured L_b behaviour of lean NG/H_2 flames (for a fixed volumetric H_2 fraction, 15% vol.) results from variations in fuel composition, with NG blends containing lowest and highest heavier HC content exhibiting analogous stretch-related behaviour to that of pure CH_4 ($\downarrow L_b - \downarrow \Phi$) and C_3H_8 ($\uparrow L_b - \downarrow \Phi$), respectively. CH_4/C_3H_8 containing a ~16:1 CH_4/C_3H_8 mol. fraction ratio exhibited L_b behaviour akin to that of pure C_3H_8 ($\uparrow L_b - \downarrow \Phi$), with H_2 addition (15%, vol.) resulting in mixtures containing a ~9:1 CH_4/C_3H_8 mol fraction ratio displaying behaviour analogous to that of CH_4 ($\downarrow L_b - \downarrow \Phi$).
- A Le_{eff} formulation based on a volume model was observed to yield best correlation with stretch-related behaviour of NG/H_2 blends (H_2 15%, vol.).
- Greatest relative changes in S_u due to variations in heavier HC content of tested NG/H_2 blends were observed at leanest conditions (Φ = 0.6). Modelling work suggests that differences in S_u are principally linked to reductions in E_a (kinetic), in agreement with conclusions presented for previously tests $C_{1\text{-}3}/H_2$ blends (Chapter 8). Experimental U_L values for NG blends display best correlation with Aramco 1.3 mechanism.
- Irrespective of inlet reactant temperature, CH_4/H_2 attained significantly leaner LBO stability limits than pure CH_4 and CH_4/C_3H_8, despite all tested blends exhibiting near-identical U_L and T_{ad}, a consequence of preferential diffusional instability, reflected in measured L_b behaviour. With respect to CH_4 and CH_4/C_3H_8, the latter attained marginally leaner limits than CH_4 at 289 K, with the opposite observed at 579 K, particularly at the higher power conditions where flame stretch is perceived to be the greatest, with measured LBO limits in correlation with measured L_b behaviour of tested fuel mixtures.

Conclusions and Future Work

Increased reliance on liquified natural gas, potentially containing high concentrations of heavier hydrocarbons, typically ethane and propane, coupled with the emerging prospect of hydrogen injection into national gas grids, presents associated combustion impacts not fully appreciated. This new reality underlines the necessity of developing understanding of fundamental combustion characteristics, ultimately guiding the design of future highly flexible, efficient and safe gas turbines. This thesis aimed to characterise fundamental combustion performance of methane-higher-hydrocarbon-hydrogen fuels, representative of fuels variations and at air fuel ratios expected in premixed low-carbon power generation facilities. From this study, the following conclusions and recommendations, as listed below, can be taken.

I. Extrapolation Methods and Quantification of Experimental Uncertainty

Spherically expanding flames require the utilisation of extrapolation relationships to yield unstretched flame speeds (S_u) devoid of stretch effects and corresponding Markstein length (L_b) value, for example the classical linear relationship between flame speed and L_b (LM(S)). A comprehensive literature review highlighted the scarcity of available S_u and L_b data (for the fuels tested), corrected using more-sophisticated and contemporary linear and non-linear relationships based on curvature and stretch (LM(C) & NM(S), respectively), which account for variations in thermo-diffusive behaviour (Lewis Number effects, Le). In order to fulfil this knowledge gap, various extrapolation models have been appraised throughout the course of this study for a variety of fuel blends under lean conditions (Φ = 0.6 – 1.0). It was concluded that failure to employ a suitable model resulted in:

- For fuels displaying Le ≈ 1 (CH_4), average relative differences in attained S_u and L_b values are < 2% and 15%, respectively, irrespective of extrapolation model employed.
- For fuels exhibiting Le >> 1, (C_2H_6, C_3H_8, C_4H_{10}), utilisation of LM(S), relative to LM(C) results in overprediction of S_u by < 10% and L_b values up to 80%, with differences increasing with decreasing Φ and increasing Le. Application of NM(S) yields underpredicted S_u and L_b values, < 3% and < 20%, respectively, relative to LM(C).
- For fuels exhibiting Le < 1 (CH_4/H_2 up to 50% vol. H_2, Φ = 0.65), utilisation of LM(S) and LM(C), relative to NM(S), results in an underprediction of S_u < 1%, and L_b values, < 20% and < 8%, respectively.

For ostensibly identical experimental conditions, large scatter in published attained flame speeds and L_b datasets employing the SEF configuration, comparable data-processing and extrapolation methodologies was observed. Thus, to better understand the nature of these discrepancies, a series of 20 experiments on lean (Φ = 0.70) and stoichiometric CH_4/air mixtures at nominally identical conditions (T_u= 298 K, P = 0.1MPa) was conducted. Experimental uncertainties related to the employed configuration were quantified using modelled results. It was observed that:

- For the combustion vessel employed, to produce results devoid of ignition or confinement influences in both planes of measurement (vertical and horizontal), a flame radius range of 8 – 35 mm, with an extrapolation range of 10 – 30 mm is recommended.
- The impact of flame radius selection, for a 10 mm radius increase yields differences in attained S_u < 3%, with larger differences in measured L_b values.
- Good repeatability was displayed for S_u, with the influence of variations in N_2/O_2 ratio of employed combustion air thought to result in substantial discrepancy in S_u measurement. As such, in order to allow for fair comparison and re-scaling, N_2/O_2 ratio of air employed should potentially be included alongside published datasets.

II. Effective Le Models and Appraised Theoretical Relationships between Le and L_b

For multi-component fuel blends, such as NG/H_2 blends, there still does not seem to exist a consensus on the correct formulation of Le to be employed, with three 'effective' Le formulations (Le_{eff}) proposed in literature, namely; a volume based Le (Le_V), diffusion based Le (Le_D) and heat-released based Le (Le_H). In order to evaluate Le_{eff} models, theoretical relationship linking L_b and Le as proposed in literature, necessitating the numerical evaluation of various fundamental flame parameters, were appraised and compared to experimentally measured data. From this qualitative exercise, the following L_{eff} models are recommended:

- A diffusional-based formulation (Le_D) yielded best correlation for measured stretch-behaviour of lean (Φ < 0.7) CH_4/H_2 mixtures containing up to 50% H_2 vol. additions.
- A heat-release based model (Le_H) resulted in best agreement for measured stretch-behaviour of lean hydrocarbon blends; CH_4/C_2H_6, CH_4/C_3H_8 and C_2H_6/C_3H_8.
- A volume-based formulation (Le_V) displayed best correlation for lean hydrogen enriched heavier hydrocarbon mixtures; C_2H_6/H_2, C_3H_8/H_2 (50% H_2 vol.) and $CH_4/C_3H_8/H_2$ mixtures (up to 18% and 15% vol., C_3H_8 and H_2, respectively).

III. Flame Propagation and Stretch Related behaviour of Investigated Fuel Mixtures

Experimental and modelling work was undertaken to measure and quantify various fundamental combustion properties of the main components of NG; CH_4, C_2H_6, C_3H_8 and C_4H_{10}. NG/H_2 relevant binary and tertiary mixtures were parametrically investigated with respect to measured stretch-related and flame propagation behaviour at lean conditions. From this work, the following can be concluded:

Pure Single Fuels:

- In agreement with literature, all hydrocarbons tested exhibit similar flame speeds at lean conditions, in the order of $C_2H_6 > C_3H_8 > C_4H_{10} \geq CH_4$. With respect to the heavier hydrocarbons (C_2+), flame speed decreases with increasing molecular weight and decreasing thermal conductivity. In terms of measured stretch related behaviour, all tested HC fuels display similar sensitivity to stretch at near stoichiometric conditions ($+L_b$, Le > 1), with diverging and opposite behaviour exhibited with decreasing Φ, between CH_4 (Le ≤ 1, $-L_b$) and the C_2+ fuels tested ($+L_b$, Le >> 1).

Binary Mixtures:

- Equal small volumetric additions of H_2 and C_3H_8 (15%) to CH_4 flames resulted in similar enhancement of burning intensity but opposite susceptibility to preferential diffusional instability, with influence of H_2 and C_3H_8 yielding greatest influence at leanest conditions. Measured behaviour in S_u and L_b is supported by numerical analysis, which suggests that H_2 and C_3H_8 enrichment to CH_4 flames result in similar reduction in overall activation energy and flame thickness.
- Significant differences in molecular mass between H_2 and C_2+ fuels tested diminish the influence of small volumetric additions of H_2 (15% vol.), with marginal changes in flame propagation and stability behaviour observed for $H_2/C_{2\text{-}4}$ (15/85%) flames.
- For ultra-lean (Φ = 0.65) CH_4 based fuels, C_2H_6 and C_3H_8 additions result in comparable influence on flame propagation and stretch sensitivity, a consequence of C_2H_6 and C_3H_8 similar thermo-diffusive properties.
- Changes in premixed laminar flame stability are a consequence of hydrodynamic (thermal expansion of gases) and preferential-diffusional instabilities (thermo-diffusive effects). For the tested $C_{1\text{-}3}/H_2$ blends (Φ = 0.65), thermal expansion was observed to remain relatively constant (<2%, 50% vol. H_2) with flame thickness decreasing with increasing H_2 content, thereby promoting hydrodynamic instabilities. Although $C_{1\text{-}3}/H_2$ blends exhibited similar decreasing Le trends, the higher mass diffusivity of H_2 and CH_4 compared to the O_2 molecule result in a promotion of thermo-diffusive instability,

reflected in –ve L_b measurements. Since the mass diffusivity of C_3H_8 (and to a lesser extent C_2H_6) is lower than that of air, diffusional-thermal effects are moderated (Le > 1, + L_b), underlining the stabilising influence of C_{2-3} HC fuels on flame stability.

- H_2 (50%, vol.) enrichment significantly augments CH_4 flame propagation, with attained S_u equivalent to that of C_2H_6 and marginally faster than C_3H_8 flames (for 50% H_2 additions), with enhancement of S_u due to H_2 enrichment following the order $CH_4 > C_2H_6 > C_3H_8$.
- For CH_4/H_2 blends, modelling and experimental work suggests that flame speed, burning intensity (Q') and production of H radical concentrations are highly correlated, in agreement with literature, with the above correlation extendable to C_2H_6/H_2 and C_3H_8/H_2 mixtures (up to 50% H_2 vol.).
- A sensitivity analysis related to the major flame enhancing pathways (thermal, kinetic, diffusive) was conducted to clarify the nature of measured augmented burning intensity of ultra-lean C_{1-3}/H_2 flames. Enhanced flame propagation of CH_4/H_2 is essentially an Arrhenius effect (kinetic), through the reduction of the global activation energy (and thus activation temperature), with diffusive and thermal pathways comparable in strength, but with opposite sensitivities, in agreement with conclusions from similar work. With respect to the C_{2-3}/H_2 blends tested, augmentations of flame propagation were also kinetic in nature, however, considerably weaker than for CH_4/H_2, in good correlation with marginal gains in measured flame speed and modest increases in volumetric heat release and H radical production.

NG/H_2 Mixtures

- For a fixed H_2 enrichment level, differences in measured S_u and L_b result from variations in CH_4:C_3H_8 mol fractions, with greatest differences observed at leanest conditions (Φ = 0.6). NG blends containing highest and lowest fractions of heavier hydrocarbons exhibit flame stretch behaviour analogous to that of pure C_3H_8 (increasing L_b with decreasing Φ) and CH_4 (decreasing L_b with decreasing Φ), respectively. Differences in S_u are principally linked to reductions in global activation energy, in agreement with sensitivity analysis presented for tested C_{1-3}/H_2 blends.
- The Wobbe Index (WI) is unable to capture changes in thermo-diffusive flame response due to variations in fuel composition. By its method of calculation, the WI masks potential changes in reactivity due to additions of H_2 and/or heavier hydrocarbons of alternative fuels.

Reaction Mechanism Appraisal

- Various reaction mechanisms, all including the H_2/CO chemistry and thus suitable for NG/H_2 fuel combustion were appraised. Overall best correlation was consistently displayed with the Aramco 1.3 mechanism for all single, binary and tertiary mixtures containing tested C_{1-3} and H_2 fuels. It should be underlined that Aramco 1.3 contained at least twice as many more species and elementary reactions than other evaluated reaction mechanisms, potentially explaining the afforded enhanced accuracy with respect to measured laminar burning velocities.

IV. Experimental investigation of premixed, turbulent, Lean Blow-Off stability limits

To practically assess the observed opposite influence of equal volumetric additions of H_2 and C_3H_8 (15% vol.) on stretch-sensitivity of lean CH_4 flames, experimental work was undertaken using a generic swirl burner. The lean blow-off (LBO) stability limits of premixed turbulent CH_4, CH_4/H_2 and CH_4/C_3H_8 flames were examined, at two different unburnt reactant temperature (289 and 579 K) and three thermal powers (25, 42 and 55 kW). From this work, the following conclusions can be taken:

- Regardless of inlet temperature and power tested, CH_4/H_2 flames stabilised at significantly leaner LBO limits than CH_4 and CH_4/C_3H_8, despite all tested mixtures displaying very similar modelled flame speeds and temperatures, a consequence of preferential diffusion, reflected in measured L_b value (– L_b, Le < 1)
- At 279 K, the CH_4/C_3H_8 flame attained marginally leaner limits than CH_4, with the opposite observed at 579 K, particularly at the highest power conditions, where flame stretch is perceived to be greatest, due to increased volumetric flowrates. Lean limits display correlation with measured L_b behaviour of fuel mixtures tested, warranting further investigation.

V. Recommendations for Future Work

Several recommendations for further investigation can be made as a result from this work:

- Performance of tests at higher values of initial ambient pressure, would facilitate further validation of chemical reaction mechanisms at conditions more representative of GT operating windows. Furthermore, upgrading of temperature and ignition systems would possibly permit to conduct experiments at leaner conditions.
- Fuel compositions could be broadened to include inert gases typically found in NG, for example N_2 and CO_2, which have been demonstrated to have the same influence as H_2 on the Wobbe Index. Investigation of the potential impact of inert fuels on stretch-sensitivity, thermo-diffusive behaviour and flame propagation, as well as greater H_2 enrichment fractions, would be valuable data for the GT industry.
- Theoretical relationships relating L_b to fundamental combustion parameters have already been derived for premixed counterflow flames, for which stretch influence can be readily quantified. Further investigation of Le_{eff} model on counterflow flames could potentially lead to universal validation of proposed recommendations, as suggested in literature.
- From the correlation displayed by attained lean limits and measured L_b behaviour of tested fuel blends, it seems that estimating turbulent flame speeds employing Le scaling merits further inquiry, thereby providing an opportunity to correlate experimentally attained U_L values with corresponding turbulent flame speeds. Quantification of various turbulent parameters would be required, allowing further characterisation of flame stretch influence on turbulent flame propagation.

References

[1] H. Ritchie and M. Roser, “Energy,” *Our World in Data*, 2020. [Online]. Available: https://ourworldindata.org/energy-production-and-changing-energy-sources. [Accessed: 31-Jan-2020].

[2] T. Letcher, *Climate Change : Observed Impacts on Planet Earth*, 2nd ed. Elsevier, 2015.

[3] R. Swart and F. Raes, “Making integration of adaptation and mitigation work: Mainstreaming into sustainable development policies?,” *Clim. Policy*, vol. 7, no. 4, pp. 288–303, 2007.

[4] BP, “Statistical Review of World Energy,” 2019.

[5] V. Smil, *Energy Transitions: Global and National Perspectives*, 2nd ed. Praeger, 2017.

[6] IPCC, “Climate change science - the status of climate change science today,” *United Nations Framew. Conv. Clim. Chang.*, no. February 2011, pp. 1–7, 2011.

[7] H. Ritchie and M. Roser, “CO2 and Greenhouse Gas Emissions,” *Our World in Data*, 2019. [Online]. Available: https://ourworldindata.org/co2-and-other-greenhouse-gas-emissions. [Accessed: 31-Jan-2020].

[8] European Political Strategy Centre, “10 Trends Reshaping Climate and Energy,” 2018.

[9] M. R. Pompeo, “On the U.S. Withdrawal from the Paris Agreement - United States Department of State,” *U.S Department of State*, 2019. [Online]. Available: https://www.state.gov/on-the-u-s-withdrawal-from-the-paris-agreement/. [Accessed: 05-Feb-2020].

[10] Global Carbon Atlas Team, “Emissions | Global Carbon Atlas,” 2018. [Online]. Available: http://www.globalcarbonatlas.org/?q=en/emissions. [Accessed: 05-Oct-2019].

[11] The Core Writing Team, R. . Pachauri, and L. . Meyer, “Climate Change 2014 Synthesis Report. Contributions of Working Groups I, II and III to the Fifth Assessment Report of the Intergovernmental Panel on Climate Change,” 2014.

[12] SHELL, “LNG Outlook 2019 factsheet,” 2019.

[13] McKincey, “Global Gas & LNG Outlook to 2035,” 2018.

[14] M. Roser and H. Ritchie, “Energy Production & Changing Energy Sources,” *Our World in Data*, 2019. [Online]. Available: https://ourworldindata.org/energy-production-and-changing-energy-sources. [Accessed: 31-Jan-2020].

[15] D. Frazier, R. Gomez, and N. Westbrook, “Coal vs . Natural Gas Energy Production Roadmap,” 2013.

[16] BP, “Energy Outlook 2019 edition,” 2019.

[17] E.I.A, “Annual Energy Outlook 2019 with projections to 2050,” 2019.

[18] P. Carpos *et al.*, “EU Reference Scenario 2016 - Energy, transport and GHG emissions - Trends to 2050,” 2016.

[19] K. B. Medlock, “Impact of Shale Gas Development on Global Gas Markets,” *Nat. Gas Electr.*, vol. 27, no. 9, pp. 22–28, 2009.

[20] GIIGNL, “Annual Report,” 2019.

[21] E. J. Moniz, H. D. Jacoby, and A. J. M. Meggs, “The Future of Natural Gas - MIT Study,” 2011.

[22] O. Tlili, C. Mansilla, D. Frimat, and Y. Perez, “Hydrogen market penetration feasibility assessment : Mobility and natural gas markets in the US , Europe , China and Japan,” *Int. J. Hydrogen Energy*, vol. 44, no. 31, pp. 16048–16068, 2019.

[23] I.E.A, “The Future of Hydrogen - Seizing today’s opportunities,” 2019.

[24] B. Pivovar, “H2 at Scale: Deeply Decarbonizing Our Energy Systems,” 2016.

[25] C. Wulf, J. Linßen, and P. Zapp, “Review of power-to-gas projects in Europe,” *Energy Procedia*, vol. 155, pp. 367–378, 2018.

[26] A. Floristean, “Gas Grid issues and Sectoral Integration,” 2018.

[27] M. Huth and A. Heilos, *Fuel flexibility in gas turbine systems: Impact on burner design and performance*. Woodhead Publishing Limited, 2013.

[28] D. J. Abbott, J. P. Bowers, and S. R. James, “The Impact of Natural Gas Composition Variations on the Operation of Gas Turbines for Power Generation,” *Futur. Gas Turbine Technol.*, no. October, p. 1, 2012.

[29] ETN, “Hydrogen Gas Turbines - The Path Towards a Zero-Carbon Gas Turbine,” 2020.

[30] F. Arafin and E. Belmont, “Combustion Flame Speeds and Stability of Associated

Natural Gas with High Concentrations of C2-C4 Alkanes," *Energy and Fuels*, vol. 32, no. 11, pp. 11821–11830, 2018.

[31] W. Lowry, J. De Vries, M. Krejci, E. Petersen, and W. Metcalfe, "Measurements and Modeling of Pure Alkanes and Alkane Blends," vol. 133, no. September 2011, pp. 1–9, 2014.

[32] P. Dirrenberger *et al.*, "Measurements of Laminar Flame Velocity for Components of Natural Gas," *Energy and Fuels*, vol. 25, no. 9, pp. 3875–3884, Sep. 2011.

[33] N. Lamoureux and C. E. Paillard, "Natural gas ignition delay times behind reflected shock waves: Application to modelling and safety," *Shock Waves*, vol. 13, no. 1, pp. 57–68, 2003.

[34] S. Taamallah, K. Vogiatzaki, F. M. Alzahrani, E. M. A. Mokheimer, M. A. Habib, and A. F. Ghoniem, "Fuel flexibility, stability and emissions in premixed hydrogen-rich gas turbine combustion: Technology, fundamentals, and numerical simulations," *Appl. Energy*, vol. 154, pp. 1020–1047, 2015.

[35] European Commission, "Shedding light on energy in the EU - A guided tour of energy statistics," 2017.

[36] C. E. Manufacturers, "Actual H-gas Wobbe Index ranges in five member states compared with the EASEE gas proposal," no. 6284937371, 2014.

[37] European Network of Transmission System Operators for Gas, "Wobbe Index and Gross Calorific Value in European networks - Analysis of ranges and variability," 2017.

[38] European Network of Transmission System Operators for Gas, "Ten-Year Network Development Plan 2017 - Annex G - Gas Quality Outlook," 2017.

[39] P. Griebel, Presentation, Topic: "Hydrogen in Gas Turbine Combustion Systems: Challenges and Opportunities," TOTeM 45: Gas Turbines for Future Energy Systems, Cardiff University, Cardiff, Wales, Sept. 3rd, 2018

[40] A. A. Konnov, A. Mohammad, V. R. Kishore, N. Il Kim, C. Prathap, and S. Kumar, "A comprehensive review of measurements and data analysis of laminar burning velocities for various fuel+air mixtures," *Prog. Energy Combust. Sci.*, vol. 68, pp. 197–267, 2018.

[41] C. K. Law, *Combustion Physics*, 1st ed. Cambridge University Press, 2006.

[42] A. C. Benim and K. J. Syed, *Flashback Mechanisms in Lean Premixed Gas Turbine Combustion*. Elsevier Inc., 2014.

[43] H. Bunsen, R. & Roscoe, "Photochemische Untersuchugen," *Poggendorffs Ann. Phys.*, vol. 100, pp. 43–88, 1867.

[44] Mallard and Le Chatelier, "Recherches sur la combustion des mélanges gazeux explosifs," *J. Phys. Théorique Appliquée*, vol. 4, no. 1, pp. 59–84, 1885.

[45] W. Mason and R. V. Wheeler, "XCII. - The 'uniform movement' during the propagation of flame," *J. Chem. Soc. Trans.*, vol. 111, pp. 1044–1057, 1917.

[46] W. R. Chapman and R. V. Wheeler, "The Propagation of Flame in Mixtures of Methane and Air. Part V. The movement of the medium in which the Flame Travels," *J. Chem. Soc.*, pp. 38–46, 1927.

[47] H. F. Coward and F. J. Hartwell, "Studies in the Mechanism of Flame Movement. Part I. The Uniform Movement of Flame in Mixtures of Methane and Air, in Relation to Tube Diameter," *J. Chem. Soc.*, pp. 1996–2004, 1932.

[48] B. Hopkinson, "Explosions of coal-gas and air," *Proc. R. Soc. London. Ser. A, Contain. Pap. a Math. Phys. Character*, vol. 77, no. 518, pp. 387–413, Apr. 1906.

[49] F. W. Stevens, "National Advisory Commitiee for Aeronautics," 1923.

[50] W. Payman, "The 'normal' propagation of flame in gaseous mixtures," *Proc. Symp. Combust.*, vol. 1–2, pp. 51–60, 1948.

[51] W. Payman and H. F. Coward, "Problems in flame propagation," *Proc. Symp. Combust.*, vol. 1–2, pp. 189–193, 1948.

[52] B. Lewis and G. Von Elbe, "Determination of the speed of flames and the temperature distribution in a spherical bomb from time-pressure explosion records," *J. Chem. Phys.*, vol. 2, no. 5, pp. 283–290, 1934.

[53] B. Lewis and G. Von Elbe, "Structure and stability of burner flames," *J. Chem. Phys.*, vol. 11, no. September 1942, pp. 75–97, 1943.

[54] J. W. Linnett, "Methods of measuring burning velocities," *Symp. Combust.*, vol. 4, no. 1, pp. 20–35, 1953.

[55] J. Powling, "A New Burner Method for Determination of Low Burning Velocities and Limits of Inflammability," *Fuel*, vol. 28, pp. 25–28, 1949.

[56] J. P. Botha and D. B. Spalding, “The laminar flame speed of propane/air mixtures with heat extraction from the flame,” *Proc. R. Soc. London. Ser. A. Math. Phys. Sci.*, vol. 225, no. 1160, pp. 71–96, Aug. 1954.

[57] L. P. H. de Goey, A. van Maaren, and R. M. Ouax, “Short Communication: Stabilization of Adiabatic Premixed Laminar Flames on a Flat Flame Burner,” *Combust. Sci. Technol.*, vol. 92, no. 1–3, pp. 201–207, Jul. 1993.

[58] B. Karlovitz, D. W. Denniston, D. H. Knapschaefer, and F. E. Wells, “Studies on Turbulent Flames,” *Proc. Combust. Inst.*, vol. 4, pp. 613–620, 1952.

[59] G. H. Markstein, “Experimental and Theoretical Studies of Flame-Front Stability,” *J. Aeronaut. Sci.*, vol. 18, no. 3, pp. 199–209, Mar. 1951.

[60] G. H. Markstein, *Nonsteady flame propagation*. Published for and on behalf of Advisory Group for Aeronautical Research and Development, North Atlantic Treaty Organization by Pergamon Press, 1964.

[61] F. Van den Schoor, ''Influence of pressure and temperature on flammability limits of combustible gases in air,'' Katholieke Universiteit Leuven, 2007.

[62] D. Pugh, “Combustion characterisation of compositionally dynamic steelworks gases,” Cardiff University, 2013.

[63] M. L. Frankel and G. I. Sivashinsky, “On Quenching of Curved Flames,” *Combust. Sci. Technol.*, vol. 40, no. 5–6, pp. 257–268, Sep. 1984.

[64] C. K. Wu and C. K. Law, “On the determination of laminar flame speeds from stretched flames,” *Symp. Combust.*, vol. 20, no. 1, pp. 1941–1949, 1985.

[65] J. H. Tien and M. Matalon, “On the burning velocity of stretched flames,” *Combust. Flame*, vol. 84, no. 3–4, pp. 238–248, 1991.

[66] P. D. Ronney and G. I. Sivashinsky, “A Theoretical Study of Propagation and Extinction of Nonsteady Spherical Flame Fronts,” *SIAM J. Appl. Math.*, vol. 49, no. 4, pp. 1029–1046, 1989.

[67] B. H. Chao, F. N. Egolfopoulos, and C. K. Law, “Structure and propagation of premixed flame in nozzle-generated counterflow,” *Combust. Flame*, vol. 109, no. 4, pp. 620–638, 1997.

[68] A. P. Kelley and C. K. Law, “Nonlinear effects in the extraction of laminar flame speeds from expanding spherical flames,” *Combust. Flame*, vol. 156, no. 9, pp. 1844–

1851, 2009.

[69] A. N. Lipatnikov and J. Chomiak, “Molecular transport effects on turbulent flame propagation and structure,” *Prog. Energy Combust. Sci.*, vol. 31, no. 1, pp. 1–73, 2005.

[70] M. Brower *et al.*, “Ignition delay time and laminar flame speed calculations for natural gas/hydrogen blends at elevated pressures,” *J. Eng. Gas Turbines Power*, vol. 135, no. 2, pp. 1–10, 2013.

[71] F. N. Egolfopoulos, N. Hansen, Y. Ju, K. Kohse-Höinghaus, C. K. Law, and F. Qi, “Advances and challenges in laminar flame experiments and implications for combustion chemistry,” *Prog. Energy Combust. Sci.*, vol. 43, pp. 36–67, 2014.

[72] D. L. Zhu, F. N. Egolfopoulos, and C. K. Law, “Experimental and numerical determination of laminar flame speeds of methane/(Ar, N2, CO2)-air mixtures as function of stoichiometry, pressure, and flame temperature,” *Symp. Combust.*, vol. 22, no. 1, pp. 1537–1545, 1989.

[73] M. I. Hassan, K. T. Aung, and G. M. Faeth, “Measured and predicted properties of laminar premixed methane/air flames at various pressures,” *Combust. Flame*, vol. 115, no. 4, pp. 539–550, 1998.

[74] C. M. Vagelopoulos, F. N. Egolfopoulos, and C. K. Law, “Further considerations on the determination of laminar flame speeds with the counterflow twin-flame technique,” *Symp. Combust.*, vol. 25, no. 1, pp. 1341–1347, 1994.

[75] X. J. Gu, M. Z. Haq, M. Lawes, and R. Woolley, “Laminar burning velocity and Markstein lengths of methane-air mixtures,” *Combust. Flame*, vol. 121, no. 1–2, pp. 41–58, 2000.

[76] Z. Chen, X. Qin, Y. Ju, Z. Zhao, M. Chaos, and F. L. Dryer, “High temperature ignition and combustion enhancement by dimethyl ether addition to methane-air mixtures,” *Proc. Combust. Inst.*, vol. 31 I, no. 1, pp. 1215–1222, 2007.

[77] T. Tahtouh, F. Halter, and C. Mounaïm-Rousselle, “Measurement of laminar burning speeds and Markstein lengths using a novel methodology,” *Combust. Flame*, vol. 156, no. 9, pp. 1735–1743, 2009.

[78] F. Halter, T. Tahtouh, and C. Mounaïm-Rousselle, “Nonlinear effects of stretch on the flame front propagation,” *Combust. Flame*, vol. 157, no. 10, pp. 1825–1832, 2010.

[79] S. C. Taylor, “Burning velocity and the influence of flame stretch,” University of Leeds, 1991.

[80] E. J. K. Nilsson, A. van Sprang, J. Larfeldt, and A. A. Konnov, “The comparative and combined effects of hydrogen addition on the laminar burning velocities of methane and its blends with ethane and propane,” *Fuel*, vol. 189, pp. 369–376, 2017.

[81] R. T. E. Hermanns, A. A. Konnov, R. J. M. Bastiaans, L. P. H. de Goey, K. Lucka, and H. Köhne, “Effects of temperature and composition on the laminar burning velocity of CH4 + H2 + O2 + N2 flames,” *Fuel*, vol. 89, pp. 114–121, 2010.

[82] O. Park, P. S. Veloo, N. Liu, and F. N. Egolfopoulos, “Combustion characteristics of alternative gaseous fuels,” *Proc. Combust. Inst.*, vol. 33, no. 1, pp. 887–894, 2011.

[83] Z. Chen, “On the accuracy of laminar flame speeds measured from outwardly propagating spherical flames: Methane/air at normal temperature and pressure,” *Combust. Flame*, vol. 162, no. 6, pp. 2442–2453, 2015.

[84] Z. Chen, “On the extraction of laminar flame speed and Markstein length from outwardly propagating spherical flames,” *Combust. Flame*, vol. 158, no. 2, pp. 291–300, 2011.

[85] F. Wu, W. Liang, Z. Chen, Y. Ju, and C. K. Law, “Uncertainty in stretch extrapolation of laminar flame speed from expanding spherical flames,” *Proc. Combust. Inst.*, vol. 35, no. 1, pp. 663–670, 2015.

[86] D. Bradley, P. H. Gaskell, and X. J. Gu, “Burning velocities, Markstein lengths, and flame quenching for spherical methane-air flames: A computational study,” *Combust. Flame*, vol. 104, no. 1–2, pp. 176–198, Jan. 1996.

[87] M. P. Burke, Z. Chen, Y. Ju, and F. L. Dryer, “Effect of cylindrical confinement on the determination of laminar flame speeds using outwardly propagating flames,” *Combust. Flame*, vol. 156, no. 4, pp. 771–779, 2009.

[88] S. Ravi, T. G. Sikes, A. Morones, C. L. Keesee, and E. L. Petersen, “Comparative study on the laminar flame speed enhancement of methane with ethane and ethylene addition,” *Proc. Combust. Inst.*, vol. 35, no. 1, pp. 679–686, 2015.

[89] D. G. Pugh, A. P. Crayford, P. J. Bowen, and M. Al-Naama, “Parametric investigation of water loading on heavily carbonaceous syngases,” *Combust. Flame*, vol. 164, pp. 126–136, 2016.

[90] E. Hu, Z. Huang, J. He, and H. Miao, “Experimental and numerical study on laminar burning velocities and flame instabilities of hydrogen-air mixtures at elevated pressures and temperatures,” *Int. J. Hydrogen Energy*, vol. 34, pp. 8741–8755, 2009.

[91] D. Lapalme, R. Lemaire, and P. Seers, “Assessment of the method for calculating the Lewis number of H2/CO/CH4 mixtures and comparison with experimental results,” *Int. J. Hydrogen Energy*, vol. 42, no. 12, pp. 8314–8328, 2017.

[92] G. Jomaas, X. L. Zheng, D. L. Zhu, and C. K. Law, “Experimental determination of counterflow ignition temperatures and laminar flame speeds of C2-C3 hydrocarbons at atmospheric and elevated pressures,” *Proc. Combust. Inst.*, vol. 30, no. 1, pp. 193–200, 2005.

[93] L. . Tseng, M. A. Ismail, G. M. Faeth, Tseng, L.K, M. A. Ismail, and G. M. Faeth, “Laminar Burning Velocities and Markstein Numbers of Hydrocarbon/air Flames,” *Combust. Flame*, vol. 95, pp. 410–426, 1993.

[94] O. Park, P. S. Veloo, and F. N. Egolfopoulos, “Flame studies of C2 hydrocarbons,” *Proc. Combust. Inst.*, vol. 34, no. 1, pp. 711–718, 2013.

[95] C. K. Law and O. C. Kwon, “Effects of hydrocarbon substitution on atmospheric hydrogen-air flame propagation,” *Int. J. Hydrogen Energy*, vol. 29, pp. 867–879, 2004.

[96] T. Chenglong, H. Zuohua, H. Jiajia, J. Chun, W. Xibin, and M. Haiyan, “Effects of N2 dilution on laminar burning characteristics of propane-air premixed flames,” *Energy and Fuels*, vol. 23, no. 1, pp. 151–156, 2009.

[97] H. Wu *et al.*, “Experimental and numerical study on the laminar flame speed of n-butane/dimethyl ether-air mixtures,” *Energy and Fuels*, vol. 28, no. 5, pp. 3412–3419, 2014.

[98] S. G. Davis and C. K. Law, “Determination of and Fuel Structure Effects on Laminar Flame Speeds of C1 to C8 Hydrocarbons,” *Combust. Sci. Technol.*, vol. 140, no. 1–6, pp. 427–449, 1998.

[99] T. Hirasawa, C. J. Sung, A. Joshi, Z. Yang, H. Wang, and C. K. Law, “Determination of laminar flame speeds using digital particle image velocimetry: Binary fuel blends of ethylene, n-butane, and toluene,” *Proc. Combust. Inst.*, vol. 29, no. 2, pp. 1427–1434, 2002.

[100] A. R. Khan, M. R. Ravi, and A. Ray, “Experimental and chemical kinetic studies of the

effect of H 2 enrichment on the laminar burning velocity and flame stability of various multicomponent natural gas blends," *Int. J. Hydrogen Energy*, vol. 44, no. 2, pp. 1192–1212, 2019.

[101] G. Yu, C. K. Law, and C. K. Wu, "Laminar flame speeds of hydrocarbon + air mixtures with hydrogen addition," *Combust. Flame*, vol. 63, no. 3, pp. 339–347, 1986.

[102] F. Halter, C. Chauveau, N. Djebaïli-Chaumeix, and I. Gökalp, "Characterization of the effects of pressure and hydrogen concentration on laminar burning velocities of methane-hydrogen-air mixtures," *Proc. Combust. Inst.*, vol. 30, no. 1, pp. 201–208, 2005.

[103] N. Donohoe *et al.*, "Ignition delay times, laminar flame speeds, and mechanism validation for natural gas/hydrogen blends at elevated pressures," *Combust. Flame*, vol. 161, no. 6, pp. 1432–1443, 2014.

[104] E. Hu, Z. Huang, J. He, J. Zheng, and H. Miao, "Measurements of laminar burning velocities and onset of cellular instabilities of methane-hydrogen-air flames at elevated pressures and temperatures," *Int. J. Hydrogen Energy*, vol. 34, no. 13, pp. 5574–5584, Jul. 2009.

[105] C. Ji, D. Wang, J. Yang, and S. Wang, "A comprehensive study of light hydrocarbon mechanisms performance in predicting methane/hydrogen/air laminar burning velocities," *Int. J. Hydrogen Energy*, vol. 42, no. 27, pp. 17260–17274, 2017.

[106] D. Bradley, M. Lawes, and R. Mumby, "Burning velocity and Markstein length blending laws for methane/air and hydrogen/air blends," *Fuel*, vol. 187, pp. 268–275, 2017.

[107] Q. Liu, X. Chen, Y. Shen, and Y. Zhang, "Parameter extraction from spherically expanding flames propagated in hydrogen/air mixtures," *Int. J. Hydrogen Energy*, vol. 44, no. 2, pp. 1227–1238, 2019.

[108] C. Tang, Y. Zhang, and Z. Huang, "Progress in combustion investigations of hydrogen enriched hydrocarbons," *Renew. Sustain. Energy Rev.*, vol. 30, pp. 195–216, 2014.

[109] V. Di Sarli and A. Di Benedetto, "Laminar burning velocity of hydrogen-methane/air premixed flames," *Int. J. Hydrogen Energy*, vol. 32, no. 5, pp. 637–646, 2007.

[110] F. Ren, H. Chu, L. Xiang, W. Han, and M. Gu, "Effect of hydrogen addition on the laminar premixed combustion characteristics the main components of natural gas," *J. Energy Inst.*, vol. 92, no. 4, pp. 1178–1190, 2019.

[111] Y. Cheng, C. Tang, and Z. Huang, “Kinetic analysis of H2 addition effect on the laminar flame parameters of the C1-C4 n-alkane-air mixtures: From one step overall assumption to detailed reaction mechanism,” *Int. J. Hydrogen Energy*, vol. 40, no. 1, pp. 703–718, 2015.

[112] F. Wu, A. P. Kelley, C. Tang, D. Zhu, and C. K. Law, “Measurement and correlation of laminar flame speeds of CO and C2 hydrocarbons with hydrogen addition at atmospheric and elevated pressures,” *Int. J. Hydrogen Energy*, vol. 36, no. 20, pp. 13171–13180, 2011.

[113] C. Tang *et al.*, “Laminar burning velocities and combustion characteristics of propane-hydrogen-air premixed flames,” *Int. J. Hydrogen Energy*, vol. 33, no. 18, pp. 4906–4914, 2008.

[114] C. Tang, Z. Huang, J. Wang, and J. Zheng, “Effects of hydrogen addition on cellular instabilities of the spherically expanding propane flames,” *Int. J. Hydrogen Energy*, vol. 34, no. 5, pp. 2483–2487, 2009.

[115] C. L. Tang, Z. H. Huang, and C. K. Law, “Determination, correlation, and mechanistic interpretation of effects of hydrogen addition on laminar flame speeds of hydrocarbon-air mixtures,” *Proc. Combust. Inst.*, vol. 33, no. 1, pp. 921–928, 2011.

[116] P. Dagaut and G. Dayma, “Hydrogen-enriched natural gas blend oxidation under high-pressure conditions: Experimental and detailed chemical kinetic modeling,” *Int. J. Hydrogen Energy*, vol. 31, pp. 505–515, 2006.

[117] Z. Huang, Y. Zhang, K. Zeng, B. Liu, Q. Wang, and D. Jiang, “Measurements of laminar burning velocities for natural gas-hydrogen-air mixtures,” *Combust. Flame*, vol. 146, no. 1–2, pp. 302–311, 2006.

[118] H. Miao, Q. Jiao, Z. Huang, and D. Jiang, “Effect of initial pressure on laminar combustion characteristics of hydrogen enriched natural gas,” *Int. J. Hydrogen Energy*, vol. 33, no. 14, pp. 3876–3885, 2008.

[119] D. R. Dowdy, D. B. Smith, S. C. Taylor, and A. Williams, “The use of expanding spherical flames to determine burning velocities and stretch effects in hydrogen/air mixtures,” *Symp. Combust.*, vol. 23, no. 1, pp. 325–332, 1991.

[120] Z. Chen, M. P. Burke, and Y. Ju, “Effects of Lewis number and ignition energy on the determination of laminar flame speed using propagating spherical flames,” *Proc. Combust. Inst.*, vol. 32 I, no. 1, pp. 1253–1260, 2009.

[121] M. L. Frankel and G. I. Sivashinsky, “On effects due to thermal expansion and lewis number in spherical flame propagation,” *Combust. Sci. Technol.*, vol. 31, no. 3–4, pp. 131–138, 1983.

[122] A. P. Kelley, J. K. Bechtold, and C. K. Law, “Premixed flame propagation in a confining vessel with weak pressure rise,” *J. Fluid Mech.*, vol. 691, pp. 26–51, 2012.

[123] E. W. Lemmon, M. O. McLinden, and and D. G. Friend, “NIST Chemistry WebBook, NIST Standard Reference Database,” *NIST Chemistry WebBook*, 2017. [Online]. Available: http://webbook.nist.gov/cgi/cbook.cgi?ID=C7732185&Units=SI&Mask=4#Notes. [Accessed: 31-Jan-2020].

[124] D. Dandy, “Transport Properties Calculator.” [Online]. Available: http://navier.engr.colostate.edu/code/code-2/index.html. [Accessed: 31-Jan-2020].

[125] B. E. Poling, J. M. Prausnitz, and J. P. O’Connell, *The properties of gases and liquids*, 5th ed. McGraw-Hill, 2001.

[126] M. W. Chase Jr., “NIST-JANAF Themochemical Tables, Fourth Edition,” *J. Phys. Chem. Ref. Data*, vol. Monograph, pp. 1–1951, 1998.

[127] A. Clarke, “Calculation and consideration of the Lewis number for explosion studies,” *Process Saf. Environ. Prot. Trans. Inst. Chem. Eng. Part B*, vol. 80, no. 3, pp. 135–140, 2002.

[128] T. H. Chung, L. L. Lee, and K. E. Starting, “Applications of Kinetic Gas Theories and Multiparameter Correlation for Prediction of Dilute Gas Viscosity and Thermal Conductivity,” *Ind. Eng. Chem. Fundam.*, vol. 23, no. 1, pp. 8–13, 1984.

[129] T. C. Horng, M. Ajlan, L. L. Lee, K. E. Starling, and M. Ajlan, “Generalized Multiparameter Correlation for Nonpolar and Polar Fluid Transport Properties,” *Ind. Eng. Chem. Res.*, vol. 27, no. 4, pp. 671–679, 1988.

[130] S. Mathur, P. K. Tondon, and S. C. Saxena, “Thermal conductivity of binary, ternary and quaternary mixtures of rare gases,” *Mol. Phys.*, vol. 12, no. 6, pp. 569–579, 1967.

[131] N. Bouvet, F. Halter, C. Chauveau, and Y. Yoon, “On the effective Lewis number formulations for lean hydrogen/hydrocarbon/ air mixtures,” *Int. J. Hydrogen Energy*, vol. 38, no. 14, pp. 5949–5960, 2013.

[132] C. R. Wilke and C. Y. Lee, “Estimation of Diffusion Coefficients for Gases and Vapors,” *Ind. Eng. Chem.*, vol. 47, no. 6, pp. 1253–1257, Jun. 1955.

[133] J. R. Fair and B. J. Lerner, “A generalized correlation of diffusion coefficients,” *AIChE J.*, vol. 2, no. 1, pp. 13–17, Mar. 1956.

[134] N. H. Chen and D. F. Othmer, “New Generalized Equation for Gas Diffusion Coefficient.,” *J. Chem. Eng. Data*, vol. 7, no. 1, pp. 37–41, Jan. 1962.

[135] D. F. Fairbanks and C. R. Wilke, “Diffusion Coefficients in Multicomponent Gas Mixtures,” *Ind. Eng. Chem.*, vol. 42, no. 3, pp. 471–475, 1950.

[136] C. J. Sun, C. J. Sung, D. L. Hu, and C. K. Law, “Response of counterflow premixed and diffusion flames to strain rate variations at reduced and elevated pressures,” *Symp. Combust.*, vol. 26, no. 1, pp. 1111–1120, 1996.

[137] C. J. Sun, C. J. Sung, L. He, and C. K. Law, “Dynamics of weakly stretched flames: Quantitative description and extraction of global flame parameters,” *Combust. Flame*, vol. 118, no. 1–2, pp. 108–128, 1999.

[138] G. Jomaas, C. K. Law, and J. K. Bechtold, “On transition to cellularity in expanding spherical flames,” *J. Fluid Mech.*, vol. 583, pp. 1–26, 2007.

[139] C. K. Law, G. Jomaas, and J. K. Bechtold, “Cellular instabilities of expanding hydrogen/propane spherical flames at elevated pressures: Theory and experiment,” *Proc. Combust. Inst.*, vol. 30, no. 1, pp. 159–167, 2005.

[140] F. Dinkelacker, B. Manickam, and S. P. R. Muppala, “Modelling and simulation of lean premixed turbulent methane/hydrogen/air flames with an effective Lewis number approach,” *Combust. Flame*, vol. 158, no. 9, pp. 1742–1749, 2011.

[141] S. P. R. Muppala, M. Nakahara, N. K. Aluri, H. Kido, J. X. Wen, and M. V. Papalexandris, “Experimental and analytical investigation of the turbulent burning velocity of two-component fuel mixtures of hydrogen, methane and propane,” *Int. J. Hydrogen Energy*, vol. 34, no. 22, pp. 9258–9265, 2009.

[142] J. K. Bechtold and M. Matalon, “The dependence of the Markstein length on stoichiometry,” *Combust. Flame*, vol. 127, no. 1–2, pp. 1906–1913, 2001.

[143] C. K. Law and C. J. Sung, “Structure, aerodynamics, and geometry of premixed flamelets,” *Progress in Energy and Combustion Science*, vol. 26, no. 4. pp. 459–505, 2000.

[144] F. N. Egolfopoulos and C. K. Law, “Chain mechanisms in the overall reaction orders in laminar flame propagation,” *Combust. Flame*, vol. 80, no. 1, pp. 7–16, Apr. 1990.

[145] K. Kumar and C. J. Sung, “Laminar flame speeds and extinction limits of preheated n-decane/O2/N2 and n-dodecane/O2/N2 mixtures,” *Combust. Flame*, vol. 151, pp. 209–224, 2007.

[146] U. C. Müller, M. Bollig, and N. Peters, “Approximations for burning velocities and Markstein numbers for lean hydrocarbon and methanol flames,” *Combust. Flame*, vol. 108, no. 3, pp. 349–356, 1997.

[147] D. G. Pugh, T. O’Doherty, A. J. Griffiths, P. J. Bowen, A. P. Crayford, and R. Marsh, “Sensitivity to change in laminar burning velocity and Markstein length resulting from variable hydrogen fraction in blast furnace gas for changing ambient conditions,” *Int. J. Hydrogen Energy*, vol. 38, no. 8, pp. 3459–3470, 2013.

[148] G. S. Settles, *Schlieren and Shadowgraph Techniques*. Springer Berlin Heidelberg, 2001.

[149] Photron, “FASTCAM-APX RS Hardware Manual Rev. 1.05,” 2006.

[150] Bronkhorst, “mini CORI-FLOW ™ M1x series - Instruction Manual,” 2019.

[151] E. Hu, Y. Chen, Z. Zhang, X. Li, Y. Cheng, and Z. Huang, “Experimental study on ethane ignition delay times and evaluation of chemical kinetic models,” *Energy and Fuels*, vol. 29, no. 7, pp. 4557–4566, 2015.

[152] Reaction Design, “CHEMKIN - PREMIX Manual,” 2000.

[153] Reaction Design, “CHEMKIN - A software package for the analysis of gas-phase chemical and plasma kinetics - Manual,” 2000.

[154] G. Dixon-Lewis, “Flame structure and flame reaction kinetics II. Transport phenomena in multicomponent systems,” *Proc. R. Soc. London. Ser. A. Math. Phys. Sci.*, vol. 307, no. 1488, pp. 111–135, 1968.

[155] G.P. Smith *et al.*,“GRI-Mech 3.0,”http://www.me.berkeley.edu/gri_mec/, 2000.

[156] H. Wang *et al.*, “USC Mech Version II. High-temperature combustion reaction model of H2/CO/C1-C4 compounds,” *Combust. Kinet. Lab. Univ. South. California, Los Angeles, CA, accessed Aug*, 2007.

[157] W. K. Metcalfe, S. M. Burke, S. S. Ahmed, and H. J. Curran, “A hierarchical and

comparative kinetic modeling study of C1 - C2 hydrocarbon and oxygenated fuels," *Int. J. Chem. Kinet.*, vol. 45, no. 10, pp. 638–675, 2013.

[158] Mechanical and Aerospace Engineering (Combustion Research) University of California at San Diego, "Chemical-Kinetic Mechanisms for Combustion Applications." [Online]. Available: http://combustion.ucsd.edu.

[159] BOC, "BOC Products." [Online]. Available: https://www.boconline.co.uk/en/products-and-supply/speciality-gas/pure-gases/air/air.html. [Accessed: 23-Oct-2019].

[160] BOC, "Air zero grade - FactSheet."

[161] G. K. Giannakopoulos, A. Gatzoulis, C. E. Frouzakis, M. Matalon, and A. G. Tomboulides, "Consistent definitions of 'Flame Displacement Speed' and 'Markstein Length' for premixed flame propagation," *Combust. Flame*, vol. 162, no. 4, pp. 1249–1264, 2015.

[162] J. Jayachandran *et al.*, "A study of propagation of spherically expanding and counterflow laminar flames using direct measurements and numerical simulations," *Proc. Combust. Inst.*, vol. 35, no. 1, pp. 695–702, 2015.

[163] E. Varea, J. Beeckmann, H. Pitsch, Z. Chen, and B. Renou, "Determination of burning velocities from spherically expanding H 2 /air flames," *Proc. Combust. Inst.*, vol. 35, no. 1, pp. 711–719, 2015.

[164] Z. Chen, Presentation, Topic: "On the determination of laminar flame speed from low-pressure and super-adiabatic propagating spherical flames," 3rd International Workshop on Laminar Burning Velocity, Lisbon, Portugal, April, 14th, 2019.

[165] R. J. Moffat, "Describing the uncertainties in experimental results," *Exp. Therm. Fluid Sci.*, vol. 1, no. 1, pp. 3–17, 1988.

[166] P. D. Ronney and H. Y. Wachman, "Effect of gravity on laminar premixed gas combustion I: Flammability limits and burning velocities," *Combust. Flame*, vol. 62, no. 2, pp. 107–119, Nov. 1985.

[167] "Student's T Critical Values." [Online]. Available: https://people.richland.edu/james/lecture/m170/tbl-t.html. [Accessed: 14-Feb-2020].

[168] M. Ó Conaire, H. J. Curran, J. M. Simmie, W. J. Pitz, and C. K. Westbrook, "A

comprehensive modeling study of hydrogen oxidation," *Int. J. Chem. Kinet.*, vol. 36, no. 11, pp. 603–622, 2004.

[169] E. Hu, Z. Huang, J. He, C. Jin, and J. Zheng, "Experimental and numerical study on laminar burning characteristics of premixed methane-hydrogen-air flames," *Int. J. Hydrogen Energy*, vol. 34, no. 11, pp. 4876–4888, Jun. 2009.

[170] S. Verhelst, R. Woolley, M. Lawes, and R. Sierens, "Laminar and unstable burning velocities and Markstein lengths of hydrogen-air mixtures at engine-like conditions," *Proc. Combust. Inst.*, vol. 30, no. 1, pp. 209–216, 2005.

[171] D. Dunn-Rankin and F. Weinberg, "Location of the Schlieren Image in Premixed Flames: Axially Symmetrical Refractive Index Fields," *Combust. Flame*, vol. 113, no. 3, pp. 303–311, 1998.

[172] D. Bradley, M. Lawes, and M. E. Morsy, "Flame speed and particle image velocimetry measurements of laminar burning velocities and Markstein numbers of some hydrocarbons," *Fuel*, vol. 243, no. November 2018, pp. 423–432, 2019.

[173] V. Brînzea, D. Răzuş, M. Mîţu, and D. Oancea, "Overall Activation Energy of Propane-Air Combustion in Laminar Flames," vol. I, pp. 35–41, 2009.

[174] L. Gas, "Gas Data Book," *U.S. Dep. Inter. Bur. Mines*, p. 22, 2001.

[175] E. R. Hawkes and J. H. Chen, "Direct numerical simulation of hydrogen-enriched lean premixed methane–air flames," *Combust. Flame*, vol. 138, no. 3, pp. 242–258, Aug. 2004.

[176] P. Flohr and P. Stuttaford, "Combustors in gas turbine systems," in *Modern Gas Turbine Systems: High Efficiency, Low Emission, Fuel Flexible Power Generation*, 2013, pp. 151–187.

[177] Y. Tan, P. Dagaut, M. Cathonnet, and J. C. Boettner, "Oxidation and ignition of Methane-Propane and Methane-Ethane-Propane mixtures: Experiments and modeling," *Combust. Sci. Technol.*, vol. 103, no. 1–6, pp. 133–151, Dec. 1994.

[178] ISO, "ISO 6976:2016 : Natural gas - Calculation of calorific values, density, relative density and Wobbe indices from composition Gaz naturel," 2016.

[179] Bright Sensors, "CALCULATOR « Bright Sensors | Gas Quality Sensors." [Online]. Available: https://www.bright-sensors.com/wobbe-index-calculator/. [Accessed: 04-Jan-2020].

[180] F. Wu, G. Jomaas, and C. K. Law, “An experimental investigation on self-acceleration of cellular spherical flames,” *Proc. Combust. Inst.*, vol. 34, pp. 937–945, 2013.

[181] O. C. Kwon, G. Rozenchan, and C. K. Law, “Cellular instabilities and self-acceleration of outwardly propagating spherical flames,” *Proc. Combust. Inst.*, vol. 29, pp. 1775–1783, 2002.

[182] J. B. Bell, R. K. Cheng, M. S. Day, and I. G. Shepherd, “Numerical simulation of Lewis number effects on lean premixed turbulent flames,” *Proc. Combust. Inst.*, vol. 31 I, no. 1, pp. 1309–1317, 2007.

[183] D. G. Pugh *et al.*, “Dissociative influence of H2O vapour/spray on lean blowoff and NOx reduction for heavily carbonaceous syngas swirling flames,” *Combust. Flame*, vol. 177, no. x, pp. 37–48, 2017.

[184] J. Runyon *et al.*, “Experimental analysis of confinement and swirl effects on premixed ch 4 -h 2 flame behavior in a pressurized generic swirl burner,” *Proc. ASME Turbo Expo*, vol. Part F1300, pp. 1–12, 2017.

[185] R. Marsh *et al.*, “Premixed methane oxycombustion in nitrogen and carbon dioxide atmospheres: Measurement of operating limits, flame location and emissions. Proceedings of the Combustion Institute,” *Proc. Combust. Inst.*, vol. 36, no. 3, pp. 3949–3958, 2017.

[186] J. Runyon, “Gas Turbine Fuel Flexibility : Pressurized Swirl Flame Stability , Thermoacoustics , and Emissions,” Cardiff University, 2017.

[187] A. Morones *et al.*, “Laminar and turbulent flame speeds for natural gas/hydrogen blends,” *Proc. ASME Turbo Expo*, vol. 4B, pp. 1–8, 2014.

[188] N. Chakraborty and R. S. Cant, “Effects of Lewis number on turbulent scalar transport and its modelling in turbulent premixed flames,” *Combust. Flame*, vol. 156, no. 7, pp. 1427–1444, 2009.

Appendix A - Ancillary Information

A.1 - Reference Properties, Constants and Co-efficients

Universal Gas Constant – R^0 = 8.314472 (J/mol·K) or 0.001987 (cal/mol·K)

The values of any molar masses were calculated using the following atomic weights, with some examples of calculated values:

Atomic Weight	
C	12.0107
H	1.00794
O	15.9994
N	14.0067
Ar	39.9480

Molar Mass (g/mol) - Y_i	
H_2	2.0159
CH_4	16.0424
N_2	28.0135
CO_2	44.0095
O_2	31.9988
H_2O	18.0153
C_3H_8	44.0956
C_2H_6	30.0690
C_4H_{10}	58.1222

The tables below list the co-efficients employed in the Shomate equation (Eqn. 3.10) in order to evaluate c_p. Co-efficients from the NIST-JANAF Thermo-Chemical Tables [126] and the NIST chemistry web-book [123]

CH_4

Temperature Range (K)		
Co-efficients	298 - 1300	1300 - 2000
A	-0.703029	85.81217
B	108.4773	11.26467
C	-42.52157	-2.11415
D	5.862788	0.13819
E	0.678565	-26.4222

H_2

Temperature Range (K)		
Co-efficients	298 - 1000	1000-2500
A	33.06618	18.56308
B	-11.3634	12.25736
C	11.43282	-2.85979
D	-2.77287	0.268238
E	-0.15856	1.97799

O_2

Temperature Range (K)		
Co-efficients	100-700	700-2000
A	31.32234	30.03235
B	-20.23531	8.772972
C	57.86644	-3.98813
D	-36.50624	0.788313
E	-0.007374	-0.7416

N_2

Temperature Range (K)		
Co-efficients	100-500	500-2000
A	28.98641	19.50583
B	1.853978	19.88705
C	-9.64746	-8.598535
D	16.63537	1.369784
E	0.000117	0.527601

The tables below list the C_p values used for the $C_{2\text{-}4}$ hydrocarbons:

C_2H_6		C_3H_8		C_4H_{10}	
Cp(J/mol·K)	Temperature (K)	Cp(J/mol·K)	Temperature (K)	Cp(J/mol·K)	Temperature (K)
35.7	100	34.06	50	38.07	50
42.3	200	41.3	100	55.35	100
52.49	298.15	48.79	150	67.32	150
52.71	300	56.07	200	76.44	200
65.46	400	68.74	273.15	92.3	273.15
77.94	500	73.6	298.15	98.49	298.15
89.19	600	73.93	300	98.95	300
99.14	700	94.01	400	124.77	400
107.94	800	112.59	500	148.66	500
115.71	900	128.7	600	169.28	600
122.55	1000	142.67	700	187.02	700
128.55	1100	154.77	800	202.38	800
133.8	1200	165.35	900	215.73	900
138.39	1300	174.6	1000	227.36	1000
142.4	1400	182.67	1100	237.48	1100
145.9	1500	189.74	1200	246.27	1200
148.98	1600	195.85	1300	253.93	1300
151.67	1700	201.21	1400	260.58	1400

The tables below list the co-efficients employed using Eqn. 3.12a and Eqn. 3.12b [127] for the determination of λ_i:

Species	Eqn.	A	B	C	D	T range (K)
O_2	3.13a	-3.27300E-04	9.96600E-05	-3.74300E-08	9.73200E-12	115 - 1470
N_2	3.13a	3.91900E-04	9.81600E-05	-5.06700E-08	1.50400E-11	116 - 1470
CH_4	3.13a	-1.86900E-03	8.72700E-05	1.17900E-07	-3.61400E-11	273-1270
C_2H_6	3.13a	-3.17400E-02	2.20100E-04	-1.92300E-07	1.66400E-10	273-1020
C_3H_8	3.13a	1.85800E-03	-4.69800E-06	2.17770E-07	-8.40900E-11	273-1270
C_4H_{10}	3.13b	5.10940E-02	4.52530E-01	5.45550E+03	1.97980E+06	273-1000

The table below list the properties employed to calculate λ_i using the Chung et al. Method [128], [129]:

Species	T_c (K)	P_c (bar)	V_c (cm^3/mol)
CH_4	190.56	45.99	98.6
C_2H_6	305.32	48.72	145.5
C_3H_8	369.83	42.48	200
C_4H_{10}	425.12	37.96	255
N_2	126.20	33.98	90.1
O_2	154.58	50.43	73.37
H_2	32.98	12.93	64.2

The table below list the binary mass diffusion co-efficient ($D_{i,j}$) calculated using the Hirschfelder [133], [134] and Wilke [132] methods:

Binary Combination	Wilke (cm/s) [132]	Hirschfelder (cm/s) [133], [134]
N_2 -> O_2	0.2213	0.2040
CH_4 -> N_2	0.2340	0.2185
CH_4 -> O_2	0.2362	0.2202
CH_4 -> C_3H_8	0.1299	0.1207
C_2H_6 -> CH_4	0.1637	0.1528
C_2H_6 -> O_2	0.1558	0.1434
C_2H_6 -> N_2	0.1582	0.1460
C_2H_6-> C_3H_8	0.9734	0.8954
C_3H_8 -> N_2	0.1232	0.1130
C_3H_8 -> O_2	0.1195	0.1095
C_4H_{10} -> O_2	0.1069	0.0976
C_4H_{10} -> N_2	0.1122	0.1027
C_4H_{10} -> H_2	0.4074	0.4225
H_2 -> C_2H_6	0.5338	0.5131
H_2-->C_3H_8	0.4202	0.4363
H_2-->CH_4	0.6724	0.7033
H_2-->N_2	0.7101	0.7390
H_2-->O_2	0.7494	0.7793

A.2 – Experimental Rig

Photograph of the experimental rig:

A.3 – MatLab Code for Data Processing

Sample MatLab Code:

```
clear all

path(path,'E:\Process');
fileFolder = fullfile('E:','Process');
dirOutput = dir(fullfile(fileFolder, '*.tif'));
fileNames = {dirOutput.name}';
tic

r=1;
A1 = imread( fileNames {r} );
A2 = medfilt2(A1,[2,2]);
B = edge (A1, 'canny', 0.055);
B2 = bwareaopen (B,20);
%figure, imshow (A1), title ('D');
%figure, imshow (A2), title ('B');
%figure, imshow (B), title ('S');
%figure, imshow (B2), title ('S2');
for k =1:190

    A = imread( fileNames {k} );
    A1 = medfilt2(A,[2,2]);
    %figure, imshow (A), title ('D');
    D = edge (A1, 'canny', 0.055);
    D2 = bwareaopen(D,20);
    %figure, imshow (D), title ('D');
    %figure, imshow (D2), title ('D2');
    %figure, imshow (B), title ('B');
    %figure,imshow(B2), title ('B2');
    E = D-B;
    E2 = D2-B2;
    %figure, imshow (E), title ('E');
    %figure, imshow (E2), title ('E2');
    C = imcrop ( E2, [46,313,540,9]);
    %figure, imshow (C), title ('C');
    ll1 = find ( C==1, 1, 'first');
    rr1 = find ( C==1, 1, 'last');
    lcol = ll1/10;
    lcol1 = ceil(lcol);
    rcol= rr1/10;
    rcol1= ceil(rcol);

    if (isempty(ll1))
        Ledge(k) = 0;
    else
        Ledge(k)= 270-lcol1;
    end;

    if (isempty(rr1))
        Redge(k) = 0;
    else
        Redge(k)= rcol1-270;
    end;

    if ((isempty(ll1))||(isempty(rr1)))
        fd(k) = 0;
        P(k) = 0;
    else
        fd(k) = rcol1-lcol1;
        P(k) = (10-(lcol1*10-ll1));
```

```
    end;
    V = imcrop ( E2, [312,58,3,540]);
    %figure, imshow (V), title ('V');
    %[X,Y,width,length]

    vl1 = find ( V==1, 1, 'first');
    vr1 = find ( V==1, 1, 'last');
    vlcol = vl1;
    vlcol1= ceil(vlcol);
    vrcol = vr1-(3*541);
    %= vr1 - ('w'*'length+1')
    vrcol1= ceil(vrcol);

    if(isempty(vl1))
        vLedge(k)=0;
    else
        vLedge(k)=270-vlcol1;
    end;

    if(isempty(vr1))
        vRedge(k)=0;
    else
        vRedge(k)=vrcol1-270;
    end;

    if((isempty(vl1))||(isempty(vr1)))
        fvd(k)=0;

    else
        fvd(k)=vrcol1-vlcol1;

    end;
    vr2 = (vr1-(3*541));
    %= vr2 = ('w'*'length+1')
    if ((isempty(vl1))||(isempty(vr2)))
        vd(k) = 0;

    else
        vd(k) = vr2-vl1;

    end;

end

Tre = transpose (Redge);
Tle = transpose (Ledge);

Tvre = transpose (vRedge);
Tvle = transpose(vLedge);

Tfd = transpose (fd);

Tvd = transpose (vd);
Tfvd = transpose(fvd);

xlswrite('Result.xls',Tfd,1,'A1');
xlswrite('Result.xls',Tre,1,'C1');
xlswrite('Result.xls',Tle,1,'D1');
xlswrite('Result.xls',Tvd,1,'F1');
xlswrite('Result.xls',Tfvd,1,'H1');
xlswrite('Result.xls',Tvre,1,'I1');
xlswrite('Result.xls',Tvle,1,'J1');
```

A.4 – Comparison of Numerical Data

Comparison of resultant density ratios generated using different reaction mechanisms

CH_4	**Aramco 1.3**[157]	**USC II**[156]	**GRI M 3.0**[155]	**San Diego**[158]
(Φ)	ρ_b/ρ_u	ρ_b/ρ_u	ρ_b/ρ_u	ρ_b/ρ_u
0.60	*0.179*	*0.179*	*0.179*	*0.179*
0.65	*0.170*	*0.170*	*0.170*	*0.170*
0.70	*0.162*	*0.162*	*0.162*	*0.162*
0.80	*0.149*	*0.149*	*0.149*	*0.149*
0.90	*0.139*	*0.139*	*0.139*	*0.139*
1.0	*0.133*	*0.133*	*0.133*	*0.133*
C_2H_6	**Aramco 1.3**[157]	**USC II**[156]	**GRI M 3.0**[155]	**San Diego**[158]
(Φ)	ρ_b/ρ_u	ρ_b/ρ_u	ρ_b/ρ_u	ρ_b/ρ_u
0.60	*0.172*	*0.172*	*0.172*	*0.172*
0.65	*0.162*	*0.162*	*0.163*	*0.162*
0.70	*0.154*	*0.154*	*0.155*	*0.155*
0.80	*0.142*	*0.142*	*0.142*	*0.142*
0.90	*0.132*	*0.132*	*0.132*	*0.132*
1.0	*0.127*	*0.126*	*0.126*	*0.126*
C_3H_8	**Aramco 1.3**[157]	**USC II**[156]	**GRI M 3.0**[155]	**San Diego**[158]
(Φ)	ρ_b/ρ_u	ρ_b/ρ_u	ρ_b/ρ_u	ρ_b/ρ_u
0.65	*0.160*	*0.160*	*0.160*	*0.160*
0.70	*0.152*	*0.152*	*0.153*	*0.152*
0.80	*0.139*	*0.139*	*0.140*	*0.140*
0.90	*0.130*	*0.130*	*0.130*	*0.130*
1.0	*0.125*	*0.124*	*0.125*	*0.124*
C_4H_{10}	**Aramco 1.3**[157]	**USC II**[156]	**GRI M 3.0**[155]	**San Diego**[158]
(Φ)	ρ_b/ρ_u	ρ_b/ρ_u	ρ_b/ρ_u	ρ_b/ρ_u
0.70	/	*0.150*	/	*0.150*
0.80	/	*0.138*	/	*0.138*
0.90	/	*0.129*	/	*0.129*

Comparison between Adiabatic Flame Temperature yielded from appraised Reaction Mechanisms

Φ	CH_4					C_2H_6					C_3H_8					C_4H_{10}				
	Aramco 1.3[157]	GRI-M 3.0[155]	USC II [156]	San Diego[158]	Aramco 1.3[157]	GRI-M 3.0[155]	USC II [156]	San Diego[158]	Aramco 1.3[157]	GRI-M 3.0[155]	USC II [156]	San Diego[158]	Aramco 1.3[157]	GRI-M 3.0[155]	USC II [156]	San Diego[158]	Aramco 1.3[157]	GRI-M 3.0[155]	USC II [156]	San Diego[158]
0.6	1663.84	1662.08	1662.6	1663.47	1706.04	1703.58	1704.7	1704.95	1717.2	1715.27	1714.79	1716.13	1723.43	1725.59						
0.65	1752.39	1751.51	1751.5	1751.6	1798.51	1794.72	1802.3	1798.96	1812.14	1809.44	1813.14	1813.83	1820.64	1825.67						
0.7	1838.35	1837.09	1837.75	1837.88	1891.01	1887.97	1892	1886.46	1905.17	1896.48	1908.31	1899.47	1915.46	1916.63						
0.8	1999.92	1998.69	1999.42	1999.35	2052.9	2049	2051.7	2049.65	2067.07	2057.3	2067.59	2060.54	2074.66	2077.45						
0.9	2136.26	2136.52	2137.35	2137.22	2181.55	2184.42	2185	2182.9	2195.19	2196.56	2200.53	2195.4	2204.55	2207.53						
1	2224.15	2227.21	2229.38	2227.84	2257.3	2266.4	2269.9	2267.75	2268.49	2272.82	2276.94	2276.19	2281.22	2283.35						

Appendix B – Uncertainty Results

B.1 – Uncertainty Analysis Results Datasets

Test details of stoichiometric CH_4/air mixtures for uncertainty analysis (Φ=1.0, 0.1 MPa)

Test N	1	2	3	4	5
Date	10-Sep-18	11-Sep-18	11-Sep-18	11-Sep-18	12-Sep-18
Temp (C)	25.7	25.4	25.3	24.7	25.7
Test N	6	7	8	9	10
Date	22-Nov-18	03-Dec-18	03-Dec-18	03-Dec-18	17-Jan-19
Temp (C)	26.1	26.2	26.3	26.3	25
Test N	11	12	13	14	15
Date	29-Aug-19	29-Aug-19	29-Aug-19	29-Aug-19	29-Aug-19
Temp (C)	26	25.4	25.2	24.6	25
Test N	16	17	18	19	20
Date	30-Aug-19	30-Aug-19	30-Aug-19	30-Aug-19	30-Aug-19
Temp (C)	25.1	24.9	24.9	24.8	24.8

Test details of Lean CH_4/air mixtures for uncertainty analysis (Φ=0.70, 0.1 MPa)

Test N	1	2	3	4	5
Date	10-Sep-18	11-Sep-18	11-Sep-18	11-Sep-18	12-Sep-18
Temp (C)	25.6	24.8	25.4	25.2	26
Test N	6	7	8	9	10
Date	22-Nov-18	03-Dec-18	03-Dec-18	03-Dec-18	17-Jan-19
Temp (C)	26.4	26.1	26.6	26.6	26.7
Test N	11	12	13	14	15
Date	29-Aug-19	29-Aug-19	29-Aug-19	29-Aug-19	29-Aug-19
Temp (C)	25.8	25.3	25.2	25.1	25.2
Test N	16	17	18	19	20
Date	30-Aug-19	30-Aug-19	30-Aug-19	30-Aug-19	30-Aug-19
Temp (C)	25.1	25.1	25	24.9	24.9

Individual Test results of stoichiometric CH_4/air mixtures for uncertainty analysis:

Flame Radius = 10 – 30 mm, Extrapolation Range 8-35 mm, Non-Linear Model NM(S)

	Φ = 0.70		Φ = 1.00	
Test N.	S_u (mm/s)	L_b (mm)	S_u (mm/s)	L_b (mm)
1	985.63	0.278	2415.03	0.608
2	1014.91	0.208	2525.11	0.571
3	1054.80	0.238	2548.85	0.735
4	1035.39	0.229	2555.81	0.633
5	1057.11	0.248	2556.38	0.675
6	1010.20	0.236	2540.95	0.538
7	1041.94	0.203	2551.70	0.604
8	1050.47	0.169	2563.25	0.639
9	1050.53	0.128	2570.20	0.648
10	996.87	0.173	2602.77	0.713
11	1060.27	0.235	2716.81	0.689
12	1076.74	0.274	2688.88	0.626
13	1079.81	0.218	2694.48	0.674
14	1091.64	0.289	2726.00	0.725
15	1082.68	0.267	2745.41	0.656
16	1058.53	0.147	2732.75	0.588
17	1087.12	0.301	2726.25	0.571
18	1057.28	0.230	2718.18	0.577
19	1056.44	0.222	2717.80	0.611
20	1054.86	0.215	2753.36	0.736

Experimental and Statistical Uncertainties

		B_{Su} (mm/s)	B_{Su} (mm/s) Excluding N_2/O_2	Average S_u (mm/s)	Stand. Dev. σ_{Su} (mm/s)	U_{Su} (mm/s)	% of Average S_u	U_{Su} (mm/s) Excluding N_2/O_2	% of Average S_u
	Tests 1-20	105.58	/	1050.16	28.47	105.74	10.07	/	
	Tests 1-10	103.53	46.15	1029.79	24.59	103.77	10.08	46.68	4.53
Φ = 0.70	Tests 11-20	107.62	47.96	1070.54	13.64	107.68	10.06	48.09	4.49
	Tests 1-20	187.68	/	2632.50	96.35	188.92	7.18	/	
	Tests 1-10	181.33	34.52	2543.00	46.77	181.93	7.15	37.57	1.48
Φ = 1.00	Tests 11-20	194.03	36.66	2721.99	18.96	194.11	7.13	37.08	1.36

Appendix C – Results Tables

All tests were conducted at T_u = 298 K (± 2 K) & P = 0.1 MPa

Camera Speed = 5000 frame/sec Purity of Fuels = 99.9 %

Individual Results: CH_4/air

Φ	ρb/ρu	Aramco 1.3 U_L (cm/s)	LM(S)			LM(C)			NM(S)		
			S_u (mm/s)	L_b (mm)	U_L (cm/s)	S_u (mm/s)	L_b (mm)	U_L (cm/s)	S_u (mm/s)	L_b (mm)	U_L (cm/s)
0.6	0.179	10.12	418.69	-0.405	7.49	417.68	-0.449	7.48	417.17	-0.474	7.47
			417.17	-0.153	7.47	417.67	-0.222	7.48	419.17	-0.256	7.5
			478.03	-0.206	8.56	479.73	-0.226	8.61	481.03	-0.253	8.59
0.65	0.1699	14.13	749.68	0.137	12.74	749.51	0.133	12.74	749.57	0.132	12.74
			752.91	0.063	12.79	752.88	0.062	12.79	752.86	0.061	12.79
			759.6	0.136	12.91	759.47	0.121	12.91	759.39	0.119	12.9
0.7	0.162	18.34	1082.04	0.307	17.52	1080.8	0.286	17.5	1080.32	0.277	17.5
			1104	0.318	17.88	1102.67	0.296	17.86	1102.02	0.285	17.85
			1075.09	0.274	17.41	1074.1	0.257	17.4	1073.42	0.248	17.38
0.8	0.1487	26.69	1764.55	0.511	26.24	1759.15	0.455	26.16	1757.15	0.432	26.13
			1787.64	0.555	26.59	1781.33	0.49	26.49	1779.04	0.464	26.46
			1756.73	0.495	26.13	1751.48	0.441	26.05	1749.3	0.418	26.02
0.9	0.139	33.43	2362.77	0.68	32.83	2350.68	0.585	32.66	2346.03	0.548	32.6
			2404.06	0.728	33.41	2389.58	0.618	33.2	2383.5	0.573	33.12
			2345.12	0.588	32.59	2335.67	0.514	32.46	2331.94	0.485	32.4
1	0.1328	37.8	2783.68	0.761	36.95	2766	0.643	36.72	2759.16	0.598	36.63
			2696.45	0.746	35.8	2679.65	0.632	35.57	2672.3	0.585	35.48
			2763.79	0.712	36.69	2747.7	0.606	36.48	2740.58	0.562	36.38

Individual Results: C_2H_6/air

Φ	ρ_b/ρ_u	Aramco 1.3 U_L (cm/s)	LM(S)			LM(C)			NM(S)		
			S_u (mm/s)	L_b (mm)	U_L (cm/s)	S_u (mm/s)	L_b (mm)	U_L (cm/s)	S_u (mm/s)	L_b (mm)	U_L (cm/s)
0.6	0.1716	15.74	912.98	2.88	15.66	857.16	1.692	14.71	839.71	1.376	14.41
			852.89	2.197	14.63	818.29	1.428	14.04	806.91	1.204	13.84
			908.71	2.196	15.59	872.52	1.434	14.97	862.48	1.222	14.8
0.65	0.1625	20.01	1181.72	1.881	19.2	1144.79	1.291	18.6	1131.63	1.104	18.39
			1173.71	1.357	19.07	1153.06	1.025	18.74	1146.09	0.913	18.62
			1173.02	1.29	19.06	1153.98	0.985	18.75	1147.37	0.88	18.64
0.7	0.1542	24.52	1444.7	1.338	22.28	1419.4	1.011	21.89	1409.8	0.896	21.75
			1460.5	1.059	22.53	1443.55	0.843	22.27	1437.7	0.767	22.18
			1510.04	1.175	23.29	1489.04	0.915	22.97	1481.25	0.823	22.85
0.8	0.1415	32.41	2142.78	0.957	30.33	2122.2	0.778	30.04	2114.58	0.712	29.93
			2179.03	0.992	30.84	2156.78	0.801	30.53	2149.91	0.736	30.43
			2226.88	0.979	31.52	2204.26	0.791	31.2	2206.67	0.763	31.23
0.9	0.1325	38.9	2879.5	1.097	38.14	2843.8	0.866	37.67	2829.84	0.782	37.48
			2747.56	1.105	36.39	2713	0.872	35.94	2698.58	0.784	35.74
			2747.56	1.092	36.39	2714.08	0.865	35.95	2700.58	0.781	35.77

Individual Results: C_3H_8/air

Φ	ρ_b/ρ_u	Aramco 1.3 U_L (cm/s)	LM(S)			LM(C)			NM(S)		
			S_u (mm/s)	L_b (mm)	U_L (cm/s)	S_u (mm/s)	L_b (mm)	U_L (cm/s)	S_u (mm/s)	L_b (mm)	U_L (cm/s)
0.65	0.16	19.44	1226.74	3.097	19.63	1143.7	1.768	18.3	1115.92	1.412	17.86
			1230.62	3.101	19.69	1147.43	1.771	18.36	1120.68	1.421	17.93
			1284.43	4.013	20.55	1159.31	2.036	18.55	1125.07	1.589	18
0.7	0.1518	23.92	1603.73	2.125	24.35	1542.35	1.4	23.42	1521.42	1.181	23.1
			1477.14	2.348	22.43	1411.21	1.495	21.43	1388.72	1.245	21.08
			1598.89	2.618	24.28	1513.93	1.596	22.99	1487.29	1.316	22.58
0.8	0.1392	31.62	2145.57	1.542	29.87	2096.9	1.12	29.2	2079.18	0.979	28.95
			2133.85	1.384	29.71	2093.92	1.035	29.15	2079.62	0.917	28.95
			2121.63	1.415	29.54	2080.75	1.054	28.97	2065.2	0.929	28.75
0.9	0.1302	37.72	2714.85	1.18	35.34	2677.57	0.922	34.86	2662.23	0.825	34.66
			2706.77	1.243	35.24	2665.56	0.958	34.7	2649.69	0.855	34.49
			2834.66	1.33	36.9	2784.55	1.003	36.25	2769.49	0.898	36.05
1	0.1246	41.4	3123.82	0.998	38.94	3091.04	0.804	38.53	3078.2	0.731	38.37
			3160.82	0.981	39.4	3127.73	0.79	38.99	3114.81	0.718	38.82
			3079.64	0.893	38.39	3052.44	0.732	38.05	3041.56	0.67	37.91

Individual Results: C_4H_{10}/air

Φ	ρ_b/ρ_u	USC II U_L (cm/s)	LM(S) S_u (mm/s)	LM(S) L_b (mm)	LM(S) U_L (cm/s)	LM(C) S_u (mm/s)	LM(C) L_b (mm)	LM(C) U_L (cm/s)	NM(S) S_u (mm/s)	NM(S) L_b (mm)	NM(S) U_L (cm/s)
0.7	0.1503	25.22	1326.65	2.864	19.94	1246.12	1.686	18.73	1222.23	1.38	18.37
			1496.23	4.397	22.49	1333.13	2.137	20.04	1285.94	1.633	19.33
			1475.45	3.979	22.18	1333.78	2.029	20.05	1293.63	1.582	19.45
0.8	0.138	32.16	1990.03	2.098	27.47	1916.57	1.394	26.46	1892.56	1.184	26.12
			1929.46	1.937	26.63	1867.45	1.323	25.78	1846.84	1.134	25.49
			1868.07	2.141	25.79	1795.95	1.408	24.79	1772.53	1.192	24.47
0.9	0.129	37.5	2601.39	1.472	33.55	2548	1.086	32.86	2531	0.962	32.64
			2546.26	1.592	32.84	2485.02	1.116	32.05	2465.51	1.004	31.79
			2589.25	1.454	33.39	2537.68	1.078	32.73	2516.43	0.943	32.45

Average Results Datasets:

CH_4/air

Φ	LM(S) S_u(mm/s)	LM(S) L_b (mm)	LM(S) U_L (cm/s)	LM(C) S_u(mm/s)	LM(C) L_b (mm)	LM(C) U_L (cm/s)	NM(S) S_u(mm/s)	NM(S) L_b (mm)	NM(S) U_L (cm/s)
0.6	437.96	-0.255	7.84	438.36	-0.299	7.85	439.12	-0.327	7.85
0.65	754.06	0.112	12.81	753.95	0.105	12.81	753.94	0.104	12.81
0.7	1087.04	0.3	17.61	1085.86	0.279	17.59	1085.25	0.27	17.58
0.8	1769.64	0.52	26.32	1763.99	0.462	26.23	1761.83	0.438	26.2
0.9	2370.65	0.666	32.94	2358.65	0.572	32.77	2353.82	0.535	32.71
1	2747.97	0.74	36.48	2731.12	0.627	36.26	2724.01	0.581	36.16

C_2H_6/air

Φ	LM(S) S_u (mm/s)	LM(S) L_b (mm)	LM(S) U_L (cm/s)	LM(C) S_u (mm/s)	LM(C) L_b (mm)	LM(C) U_L (cm/s)	NM(S) S_u (mm/s)	NM(S) L_b (mm)	NM(S) U_L (cm/s)
0.6	891.53	2.424	15.3	849.32	1.518	14.57	836.37	1.267	14.35
0.65	1176.15	1.509	19.11	1150.61	1.1	18.7	1141.7	0.966	18.55
0.7	1471.75	1.19	22.7	1450.67	0.923	22.38	1442.92	0.828	22.26
0.8	2182.9	0.976	30.9	2161.08	0.79	30.59	2157.05	0.737	30.53
0.9	2791.54	1.098	36.98	2756.96	0.868	36.52	2743	0.782	36.33

C_3H_8/air

Φ	LM(S) S_u (mm/s)	LM(S) L_b (mm)	LM(S) U_L (cm/s)	LM(C) S_u (mm/s)	LM(C) L_b (mm)	LM(C) U_L (cm/s)	NM(S) S_u (mm/s)	NM(S) L_b (mm)	NM(S) U_L (cm/s)
0.65	1247.26	3.403	19.96	1150.15	1.858	18.41	1120.55	1.474	17.93
0.7	1559.92	2.364	23.68	1489.16	1.497	22.61	1465.81	1.248	22.26
0.8	2133.68	1.447	29.71	2090.52	1.07	29.11	2074.67	0.942	28.89
0.9	2752.09	1.251	35.83	2709.22	0.961	35.27	2693.8	0.86	35.07
1	3121.42	0.957	38.91	3090.4	0.775	38.52	3078.19	0.706	38.37

C_4H_{10}/air

Φ	LM(S) S_u (mm/s)	LM(S) L_b (mm)	LM(S) U_L (cm/s)	LM(C) S_u (mm/s)	LM(C) L_b (mm)	LM(C) U_L (cm/s)	NM(S) S_u (mm/s)	NM(S) L_b (mm)	NM(S) U_L (cm/s)
0.7	1432.78	3.747	21.54	1304.34	1.951	19.61	1267.27	1.531	19.05
0.8	1929.19	2.058	26.63	1859.99	1.375	25.67	1837.31	1.17	25.36
0.9	2578.96	1.506	33.26	2523.57	1.093	32.54	2504.31	0.97	32.29

Individual Results: CH_4/H_2 Blend (85/15) vol.%

Φ	ρ_b/ρ_u	Aramco 1.3 U_L (cm/s)	LM(S) S_u (mm/s)	LM(S) L_b (mm)	LM(S) U_L (cm/s)	LM(C) S_u (mm/s)	LM(C) L_b (mm)	LM(C) U_L (cm/s)	NM(S) S_u (mm/s)	NM(S) L_b (mm)	NM(S) U_L (cm/s)
0.55	0.1906	7.5	379.86	-0.944	7.24	372.92	-1.253	7.11	368.91	-1.469	7.03
			394.53	-0.832	7.52	388.76	-1.135	7.41	385.61	-1.395	7.35
0.6	0.1801	11.43	604.97	-0.636	10.89	601.37	-0.748	10.83	600.85	-0.792	10.82
			596.19	-0.598	10.73	592.87	-0.7	10.67	591.5	-0.754	10.65
			578.07	-0.78	10.41	572.73	-0.955	10.31	572.49	-1.017	10.31
0.65	0.1712	15.72	926.26	-0.25	15.85	925.52	-0.266	15.84	925.79	-0.268	15.85
			912.84	-0.417	15.62	910.66	-0.461	15.59	910.42	-0.478	15.58
			940.6	-0.469	16.1	937.73	-0.527	16.05	937.93	-0.543	16.05
0.7	0.1636	20.24	1220.33	-0.232	19.97	1219.45	-0.246	19.95	1219.54	-0.249	19.96
			1291.03	0.025	21.12	1291.02	0.025	21.12	1291.02	0.025	21.12
			1285.44	-0.243	21.03	1284.42	-0.258	21.02	1284.23	-0.264	21.01
0.8	0.1504	29.16	1963.51	0.266	29.53	1961.8	0.25	29.5	1961	0.243	29.49
			1980.16	0.075	29.78	1980.15	0.066	29.78	1980.14	0.064	29.78
			2002.9	0.115	30.12	2003.81	0.112	30.14	2002.92	0.111	30.12
0.9	0.1406	36.71	2553.41	0.341	35.89	2549.86	0.315	35.84	2548.47	0.304	35.82
			2433.46	0.374	34.2	2429.91	0.342	34.15	2427.26	0.328	34.12
			2646.76	0.418	37.2	2640.93	0.372	37.12	2638.61	0.362	37.09

Individual Results: C_2H_6/H_2 Blend (85/15) vol.%

Φ	ρ_b/ρ_u	Aramco 1.3 U_L (cm/s)	LM(S) S_u (mm/s)	LM(S) L_b (mm)	LM(S) U_L (cm/s)	LM(C) S_u (mm/s)	LM(C) L_b (mm)	LM(C) U_L (cm/s)	NM(S) S_u (mm/s)	NM(S) L_b (mm)	NM(S) U_L (cm/s)
0.55	0.1815	12.6	632.92	2.064	11.49	610.31	1.38	11.08	601.12	1.153	10.91
			628.37	2.065	11.41	605.77	1.378	11	597.57	1.161	10.85
			715.38	3.111	12.99	664	1.751	12.05	649.92	1.41	11.8
0.6	0.1713	16.74	930.46	1.674	15.94	906.56	1.191	15.53	897.1	1.026	15.37
			939.19	1.912	16.09	904.92	1.262	15.51	898.28	1.115	15.39
			934.82	1.79	16.02	905.74	1.23	15.52	897.69	1.07	15.38
0.65	0.1628	20.86	1196.02	1.102	19.47	1181.19	0.871	19.23	1175.63	0.787	19.14
			1211.02	1.182	19.72	1194.09	0.92	19.44	1187.27	0.824	19.33
			1175.54	1.033	19.14	1162.52	0.827	18.93	1156.43	0.735	18.83
0.7	0.1549	25.26	1490.15	0.981	23.09	1474.98	0.782	22.85	1469.22	0.723	22.76
			1536.03	0.868	23.8	1523.48	0.717	23.6	1518.94	0.661	23.53
			1510.41	1.03	23.4	1493.58	0.824	23.14	1487.5	0.75	23.05
0.8	0.142	33.84	2258.19	1.064	32.06	2231.13	0.844	31.67	2220.62	0.763	31.53
			2154.95	0.849	31.59	2137.85	0.703	31.35	2132.46	0.651	31.27
			2232.39	0.972	31.7	2210.56	0.785	31.39	2201.41	0.714	31.26
0.9	0.1328	40.55	2854.35	0.89	37.92	2830.46	0.734	37.6	2824.06	0.681	37.52
			2777.61	0.981	36.9	2749.73	0.794	36.53	2740.8	0.729	36.41
			2799.27	0.741	37.19	2783.65	0.633	36.98	2782.53	0.603	36.96

Individual Results: C_3H_8/H_2 Blend (85/15) vol.%

Φ	ρ_b/ρ_u	Aramco 1.3 U_L (cm/s)	LM(S) S_u (mm/s)	LM(S) L_b (mm)	LM(S) U_L (cm/s)	LM(C) S_u (mm/s)	LM(C) L_b (mm)	LM(C) U_L (cm/s)	NM(S) S_u (mm/s)	NM(S) L_b (mm)	NM(S) U_L (cm/s)
0.6	0.1689	16.05	942.43	3.178	15.92	877.99	1.811	14.83	856.76	1.447	14.47
			947.01	3.34	15.99	878.48	1.87	14.84	858.52	1.51	14.5
			951.58	3.505	16.07	878.96	1.939	14.84	860.27	1.573	14.53
0.65	0.1601	20.32	1221.15	2.475	19.55	1178.32	1.55	18.86	1165.08	1.285	18.65
			1254.62	2.114	20.08	1205.64	1.404	19.3	1188.32	1.179	19.02
			1240.59	2.15	19.86	1186.56	1.42	19	1173.36	1.2	18.78
0.7	0.1524	24.58	1552.94	1.66	23.67	1514.06	1.187	23.07	1500.65	1.034	22.87
			1552.96	1.502	23.67	1520.07	1.103	23.16	1508.35	0.969	22.99
			1543.51	1.492	23.52	1510.84	1.095	23.02	1499.19	0.962	22.85
0.8	0.1399	32.44	2208.24	1.141	30.9	2178.93	0.894	30.49	2168.46	0.808	30.35
			2270.92	1.14	31.78	2241.69	0.897	31.37	2232.51	0.815	31.24
			2246.71	1.078	31.44	2220.25	0.857	31.07	2211.34	0.779	30.95
0.9	0.1307	39.07	2804.9	0.926	36.65	2779.34	0.757	36.31	2770.84	0.696	36.2
			2861.74	0.928	37.39	2834.35	0.754	37.03	2827.33	0.698	36.94
			2867.71	0.993	37.47	2838.46	0.802	37.08	2829.15	0.735	36.96

Individual Results: C_4H_{10}/H_2 Blend (85/15) vol.%

Φ	ρ_b/ρ_u	USC II U_L (cm/s)	LM(S) S_u (mm/s)	LM(S) L_b (mm)	LM(S) U_L (cm/s)	LM(C) S_u (mm/s)	LM(C) L_b (mm)	LM(C) U_L (cm/s)	NM(S) S_u (mm/s)	NM(S) L_b (mm)	NM(S) U_L (cm/s)
0.7	0.1508	25.68	1402.61	3.238	18.13	1302.45	1.792	16.84	1270.7	1.453	16.43
			1528.97	3.619	19.76	1398.84	1.922	18.08	1360.86	1.516	17.59
			1540.81	3.706	19.92	1406.12	1.951	18.18	1368.4	1.54	17.69
0.8	0.1383	32.98	1987.18	1.923	27.47	1924.02	1.317	26.6	1902.24	1.128	26.3
			1998.98	1.929	27.64	1934.47	1.317	26.75	1911.62	1.124	26.43
			2051.96	2.196	28.37	1968.16	1.425	27.21	1944.67	1.214	26.89
0.9	0.1293	38.44	2579.4	1.34	33.34	2533.05	1.009	32.74	2516.22	0.895	32.53
			2620.41	1.283	33.87	2578.37	0.982	33.33	2563.69	0.879	33.14
			2634.58	1.571	34.06	2575.46	1.102	33.29	2558.33	1.012	33.07

Average Results CH_4/H_2 Blend (85/15) vol.%

Φ	LM(S)			LM(C)			NM(S)		
	S_u (mm/s)	L_b (mm)	U_L (cm/s)	S_u (mm/s)	L_b (mm)	U_L (cm/s)	S_u (mm/s)	L_b (mm)	U_L (cm/s)
0.55	387.2	-0.888	7.38	380.84	-1.194	7.26	377.26	-1.432	7.19
0.6	593.07	-0.671	10.68	588.99	-0.801	10.61	588.28	-0.855	10.59
0.65	926.57	-0.379	15.86	924.63	-0.418	15.83	924.71	-0.43	15.83
0.7	1265.6	-0.15	20.71	1264.96	-0.16	20.7	1264.93	-0.163	20.7
0.8	1982.19	0.152	29.81	1981.92	0.143	29.81	1981.35	0.139	29.8
0.9	2544.54	0.377	35.77	2540.23	0.343	35.71	2538.11	0.331	35.68

Average Results C_2H_6/H_2 Blend (85/15) vol.%

Φ	LM(S)			LM(C)			NM(S)		
	S_u (mm/s)	L_b (mm)	U_L (cm/s)	S_u (mm/s)	L_b (mm)	U_L (cm/s)	S_u (mm/s)	L_b (mm)	U_L (cm/s)
0.55	658.89	2.413	11.96	626.69	1.503	11.38	616.21	1.241	11.19
0.6	934.82	1.793	16.02	905.74	1.226	15.52	897.69	1.07	15.38
0.65	1194.19	1.106	19.44	1179.27	0.873	19.2	1173.11	0.782	19.1
0.7	1512.2	0.96	23.43	1497.35	0.775	23.2	1491.89	0.711	23.11
0.8	2215.18	0.962	31.78	2193.18	0.777	31.47	2184.83	0.71	31.35
0.9	2810.41	0.871	37.33	2787.94	0.72	37.04	2782.46	0.671	36.96

Average Results C_3H_8/H_2 Blend (85/15) vol.%

Φ	LM(S)			LM(C)			NM(S)		
	S_u (mm/s)	L_b (mm)	U_L (cm/s)	S_u (mm/s)	L_b (mm)	U_L (cm/s)	S_u (mm/s)	L_b (mm)	U_L (cm/s)
0.6	947.01	3.342	15.99	878.48	1.875	14.84	858.52	1.51	14.5
0.65	1238.78	2.247	19.83	1190.17	1.458	19.05	1175.58	1.22	18.82
0.7	1549.81	1.551	23.62	1514.99	1.128	23.09	1502.73	0.989	22.9
0.8	2241.96	1.12	31.37	2213.63	0.883	30.98	2204.1	0.801	30.84
0.9	2844.78	0.949	37.17	2817.38	0.771	36.81	2809.11	0.71	36.7

Average Results C_4H_{10}/H_2 Blend (85/15) vol.%

Φ	LM(S)			LM(C)			NM(S)		
	S_u (mm/s)	L_b (mm)	U_L (cm/s)	S_u (mm/s)	L_b (mm)	U_L (cm/s)	S_u (mm/s)	L_b (mm)	U_L (cm/s)
0.7	1490.8	3.521	19.27	1369.13	1.888	17.7	1333.32	1.503	17.24
0.8	2012.7	2.016	27.83	1942.21	1.353	26.85	1919.51	1.155	26.54
0.9	2611.46	1.398	33.76	2562.29	1.031	33.12	2546.08	0.928	32.91

Individual Results: 98% CH_4 – 2% C_3H_8 (vol.%)

Φ	ρ_b/ρ_u	Aramco 1.3 U_L (cm/s)	LM(S) S_u (mm/s)	LM(S) L_b (mm)	LM(S) U_L (cm/s)	LM(C) S_u (mm/s)	LM(C) L_b (mm)	LM(C) U_L (cm/s)	NM(S) S_u (mm/s)	NM(S) L_b (mm)	NM(S) U_L (cm/s)
0.6	0.1785	10.41	542.87	0.243	9.69	541.89	0.239	9.67	541.46	0.237	9.67
			530.16	0.222	9.47	530.05	0.217	9.46	529.74	0.215	9.46
			526.25	0.141	9.4	526.11	0.136	9.39	526.05	0.134	9.39
0.65	0.1695	14.42	933.27	0.561	15.81	929.92	0.494	15.76	928.82	0.469	15.74
			841.07	0.287	14.25	840.33	0.269	14.24	840.6	0.267	14.24
			846.05	0.336	14.34	844.91	0.311	14.32	844.49	0.301	14.31
0.7	0.1614	18.63	1144.1	0.592	18.47	1139.49	0.518	18.39	1137.88	0.49	18.37
			1154.62	0.612	18.64	1149.75	0.534	18.56	1148.5	0.507	18.54
			1142.32	0.55	18.44	1137.17	0.463	18.36	1138.36	0.486	18.38
0.8	0.1482	26.95	1763.47	0.555	26.13	1757.92	0.489	26.05	1756.12	0.465	26.02
			1784.43	0.53	26.44	1778.93	0.47	26.36	1776.33	0.443	26.32
			1714.64	0.676	25.41	1705.85	0.581	25.28	1704.08	0.551	25.25
0.9	0.1385	33.67	2337.69	0.872	32.38	2319.61	0.724	32.13	2316.9	0.68	32.09
			2351.15	0.876	32.57	2332.62	0.726	32.31	2329.55	0.681	32.27
			2342.32	0.788	32.44	2326.81	0.664	32.23	2323.72	0.624	32.19
1	0.1323	38.01	2706.29	1.051	35.82	2674.93	0.837	35.4	2668.32	0.772	35.31
			2678.4	0.966	35.45	2653.02	0.786	35.11	2646.29	0.726	35.02
			2700.2	1.065	35.74	2669.36	0.85	35.33	2662.91	0.785	35.24

Individual Results: Individual Results: 96% CH_4 – 4% C_3H_8 (vol.%)

Φ	ρ_b/ρ_u	Aramco 1.3 U_L (cm/s)	LM(S) S_u (mm/s)	LM(S) L_b (mm)	LM(S) U_L (cm/s)	LM(C) S_u (mm/s)	LM(C) L_b (mm)	LM(C) U_L (cm/s)	NM(S) S_u (mm/s)	NM(S) L_b (mm)	NM(S) U_L (cm/s)
0.6	0.1781	10.55	536.52	0.402	9.55	535.48	0.367	9.54	535.08	0.352	9.53
			511.72	0.62	9.11	509.45	0.538	9.07	508.53	0.505	9.06
0.65	0.169	14.69	874.68	0.463	14.78	872.77	0.419	14.75	873.49	0.414	14.76
			875.61	0.514	14.79	872.86	0.456	14.75	872.08	0.436	14.73
			867.27	0.431	14.65	865.46	0.392	14.62	864.57	0.373	14.61
0.7	0.161	18.92	1180.35	0.803	19	1172.21	0.674	18.87	1168.66	0.621	18.81
			1161.83	0.558	18.7	1157.78	0.493	18.64	1156.58	0.469	18.62
			1182.71	0.763	19.04	1175.3	0.646	18.92	1172.24	0.599	18.87
0.8	0.1478	27.22	1819.29	0.828	26.88	1806.01	0.691	26.69	1802.26	0.644	26.63
			1820.37	0.773	26.9	1808.72	0.653	26.73	1806.29	0.614	26.69
			1761.79	0.77	26.03	1750.73	0.652	25.87	1749.02	0.616	25.84
0.9	0.1382	33.9	2385.87	0.941	32.96	2364.14	0.769	32.66	2358.78	0.714	32.59
			2387.11	0.861	32.98	2368.06	0.713	32.72	2363.8	0.666	32.66
			2404.05	0.892	33.21	2383.47	0.733	32.93	2379.74	0.686	32.88
1	0.132	38.2	2680.45	0.855	35.38	2660.12	0.711	35.11	2658.56	0.673	35.09
			2700.03	0.956	35.63	2674.38	0.778	35.3	2669.68	0.726	35.23
			2767.15	1.12	36.52	2732.83	0.886	36.07	2720.27	0.8	35.9

Individual Results: 94% CH_4 – 6% C_3H_8 (vol.%)

Φ	ρ_b/ρ_u	Aramco 1.3 U_L (cm/s)	LM(S) S_u (mm/s)	LM(S) L_b (mm)	LM(S) U_L (cm/s)	LM(C) S_u (mm/s)	LM(C) L_b (mm)	LM(C) U_L (cm/s)	NM(S) S_u (mm/s)	NM(S) L_b (mm)	NM(S) U_L (cm/s)
0.6	0.1776	10.93	595.85	1.079	10.58	588.61	0.854	10.45	585.62	0.769	10.4
			558.5	0.918	9.92	553.47	0.751	9.83	551.4	0.687	9.79
			576.97	0.984	10.25	570.79	0.798	10.14	568.03	0.722	10.09
0.65	0.1685	14.94	872.92	0.504	14.71	870.39	0.45	14.67	870.56	0.438	14.67
			926.56	0.789	15.61	920.14	0.662	15.51	918.47	0.62	15.48
			902.87	0.651	15.21	898.65	0.564	15.14	897.59	0.534	15.13
0.7	0.1605	19.15	1242.67	0.812	19.95	1233.71	0.679	19.81	1230.76	0.631	19.76
			1224.4	0.826	19.66	1215.12	0.687	19.51	1212.26	0.639	19.46
0.8	0.1474	27.45	1865.62	0.847	27.5	1851.55	0.705	27.29	1847.37	0.656	27.23
			1846.8	0.887	27.22	1831.76	0.733	27	1826.26	0.676	26.92
			1841.95	0.82	27.15	1828.31	0.684	26.95	1824.43	0.637	26.89
0.9	0.1377	34.1	2424.99	0.924	33.39	2403.56	0.758	33.1	2398.47	0.705	33.03
			2397.92	0.91	33.02	2376.91	0.747	32.73	2370.84	0.692	32.65
			2381.54	0.892	32.79	2361.73	0.736	32.52	2358.24	0.689	32.47
1	0.1315	38.42	2740.46	0.868	36.04	2718.75	0.719	35.75	2716.18	0.677	35.72
			2744.01	1.028	36.09	2713.36	0.822	35.68	2703.99	0.752	35.56
			2715.87	0.962	35.72	2689.85	0.783	35.37	2682.79	0.723	35.28

Individual Results: 92% CH_4 – 8% C_3H_8 (vol.%)

Φ	ρ_b/ρ_u	Aramco 1.3 U_L (cm/s)	LM(S) S_u (mm/s)	LM(S) L_b (mm)	LM(S) U_L (cm/s)	LM(C) S_u (mm/s)	LM(C) L_b (mm)	LM(C) U_L (cm/s)	NM(S) S_u (mm/s)	NM(S) L_b (mm)	NM(S) U_L (cm/s)
0.6	0.1772	11.15	660.29	1.177	11.7	650.87	0.914	11.53	647.51	0.822	11.47
			638.79	1.096	11.32	630.82	0.865	11.18	627.61	0.779	11.12
			649.97	1.263	11.51	639.74	0.968	11.33	636.66	0.873	11.28
0.65	0.1681	15.19	942.49	0.843	15.84	935.11	0.699	15.72	932.53	0.647	15.67
			904.99	0.82	15.21	898.46	0.685	15.1	897.03	0.642	15.08
			931.15	0.937	15.65	922.51	0.765	15.51	919.45	0.702	15.45
0.7	0.1601	19.39	1311.82	1.011	21.01	1297.55	0.811	20.78	1294.42	0.749	20.73
			1265.12	0.943	20.26	1253.15	0.768	20.07	1249.43	0.707	20.01
			1226.53	0.745	19.64	1219.11	0.632	19.52	1216.86	0.592	19.49
0.8	0.147	27.67	1869.45	0.916	27.47	1852.96	0.751	27.23	1848.48	0.696	27.17
			1871.01	0.92	27.5	1854.4	0.754	27.25	1850.77	0.701	27.2
			1849.11	0.757	27.18	1837.56	0.641	27.01	1835.06	0.603	26.97
0.9	0.1373	34.29	2454.59	1.073	33.71	2425.96	0.855	33.32	2416	0.777	33.18
			2416.43	0.973	33.19	2392.69	0.789	32.86	2386.96	0.73	32.78
			2445.58	0.945	33.59	2422.65	0.77	33.27	2416.93	0.714	33.19
1	0.1313	38.58	2796.21	1.038	36.71	2764.77	0.83	36.3	2757.4	0.764	36.2
			2809.61	1.102	36.88	2775.51	0.874	36.44	2765.38	0.797	36.3
			2756.39	0.941	36.19	2731.48	0.77	35.86	2727.51	0.719	35.81

Individual Results: 90% CH_4 – 10% C_3H_8 (vol.%)

Φ	ρ_b/ρ_u	Aramco 1.3 U_L (cm/s)	LM(S) S_u (mm/s)	LM(S) L_b (mm)	LM(S) U_L (cm/s)	LM(C) S_u (mm/s)	LM(C) L_b (mm)	LM(C) U_L (cm/s)	NM(S) S_u (mm/s)	NM(S) L_b (mm)	NM(S) U_L (cm/s)
0.6	0.1767	11.38	656.95	1.273	11.61	646.29	0.972	11.42	642.97	0.873	11.36
			679.95	1.282	12.02	668.86	0.978	11.82	665.22	0.877	11.76
0.65	0.1677	15.37	952.94	1.068	15.98	941.16	0.844	15.79	937.47	0.769	15.72
			937.55	1.076	15.73	926.24	0.853	15.54	921.51	0.768	15.46
			940.76	0.997	15.78	930.81	0.802	15.61	927.34	0.733	15.55
0.7	0.1597	19.65	1223.94	0.89	19.55	1213.47	0.732	19.38	1209.57	0.673	19.32
			1267.33	0.924	20.24	1255.88	0.756	20.06	1251.6	0.694	19.99
			1221.7	0.696	19.51	1215.05	0.596	19.41	1213.41	0.562	19.38
0.8	0.1466	27.86	1929.32	1.034	28.28	1908.46	0.83	27.97	1902.76	0.763	27.89
			1903.05	0.729	27.9	1892.25	0.621	27.74	1892.14	0.595	27.74
			1849.11	0.757	27.1	1837.56	0.641	26.94	1835.06	0.603	26.9
0.9	0.1371	34.48	2443.43	0.86	33.49	2424.49	0.714	33.23	2420.41	0.668	33.17
			2467.77	1.029	33.82	2441.2	0.827	33.46	2433.88	0.76	33.36
			2487.99	1.106	34.1	2457.68	0.876	33.69	2449.09	0.8	33.57
1	0.131	38.72	2860.93	1.067	37.47	2827.23	0.848	37.03	2820.06	0.782	36.93
			2790.08	1.146	36.54	2754.25	0.902	36.07	2743.69	0.821	35.93
			2777.44	1.031	36.37	2746.34	0.896	35.97	2739.73	0.761	35.88

Individual Results: 85% CH_4 – 15% C_3H_8 (vol.%)

Φ	ρ_b/ρ_u	Aramco 1.3 U_L (cm/s)	LM(S) S_u (mm/s)	LM(S) L_b (mm)	LM(S) U_L (cm/s)	LM(C) S_u (mm/s)	LM(C) L_b (mm)	LM(C) U_L (cm/s)	NM(S) S_u (mm/s)	NM(S) L_b (mm)	NM(S) U_L (cm/s)
0.6	0.1759	11.83	687.07	1.781	12.08	667.8	1.248	11.74	660.81	1.075	11.62
			670.79	1.628	11.8	654.31	1.167	11.51	647.92	1.01	11.4
			664.96	1.755	11.69	646.49	1.231	11.37	640.16	1.065	11.26
0.65	0.1668	15.9	894.35	1.24	14.92	880.99	0.958	14.7	875.65	0.854	14.61
			1025.56	1.389	17.11	1006.12	1.037	16.78	999.59	0.921	16.67
			991.01	1.231	16.53	975.91	0.948	16.28	970.28	0.848	16.19
0.7	0.1589	20.12	1235.18	1.014	19.62	1222.06	0.816	19.42	1216.6	0.739	19.33
			1263.75	0.991	20.08	1250.61	0.798	19.87	1245.46	0.726	19.79
			1270.84	0.888	20.19	1260.38	0.733	20.02	1255.79	0.671	19.95
0.8	0.1457	28.31	1817.83	0.999	26.49	1799.1	0.806	26.22	1791.17	0.731	26.1
			1877.07	0.9	27.36	1860.77	0.739	27.12	1854.05	0.677	27.02
			1889.35	0.931	27.54	1872.02	0.76	27.28	1864.75	0.694	27.18
0.9	0.1362	34.93	2434.72	1.008	33.15	2408.87	0.811	32.8	2399.03	0.738	32.67
			2374.61	0.87	32.33	2354.88	0.718	32.07	2347.22	0.66	31.96
			2375.97	0.988	32.35	2352.05	0.8	32.03	2342.36	0.727	31.89
1	0.1301	39.19	2626.36	0.958	34.16	2600.97	0.779	33.83	2591.52	0.712	33.71
			2501.85	1.176	32.54	2466.62	0.915	32.08	2452.46	0.818	31.9
			2603.01	0.689	33.86	2589.16	0.591	33.68	2583.58	0.552	33.6

Average Results: 98% CH_4 – 2% C_3H_8 (vol.%) Blend

Φ	LM(S)			LM(C)			NM(S)		
	S_u (mm/s)	L_b (mm)	U_L (cm/s)	S_u (mm/s)	L_b (mm)	U_L (cm/s)	S_u (mm/s)	L_b (mm)	U_L (cm/s)
0.6	533.09	0.202	9.52	532.68	0.197	9.51	532.42	0.195	9.51
0.65	873.46	0.394	14.8	871.72	0.358	14.77	871.3	0.346	14.76
0.7	1147.01	0.585	18.52	1142.14	0.505	18.44	1141.58	0.494	18.43
0.8	1754.18	0.587	26	1747.57	0.514	25.9	1745.51	0.486	25.87
0.9	2343.72	0.845	32.46	2326.35	0.705	32.22	2323.39	0.662	32.18
1	2694.96	1.027	35.67	2665.77	0.824	35.28	2659.17	0.761	35.19

Average Results: 96% CH_4 – 4% C_3H_8 (vol.%) Blend

Φ	LM(S)			LM(C)			NM(S)		
	S_u (mm/s)	L_b (mm)	U_L (cm/s)	S_u (mm/s)	L_b (mm)	U_L (cm/s)	S_u (mm/s)	L_b (mm)	U_L (cm/s)
0.6	524.12	0.511	9.33	522.47	0.452	9.3	521.8	0.429	9.29
0.65	872.52	0.469	14.74	870.36	0.422	14.7	870.05	0.408	14.7
0.7	1174.96	0.708	18.91	1168.43	0.604	18.81	1165.83	0.563	18.77
0.8	1800.48	0.79	26.6	1788.49	0.665	26.43	1785.86	0.625	26.39
0.9	2392.34	0.898	33.05	2371.89	0.739	32.77	2367.44	0.689	32.71
1	2715.88	0.977	35.84	2689.11	0.792	35.49	2682.84	0.733	35.41

Average Results: 94% CH_4 – 6% C_3H_8 (vol.%) Blend

Φ	LM(S)			LM(C)			NM(S)		
	S_u (mm/s)	L_b (mm)	U_L (cm/s)	S_u (mm/s)	L_b (mm)	U_L (cm/s)	S_u (mm/s)	L_b (mm)	U_L (cm/s)
0.6	577.11	0.993	10.25	570.96	0.801	10.14	568.35	0.726	10.09
0.65	900.78	0.648	15.18	896.39	0.559	15.11	895.54	0.53	15.09
0.7	1233.53	0.819	19.8	1224.42	0.683	19.66	1221.51	0.635	19.61
0.8	1851.46	0.851	27.29	1837.2	0.708	27.08	1832.68	0.656	27.01
0.9	2401.48	0.909	33.07	2380.73	0.747	32.78	2375.85	0.695	32.72
1	2733.44	0.953	35.95	2707.32	0.775	35.6	2700.99	0.717	35.52

Average Results: 92% CH_4 – 8% C_3H_8 (vol.%) Blend

Φ	LM(S)			LM(C)			NM(S)		
	S_u (mm/s)	L_b (mm)	U_L (cm/s)	S_u (mm/s)	L_b (mm)	U_L (cm/s)	S_u (mm/s)	L_b (mm)	U_L (cm/s)
0.6	649.68	1.179	11.51	640.47	0.916	11.35	637.26	0.825	11.29
0.65	926.21	0.867	15.57	918.69	0.717	15.44	916.33	0.664	15.4
0.7	1267.82	0.9	20.3	1256.6	0.737	20.12	1253.57	0.683	20.07
0.8	1863.19	0.864	27.38	1848.31	0.715	27.16	1844.77	0.667	27.11
0.9	2438.87	0.997	33.49	2413.77	0.804	33.15	2406.63	0.74	33.05
1	2787.4	1.027	36.59	2757.25	0.824	36.2	2750.1	0.76	36.1

Average Results: 90% CH_4 – 10% C_3H_8 (vol.%) Blend

Φ	LM(S)			LM(C)			NM(S)		
	S_u (mm/s)	L_b (mm)	U_L (cm/s)	S_u (mm/s)	L_b (mm)	U_L (cm/s)	S_u (mm/s)	L_b (mm)	U_L (cm/s)
0.6	668.45	1.277	11.81	657.57	0.975	11.62	654.1	0.875	11.56
0.65	943.75	1.047	15.83	932.74	0.833	15.64	928.77	0.757	15.58
0.7	1237.66	0.837	19.77	1228.13	0.695	19.61	1224.86	0.643	19.56
0.8	1893.83	0.84	27.76	1879.42	0.697	27.55	1876.65	0.654	27.51
0.9	2466.4	0.998	33.81	2441.13	0.806	33.46	2434.46	0.743	33.37
1	2809.48	1.082	36.79	2775.94	0.882	36.35	2767.83	0.788	36.25

Average Results: 85% CH_4 – 15% C_3H_8 (vol.%) Blend

Φ	LM(S)			LM(C)			NM(S)		
	S_u (mm/s)	L_b (mm)	U_L (cm/s)	S_u (mm/s)	L_b (mm)	U_L (cm/s)	S_u (mm/s)	L_b (mm)	U_L (cm/s)
0.6	674.27	1.721	11.86	656.2	1.215	11.54	649.63	1.05	11.43
0.65	970.31	1.287	16.19	954.34	0.981	15.92	948.51	0.874	15.82
0.7	1256.59	0.964	19.96	1244.35	0.783	19.77	1239.28	0.712	19.69
0.8	1861.42	0.943	27.13	1843.97	0.769	26.87	1836.66	0.701	26.77
0.9	2395.1	0.956	32.61	2371.93	0.776	32.3	2362.87	0.708	32.17
1	2577.07	0.941	33.52	2552.25	0.761	33.2	2542.52	0.694	33.07

Individual Results: Ultra-Lean (Φ = 0.65) CH_4/C_3H_8 Blend

% (vol.) of C_3H_8 in CH_4	ρ_b/ρ_u	Aramco 1.3	LM(S)			LM(C)			NM(S)		
		U_L (cm/s)	S_u (mm/s)	L_b (mm)	U_L (cm/s)	S_u (mm/s)	L_b (mm)	U_L (cm/s)	S_u (mm/s)	L_b (mm)	U_L (cm/s)
0%	0.1699	14.13	749.68	0.137	12.74	749.51	0.133	12.74	749.57	0.132	12.74
			752.91	0.063	12.79	752.88	0.062	12.79	752.86	0.061	12.79
			759.6	0.136	12.91	759.47	0.121	12.91	759.39	0.119	12.90
2%	0.1695	14.42	933.27	0.561	15.81	929.92	0.494	15.76	928.82	0.469	15.74
			841.07	0.287	14.25	840.33	0.269	14.24	840.6	0.267	14.24
			846.05	0.336	14.34	844.91	0.311	14.32	844.49	0.301	14.31
4%	0.169	14.69	874.68	0.463	14.78	872.77	0.419	14.75	873.49	0.414	14.76
			875.61	0.514	14.79	872.86	0.456	14.75	872.08	0.436	14.73
			867.27	0.431	14.65	865.46	0.392	14.62	864.57	0.373	14.61
6%	0.1685	14.94	872.92	0.504	14.71	870.39	0.45	14.67	870.56	0.438	14.67
			926.56	0.789	15.61	920.14	0.662	15.51	918.47	0.62	15.48
			902.87	0.651	15.21	898.65	0.564	15.14	897.59	0.534	15.13
8%	0.1681	15.19	942.49	0.843	15.84	935.11	0.699	15.72	932.53	0.647	15.67
			904.99	0.82	15.21	898.46	0.685	15.10	897.03	0.642	15.08
			931.15	0.937	15.65	922.51	0.765	15.51	919.45	0.702	15.45
10%	0.1677	15.37	952.94	1.068	15.98	941.16	0.844	15.79	937.47	0.769	15.72
			937.55	1.076	15.73	926.24	0.853	15.54	921.51	0.768	15.46
			940.76	0.997	15.78	930.81	0.802	15.61	927.34	0.733	15.55

Individual Results: Ultra-Lean (Φ = 0.65) CH_4/C_3H_8 Blend

% (vol.) of C_3H_8 in CH_4	ρ_b/ρ_u	Aramco 1.3 U_L (cm/s)	LM(S) S_u (mm/s)	LM(S) L_b (mm)	LM(S) U_L (cm/s)	LM(C) S_u (mm/s)	LM(C) L_b (mm)	LM(C) U_L (cm/s)	NM(S) S_u (mm/s)	NM(S) L_b (mm)	NM(S) U_L (cm/s)
15%	0.1668	15.9	894.35	1.24	14.92	880.99	0.958	14.70	875.65	0.854	14.61
			1025.56	1.389	17.11	1006.12	1.037	16.78	999.59	0.921	16.67
			991.01	1.231	16.53	975.91	0.948	16.28	970.28	0.848	16.19
25%	0.1653	16.76	1043.1	1.617	17.24	1017.98	1.163	16.82	1007.79	1.005	16.66
			1063.85	1.515	17.58	1040.41	1.105	17.19	1032.89	0.975	17.07
			1027.15	1.451	16.98	1006.39	1.074	16.63	998.38	0.942	16.50
30%	0.1648	17	1130.5	2.423	18.63	1077.65	1.526	17.76	1061.25	1.275	17.49
			1084.12	2.399	17.86	1032.89	1.506	17.02	1018.05	1.265	16.78
			1148.43	2.436	18.92	1094.05	1.529	18.03	1078.11	1.282	17.77
40%	0.1637	17.62	1160.77	2.381	19.00	1108.1	1.51	18.14	1088.8	1.247	17.82
			1250.45	2.913	20.47	1173.59	1.71	19.21	1146.97	1.376	18.77
			1149.02	2.262	18.81	1100.32	1.457	18.01	1082.55	1.211	17.72
50%	0.1628	18.09	1287.42	3.663	20.96	1177.58	1.945	19.17	1143.96	1.525	18.62
			1259.51	3.226	20.50	1169.38	1.811	19.03	1143.24	1.459	18.61
70%	0.1615	18.69	1346.36	3.848	21.75	1219.77	1.974	19.70	1186.19	1.553	19.16
			1305	3.467	21.08	1200.15	1.877	19.39	1172.99	1.508	18.95
85%	0.1606	19.17	1339.68	4.051	21.52	1209.07	2.057	19.42	1175.7	1.62	18.89
			1318.86	3.928	21.19	1210.93	2.138	19.45	1179.35	1.707	18.95
100%	0.16	19.44	1226.74	3.097	19.63	1143.7	1.768	18.30	1115.92	1.412	17.86
			1230.62	3.101	19.69	1147.43	1.771	18.36	1120.68	1.421	17.93
			1284.43	4.013	20.55	1159.31	2.036	18.55	1125.07	1.589	18.00

Individual Results: Ultra-Lean ($\Phi = 0.65$) CH_4/C_2H_6 Blend

% (vol.) of C_2H_6 in CH_4	ρ_b/ρ_u	Aramco 1.3 U_L (cm/s)	LM(S) S_u (mm/s)	LM(S) L_b (mm)	LM(S) U_L (cm/s)	LM(C) S_u (mm/s)	LM(C) L_b (mm)	LM(C) U_L (cm/s)	NM(S) S_u (mm/s)	NM(S) L_b (mm)	NM(S) U_L (cm/s)
0%	0.1699	14.13	749.68	0.137	12.74	749.51	0.133	12.74	749.57	0.132	12.74
			752.91	0.063	12.79	752.88	0.062	12.79	752.86	0.061	12.79
			759.6	0.136	12.91	759.47	0.121	12.91	759.39	0.119	12.9
2%	0.1697	14.41	817.57	0.158	13.87	817.33	0.153	13.87	817.43	0.152	13.87
			825.83	0.115	14.01	825.7	0.112	14.01	825.66	0.111	14.01
			816.98	0.089	13.86	816.89	0.087	13.86	816.85	0.086	13.86
4%	0.1694	14.67	846.7	0.383	14.34	845.2	0.351	14.32	844.46	0.336	14.3
			833.57	0.325	14.12	832.55	0.302	14.1	832.09	0.292	14.09
			809.02	0.258	13.7	808.39	0.243	13.69	808.15	0.237	13.69
6%	0.1691	14.91	861.82	0.432	14.58	859.93	0.391	14.54	859.06	0.373	14.53
			845.38	0.311	14.3	844.45	0.29	14.28	843.88	0.279	14.27
			831.63	0.455	14.07	829.6	0.41	14.03	828.67	0.391	14.02
8%	0.1689	15.18	873.55	0.491	14.75	871.07	0.438	14.71	870.02	0.416	14.69
			845.92	0.446	14.28	843.98	0.403	14.25	843	0.383	14.24
			855.13	0.411	14.44	853.39	0.373	14.41	852.61	0.357	14.4
10%	0.1686	15.4	893.4	0.498	15.07	890.8	0.445	15.02	889.74	0.423	15
			887.45	0.659	14.97	883.04	0.568	14.89	881.58	0.534	14.87
			846.01	0.452	14.27	843.97	0.408	14.23	842.93	0.388	14.21
15%	0.1681	15.89	906.18	0.604	15.23	902.48	0.528	15.17	900.83	0.496	15.14
			895.16	0.557	15.05	891.9	0.49	14.99	890.6	0.463	14.97
			904.36	0.661	15.2	899.88	0.57	15.13	897.88	0.532	15.09

Individual Results: Ultra-Lean ($\Phi = 0.65$) CH_4/C_2H_6 Blend

% (vol.) of C_2H_6 in CH_4	ρ_b/ρ_u	Aramco 1.3	LM(S)			LM(C)			NM(S)		
		U_L (cm/s)	S_u (mm/s)	L_b (mm)	U_L (cm/s)	S_u (mm/s)	L_b (mm)	U_L (cm/s)	S_u (mm/s)	L_b (mm)	U_L (cm/s)
25%	0.1671	16.76	959.13	1.101	16.03	947.04	0.868	15.82	941.85	0.778	15.74
			957.83	0.838	16	950.46	0.696	15.88	947.59	0.642	15.83
			972.73	1.024	16.25	962.11	0.821	16.08	958.29	0.748	16.01
30%	0.1667	17.05	973.03	1.228	16.22	958.25	0.946	15.98	952.33	0.843	15.88
			946.97	0.54	15.79	953.09	0.656	15.89	950.69	0.609	15.85
			978.66	1.007	16.32	968.15	0.809	16.14	964.05	0.735	16.07
40%	0.1659	17.75	1039.77	1.152	17.24	1025.43	0.899	17.01	1019.33	0.803	16.91
			1010.81	1.24	16.76	994.87	0.951	16.5	988.48	0.846	16.39
			1002.48	1.361	16.63	983.69	1.019	16.31	977.42	0.906	16.21
50%	0.1651	18.28	1071.93	1.17	17.7	1057.28	0.914	17.46	1050.84	0.815	17.35
			1071.96	1.421	17.7	1051.14	1.058	17.36	1042.95	0.93	17.22
			1093.4	1.321	18.05	1074.46	0.994	17.74	1066.97	0.884	17.62
70%	0.1639	19.13	1090.75	1.478	17.88	1068.41	1.092	17.51	1061.62	0.969	17.4
			1110.76	1.482	18.2	1088.1	1.095	17.83	1079.96	0.964	17.7
			1106.25	1.208	18.13	1090.86	0.942	17.88	1086.19	0.853	17.8
85%	0.1632	19.6	1190.86	1.753	19.43	1158.13	1.233	18.9	1147.3	1.069	18.72
			1141.52	1.343	18.63	1121.86	1.018	18.3	1115.21	0.907	18.2
			1156.38	1.386	18.87	1135.55	1.044	18.53	1126.71	0.917	18.38
100%	0.1625	20.01	1181.72	1.881	19.2	1144.79	1.291	18.6	1131.63	1.104	18.39
			1173.71	1.357	19.07	1153.06	1.025	18.74	1146.09	0.913	18.62
			1173.02	1.29	19.06	1153.98	0.985	18.75	1147.37	0.88	18.64

Individual Results : Ultra-Lean (Φ = 0.65) C_2H_6/C_3H_8 Blend

% (vol.) of C_2H_6 in C_3H_8	ρ_b/ρ_u	Aramco 1.3	LM(S)			LM(C)			NM(S)		
		U_L (cm/s)	S_u (mm/s)	L_b (mm)	U_L (cm/s)	S_u (mm/s)	L_b (mm)	U_L (cm/s)	S_u (mm/s)	L_b (mm)	U_L (cm/s)
0%	0.1625	20.47	1181.72	1.881	19.20	1144.79	1.291	18.60	1131.63	1.104	18.39
			1173.71	1.357	19.07	1153.06	1.025	18.74	1146.09	0.913	18.62
			1173.02	1.29	19.06	1153.98	0.985	18.75	1147.37	0.88	18.64
30%	0.1609	20.26	1254.78	2.47	20.19	1170.54	1.548	18.83	1144.86	1.278	18.42
			1263.76	2.525	20.33	1173.15	1.569	18.87	1145.42	1.293	18.43
			1244.21	2.618	20.02	1160.77	1.602	18.67	1135.06	1.312	18.26
50%	0.1603	20.19	1289.1	2.847	20.66	1213.16	1.691	19.44	1187.31	1.37	19.03
			1295.28	3.057	20.76	1210.49	1.763	19.40	1182.67	1.416	18.95
			1267.2	3.109	20.31	1182.31	1.78	18.95	1154.25	1.425	18.50
70%	0.1598	20.1	1254.3	3.085	20.04	1194.44	1.766	19.08	1173.65	1.424	18.75
			1247.16	3.221	19.93	1185.53	1.808	18.94	1164.43	1.447	18.60
			1240.23	3.085	19.81	1174.75	1.766	18.77	1152.26	1.424	18.41
100%	0.16	19.44	1226.74	3.097	19.63	1143.7	1.768	18.30	1115.92	1.412	17.86
			1230.62	3.101	19.69	1147.43	1.771	18.36	1120.68	1.421	17.93
			1284.43	4.013	20.55	1159.31	2.036	18.55	1125.07	1.589	18.00

Average Results for Ultra-Lean (Φ = 0.65) – CH_4/C_3H_8 Blend

% (vol.) of C_3H_8 in CH_4	LM(S)			LM(C)			NM(S)		
	S_u (mm/s)	L_b (mm)	U_L(cm/s)	S_u (mm/s)	L_b (mm)	U_L(cm/s)	S_u (mm/s)	L_b (mm)	U_L(cm/s)
0%	754.06	0.110	12.81	753.95	0.110	12.81	753.94	0.100	12.81
2%	873.46	0.390	14.8	871.72	0.360	14.77	871.3	0.350	14.76
4%	872.52	0.470	14.74	870.36	0.420	14.7	870.05	0.410	14.7
6%	900.78	0.650	15.18	896.39	0.560	15.11	895.54	0.530	15.09
8%	926.21	0.870	15.57	918.69	0.720	15.44	916.33	0.660	15.4
10%	943.75	1.050	15.83	932.74	0.830	15.64	928.77	0.760	15.58
15%	970.31	1.290	16.19	954.34	0.980	15.92	948.51	0.870	15.82
25%	1044.7	1.530	17.27	1021.6	1.110	16.88	1013.02	0.970	16.74
30%	1121.02	2.420	18.47	1068.2	1.520	17.6	1052.47	1.270	17.34
40%	1186.75	2.520	19.42	1127.34	1.560	18.45	1106.11	1.280	18.1
50%	1273.47	3.440	20.73	1173.48	1.880	19.1	1143.6	1.490	18.61
70%	1325.68	3.660	21.41	1209.96	1.930	19.54	1179.59	1.530	19.05
85%	1329.27	3.990	21.35	1210	2.100	19.44	1177.52	1.660	18.92
100%	1247.26	3.400	19.96	1150.15	1.860	18.41	1120.55	1.470	17.93

Average Results for Ultra-Lean (Φ = 0.65) – CH_4/C_2H_6 Blend

% (vol.) of C_2H_6 in CH_4	LM(S)			LM(C)			NM(S)		
	S_u (mm/s)	L_b (mm)	U_L(cm/s)	S_u (mm/s)	L_b (mm)	U_L(cm/s)	S_u (mm/s)	L_b (mm)	U_L(cm/s)
0%	754.06	0.110	12.81	753.95	0.110	12.81	753.94	0.100	12.81
2%	820.12	0.120	13.91	819.97	0.120	13.91	819.98	0.120	13.91
4%	829.76	0.320	14.06	828.71	0.300	14.04	828.23	0.290	14.03
6%	846.28	0.400	14.31	844.66	0.360	14.29	843.87	0.350	14.27
8%	858.2	0.450	14.49	856.15	0.400	14.46	855.21	0.390	14.44
10%	875.62	0.540	14.77	872.6	0.470	14.72	871.41	0.450	14.7
15%	901.9	0.610	15.16	898.09	0.530	15.1	896.44	0.500	15.07
25%	963.23	0.990	16.09	953.2	0.800	15.93	949.24	0.720	15.86
30%	966.22	0.930	16.11	959.83	0.800	16	955.69	0.730	15.93
40%	1017.69	1.250	16.88	1001.33	0.960	16.61	995.07	0.850	16.5
50%	1079.1	1.300	17.82	1060.96	0.990	17.52	1053.59	0.880	17.4
70%	1102.59	1.390	18.07	1082.45	1.040	17.74	1075.92	0.930	17.63
85%	1162.92	1.490	18.97	1138.51	1.100	18.58	1129.74	0.960	18.43
100%	1176.15	1.510	19.11	1150.61	1.100	18.7	1141.7	0.970	18.55

Average Results for Ultra-Lean (Φ = 0.65) – C_2H_6/C_3H_8 Blend

% (vol.) of C_2H_6 in C_3H_8	LM(S)			LM(C)			NM(S)		
	S_u (mm/s)	L_b (mm)	U_L(cm/s)	S_u (mm/s)	L_b (mm)	U_L(cm/s)	S_u (mm/s)	L_b (mm)	U_L(cm/s)
0%	1176.15	1.51	19.11	1150.61	1.1	18.7	1141.7	0.97	18.55
30%	1254.25	2.54	20.18	1168.15	1.57	18.79	1141.78	1.29	18.37
50%	1283.86	3	20.57	1201.99	1.74	19.26	1174.74	1.4	18.83
70%	1247.23	3.13	19.93	1184.91	1.78	18.93	1163.45	1.43	18.59
100%	1247.26	3.4	19.96	1150.15	1.86	18.41	1120.55	1.47	17.93

Individual Results: Ultra-Lean (Φ = 0.65) H_2/CH_4 Blend

% (vol.) of H_2 in CH_4	ρ_b/ρ_u	Aramco 1.3 U_L (cm/s)	LM(S)			LM(C)			NM(S)		
			S_u (mm/s)	L_b (mm)	U_L (cm/s)	S_u (mm/s)	L_b (mm)	U_L (cm/s)	S_u (mm/s)	L_b (mm)	U_L (cm/s)
0%	0.1699	14.13	749.68	0.137	12.74	749.51	0.133	12.74	749.57	0.132	12.74
			752.91	0.063	12.79	752.88	0.062	12.79	752.86	0.061	12.79
			759.6	0.136	12.91	759.47	0.121	12.91	759.39	0.119	12.90
10%	0.1708	14.91	783.1	-0.136	13.40	782.93	-0.14	13.40	782.94	-0.141	13.40
			859.53	-0.206	14.71	859.05	-0.217	14.70	858.96	-0.221	14.70
			847.87	-0.21	14.51	847.4	-0.221	14.50	847.46	-0.224	14.50
15%	0.1712	15.72	926.26	-0.25	15.85	925.52	-0.266	15.84	925.79	-0.268	15.85
			912.84	-0.417	15.62	910.66	-0.461	15.59	910.42	-0.478	15.58
			940.6	-0.469	16.10	937.73	-0.527	16.05	937.93	-0.543	16.05
25%	0.1717	16.87	934.18	-0.507	16.04	930.77	-0.576	15.98	929.47	-0.611	15.96
			1035.09	-0.542	17.77	1030.88	-0.62	17.70	1029.5	-0.658	17.68
			981.39	-0.434	16.85	978.8	-0.484	16.81	977.86	-0.508	16.79
30%	0.1717	17.81	1056.75	-0.457	18.15	1053.49	-0.513	18.09	1052.22	-0.542	18.07
			1043.96	-0.536	17.93	1039.31	-0.617	17.85	1037.08	-0.663	17.81
			1062.55	-0.54	18.25	1057.94	-0.621	18.17	1056.79	-0.656	18.15
40%	0.1724	19.83	1242.99	-0.61	21.43	1235.9	-0.716	21.31	1233.38	-0.769	21.27
			1221.66	-0.569	21.07	1216.09	-0.656	20.97	1214.33	-0.697	20.94
			1222.34	-0.591	21.08	1215.69	-0.691	20.96	1212.35	-0.749	20.91
50%	0.173	22.97	1412.63	-0.833	24.44	1407.02	-0.894	24.34	1401.84	-0.984	24.25
			1511.53	-0.624	26.15	1505.52	-0.716	26.05	1501.47	-0.765	25.98
			1469.87	-0.653	25.43	1465.5	-0.697	25.35	1457.19	-0.752	25.21

Individual Results: Ultra-Lean (Φ = 0.65) H_2/C_2H_6 Blend

% (vol.) of H_2 in C_2H_6	ρ_b/ρ_u	Aramco 1.3 U_L (cm/s)	LM(S)			LM(C)			NM(S)		
			S_u (mm/s)	L_b (mm)	U_L (cm/s)	S_u (mm/s)	L_b (mm)	U_L (cm/s)	S_u (mm/s)	L_b (mm)	U_L (cm/s)
0%	0.1625	20.01	1181.72	1.881	19.2	1144.79	1.291	18.6	1131.63	1.104	18.39
			1173.71	1.357	19.07	1153.06	1.025	18.74	1146.09	0.913	18.62
			1173.02	1.29	19.06	1153.98	0.985	18.75	1147.37	0.88	18.64
15%	0.1628	20.86	1196.02	1.102	19.47	1181.19	0.871	19.23	1175.63	0.787	19.14
			1211.02	1.182	19.72	1194.09	0.92	19.44	1187.27	0.824	19.33
			1175.54	1.033	19.14	1162.52	0.827	18.93	1156.43	0.735	18.83
30%	0.1639	21.56	1298.08	0.778	21.27	1289.47	0.655	21.13	1285.83	0.605	21.07
			1237.87	0.855	20.29	1227.96	0.708	20.12	1224.41	0.654	20.07
			1280.79	0.873	20.99	1270.23	0.721	20.82	1266.01	0.662	20.75
50%	0.1658	23.31	1347.97	0.374	22.35	1345.69	0.343	22.31	1344.68	0.329	22.29
			1421.06	0.226	23.56	1420.22	0.215	23.55	1419.75	0.209	23.54
			1444.28	0.215	23.95	1443.45	0.201	23.93	1443.04	0.199	23.92

Individual Results: Ultra-Lean (Φ = 0.65) H_2/C_3H_8 Blend

% (vol.) of H_2 in C_3H_8	ρ_b/ρ_u	Aramco 1.3 U_L (cm/s)	LM(S) S_u (mm/s)	LM(S) L_b (mm)	LM(S) U_L (cm/s)	LM(C) S_u (mm/s)	LM(C) L_b (mm)	LM(C) U_L (cm/s)	NM(S) S_u (mm/s)	NM(S) L_b (mm)	NM(S) U_L (cm/s)
0%	0.16	19.44	1226.74	3.097	19.63	1143.7	1.768	18.3	1115.92	1.412	17.86
			1230.62	3.101	19.69	1147.43	1.771	18.36	1120.68	1.421	17.93
			1284.43	4.013	20.55	1159.31	2.036	18.55	1125.07	1.589	18
15%	0.1601	20.32	1221.15	2.475	19.55	1178.32	1.55	18.86	1165.08	1.285	18.65
			1254.62	2.114	20.08	1205.64	1.404	19.3	1188.32	1.179	19.02
			1240.59	2.152	19.86	1186.56	1.421	19	1173.36	1.195	18.78
30%	0.1608	20.99	1252.33	2.02	20.14	1192.43	1.355	19.17	1172.66	1.16	18.86
			1232.83	2.171	19.82	1187.33	1.424	19.09	1170.22	1.197	18.82
			1214.37	2.02	19.53	1168.22	1.278	18.78	1151.6	1.086	18.52
50%	0.1624	22.6	1280.46	0.996	20.8	1267.28	0.804	20.58	1261.68	0.729	20.49
			1287.27	0.882	20.91	1276.61	0.728	20.74	1272.05	0.666	20.66
			1342.98	0.942	21.81	1330.61	0.769	21.61	1325.32	0.701	21.53

Average Results: Ultra-Lean (Φ = 0.65) H_2/CH_4 Blend

% (vol.) of H_2 in CH_4	LM(S)			LM(C)			NM(S)		
	S_u (mm/s)	L_b (mm)	U_L (cm/s)	S_u (mm/s)	L_b (mm)	U_L (cm/s)	S_u (mm/s)	L_b (mm)	U_L (cm/s)
0%	754.06	0.11	12.81	753.95	0.11	12.81	753.94	0.1	12.81
10%	830.17	-0.18	14.21	829.79	-0.19	14.2	829.78	-0.2	14.2
15%	926.57	-0.38	15.86	924.63	-0.42	15.83	924.71	-0.43	15.83
25%	983.55	-0.49	16.89	980.15	-0.56	16.83	978.94	-0.59	16.81
30%	1054.42	-0.51	18.11	1050.25	-0.58	18.03	1048.69	-0.62	18.01
40%	1229	-0.59	21.19	1222.56	-0.69	21.08	1220.02	-0.74	21.04
50%	1464.67	-0.7	25.34	1459.35	-0.77	25.25	1453.5	-0.83	25.15

Average Results: Ultra-Lean (Φ = 0.65) H_2/C_2H_6 Blend

% (vol.) of H_2 in CH_4	LM(S)			LM(C)			NM(S)		
	S_u (mm/s)	L_b (mm)	U_L (cm/s)	S_u (mm/s)	L_b (mm)	U_L (cm/s)	S_u (mm/s)	L_b (mm)	U_L (cm/s)
0%	1176.15	1.51	19.11	1150.61	1.1	18.7	1141.7	0.97	18.55
15%	1194.19	1.11	19.44	1179.27	0.87	19.2	1173.11	0.78	19.1
30%	1272.25	0.84	20.85	1262.55	0.69	20.69	1258.75	0.64	20.63
50%	1404.43	0.27	23.28	1403.12	0.25	23.26	1402.49	0.25	23.25

Average Results: Ultra-Lean (Φ = 0.65) H_2/C_3H_8 Blend

% (vol.) of H_2 in CH_4	LM(S)			LM(C)			NM(S)		
	S_u (mm/s)	L_b (mm)	U_L (cm/s)	S_u (mm/s)	L_b (mm)	U_L (cm/s)	S_u (mm/s)	L_b (mm)	U_L (cm/s)
0%	1247.26	3.4	19.96	1150.15	1.86	18.41	1120.55	1.47	17.93
15%	1238.78	2.25	19.83	1190.17	1.46	19.05	1175.58	1.22	18.82
30%	1233.18	2.07	19.83	1182.66	1.35	19.02	1164.83	1.15	18.73
50%	1303.57	0.94	21.17	1291.5	0.77	20.98	1286.35	0.70	20.89

Individual Results: NG 1 (68/17/15) – ($CH_4/C_3H_8/H_2$) vol.%

Φ	ρ_b/ρ_u	Aramco 1.3 U_L (cm/s)	LM(S) S_u (mm/s)	LM(S) L_b (mm)	LM(S) U_L (cm/s)	LM(C) S_u (mm/s)	LM(C) L_b (mm)	LM(C) U_L (cm/s)	NM(S) S_u (mm/s)	NM(S) L_b (mm)	NM(S) U_L (cm/s)
0.6	0.1755	13.36	802.02	0.939	14.08	794.43	0.764	13.94	791.56	0.699	13.89
			766.58	0.654	13.46	763.11	0.568	13.39	762.58	0.541	13.39
			849.21	0.685	14.91	844.66	0.587	14.83	842.71	0.546	14.79
0.7	0.1587	22.15	1387.06	0.589	22.01	1381.51	0.516	21.92	1379.15	0.485	21.89
			1424.37	0.489	22.6	1420.34	0.437	22.54	1418.55	0.414	22.51
			1338.28	0.5	21.24	1334.42	0.45	21.18	1332.77	0.42	21.15
0.8	0.1456	30.95	1972.05	0.535	28.72	1965.55	0.474	28.62	1962.82	0.448	28.58
			2054.77	0.585	29.92	2046.7	0.513	29.81	2043.5	0.483	29.76
			2012.42	0.655	29.31	2002.83	0.566	29.17	1998.72	0.529	29.11

Average Results: NG 1 (68/17/15) – ($CH_4/C_3H_8/H_2$) vol.%

Φ	LM(S) S_u (mm/s)	LM(S) L_b (mm)	LM(S) U_L (cm/s)	LM(C) S_u (mm/s)	LM(C) L_b (mm)	LM(C) U_L (cm/s)	NM(S) S_u (mm/s)	NM(S) L_b (mm)	NM(S) U_L (cm/s)
0.6	805.94	0.759	14.15	800.73	0.639	14.06	798.95	0.595	14.02
0.7	1383.23	0.525	21.95	1378.76	0.466	21.88	1376.82	0.441	21.85
0.8	2013.08	0.591	29.32	2005.02	0.517	29.2	2001.68	0.487	29.15

Individual Results: NG 2 (73.1/11.9/15) – ($CH_4/C_3H_8/H_2$) vol.%

Φ	ρ_b/ρ_u	Aramco 1.3 U_L (cm/s)	LM(S) S_u (mm/s)	LM(S) L_b (mm)	LM(S) U_L (cm/s)	LM(C) S_u (mm/s)	LM(C) L_b (mm)	LM(C) U_L (cm/s)	NM(S) S_u (mm/s)	NM(S) L_b (mm)	NM(S) U_L (cm/s)
0.6	0.1765	12.92	801.69	0.514	14.15	799.3	0.459	14.11	798.14	0.433	14.09
			846.59	0.262	14.95	845.89	0.247	14.93	845.56	0.24	14.93
			841.94	0.302	14.86	841.45	0.285	14.85	842.16	0.287	14.87
0.7	0.1596	21.74	1407.21	0.374	22.46	1404.85	0.343	22.43	1403.81	0.33	22.41
			1486.7	0.276	23.73	1485.33	0.259	23.71	1484.68	0.251	23.7
			1442.49	0.33	23.03	1440.92	0.3	23	1440.1	0.29	22.99
0.8	0.1467	30.38	2094.21	0.436	30.72	2089.42	0.394	30.65	2087.42	0.376	30.62
			2071.39	0.292	30.39	2069.34	0.274	30.36	2068.37	0.265	30.34
			2049	0.378	30.06	2045.76	0.346	30.01	2044.38	0.332	29.99

Average Results: NG 2 (73.1/11.9/15) – ($CH_4/C_3H_8/H_2$) vol.%

Φ	LM(S) S_u (mm/s)	LM(S) L_b (mm)	LM(S) U_L (cm/s)	LM(C) S_u (mm/s)	LM(C) L_b (mm)	LM(C) U_L (cm/s)	NM(S) S_u (mm/s)	NM(S) L_b (mm)	NM(S) U_L (cm/s)
0.6	830.07	0.359	14.65	828.88	0.33	14.63	828.62	0.32	14.63
0.7	1445.47	0.325	23.07	1443.7	0.301	23.05	1442.86	0.29	23.03
0.8	2071.53	0.369	30.39	2068.17	0.338	30.34	2066.72	0.325	30.32

Individual Results: NG 3 (76.5/8.5/15) – ($CH_4/C_3H_8/H_2$) vol.%

Φ	ρ_b/ρ_u	Aramco 1.3 U_L (cm/s)	LM(S) S_u (mm/s)	LM(S) L_b (mm)	LM(S) U_L (cm/s)	LM(C) S_u (mm/s)	LM(C) L_b (mm)	LM(C) U_L (cm/s)	NM(S) S_u (mm/s)	NM(S) L_b (mm)	NM(S) U_L (cm/s)
0.6	0.1773	12.57	736.89	0.156	13.06	736.67	0.151	13.06	736.58	0.148	13.06
			740.42	0.218	13.13	740	0.208	13.12	739.76	0.202	13.11
			756.42	0.201	13.41	756	0.192	13.4	755.76	0.189	13.4
0.7	0.1604	21.4	1337.72	0.246	21.45	1336.75	0.232	21.44	1336.24	0.226	21.43
			1218.41	0.298	19.54	1217.07	0.277	19.52	1216.45	0.268	19.51
			1376.97	0.24	22.08	1375.94	0.23	22.06	1375.43	0.22	22.06
0.8	0.1474	30.09	2122.43	0.419	31.28	2117.96	0.38	31.21	2115.98	0.363	31.18
			2200.82	0.365	32.43	1997.74	0.336	29.44	1996.28	0.322	29.42
			2121.28	0.304	31.26	2118.98	0.284	31.23	2118.25	0.276	31.22

Average Results: NG 3 (76.5/8.5/15) – ($CH_4/C_3H_8/H_2$) vol.%

Φ	LM(S) S_u (mm/s)	LM(S) L_b (mm)	LM(S) U_L (cm/s)	LM(C) S_u (mm/s)	LM(C) L_b (mm)	LM(C) U_L (cm/s)	NM(S) S_u (mm/s)	NM(S) L_b (mm)	NM(S) U_L (cm/s)
0.6	744.58	0.192	13.2	744.23	0.183	13.19	744.04	0.18	13.19
0.7	1311.04	0.261	21.02	1309.92	0.246	21.01	1309.37	0.238	21
0.8	2148.18	0.363	31.66	2078.23	0.333	30.63	2076.84	0.32	30.61

Individual Results: NG 4 (78.2/6.8/15) – ($CH_4/C_3H_8/H_2$) vol.%

Φ	ρ_b/ρ_u	Aramco 1.3 U_L (cm/s)	LM(S) S_u (mm/s)	LM(S) L_b (mm)	LM(S) U_L (cm/s)	LM(C) S_u (mm/s)	LM(C) L_b (mm)	LM(C) U_L (cm/s)	NM(S) S_u (mm/s)	NM(S) L_b (mm)	NM(S) U_L (cm/s)
0.6	0.1777	12.38	734.46	0.105	13.05	734.35	0.102	13.05	734.37	0.101	13.05
			725.81	0.011	12.9	725.83	0.012	12.9	725.89	0.012	12.9
0.7	0.1608	21.18	1358.82	0.185	21.85	1358.26	0.177	21.84	1357.94	0.173	21.84
			1410.91	0.127	22.69	1410.62	0.123	22.69	1410.53	0.122	22.68
			1383.1	0.31	22.24	1381.54	0.29	22.22	1380.68	0.28	22.2
0.8	0.1478	29.94	1943.33	0.418	28.72	1939.3	0.38	28.66	1937.57	0.363	28.63
			1929.72	0.344	28.51	1926.89	0.318	28.47	1925.67	0.306	28.45
			2018.2	0.353	29.82	2015.08	0.325	29.78	2013.61	0.312	29.75

Average Results: NG 4 (78.2/6.8/15) – ($CH_4/C_3H_8/H_2$) vol.%

Φ	LM(S) S_u (mm/s)	LM(S) L_b (mm)	LM(S) U_L (cm/s)	LM(C) S_u (mm/s)	LM(C) L_b (mm)	LM(C) U_L (cm/s)	NM(S) S_u (mm/s)	NM(S) L_b (mm)	NM(S) U_L (cm/s)
0.6	730.14	0.058	12.98	730.09	0.057	12.97	730.13	0.057	12.98
0.7	1384.28	0.208	22.26	1383.47	0.197	22.25	1383.05	0.191	22.24
0.8	1963.75	0.372	29.02	1960.43	0.341	28.97	1958.95	0.327	28.95

Individual Results: NG 5 (79.9/5.1/15) – ($CH_4/C_3H_8/H_2$) vol.%

Φ	ρ_b/ρ_u	Aramco 1.3 U_L (cm/s)	LM(S) S_u (mm/s)	LM(S) L_b (mm)	LM(S) U_L (cm/s)	LM(C) S_u (mm/s)	LM(C) L_b (mm)	LM(C) U_L (cm/s)	NM(S) S_u (mm/s)	NM(S) L_b (mm)	NM(S) U_L (cm/s)
0.6	0.1782	12.13	667.29	-0.036	11.89	667.3	-0.036	11.89	667.4	-0.034	11.89
			680.78	0.077	12.13	680.72	0.076	12.13	680.68	0.075	12.13
			724.32	-0.158	12.91	724.1	-0.164	12.9	724.14	-0.166	12.9
0.7	0.1613	20.97	1254.26	0.068	20.23	1254.21	0.067	20.23	1254.21	0.067	20.23
			1365.63	0.22	22.02	1364.85	0.209	22.01	1364.46	0.204	22
			1298.64	0.15	20.94	1298.26	0.15	20.94	1298.08	0.14	20.93
0.8	0.1482	29.73	1973.58	0.19	29.25	1973.39	0.188	29.24	1973.29	0.187	29.24
			2076.04	0.349	30.76	2072.99	0.322	30.72	2071.61	0.31	30.7
			1966.28	0.238	29.14	1964.87	0.225	29.12	1964.25	0.219	29.11

Average Results: NG 5 (79.9/5.1/15) – ($CH_4/C_3H_8/H_2$) vol.%

Φ	LM(S) S_u (mm/s)	LM(S) L_b (mm)	LM(S) U_L (cm/s)	LM(C) S_u (mm/s)	LM(C) L_b (mm)	LM(C) U_L (cm/s)	NM(S) S_u (mm/s)	NM(S) L_b (mm)	NM(S) U_L (cm/s)
0.6	690.8	-0.039	12.31	690.7	-0.041	12.31	690.74	-0.042	12.31
0.7	1306.18	0.147	21.06	1305.77	0.141	21.06	1305.58	0.138	21.05
0.8	2005.3	0.259	29.72	2003.75	0.245	29.69	2003.05	0.239	29.68